Cranfield University

Adrian James Clarke

The Conceptual Design of Novel Future UAV's Incorporating Advanced Technology Research Components

School of Engineering

Doctor of Philosophy (PhD) Thesis

Cranfield University

School of Engineering

Doctor of Philosophy (PhD) Thesis

2011

Adrian James Clarke

The Conceptual Design of Novel Future UAV's Incorporating Advanced Technology Research Components

Supervisor: Prof. J. P. Fielding

Academic Year 2010 to 2011

This thesis is submitted in partial fulfilment of the requirements for the degree of Doctor of Philosophy (PhD)

Abstract

There is at present some uncertainty as to what the roles and requirements of the next generation of UAVs might be and the configurations that might be adopted. The incorporation of technological features on these designs is also a significant driving force in their configuration, efficiency, performance abilities and operational requirements. The objective of this project is thus to provide some insight into what the next generation of technologies might be and what their impact would be on the rest of the aircraft.

This work involved the conceptual designs of two new relevant full-scale UAVs which were used to integrate a select number of these advanced technologies. The project was a CASE award which was linked to the Flaviir research programme for advanced UAV technologies. Thus, the technologies investigated during this study were selected with respect to the objectives of the Flaviir project. These were either relative to those already being developed as course of the Flaviir project or others from elsewhere. As course of this project, two technologies have been identified and evaluated which fit this criterion and show potential for use on future aircraft. Thus we have been able to make a contirubtion knowledge in two gaps in current aerospace technology.

The first of these studies was to investigate the feasibility of using a low cost mechanical thrust vectoring system as used on the X-31, to replace conventional control surfaces. This is an alternative to the fluidic thrust vectoring devices being proposed by the Flaviir project for this task. The second study is to investigate the use of fuel reformer based fuel cell system to supply power to an all-electric power train which will be a means of primary propulsion. A number of different fuels were investigated for such a system with methanol showing the greatest promise and has been shown to have a number of distinct advantages over the traditional fuel for fuel cells (hydrogen).

Each of these technologies was integrated onto the baseline conceptual design which was identified as that most suitable to each technology. A UCAV configuration was selected for the thrust vectoring system while a MALE configuration was selected for the fuel cell propulsion system. Each aircraft was a new design which was developed specifically for the needs of this project. Analysis of these baseline configurations with and without the technologies allowed an assessment to be made of the viability of these technologies.

The benefits of the thrust vectoring system were evaluated at take-off, cruise and landing. It showed no benefit at take-off and landing which was due to its location on the very aft of the airframe. At cruise, its performance and efficiency was shown to be comparable to that of a conventional configuration utilizing elevons and expected to be comparable to the fluidic devices developed by the Flaviir project. This system does however offer a number of benefits over many other nozzle configurations of improved stealth due to significant exhaust nozzle shielding.

The fuel reformer based fuel cell system was evaluated in both all-electric and hybrid configurations. In the ell-electric configuration, the conventional turboprop engine was completely replaced with an all-electric powertrain. This system was shown to have an inferior fuel consumption compared to a turboprop engine and thus the hybrid system was conceived. In this system, the fuel cell is only used at loiter with the turboprop engine being retained for all other flight phases. For the same quantity of fuel, a reduction in loiter time of 24% was experienced (compared to the baseline turboprop) but such a system does have benefits of reduced emissions and IR signature. With further refinement, it is possible that the performance and efficiency of such a system could be further improved.

In this project, two potential technologies were identified and thoroughly analysed. We are therefore able to say that the project objectives have been met and the project has proven worthwhile to the advancement of aerospace technology. Although these systems did not provide the desired results at this stage, they have shown the potential for improvement with further development.

Keywords:
Thrust vectoring, fuel cells, fuel processing, alternative fuels, aircraft performance

Acknowledgements

This thesis is dedicated to Frank Clarke. My great uncle, who worked in Woomera Australia as a designer of the Black Arrow Rocket and then worked on the subsequent missile projects. He has always been somebody to look up to and his work has been an inspiration for my own career.

The author would like to thank the following people for their continual help and support during my studies,

- Prof. Fielding (my supervisor) – For his continued support and advise, especially through the most difficult times.
- My family – For their love, support and patience.
- BAE Systems (Case Award sponsors) - For their financial support, without which this project would not have been possible.
- The 2007-2008 Flaviir Team – Especially, Craig Lawson, Robert Jones and Andrew Mills. It was a very interesting and rewarding year and I was proud to be a key part of the original team which turned the project around and tuned it in to an ultimate success.
- The library staff – Especially Tricia Fountain and Sharon Hinton for their warm welcome, help and for always being there when I really needed somebody to talk to. Additional thanks is also due for them always being kind enough to remove the continual bar on my library account (for never returning books on time).
- Thanks also goes out to a special group of people who helped me through the darkest times. Any time, day or night, they were always there to turn to and always willing to give up hours of their time to listen to others and offer their comfort and support. I am glad to be part of the group and am now pleased to be able play an active part in helping others in the same situation.

We are pressed on every side by troubles, but we are not crushed. We are perplexed, but not driven to despair. We are hunted down, but never abandoned by god. We get knocked down, but we are not destroyed. - 2 Corinthians 4:8

Fairy Tales are more than true; not because they tell us that dragons exist, but because they tell us that dragons can be beaten. - G. K. Chesterton

Table of Contents

Additional Table of Contents for the Appendices

Notation

1.1 Notation for baseline aircraft design studies

AR - Wing aspect ratio
b - Wing span
C_{DZ} - Zero lift drag coefficient
C_L - Lift coefficient
C_{Lp} - Rolling moment derivative
$C_{L\alpha}$ - Lift curve slope
C_m - Pitching moment coefficient
C_{m0} - Zero lift pitching moment coefficient
$C_{n\beta}$ - Yawing moment derivative
C_P - Propeller power coefficient
C_{Root} - Wing root chord
C_T - Propeller thrust coefficient
C_{Tip} - Wing tip chord
J - Propeller advance ratio
K - Lift induced drag coefficient
K_n - Static stability static margin
L/D - Lift to drag ratio
L_δ - Rolling moment control power coefficient
N - Load factor
nD - Propeller tip speed factor
N_ξ - Yawing control power coefficient
P_{Engine} - Engine design power output
S - Reference wing area
SP - Structural parameter
T_{Engine} - Engine design thrust
t/c - Wing thickness to chord ratio
T/W - Thrust loading
V - Aircraft velocity
V_{Stall} - Aircraft stalling speed
W_e - Aircraft empty weight
W_f - Fuel weight
W_0 - All-up aircraft mass
W/S - Wing loading
X_{AC} - Location of aerodynamic centre
α - Angle of attack

α_{0L} - Wing angle of zero lift
Γ - Wing dihedral
ε_t - Wing twist
$\Lambda_{1/4}$ - Quarter chord sweep angle
λ - Wing taper ratio
ϕ - Roll angle

1.2 Additional notation for performance analysis studies

a - Speed of sound
Alt - Altitude
AR - Aspect ratio
a_X - Acceleration in the x-direction
a_Z - Acceleration in the z-direction
c - Speed and altitude scaled specific fuel consumption
c' - Design specific fuel consumption
$\bar{c}$ - Mean aerodynamic chord of the wing
ΔC_{Di} - Increment in lift induced drag due to elevon deflection
$\Delta C_{Di(GE)}$ - Increment in lift induced drag due to the ground effect
ΔC_{DZ} - Increment in zero lift drag due to elevon deflection
$\Delta C_{DZ(Landing)}$ - Increment in zero lift drag of the aircraft in the landing configuration
$C_{L(Basic)}$ - Lift coefficient of an aircraft operating away from the ground
$\Delta C_{L(GE)}$ - Increment in lift coefficient due to the ground effect
$C_{L(incGE)}$ - Lift coefficient including the ground effect
$C_{L(\max)}$ - Maximum wing lift coefficient
C_{L0} - Lift coefficient at zero angle of attack
$C_{M(elevons)}$ - The pitching moment due to deflection of the elevons
$C_{M(HT)}$ - Moment due to the horizontal component of deflected thrust
$C_{m0(Krugers)}$ - Moment due to deflection of the kruger flaps
$C_{M(LW)}$ - Moment due to the lift of the wing
$C_{M0(wf)}$ - The zero lift pitching moment of the wing-fuselage
$C_{M(Total)}$ - Sum of moments acting about the aircraft centre of gravity
$C_{M(VT)}$ - Moment due to the vertical component of deflected thrust
$C_{m\alpha}$ - Pitching moment coefficient as a function of angle of attack
D - Drag force
F_R - Friction force
F_X - Resultant force in the x-direction
F_Z - Component of thrust acting in the z-direction
g - Acceleration due to gravity

H - Height
i_W - Incidence of the wing
K_{Basic} - Lift induced drag of an aircraft operating away from the ground
$K_{(incGE)}$ - Lift induced drag including the ground effect
L - Lift force
ΔL - Lift coefficient increment due to high lift devices
L_{Drag} - Component of drag acting in the z-direction
L_{Lift} - Component of aerodynamic lift acting in the z-direction
L_{NJ} - Resultant thrust from the nose jet
$L_{NJ(@M0.2)}$ - Resultant thrust from the nose jet at Mach 0.2
$L_{NoseJet}$ - Component of thrust from the nose jet acting in the z-direction
L_{Thrust} - Component of deflected thrust acting in the z-direction
L_{Total} - Total lift acting on the aircraft
m_{AC} - Aircraft mass
q - Dynamic pressure
Q_f - Mass flow rate of fuel per unit time
R - Resultant force, bypass ratio
$R_{Main-gear}$ - Reaction force acting on the main gear, similar for the nose gear
$Scale_{NJ-Mach}$ - Nose jet thrust scale factor for Mach number effects
SFC - Specific fuel consumption at off-design thrust conditions
$SFC_{M0.2}$ - Take-off specific fuel consumption at Mach 0.2
$SFC_{M-Scale}$ - Take-off SFC scale factor for Mach number effects
SFC_{TO} - Specific fuel consumption at take-off
S_G - Ground run distance
t - Time
T - Thrust
$\%T$ - Throttle setting
$T_{Available}$ - Available thrust for climb
T_{Drag} - Component of drag acting in the x-direction
$T_{Engine-X}$ - Component of deflected thrust acting in the x-direction
$T_{Engine(Vectored)}$ - Vectored engine thrust
T_{Lift} - Component of deflected thrust acting in the z-direction
T_{Max} - Design thrust
$T_{M0.2}$ - Available take-off thrust at Mach 0.2
$T_{M-Scale}$ - Thrust scale factor for Mach number effects
$T_{NoseJet}$ - Component of thrust from the nose jet acting in the x-direction
T_{TO} - Available take-off thrust
$Temp$ - Temperature of surrounding air

T_X - Component of deflected thrust acting in the x-direction
T_Z - Component of deflected thrust acting in the z-direction
V_1 - Take-off decision speed
$V_{Approach}$ - Landing approach speed
V_{LOF} - Take-off lift off speed
V_{Final} - Touchdown speed
V_R - Take-off rotation speed
V_X - Velocity component in the x-direction
V_Z - Velocity component in the z-direction
$V_{Z(0)}$ - Initial vertical descent velocity
W - Weight
X_{ACW} - Location of the aerodynamic centre of the wing
X_{CG} - Location of the aircraft centre of gravity from the aircraft reference point
$X_{Inertia}$ - Inertia acting in the x-direction
X_{MAC} - Location of the mean aerodynamic chord of the wing from the aircraft ref. point
$Z_{Inertia}$ - Inertia acting in the z-direction
β - Flight path angle
δ_f - Elevon deflection
γ - Flight path angle
μ_B - Friction coefficient due to the application of the aircraft brakes
μ_R - Friction coefficient
ρ - Density
σ - Density ratio
τ - Thrust scaling factor
ϕ - Engine plume deflection angle

1.3 Additional notation for thrust vectoring analysis studies

A_C - Inlet capture area
C_A - Nozzle angularity coefficient
C_D - Nozzle discharge coefficient
C_{fg} - The nozzle thrust loss factor
C_V - Nozzle velocity coefficient
dA - The deflection angle of the thrust vectoring vanes
D_{Inlet} - Inlet drag
D_{Nozzle} - Nozzle drag
dR - The deflection of the exhaust jet plume
e_n - Nozzle polytropic efficiency
K_{Total} - Coefficient for total losses in the nose jet system

$\dot{m}_0$ - Engine mass flow rate
$\dot{m}_8$ - Mass flow rate of exhaust gases through the nozzle throat
$\dot{m}_{Bleed}$ - Mass flow rate of engine bleed
$\dot{m}_{Cooling}$ - Mass flow rate of engine cooling air
$\dot{m}_{Engine}$ - Engine mass flow rate
$\dot{m}_{Inlet}$ - Total inlet mass flow rate NPR - The nozzle pressure ratio
P_t - Total pressure
P_{t8} – Total pressure of the exhaust gases at the nozzle throat
SF - Engine sizing scale factor
SF_{Thrust} - Engine thrust scale factor for Mach number effects
SF_{TSFC} - Thrust specific fuel consumption scale factor for Mach number effects
T_{t4} - Turbine entry temperature
T_{t8} – Total temperature of the exhaust gases at the nozzle throat
TR - Throttle ratio
$TSFC$ - Thrust specific fuel consumption
α - Engine bypass ratio
γ_{6A} - Ratio of specific heats of the gases at the nozzle entry (mixer exit)
ε - Engine cooling air requirements
η_{Nozzle} - Nozzle efficiency
π_C - Compressor pressure ratio
$\pi_{Component}$ - Component total pressure ratio
π_f - Fan pressure ratio
ϕ_{Inlet} - Inlet installation loss factors
ϕ_{Nozzle} - Nozzle installation loss factors

1.4 Additional notation for fuel cell system studies

A - Area
AR_{Matrix} - Aspect ratio of heat exchanger matrix
C - Sutherland's constant, equation constant
C_P - Specific heat at constant pressure
$\overline{C_P}$ - Specific heat at constant pressure on a molar basis
C_{Rate} - Heat exchanger capacity rate
$\overline{C_V}$ - Specific heat at constant volume on a molar basis
D - Diameter, depth
E – Potential
f - Friction factor, fuel flow rate on a molar basis
F - Shape factor (taken as 1), faraday constant, fuel cell power output
g - Acceleration due to gravity (9.81 m/s^2)
G - Mass velocity, gibbs free energy of formation

H - Geopotential altitude, enthalpy, higher heating value
h - Convection coefficient, height
h_{fg} - Heat of evaporation
h_{HHV} - Higher heating value
i - Current density
I - Current
k - Ratio of specific heats, thermal conductivity
K - Loss factor
L - Length, temperature gradient
LPM - Litres per minute
$\dot{m}$ - Mass flow rate
m - Mass
m_0 - Mean molecular mass
m,n,p – Number of moles of each element
M – Molecular mass, mass
N - Number of.
NTU - NTU number
n - Number of cells in a fuel cell stack
nu - Viscosity
Nu - Nusselt number
P - Pressure, power output, perimeter
Pr - Prandtl number
Q - Volumetric flow rate, heat output/input
r - Gas concentration
R - Gas constant
Ra - Rayleigh number
R_{Con} - Convective thermal resistance
Re - Reynolds number
r_H - Hydraulic radius
R_{Rdv} - Radiative thermal resistance
R_{Th} - Combined thermal resistance
R_u - Universal gas constant
S - Stoichiometric ratio, separation
$SLPM$ - Standard litres per minute
T - Temperature
t - Temperature, thickness
u - Velocity
U_{Air} - Overall heat transfer coefficient
V - Voltage, velocity, volume
V_0 - Freestream velocity
w - Width
W - Width, work output/input
χ - Quantity of oxygen to attain desired reforming reaction
X - Fraction of water recovered

X_{HT} - Heat exchanger heat transfer relation
y - Molar fraction
α - Ratio of free flow area to frontal area, thermal diffusitivity
β - Gas concentration, thermal expansion coefficient
β_{Fin} - Fin area ratio
γ - Ratio of specific heats
ε - Equivalence ratio for autothermal reforming, heat transfer epsilon factor
η - Efficiency
μ - Dynamic viscosity
ν - Kinematic viscosity
ρ - Density
σ - Stefan-Boltzman constant (5.67E-8 $Wm^{-2}K^{-4}$)
ϕ - Relative humidity
ω - Humidity ratio

1 Introduction

1.1 Project objectives

This project was a CASE award which was partly funded by the EPSRC and BAE Systems and linked to the Flaviir project. The project definition laid down at the start of the project was: 'To perform a number of new conceptual designs of relevant full-scale UAVs which will each integrate a number of advanced technologies, selected from either those which are currently being developed within the FLAVIIR research programme or others from elsewhere'.

The Flaviir project is a £6.5M BAE Systems/EPSRC funded research project whose aim is to investigate technologies which could possibly be used for the next generation of UAVs. Those being investigated range from low cost manufacturing methods, "flapless" controls, novel control algorithms to prediction methods to enhance the design cycle. 11 universities are involved in the research effort with Cranfield being responsible for the design and development of an advanced demonstrator UAV. This demonstrator is used to integrate and evaluate in-flight the technology components developed by the partner universities. In particular, this is used to test fluidic thrust vectoring and circulation control systems for flapless pitch and roll control respectively.

At present there is little published work being carried out to investigate what the next generation of UAVs might look like, the roles they might be able to perform and the additional markets (civil and military) that they could be expected to fill. This area has therefore been identified as a technology gap, which was the foundation of this research project. Work in this area will not only contribute to the evolution of the next generation of unmanned air vehicles but may also increase the future potential for the work of the FLAVIIR programme. Throughout the course of this project, the complexity, cost and time to develop viable solutions incorporating a number of these technologies was explored. This led to an assessment of the viability of these technologies.

The current range of UAV designs and the design methodologies used to create them can be restrictive in the sense that they are biased towards conventional configurations and the integration of existing technology. When these traditional procedures are applied to the design of novel UAV configurations utilising advanced concepts, there are concerns that the optimal solution could be either dismissed or overlooked. There is also an increasing risk that current design practices could even deem a good concept either non-viable or not cost-effective. Throughout the course of the project, new UAV designs were developed which were purposely designed around a number of the newly emerging technologies. As this will use new concepts, rather than the adaptation of existing designs, this will give a more realistic perspective of the viability of these technologies.

1.2 Work on the Flaviir project

During the course of these studies as well as working on this PhD, the author also had the opportunity to become involved in the development of the flying demonstrator for the industry-based Flaviir research programme. This work was not only an opportunity for the author to gain valuable industrial experience but to also gather insight which will contribute to the development of new UAV designs incorporating these technologies. The roles held by the author on the Flaviir project are,

- 10/2007-10/2008 (Full-time) Lead Structural Designer. Work involved extensive design work and close liaison with others to progress the demonstrator UAV from a conceptual design through the preliminary design, detail design and airframe manufacturing phases. In particular this has involved the design of external shell panels, main structure detail, patterns for mould tools, payload bay structure, nose and main landing gears and attachments, engine and APU installation and cowlings, intakes and mountings, wing tips, trailing edge devices and mountings, component positioning, pipe work and wiring routing, fuel tank sizing and integration., fuel tank supporting structure, centre of gravity and weight estimation.
- 10/2005-10/2007 (Part-time) Design/Systems Integration Engineer and CAD Manager. Work involved investigating possible system configurations and their layout within the airframe.

This project was an excellent opportunity for the author to put into practice many skills within a real world environment as well as work alongside other engineers and learn many new skills. This also gave a good context for the work carried out for this PhD.

1.3 Summary of work

This work was carried out over four phases. This project began by investigating the current UAV market as well as typical aircraft design flight profiles and specifications. Past and current aircraft design methodologies were then researched and an optimisation tool developed for the design and evaluation of future designs. This work enabled areas to be identified in the design process where it may prove to be inefficient and need to be adapted in order to be able to cater for new technologies and unconventional aircraft. The first phase of this project concluded with the design and analysis of a baseline MALE and UCAV UAV which will be used to integrate new technologies.

The second phase of the project involved a broad literature search for possible technologies, which generated a list of over 100 candidate technologies. This list was down-selected to just two by marking each technology against selection criteria which were chosen in accordance with the initial project goals and requirements. Low-cost mechanical thrust vectoring and fuel cell propulsion were selected as candidate technologies by means of this process. The third and fourth phases of the project commenced with an extensive literature review of each of the technologies. In the case of mechanical thrust vectoring, this has encompassed a survey of the different forms of mechanical and fluidic thrust vectoring. Whilst the fuel cell study has covered the review of fuel cell systems, alternative fuels and fuel reformers.

Each of these technologies were then sized and integrated on the corresponding baseline UAV designs. This was followed by an analysis of the performance of each of the

modified UAV designs which could then be compared to the performance of the baseline configuration. The work finally concluded with a review of the integration issues encountered and a study of the benefits and drawbacks of these new technologies. Suggestions were then made as to the applicability and benefits of these technologies to other UAV types within both the civil and military markets.

In conjunction with the research work, significant time was invested gathering the skills and tools required in order to able to fulfil the objectives of this project. As an example of this, the integration of the thrust vectoring system on the UCAV required detailed knowledge of engine operating characteristics. This necessitated the need to build the skills and knowledge required in order to be able to perform the conceptual design a turbofan engine which is sufficient to provide the required data. This PhD has therefore not only given the author the opportunity to make significant contribution to knowledge but also the opportunity to develop and put into practice the skills and understanding needed to be an aircraft designer.

1.4 Thesis structure

This section gives an overview of the structure of the thesis and how this relates to the work carried out in the different phases of the project. Chapters 2 and 3 cover Phase 1 of the project. Specifically, Chapter 2 gives an outline of the initial literature review which covers aircraft design methodologies and the selection of a baseline UAV configuration from a review of existing UAVs. Chapter 3 then discusses the design of the 2 baseline UAV configurations which is based on design requirements from similar existing designs. Phase 2 of the work is described in Chapter 4 which covers the selection of 2 technologies from an extensive literature review of potential technologies. .

Phase 3 of the project which involved the study of the thrust vectoring system, commenced with an extensive literature review given in Chapters 5 and 6. An overview of the sizing and integration of this system on the UCAV is then given in Chapters 7 and 8. The detailed calculations for this are given in Appendices B and C which covers the conceptual design of an engine and the rescaling of thrust vectoring nozzle test data to suit. This phase concludes with a performance analysis of the modified aircraft which is described in Chapter 16, the methodology for which is given in Appendix D.

Phase 4 of the project involved a study of the use of fuel cells as a primary propulsion source. This commenced with a review of fuel cell systems and fuel processors as given in Chapters 9, 10, 12 and 13, which was carried out in conjunction with a review of alternative fuels as given in Chapter 11. An overview of the sizing and integration of this system on the MALE is then given in Chapters 14 and 15. The detailed calculations for which are given in Appendices E through to I. Appendix E derives the fuel cell requirements and gives and overview of the fuel cell and fuel processor systems. Appendix H gives the methodology used to design and analyses the system while Appendix I works through the process used to size some of the ancillary equipment. Appendices F and G cover the derivation of the equations used in the analysis and are included purely for reference. This project phase concludes with a performance analysis of the modified aircraft which is described in Chapter 16, the methodology for which is given in Appendix J.

2 Initial literature review

2.1 A review of aircraft design methodologies

The aim of this research study was to summarise the different aircraft design methods proposed in the literature and their applicability to the design of UAVs. The actual process followed to design an aircraft will be specific to the type of aircraft and will also vary from one company to another, as well as from one designer to another. There are therefore many different aircraft design approaches and it has been necessary to limit this study to those found in the main texts on the subject. This encompassed those methods proposed by Howe [1], Jenkinson [2], Raymer [3], Stinton [4], Loftin [5], Roskam [6-13] and Torenbeek [14].

2.1.1 An overview of the aircraft design process

The design process begins with a customer or executive design brief which is a brief statement of what is needed and an invitation for proposals. The next stage is the initial project study phase which involves a review of the current market and similar aircraft to enable a design specification and flight profile to be drawn up. At this stage, an assessment is also made of emerging technologies which could be incorporated on the design.

The project will then enter the conceptual design phase where a variety of design solutions are brainstormed and a small number of the most viable solutions are down-selected. At this stage, the designer is working with basic estimation methods based on statistical data. These do not offer results of great detail but are sufficient to be able to make first pass estimates of the size, mass, performance and layout of the configurations. At this stage in the process, an assessment is being made of the feasibility of a number of configurations and it is important that to keep the analyses as simple as possible so that costs and time invested are kept to a minimum. The configurations are therefore simplistic with components being represented by points, lines and boxes. The results from this phase enable the final configuration to be down-selected from a trade-off of the different designs. At this point, the project will be subject to a review to ensure its viability and protect any financial investment.

The most promising design will then enter the initial preliminary design phase, during which more detail will be added to the design. The design will also be subjected to more detailed and time consuming analysis methods for aerodynamics, stability, mass and performance. At this stage, consideration is also given to the layout of the structure and the size and location of the systems. The external profile of the aircraft will at this point be frozen following the completion of design review. Other design teams will now be becoming more involved in the design process. The structures team will be deriving the airframe loads and estimating the size of the structural members while the aerodynamics team will be carrying out detailed CFD and wind tunnel testing.

The final design stage is the detail design phase where the structural components evolve from blocks to fully detailed assemblies which are stressed and tested. The systems team will source the components and sub-systems, design the circuits and test the systems on an iron bird test rig. The flight dynamics team will build a flight simulator model to test the flight characteristics of the aircraft using aerodynamic and stability coefficients derived by the aerodynamics team.

The design will finally enter the manufacturing phase where a prototype will be manufactured often by very manual processes. This test vehicle is used for a phase of full-scale testing which will test the flight characteristics and structural strength of the aircraft. This may be followed by a phase of evaluation and design revision in which any critical parts will be redesigned, pilot opinion ratings collated and aerodynamic fixes added where necessary. Successful completion of the prototype testing will ultimately lead to the aircraft being certified by the necessary body, its mass production and its entry to service. As the design progresses through the different stages above, more and more specialised departments join the project and the amount of financial injection required increases as a result. From the discussion above, it is clear to see how the success of the project is pinned on the work of the conceptual design team and therefore the following section will take a closer look at this crucial design stage.

2.1.2 A closer look at the conceptual design phase

Any new aircraft design commences with the conceptual design phase which develops the lines and size of an aircraft from a blank sheet of paper. This process begins with sketches of possible design configurations which the designer believes that the final aircraft form may follow. At this point in the design process, the designer is working from their experience and a review of existing aircraft designed to meet a similar role. The most promising of these designs are selected by means of an initial design review and then further analysed by the conceptual design analysis process. This process enables the feasibility of each design to be assessed and therefore enables a selection of the final configuration to be made.

During the conceptual design phase, statistical estimations are used to size a design and predict how it might perform in its final form. A process known as parametric analysis enables the design parameters to be varied to determine the range of parameters which are able to meet the specified performance constraints. This process ensures that the design is able to meet all the performance criteria early on in the process, which can reduce the design man hours required. Where time is critical, such an analysis can utilise non-dimensionalised parameters and charts but where greater accuracy is required calculations based on detailed flight performance derivations can be used.

Within these performance boundaries, the baseline as-drawn design can then be optimised in terms of its mass, cost or some other parameter. Having decided upon what appears to be a feasible solution, the design will then be further analysed with more detailed methods to make a better prediction of its mass, performance and stability. It may be necessary to return to an earlier stage in the design to modify the configuration if the design proves inadequate in these later stages. Where more than one design has been analysed in parallel, at this point a selection of the final design can be made.

2.1.3 The aircraft design process applicable to UAV's

As already mentioned the aircraft design process will differ according to the class of aircraft as well as differing from company to company and designer to designer. For example, the payload provision and design mission will be specific to the aircraft and each design will also have a different design focal point. In the case of a civil airliner, the design focal point is likely to be to carry as much cargo and as many people as you can as fastly and as cheaply as you can over as long a range as is possible. A military aircraft might instead focus on being able to move as quickly as it can with the smallest possible Radar Cross-Section and its economy moves further down the list of design priorities. The methodology presented above is not definitive but is an example of what a designer's typical design process might consist of and could easily be debated.

The design process for a UAV is expected to be in some ways similar to that used for a manned aircraft. Since there are no life forms aboard the aircraft, the following differences are expected.

- No cockpit or cabin is required.
- A smaller environmental control system can be used, whose purpose is to maintain a reasonable operating environment for the avionics.
- Significant more flexibility is available in the design of the aircraft since it no longer has to accommodate a large cabin or cockpit. Smaller and slender configurations can be used as a result with better aerodynamic characteristics.
- In some cases, the aircraft may be able to be designed for a shorter service life since they may be used for shorter periods. In such cases, the airframe will be subjected to less flight hours and therefore fatigue may be less of an issue. Military units may be packed away in crates during peace time.
- Safety and redundancy constraints may also be less of an issue since there are no souls on board. The concern to protect an expensive aircraft, people on the ground and valuable on-board equipment is still an issue though.

2.2 Review of existing UAVs and down-selection of the baseline configurations

A review of existing UAVs involved a stage of information gathering and familiarisation with the current UAV market. The UAVs collated where then categorised according to their size and intended mission. This gave an opportunity to narrow down the vast UAV market, to be able to identify the UAVs that are of most relevance to this particular project. Two distinct categories were felt to be most applicable to this project as well as being of interest to current UAV customers and developers. The first is those covered those under the title UCAV (Unmanned Combat Air Vehicle), such as the X-45 family (A, B and C variants), X-47 family (A and B variants) and the EADS Barracuda. The second category is those under the title MALE (Medium Altitude Long Endurance) such as the Predator family (RQ-1, MQ-1 and B), Hermes 1500, Heron, Hunter and BAE Herti. Since information on these existing UAVs is readily available elsewhere, data for these will not be included here.

3 Baseline UAV design

Thesis size limitations necessitate that the description of the design process followed for the baseline configurations is kept as brief as possible. This section will therefore be kept as concise as possible with a very brief outline of the processes followed and only the most important results included. Where possible references for the methods used will be included to enable the reader to follow the methodology used if they so wish. The layout of this section follows the same course as that used to design aircraft. It progresses from the initial sizing of the aircraft through to the more detailed methods.

3.1 Design requirements and design flight profiles

Before any air vehicle can be designed, design requirements and a design flight profile are required. The design flight profile is an idealic representation of a typical mission which the aircraft would be required to complete while the design requirements are used to specify other parameters such as field length. These are a critical part of the design process and are used to specify the required operating characteristics and can therefore dictate the eventual commercial success of the aircraft in relation to its competetors. These are normally specified by either the customer or the companies executives. In the case of this project a small selection of vehicles were identified upon which the new design will be based. The specifications of these not only give an indication of the size of this design but can also be used to define typical design requirements and design flight profiles. These will be presented in the following sections.

3.1.1 UCAV design requirements

The design objective for the UCAV was to deliver a lethal payload of 2x GBU-31 JDAM bombs of a weight of 2000lb each to a target. Design flight profiles of simular existing UCAV designs were not available in the public domain and one from the Cranfield U-99 TUAV [15] group design project had to be used instead. Although two flight profiles had been defined for the U-99 project, its primary flight profile was sufficient for the needs of this project. The design cruise speed was however increased to M0.9 for the purposes of this project. Although a weapons release is dictated in the mission profile, it was decided not to incorporate this in the aircraft design work. The rationale for this is that it may be necessary to bring the expensive and deadly weapons home if the target cannot be identified.

UCAV design flight profile and design requirements

(Modified version of the Cranfield U-99 TUAV requirements)

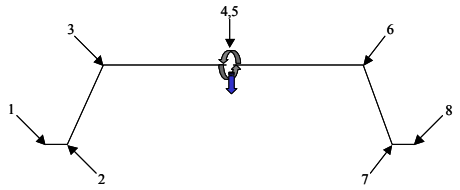

High Altitude Deep Penetration (Primary Mission)

Mission Segment	Description	Altitude (ft)	Speed (Mach)	Distance (nm)
1 - 2	Engine start, Taxi and Take-off			
2 - 3	Climb and Accelerate	≈0 to 40,000	≈0 to ≥0.7 (0.8 Typical)	
3 - 4	Cruise segment 1 (outbound leg)	40,000	≥0.7 (0.8 Typical)	≥750
4 - 5	Weapon release (454kg)	(at appropriate altitude and speed with 1.5 turns)		
5 - 6	Cruise segment 2 (inbound leg)	40,000	≥0.7 (0.8 Typical)	≥750
6 - 7	Descent	40,000 to ≈0	≥0.7 (0.8 Typical) to ≈0	
7 - 8	Landing, Taxi and shutdown			
(6% fuel remaining (includes useable fuel) at point 8)				

Design requirements

- Payload = 4000lb
- Mission radius = ≥ 750nm
- Field performance (take-off and landing) = ≤ 3500ft
- Cruise speed = ≤ M0.9
- Cruise altitude = 40,000ft
- Design max. Mach no. (M_D) = 0.95
- Limit manoeuvre factors at combat mass = +7.5 and –3
- Airframe life = 500hrs

Figure 3-1

3.1.2 MALE design requirements

In the case of the MALE UAV, there was fortunatly a design flight profile available in the public domain for the simular existing MQ-9B Predator B UAV which was sufficent for the needs of this project.

MALE UAV design flight profile and design requirements

(Modified version of the MQ-9B Predator B requirements)

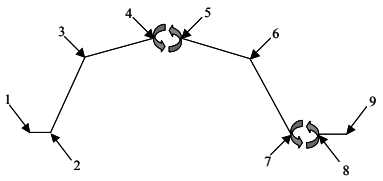

Predator (Tier II) Mission Profile

Mission Segment	Description	Altitude (ft)	Speed (Mach)	Distance
1 - 2	Engine start, Taxi and Take-off	0 to 50		2650ft
2 - 3	Climb	50 to 15,000		60nm max.
3 - 4	Cruise Climb Ingress	15,000 to 25,000		500nm
4 - 5	Loiter	25,000		24 hour
5 - 6	Egress	25,000 to 15,000		500nm
6 - 7	Descent	15,000 to S.L.		60nm max.
7 - 8	Reserve Loiter	Sea Level		1 hour
8 - 9	Landing, Taxi and Shutdown	Sea Level		2650ft

Design requirements

- Internal payload = 800lb
- External payload = 3,000lb
- Endurance (clean) = 35 hrs
- Max level speed = 240kt
- Cruising speed = 210kt
- Max rate of climb at S.L. = 2,500ft/min
- Max operating altitude = 51,000ft
- Max range = 6,622nm
- Field performance (take-off and landing) = ≤ 5000ft (1524m)
- Limit load factors (as for GA Utility Aircraft) = +4.4 to -1.8

Figure 3-2

3.2 The conceptual design of the baseline configurations

At the conceptual design stage we are using statistical sizing relations to explore a number of different design concepts before we make our final selection. The parametric analysis carried out as part of this work not only verifies that the design is able to meet our performance requirements but also gives us a insight into the optimal size of the wing and engine to meet our needs. This ensures that the design is able to meet all of the performance constraints and neither the wing nor engine is unnecessarily oversized with

the optimal being one which is just able to meet the most prominent performance constraints.

This work necessitated the need for an optimisation tool which would enable optimal design choices to be made within our performance constraints. In the absence of such a ready made tool, a 25 point spreadsheet based optimisation tool was developed specifically for this task by the author. The parametric analysis part of the tool is able to analyse the performance of an aircraft for a range of values of wing loading (weight/wing area) and thrust loading (thrust/weight) and then express the results graphically so the boundaries of the solution space can be clearly identified. The optimisation part then allows the optimal size of each component to be determined at this design point. This enables a range of wing design values such as aspect ratio and thickness/chord ratio to be explored to determine the configuration with minimal mass. Such a process is a complex trade-off between structural weight and the mission fuel requirements via the drag of the configuration. An additional capability of the tool is its ability to perform sensitivity studies of the T/W and W/S parameters by imposing lines of constant mass on the parametric output chart. The differences in the designs meant that the tool had to be specifically tailored towards the design of the UCAV and MALE respectively. In each case, a variety of aircraft design relations were used from Howe [1], Mattingly [16] and Raymer [3].

3.2.1 The conceptual design of the UCAV

The design brief for the UCAV was to design a stealthy configuration which is able to efficiently deliver a lethal payload over a long range. The final UCAV design was based on a true delta planform with a straight wing trailing edge. Such a configuration may not have normally been regarded as being stealthy, but developments in this area have seen the introduction of designs such as the Eurofighter with such a wing planform. As the aircraft is only required to operate at transonic speed, aerodynamic requirements would dictate only a small amount of sweep but in this example, it is dictated by centre of gravity requirements instead. A particular feature of a true delta is that wing sweep can be shown to be related to the aspect ratio, whereby a reduction in aspect ratio will result in an increase in wing sweep. This not only has the desired effect of shifting the wing fuel tanks and therefore the aircraft centre of gravity aft but also shifts the aerodynamic centre of the wing aft although at a lesser rate. By modelling a number of different configurations of different aspect ratio a relationship between aspect ratio and centre of gravity was determined. In conjunction with a relationship for the aerodynamic centre of the wing as a function of wing sweep, the solution for neutral stability (when the two parameters coincide) can be determined. This gave an aspect ratio of 2.54 and quarter chord wing sweep of 44º. A taper ratio of 0.1 was selected to retain good stall characteristics while keeping the shape of the delta.

The resulting parametric chart for this configuration is presented below, from which the optimal configuration can be seen to lie within the boundaries of the landing and specific excess power constraints. This results in the solution W/S = 1588.6, T/W = 0.62 and W_0 = 8650.5kg. Other specifications are, t/c = 0.12, W_e = 4523.5kg, W_f = 2312.6kg, S = 53.42m^2, b = 11.65m, C_{Root} = 8.34m, L/D_{Max} = 11.0, T_{Engine} = 52.73kN.

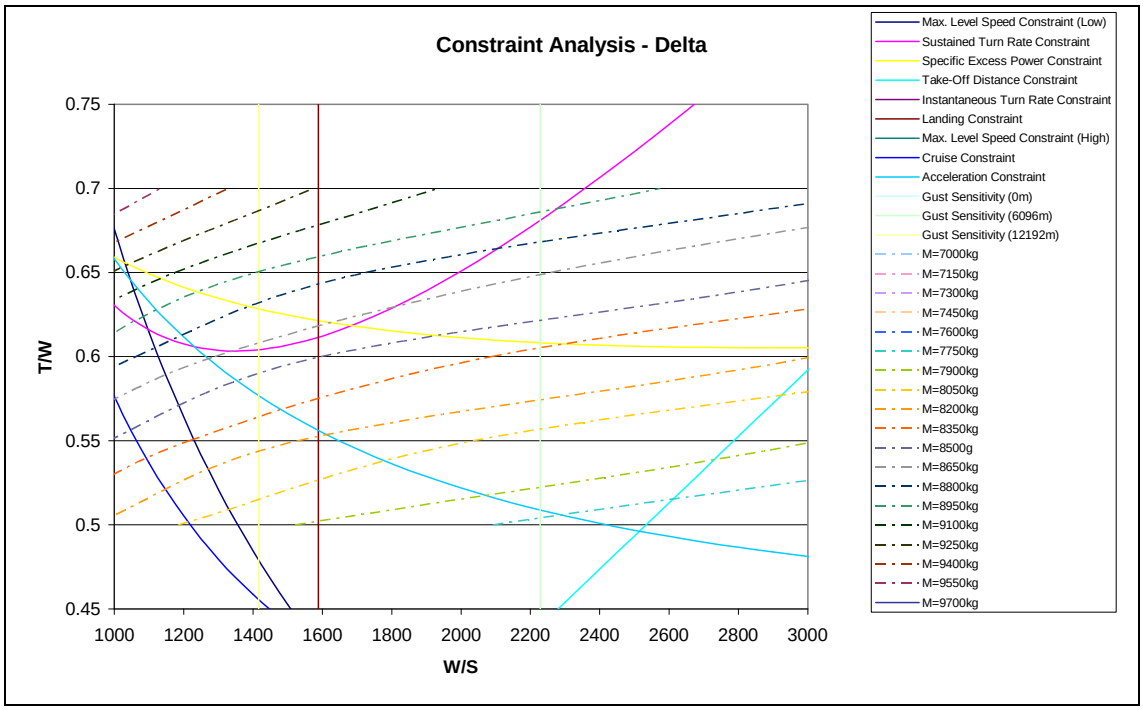

Chart 3-1

3.2.2 The conceptual design of the MALE

The design brief for the MALE was, to design a configuration which is able to efficiently loiter for long periods at medium altitudes. It should also have sufficient operational flexibility and be capable of delivering a lethal payload as required. The optimiser tool highlighted the potential of using a wing with the highest aspect ratio possible as used on sailplane. Within the methodology, an additional constraint known as the structural parameter had to be incorporated to take into account the structural limitations of such wing designs. This parameter is used to restrict the maximum aspect ratio to a realistic value with respect to our wing thickness from the relation below.

$$AR = \frac{\left(SP \cdot Cos\Lambda_{C/4}\right)^{1.6}}{N^{0.8}} \cdot \left(\frac{t}{c}\right)^{0.4} \qquad \text{Eq 3-1}$$

The value of the structural parameter for this study was estimated as 24.5 from similar existing designs such as the Predator B. When combined with a t/c figure of 17% from the optimiser, this gave a maximum realistic wing aspect ratio of 16.83. Wing sweep was not required for this low speed design but it was deemed good practice to incorporate a straight rear spar and thus a straight trailing edge device hinge line. The remaining unknown was the wing taper ratio which was assumed a value of 0.45 to correspond to the equivalent elliptical planform of a wing with zero sweep.

The resulting parametric chart for this configuration is presented below, from which the optimal configuration can be seen to lie within the boundaries of the high altitude maximum lift coefficient (C_L = 0.8) and high altitude cruise power constraints. This results in the solution W/S = 1408.9, T/W = 0.295 and W_0 = 3428.7kg (unarmed). Other

design specifications are, $W_e = 1054.5kg$, $W_f = 2011.4kg$, $S = 23.87m^2$, $b = 20.04m$, $C_{Root} = 1.64m$, $L/D_{Max} = 21.3$, $P_{Engine} = 591.0kW$.

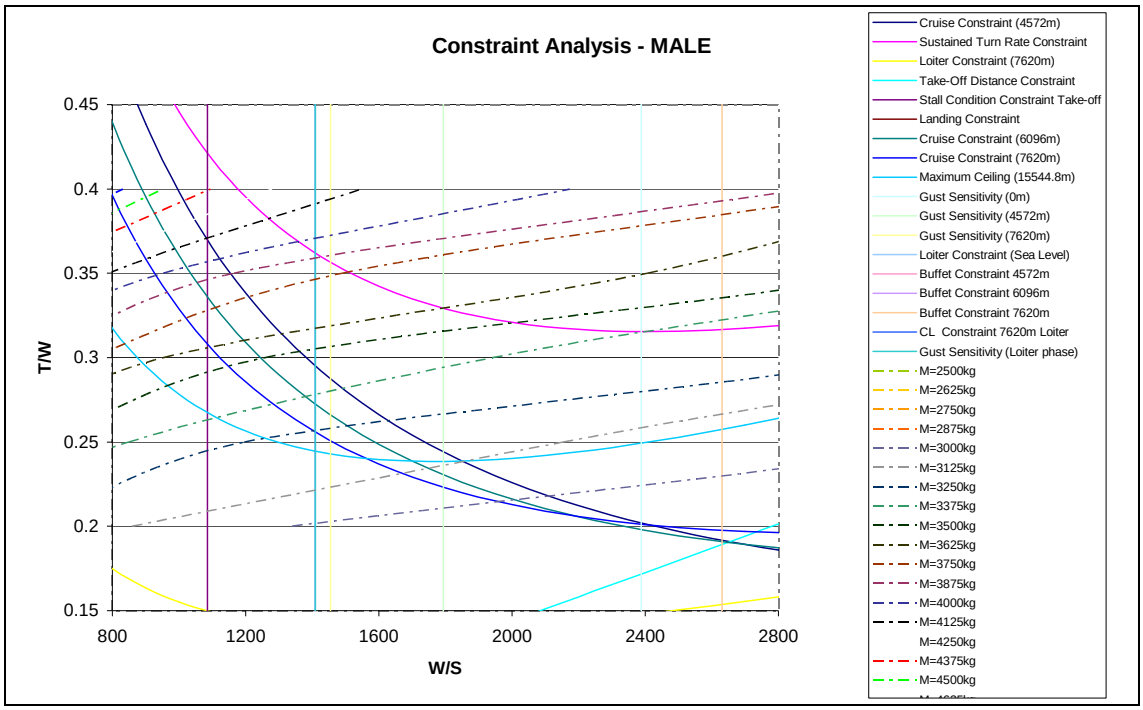

Chart 3-2

3.3 Details of the final baseline configurations

At this stage it was sufficient to represent the internal components as simple boxes, whose size were estimated during the conceptual design phase. The layout of the aircraft had to be carried out in conjunction with the static stability analysis to achieve a centre of gravity relative to the desired degree of stability. The consumption of fuel means that the centre of gravity and the stability will however be variable and so a number of points throughout the flight must be analysed. Integration of the fuel system at was limited to consideration of the size, shape and location of the fuel tanks. This is a particularly exhausting task since they have to be designed around centre of gravity and geometrical imitations. Integration of the engine not only had to take into account its location but also clearance requirements for cooling and maintenance. The physical size and mass of an engine were determined as a function of output power by means of rubber engine sizing relations. The engine intakes were sized using relations from Roskam [7] which determine the total intake mass flow rate required as the sum of that for engine and that for engine cooling. The final intake size is determined from the analysis of a number of different flight conditions to find the critical condition.

At this stage, the aerodynamic surfaces also became better defined with the selection of airfoils, high lift devices, control surfaces, washout and dihedral. The details of the high lift devices and control surfaces will be covered in later sections. At the conceptual design phase it is sufficient to make a selection from existing airfoils which will be better tailored to the design by the aerodynamics team at a later stage. Selection of the

right starting airfoil needed to take into account the operating regime and desired performance of the aerodynamic surfaces. The correct selection of an initial airfoil proved to be vital to making the best possible aircraft performance predictions as early as possible in the design process.

3.3.1 The UCAV configuration

The aerodynamic design of the wing for a tailless aircraft is a balance of flight performance, stability, control and stall behaviour. The absence of a tail and therefore longitudinal dihedral (generated by the setting angles of the wing and stabiliser) means that the wing has to not only generate lift but also provide a means of controlling and stabilising the aircraft. Swept back flying wing typically utilise the combination of a number of aerodynamic design features to generate such longitudinal balance. This can include, sweep and washout, tailored wing sections, the deflection of elevator flaps and reflexed airfoil sections at the wing root. It can be summarised that the secret of a flying wing lies merely in its lift distribution, which can be analysed as three separate distributions - basic, washout and flap deflection.

The tailless transonic configuration of the UCAV dictated the need for high speed/low pitching moment airfoils. The high wing sweep and taper meant that wing tip stall would be a problem and an airfoil with smooth stalling characteristics was required for the wing tips. The high speed NACA 6A (straight trailing edge) series of airfoils offered the best design flexibility for such an application. At the highly loaded wing root, a cambered NACA 65A112 was selected to meet the design lift coefficient. This was blended out to a NACA 64A012 give the lift performance required at the root along with good stall characteristics at the tip.

Wing tip elevons were selected for this design as these not only provide the best roll moment arm but can also increase the wash-out at the wing tips. When deflected upwards, these can reduce the aerodynamic load on the wing tips and are therefore beneficial to the stall characteristics of the wing. A statistical estimate of 2º was used for the dihedral of an equivalent straight wing. However, since 10º of sweep results in 1º of effective dihedral, the effective dihedral of this wing (44º sweep) was 4.4º and so 2.4º of anhedral was used. The airfoil choices resulted in C_{m0r} = -0.016 and C_{m0t} = 0, which meant that wash-out was required to generate the positive overall pitching moment required for stability. The amount of wash-out required was determined from the equation below taken from Roskam [11].

$$C_{m0w} = \frac{A \cdot \left(Cos\Lambda_{1/4}\right)^2}{A + \left(2 \cdot Cos\Lambda_{1/4}\right)} \cdot \frac{C_{m0r} + C_{m0t}}{2} + \left(\frac{\Delta C_{m0}}{\varepsilon_t}\right) \cdot \varepsilon_t \qquad \text{Eq 3-2}$$

Early work indicated that a C_{m0w} value of 0.006 was desirable which meant a value of ε_t = -6.17° was required. These results were validated with a wing lift distribution using the methods of ESDU 83040 [17] and further validated with a vortex lattice analysis. Using the methods of Roskam [11], the wing zero lift angle was determined as 1.95º at M0.15 and 1.88º at M0.9. The size and location of the wing fuel tanks is consistent with the conceptual design work to align the centre of gravity and aerodynamic centre.

3.3.2 The MALE configuration

The low speed medium altitude operation of the MALE dictated the need for airfoils optimised for loiter periods. Since the parametric analysis indicated a root t/c of 17% was required the LS(1)-0417 was the perfect candidate. This was complimented with the 13% t/c LS(1)-0413 at the tip with a smooth blend between. This combination is well established and has seen use on similar designs such as the Predator. A statistical estimate of 3º wash-out was incorporated to prevent the adverse effects of wing tip stall by shifting the lift distribution inwards. A statistical estimate of 2º wing dihedral was also incorporated to improve the lateral stability characteristics of the aircraft. The considerably large fuel requirement of the MALE necessitated the need to utilise as much space as possible for the stowage of fuel. The final configuration has consisted of as much fuel as possible being held in the wings with the remainder being held in a fuselage fuel tank.

3.4 The final layout of the baseline configurations

3.4.1 The baseline MALE UAV configuration

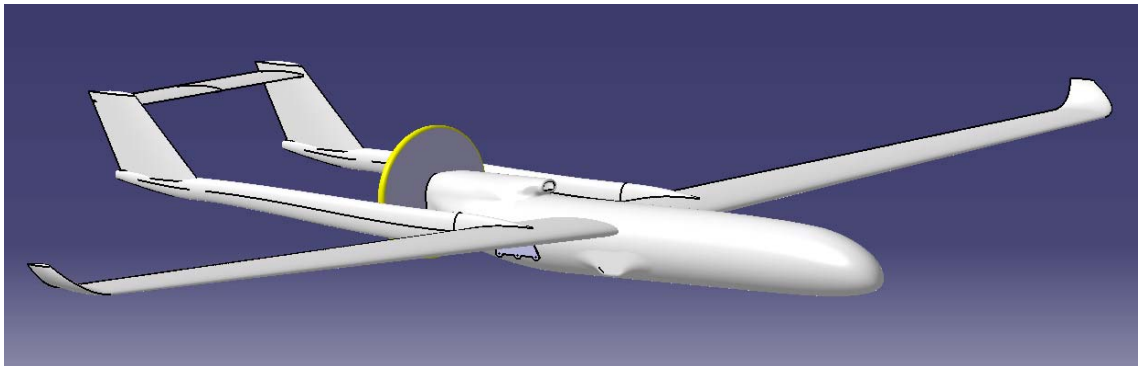

Figure 3-3 – The final MALE configuration

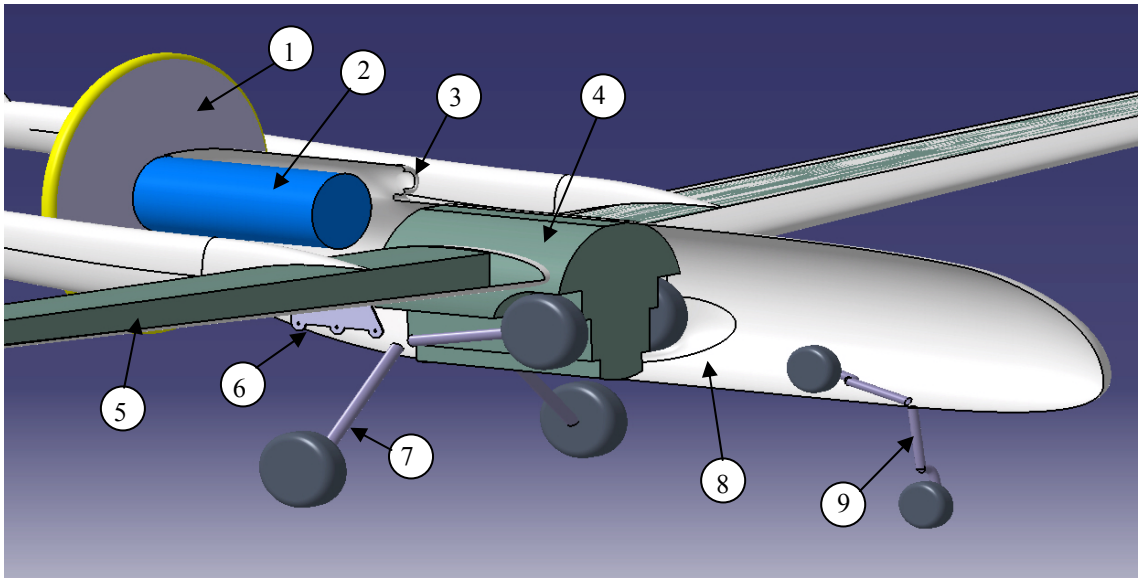

Figure 3-4 – Internal view of the final MALE UAV configuration

Baseline MALE component breakdown

Item	Description
1	Propellor
2	Turboprop engine
3	Turboprop pitot air inlet
4	Fuselage fuel tank
5	Wing fuel tanks
6	Wing hard points
7	Main landing gear
8	Location of systems
9	Nose landing gear

Table 3-1 – Component breakdown for the MALE UAV

3.4.2 The baseline UCAV configuration

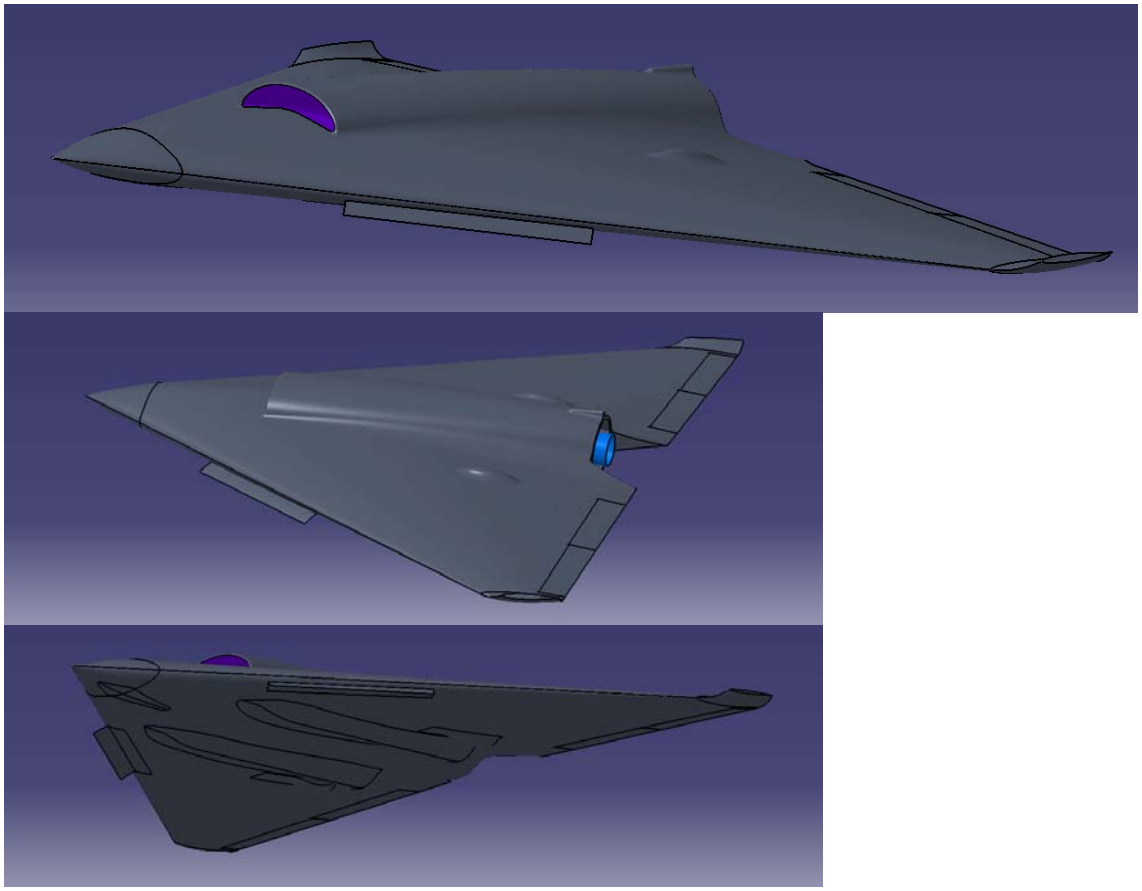

Figure 3-5, 3-6, 3-7 – The final Delta UCAV configuration

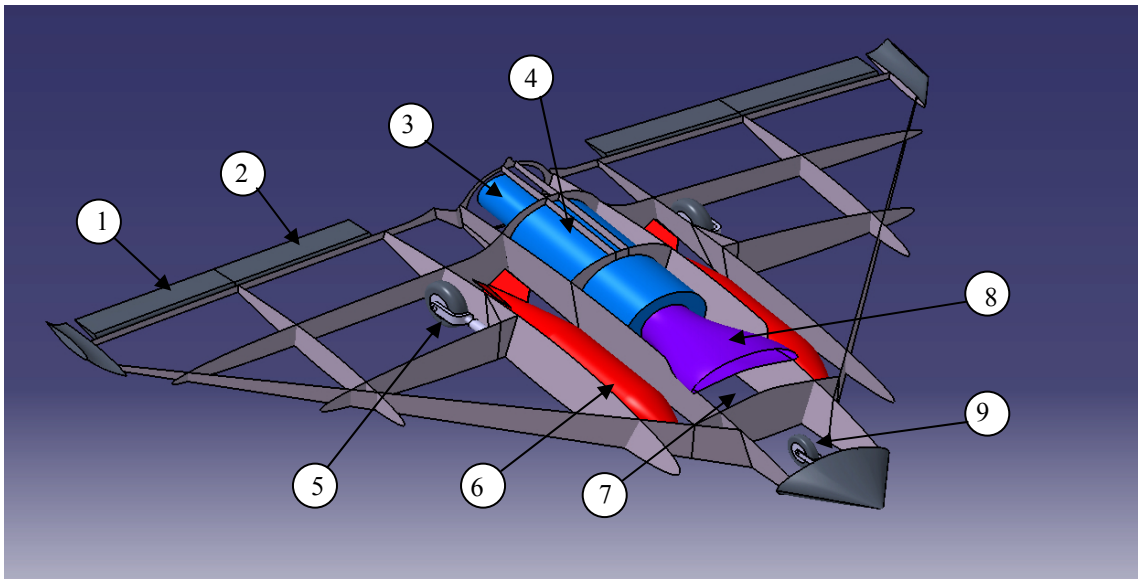

Figure 3-8 – Internal view of the final Delta UCAV configuration

Baseline UCAV component breakdown

Item	Description
1	Elevons
2	Drag rudders
3	Main engine jet pipe
4	Low by-pass ratio turbofan engine
5	Main landing gear
6	JDAMS (2 off)
7	Location of systems
8	S-duct inlet
9	Nose landing gear

Table 3-2 – Component breakdown for the Delta UCAV

3.5 Analysis of the baseline configurations

3.5.1 Longitudinal static stability

Longitudinal static stability is the ability of an aircraft to return to its undisturbed flight state following a disturbance around the pitch axis. This is however the starting point when designing a stable aircraft configuration and the lateral and dynamic characteristics must be verified soon after. Since the static stability of the aircraft is dependant on the centre of gravity, its analysis was carried out in conjunction with the general layout of the aircraft. It should be noted that a trade-off exists between static stability and manoeuvrability and the degree of stability or manoeuvrability required is relative to the role of the aircraft. The stability if an aircraft is usually expressed by the static margin (K). This is by definition the distance from the neutral point to the centre of gravity expressed as a percentage of the MAC, as given by the equation below.

$$K = \left(\overline{X_{np}} - \overline{X_{cg}}\right) \times 100\% \qquad \text{Eq 3-3}$$

The neutral point is the centre of gravity location where the aircraft pitching moment remains constant for a variation in the angle of attack and can be regarded as the aerodynamic centre. The location of this point was determined by an expression given by Raymer [3] which is derived from the derivative of the sum of the moments acting on the aircraft with respect to its angle of attack. The results are presented below.

Static stability results

UCAV	Kn (%)
End of take-off	2.0
Start of cruise outbound	5.3
Start of cruise inbound	5.5
End of cruis inbound	5.7
Start of landing	2.4

MALE	Kn (%)
End of take-off	7.3
Start of cruise 1	7.0
Start of loiter	7.1
End of loiter	6.5
End of cruise 2	6.2
Start of landing	6.4

Table 3-3

3.5.2 Aerodynamic characteristics

Predictions of the zero lift and lift induced drag components were made during the conceptual design work for each configuration. A polynomial equation was fitted to each set of data to arrive at the expressions given below. Also included is curve fit expressions obtained for data obtained from ESDU 70011 [18] for the wing lift curve slope and aerodynamic centre.

UCAV

$$C_{DZ} = 0.2493M^6 - 0.6863M^5 + 0.7388M^4 - 0.3926M^3 + 0.1067M^2 - 0.0162M + 0.0128$$

$$K = 0.0882M^4 - 0.1134M^3 + 0.0551M^2 - 0.011M + 0.1677$$

$$C_{L\alpha} = 4.9629M^4 - 7.9647M^3 + 5.0877M^2 - 1.0231M + 2.8036$$

$$X_{AC} = 0.2472M^4 - 0.3881M^3 + 0.2405M^2 - 0.0471M + 0.3333$$

MALE

$$C_{DZ} = 0.0002M^2 - 0.0044M + 0.0217$$

$$K = 0.0055M^4 - 0.0048M^3 + 0.0016M^2 - 0.0002M + 0.0237$$

$$C_{L\alpha} = 5.2681M^4 - 3.8586M^3 + 3.5794M^2 - 0.236M + 5.2085$$

$$X_{AC} = -0.1399M^4 + 0.2036M^3 - 0.1115M^2 + 0.0233M + 0.2445$$

Eq 3-4 to 3-11

3.5.3 High lift devices

The trailing edge devices of the MALE and UCAV were selected and sized to meet the lift enhancement requirements specified in the conceptual design analysis work. In the case of the MALE, simplistic trailing edge plain flaps located inboard of the ailerons proved to be more able to meet the required lift increment. Statistical methods were deemed sufficient for MALE, to roughly size the devices. This resulted in flaps with a width of 20% of the wing chord and a length of 8 to 50% of the wing semi-span.

Of the high lift devices studied, the Kruger flap was selected as the device most suited to the UCAV. As the trailing edge of the wing already incorporates drag rudders and elevons, the addition of a further device would reduce the space available for these. Whereas trailing edge devices can have a negative effect on the pressure gradient across the top surface of the wing, leading edge devices offer a means of increasing the flow

over the top surface of the wing. This has the effect of adding energy to the flow and therefore delaying the onset of flow separation, which results in a much higher operating angle of attack. Although the use of a leading edge device means that the aircraft must operate at higher angles of attack (since they have the effect of increasing the angle of zero lift), this is not considered a problem for unmanned aircraft. They also have the additional benefit of the potential for increased manoeuvrability at transonic speeds by having a positive effect on the buffet characteristics.

The first stage in sizing the Kruger flaps was to estimate maximum lift available from the clean wing. The best method for this task was found to be the advanced leading edge sharpness parameter method from Raymer [3], which is specifically aimed at low aspect ratio wings. This chart based approach gave a C_{L-Max} value of 0.9 for our wing. Using the estimate of maximum lift coefficient from the conceptual design work, including an allowance of 5% for the loss of lift due to trimming, the total lift enhancement required is 0.221. A first pass estimate of the performance of Kruger flaps (from Roskam [11]), sufficient for sizing work is,

$$\left(\Delta C_{L-Max}\right)_{Kruger} = 7.11 \cdot \left(\frac{c_{lef}}{c}\right) \cdot \left(\frac{b_{lef}}{b_e}\right)^2 \cdot \left(Cos\Lambda_{c/4}\right)^2 \qquad \text{Eq 3-12}$$

To be able to use this expression, estimates of the geometry were made from similar configurations and ESDU 94027 [19] to give the following. The setback of the Kruger flap hinge line from the leading edge = 2%. The chord of the Kruger flap = 5%. The backwards deflection angle of the Kruger flap from the wing chord line = 35°.

An iterative process was used to size the devices to meet the desired value of lift enhancement. The final configuration extends from 30 to 55% of the semi-span to give a lift increment of 0.235. The aircraft pitching moment increment due to the deflection of these devices was determined by methods of Roskam [11]. This method gives the increment in pitching moment, as a function of the configuration geometry, aircraft pitching moment (also determined by Roskam methods); aircraft lift coefficient and the location of the centre of gravity. Since the Kruger flaps are only deployed during the take-off and landing phase, only these flight phases were analysed to give,
$\Delta C_{m(Take-off)}$ = -0.001 and $\Delta C_{m(Landing)}$ = -0.00125.

3.5.4 Landing gear layout and analysis

For these studies, a conceptual design of the landing gear was sufficient to determine its geometry, longitudinal and lateral location, tyre sizes and interaction with the runway surface. As the centre of gravity is a function of this process, it is also dependent on other design stages. This work followed the methodology of Raymer [3]. The ground handling is a function of the longitudinal and lateral location of the landing gear. The longitudinal location was set so that the nose gear load fraction lies between the preferred ranges of 8-20%. The lateral location of the main gear was set so that the overturn angle was kept within the 63 degrees limit. The design work had to also take into account its retraction and length which had to sufficient to ensure there was adequate clearance during take-off and landing rotation. The tyres were selected from the Goodyear Aircraft Tire Data Book to be capable of carrying the aircraft static and dynamic ground loads. An analysis of the aircraft flotation characteristics for the given

tyre/landing gear configuration was given by the Load Classification Number (LCN). These were compared to specified ranges for different runway surfaces to determine the aircraft's suitability to operate from a range of airfields. A summary of the results for the UCAV and MALE are given in the table below.

Landing gear configuration details

	UCAV	MALE
Max. static nose gear load fraction (%)	20.0	13.5
Min. static nose gear load fratction (%)	15.1	11.5
Overturn angle (deg)	48.7	54.0
Nose gear tyre type (Goodyear)	461B-3072-TL	504T41-2
Main gear tyre type (Goodyear)	461B-3356-TL	708C01-1
LCN nose gear	5.9	1.7
LCN main gear	11.1	5.7

Table 3-4

3.5.5 Control surface sizing and analysis for the MALE

As the MALE was not intended to be used for any detailed control analysis work, statistical methods were sufficient to roughly size the control surfaces as follows.

- Ailerons – Width of 20% of the wing chord and with a length of 50 to 95% of the wing semi-span.
- Elevator – Width of 25% of the horizontal tail chord and with a length of 100% of the horizontal tail span.
- Rudder – Width of 25% of the vertical tail chord and with a length of 14% to 92% of the vertical tail span.

In a similar way, the horizontal and vertical tail surfaces were roughly sized using tail volume coefficients, respective of this class of aircraft. It was still advantageous to carry out a carpet plot analysis to explore the effect of variations in centre of gravity and tail area on the tail plane setting angle to trim. This enabled the angle of the horizontal tail plane to be set so that the elevator deflection and trim drag is kept to a minimum. The result is a tail plane setting angle of -2 deg. A further analysis was carried out to verify that there is sufficient elevator deflection available to trim the aircraft at various points throughout its flight. The results below show the maximum elevator deflection of -15.4º during landing approach to be well within acceptable limits. During the loiter phase, the elevator deflection ranges from -5.1 to 4.0º which indicates that the tail plane is correctly set.

3.5.6 Control surface sizing and analysis for the UCAV

In the case of the UCAV, an in-depth analysis of its control characteristics was required for later work. This involved an analysis of the roll, pitch and yaw requirements and analytical sizing of the corresponding control surfaces. The control configuration of the UCAV consists of,

- Elevons – These are located outboard on the wing which deflected differentially provides roll control and deflected collectively provides pitch control.
- Drag-rudders – These are located inboard of the elevons and can open and close to provide a means of yaw control. When closed, they can also work as a plain flap trailing edge high lift device for take-off and landing.

The yaw control power required to meet airworthiness requirements was determined as $-N_{\xi} \cdot \varsigma$ = 0.004189, to counteract a 15.43m/s cross-wind at 1.3 V_{Stall}. The aircraft was approximated as a flying wing and Datcom methods [20] were used to determine the yawing moment derivative $C_{n\beta}$ (in wind axes). Assuming a maximum deflection of 60° an expression from Roskam [21] was used to size the drag rudders. The result was drag rudders of 8% constant chord (measured at the mid point of the drag rudder) which extend from 28% to 60% of the wing half span to give $-N_{\xi}$ = 0.00443.

The roll performance requirement of 0-45 degrees in 1.4 seconds and at a speed of $1.3V_{Stall}$ from the MIL Type A, Level 1 airworthiness requirements was deemed applicable for the UCAV. The aircraft was approximated as a flying wing and the method of ESDU 06.01.01 [22] used to determine the rolling moment derivative C_{Lp} (in wind axes). When transformed into dimensional American notation the result was $L_{P(Dim)}$ = -1.065 (1/s). Assuming that the maximum deflection of the control surface is 16º, the control power derivative required can then be determined by solving the expression below from Roskam [21].

$$\phi(t) = -\left\{\frac{L_{\delta} \cdot \delta}{L_P}\right\} \cdot t + \left\{\frac{L_{\delta} \cdot \delta}{{L_P}^2}\right\} \cdot \left(e^{Lp \cdot t} - 1\right) \qquad \text{Eq 3-13}$$

This gave an American dimensional derivative value of $L_{\delta(Dim)}$ = 4.455 or a value of $L_{\delta} = C_{L\delta} = 0.0703$ in non-dimensional format. An iterative process was then used to size the elevons using ESDU 88013 [23]. The final elevon has a constant chord of 15% (measured at the mid point of the elevon) and extends from 60% to 93% of the wing half span to gives a control power derivative of L_{ξ} = -0.0725. In a separate analysis, the size of the elevons was also shown to be sufficient for pitch control at their critical phases and they were therefore fixed at this value.

In the case of the pitch control surfaces, the airworthiness requirements simply state that there must be sufficient control authority available at all phases during a flight. The take-off rotation phase when the aircraft is flying at a low speed and the high lift devices are extended proved to be the most control power critical. This analysis was based on the sum of moments about the main wheel ground contact points at the point of initiation of the take-off rotation. At this instant, the nose wheel is just resting on the ground and the aircraft has an angular acceleration of 8 deg/sec^2 about the ground contact point. The rotational inertia of the aircraft was based on a statistical estimate from Roskam [10], modified with the parallel axis theorem. This analysis was complicated by the number of design variables involved such as, landing gear setting angle, wing setting angle, take-off speed, landing gear location and length. Each of these needed to be properly explored in order to arrive at the best compromise of design choices and a landing gear setting angle of 5º was finally selected. The elevon size could finally be determined and its range of deflection verified at other flight phases via more straight forward trim analyses. In this case, moments were taken about the centre of gravity. This analysis is complicated by the fact that deflection of the elevon will not only modify the wing pitching moment but also the lift coefficient. The results showed a deflection of -3.5º during landing approach and a range of -0.19 to 0.17º during cruise confirmed that the aerodynamic characteristics of the aircraft are well balanced.

3.5.7 Refined drag predictions

The original drag estimates from the conceptual design phase were based on statistical predictions which required only a rough estimate of the aircraft configuration. As the design became more defined, a better estimate of the drag components could be made. Since the lift induced drag component is primarily based on the primary lifting surface, the original subsonic-transonic predictions were still adequate. In the later design stages, the aircraft is sufficiently detailed to make a better estimate of the profile drag using the methods of Raymer [3]. The nature of the flow in the transonic regime meant that to obtain a drag estimate in this regime, it was necessary to graphically interpolate between estimates for the subsonic and supersonic regimes. This process involved determining the profile drag of each of the component parts that makes up the external surface. For each component, a flat-plate skin-friction drag coefficient is used to estimate its surface friction and a form factor to estimate its pressure drag due to viscous separation. These are then factored to allow for component interference and multiplied by the component wetted area to give the drag for that part. The sum of these, including additional allowances for miscellaneous drag items, leakages and protuberances allows us to arrive at the total drag of the aircraft. In the supersonic regime, an additional term known as the wave drag is included to account for the pressure drag due to shock wave formation on the surface of the aircraft. This term is directly related to the volume distribution of the aircraft but there was insufficient time to carry out an analysis to optimise this term. In the case of the supersonic analysis, the component interference and form factors are included within the wave drag term.

Thesis size limitations have meant that it has not been possible to include the resulting drag polars here. As these refined results were similar to the original estimates, the original predictions were retained in the later performance analysis work.

3.5.8 Refined mass estimations

As for the drag estimates, the estimates from the conceptual design work were sufficient to give a first pass estimate with minimal knowledge of the final configuration. As the design becomes more defined, these figures can be verified with more detailed methods such as the mass prediction formulae from Howe [1]. These predict of the mass of the aircraft on a component level, which results in a greater degree of accuracy but requires component level knowledge of the aircraft. Since many of the different component masses are determined as functions of the gross aircraft mass, the process is iterative and time consuming. The results for the MALE and UCAV are presented below, but due to the size of the full results, only the results for each assembly subset are given. Also included are the earlier conceptual design estimates for comparison.

Component level mass estimation	Conceptual estimates		Refined estimates	
	UCAV	MALE	UCAV	MALE
Wing (kg)	661.4	208.7	991.8	283.3
Fuselage (including emenage and undercariage) (kg)	1319.0	246.7	1168.1	287.3
Installed powerplant (kg)	1505.1	222.0	1314.9	367.9
Systems (kg)	1038.1	377.2	1225.5	423.0
Payload for primary mission (kg)	1814.4	362.9	1814.4	362.9
Fuel (including allowance and reserve) (kg)	2312.6	2011.4	2312.6	2011.4
Total all-up mass (kg)	8650.5	3428.7	8827.1	3735.7

Table 3-5

3.5.9 Refined performance predictions

During the conceptual design phase, we have relied upon weight fractions to determine the fuel burn and the constraint analysis to ensure our engine meets our performance requirements. It was however essential that these results were verified by more advanced analytical methods which are able to predict the performance of the aircraft throughout its flight. This not only verified that the engine was able to deliver the required performance but also provided better estimates of fuel consumption. This work was based on direct derivations of aircraft performance from first principles which were incorporated into macro driven spreadsheets. This work eventually became the basis for later work and because of this a separate section has been devoted to its discussion within the appendices [Appendix A]. The fuel consumption results for the MALE and UCAV are presented below.

Fuel consumption estimates from conceptual and refined analyses

	Original	Refined
UCAV	m_f (kg)	m_f (kg)
Take-off	259.5	23.4
Climb and accelerate	190.9	363.2
Cruise outbound	887.6	1023.4
Weapons release	0.0	0.0
Cruise inbound	791.6	970.0
Descent	32.6	130.5
Landing	19.5	3.0
Reserve (additional 6%)	130.9	150.8
Total fuel estimate	2312.6	2664.3

	Original	Refined
MALE	m_f (kg)	m_f (kg)
Take-off	68.6	1.8
Climb and accelerate	16.3	50.4
Cruise outbound	151.2	237.6
Loiter (35 hours)	1555.0	1417.3
Cruise inbound	74.1	196.1
Descent	7.8	14.4
Loiter sea level (1 hour)	13.8	16.1
Landing	10.8	0.0
Reserve (additional 6%)	113.9	116.0
Total fuel estimate	2011.4	2049.6

Table 3-6

3.5.10 Dynamic stability analysis of the UCAV

Although the static stability of the UCAV was favourable, it was necessary to verify its dynamic stability characteristics. Its unconventional configuration meant that simplistic reduced order analytical models could not be used and a more complete analysis was required. The Class II, CAT A, Level 1 airworthiness requirements were identified as being most applicable to the size and mission requirements of this aircraft. The space state format of the decoupled equations of longitudinal and lateral motion referred to the body axes were used for this analyses as given by Cook [24]. This relies on two matrices of derivatives in concise form, one for aerodynamic terms (body axes) and the other for control terms. Determination of the stability derivates was lengthy and followed the methods of Datcom [20]. Various transformation stages were required to obtain their required concise form. These were obtained for a range of speeds from Mach 0.15 to 0.9 and also at three flight phases to allow for centre of gravity variations.

Matlab was used to carry out the matrix algebra to determine the transfer function matrix of the system in the Laplace 'S' domain format. The numerator of this gives the control response transfer functions and the denominator $\Delta(s)$ is the characteristic polynomial. When the characteristic polynomial is set to zero, the resulting characteristic equation can be used to find the open loop stability of the aircraft. In the case of the longitudinal motion, this factors in to two pairs of complex roots representing the phugoid and the short period oscillation. The undamped natural frequency and damping ratio can finally be determined for each mode. For the lateral case, the characteristic equation factors into a complex pair of roots and two real roots

which represent the dutch roll, spiral and roll subsidence modes respectively. To be stable, real roots must be negative and complex roots must have negative real parts

The results for the longitudinal analysis gave negative real parts for both pairs of complex roots which imply that the aircraft is stable in both the phugoid and short period oscillation longitudinal stability modes. In the case of the lateral analysis, negative real roots implied a stable configuration for the spiral mode and the roll subsidence modes. The complex pair of roots however has positive real parts which imply that the aircraft is unstable in the dutch roll mode. This is to be expected however due to the absence of a vertical tail and the solution to this would be to use a yaw damper.

3.5.11 Propeller analysis for the MALE

In the constraint analysis work, estimates of the thrust required from the propeller were made. To be able to determine the input power required to drive the propeller, it is necessary to determine the efficiency of the propeller at a number of flight conditions. This is a measure of the propellers ability to transform power into thrust. CFD and experimental data for an actual propeller design give the best results but the design of a propeller is a complex, time consuming and costly process. The design process typically begins with an analytical methods based on a combination of momentum and blade element theories. Each theory on its own is insufficient to fully describe the actual characteristics of the propeller but an analysis using a combination of the two has shown to produce very good results. Such an analysis is also beyond the scope of this work. Instead, relations from Howe [1] based on statistical data were used to first roughly size the propeller. As this design uses a turboprop engine allowance had to be made for the additional component of thrust from its jet exhaust. This was assumed to be 5% of the total thrust due to the possible complexity of a suitable exhaust system and will obviously not exist for an electric propulsion system. The number of propeller blades required was predicted from similar existing designs as 3. These expressions also relied on estimates of tip speed factor nD (taken as 75), engine power off takes (taken to be 5%) and maximum tip speed (taken as Mach 0.85). The final size of the propeller must be verified at different flight conditions to determine the critical design condition which in this case is high altitude cruise condition.

Generalised propeller charts where then used (as can be obtained from manufacturer's data and research papers) to determine the performance of a typical propeller. Such charts eliminate the need for detailed knowledge of factors such as blade shape, blade twist and the blade airfoils. The Hamilton Standard charts [25] as used for this work are available for a range of values of a parameter known as the activity factor. This is related to the shape of the blade and is an indicator of the amount of power the propeller blade absorbs. The activity factor is typically related to the type and size of the aircraft with a value of 100 being a good estimate for a light aircraft similar to the MALE. To be able to use charts we also need to make an estimate of the design lift coefficient of the blade airfoils. A figure of 0.5 was deemed typical for a light aircraft propeller and therefore suitable for this work. The charts are based on the advance ratio (J) which is analogous to the angle of attack of a wing and the power and thrust coefficients (C_P and C_T) which are a function of the power absorbed and thrust produced. As an estimate of

the propeller input power is required to be able to use the charts, input to the process, either a graphical or iterative solution is required. The absence of forward speed during take-off results in an advance ratio of zero and therefore a set of static propeller charts were used instead (based on the ratio of thrust coefficient to power coefficient).

The efficiency figure obtained from the charts must finally be factored to take account of installation losses. In the case of a pusher propeller like this, a loss of efficiency is experienced due to the wake of the wing and blockage from the presence of the fuselage. Determination of the actual figure can be quite complex and must be verified by experimentation. Typical figures range from 2-5% and our design is assumed to lie in the middle of this range. The final results are presented in the figure below for the range of flight conditions experienced by the aircraft. This includes data for both the turboprop and fuel cell powered aircraft, denoted by TP and FC respectively.

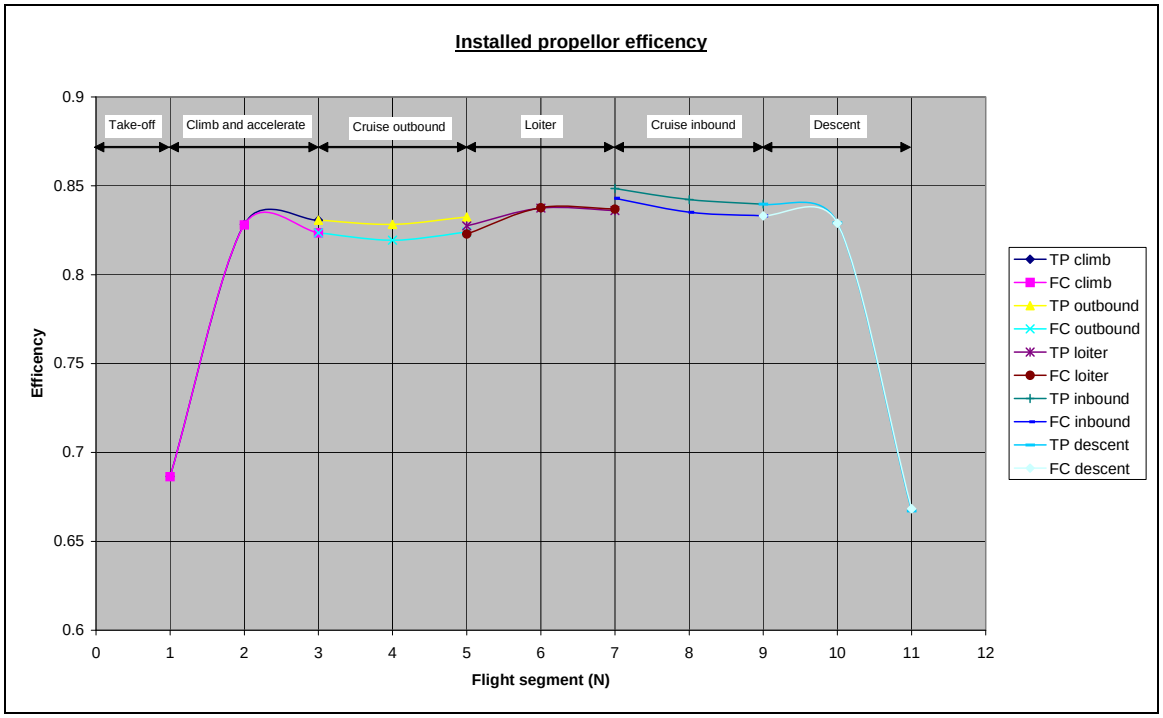

Chart 3-3

4 Technologies selection

The goal of this PhD is to perform a number of new conceptual designs of full-scale UAVs which will each integrate a selected number of advanced technologies. The choice of technologies includes those technologies which were being developed a part of the FLAVIIR (Flapless Air Vehicles Integrated Industrial Research) research programme as well as a choice of others from elsewhere. To be able to complete this task it was necessary to carry out a literature review of current technologies and down-select this list to those most relevant to this project. This section discusses the process followed to determine the technologies to be integrated.

4.1 Identification of potential UAV technologies

An extensive literature review was carried out to survey the possible technologies that could be implemented on the aircraft. The number of advanced projects and emerging technologies reported in the literature proved vast, some of which had a reasonable amount of data available while others had very little. At this stage only a very brief study of each technology was carried out which was sufficient enough to identify their key points without any in-depth detail. This was, however, sufficient to select those with the greatest potential to this project. This review was time consuming and the final list of possible technologies amounted to 100+.

4.2 The down-selection of potential technologies

The purpose of the technology selection process was to identify those forthcoming technologies from the list of 100+ technologies which are most closely matched to the project objectives. The time limitations of this project meant that there was only sufficient time carry out an in-depth study of 2 technologies. It would have been possible to study more but the time invested in each would have been much less. This would have led to a less detailed study with the risk of important design considerations being overlooked. It was therefore felt that an in-depth study of 2 technologies was the best option. Within this section, an overview is given of the down-selection methodology employed in the search for these 2 ideal technologies. Potential technologies should meet a number or all of the following requirements and should:

- Be applicable to the class of aircraft which the technologies are being applied to, which in this case is one or both of the baseline UAVs.
- Ideally have some relevance to the goals of the FLAVIIR programme although the project objectives states that others outside the programme can also be used.
- Have a realistic chance of success.
- Be of interest to both commercial as well as academic parties both within and outside the project and possibly lead on to further research studies both at Cranfield and elsewhere.
- Offer a significant operational benefit to the aircraft in terms of performance, cost, maintenance etc.
- Project timescales imply that there should be sufficient literature available to implement the technologies on the baseline designs without further extensive experimental or theoretical development of the technologies.

4.2.1 The QFD down-selection process

A number of different methods were briefly reviewed for the down-selection process but many of these proved very time consuming or relied upon third party computer programs which were not available. The ideal method had to be an easy to understand and implement method which could effectively match the list of technologies to the requirements. The method finally employed was the QFD (Quality Function Deployment) method which is based on the familiar graphical 'House of Quality' decision making process. This process is defined as the objective comparison of a number of different systems or processes, the results of which are stored logically within a results matrix. This decision tool was selected in preference to other methods as it is able to offer the following benefits:

- The output is the well-known graphical 'House of Quality' format which can be easily interpreted by many people from different disciplines
- The relatively simple process can be easily incorporated into a spreadsheet with no extra programs or tools being required.
- Participant inputs can be scaled according to their experience and specialism.
- Customer requirements are easily changed as required.
- The layout of the matrix produces a record of the many decisions and therefore generates a valuable audit trail of events.
- The process can also be used to consider the interactions that exist between each of the separate parameters themselves.

A good example of the method in use is reported by Boeing Phantom Works in their technology selection work on the 1997 FATE programme [26].

4.2.2 The QFD methodology

The construction of a QFD matrix involves the following stages:

1. Each of the different systems/processes must be accurately defined. Collectively the competing solutions/processes are known as the 'HOWs'.
2. The customer requirements must be identified and clearly defined. These are known as the 'WHATs', which will be used to quantatively compare the 'HOWs'. Examples include, an performance increase or reductions in mass, cost or weight.
3. The customer requirements must be prioritised by means of weighting factors known as WHYs.
4. The HOWs, WHYs and WHATs are used along with some simple QFD maths to generate 'HOW MUCHes. The HOW MUCHes are a scoring system for each system/process solution which indicate how successful each solution is at meeting the customer requirements (WHATs).

The standard QFD matrix presented above can also be extended with an optional correlation of the systems/processes being considered. This is recognised as the roof section of a standard house of quality diagram which is used to identify relationships that exist between the competing systems/processes. This allows the full effect of the addition of more than one system or process to be accounted for. To produce more reliable and accurate results the expert's input into the matrix can also be weighted to take account of their experience and specialism.

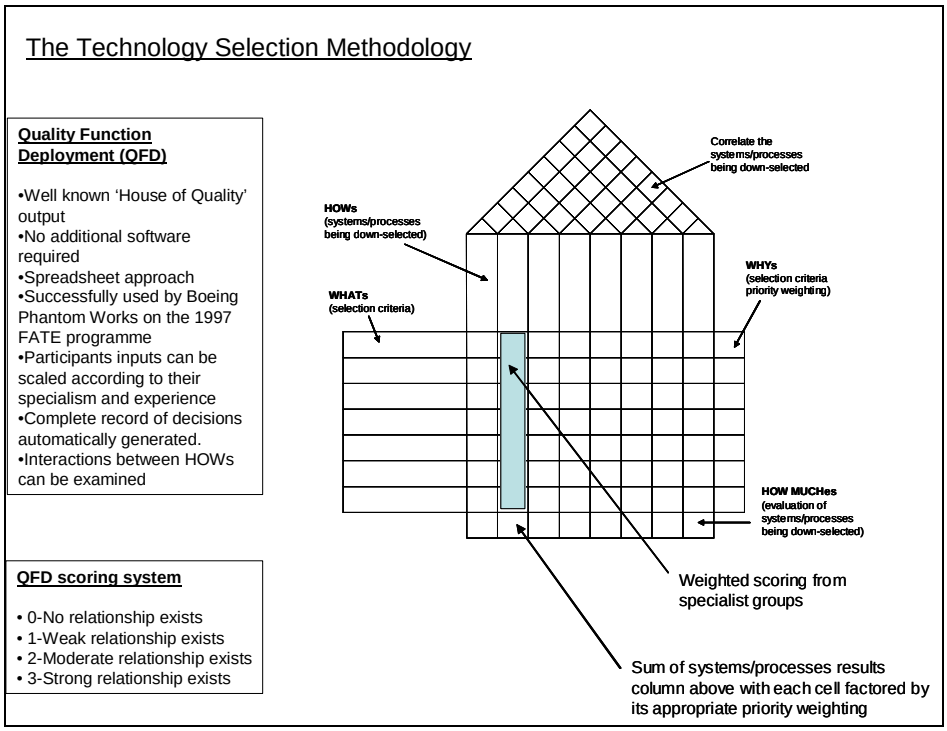

Figure 4-1

The scoring system used for the QFD matrix enables a representation of whether and if so how much the proposed systems/processes (HOWs) influence the customer requirements (WHATs). A standard linear scoring system with a scale of 0 to 3 is sufficient to represent a range of relationships from none to strong. Although a non-linear scoring system is recommended by Boeing Phantom Works, the linear system ensures that less favourable technologies are not dismissed too early in the project.

4.2.3 The QFD process applied to this project

This section gives an overview of the application of the QFD process to this project.

The HOWs (competing systems and processes) is the extensive list of 100+ potential technologies identified in the broad technology review. These were categorised according to the flight vehicle areas influenced by the technologies which ranges from stability and control to stealth and operation. It has been impossible to include the complete list of technologies within this thesis due to the limitation on its size.

The WHATs (customer or design board requirements) were carefully selected in accordance with the project objectives. Since the project is directly related to the FLAVIIR programme, the requirements where selected in accordance with the criteria laid down in the BAE Systems 'grand challenge' statement.
'To develop technologies for a maintenance free, low cost UAV without conventional control surfaces and without performance penalty over conventional craft.'
This led to the specification of requirements which were categorised under the headings of performance and cost.

The WHYs (requirements priority weights) were carefully selected in accordance with the project objectives. This enabled the list of requirements to be skewed towards the BAE 'grand challenge' statement and project objectives.

The Technology Selection Process Inputs

HOWs
(The competing systems and processes)

WHYs
(Requirements priority weights)

WHATs
(Customer or design board requirements)
1. To satisfy the project objectives.
2. To meet the criteria laid down by the BAE Systems 'Grand Challenge' [***To develop technologies for a maintenacne free, low cost UAV without conventional control surfaces and without performance penalty over conventional craft***].

Technology categories

- Stability and control
- Configuration design
- Materials
- Design methods
- Aerodynamics
- Subsystems and avionics
- Structures
- Propulsion
- Manufacturing
- Performance
- Cost
- Armament
- Maintainability
- Reliability
- Weight estimation
- Stealth
- Safety
- Operation
- Environmental impart
- Other

Performance		Weight Factor
Capability	Payload capability increase	7
	Mission Radius/Endurance increase	7
	Field Performance. Take-off and landing distance decrease	4
	Cruise speed/loiter time increase	3
	Cruise/loiter altitude increase	3
	Agility increase	4
	Autonomy increase	5
Mass	Systems mass decrease	6
	Powerplant mass decrease	6
	Structural mass decrease	6
Operational	Suscepability decrease	5
	Vulnerability decrease	5
	Durability increase	10
	Reparability increase	9
	Environmental impact decrease	2
	Transportability increase	7
Development	Technology risk/readiness level decrease	7
	Project intellectual assets increase	8
Costs		
Operational costs	Maintenance and support costs decrease	10
	Design mission fuel costs decrease	9
Program costs	Research, Development, Test & Evaluation (RDT&E) costs decrease	8
	Component manufacturing costs decrease	10
	Air vehicle assembly costs decrease	10
End of life costs	Final disposal costs decrease	3

Figure 4-2

The HOW MUCHes (results from the selection phase) enabled the list of technologies to be short-listed to the 10 most relevant to this project. The full 'House of Quality' results matrix for this project is too big to be included in this thesis. These 10 were manually further down-selected to just 2. This manual selection process enabled additional requirements to be accounted for in the selection process.

4.3 The final selected technologies and rationale

The two technologies selected for investigation in this project are:

- Low cost mechanical thrust vectoring approaches
- Fuel cells as a primary propulsion sources

The rationale for their selection will be given in the following sections.

4.3.1 Rationale for low cost mechanical thrust vectoring systems

Recently, there has been significant interest in the use of thrust vectoring systems to replace conventional flight control surfaces. Such a system would enable the aircraft to be controlled and/or trimmed by vectoring the engine exhaust gases. Conventional control surfaces are well known for their contribution to drag of and where they are used for trim considerable trim drag can also result. Such conventional devices also require regular maintenance and the radar cross-section of the aircraft is also increased as a result of their presence. The elimination of such devices is therefore expected to result in an increase in the performance of the aircraft and a reduction in maintenance.

The idea of using thrust vectoring for control and/or trim is not new and a small number of research studies have already been carried out in this area. Until now this has concentrated on the use of fluidic thrust vectoring devices for this purpose. Although fluidic devices have a number of benefits associated with them compared to mechanical thrust vectoring devices, they also come with their own set of problems. In particular, the research work of the Flaviir project has shown them to have considerable air flow demands necessary for their operation. Although mechanical thrust vectoring has traditionally been disregarded for such roles due to their cost, complexity and weight, there are a number of low cost devices receiving interest lately. Such low cost devices have traditionally been proposed as a means to improve the manoeuvrability of an aircraft and this project aims to investigate their viability for control and/or trim instead.

4.3.2 Rationale for the use of fuel cells for propulsion

Since the advent of the industrial revolution, the world's power requirements have seen continual growth. This is not only to meet the needs of mass manufacturing but to also satisfy the needs of the revolution in personal transport. This need has until now been met with the combustion of hydrocarbon based fossil fuels such as coal and oil derived products. The rapidly diminishing finite supply of fossil fuels as well as the degenerative environmental impact associated with their use, means that alternatives are being sought. Aircraft as well as other forms of transport are seeking alternative means.

The dependency of current aerospace propulsion devices on fuels derived from crude oil has made them vulnerable to rising oil prices and fuel availability. Air transport is reported to be responsible for about 10% of global warming via the greenhouse gas CO_2. With a further increase in air transport expected over the next few years, the level of pollution will increase accordingly. Research is underway to determine ways to improve the fuel efficiency and reduce the emissions from conventional aircraft engines. A number of alternative studies are also underway into the use of alternative fuels such as hydrogen and alternative power sources such as fuel cells. The studies carried out to date have dismissed the commercial use of fuel cells onboard aircraft due to problems of weight and hydrogen storage. The aim of this project is thus to investigate the current level of technology of fuel cells and the fuel choices available for such devices.

4.3.3 Matching of the selected technologies to the baseline aircraft

The selected technologies can clearly be seen to be more appropriate to one type of aircraft than the other and as a result, the technologies have been paired to the baseline aircraft accordingly.

- Low cost mechanical thrust vectoring – Most suited to the UCAV. The MALE UAV is not suitable because of its propeller configuration.
- Fuel cells for propulsion – Most suited to the MALE. The UCAV is not suitable because of its high thrust requirements necessitating the need for jet propulsion.

In the case of the thrust vectoring system we have the choice of a pitch only, pitch and yaw or pitch, roll and yaw system. It has been decided to opt for a pitch only system to replace the function of the elevators in the first instance, to keep the analysis to a manageable level. The UCAV is however well suited to the future integration of a pitch and yaw system, in which case it would replace the elevators and drag rudders.

5 Thrust vectoring literature review

5.1 What is thrust vectoring?

On a conventional aircraft, the line of action of the thrust from its engines is typically approximately parallel to the centreline of the aircraft. Thrust vectoring is a technique whereby the thrust line is deflected away from the centreline. When resolved into its components, this deflected thrust generates an additional component of thrust perpendicular to the centreline. This can have many benefits, the most common of these being reduced take-off and landing field length and/or improved manoeuvring capabilities. An obvious drawback to deflecting the thrust is that the resolved component of thrust along the aircraft centreline is reduced as the thrust vectoring angle increases. This necessitates the need to increase the engine thrust in order to maintain the momentum of the aircraft parallel to its axis.

5.2 The dawn of thrust vectoring - VTOL and STOL

Thrust vectoring first appeared when the idea of an aircraft being able to take-off and land vertically was first conceived. Although helicopters already have this inherent ability, they also have a number of drawbacks including lower achievable flight speeds. There was therefore a need for a hybrid between the two different craft, and thrust vectoring offered a solution to extending the capabilities of a fixed wing aircraft.

A variation of the vertical take-off and landing (VTOL) concept is the short take-off and landing (STOL) concept. Where as VTOL aircraft do not require a runway, STOL aircraft still require a runway, although a much shorter one than would be required for the same size and weight of aircraft. This gives STOL aircraft an obvious operational advantage of being able to operate from an increased number of airfields. STOL as opposed to VTOL has the additional benefit of significantly reduced vertical thrust requirements. Extending the concept even further, a hybrid of the VTOL and STOL concepts is known as, STOVL (short take-off and vertical landing). This concept is not only capable of short take-off but also has the capability of a vertical landing. Since the landing weight is always significantly less than the take-off weight, the vertical thrust requirements are significantly reduced for such a concept.

It should be noted that a VTOL aircraft is also STOL and STOVL capable but is less efficient. Since the thrust requirements for vertical lift are dominant for a VTOL aircraft, the engine is oversized (larger and heavier than is required) for all other flight phases. Afterburners have been explored to provide the additional thrust required for these critical phases but the excessive heat from the impinging hot exhaust gases can however damage the runway surface.

Over the years, a number of methods have been explored to give an aircraft VTOL capability, all of which have the same goal of generating the vertical thrust required. Some of the concepts explored are grouped into the categories below:

- Swivelling the whole engines – Rather than deflecting the thrust, the wing tip mounted jet engines rotate through 90º. A variant of this is the tilt-rotor which uses two wing mounted turboprop engines fitted with hybrid propeller/rotors. When airborne, the engines return to their normal forward position. Since the take-off and landing phases are no longer critical constraints for wing size, a smaller wing can be used. This concept can become complex when consideration is given to the engines ancillaries, off-takes and the many connections required (electrical/pneumatic/hydraulic/fuel), which all have to rotate as well. Safety considerations dictate that a minimum of two engines must be used for such a concept.
- Using vertically aligned secondary engines - whose sole purpose is to provide vertical thrust during take-off and landing and are switched off at all other times. The downside of this is their dead weight and volume during normal flight.
- Deflecting the thrust of the main engines – Swivel/rotating nozzles and/or vanes allow the exhaust gases of a turbofan engine to be deflected by up to 90º.
- Using ducted high energy gas – either bled from the engine or generated by engine shaft driven remote lift fans.

A selection of common deflector nozzle configurations which includes, switch-in deflector nozzle, swivelling nozzle and contra-rotating nozzle, are presented in the figures below.

.

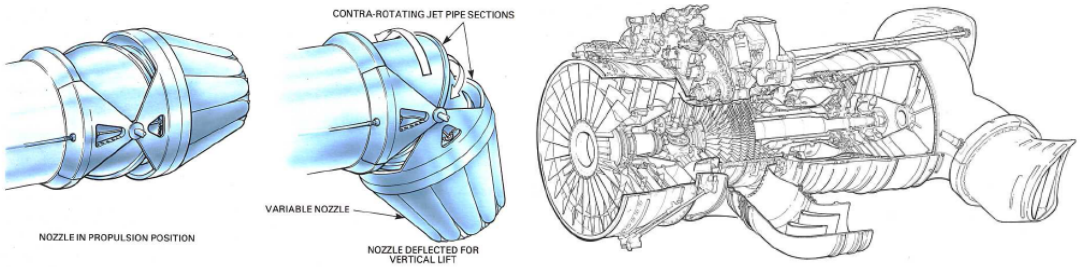

Figure 5-1 and 5-2 – Common deflector nozzle configurations [27]

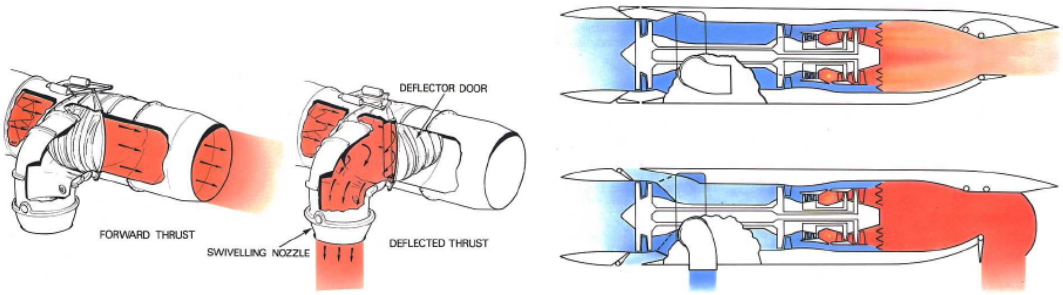

Figure 5-3 and 5-4 – More common deflector nozzle configurations [27]

With all the VTOL thrust vectoring concepts mentioned above, it should be noted that additional systems are required to provide aircraft control since the conventional aerodynamic flight control surfaces are ineffective during such manoeuvres. This increases the complexity of the system even further. Examples of such control approaches include differential engine throttling and reaction control jets.

5.3 Thrust vectoring as an alternative means of aircraft control

Besides offering the benefits of VTOL and STOL capability mentioned above, thrust vectoring systems are also able to offer an alternative means of aircraft control. Since the dawn of aviation, conventional aircraft have until recently relied heavily upon aerodynamic control surfaces for control about their three axis (pitch, roll and yaw axis). The ailerons, elevators and rudder (or in some cases the elevons, ruddervator or flapperons) have been until now regarded as the life-lines of the aircraft from a control perspective. Although these control methods have stood the test of time, they are not, however, without their drawbacks as will be discussed below.

5.3.1 The limitations of conventional control surfaces

The control force attainable (L_C) from conventional aerodynamic control devices can be shown to be proportional to and limited by:

- V^2 - The square of the aircraft's speed. This shows the strong dependence of the control force on the flight speed. At low flight speeds this nay result in only marginal control power being available while at high subsonic speeds the control surfaces may prove to be oversized and merely adding drag to the aircraft. At supersonic speeds the onset of shock waves produces a completely different flow system in which subsonic control surfaces will prove to be inadequate
- ρ - The density of the surrounding atmosphere. A decrease in ρ at high altitudes will result in a decrease in the control force attainable.
- $dCL/d\eta$ - The change in lift curve slope of a lifting surface with respect to the deflection of its control surface. The product $dCL/d\eta*\eta$, can be thought of as a means of altering the camber of the wing (and therefore altering the zero lift angle of the wing) to give a ΔC_L. This will however also have either a positive or negative impact on the stall margin of the wing with control deflection.
- η - The deflection angle of a control surface. This is typically limited by aerodynamic and aero-elastic effects
- S_C - The planform area of the control surface. The perfect balance of control surface size is difficult to achieve since the control surface will either be either marginal or oversized under different conditions

This list is by no means exhaustive, but the main parameters listed here are sufficient for some of the limitations of conventional control surfaces to be highlighted.

Summarising the points above, the conventional control surfaces can be seen to lose effectiveness while flying at either high altitudes, low speeds or high angles of attack close to the stall. Fortunately, thrust vectoring offers a means to be able to overcome some of these problems by replacing or supplementing the control force from a conventional control surface with the thrust components from a vectored exhaust jet.

5.3.2 Thrust vectoring for aircraft trim

As well as extending the control envelope of an aircraft, thrust vectoring has also been proposed as a means of improving the cruise efficiency by eliminating the need to trim the aircraft by means of the elevator. Since the associated elevator trim drag can reduce the efficiency noticeably it has been proposed that thrust vectoring can be used to trim

the aircraft instead. Such a configuration is being investigated in the SAX-40 design project, which has shown that the trim drag associated with conventional aircraft can be almost eliminated.

5.3.3 The advantages of using thrust vectoring for aircraft control

The benefits available from the incorporation of thrust vectoring on an aircraft are:

1. **Increase in aircraft efficiency.** Thrust vectoring has been shown to improve the efficiency of an aircraft as a whole when used control or trim
2. **Reduction in control surface size for conventional flight.** When used for control, the additional control power available from the thrust vectoring enables conventional control surfaces to be significantly reduced in size or even eliminated. This can lead to a reduction in drag, weight, maintenance, cost and radar vulnerability of the aircraft.
3. **Expansion of the control envelope.** Where manoeuvrability and agility are important, thrust vectoring allows the control envelope of the aircraft to be expanded, especially in the low speed and/or high angle of attack regimes. Since thrust vectoring systems do not have the same aerodynamic limitations as conventional control surfaces, we are now also able to extend our manoeuvring capabilities into the "post-stall" regime. Such manoeuvring abilities do not however impose any extra load on the aircraft structure, since the aerodynamic surfaces in a post-stall manoeuvre are operating beyond their stall margins and therefore lower 'g' loads are experienced.
4. **Low speed manoeuvre capabilities.** Although speed is the key for a fighter pilot, there are instances where low speed flight is inevitable. Studies have identified this as being the regime where thrust vectoring is most beneficial to a fighter pilot.
5. **Reduction in control surface size for manoeuvrability.** It can be shown that the pitch and yaw control requirements increase with an increase in the aircrafts angle of attack. It can also been noted that for a given roll rate, the pitch and yaw requirements increase exponentially with angle of attack. This would normally imply the need for exceptionally large and heavy conventional control surfaces for aircraft operating at low speeds and high angles.
6. **Reduction in lifting surface size.** The vectored exhaust jet can also supplement the lift from the wings or other lifting surfaces, allowing them to be reduced in size.
7. **Reduction in field length.** The vectored exhaust jet is reported to be able to supplement the lift from the wings during take-off and landing and thereby reducing the field length. This has is also particularly attractive for carried based aircraft. In cases when aerodynamic control surfaces are retained for control, sufficient forward speed may be required before adequate control power is available.
8. **Provide lift in the 'post-stalled' domain.** The vectored exhaust jet is able to provide a means of lift when the aircraft is operating in flight regimes where the lifting surfaces have stalled.
9. **Possibility of the complete elimination of control surfaces.** In the case of pure vectored aircraft, the control surfaces and their associated actuators can be completely eliminated. This has many benefits including a reduction in mass and

maintenance requirements, which is offset to some extent by the increases in mass and maintenance of the engine nozzle.

10. **Reduced roll inertia.** Elimination of ailerons in favour of thrust vectoring roll control can improve the roll inertia as a result of the aircraft's mass becoming more concentrated on it longitudinal axis.
11. **Large control forces are possible.** Especially at high throttle settings, large control forces and therefore very rapid manoeuvres are possible.
12. **Improved combat manoeuvring.** Combat manoeuvre analysis studies have shown thrust vectoring to offer improved turn rates and smaller minimum turn radiuses in the post-stalled domain.

5.3.4 The disadvantages of using thrust vectoring for aircraft control

The drawbacks of incorporating of thrust vectoring on an aircraft are:

1. **Cost, complexity and mass.** Existing thrust vectoring systems have proven to be heavy, complex and costly systems.
2. **Systems can be application specific.** Particular thrust vectoring systems do not have the same benefits for all aircraft configurations. Certain systems might prove to be vital to the survival of combat aircraft but may have little benefit on a recreational aircraft.
3. **Dependency on engine power.** Loss of engine power can lead to complete loss of control power for pure vectored aircraft and degradation of control power for partially vectored aircraft.
4. **Aft fuselage located heavy mass.** Existing mechanical thrust vectoring nozzles have proven to be heavy (~50% heavier than conventional nozzles). Since nozzles are located at the very rear of an aircraft, the centre of gravity of the aircraft is offset to the rear with an increase in the pitch inertia of the aircraft.
5. **Dependency on engine operating conditions.** Control power is engine thrust dependant, which itself is altitude and speed dependant.
6. **Lack of control power for landing.** During landing the engine is throttled back and their may be insufficient control power for a pure vectored aircraft. It may be necessary to increase the engine thrust during the landing approach to overcome this problem.
7. **Engine lag influence.** As thrust vectoring is thrust dependant, control power may also be subject to the thrust build-up lag often experienced with jet engines.
8. **Control system complexity.** A complex control system is required which can take into account altitude, speed, thrust variations and vectoring requirements.
9. **Engine thrust – vectoring angle interdependence.** When the thrust is deflected, the component of thrust parallel to the aircraft centre-line is reduced which results in a loss of momentum of the aircraft. A control system is required which is capable of increasing the engine thrust to compensate.
10. **Maintenance.** Existing thrust vectoring systems have proven to be very complex, particularly the multi-axis vectoring systems which contain a large number of moving parts. This necessitates an increase in maintenance.

5.3.5 The special case of the pure sideslip manoeuvre

A pure sideslip manoeuvre is one where the aircraft translates sideways without any change in the pitch or roll of the aircraft. In their simplest form they can be generated in a twin engine aircraft by deflecting the thrust on one engine while reducing the thrust on the other to prevent any unwanted aircraft yaw. Alternatively, both engines can be vectored in the desired direction. Vectored canard and extended nose vectoring jet configurations are also able to perform pure sideslip manoeuvres by deflecting all of their jets in one direction. The deflection angle of each jet must however take into account the thrust level and moment arm of each jet to keep the aircraft in balance.

5.4 Different thrust vectoring approaches

As will be presented later, considerable research effort has already been expended in investigating different approaches to deflecting thrust for purpose of aircraft control. The extent of thrust vectoring onboard the aircraft, the propulsion system used and its vectoring capabilities allow the system to be categorised as follows. The aircraft may be categorised as either pure vectored or partially vectored. The propulsion system, including the thrust vectoring nozzle, may be categorised as either internal or external thrust vectoring. Finally, the vectoring capabilities allow the system to be categorised as either 1-D or 2-D. These terms will be explained in more detail in the sections below.

5.4.1 Pure vs. partially vectored aircraft

A pure vectored aircraft is defined as one whose entire set of traditional aerodynamic control surfaces has been replaced with a thrust vectoring system capable of providing pitch, roll and yaw aircraft control. Such a configuration has a fully movable exhaust nozzle which allows the engine exhaust to be deflected in multiple directions. This sometimes also includes thrust reversal capability. The elimination of flight control surfaces can sometimes be extended to the elimination of stabiliser surfaces as well to create a pure flying wing. It should be noted however that a sophisticated flight and propulsion control system is required for such a configuration.

Since the control power moment available is a direct consequence of the length of the moment arm, vectoring jets located outboard on the wings offer the best control authority for yaw and roll control. There are also some aerodynamic benefits to such a configuration. In particular, the wing area in vicinity of wing mounted thrust vectoring nozzles is influenced by super-circulation effects.

In such a pure vectored configuration, the control authority can be further increased with the addition of differentially vectored canards or nose jets. In such an arrangement, the canards can be fixed or variable and typically use bleed air from the low pressure fan of a turbofan engine. In some cases, these are a necessity to balance some of the adverse moments that can be encountered.

The partially vectored aircraft is a hybrid between a conventional aircraft with aerodynamic control surfaces and the pure vectored aircraft discussed above. Not all of the conventional control surfaces (rudders, ailerons, elevators etc) may be present on a

partially vectored aircraft and the addition of any one or more of these on a purely vectored aircraft is regarded as a partially vectored aircraft. Since externally vectored aircraft are also to some extent affected by the surrounding flow environment (and therefore susceptible to certain aerodynamic limitations), these aircraft can also be classified as partially vectored. One of the main drawbacks of such a configuration is the need for a considerably more complex control system than for a purely vectored aircraft due to the phasing of aerodynamic and thrust vectoring control.

5.4.2 Internal vs. external thrust vectoring

External thrust vectoring (also referred to as post-nozzle or impingement) uses obstructions in the exhaust jet such as post-exit single or multi-axis paddles to deflect the exhaust jet from an axi-symmetric nozzle. An example of this is the paddles vectoring system as used on the X-31, which will be covered in more detail in a later section. Such an arrangement does however require heavy hydraulic actuators to operate the paddles. This type of system is capable of providing either pitch only, yaw-pitch or yaw-pitch-roll control. The benefits of this system are its simplicity and its ease of incorporation on existing aircraft. This can however experience considerable thrust losses, and it therefore less efficient than some other thrust vectoring approaches. The large gaps between the paddles also result in an additional inefficiency since a significant portion of the jet flow is able to escape un-deflected. As already mentioned, due to the protrusion of the paddles into the surrounding flow, the behaviour of the system is also influenced by the external flow. The additional length of the paddles results in a longer overall propulsion system and aircraft. Such a system is however designed around axi-symmetric nozzles, which means that super-circulation lift-gains can not be achieved. From a stealth perspective, the IR signature of the aircraft is increased as a result of the hot exhaust gases impinging on the paddles and heating them up. Three and four vane derivatives of this thrust vectoring system are available, though the three vane has received the most attention due to the weight saving in comparison with the four vane version.

Internal thrust vectoring nozzles (also known as annular nozzles) are more complex and heavier than their external vectoring counterparts. Within such a nozzle, the exhaust jet is turned within the actual nozzle and therefore they exhibit a greater efficiency. They do however sometimes require a significant number of large hydraulic rams and actuators which contributes to their weight and complexity.

5.4.3 Axi-symmetric vs. rectangular thrust vectoring nozzles

The obvious difference between the axi-symmetric (circular) and rectangular nozzles is in their cross-section. As will be discussed, each has their own merits and limitations. Rectangular nozzles can either be of low aspect ratio and located on the aircraft mid-plane or of high aspect ratio and blended into the trailing edge of the wing. The rectangular shape offers improved exhaust gas cooling and therefore lower exhaust gas IR signatures. The high aspect ratio nozzles offer improved wing aerodynamic efficiency (by means of super-circulation), improved yaw and roll vectoring capability and structural integration. They do however have problems associated with uneven internal flow and distortion due to temperature gradients.

The axi-symmetric nozzles are typically located on the aircraft mid-plane (in the case of a single engine aircraft). Their complex construction typically consists of a large number of smaller movable metal flaps around its perimeter, that can be simultaneously deflected together to deflect the thrust line. These nozzles can be configured to provide both yaw and pitch control but are limited to low deflection angles. Although these nozzles can exhibit high thrust efficiencies, the large number of flaps has the drawbacks of gas leakage and thrust losses as well as velocity and thermal boundary layers. As with any axi-symmetric nozzle, super-circulation lift gains are not possible (since the nozzle must be fully integrated with the trailing edge for such benefit). The IR signatures of these nozzles are higher than some of the high aspect ratio diverging nozzles.

5.4.4 Single vs. multi-axis thrust vectoring

Single-axis thrust vectoring is limited to providing control about only one of the aircrafts axis, which is typically pitch or yaw. In contrast, multi-axis thrust vectoring is able to provide control about two or all three of the aircraft's axes.

Multi-axis thrust vectoring has received extensive study (in the form of analytical evaluations and simulator and flight evaluations) over the past years to assess its benefits for combat aircraft. In contrast to pitch control/thrust reversing systems, thrust vectoring about the yaw/pitch axes was determined to have better agility payoffs.

5.5 An overview thrust vectoring theoretical principles

When the exhaust gases are deflected by an angle θ, a force perpendicular to the aircrafts longitudinal axis and a moment about the centre of gravity is produced which are proportional to Sin θ. At the same time a loss in axial thrust is experienced which is proportional to (1-Cos θ). When the exhaust gases are vectored, losses are encountered within the nozzle as a result of the turning process. These are accounted for by a slight reduction in gross thrust coefficient as a function of vector angle, which are characteristic of each particular nozzle.

The components of thrust along the X,Y,Z (forward, sideslip, heave) axes for a pitch and yaw thrust vectoring nozzle can then be determined from the relations below,

$$T_x = C_{fg} \cdot T_i \cdot Cos\delta_z \cdot Cos\delta_y \quad \text{Eq 5-1}$$

$$T_y = C_{fg} \cdot T_i \cdot Cos\delta_z \cdot Sin\delta_y \quad \text{Eq 5-2}$$

$$T_z = C_{fg} \cdot T_i \cdot Sin\delta_z \cdot Cos\delta_y \quad \text{Eq 5-3}$$

Where δ_z and δ_y are the deflection angles of the thrust line in the pitch and yaw directions respectively. C_{fg} is the nozzle thrust coefficient, which is used to take account of thrust losses due to the configuration of the nozzle as well as the turning of the flow within the nozzle. The final term T_i is the ideal un-vectored thrust from the nozzle which is given by,

$$T_i = \dot{m}_{actual}\left[RT_T \frac{2\gamma}{\gamma - 1}\left(1 - \left\{ \frac{P_a}{P_T} \right\}^{\frac{\gamma-1}{\gamma}} \right) \right]^{1/2} \qquad \text{Eq 5-4}$$

The terms in this expression are,

- P_a – Ambient pressure
- P_T – Total pressure at the nozzle throat
- T_T – Total temperature at the nozzle throat
- $\dot{m}_{actual}$ - The actual mass flow rate through the nozzle
- R and γ – Gas constant and ratio of specific heats of the exhaust gases

5.6 The impact of engine and nozzle technology developments

In the design of any new fighter engine, its demanding relationship with other systems now dictates a 'whole system engineering' approach in which engines are no longer considered as separate units. A particularly close relationship exists between the engine and exhaust nozzle and any engine developments will have a considerable impact on the performance of the exhaust nozzle. An example of this is the 'Variable Cycle Engine' concept which is being actively chased by engine companies. This operates as a turbofan during subsonic flight and a turbojet during supersonic flight and is able to cater for both high and low jet velocities requirements. Such a propulsion unit is able to offer significant improvements in efficiency throughout the flight envelope. Such a development would however require a nozzle which has the flexibility to be able to adapt to the wide variation in engine operating conditions if the full potential of such a configuration is to be realised.

5.6.1 Engine control developments

Of benefit to the development of thrust vectoring system is the progressive change from hydro-mechanical to FADEC (Full Authority Digital Electronic Control) engine control systems. The advantage of such systems is that they are fully integrated with the aircraft flight controls and is therefore especially useful to bring together the different control systems necessary for a pure or partially vectored aircraft. The FADEC systems are currently considered the best solution for advanced fighters as they are able to significantly reduce the workload that the pilot has to cope with.

5.6.2 Material advancements

The advent of new materials such as RCC composites and other ceramic/ceramic composites are expected to allow engines to be able to operate at temperatures up to 4000°F. This is expected to offer major improvements to the SFC and thrust of the engine. The use of RCC materials is however not limited to engine components and thrust vectored nozzles/transition ducts are expected to be manufactured from these materials as well. These materials have the ability to maintain their strength at temperatures in excess of 4000ºF (limits of 1600ºF are typical for conventional metallic materials). This means that no cooling is required to protect the RCC materials. They also offer the benefit of having negligible thermal expansion compared to the metallic

equivalents which results in increased durability and reliability. From a stealth perspective, RCC materials also have an excellent ability to absorb radar waves.

The current major difficulty associated with RCC materials is the current lack of efficient manufacturing processes available, although development work is underway. RCC materials must also be impregnated with carbides etc to prevent oxidation of the carbon fibres and the matrix at elevated temperatures. This is inarguably the best treatment for RCC materials since no surface coatings are able to offer the same durability and oxidation protection.

Another similar material development is 'single crystal turbine blades' which are formed from super-alloys. These are directly applicable to aircraft engines and offer the benefits of increased turbine durability, improved cycle performance. They are also able to cater for advanced internal cooling methods. However, such developments are likely to increase the turbine entry temperature of the engine, which the exhaust nozzle must also ultimately bear.

5.7 Stealth and survivability considerations

Studies have identified thrust vectoring as one of the essential technologies for the next generation of high performance stealth aircraft. Some of its benefits for a combat aircraft are discussed in the sections below.

5.7.1 Aircraft agility

Aircraft agility is important to the survival of a combat aircraft especially during 'energy and angles' fights and can be divided into 2 areas, that of manoeuvrability and that of controllability. Agility can also be further separated into pitch, torsional and axial agility. Thrust vectoring is a tool which is able to add super-manoeuvrability and super-controllability abilities to combat aircraft. These are attributes which enable the aircraft to perform complex post-stall, de-coupled (sharp translations independent of other manoeuvres) and controlled side-slip manoeuvres.

The maximum turn rate of an aircraft is also significantly improved along with its ability to sustain high turn rate manoeuvres with thrust vectoring. This improved manoeuvring effectiveness means that the duration of high 'g' manoeuvres is also considerably reduced. It is worth noting that the pure vectored aircraft have a greater manoeuvrability and post-stall super-manoeuvrability capability than their partially vectored relatives. This is due to their complete elimination of control surfaces and in some cases stabiliser surfaces. Even so, pilots have reported that multi-axis thrust vectoring is a tool which is very effective under specific circumstances but does not need to be used at every opportunity.

Such enhanced manoeuvring capabilities must also be accompanied by efficient and precise controllability of the aircraft during all phases. This necessitates the need for adequate control power and precise aircraft handling qualities. Since thrust vectoring also enables the different means of control (such as pitch and yaw vectoring combined

with thrust reversal) to be combined, the execution of such complex manoeuvres is now realistically possible.

5.7.2 Survivability

In a combat situation, enhanced manoeuvring capabilities result in the higher probability of a kill and therefore reduced combat engagement times. Manoeuvres such as the ability of the aircraft to point in one direction while translating in another direction not only allow the aircraft to out manoeuvre other aircraft and missiles, but capture and maintain a target in its sights (rapid nose pointing and shooting).

Partially vectored aircraft have a distinct advantage over pure vectored aircraft, since the survivability of a partially vectored aircraft is higher than for a pure vectored aircraft due to the additional flight control redundancy. In the event of the failure or damage of a flight control system or surface, the aircraft has a much greater chance of still being able to complete its mission.

5.7.3 Radar cross section and IR signatures

In cases where the empennage/control surfaces have been reduced/eliminated, as on partially/pure vectored aircraft, there is an accompanying significant reduction in the number of RADAR reflecting edges, discontinuities and flat surfaces on the aircraft surface. Complex thrust vectoring exhaust nozzle with lots of surfaces, edges and moving parts, are however detrimental to the RCS signatures. In general however; the stealth characteristics of a pure vectored aircraft are improved.

The propulsion system of any aircraft is well known for its contribution to the RCS and IR signatures of an aircraft. This can however be improved by shielding the engine inlets and nozzles from below. S-duct inlets are effective at shielding the engine compressor from the front, as these are able to trap any radar waves inside the inlet. Such design features do however have an impact on the installed engine performance and therefore the performance of an attached nozzle.

In cases where a reduced IR signature is paramount, higher rates of nozzle cooling are required to cool the exhaust gases. This does however dictate the need for a larger engine

5.8 Future development opportunities

Studies have shown that substantial thrust penalties could be present with certain thrust vectoring nozzles due to coolant bypass flow and leakage. Further development work is therefore necessary in order to overcome these problems. The evolution of the next generation of UAVs incorporating this technology needs to continue the evolutional process used so far, whereby current partially vectored aircraft help pave the way for pure vectored aircraft. It is however necessary to develop the experience and tools required before these more advanced concepts can become reality.

Studies have shown that the use of thrust reversal is not essential for vectored combat manoeuvres; it is the combined use of pitch and yaw vectoring which is most significant. It has therefore been concluded that in-flight thrust reversal capability is becoming a less attractive option on today's aircraft with its only real benefit being to the landing field length. The elimination of these devices can actually have a positive impact with weight and cost savings as well as a reduction in the complexity of the nozzle. There are also stealth benefits to be gained by its removal, as a result of the accompanying reduction in the number of edges and crevices that can contribute to the RCS signature of the nozzle.

5.9 Fluidic thrust vectoring concepts

Fluidic flow control of an exhaust nozzle was originally conceived in the 1950/60's as a means of controlling the nozzle throat area of rocket engines. Such thrust vectoring systems involve the manipulation of a primary exhaust flow with a secondary air stream. This secondary air stream typically uses bleed air from the engine compressor or fan, which moves their operating point from the optimum and therefore has an impact on engine performance. Both pitch and yaw vectoring is possible with these systems. A number of different fluidic thrust vectoring approaches have been investigated over time such as,

- Co-flow
- Counter-flow
- Synthetic jet actuators
- Shock vector control
- Sonic throat skewing

These will be briefly discussed in the sections which follow.

5.9.1 Co-flow thrust vectoring

Co-flow thrust vectoring works on the coanda principle in which a jet remains attached to and is deflected around a convex surface. This effect can be increased by passing a thin layer of high velocity turbulent air tangentially to the surface. This particular system works by blowing a secondary air stream (momentum injection) across the coanda surface. This secondary air flow follows the profile of the coanda surface and entrains the primary flow (from the engine exhaust) into a curved path.

Although the coanda principle has proven to be effective for blown high lift devices, its use as a means of vectoring and exhaust jet has previously been fraught with difficulties. Early research work reported such a system as being very difficult to control with the recommendation that variable coanda surfaces were required to achieve linear control. Early systems were limited to vectoring angles of about 9º.

Interest in co-flow thrust vectoring was revived by M.S.Mason [28], who concluded that the maximum vectoring angle could be increased to about 12.5º by further increasing the secondary mass flow rate. At this point however, the system is considered saturated and no further deflection is possible. The secondary flow required was however considerable, with at least 5% being required to initiate system operation. Although the

control in linear, an initial dead zone exists and therefore a certain amount continual blowing is required to overcome this problem.

Co-flow systems have also been investigated as part of the Flaviir project. The system consisted of a high aspect ratio nozzle with thin secondary slots. Secondary air supply was from a compressor constructed from a turbocharger compressor wheel. Early studies investigated the effect of secondary gap height and coanda surface diameter, as well as other geometric variable. This led to the development of an early system whose effectiveness was demonstrated on model aircraft. These where however of very low wing loading and therefore there may be a noticeable difference in effectiveness on actual aircraft. Later on, a swept exhaust nozzle was also tested, which demonstrated better efficiency, better vectoring performance and retained the linear control characteristics with no control dead zone. This early research work did however only demonstrate the effectiveness of this system for low subsonic primary jet Mach numbers [Ref. 29]. It was also reported that "the system becomes increasingly inefficient for high primary jet Mach numbers which require supersonic secondary flow for adequate control effectiveness". Even under the early tests, secondary jet Mach numbers of up to 0.73 were tested.

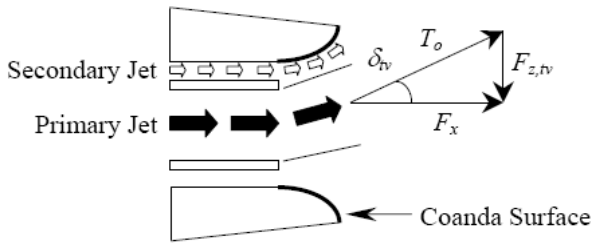

Figure 3 *Coflow thrust vectoring concept used in the present work (aircraft coordinate system)*

Figure 5-5 – The coflow thrust vectoring principle [28]

5.9.2 Counter-flow thrust vectoring

Counter-flow thrust vectoring works on a simulate principle to a co-flow thrust vectoring system as shown in the figure below. The main difference being that in this system, the secondary flow is sucked (momentum removal) rather than then blown across the coanda surface and therefore in a counter direction to that of the primary flow. The mechanics of vectoring the primary flow in this system are a result of asymmetric separation in the interaction zone between the primary and secondary flows. The counteracting secondary suction flow acts to alter the region of separation in the nozzle and therefore influences the angle at which the primary jet leaves the nozzle.

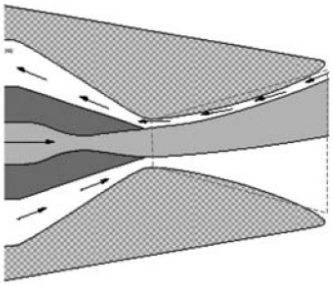

Figure 5-6 – The counter-flow thrust vectoring principle [30]

Although vectoring angles of 16º and thrust efficiencies of 92-97% have been reported, this system does have a serious drawback. At high vectoring angles, the system can experience phenomena known as hysteretic jet attachment. This is where the primary flow attaches itself to the suction collar due to the coanda effect entraining the flow to the surface of the nozzle. This results in complete loss of vectoring control and the system must be switched of and restarted in order to regain control. Such a sudden loss of control could prove to be catastrophic for a thrust vectored aircraft. A reasonable vectoring angle can be achieved with careful design of the suction collar but a limit must be imposed on the vectoring angle in order to prevent flow attachment. Throat area control is not possible with such systems.

Although the secondary mass flow ratio is only about 1% of the primary flow, a viable vacuum source must still be sought. This would most likely be a turbopump (driven by the engine).

5.9.3 Pulsed jet actuators

These are also known as ‘zero mass flux actuators’, with each consisting of an oscillating diaphragm which repeatedly draws in and ejects a small amount of the primary flow into a cavity via an orifice. The repetitive nature in which the fluid is ejected is sufficient for it to resemble a constant jet of secondary flow. Since each diaphragm is driven by a piezoelectric driver no mechanical or fluid connections are required to enable these to operate. When PJA’s are placed on alternative sides of a primary flow, they can be operated alternately to create a low pressure region on that side which deflects the flow in that direction. The response time of the system can be varied by varying the frequency of oscillation of the jet actuators.

Such a system does have the distinct benefit over other fluidic systems that it does not require air from a secondary source such as engine bleed. Initial studies have only been carried out at low primary jet velocities and this has shown the vectoring angle to decrease with increases in the primary jet velocity. Initial indications have therefore shown that this system would be unlikely to vector the high speed/pressure flows experienced within an actual exhaust nozzle.

5.9.4 Shock vector thrust vectoring

In this system, a secondary flow is injected asymmetrically into the divergent section of a convergent-divergent nozzle. This creates a low pressure region downstream of the injection port which is seen as a disturbance by the flow and results in a strong oblique shock wave being formed. The change in flow properties which are typical across a shock wave, causes the flow to change direction and be vectored away from the injection port as it passes through the oblique shock. Since vectoring takes place at supersonic speeds, thrust losses can occur as a result of the primary flow passing through the oblique shock which has a knock on effect on the thrust efficiency. Vectoring angles of more than 19º have been achieved in static tests. In practice, the resulting freestream velocities are seen to vary the pressure differential at the nozzle exit, which moves the shock wave attachment point further into the nozzle. This has the effect of reducing the effectiveness of the nozzle. This system is reported to have a greater efficiency than equivalent mechanical systems with a secondary mass flow requirement of 6-10%. The drawback of such a system is when the oblique shock wave becomes too strong and its other end impinges on the opposite nozzle wall. When this happens, a reflected shock wave of reduced intensity is generated which vectors the primary flow in the opposite direction. This results in a degradation of thrust vectoring performance and thrust efficiency. Another problem with this system is, in order to achieve large vectoring angles; the system must operate at highly over-expanded conditions which results in over-expansion loses. The throat area remains unaffected by this thrust vectoring method but can be varied by mechanical means if required.

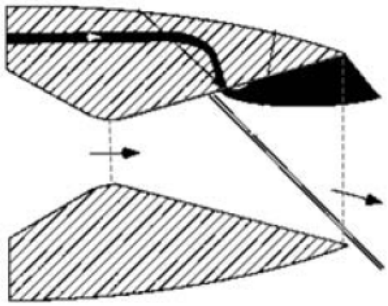

Figure 2-7 – The shock vector thrust vectoring principle [30]

Thrust vectoring efficiencies of 0.9-4 deg per percent of flow injection and thrust efficiencies of 0.86-0.94 have been demonstrated.

5.9.5 Sonic throat skewing (shifting)

In this system, secondary flow is injected into either the throat or divergent section of a supersonic convergent-divergent nozzle to vector the flow. The working principle here is the creation of virtual aerodynamic surfaces which have the same function as mechanical surfaces. The conventional throat of the nozzle and its shock wave is skewed (shifted) to the new minima of these virtual surfaces. Since the vectoring takes place on he subsonic side of the nozzle throat shockwave and therefore at lower speeds, the thrust losses due to vectoring are lower. The injection points are typically located at different points long the nozzle axis which has the effect of skewing the sonic plane

from the geometric throat to coincide with the injection points. The vectoring angle which can be achieved is dependent on the offset between the injection points as well as other factors such as the expansion ratio. In this system, the flow is turned at subsonic speeds before it passes the shock wave and therefore the thrust losses are lower than for shock vector control.

Whereas other fluidic nozzles require an additional mechanical means in order to control the area of the throat, this nozzle is able to achieve this without any additional systems (only at zero vectoring angles however). By operating the injectors symmetrically, the thickness of the boundary layer at the throat is increased which decreases the effective area of the throat. The vectoring effectiveness (secondary flow requirements) was reported to be comparable to shock vectoring methods.

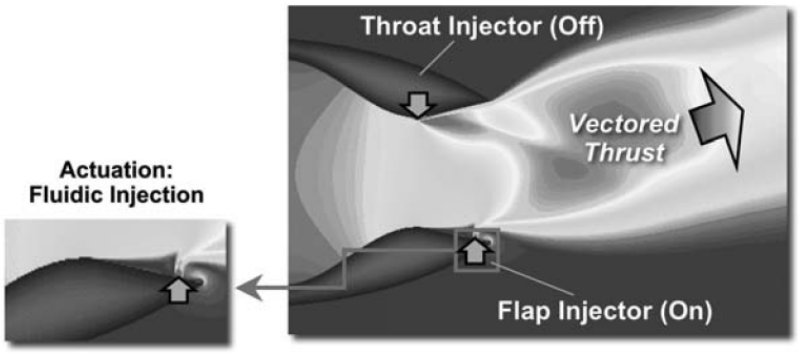

Figure 5-8 – The sonic throat skewing principle [30]

CFD tests by Lockheed Martin, predicted a response rate of 100 deg/s to a step input for this system. In practice a slightly lower rate will however be experienced. Since the ideal predictions are a magnitude higher than found on conventional systems, the system is deemed more than adequate for aircraft use. An extension of this method is the dual throat nozzle concept (DNT).

6 Thrust vectoring studies and examples

6.1 Existing thrust vectoring research effort and thrust vectored aircraft

A significant amount of research effort has been expended to thrust vectoring over the last few years. Some of the effort has not progressed beyond the experimental stage, while at the other end of the scale, a handful of thrust vectored production aircraft exist. A number of these developments are listed below and have been categorised according to their thrust vectoring abilities.

	Manufacturer	Model	Main Engine	Additional Notes
VTOL/STOL	Bell/Boeing	V-22 Osprey	2xTurboprop	Tiltrotor
	Boeing	X-32	P&W F135 A/B	
	Dornier	Do31	2xPegasus	+8x RB162 lift engines
	EWR	VJ 101	4xRB-145 (rotating)	+2x RB145 in fuselage
	BAE	Harrier	RR Pegasus	
	Lockheed Martin	F-35B JSF	F135/F136 A/B	+ Low pressure shaft driven lift fan for lift
	VFW	VAC 191B	RR RB 193-12	+2x RR RB162-81 lift engines
	Yakovlev	YAK-38	R-28 V-300	+2x RD-38 lift engines
2-d Maneuver	Lockheed Martin	F-22 Raptor	2x P&W F119-PW-100 A/B	Pitch only vectoring (+/- 20 deg)
	McDonnell Douglas	F-15 S/MTD	P&W F-100-PW-200 A/B	P&W 2-d TV Nozzle (+/- 20 deg)
	McDonnell Douglas	X-36	Williams F112	Yaw only
	Boeing	X-45A		Yaw only
	Sukhoi	Su-30	2x AI-31FL A/B	2-d (+/-15 deg)
	Sukhoi	Su-35	2x Saturn 117S A/B	
	Sukhoi	Su-37	2x AI-31FU	2-d (+/-15 deg)
3-d Maneuver	Lockheed Martin	F-16 MATV	GE F110-GE-100 A/B	
	McDonnell Douglas	F-15 ACTIVE	2x P&W F-100-PW-200 A/B	P&W P/YBBN TV Nozzles (20 deg 3-d)
	McDonnell Douglas	F-18 HARV	2x GE F404-GE-400 A/B	
	Mitsubishi	ATD-X	2x IHI XF5 A/B	3 paddles
	Mikoyan	MiG-29OVT	2x Klimov RD-33MK A/B	
	Rockwell MBB	X-31	GE F404-GE-400	3 paddles for pitch and yaw
	Sukhoi	Su-35BM	2x Saturn 117S A/B	
	Lockheed Martin	X-44		Full pitch/yaw/roll TV control

Table 6-1

6.2 Internal mechanical thrust vectoring concepts

Numerous thrust vectoring nozzle configurations have been explored over time. Many of these are however quite old compared to the configurations discussed below and there are a number for which little information is available. This review will thus be restricted to the most current concepts which have shown the most promise.

6.2.1 PYBBN nozzle

The axi-symmetric PYBBN (Pitch Yaw Balanced Beam Nozzle) nozzle is able to vector the thrust by 20° within a full 360° envelope. It was tested on a F100-PW-229 engine which was fitted to redundant MATV project test aircraft, but can be retrofitted to any F100 engine. The redundancy of the system is also good with duplex actuators being used for the engine-nozzle system. The balanced beam configuration is a means to

reduce the forces required to deflect the nozzle and thus reduce the size of any the accompanying actuators.

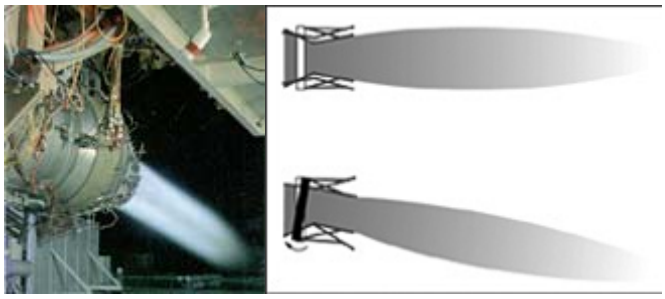

Figure 6-1 and 6-2 [Ref 31]

6.2.2 Axi-symmetric Vectoring Exhaust Nozzle (AVEN)

The General Electric AVEN nozzle program was born around a requirement to provide a simple means of multi-axis thrust vectoring which could be retro-fitted to any F-16 with a digital flight control. The nozzle was coupled to a GE F110-GE-100 engine and tested as part of the VISTA and MATV programmes. Although this was designed around a F110 engine, it is adaptable to other engine designs, including the very similar F404. The nozzle has the ability to be vectored in any direction by over 20° and has a low external profile, but is heavy and a significant amount of ballast is required in the nose of the aircraft to compensate.

The AVEN nozzle was derived from a standard convergent-divergent F110 nozzle by replacing the compression links with a load carrying flap/frame system which was connected to a movable ring. This could be either tilted to vector the thrust or translated fore and aft to adjust the exhaust area. The position of the ring is maintained relative to the engine centreline with three ring support mechanisms. Thermal resistant seals also had to be included between the divergent flaps of the nozzle to maintain its efficiency. Nozzle vectoring requirements are passed from a digital Vector Electronic Control Unit to a Nozzle Control Valve (which is a set of electro-hydraulic servo valves). The divergent section of the nozzle is then manipulated via three equally spaced actuators and the throat area by four actuators (which are adoptions of the F110 hydraulic nozzle actuators). The layout of the nozzle is shown in the figure below.

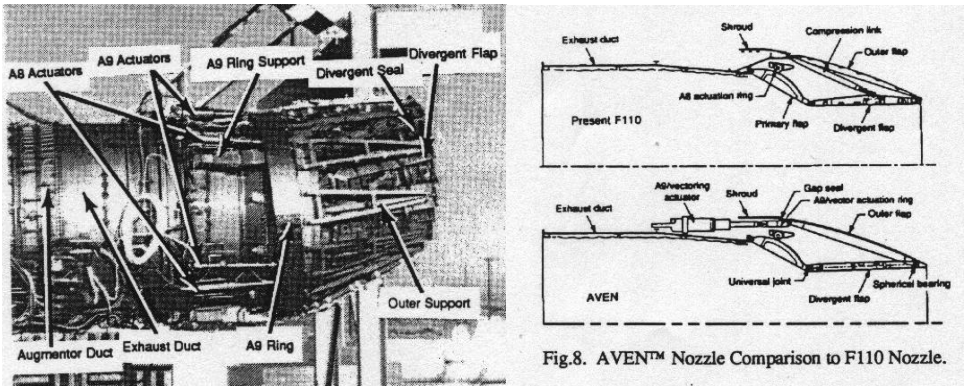

Figure 6-3 and 6-4 [Ref 32]

Since the thrust is vectored in the divergent section of the nozzle, aft of the chocked nozzle throat, the engine is unaffected by pressure fluctuations from the nozzle.

6.2.3 ADEN nozzle

The ADEN nozzle is a 2-d thrust vectoring nozzle which can be extended to include directional thrust vectoring with the addition of articulated sidewalls. In its simplest format this nozzle consists of a variable external expansion ramp (VEER) which is rotated in the vertical direction to control longitudinal thrust vectoring angle. The resulting exhaust flow field from this nozzle is rectangular.

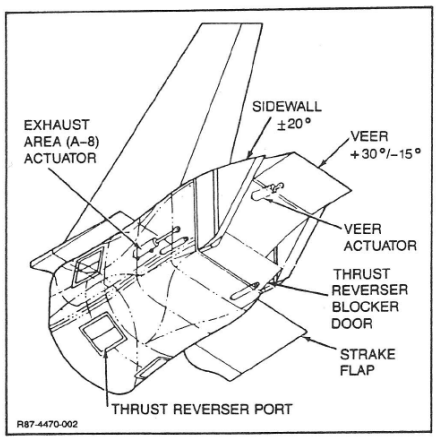

Fig. 2 X-29A/ADEN Two-Axis Vectoring Nozzle Conceptual Design

Figure 6-5 [Ref 33]

6.2.4 Lyulka Saturn AL-31FU/P

The Lyulka Saturn AL-31P and AL-31FU are thrust vectoring capable production versions of the AL-31 range of military turbojet engines. The AL-31 range of engine are reported as having high gas dynamic stability and strength and able to maintain reliable engine performance in extreme conditions of inlet distortion. Such an engine has thus until now been an excellent choice for a highly manoeuvrable aircraft.

The AL-37FU engine is fitted with a 2-d (pitch) afterburning-articulating/steerable nozzle and is currently fitted to the Su-37 and Su-47 aircraft. This titanium nozzle has the ability to deflect the thrust by ±15° at a rate of 30°/sec. When fitted to twin engined aircraft, the nozzles can be deflected collectively, differentially or even unsymmetrically.

The 83kN AL-31FP engine, which is fitted with a prototype 3-d vectoring nozzle, is only 110kg heavier and 0.4m longer than the baseline AL-31F engine with the same thrust output. The AL-31F family of engines (plus the improved 117S) are upgradeable to the AL-31FP at any time without any changes to the airframe. The AL-31FP is currently used in the SU-30MKI and has demonstrated vectoring capabilities 32 degrees in the horizontal plane and 15 degrees in the vertical plane.

Figure 6-6, 6-7, 6-8 [Ref 34]

6.3 Mechanical thrust vectoring research projects

6.3.1 McDonnell Douglas F-15 S/MTD (STOL and Manoeuvre Technology Demonstrator)

The goal of the S/MTD programme was to demonstrate six emerging technologies, which include thrust vectoring, integrated flight propulsion control systems, enhanced lift systems, enhanced avionics systems, low grade runway landing gear and advanced post stalled engine intakes (which reduce flow distortion). An F-15 airframe (capable of Mach 2.1) was used as a test bed, which was fitted with canards, derived from the stabiliser of an F/A-18. This was fitted with two P&W F-100-PW-200 turbofan engines which were fitted with 2-d converging-diverging thrust vectoring nozzles. A combination of movable nozzles and vanes in the jet pipe was able to produce deflection angles of +/-20°. The complex flight control system allowed the thrust vectoring nozzle to be integrated with the operation of the canards and elevators to provide enhanced manoeuvrability.

The work investigated ways to reduce the field length required by the aircraft to increase its operational flexibility, by means of the combined operation of thrust reversing, thrust vectoring and canards. This allowed the take-off rotation speed to be reduced to 43mph, the take-off roll distance to be reduced by 25% and the landing field length to be reduced from 2,300m to just 500m. The work also investigated some of the enhanced manoeuvres which could be possible with such a configuration. This included rapid in-flight deceleration with thrust reversal and using the canards as airbrakes as well as controlled flight at angles of attack of about 85° (without tail surfaces).

6.3.2 NASA F-15 Advanced Control Technology for Integrated Vehicles (ACTIVE) programme

The 1993-1999 ACTIVE programme was a research collaboration between a number of parties to enhancing the performance and manoeuvrability of future aircraft (civil and military). Of particular interest was the feasibility of replacing conventional aerodynamic with multi-axis thrust vectoring nozzles. This project reused the aircraft of the earlier S/MTD programme with replacement P&W F-100-229 engines fitted, along with newly developed 3-d P&W PYBBN axi-symmetric thrust vectoring nozzles. These

nozzles enable the thrust to be vectored by 20° in both the pitch and yaw directions or any combination of these, while retaining an acceptable top speed of Mach 2.0. Such a configuration required a control system capable of controlling the nozzle, engine and conventional control surfaces.

The flight tests demonstrated both pitch and yaw vectoring at speeds up to Mach 2. Yaw vectoring of the aircraft while at 30° angle of attack was also successfully demonstrated. Finally, an adaptive performance software program (developed as part of the project) was demonstrated which could optimise the nozzle and control surface deflections for minimum drag. The aircraft later went on to be reused once again in the 1999 IFCS (Intelligent Flight Control System) programme as well as also being able to lend itself to other research activities outside the ACTIVE programme.

6.3.3 General Dynamics F-16 Multi-Axis Thrust Vectoring (MATV) programme

The goal of the MATV programme was to investigate high angle of attack flight at altitudes above 20,000ft with Multi-Axis Thrust-Vectoring. The aircraft used was a modified F-16 which originated from the 1988 VISTA (Variable stability In-flight Simulator Test Aircraft) programme, where it was originally used to perform variable stability test flights. The variable stability computers and controls were removed for the MATV project and the aircraft was fitted with a P&W F100-PW-220 turbofan engine (with afterburner) and AVEN thrust vectoring nozzle. This enabled the aircraft to perform super-manoeuvres in the post-stalled domain, while also being able to fly at speeds in excess of Mach 2. The same aircraft was also used for testing the P&W PYBBN.

6.3.4 NASA F/A-18 High Angle of Attack Research Vehicle (HARV) programme

The NASA HATP (High Angle-of-Attack Technology Program) used a HARV (High Alpha Research Vehicle) F-18 aircraft to investigate controlled flight at high angles of attack. This 1987-96 project was the first NASA project to demonstrate mechanical thrust vectoring and high alpha flight at subsonic speeds. The X-31 and F-15 ACTIVE projects later went on demonstrate high alpha flight at supersonic speeds.

The test aircraft was fitted with two modified GE-F404-400 turbofan engines in which the divergent sections of each nozzle was removed and three inconel paddles were externally mounted around each exhaust. This configuration allowed pitch and yaw vectoring of the aircraft from coordinated deflection of the vanes into the thrust stream. Removal of the nozzle divergent section meant that the aircraft was limited to subsonic flight. Hinged forebody strakes were also added which were able to provide control at high angles of attack by interacting with vortices generated in this domain. Flight control system improvements included new control laws to integrate the thrust-vectoring nozzle with the existing control surfaces to achieve the optimal benefit from each device. In total, the aircraft modifications added 3,750lbs to the weight of the aircraft

Controlled flight at 70° angle of attack and high roll rates at 65° alpha were demonstrated. However, there were a number of disadvantages associated with this system and as a result, internal thrust vectoring concepts were given preference in subsequent NASA research efforts.

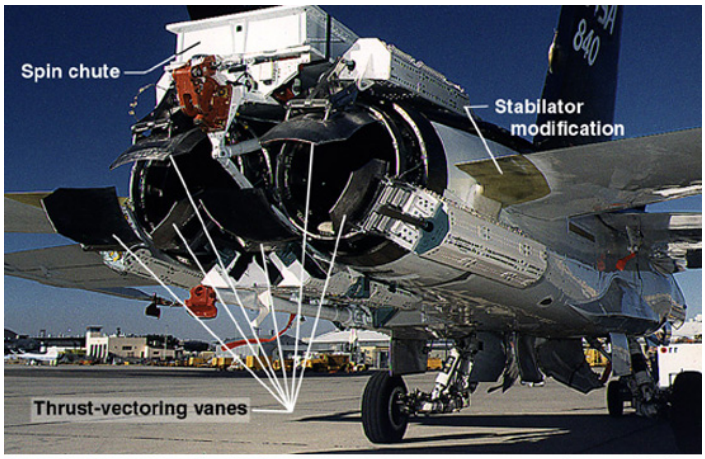

Thrust-vectoring control system. (NASA photo EC90-177-4 with text added).

Figure 6-9 [Ref 35]

6.3.5 The STOL Exhaust Nozzle (STOLEN) Concepts Program

The objective of the 1980s STOLEN project was to investigate a number of potential exhaust vectoring concepts suitable for STOL. The specifications for the project were to devise advanced tactical fighter concepts able to meet a field length requirement of either 700 or 1000ft. This necessitated the need for high vector angles to reduce the axial thrust and increase lift.

The STOL concepts investigated were based on variants of existing VTOL and CTOL nozzle designs and included, both side and rear exhaust vectoring systems with axi-symmetric and non axi-symmetric nozzles. These were fitted to either a RB406-03 military turbofan (with a variable area mixed exhaust) or a RB420-02 separate flow engine (where the bypass fan flow exhausts through two variable area side nozzles and the core flow is exhausted through a single variable area rear nozzle). The thrust from the core flow was supplemented with an afterburner and that of the side nozzles was supplemented with a plenum chamber burner (located just before each side nozzle).

Four aircraft configurations were studied, Aero Balanced Deflected Thrust (ABDT), Jet Balanced Deflected Thrust (JBDT), Vectored Fan Thrust (VFT), Vectored Total Thrust (VTT). These investigated the use of blown canards and a fan air driven pitch pipe to counteract the pitching moment due to the thrust vectoring nozzle as well as investigating the use of front nozzles for thrust vectoring. The thrust vectoring nozzles used were, VACS, RAMP, 2D-CD and CRD TRBPN. These ranged from rotating side mounted elbow ducts with variable area nozzles to movable plates and deflector doors and allowed the thrust to be deflected by up to 70º. The conclusion was that side mounted ducts gave the shortest ground roll results. Adding STOL capabilities to a tactical aircraft was estimated to incur a mere 3% increase in TOGW.

6.3.6 Rockwell-MBB X-31

Following on from the HARV programme, was the NASA X-31 Enhanced Fighter Manoeuvrability (EFM) programme, in which the aircraft was used to test the tactical benefits of thrust vectoring. Thrust vectoring was combined with a sophisticated coupled flight control system to enable the effectiveness of controlled manoeuvres at high angles of attack to be tested while in an air combat situation. The horizontal tail surfaces were removed and the single thrust vectoring nozzle was supplemented with canards and aft fuselage fixed strakes to further increase its manoeuvrability and stability.

The three paddle thrust vectoring system (as fitted to the F-18 HARV) was fitted to the exhaust of a GE F404-GE-400 turbofan engine. The carbon-carbon composite paddles (capable of withstanding temperatures of up to 1500ºC) were mounted directly to the airframe and provided both pitch and yaw control. Although the design speed of the X-31 was Mach 0.9 (40,000ft), the thrust vectoring system was tested at Mach 1.28 (35,000ft).

The design of the X-31 demonstrator aircraft descended from the earlier HiMAT and (Highly Manoeuvrable Aircraft Technology Program) in which tests were carried on a remotely piloted research vehicle. The design of the thrust vectoring system was built on experience gained from the SNAKE programme (Super Normal Attitude Kinetic Enhancement) which investigated the use of paddles as a low cost means of thrust vectoring. In the development of the multi-axis X-31 thrust vectoring system, 498 paddle and nozzle configurations were tested and then used to down select the final configuration. Initial tests revealed a weakness in the post-stalled pitch control of the aircraft, which was fixed with the addition of aft fuselage strakes to the aircraft.

The X-31 programme successfully demonstrated controlled flight at 70° AoA and the execution of a Herbst manoeuvre (rapid 180° turn using a post stalled manoeuvre). The X-31 has since been involved in the NASA Vectoring, Extremely Short Take-off and Landing, Control and Tailless Operation Research (VECTOR) project. This goal of this project was to research the autonomous short landing of an aircraft at a high angle of attack. As well as building on the work of the X-31 programme, this project integrated a modified EuroJet EJ200 engine with a novel axi-symmetric thrust vectoring nozzle. The nozzle was developed by Industria de Turbo Propulsores (Spain) and is able to offer multi-axis vectoring capability while being capable of varying its throat and exit areas with a minimal number of control actuators.

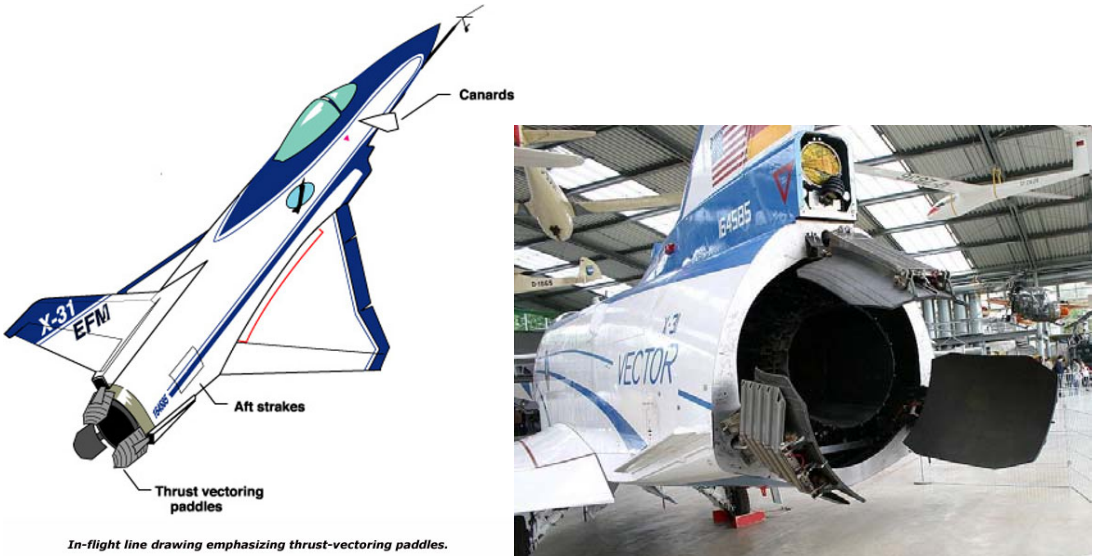

Figure 6-10 [Ref 36] and 6-11 [Ref 37]

6.3.7 Boeing X-32

The Boeing X-32 was a Mach 1.6 capable (at altitude) direct lift STOVL demonstrator aircraft, designed around the requirements of the Joint Strike Fighter competition. The aircraft used three-poster thrust vectoring system, powered by a P&W F135 afterburning turbofan engine located in the forward fuselage. The exhaust gases were directed to lift nozzles at the rear of the engine and a pitch axis thrust vectoring nozzle (via a afterburner) at the rear of the aircraft. The three lifting nozzles are fixed and do not rotate, instead the exhaust gases are ducted to them. During testing, it was noted that the hot exhaust gases had a tendency to get sucked back into the engine, which caused it to overheat along with a loss in thrust. The contract was ultimately lost to the Lockheed Martin X-35 and the X-32 was retired to a museum.

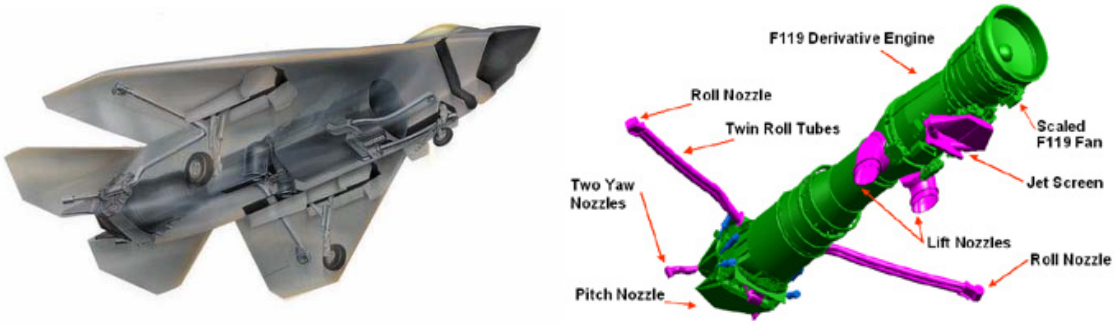

Figure 6-12 and 6-13 [Ref 38]

6.3.8 Lockheed Martin X-35

The X-35 was the Mach 1.6 capable rival to the X-32 and winner in the JSF competition. The aircraft later went on to production with the F-35 designation. The aircraft comes in three variants, a conventional fighter, a STOVL fighter and a carrier capable fighter. The STOVL variant, as is discussed here, is the baseline of the three

configurations. The carrier capable variant of the aircraft was given a bigger wing and tail surfaces as well as a strengthened landing gear. The conventional fighter configuration variant of the aircraft enables the lift fan to be replaced with a large fuel tank for increased range.

The Lockheed Martin lift system consisted of a vertical contra-rotating lift fan which was situated at the middle of the aircraft (just behind the cockpit) and shaft driven from a P&W F119 engine. Propulsive lift comes from a combination of thrust from the lift fan and vectored exhaust gases from a three bearing pitch-axis vectoring main engine nozzle. The shaft-driven fan arrangements ability to move a large mass of slower moving air made it more efficient than other concepts and is able to support almost half of the aircrafts weight. As it does not use high velocity hot exhaust gases it is also less likely to damage runway surfaces. During normal flight, the lift fan is disengaged and the lift fan bay concealed with upper and lower clamshell doors. At low speeds, a further set of doors open to uncover an auxiliary intake for the engine. Roll control is provided by roll-post nozzles located on each wing tip, which uses air from the LP turbine of the main engine. Although the lift system is unnecessary weight during normal flight, it has the added benefit of enabling heavier payloads to be carried while still achieving a satisfactory field length. Although the X-35 was designed with stealth in mind, the unshielded circular nozzle does make the aircraft vulnerable from the rear.

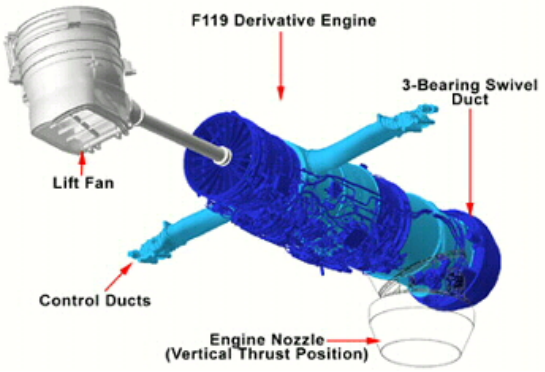

Figure 6-14 [Ref 39] and 6-15 [Ref 40]

6.3.9 McDonnell Douglas X-36

The unmanned X-36 was a 28% scale prototype of a possible low-observable fighter configuration, which was used to research tailless fighter agility. Its low observable features included, no tail, aligned edges, a wide flat exhaust. Conventional control surfaces were eliminated with aircraft control being instead achieved with: all moving canards, split ailerons and an advanced thrust vectoring. The thrust vectoring system was only used to supplement the directional control from the drag rudders on the wing tips. It used a Williams F112 turbofan engine and was reported to be capable of 234mph but unstable in the pitch and yaw axes, necessitating the need for an advanced flight control system.

During flight testing, the aircraft demonstrated, stable flight at 40° AoA, 360° rolls at 15° AoA and rapid turning/rolling manoeuvres at 35° AoA. At the end of the project

there were still concerns about its safety in the event of a flight control effecter failure. This led to the aircraft being later used to test Reconfigurable Control for Tailless Aircraft (RESTORE) software developed by the AFRL. Although the X-36 was shown to be very successful, the full-scale design was never produced. Instead it is believed that the experienced gained was used in the design of the X-45A UCAV.

Figure 6-16 [Ref 41]

6.3.10 Lockheed Martin X-44 MANTA

Following the advancements made by the F-15 Active and X-31 Vector programmes, the US Air Force and NASA initiated the X-44 MANTA (Multi-Axis No-Tail Aircraft) flight test programme. The goal of the project is to demonstrate the feasibility of a pure thrust vectored aircraft. The tail plane will be completely removed, with pitch, yaw and roll control being provided by a 3-d thrust vectoring nozzle. It is reported that the stealthy aircraft will be a converted F-22 with a large delta wing, fluidic nozzles and supersonic cruise aerodynamics.

6.3.11 Mitsubishi ATD-X

The Mitsubishi ATD-X is a Japanese advanced technology demonstrator aircraft which is not expected to fly until 2016 and therefore little information available. The ATD-X will be used to research the viability of advanced technologies which include 3-d thrust vectoring. The thrust vectoring system planned consists of 3 paddles on each engine nozzle, as seen on some of the US X designated aircraft. It is however thought that the uncovered nozzles may give rise to a stealth penalty of the aircraft.

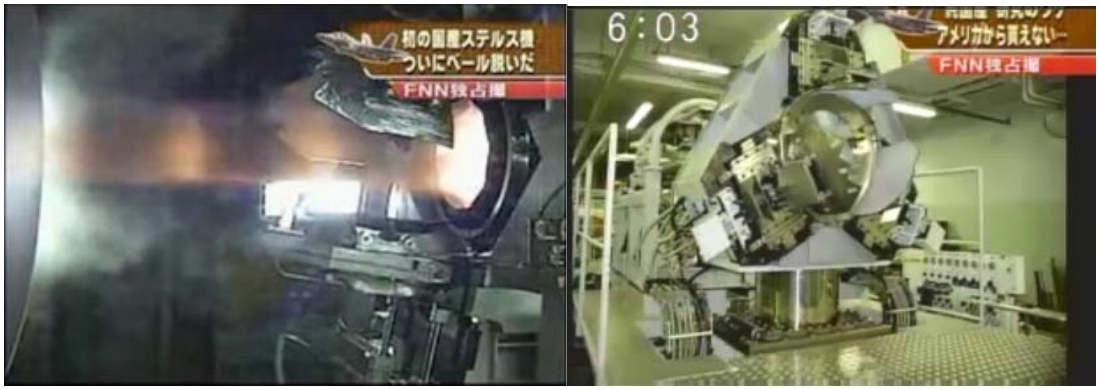

Figure 6-17 to 6-20 [Ref 42]

6.3.12 Harrier

No study of thrust vectoring systems is complete without mentioning the Harrier since this lead the way in the development of vectored propulsion theory and practice. The Harrier relies on its four poster thrust vectoring system for VTOL capabilities rather than super-manoeuvrability. During take-off and landing, the four nozzles of the Pegasus engine thrust are rotated to deflect the thrust downwards. During normal flight, the nozzles return to their normal position for forward propulsion of the aircraft. Pitch and roll control was achieved with reaction control valves (which used air bled from the engine) located on the nose, tail and wing tips of the aircraft.

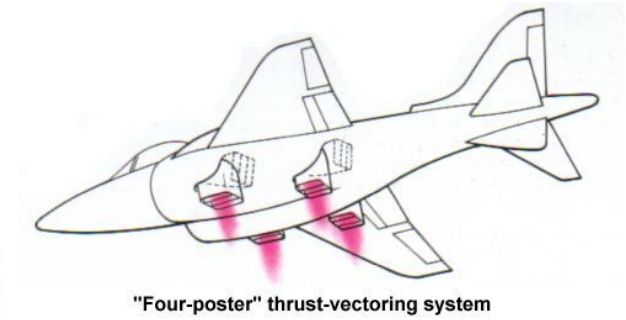

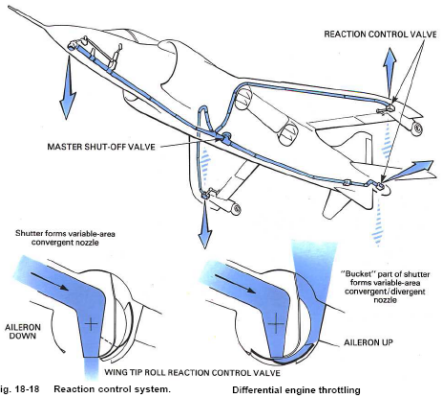

Figure 6-21 [Ref 39] and 6-22 [Ref 27]

6.3.13 Grumman X-29A

The initial goal of the cancelled X-29A project was to evaluate a forward swept winged aircraft at an angle of attack up to 40º without thrust vectoring and up to 90º with multi-axis thrust vectoring. The aircraft was a close coupled variable incidence lifting canard design in which the flow field of the canard and wing interact favourably with each other. The relaxed stability aircraft (35% statically unstable) relies upon a full authority digital fly-by-wire flight control system. The partially thrust vectored aircraft used an ADEN (Augmented Deflector Exhaust Nozzle) thrust vectoring nozzle fitted to a GE F404-GE-400 engine and retained the original aerodynamic flight control surfaces. Lateral-directional manoeuvres which were not possible at high angle of attack

manoeuvres for the normal aircraft (due to masking of the rudder by the fuselage) could be successfully carried out with directional thrust vectoring. The benefits of longitudinal thrust vectoring were assessed as a 17% reduction in take-off speed, 37% reduction in take-off distance and 20% reduction in take-off time.

6.3.14 F-22 Raptor

The F-22 raptor used the first ever production thrust vectoring nozzles fitted to two P&W F119-100 engines. The pitch only mechanical vane thrust vectoring system is capable of delivering up to 20 degrees pitch vectoring to enhance the maneuverability of the aircraft.

Figure 6-23 [Ref 43} and 6-24 [Ref 44]

6.3.15 X-45

Little in known about the X-45 thrust vectoring system except that it builds on the experience of the X-36 aircraft, is an internal thrust vectoring system and is used for yaw control only.

6.3.16 Thrust vectoring for the Eurofighter

The European fighter aircraft (EFA) is not currently equipped with any form of thrust vectoring and concerns have been raised that this may make the aircraft vulnerable. As a result, on-going research work is being carried out to investigate a modified nozzle which could be used to add thrust vectoring capability to the aircraft. The convergent-divergent thrust vectoring nozzle which was developed by ITP has the ability to vector the thrust by 30º in three dimensions. This nozzle is based on three concentric rings enabling it to offer variable area control for the throat and exit areas to further improve its efficiency. It is also claimed to be the lightest in its category.

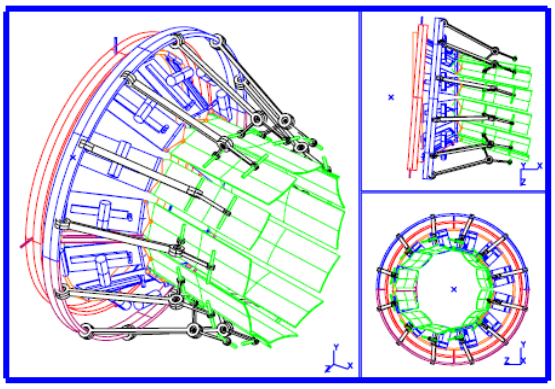

Fig. 9.- Nozzle Movement in vectoring

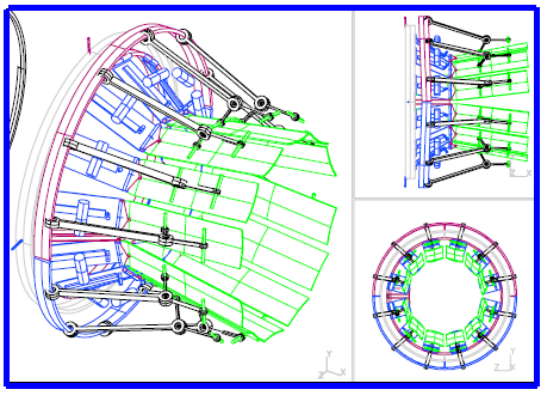

Fig. 12.- Nozzle Movement in A9 control

Figure 6-25 and 6-26 [Ref 45]

6.3.17 The B2

To reduce the radar signature of this stealth aircraft, there is no conventional tail and alternative means of aircraft control have been incorporated. Pitch and roll control are achieved with three elevons located on each side of the aircraft. Yaw control is achieved with the use of drag rudders located at the extremities of each wing and are able to function as both an airbrake and rudder as required. Unfortunately, the drag rudders are inoperative at deflections below 5º and therefore have to be left slightly open in flight. As this is detrimental to the stealth characteristics of the aircraft, differential engine operation is used for yaw control instead where possible. Although this is not thrust vectoring in the true sense it is still worth including in any study.

6.3.18 Sukhoi-37

This uses two Lyulka Saturn AL-31FU thrust vectored engines to enhance its maneuverability. These 2-d nozzles are able to vector by -15º to +15º in the pitch plane but can also be deflected differentially or collectively to achieve the desired control. Although they are integrated into the digital flight control system, they can be operated either automatically by the FCS of manually by the pilot.

6.4 Fluidic thrust vectoring research effort

A number of research studies have been carried out in to fluidic thrust vectoring. The key players in this field to date have been NASA but another significant contribution has been made by the recent Flaviir project. In addition, there has been a number of smaller research efforts conducted at many of the universities such as the Florida State University. The only commercial non-mechanical thrust vectoring nozzle reported to date is the Exact nozzle as developed by Williams for the Cirrus aircraft [46]. There is however expected to be other non-commercial nozzles in use on military aircraft but as to be expected no information is available.

6.4.1 Fluidic research at NASA

NASA has been actively researching fluidic thrust vectoring for some time with reports being available which date back to the early 1990's. The objective of their research efforts was to evaluate the use of fluidic thrust vectoring nozzles as a means to reduce the weight and observability of an aircraft. A range of fluidic concepts were explored which were able to offer, thrust-vector angle control, throat area control and expansion control. The fluidic thrust vectoring concepts being researched by NASA were:

- Shock vector control method
- Throat shifting method
- Counter flow method

These were tested and evaluated by a range of both computational and experimental studies at NASA Langley Research Centre. The latest update on fluidic thrust vectoring within NASA dates however back to 2003 with no more up to date information being available. It is therefore unknown whether NASA is still active in this research area.

6.4.2 The Flaviir project

Amongst other technologies, the Flaviir project investigated the viability of replacing conventional control surfaces with fluidic devices. Fluidic circulation control devices were retro-fitted in place of conventional ailerons and a fluidic thrust vectoring nozzle replaced a conventional straight through jet pipe. The fluidic thrust vectoring nozzle was based on the co-flow concept, which differs from the counter-flow concept by the direction of the secondary flow. The secondary air is therefore blown out of the nozzle instead of being sucked in a direction against the primary flow.

The research effort was initiated by Mark Mason [28] and the concept further developed by later students after it became part of the Flaviir project sponsored by BAE/EPSRC. Development followed a series of computation and experimental studies, in which the control and flow characteristics were evaluated and refined. The concept was finally evaluated on a series of model aircraft with promising resulting being reported. A larger scale nozzle was then built and tested, which unfortunately highlighted a number of problems at this larger scale and the nozzle was never tested on the Flaviir flying demonstrator. The nozzle does show promise but possibly only for smaller air vehicles. The problems highlighted in its development are control instability, control dead-zones, manufacturing difficulties due to the required tolerances and the provision of a large amount of the secondary jet. The greatest difficulty for the flying demonstrators proved to be the provision of a mass flow rate of air sufficient for the secondary jet. The only practical way to achieve this was to use engine bleed air but the amount of bleed required would have been too detrimental to the performance of the main engine. Therefore, a secondary engine was used whose sole purpose was to supply bleed air.

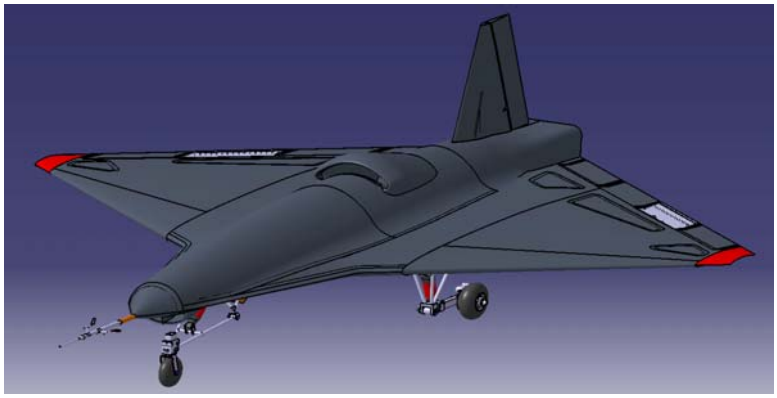

Figure 6-27 – Configuration of the Flaviir Demon demonstrator UAV

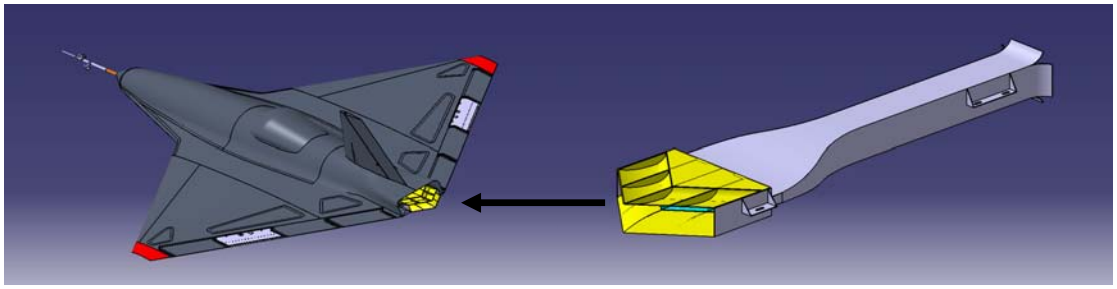

Figure 6-28 and 6-29 – The co-flow thrust vectoring nozzle developed as part of the Flaviir project [Courtesy of Manchester University]

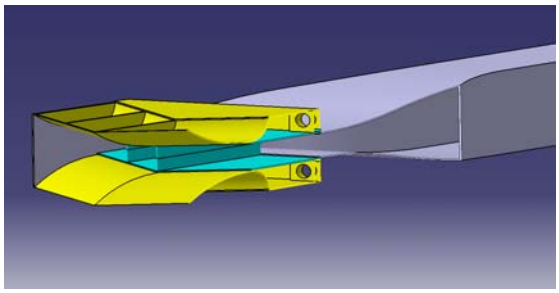

Figure 6-30 – Cross-section through the co-flow thrust vectoring nozzle developed as part of the Flaviir project [Courtesy of Manchester University]

6.4.3 The Cirrus Vision aircraft and the Williams Exact nozzle

The Exact nozzle developed by Williams for the Cirrus Vision aircraft is reported as being a pressure ratio thrust vectoring nozzle [46]. This nozzle allows the thrust from the top mounted engine to be vectored as required to increase the cruise speed and improve the pitch-thrust coupling effect and thus the handling at low speeds. The most significant vectoring takes place at low altitudes and low speeds with it being straighter at high altitude cruise. The nozzle was developed specifically for the Cirrus Vision aircraft with several nozzle geometry configurations being tested on the aircraft to arrive at the optimal geometry to achieve the best handling characteristics.

The nozzle itself is reported as using the coanda effect with no moving parts and with little more being known about its operating details. The presence of a coanda surface would initially suggest that it is either of a co-flow or counter-flow type but the axi-symmetric design of the nozzle exit could indicate a different means. It is possible that there is no secondary flow and the angle of the primary jet is dependent on the operating characteristics of the nozzle and the ability of the flow to follow the coanda surface.

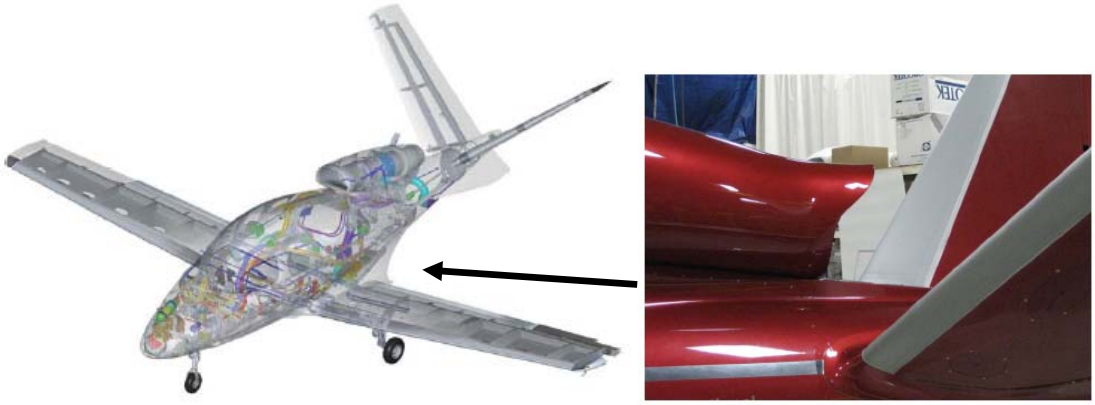

Figure 6-31 and 6-32 – The Williams Exact thrust vectoring nozzle [Ref 46 – Cirrus Update 2010]

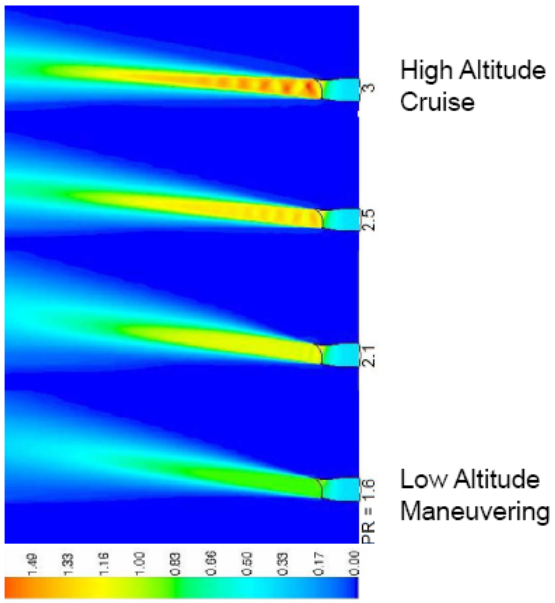

Figure 6-33 – CFD results for the Williams Exact thrust vectoring nozzle at high and low altitude operation [Ref 46 – Cirrus Update 2010]

7 Design and integration considerations for thrust vectoring systems

7.1 An overview of the fundamental concepts

7.1.1 An overview of exhaust nozzles

The simplest of all the exhaust nozzles is the convergent nozzle. Their performance is limited, but with careful design, they are able to offer satisfactory performance up to transonic speeds. They are, however, only efficient over a narrow operating range but this can be expanded with a variable area configuration. When it is necessary to meet high speed and performance requirements, full expansion from a convergent nozzle can not always be achieved, and in such cases a convergent-divergent nozzle is required. Variable geometry derivatives are able to offer the benefits of higher performance and efficiencies throughout a wider aircraft flight envelope. When the performance of the convergent-divergent nozzle (including the thrust vectoring variants) configurations needs to be extended for short periods, an afterburner can be used. These are fitted upstream of the nozzle and typically necessitate the need for a variable geometry nozzle to allow the nozzle throat area to be increased (to maintain constant flow and the correct back pressure). A more detailed overview of the common exhaust nozzles is given in Appendix C and the reader is advised to refer to this section for more information.

Thrust vectoring nozzles do share similarities with other exhaust nozzles and can still be categorised as being convergent or convergent-divergent according to their operating requirements. The internal vectoring nozzles for example can be seen to retain their convergent-divergent geometry when vectored, although now with a deflected flow path. It is possible to offer convergent nozzles with thrust vectoring capabilities, but their performance will be limited. The majority of thrust vectoring nozzles are therefore of the convergent-divergent type and are categorised as 2-d or 3-d according to their vectoring abilities. As to be expected, the mass, cost and complexity of the nozzle will however be increased somewhat as a result of increasing nozzle performance abilities. Therefore, the use of a convergent-divergent configuration, afterburners and/or thrust vectoring should be justified otherwise a more simplistic approach should be adopted.

7.1.2 The engine and exhaust nozzle sizing process

In order to maximise its performance, exhaust nozzles should be designed to achieve full expansion. However, since the performance of an exhaust nozzle is directly related to the performance of the accompanying engine, the design of the nozzle is complex and must be integral with the design of the engine. The final nozzle configuration is therefore a trade-off between many requirements. For example, nozzles can be designed purely to achieve maximum possible thrust but this can lead to problems of high temperatures, pressures and possible engine surge. A more detailed overview of the engine and exhaust nozzle sizing process is given in Appendix C and the reader is advised to refer to this section for more information.

7.2 Thrust vectoring nozzle design and integration

This discussion builds on the discussion for the design and integration of a general exhaust nozzle as given in Appendix C and the reader is advised to refer to this section for background reading. It should be noted that the scale of the benefits attainable from a thrust vectoring system is dependent on many design factors. In order to reap the most benefit from such a system, it must be integrated into the design as early as possible, preferably at the conceptual design stage. An example of this is that conventional control surfaces will be redundant and only act to hinder aircraft performance on an aircraft which uses thrust vectoring as its primary means of flight control. The class of aircraft on to which the system is to be fitted, must also be considered since a thrust vectoring system designed for a combat aircraft is unlikely to realise its potential on a reconnaissance aircraft.

Since the design and integration of an exhaust nozzle can be considerably complex and encompass so many different streams of aeronautical engineering, it is not possible to go into great depth within the constraints of this thesis. Therefore only an overview of some of the design and integration considerations will be given in the sections below.

7.2.1 Thrust vectoring nozzle design requirements

As with any other part of the aircraft, any exhaust nozzle will be designed to meet design requirements laid down by the airworthiness regulations, customer and other internal design groups. A thrust vectoring nozzle will be subject to additional design requirements such as:

- Max sustainable TV angle. This will always be less than the nozzle deflection angle. (20-25 degrees is reasonable for a mechanical paddle system)
- Total system weight. This includes all the actuators, control systems, hydraulic pumps and other ancillary equipment.
- Nozzle efficiency when vectored. This accounts for losses in engine thrust due to vectoring.
- Thrust vectoring efficiency. The deflection angle of the thrust line of action will be less than the nozzle deflection angle, which is accounted for by this term.
- Complexity and Maintainability. The higher moving part count of thrust vectoring nozzles makes them more complex than other nozzles and they require more frequent maintenance as a result.
- Safety. This includes the ability to vector the thrust in a controlled manner without failure as well as the controllability of an aircraft in the event of engine failure/flame-out.
- Observability. This covers the effect of the system on RADAR and infrared signatures. One method of reducing the radar cross-section of the nozzle is by shaping to a flattened arrowhead shape (as used on the X-45A). One of biggest infrared emitters is hot exhaust gases which heat up the metal parts, which can be reduced by nozzle cooling or shielding.
- Operational Effectiveness. How will the thrust vectoring nozzle affect the rest of the aircraft, engine and aircraft systems. This includes factors such as boat-tail drag, super-circulation lift gains (from integrated high aspect ration nozzles) and the impact on engine performance as a result of bleed air and power off-takes.

As a result of their extended manoeuvring capabilities, post-stalled manoeuvre capable aircraft are subject to additional design requirements. Research by Herbst determined the following requirements in such cases:

- Adequate control power must be available about all 3 axes for Mach numbers down to 0.1 and angles of attack up to 70 degrees.
- Sufficient aircraft stability and engine intake performance is necessary for Mach numbers up to 0.6 and angles of attack up to 70 degrees.
- The aircraft thrust loading (T/W) should ideally be no less then 1.2.
- Intelligent flight control systems are required which are capable of calculating the control inputs required for coordinated flight manoeuvres with regards to the main velocity vector.

7.2.2 Exhaust system layout

As shown in the figure below, the exhaust nozzle of a buried installation is only one part of the exhaust system. The propelling nozzle is located at the very rear of the aircraft and is connected to the exhaust cone of the main engine via a jet pipe. The total length of the exhaust system is dictated by the layout of the aircraft configuration and in particular the positioning of the engine within the fuselage. The respective lengths of the jet pipe and nozzle are, however, design choices. The length of a thrust vectoring nozzle for example is a trade-off between the weight savings possible with a short nozzle and the nozzle length required to overcome internal flow problems such as separation, non-uniformity and swirl.

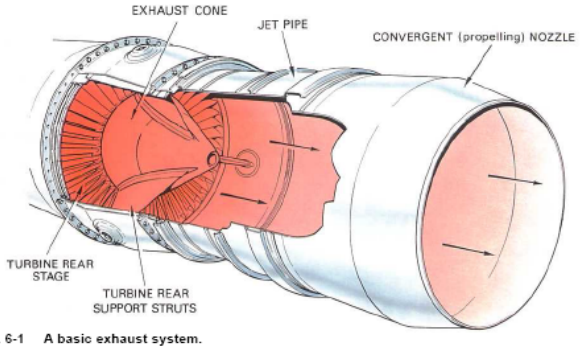

Fig. 6-1 A basic exhaust system.

Figure 7-1 – A typical buried engine complete exhaust system [27]

7.2.3 Jet pipe design

The jet pipe may at first sight appear to be a simple transition section connecting the propelling nozzle to the exhaust cone but its design is, however, more complex. For example, its area is gradually increased in order to be able to act as a diffuser to reduce the speed of the high speed gases entering the jet pipe. This helps to reduce friction losses associated with the gases moving through the exhaust system. Since the gases pass through flow straighteners before entering the exhaust system, losses due to swirl are less of a problem. When high aspect ratio nozzles are used, the jet pipe becomes a circular to rectangular transition duct, which must be designed so that the exit velocity profile remains as uniform as possible in order to minimise pressure losses.

7.2.4 Cooling requirements

The high temperature of the exhaust gases passing through the nozzle necessitates the need for high temperature materials and appropriate cooling methods. The nozzle components which are directly impinged on by the hot exhaust gasses have the most severe cooling requirements. This means that thrust vectoring nozzles have significantly greater cooling requirements than conventional nozzles and typically use film cooling methods. The shape and therefore the internal surface area of a nozzle also have an impact on cooling requirements (as is the case for 2-d vectoring nozzles which are usually rectangular). It should also be noted that the temperature across the surface of a nozzle may not be uniform (especially in the case of 2-d nozzles which experience a non uniform field in mid flap compared to the corners). These temperature fields can result in internal stresses and distortion of the nozzle and therefore the nozzle must be cooled in accordance.

Since engine bleed air is used for cooling the nozzle, the engine size and weight or even influence the choice of engine cycle selected is influenced by the nozzle cooling requirements. There is a perfect balance with regards the amount of cooling air to use. There must be sufficient cooling air to protect the structural integrity of the nozzle but not too much which would result in a significant detriment in engine thrust. A solution to the cooling flow requirements of nozzles may be the use of an ejector system, which may also result in an improved propulsion system. This does, however, have the disadvantage of complicating the propulsion system installation as in-depth consideration of the inlet and nozzle installations is required. The cooling of very high temperature can be further improved by using a double wall construction for the nozzle walls. This has an added benefit that the external wall also acts like an insulating blanket to reduce noise. In such an arrangement, cooling air is drawn between the nozzle walls by the ejector principle.

Although cooling is a major problem for current thrust vectoring nozzles, this will be less of an issue for the next generation of nozzles manufactured from RCC materials. Such materials are able to maintain their shape and structural integrity at higher temperatures and therefore have lower cooling requirements. These are, however, still in the early stages of development.

7.2.5 Weight and centre of gravity considerations

The weight of a nozzle is relative to its functional ability and its complexity and thrust vectoring nozzles can be considerably heavy. Although the weight of the aircraft is increased as a result, of greater concern is the location of this additional mass at the rear of the aircraft. This not only shifts the centre of gravity rearwards but also increases the pitch inertia of the aircraft. Potential weight savings are available with the advent of new mechanical thrust vectoring nozzle concepts as well as the use of novel materials. The new class of fluidic thrust vectoring nozzles are also reported to offer significant weight savings but these are still in their infancy. In the case of 2-d rectangular converging-diverging nozzles, weight savings may be made by designing the nozzle so that the sidewalls are cut back to be shorter than the diverging flaps. The amount of side wall that can be cut back can be determined by examination of the Mach lines within the nozzle exit as shown in the figure below.

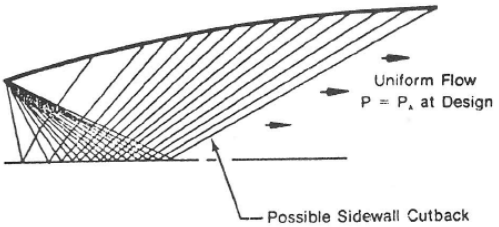

Fig. 15. **Figs. 8 and 12 show that the *sidewalls* of pitch-only, vectored, 2*D*-*CD* nozzles, may be shorter than the diverging flaps.** This is done to reduce nozzle weight (49).

Figure 7-2 – Guidelines for potential nozzle cut-back for weight saving [47]

7.2.6 Metallurgical considerations

A well known restriction in the technological expansion of engines is the temperature limits imposed by current materials. Since increases in engine operating temperature are also imposed on the exhaust system, the exhaust system is also subject to material limitations. Current exhaust systems have to be manufactured from nickel or titanium and use some form of cooling to withstand the high temperatures currently experienced.

A new breed of Reinforced Carbon-Carbon composite materials are being developed which are able to reduce the amount of cooling required for intended hot engine components such as turbine blades and exhaust nozzles. As well as being able to reduce cooling requirements, nozzles constructed from these materials also offer reductions in leakage losses. Overall this leads to an improvement in performance of the propulsion system. These new materials also offer significant weight reductions and enable complex assemblies to be co-formed, which reduced part counts and assembly times. Such materials also have stealth benefits as they are reported be excellent absorbers of electromagnetic waves.

7.2.7 Afterburners

Where an afterburner is required, the complexity, mass and cost of the nozzle can increase considerably. The increase in exhaust gas temperature and thrust associated with afterburners demands the use of a more robust nozzle able to withstand the higher internal stresses and temperatures. It should be remembered that these higher temperatures will also dictate the need for a means of increased nozzle cooling. The incorporation of an afterburner will also have the impact of lengthening the complete engine exhaust and may therefore lengthen and increase the mass of the rear fuselage.

7.2.8 The relationship between engine and nozzle

The inter-relation between engine and nozzle is complicated with many factors to consider. The performance of the nozzle is dependant on factors such as engine throttle setting, nozzle pressure ratio (NPR) and exhaust gas composition (which is dependant on the air/fuel ratio and the combustion efficiency). Engine swirl can have a considerable impact on the performance of a nozzle, which is overcome with flow straighteners. The behaviour of the flow within the engine and nozzle can be complex and the exact performance of a nozzle can only be properly investigated experimentally.

When designing a thrust vectoring system for agility, we also need to give consideration to the response time of the engine. Many current engines are reported to fall short of this requirement and engine developments are required in this area, especially to compressor stall margins and digital flight control systems. This short fall in requirements is not necessarily a design restriction, however, since performance limitations are sometimes imposed by a manufacturer to preserve engine life.

Modifications may be required to an engine which is fitted with a thrust vectoring nozzle since the operation of the nozzle will generate pressure distortions within the engine. When the distance between the engine and nozzle is short, this can cause the fan and turbine blades to vibrate. In such an event, snubbers can be fitted to the fan blades and shrouds to the turbine tips. This is however not an issue for convergent-divergent nozzles since the pressure fluctuations are prevented from being reflected back to the engine by the shock wave at the nozzle throat.

7.2.9 Stability and control and aerodynamic considerations

As already discussed, the installation of a thrust vectoring nozzle will move the aircraft centre of gravity and increase the pitch inertia of the aircraft. In addition to this, the rear of the fuselage may have to be increased to accommodate the nozzle, which will have an impact on the aerodynamic pitch damping of the aircraft. Collectively, these will have an impact on the aircraft static and dynamic stability and control characteristics.

The aerodynamics of the aircraft can also be significantly affected by a thrust vectoring nozzle and in particular the boat-tail drag of the aircraft will be affected by increases in the rear fuselage. In the case of high aspect ratio nozzles, it is possible to carefully blend them in to the trailing edge of a lifting surface to create phenomena known as super-circulation. In such a situation the aircraft aerodynamics are improved due to the generation of favourable interference effects between the exhaust flow and the airflow over the lifting surface. In cases where thrust vectoring is used to contribute to the lift produced by the wings, it is possible to reduce the size of the wings and their accompanying drag.

7.2.10 Detailed nozzle design

The detail design of mechanical thrust vectoring nozzles is a complex process which encompasses many of the different branches of mechanical engineering. Some of the engineering design parameters which need to be considered include:

- Engine operational factors – Thrust requirements, efficiency, engine technology limits, aero-thermodynamics, IR and heat transfer variables
- Design and manufacture - Structural and materials technology limits, manufacturing constraints, mass, installation considerations and cost
- Operational factors - Reliability, durability, safety, cost and maintenance

In particular, careful selection of nozzle materials and its structural layout is essential to prevent distortion of the nozzle. Installation and assembly of the exhaust system must also take into account the expansion and contraction of the different sections, which

requires careful design of the joints and mounts. Failure to do so can result in severe distortion and damage to the nozzle and surrounding structure.

7.2.11 Integration of the next generation of technology

Integration is a discipline which is continually changing as new technologies and engineering approaches are evolving. The integration of a propulsion unit into an airframe has traditionally dealt with aspects such as:

- Space allocation within the airframe and optimisation of the surrounding aircraft aft-body profile.
- Aircraft configuration considerations. The aircraft configuration may have to be modified to compensate for the rearward shift of the centre of gravity by shifting the aerodynamic centre of the aircraft. The easiest way to achieve this is by repositioning the wings on the fuselage.
- Weight and centre of gravity considerations.
- Aerodynamic considerations.
- Stability and control considerations.
- Engine-inlet matching. This takes into consideration airflow requirements and distortion effects.
- Engine bleed air and power extraction requirements.

The advent of new technologies has considerably increased the complexity of airframe/engine integration. For example, the incorporation of electronic control systems (instead of the earlier mechanical inputs) require numerous inputs from the pilot, environment, airframe and engine in order to optimise the performance of the engine/airframe combination.

Thrust vectoring has been noted to be one of the most extreme cases of airframe/propulsion integration and the design and integration of the next generation of exhaust nozzles is not straightforward. In such cases, there are barriers which still have to be overcome such as:

- The desires to maintain inter-changeability between engines from different manufacturers.
- Negative views of highly integrated systems being risky.
- Contractual working environments between engine and airframe manufacturers where teamwork is often not viable.
- Difficulties in the exchange of data between airframe and engine manufacturers.
- The need to recognise the airframe/engine assembly as a single system.

7.2.12 Airframe considerations

An important consideration when integrating a thrust vectoring nozzle into an airframe is ensuring that that there is sufficient strength within the airframe to withstand additional loads generated. Such a task does, however, require prior knowledge of the loads likely to be experienced. Whereas the loads generated by a conventional nozzle are primarily parallel to the axis of the aircraft, a thrust vectoring nozzle is able to generate considerable loads perpendicular to the aircraft axis.

As well as designing the airframe to withstand the control forces generated by the nozzle itself, consideration must also be given to the airframe loads generated by thrust vectoring manoeuvres. According to Gal-Or [47], the load factors on a post-stall technology vectored aircraft during a manoeuvre is dependent on:

- The design of the thrust vectoring system
- The magnitude and direction of the deflected exhaust jet which is time dependent
- Engine throttle settings
- Manoeuvre turn rate and radius
- Aircraft angles of attack and sideslip
- Aircraft speed and altitude just prior to and during the manoeuvre
- Weight and drag components
- Other control deflections and resultant loads

This extensive but not exhausted list of dependant variables highlights the fact that the load factors generated as a result of a thrust vectored manoeuvre can not be accurately predicted by classical methods.

A designer must finally give consideration to the impact of the high exhaust temperatures and ways of preventing heat conduction to the surrounding aircraft structure. Either blowing air around the jet pipe, or lagging the system with an insulating blanket, are the common ways to overcome this problem. The blankets are made from a fibrous/stainless steel sandwich which has the added benefit of reducing noise.

7.2.13 Safety considerations

The development of thrust vectored aircraft must be accompanied by stringent safety assessments to ensure that there is sufficient control redundancy in the event of a failure. In such cases, aircraft relying on thrust vectoring for primary flight control are likely to find that the reliability requirements of the engine and flight control system may prove to be excessive. On the other hand, thrust vectoring would prove to be beneficial to the control redundancy of an aircraft if it is used to augment existing systems.

Of particular concern for thrust vectored aircraft is the total engine failure of both single and multiple engined aircraft. A thrust vectored aircraft should be designed so that in such an event, there is still sufficient control of the aircraft while the engine is either restarted or the aircraft is safely landed. Post-exit nozzle flaps are particularly attractive from this respect as they can be sufficiently sized in order to be able to operate as conventional aerodynamic control surfaces. Depending on the configuration these can provide both pitch and roll control. Where canards are used, they can be controlled differentially to enable roll control and a certain amount of yaw control can be obtained if they have dihedral. Should a nose vectoring jet remain operative when all other vectoring systems have failed, this can be used to provide a certain amount of control. A pneumatic buffer tank may prove useful in such circumstances. In the case of twin engined aircraft; these can be controlled with only one engine operative by using the inoperative external vectoring flap as an aerodynamic aileron and reducing the thrust of the other engine.

7.2.14 A note on engine inlets for thrust vectoring systems

Any engine/nozzle system must consider the effect which large pitch, yaw and sideslip angles have on the performance of engine intakes, since this will ultimately affect the performance of the engine. This is especially an issue for thrust vectored aircraft due to the increase of this effect during super manoeuvres and their reliant on engine power for aircraft control. The design of the intake needs to give consideration to the behaviour of the flow field surrounding the aircraft since this can have a significant impact on its performance. This is a particular problem or thrust vectored aircraft executing complex large angle of attack manoeuvres, since the flow field can become extremely distorted and complex. In such cases, a post-stall capable engine intake must be used since the engine is extremely susceptible to engine stall at these extreme flight conditions. Such inlet configurations are of variable geometry and be able to supply air from the upper and lower wing surfaces.

7.2.15 Flight and propulsion control systems

The benefits of thrust vectoring are dependant on the effective control of the engine and nozzle in relation to the pilot's requirements and the aircraft operating conditions. A selection of some of the requirements which such a flight/engine control systems must meet are,

- A properly designed flight and propulsion control system must be tailored to maintain the correct load/acceleration proportions relative to the pilot's requirements.
- Thrust vectoring control forces must be governed to ensure aircraft and inhabitant limitations are not exceeded.
- Vectoring capability should be selectable by the pilot but then become transparent and its control integrated within the flight control system.
- Thrust losses due to vectoring must be accounted for by increasing the engine thrust as required.
- Allowance must be made for compressor stall margins since engine operating conditions can be directly affected by nozzle geometry via reflected pressure fluctuations.
- Allowance must be made for altitude effects which result in a reduction of engine power and therefore thrust vectoring control power.
- Partially vectored aircraft control systems must make allowance for the control force generated by the aerodynamic control surfaces.
- The thrust vectoring control system must take into account discrepancies between the deflection angles of the exhaust nozzle and exhaust plume.
- The effectiveness of the thrust vectoring system will be dependant on the aircraft operating conditions which must be allowed for.
- Allowance must be made for the response rate of the engine as well as that of the thrust vectoring nozzle to ensure that the system is able to act within the desired timeframe.
- Coupling effects must be allowed for between the payload, weapons, propulsion system and airframe. In such cases, the flight dynamics of an aircraft with and without external payload will be different and need to be accounted for.

A simplistic layout of such a control system is shown in the figure below, which highlights some of the interactions between the different systems.

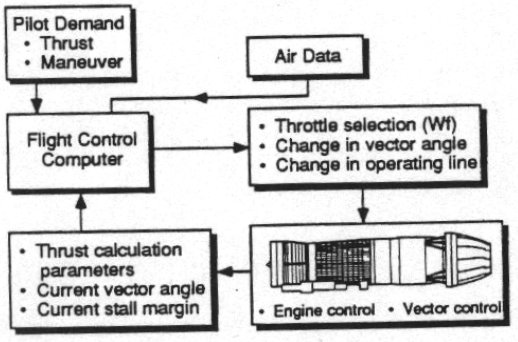

Figure 7-3 [Ref 32]

7.2.16 Modification of existing aircraft

Existing aircraft modified to incorporate thrust vectoring systems a subject to the same design considerations as those listed above. In this case however, the engineer must work within the constraints of the existing airframe which include volume, propulsion, mass and centre of gravity and flight control system constraints. For example, the addition of a heavy nozzle at the rear of the aircraft will need to be counteracted with ballast at its nose. The existing flight control system must also be replaced with one able to co-ordinate the control of the thrust vectoring nozzle with the conventional aerodynamic flight controls. Extensive testing of the modified aircraft configuration will then be required since the flight dynamics will be affected by the interaction with other components such as the wings. As already discussed, external vectoring systems will also work as aerodynamic control devices as well as being influenced by the external flow.

7.2.17 Integration of high aspect ratio nozzles

High aspect ratio nozzles are able to offer benefits of super-circulation, reduced boat-tail drag and lower IR signatures. The nozzle aspect ratio has been shown by experimental testing to be the most important parameter for the performance of these nozzles. To be able to take advantage of the super-circulation phenomena, the nozzle must be integrated into the trailing edge of the wing. In such cases, the nozzle can be integrated in to the wing structure to reduce weight, with the wing skin and structure forming part of the nozzle. Streamlined-flow-distributors/struts may be required inside such nozzles to distribute the flow evenly, reduce swirl across the throat and exit areas and improve the structural strength. NAR does however have an impact on the overall length of the exhaust system, since the circular to rectangular transition sections will have to be extended to maintain a favourable internal flow distribution. Due to their increased heat transfer area, the transition ducts may require significant cooling. This can however be improved by the use of internal wing mixers and inlet passages for cooling airflows

8 Sizing and integration of the UCAV thrust vectoring system

8.1 Thrust vectoring system requirements for the UCAV

Recent proposals have been made to utilise fluidic thrust vectoring devices for control and trim. Such a proposal is intended to reduce the trim drag associated with conventional control surfaces. Fluidic devices were envisioned as a means of being able to utilise the benefits of thrust vectoring without the many drawbacks associated with mechanical devices. However these devices have proven to be fraught with their own problems. These include unstable control regions, control dead zones and high secondary air flow requirements. The co-flow devices in particular have been shown to require a significant amount of secondary air which can only practically be obtained from engine bleed air. The use of engine bleed air is however accompanied with a decrease in engine performance and an increase in fuel consumption. This has raised the question whether such a task could be accomplished with a refined mechanical thrust vectoring system.

Mechanical thrust vectoring systems have traditionally been envisioned as a means of generating vertical lift or enhancing the manoeuvring capabilities of an aircraft. The primary objective of this work is however to investigate the effectiveness of mechanical thrust vectoring systems for aircraft control and trim. The ideal mechanical thrust vectoring system is one which:

- Is mechanical and not fluidic.
- Has a response time which is sufficient to meet aircraft control and dynamic stability requirements.
- Is able to offer a performance advantage compared to a conventional aircraft.
- Preferably is light weight, low cost and simplistic.
- Is safe and reliable
- Has a sufficient degree of accuracy and repeatability

8.2 Selection of the candidate thrust vectoring system

Our earlier review of existing thrust vectoring systems highlighted the fact the majority of mechanical thrust vectoring systems have a number of associative drawbacks. These include mass, complexity, maintenance requirements and cost. It is these drawbacks that prompted the research and development of fluidic devices. Since many of these mechanical devices were intended to enhance lift and/or manoeuvrability, they may be over-engineered for less demanding aircraft control and trim tasks. The result is that these systems will be overly complex, expensive and heavy.

A system of particular interest to this study is the low cost paddles vectoring system as investigated by NASA for their X-31 and F/A-18 aircraft. This utilises post-exit paddles which are deflected into the exhaust flow in order to change the direction of the resultant thrust. This system was tested extensively on the X-31 and F/A-18, but was

later abandoned, probably with the advent of more refined devices which offered improved manoeuvrability. This system has however recently been receiving renewed interest on the Mitsubishi ATD-X as a low-cost mean to enhance the manoeuvrability of the aircraft. Compared to other mechanical thrust vectoring concepts, this system offers distinct benefits of being low cost and light weight. This work aims to answer the question, 'can such a system be utilised to control and/or trim an aircraft and if so what are the benefits/penalties associated with it'.

8.3 An overview of the final thrust vectoring system

The thrust vectoring system envisioned for this project is a re-scaled variant of that used for the X-31 and F/A-18. This consists of three large external thrust vectoring paddles which are equally spaced around the circumference of the exhaust nozzle exit. Each of these paddles is connected to a heavy duty hydraulic actuator which deflects the paddle into and out of the exhaust flow as required. The range of movement of each paddle is +35º to -60º. The control of each actuator must therefore be integrated into the flight control system if it is to be transparent to the pilot/operator. The paddle shells are constructed from a RCC (reinforced carbon-carbon) material which is affixed to a metallic (Nimonic) backing structure which is used to transfer loads to and from the mountings and actuator. A more detailed overview of the system will follow.

Only the pitch control aspect of this system will be investigated as part of this study. This is however not restricted to control about the pitch axis and is also able to deliver yaw control by means of the simultaneous deflection of two paddles. The system is however unable to offer any significant roll control due to the lack of any significant moment arm and thus and alternative roll control device is required. A four paddle variant of this system was also investigated by NASA which utilised four equally spaced paddles instead of three. Although this is potentially easier to control with the need to deflect only 1 vane at a time, this was abandoned in favour of the lighter three paddle variant.

While in flight, the thrust vectoring system can be shown to have sufficient control power to be able to moments about the aircraft's centre of gravity which are sufficient to manoeuvre and trim the aircraft. During take-off and landing however it was envisioned that the thrust vectoring system would be used to generate an additional component of lift. In such cases an alternative means of aircraft control is required such as conventional aerodynamic control surfaces. If we are to meet the objectives of the BAE Grand Challenge (to eliminate conventional flight control surfaces), we must find a means to be able to dispense with conventional control surface. The aircraft was thus equipped with a nose jet control system which is intended to replace the function of the conventional aerodynamic pitch control surfaces. This system is only active during take-off and landing with the thrust vectoring system being used for control during all other flight phases.

The nose jet pitch control system utilises engine bleed air to generate a downward thrust from two downward jets of air located at the nose of the aircraft. The downward thrust is generated by a pair of convergent-divergent nozzles which are located on either side of the nose landing gear within the nose gear bay. Upon retraction of the nose gear, the

nozzles are covered by the nose landing gear bay doors to reduce the drag of the aircraft. The nozzles are connected to the engine bleed port via ducting which runs down each side of the aircraft. The quantity of bleed entering each duct is regulated with a butterfly valve at the bleed port exit. The reader is advised to refer to Appendix B for a more detailed breakdown of the system components.

8.4 Design and sizing the vectoring and pitch control systems

It the sections which follow, an overview will be given of the design process for the thrust vectoring and nose jet control systems. An introduction will also be given to the impact of these systems on the engine performance, which will give the reader an appreciation of the complexity of the design process. Included in Appendix C is an overview of detailed nozzle and inlet design which have been included to give the reader an appreciation of the complexity of the engine nozzle design task. We will however be utilising an existing nozzle concept for this study and will be concentrating on the integration considerations.

8.4.1 The inter-relation with the engine performance

Neither the thrust vectoring nor pitch control system can be considered in isolation of each other or in isolation of the engine. In the case of the thrust vectoring system, each deflection of the exhaust nozzle results in a different exhaust nozzle configuration with different internal flow characteristics. This is however further complicated by the fact that the performance of a typical engine can also be shown to be influenced by the characteristics of the exhaust nozzle configuration. The engine configuration and its resulting performance will thus be dependent on the deflection of the thrust vectoring nozzle.

In the case of the pitch control system, the total control force from the nose jet nozzles is dependent on the mass flow rate of engine bleed. The performance of the engine is however also dependent on the fraction of engine bleed. Thus, the performance of the engine is dependant on the total control force from the nose jets. Taking into consideration the relations discussed above, we can see that the thrust vectoring nozzle and nose jet will also be related via the engine performance. The reader is advised to refer to Appendices B and C for further details of these relationships.

8.4.2 Sizing the thrust vectoring system

To be able to utilise the test results from NASA, it was essential that the geometry of the thrust vectoring system retains the original proportions specified by NASA. The approach adopted here for sizing the system was to generate a model of the system to the exact dimensions specified by NASA. This was then re-scaled so that the diameter of the jet pipe of the NASA model matches that of the UCAV.

It should be noted that the loss coefficient of a duct will only be affected by variations in the geometry and/or flow conditions. It is therefore possible to linearly scale an existing duct design without affecting its loss coefficient. Thus, by linearly scaling the NASA thrust vectoring system, the original NASA test results will remain unaffected.

These results are however only valid for the flow conditions investigated in the NASA experiments. Although NASA did test the system over a range of flow conditions with the intention of covering all eventualities. However, a problem was uncovered when trying to utilise this data for this particular study. It was discovered that was a mis-match between characteristics of the unvectored nozzles (with no vectoring paddles installed) of the NASA test rig and the engine of our UCAV. Therefore, it was necessary to rescale the NASA test results so that the data for the unvectored test rig nozzle matches the characteristics of the unvectored nozzle of the UCAV. The reader is advised to refer to Appendix B for further details of this process.

8.4.3 Design of the nose jet pitch control system

As already discussed, the pitch control system utilises air bled from the main engine to generate a vertical thrust at the nose of the aircraft. The system utilises an arrangement of valves and ducting to deliver the bleed in a controllable manner from the main engine to the convergent-divergent nozzles located in the nose landing gear bay. Butterfly valves located at the engine bleed port exits were selected as the best means of regulating the flow to the nozzles. Such valves offer benefits of precise control and fast response times. As a result of the range of operating conditions that the nozzle has to operate over, a variable area nozzle would have provided the best solution to keep the system as efficient as possible. However, such a nozzle would result in additional mass, volume and complexity and thus it was decided to opt for a fixed nozzle arrangement instead. The various components in the system were sequentially sized by an iterative process to achieve the desired flow conditions in each component. However, a full description of this complex design process is beyond the scope of this discussion and the reader is advised to refer to Appendix B for further details.

An important design consideration is the point along the main engine at which the air is bled from. This not only influences the performance of the pitch control system but also the performance of the engine. Bleeding from the LP compressor is less detrimental to engine performance but the low pressure air does necessitate the need for large mass flow rates to achieve the desired control system thrust. This implies the need for large diameter ducting which has a greater weight and occupies more space within the aircraft. The low temperatures involved however mean that it may be possible to utilise composite sandwich ducting, in which case the sandwich core also acts as an insulation material. Bleeding from the HP compressor on the other hand generates higher pressure air which implies a smaller mass flow rate and thus smaller diameter ducting. This is however more detrimental to the engine thrust. The bleed air is however at a higher temperature which necessitates the need for high temperature ducting such as Nimonic Alloy 75. This ducting must however also incorporate expansion joints to relieve thermal stresses and be well insulated to protect surrounding equipment and structure. Insulation will however add weight and occupy a significant amount of space. The convergent-divergent nozzles are envisioned to be constructed from a nickel alloy.

8.5 The analysis of the vectoring and control systems

The analysis of the thrust vectoring is concerned with determining whether such a system is able to offer any benefits in performance at the take-off, cruise and landing

phases. In the case of the take-off and landing phases, we are primarily interested in whether the take-off and landing field lengths could be reduced. At cruise we are interested in whether a reduction in the drag and thus the fuel consumption of the aircraft could be realised. The reader is advised to refer to the evaluation section of this thesis for a more detailed discussion of this analysis work.

In order to be able to carry out these evaluative studies, we need to generate a number of representative analytical models to determine:

- The specific fuel consumption of the engine as a function of the nozzle vectoring angle and nose jet force at take-off and landing conditions.
- The maximum available engine thrust as a function of the nozzle vectoring angle and nose jet force (via the engine bleed) at take-off and landing conditions.
- The vertical thrust from the nose jet pitch control system as a function of engine bleed at take-off and landing conditions.
- The engine throttle setting as a function of the nozzle vectoring angle and engine thrust at cruise conditions.
- The specific fuel consumption of the engine as a function of the nozzle vectoring angle and engine throttle setting at cruise conditions.

The generation of such analytical models requires detailed knowledge of the engine operating characteristics and how these are affected by variations in parameters such as the nozzle characteristics and engine bleed setting. Such engine data can however only be realistically be predicted from an engine simulation model due to the complexity of the inter-relation between all the different engine components. One such engine simulation model is the AEDsys package developed by Mattingly [16], as was used for this study. This is an engine conceptual design package which requires minimal component level knowledge of the engine. It has proven to be sufficient to predict the performance of the engine over a range of engine operating conditions (off-design conditions) and is thus well suited to this study.

The engine analysis work utilised a baseline engine performance model which was representative of the unvectored engine configuration. This model could then be modified as required to take into account the variations in each of the engine parameters being studied. At cruise for example we would have a different engine model for each nozzle vectoring angle (and thus nozzle configuration) being investigated. The analysis is somewhat more complicated at take-off and landing as we will have a different model for each nozzle deflection angle and each engine bleed setting. Each on-design model can finally be tested over the range of off-design flight conditions of interest to generate the required database of test results. The required analytical models can finally be generated by fitting a polynomial expression to each data set in the database. In the case of take-off and landing, it was necessary to derive additional correction factors to take into account for variations in engine performance as a result of variations in the speed of the aircraft. The reader is advised to refer to Appendix C for further details of the engine design and analysis work.

8.6 Integration of the vectoring and pitch control systems

This section gives an overview of the integration of the thrust vectoring and nose jet pitch control systems. As with the modification of any aircraft configuration or integration of any systems, consideration needs to be given to general design considerations. These include aircraft stability and control, component positioning and space allocation within the airframe, mass, aircraft performance and additional power-off takes. An overview of initial engine installation considerations has been included in appendix C as background reference material for the reader.

8.6.1 The integration of the thrust vectoring system

As already mentioned, the thrust vectoring system was sized by rescaling a model of the system proposed by NASA. The model was constructed to the exact dimensions specified by NASA and then re-scaled to match the diameter of the jet pipe of the UCAV. This system was then integrated onto the aircraft whilst keeping the same relative position of the paddles with respect to the jet pipe as specified by NASA.

The most significant integration consideration which had to be taken into account was the additional length of the paddles. If the paddles were to be simply retro-fitted on the end of the nozzle of the conventional UCAV then there is a risk that they could come into contact with the ground during high angle of attack manoeuvres. The aft fuselage thus needed to be shortened so that the aft point of the paddles is within the bounds of the original length of the fuselage. The other main integration consideration is the provision of sufficient surrounding aircraft structure to provide mountings for the vectoring paddles and hydraulic paddles actuators. The degree of any elasticity in the structure must be determined and accounted for by the thrust vectoring control system.

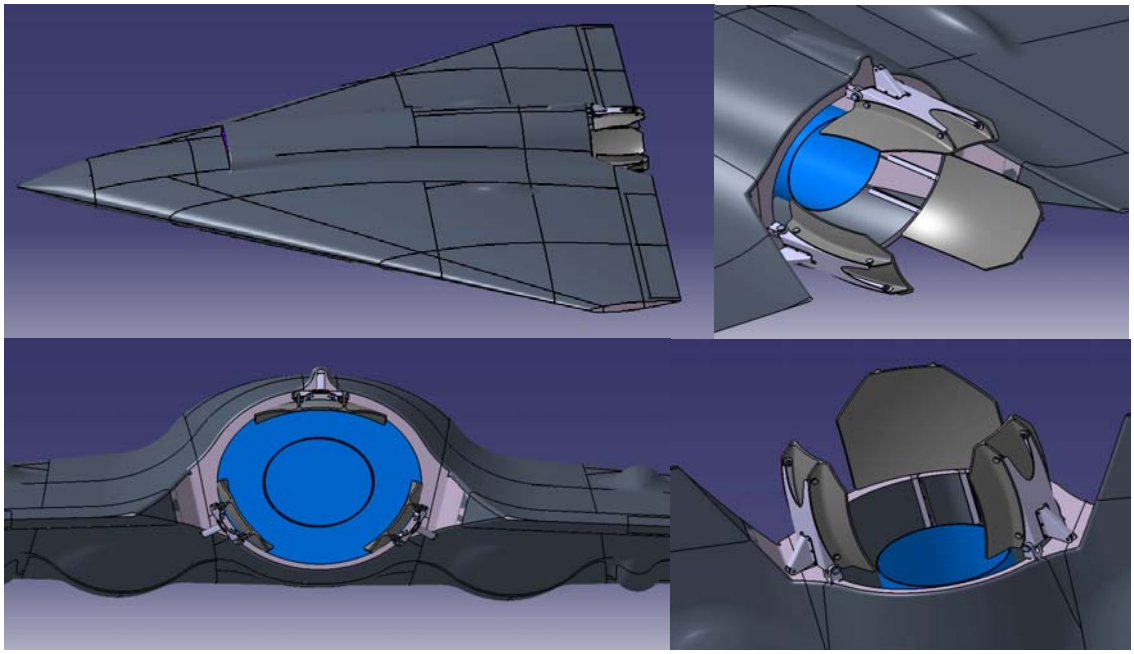

Figure 8-1 to 8-4 – External views of the paddles thrust vectoring system installed in the UCAV

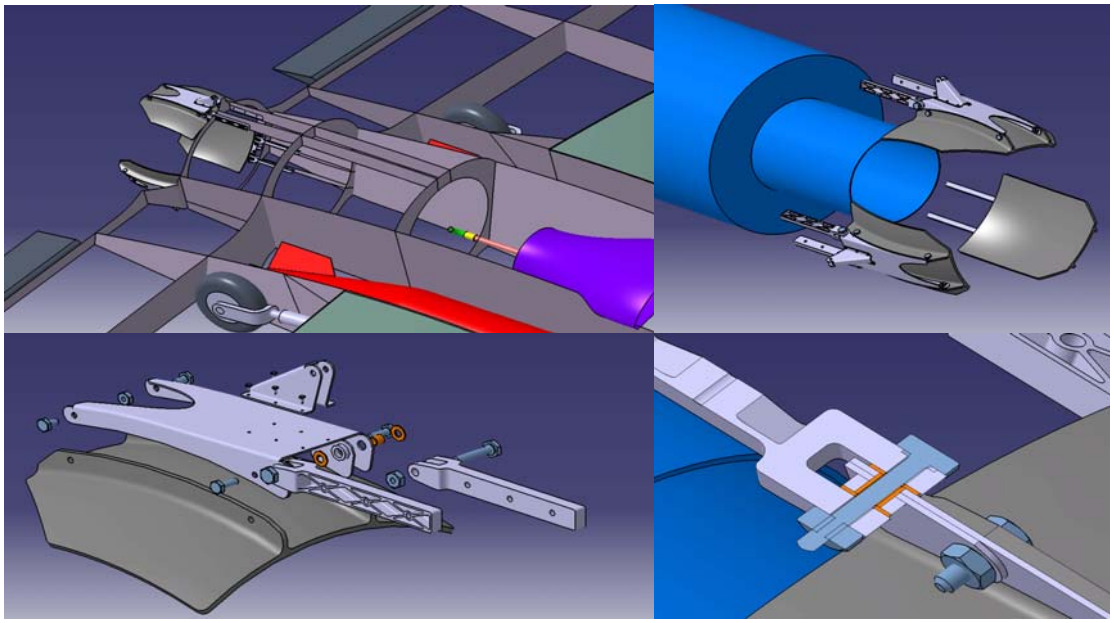

Figure 8-5 to 8-8 – The accompanying paddles supporting structure, alignment relative to the jet pipe and an exploded and sectional view of the assembly

8.6.2 The integration of the nose jet pitch control system

Integration of the nose jet pitch control system is primarily concerned with determining the most efficient ducting runs between the main engine and the pitch control nozzles at the front of the aircraft. The high temperature of the ducting means that particular consideration needs to be given to routing it away from sensitive equipment. Allowance also needs to be made for the volume occupied by any insulation material. The two nozzles are themselves located one on either side of the nose landing gear, within the nose gear bay. As the nozzles are only required for take-off and landing, they are thus concealed for all other flight phases to keep the drag of the aircraft to a minimum.

The most significant sources of loads in this system are expected to be due to pressure and momentum changes at bends and regions of cross-sectional area changes. In addition, allowance needs to be made for the hoop stress in the ducting due to the internal pressure. Thermal loads can be assumed to be insignificant due to the incorporation of expansion joints into the ducting runs.

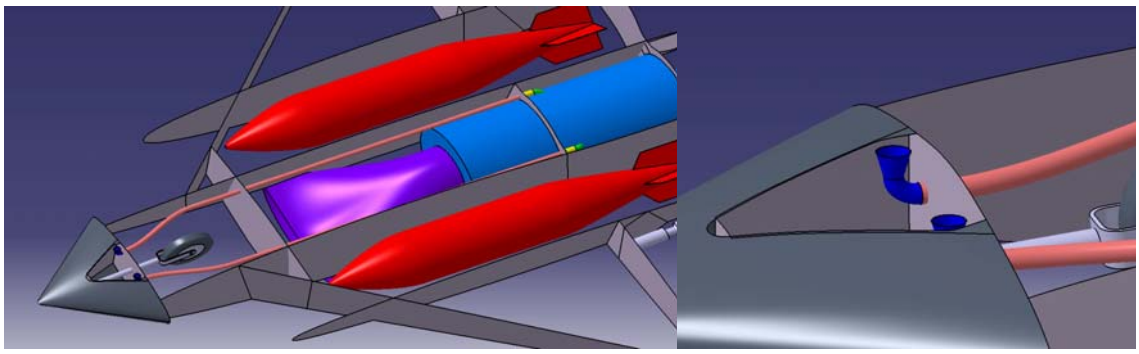

Figure 8-9 and 9-10 – The layout of the pitch control system and location of the nose jets

9 Fuel cells literature review

9.1 An overview of fuel cells and their working principles

9.1.1 What is a fuel cell?

Fuel cells were invented in about 1840 but have recently been revived as an ideal candidate in the search for an alternative power source. These electrochemical devices generate an electric current as a result of a chemical reaction between a fuel (typically hydrogen) and an oxidant with the only by-products of the process being heat and water. Since no combustion takes place, efficiencies of more than twice that of a conventional IC engine are possible. As shown in the figure below, a fuel cell system consists of a stack of identical cells which are combined to achieve the desired power output. Each individual cell assembly consists of an electrolyte membrane which is sandwiched between two catalyst impregnated anode and cathode electrodes. This basic cell is further sandwiched between two bipolar plates which are used to deliver the reactants to the working fuel cell. The sizing of a fuel cell stack is considerably simpler than for an IC engine since the power output of the stack is simply a function of the number of cells used.

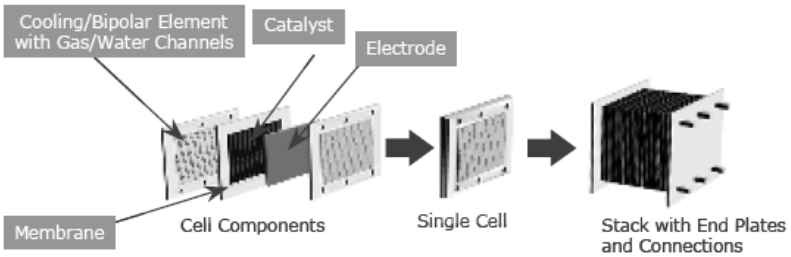

Figure 2. Several fuel cells are typically combined to form a stack that has a higher combined voltage and current.

Figure 9-1 - The components of a fuel cell stack [48]

9.1.2 Fuel cell working principles

It should be noted that the electrochemical reactions which take place at each electrode vary according to the fuel cell type and therefore the electrolyte used. This discussion will however be restricted to the most common type of fuel cell, which is the acid electrolyte hydrogen fuel cell. The working principles of a fuel cell are best understood by examining a cross-section through an anode/membrane/cathode cell assembly as shown in the figure below.

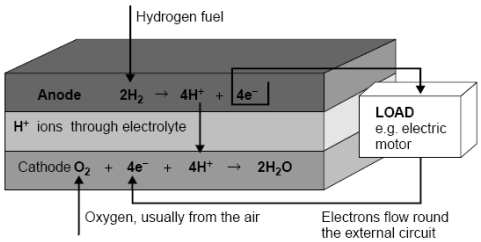

Figure 4.3 The reactions at the electrodes, and the electron movement, in a fuel cell with an acid electrolyte

Figure 9-2 – Fuel cell electrochemical reactions [49, p84]

The overall chemical reaction for a hydrogen fuel cell is $2H_2 + O_2 \rightarrow 2H_2O$ which is the result of the separate chemical reactions at the anode and cathode. At the anode there is the chemical reaction $2H_2 \rightarrow 4H^+ + 4e^-$ which ionises the hydrogen to release electrons and create H^+ ions. At the cathode, there is the reaction $O_2 + 4e^- + 4H^+ \rightarrow 2H_2O$ where H^+ ions from the electrolyte and electrons from the anode react with oxygen to form water. In order to sustain the chemical reactions, an external electrical circuit is required to supply a continual supply of electrons at the cathode from the anode. This external flow of electrons can be utilised by connecting an external load across the electrodes. The H^+ ions required from the anode are transported to the cathode through the electrolyte which is sandwiched between the two electrodes. In this case, two hydrogen molecules are required for each oxygen molecule in order to maintain the reaction process.

9.1.3 The potential benefits of fuel cells

Fuel cell systems have many benefits in comparison to conventional internal combustion engines, as discussed below,

- Higher efficiency – Fuel cells have been shown to be considerably more efficient than IC engines (approx. 50% vs. 15%). Their efficiency is expected to rise to about 60% in the future, as a result of their ongoing development.
- Wider efficiency band – The maximum efficiency of an IC engine is limited to a narrow operating range, but fuel cell engines show flatter results with a high efficiency being possible of a wide range of operating conditions.
- Modularity – IC engines are of fixed size and require considerable design effort to rescale them to meet different power requirements. Fuel cell stacks can, however, easily cater for a wide range of power requirements by varying the number of cells within the stack. Where required, more than one fuel cell stack can be used which gives an endless range of possibilities.
- Safety – The modularity of fuel cell assemblies means that failure of a single cell will only result in a small degradation of performance and not total loss.
- Fuel flexibility – Fuel cells are not restricted to pure hydrogen and with the necessary additional equipment they are capable of handling a wide variety of hydrogen based fuels including conventional hydrocarbons.
- Zero emissions when using hydrogen – The emissions from a fuel cell operating directly on hydrogen are zero but the environmental impact of the production of the hydrogen must be taken into account.

- Low emissions when using fuel reformers - The use of on-board reformers to generate hydrogen still show considerably lower emissions compared to IC engines. CO_2 is typically a third of that of an IC engine and other emissions such as CO, NO_X, SO_X, and HC are reduced to levels that are undetectable
- Low noise – Since the basic fuel cell has no moving parts and its function does not involve a combustion process, their noise output is less than that of an IC engine. The main sources of noise within a fuel cell system originate from the accompanying balance of plant such as compressors.
- Ready supply of waste heat - A by-product of the electrochemical process is heat, which can then be used for other processes or for onboard equipment such as fuel reformers. The utilisation of this waste heat can increase the efficiency of the system as a whole and reduce emissions.
- Rapid load following capability – Fuel cells are capable of immediate response to changes in demand.

9.1.4 Challenges still to be overcome

The cost, size and weight of fuel cells and their associated systems is at present inferior to conventional IC engines. The current technical progress of fuel cells is a major drawback for their vehicular use and additional research effort is required. To reduce costs current manufacturing processes must also be reviewed. Pure hydrogen is the preferential fuels but practical constraints dictate the use of other fuels which can be vulnerable to fuel tolerance issues. These are a major cause for concern since fuel contaminants can have a direct impact on fuel cell performance and lifespan. The use of other fuels also dictates the need for a fuel reformer but such systems are not as efficient as using pure hydrogen systems and further development work is required.

Although the emissions from fuel cells are low, their operation at high altitudes can still present environmental issues since the water by-product (in a steam state) has been shown to be a greenhouse gas in itself. One approach to prevent this would be to fly at a lower altitude so that the output steam is able to return to its liquid state in the atmosphere. Where this is not possible, the water can be captured and stored. This will increase the landing weight of an aircraft but it may be possible to utilise some of the water onboard the aircraft or dump it just before landing.

9.1.5 Rival hydrogen powered propulsion systems

Hydrogen can not only be used as a fuel in fuel cell engines but also as a fuel in conventional IC engines. In such engines, emissions such as CO, CO_2 and HC are negligible with only NO_X remaining. When allowance is made for power off-takes, the efficiency of a fuel cell is less than initially predicted and a hydrogen IC engine with a hybrid power train could prove to be a considerably competitive alternative. Such engines would also offer the benefits of technological maturity, reduced cost and complexity. Fuel cells however still offer a better efficiency and lower emissions making them the ultimate long term solution. In the short term however, hydrogen fuelled IC engines are a logical step in the right direction.

9.2 The different types of fuel cells

9.2.1 Electrolytes and membranes of the different fuel cell types

Numerous different fuel cells have been explored over time which can be characterised according to the electrolyte that they use and the accompanying reactions. The most common fuel cells types and their application in industry are summarised below.

Table 4.1 Data for different types of fuel cell

Fuel cell type	Mobile ion	Operating temp.	Applications and notes
Alkaline (AFC)	OH^-	50–200°C	Used in space vehicles, e.g. Apollo, Shuttle.
Proton exchange membrane (PEMFC)	H^+	30–100°C	Vehicles and mobile applications, and for lower power CHP systems
Direct methanol (DMFC)	H^+	20–90°C	Suitable for portable electronic systems of low power, running for long times
Phosphoric acid (PAFC)	H^+	~220°C	Large numbers of 200 kW CHP systems in use
Molten carbonate (MCFC)	CO_3^{2-}	~650°C	Suitable for medium to large scale CHP systems, up to MW capacity
Solid oxide (SOFC)	O^{2-}	500–1000°C	Suitable for all sizes of CHP systems, 2 kW to multi MW

Table 7-1 – A summary of the different fuel cell types [49, p85]

The electrolyte used will influence the nature of the reactions which take pace as well as the type of fuel which can be used. The most effective electrolytes to use are those with free H^+ ions, such as acids. Certain polymers called 'proton exchange membranes' also contain mobile H^+ ions and work in a similar way to the acids. Such electrolytes are fundamental to the operating principle of the fuel cell as only the H^+ ions are able to pass through and not electrons. This forces the electrons travel around the electrical circuit as opposed to through the electrolyte in order to complete the reaction. An overview of the common fuel cell types is given in the sections below.

9.2.1.1 Alkaline fuel cell (AFC)

The low operating temperatures (less than 100˚C) of alkaline fuel cells has made them particularly attractive for vehicular use. They have already been successfully used in a number of demonstrator vehicles as well as on both the Apollo and the Shuttle orbiters. They however suffer from slow reaction rates and electrodes with an embedded platinum catalyst are typically used as a result. Both of the reactant gas streams must also be scrubbed before entering the fuel cell in order to remove carbon compounds. This typically involves passing the gases through precious metal membranes which requires a considerable pressure difference and adds additional complexities to the system. Compared to PEM fuel cells, the alkaline fuel cell is considerably cheaper but their power output is lower and PEM fuel cells are more favourable as a result.

9.2.1.2 Phosphoric acid fuel cell (PAFC)

These were the first commercial fuel cells and there are currently many PAFC systems successfully operating in Europe and the USA. Their higher operating temperatures (of about 220˚C) result in start/stop and high thermal inertia problems. These systems have

proved their worth in fixed applications which require a steady continual operation such as generators for decentralised stationary power systems. They can also be used in ships and locomotives but are not a particularly viable solution for other vehicles.

9.2.1.3 Solid oxide fuel cell (SOFC)

SOFC's consist of a solid zirconia based electrolyte sandwiched between a nickel and YSZ (yttria-stabilised zirconia) anode and a LaSr (strontium and lanthanum) and magnesium oxide cathode. They have a high power density and typically operate at temperatures in the region of 600-1000˚C while remaining in a solid state. Their high temperature makes them more tolerant to fuel impurities and means that they are able use hydrocarbon fuels directly without a reformer. This also allows high reaction rates to be achieved with expensive catalysts. They are currently being used for stationary power applications (up to 10MW) but are also currently being investigated a replacement for aircraft APU's (as a result of their ability to run directly on kerosene). The SOFC unfortunately needs to be manufactured from ceramic materials which makes them expensive to manufacture and causes handling problems. Their high operating temperature means that longer starting times are required and PEM fuel cells are more favourable for vehicle applications. A variant of the SOFC is the protonic ceramic fuel cell but this is not common.

9.2.1.4 Molten carbonate fuel cell (MCFC)

The MCFC is set apart from the other fuel cell types in that it typically operates with carbon dioxide. This is another high temperature fuel cell which uses a corrosive complex lithium, potassium and sodium carbonate electrolyte mixture and is only really suitable for large systems of continual operation. The high operating temperature means that expensive catalysts are not required to achieve high reaction rates and conventional gases can be used without an onboard fuel reformer. They have the same response characteristics as the PAFC and are well suited to the same stationary and steady operation applications.

9.2.1.5 Polymer electrolyte membrane fuel cell (PEMFC)

PEM fuel cells are one of the simplest types of fuel cell. They use a solid polymer (mobile proton) electrolyte which results in a reaction process the same as that for an acid electrolyte fuel cell. Their low operating temperature necessitates the need for novel electrodes and catalysts to overcome otherwise slow reaction rates. Very small amounts of platinum are typically used as the catalyst with effort being expended to reduce the amount required and therefore further reduce the costs. Of particular concern to these fuel cells is the presence of CO which is damaging to the platinum catalyst and new platinum-ruthenium-tungsten catalyst compounds are being developed to overcome this problem. A more recent novel technique involves using electrical pulses to raise the potential of the anode which oxidises the absorbed CO into CO_2. Water management is also difficult especially with larger stacks, which can limit the size of a stack.

These were originally used for the short Gemini space missions but early problems associated with their extended use led to the use of alkaline fuel cells for the Apollo and

Space Shuttle missions. They have since seen considerable improvement and the added benefit of a solid electrolyte has led to them being the most commonly used type for vehicular applications. As a result of the impressive recent developments, NASA has decided to replace the AFC systems on the space shuttle with PEMFC systems.

9.2.1.6 Direct methanol fuel cells (DMFC)

Methanol has recently been considered as a particularly attractive alternative to pure hydrogen. Its use within indirect methanol fuel cells necessitates the need for an accompanying fuel reformer to extract the hydrogen. Direct methanol fuel cells have the ability to use the liquid methanol directly without having to extract the hydrogen first. The fuel system is therefore much simpler and humidification and thermal management systems are not required either since a controlled mixture of methanol and water is used as both the fuel and coolant. They are not as efficient as other fuel cell types due to fuel being able to travel straight through the membrane without reacting by means of concentration gradient diffusion and proton migration electro-osmotic drag (fuel crossover). A suitable catalyst is also required as a result of sluggish kinetics. DMFC's are not as developed as other systems and are only currently of very low power output and therefore only suitable for low power applications such as portable electronic equipment. Daimler has however already successfully tested a 3kW go-kart and they do show potential to be used in vehicles in the future with further development work.

9.2.2 Recommended systems suitable for propulsion

As well as being the most technically advanced, the PEM fuel cell has for some time been regarded as the type currently showing most promise for mobile applications. Compared to other types, they offer benefits of low operational temperatures (40-100 degrees), short transient and start-up periods and respectable efficiencies. The SOFC has also received significant interest for vehicles as a result of their higher efficiency and better tolerance of fuel impurities. They are however presently not viable due to their higher operating temperature and lower power densities. However, on-going development work may make them more viable in the near future. At present, the majority of fuel cell powered cars use the PEM fuel cells and they have also been shown to be an excellent choice for the aerospace industry.

9.3 The PEM fuel cell in greater detail

9.3.1 Predicting the efficiency of a fuel cell

In this analysis, the fuel cell can be considered as a black box with hydrogen and oxygen entering and electrical energy, heat and water leaving. In such studies, it is typical to use a parameter known as the Gibbs free energy which is defined as the energy available to do external work. The Gibbs energy, which is dependant on the temperature and state of a substance, is determined for the reactants entering and the products leaving the fuel cell. The energy released from the fuel cell is then taken as the difference between the Gibbs input and the Gibbs output. In order to be able to accurately compare the efficiency of a fuel cell with that of an IC engine, the change in enthalpy of formation of the products is typically used instead. This the electrical

energy output of the fuel cell to be compared to the heat that would be produced if the fuel was burnt as in an IC engine. The comparable efficiency of the fuel cell can then be determined as the ratio of the electrical energy produced per mole of fuel to the change in enthalpy of formation. The change in enthalpy of formation is dependant on weather the final state of the products of the reactions are a liquid or gas.

The maximum efficiency of the fuel cell (comparable IC engine carnot limit) can be determined for a fuel cell from the following equation, which assumes that the electrical energy equals the Gibbs energy.

$$\eta_{FuelCell(Max)} = \frac{\Delta G}{\Delta H} \cdot 100\% \qquad \text{Eq 9-1}$$

This is dependant on the operating temperature of the fuel cell with a drop in efficiency and EMF typically being experienced with an increase in temperature. The operating temperature must therefore be chosen with care with a figure of 80ºC being typical for vehicular PEM fuel cells. In the ideal case of 100% efficiency, the maximum voltage obtainable for a single cell is 1.48V for the higher heating value (HHV) of hydrogen or 1.25V for the lower heating value (LHV). The efficiency of a single cell can then be determined by inputting the average voltage of one cell into the equation below.

$$\eta_{FuelCell} = \frac{V_{Cell}}{V_{Cell(100\%)}} \qquad \text{Eq 9-2}$$

The maximum voltage of a fuel cell is obtained when 100% of the Gibbs free energy is converted into electrical energy as given by the equation below (F = Faraday constant).

$$V_{Max} = \frac{\Delta G}{2 \cdot F} \qquad \text{Eq 9-3}$$

9.3.2 An introduction to fuel cell operating characteristics

The operating characteristics of a fuel cell are governed by internal resistances which cause a voltage drop proportional to the current being drawn. An example of typical fuel cell operating characteristics is shown in the figure below.

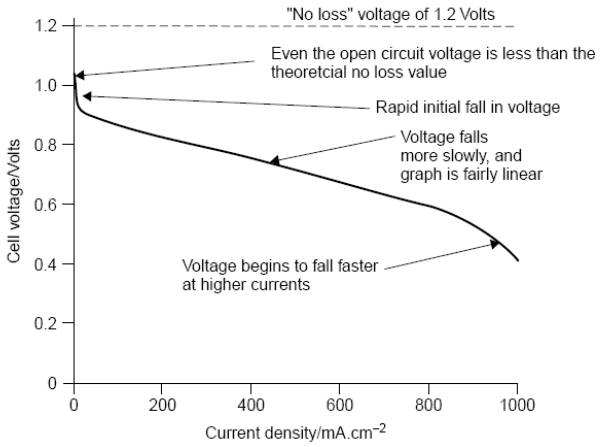

Figure 4.10 Graph showing the voltage from a typical good quality PEM fuel cell operating on air at about 80°C

Figure 9-3 - Typical fuel cell polarization curve [Ref 49]

Three characteristic operating regions are apparent from the voltage drop curve in the above graph, which are.

1. The initial rapid voltage drop at low currents is referred to as the activation energy, which is the energy required to maintain the reactions at the electrodes.
2. The steady linear voltage drop which dominates the fuel cell characteristics is referred to as the ohmic voltage loss, which is a result of the resistance of the electrolyte and electrodes.
3. The increased voltage drop at high currents is referred to as the 'concentration voltage loss'. This results from a reduction in available oxygen to complete the reaction as a result of a build-up of remnant nitrogen from the air.

Continual research and development effort is aiming towards a reduction in these voltage losses but at present a typical fuel cell voltage is approximately 0.65-0.7 V (for currents up to 1A per cm^2). This corresponds to an efficiency of about 50% (HHV) which is further reduced when allowance is made for balance of plant power off-takes. In contrast to an IC engine, as can be seen from above, a fuel cell is capable of high efficiencies at low power outputs and therefore has a wider useful operating range.

9.3.3 Impact of pressure and concentration on fuel cell performance

In addition to operating temperature, the performance of a fuel cell is also affected by operating pressure, which also has an impact on the values of Gibbs free energy. Likewise, gas concentration will also have a similar impact on the Gibbs free energy. For a pressure change from P1 to P2, the resulting voltage change can be predicted by the Nernst equation below.

$$\Delta V = \frac{R \cdot T}{4 \cdot F} \cdot \ln\left(\frac{P_2}{P_1}\right) \qquad \text{Eq 9-4}$$

This expression is however most suited to high temperature fuel cells as it under predicts the voltage drop of low temperature fuel cells (such as PEM). This discrepancy is related to activation energy which has in this case been shown to be influenced by both pressure and concentration. In practice, allowance must also be made for the power off-take of an air compressor which is required to generate the pressure and thus voltage increase. Fuel cells intended for vehicle applications generally operate at pressures of 1.5 - 2.0 bars primarily to aid the balance of water within the cell.

9.3.4 The impact of fuel and air quality on fuel cell performance

In addition to temperature, pressure and gas concentration, other factors which are likely to result in degradation in fuel cell output voltage and therefore performance are,

- The use of air instead of pure oxygen.
- The use of hydrogen based fuels as opposed to pure hydrogen. The hydrogen obtained from reforming fuels such as methanol is typically diluted with CO_2.

9.3.5 Water management

The fuel cell cathode is not only used to deliver oxygen to the fuel cell membrane but is also used to expel the water which is formed as a by-product of the electrochemical

process. The continual flow of air that is fed to the electrode evaporates off and then carries the excess water out of the fuel cell. It is however critical that the level of hydration in a PEM fuel cell is carefully maintained at the correct level to avoid a degradation in its performance. It can be shown that the proton conductivity of the electrolyte is directly proportional to the electrolyte water content and insufficient water will result in a loss in performance. Too much water on the other hand will block the pores in the electrodes or the gas diffusion layer as a result of flooding which will also result in a loss in performance.

In a small number of situations water, which is produced at the cathode, is able to diffuse through the thin electrolyte membrane and keep the whole system suitably hydrated. This is, however, difficult to control due to water molecules migrating in the opposite sense by electro-osmotic drag and the drying effect of fuel cell operating temperatures. In practical PEM fuel cell systems however, the air and/or hydrogen are humidified by injecting water in to them prior to them entering the fuel cell. It is necessary to use pure water for this process and it is typical to condense and recirculate water from the water vapour exhausted from the fuel cell. Fortunately, higher operating pressures not only increase the performance of the fuel cell but also slightly alleviate the problem of electrolyte drying. This means that less additional water vapour is required to keep the electrolyte hydrated.

9.3.6 Thermal management

Compared to IC engines, fuel cells are more efficient and generate less heat but have more waste heat to dispose of. Whereas IC engines are able to dispense an significant proportion of their waste heat via their exhaust, the waste air exiting the fuel cell will only be at about 85ºC and will therefore carry little waste heat. IC engines are also able to dispense heat by forced convection and radiation from the external surfaces; this is however less effective for fuel cells due to their cooler external surfaces. There are therefore fewer mechanisms for the removal of excess heat from a fuel cell compared to an IC engine and the performance requirements of a fuel cell cooling system are greater as a result.

Small fuel cells (up to 100W) can be sufficiently cooled by supplying excess air to the cathode to remove the waste heat. At higher powers the cooling air flow requirements become excessive leading to excess water evaporation and unfavourable drying of the electrodes and electrolyte. Alternative cooling methods are therefore required for larger fuel cell systems. Medium sized fuel cells (up to 2-3kW) may be cooled by passing an additional cooling air flow through dedicated cooling passages in the bipolar plates. Such an arrangement is shown in the figure below.

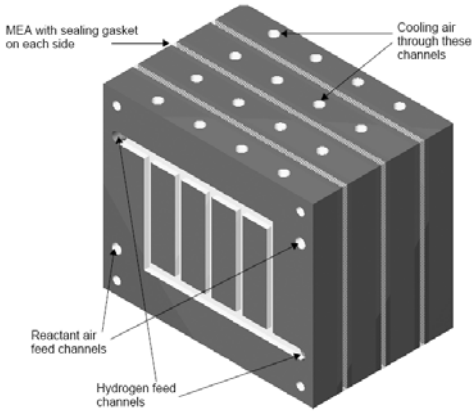

Figure 4.21 Three cells from a PEM fuel cell stack where the bipolar plated incorporate channels for cooling air, in addition to channels for reactant air over the electrodes

Figure 9-4 – The arrangement of reactant and coolant passages in a stack [49]

In the case of large fuel cells (over 2-3kW) the cooling air is substituted with cooling fluids (such as water), in order to maintain even cooling. The cooling water is re-circulated through a radiator which considerably larger than for an IC engine since typically twice as much heat needs to be dispersed.

9.4 Fuel cell construction

9.4.1 The main parts of a fuel cell

Each single fuel cell assembly consists of membrane electrolyte sandwiched between anode and cathode electrodes. These are typically 1mm thick, which is made up from:

- 0.03mm thick anode and cathode electrode plates
- 0.2 – 0.5mm anode and cathode gas diffusion layers.
- A 0.05 to 0.1mm sandwich layer of electrolyte.

The most common arrangement for a fuel cell stack consists of a series of flat plates which are clamped and sandwiched together. To alleviate the sealing problems associated with the planar designs the different layers can be built as a series of concentric circles to create a tubular design. The planar configurations typically have higher power densities and will be the only type considered here.

9.4.2 Fuel cell electrodes

The reactions which take place between all the fuel cell elements take place on the electrode surfaces. These reactions are however typically too slow to produce a significant current and therefore power output, which must be improved by:

- Increasing the area of the electrodes. For this reason, the performance of a fuel cell is typically expressed in terms of the current per cm^3. Porous surfaces enable the electrode area to be increased when viewed on a microscopic level.
- Increasing the operating temperature of the fuel cell. This is beneficial to the reactions but long start-up times are required and the transient operation is poor.
- Coating the electrodes with a catalyst layer to provoke the reaction. The catalyst required is specific to the fuel cell, with platinum typically being used for PEM

cells. Catalysts can however (especially platinum) be very expensive and it is necessary to use them sparingly.

Within PEM fuel cells, very fine particles of the catalyst are typically supported within a surface layer of carbon particles which is connected to the electrode surface by means of a porous but highly conductive gas diffusion layer. This allows the contact between the reactants and catalyst to be maximised while maintaining a good electrical contact between the parts of the electrode. At the cathode, the gas diffusion layer also allows the water by-product to be removed. Carbon based materials such as carbon felt or carbon paper are normally used for this purpose. A certain amount of the electrodes typically extends beyond the catalyst to further increase the contact with the reactants.

9.4.3 Fuel cell membranes

The best and most common material used for the polymer electrolyte membranes of PEM fuel cells is the fluoroethylene material Nafion. Fluoroethylene materials are particularly suited to such an application since:

- They offer a high resistance to chemical attack
- They offer good mechanical strength and durability, which allows them to be manufactured in very thin films of down to 50μm
- They are good proton conductors. When the material is kept well hydrated the H+ ions are able to freely move within the material.
- They are highly hydrophobic. This material property is particularly beneficial to operation of fuel cells as it promotes the expulsion of water from electrodes and therefore helps to prevent flooding.

The main disadvantages of the material are, it is expensive to manufacture and must be kept sufficiently hydrated for the electrolyte to function properly.

9.4.4 Fuel cell manufacture and construction

The construction of a fuel cell stack consists of the assembly of a number of repeating fuel cell units to achieve the desired power output. The cells in a stack are connected in series whereby the anode of one cell is connected to the cathode of the next and so on Careful connection between the cells is however required if significant voltage drops as a result of the connections between cells is to be avoided. The layout of a single cell within a stack is shown below, which shows the grooved backing plates which are used to channel the gases and make electrical connection with the electrodes.

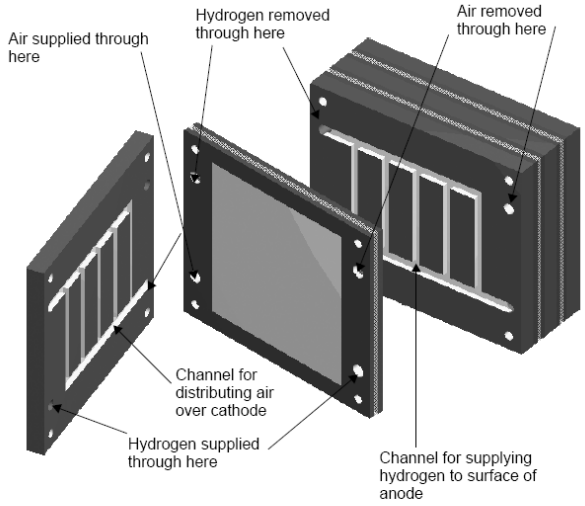

Figure 4.15 A simple bipolar plate with internal manifolding, as is usually used in PEM fuel cells. The reactant gases are fed to the electrodes through internal tubes

Figure 9-5 – Reactant channelling within a stack [49]

The backing plates are typically manufactured from either Stainless Steel or Graphite. These materials each have their benefits and drawbacks: Stainless Steel plates face problems of corrosion while Graphite plates are brittle and require careful manufacture. When used within a stack, they have grooves on both sides to produce a 'bipolar plate' which is used to link the anode and cathode of adjacent cells, while keeping the supply gases safely separated. A bi-polar plate is typically made larger than the electrodes and also used to channel the gases though the complete stack. This significantly simplifies connections to the fuel cell stack, as only electrical and gas connections need to be made on the end plates of the stack. The porosity of the electrodes results in an additional complication when fuel cells are clamped together within a stack, since gas leakage will occur if the edges of the electrodes are not properly sealed. It is typical to increase the size of the electrolyte layer and use a sealing gasket around the edges of the electrodes to prevent such leakage, as shown in the figure below.

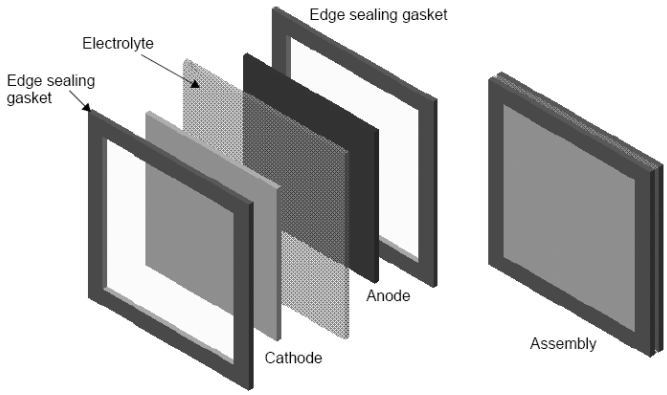

Figure 4.14 The construction of anode/electrolyte/cathode assemblies with edge seals. These prevent the gases leaking out of the edge of the porous electrodes

Figure 9-6 – Exploded view of a fuel cell membrane-electrode assembly [49]

The complexity of the bi-polar plates is further increased when additional passages are incorporated for a cooling medium. In such cases, each bi-polar plate normally has to be manufactured in two halves in order to be able to manufacture the cooling channels which results in an increase in cost, weight, size, complexity and the number of component joints.

9.5 High altitude fuel cell operation

9.5.1 Introduction

Until now the use of fuel cells has been primarily limited to sea level applications. Operation of a fuel cell at higher than atmospheric pressures is already well understood for its performance benefits. Until now, there has been little research effort for cases where they are operated at lower than standard sea level atmospheric pressure conditions. This is because until now fuel cells have only been used for sea level installations and since degradation in performance is expected at such operating conditions, they have generally been avoided. Along with the interest in the use of fuel cells in the aerospace industry is the need to investigate their performance under low pressure conditions. The research efforts that have been carried out in this area will be discussed in a later section.

9.5.2 Low pressure fuel cell applications

There are already a small number of fuel cell installations which operate within low pressure environments such as on the Apollo and space shuttle orbiters and the Boeing fuel cell demonstrator aircraft. These have however relied on high pressure bottled oxygen and hydrogen and thus have ignored the problem of low pressure operation. GA aircraft and UAVs operating at low altitudes are unlikely to see a serious deterioration in the performance of a fuel cell using atmospheric air. The effect of much higher altitudes will be more significant and any performance degradation can no longer be ignored. Operation under such conditions is likely to necessitate the need for a larger fuel cell, resulting in increased cost, complexity, volume and weight.

9.5.3 De-rate performance prediction methods

A number of manufacturers currently specify altitude ‘de-rate’ factors for the un-pressurised operation of their fuel cells at altitude. An example of such a de-rate factor would be a power output decrease of 1.5% per 1000ft for altitudes above 1000ft. These are however generally only applicable for altitudes up to 10,000ft and therefore are not applicable to typical aircraft cruising altitudes of 20,000+ft.

9.5.4 Current low pressure operation research efforts

It is evident that, for fuel cell powered aircraft to become viable some form of reliable analytical method is required to predict the performance of a fuel cell at high altitudes. Such a tool would enable the performance of the fuel cell to be accurately predicted not only at high altitudes but throughout the complete flight profile. In order to meet

airworthiness requirements, fuel cells must also demonstrate that they are reliably able to produce sufficient power even under the most hostile of environments. Three research efforts which have been aimed at bridging this gap in knowledge will be discussed in the sections below.

9.5.4.1 Cessna-Boeing aircraft battery replacement research

In this project, fuel cells were investigated as a replacement for the batteries used on-board aircraft. Experimental tests were carried out on a Ballard Nexa 1.2kW PEM fuel cell within a basic altitude test chamber, which showed a net power decrease from 1300W at sea level conditions to 970W at 5000ft. The air supply was identified as being responsible for the power loss.

9.5.4.2 U.S. Environmental Protection Agency high altitude fuel cell bus operation

This research was conducted as was part of phase 2 of the Ballard fuel cell bus research programme. Its powerplant consisted of 20 13kW PEM fuel cells which were tested at an altitude of 7400ft in Mexico City. Operation at this altitude showed a 24% decrease in current compared to equivalent operation at sea level conditions. The research also identified the air supply system to be responsible for the power loss.

9.5.4.3 General high altitude research by the National Fuel Cell Centre (NFCC)

The aim of this project was to investigate how the performance of a fuel cell is affected by variations in both ambient pressure and oxygen concentration. This is the most significant contribution to high altitude fuel cell operation. A summary of this research is presented below but further details can be obtained from Ref [50].

9.5.4.3.1 Experimental testing and analysis

This involved the experimental testing of an annular type PEM fuel cell (supplied by DCH Enable Fuel Cell Corp.) at a range of pressures from 0 to 53,500ft within a vacuum chamber. The air was cooled by means of cold boil-off nitrogen gas fed to a flat plate heat exchanger and the relative humidity was controlled by means of a desiccant dryer system. Ultra-high purity hydrogen was used. The results were later compared to current theoretical analyses to offer possible explanations for the mechanisms that govern such behaviour. The results presented a distinction between voltage losses due to concentration changes and voltage losses due to total pressure reductions. For the same percentage reduction, total pressure reductions are shown to have the greater effect on performance.

The concentration of oxygen in air is constant for altitudes up to 262,000ft and total pressure is typically the main contributor to reduced performance. Limitations of the analysis methods meant that the results were only analysed up to 35,000ft. Oxygen concentration was varied by changing the airflow and thus the stoichiometric ratio but this is complicated by the fact that it is also dependant on the water content of the

cathode. In these experiments, neither of these varied by an amount considered to be significant.

9.5.4.3.2 Results

The results obtained are valid for the 15-70% humidity range and inlet air temperature range of -60 to +20˚C. The results were initially obtained as a number of voltage vs. current curves for a number of different pressure and airflow combinations. In such tests, the fuel cell was operating in the transition region, where its characteristics are dominated by activation and ohmic losses. These results showed airflow to have little effect at high pressures but a large effect at low pressures, which led to the development of the Air Flow – Pressure interaction contour graph below.

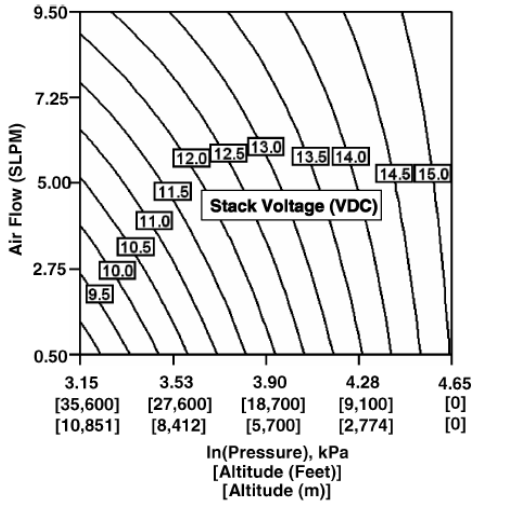

Fig. 2 Interaction of ambient pressure and airflow and their effects on stack voltage for a fixed external resistance (50 Ω).

Figure 9-7 – Results from the study into the performance of fuel cell at high altitudes [50]

As can be seen, this voltage drop with decreasing airflow can be considered to be less significant at high pressure than low pressure conditions.

9.5.4.3.3 Theoretical analysis

The effect of high altitude conditions on a fuel cell are thought to be a result of variations of both the Nernst potential and cell polarizations which will reduce the voltage and efficiency of the fuel cell for a given power setting. The theoretical analysis is based on a form of the Nernst equation below, which is presented in terms of the total pressure of the anode and cathode. This expression shows the performance of the fuel cell to be dependant on partial pressure, which itself is dependant on both concentration and total pressure.

$$E = E^0 + \frac{RT}{nF}\ln\frac{pH_2\left(pO_2\right)^{1/2}}{pH_2O} \qquad \text{Where, } pO_2 = xO_2P_T \qquad \text{Eq 9-5 and 9-6}$$

The Nernst equation is insufficient on its own and irreversible losses such as activation, ohmic and mass diffusion also need to be accounted for. These are however dependant on the regime within with the fuel cell operates and have also been shown to have an effect on whether it is the concentration or total pressure that is the most relevant. Total pressure has been shown to be more significant than concentration at low current densities.

The theoretical analysis predicts that the voltage loss should be equally affected by either a change in the total pressure or concentration. This is however not what has been observed in practice, with total pressure having a greater influence on the voltage than the oxygen partial pressure. Reductions in both concentration and total pressure also gave rise to losses greater than predicted and further work is required in this area. Experimental results therefore remain the most reliable at present.

9.5.4.3.4 Evaluation of the research effort

The author of this thesis conducted an in-depth review of the results presented for this research effort with a view to fitting a convenient analytical expression to the results. In the process however it was discovered that the results were unreliable due to temperature variations during testing. These results were therefore not used for this project. Full details of the evaluation of the results and the derivation of the general analytical expression are given in Appendix F.

9.5.5 Fuel cells – Design for high altitude operation

Where fuel cells are operated under high altitude conditions a number of design features can be implemented to tailor them for improved performance under such conditions. Such modifications include:

- Modifying the electrolyte concentration in the catalyst layer to improve mass diffusion at low pressures.
- Optimise the catalyst layer thickness for low pressure conditions. The design operating region on the V-i curve not only has an impact on the reaction rate but also has a significant impact on the optimal catalyst layer design. Thicker catalyst layers are favourable for low current operation but result in increased total pressure losses and are therefore less suitable for low pressure operation. Thinner catalyst layers are favourable for high current operation and low pressure operation but result in lower reaction rates.
- Design of the fuel cell backing layer with respect to oxygen concentration. It is independent of total operating pressure.

10 Fuel cell research projects

10.1 An overview of fuel cell development

The first serious use of mobile fuel cells was for space missions onboard the 1960's Apollo Orbiter. More recently fuel cell technology has received serious interest for stationary power generation, automotive propulsion and small scale electrical equipment power supply. Their continual development has resulted in significant improvements in performance, weight, volume and cost. Their continued improvement has now reached a stage where the readiness of the technology and the power/weight of these units have reached levels which are attractive for use in the aerospace sector. Fuel cell technology is not without its problems, but it is currently considered to be the best replacement for oil dependant propulsion systems and is being eagerly followed up by many sectors.

10.2 Automotive research effort

Within the automotive industry fuel cells are seen as serious contenders to IC engines and the majority of major motor companies are investing considerable time and money to advance the technology for vehicular use. To-date fuel cells have been demonstrated in a number of concept cars, which have proven the capability of the technology with very respectable performance figures. There are many challenges which still need to be overcome before they can become commercially widespread but their development is advancing at a respectable rate. It is fair to say that the application of fuel cells in the automotive industry may always be ahead of the aerospace industry since the development of these vehicles is not held back by strict airworthiness requirements. The most recent developments in the automotive industry are summarised in the table below.

Automotive research efforts - Copied from www.fuelcells2000.org carchart

Manufacturer	Vehicle	Year	Propulsion	Fuel cell size/type	FC Mfr.	Fuel type
Audi	Q5 HFC	2010	FC/Batt. hybrid	131 bhp	N/A	Comp. hydrogen
	A2	2004	FC/Batt. hybrid	66kW PEM	Ballard	Comp. hydrogen
BMW	FC hybrid 1-series	2009	FC/Batt. hybrid	5kW PEM	UTC Power	N/A
Daihatsu	MOVE FCV-K II	2001	FC/Batt. hybrid	30kW PEM	Toyota	Comp. hydrogen
Daimler	M' -Benz F-800	2010	FC/Batt. hybrid	N/A	N/A	Comp. hydrogen
	B-Class Zero F-Cell	2009	FC/Batt. hybrid	90kW PEM	N/A	Comp. hydrogen
	Blue Zero F-Cell	2009	Fuel Cell	N/A	N/A	N/A
	EcoVoyager	2008	FC/Batt. hybrid	45kW PEM	N/A	Comp. hydrogen
Fiat	Panda	2007	Fuel Cell	60kW PEM	Nuvera	Comp. hydrogen
Ford	Airstream/HySeries	2007	FC/plug-in hybrid	HySeries Drive	Ballard	N/A
	Explorer	2006	FC/Batt. hybrid	60kW PEM	Ballard	Comp. hydrogen
GM	Provoq	2008	FC/Batt. hybrid	88kW PEM	GM	Comp. hydrogen
	HydroGen4	2007	FC/Batt. hybrid	93kW PEM	N/A	N/A
	Equinox FCEV	2006	FC/Batt. hybrid	93kW PEM	N/A	N/A
Honda	FC Sport	2008	Fuel Cell	PEM	Honda	Comp. hydrogen
	FCX Clarity	2007	Fuel Cell	100kW PEM	Honda	Comp. hydrogen
	PUYO	2007	Fuel Cell	N/A	N/A	N/A
	FCX	2006	Fuel Cell	100kW PEM	Honda	Comp. hydrogen
Hyundai	Tucson ix35 FCEV	2010	FC/SuperCap.	100kW PEM	N/A	Comp. hydrogen
	i-Blue	2007	Fuel Cell	100kW PEM	N/A	Comp. hydrogen
	Tuscon II	2007	FC/Batt. hybrid	100kW PEM	Kia	Comp. hydrogen
Kia	Borrego/Mojave	2008	FC/Batt. hybrid	115kW PEM	Kia	Comp. hydrogen
	Sportage II	2008	FC/Batt. hybrid	100kW PEM	Kia	Comp. hydrogen
Peugeot-Citroen	307cc FiSyPAC	2009	FC/Batt. hybrid	N/A	N/A	N/A
	H2 Origin Van	2008	FC/Batt. hybrid	10kW PEM	Intelligent Energy	Comp. hydrogen
Renault	Scenic FCV H2	2008	FC/Batt. hybrid	90kW	Nissan	N/A
Suzuki	SX4-FCV	2008	Fuel Cell	80kW PEM	GM	Comp. hydrogen
Toyota	FCHV-adv	2008	FC/Batt. hybrid	Toyota FC Stack	N/A	N/A
Volkswagen	Passat Lingyu	2008	FC/Batt. hybrid	55kW PEM	SAIC	N/A
	Tiguan HyMotion	2008	FC/Batt. hybrid	80kW HTFC	VW	N/A
	Space-Up Blue	2007	FC/Batt. hybrid	45kW PEM	VW	N/A
	Touran HyMotion	2007	FC/Batt. hybrid	80kW PEM	VW	N/A

Table 10-1

Work in the automotive industry has however not been limited to cars and vans with fuel cell buses, trucks and scooters also being developed. Compared to other vehicles, buses have the benefit of virtually continual operation which can relieve some of the problems experienced with other vehicles. These include long periods of on-board hydrogen storage, long warm-up and shut down cycles and cost recuperations. As a result, hydrogen buses have already been successfully used in several major cities.

10.3 Current PEM fuel cell developers

Of all the fuel cell types, the PEM fuel cell is one of the most mature and is showing the most promise for vehicles. These have the advantages of low operating temperature (60-80ºC), compact size, low weight, high efficiency and quick start-up times. PEM fuel cells have not always been attractive candidates however, due to their use of platinum, but, fortunately, recent research effort has reduced the platinum content making them more cost effective than in the 1970's. To date these fuel cells have typically used hydrogen, but systems coupled to methanol fuel processors are also showing promise. Automotive PEM fuel cells are currently being developed by a number of companies, such as Ballard, GM, Nuvera, UTC and VW. Ballard was at one time considered to be the leaders in this field with their Mk900 series fuel cells being incorporated in the majority of early automotive research projects.

10.4 Other applications of fuel cells

Fuel cells have not only been considered for use within aircraft and cars and a number of other research projects have investigated their use within:

- Marine Vehicles – Such as boats, submarines and yachts. Fuel cell systems up to 300kW have been developed for such applications.
- Utility vehicles – Such as trucks, tractors and forklifts. The most relevant vehicles in this area have been 65kW aircraft tow tractors developed by Entwhistle and Hydrogenics.
- Motorcycles and scooters – The majority of these demonstrator projects have been in the low power range with the biggest being the ECN Fresco scooter which uses a 12kW PEM fuel cell.
- Unmanned Aerial Vehicles – The most significant demonstrator vehicles in this area have been the Aerovironment Puma and DLR HyFish, each with a 1kW fuel cell. Other projects have been on a much smaller scale and are not relevant to this project.
- Other vehicles – Such as all-terrain vehicles, wheelchairs, trains and golf carts. The most relevant development in this area has been the 10kW Quantum Aggressor ATV vehicle. Other systems have been of low power.

10.5 Aerospace research projects

10.5.1 DLR Antares DLR-H2 fuel cell airplane

This demonstrator aircraft was developed as part of the Fuel Cell Labs research project run by DLR to develop fuel cells to be used as reliable on-board power supplies in civil aviation applications. This aircraft is to be used as a flying test bed aircraft for the development of fuel cells for such purpose, and will optimise the time needed for testing of the much larger Airbus A320 ATRA research aircraft also being used by DLR. On the ATRA aircraft, fuel cells have been implemented as an auxiliary power supply for hydraulic pumps used for steering. Plans are already in place to extend their use as an on-board power supply for wide body airliners.

The DLR-H2 aircraft is based on the self-launching Antares 20E single seater motor glider built by Lange Aviation. This production glider with a 20m wingspan and weight of 660kg already uses a battery powered electrical propulsion system which made it the ideal candidate for this project. The aircraft was retrofitted with a 25kW fuel cell system specially prepared as a collaborative effort between DLR Institute of Technical Thermodynamics, BASF Fuel Cells and Serenergy A/S. The fuel cell is used as the primary power source for propulsion and delivers sufficient power to enable it to take-off using fuel cell power alone. The propulsion system enables the aircraft to fly at a maximum speed of 170km/h but in normal straight and level flight, only 10kW is required, enabling the fuel cell to operate at an efficiency of 52%. The aircraft wings were strengthened to enable an external pod to be added underneath each wing with the left pod housing the fuel cell system and the right pod housing the hydrogen tank. The power train consisting of the motor, controller and propeller was specifically developed by Lange Aviation. In 2010 the aircraft made history as the first aircraft to take-off using power from the fuel cells, as well as setting an altitude record of 2560m.

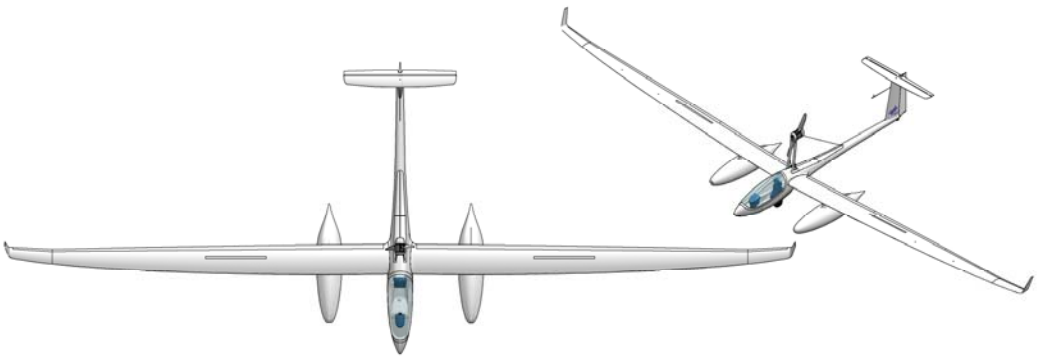

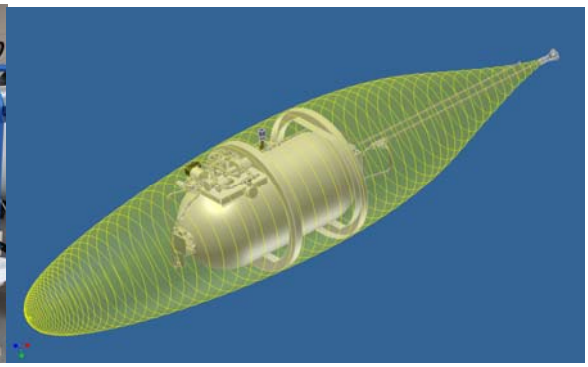

Figure 10-1, 10-2 and 10-3 – The DLR Antares fuel cell airplane [51]

Although the design range and endurance of the Antares DLR-H2 is a respectable 700km and 5 hours respectively, DLR is developing an improved performance version, the DLR-H3 in collaboration with Lange Aviation. The DLR-H3 will use four external pods to give it a design range and endurance of 6km and 50 hours respectively. The wingspan and weight have increased to 23m and 1250kg respectively, but it is also capable of carrying payloads up to 200kg. First flight of this aircraft is expected in 2011 and it is intended to become the first piloted aircraft to perform a complete powered flight by fuel cell alone.

10.5.2 FASTec/ATP fuel cell E-plane

This project was lead by the Foundation for Advanced Science and Technology Education organisation with the aim of converting a 2 seater composite DynAero Lafayette III aircraft to electric power. Development of the E-plane was to be carried out over three phases. The first phase will focus on converting the aircraft to electrical power using lithium ion batteries and a brushless permanent magnet motor from UQM which will give the aircraft a range of 100 miles. In the second project phase a 10-15kW fuel cell will be used to augment the batteries to give it a range of 250 miles. In this configuration, the fuel cell will provide power for the steady cruise phases, with additional power coming from the batteries as required. In its final phase, a larger fuel cell will be used to replace all the batteries, which is capable of delivering a 500 mile range. In this configuration, a number of batteries will be carried on-board solely to provide power in the event of emergency. The E-Plane was intended to be used to demonstrate emerging technologies in worldwide education programs, but the project has been relatively quiet since late 2003 when they were actively seeking sponsors.

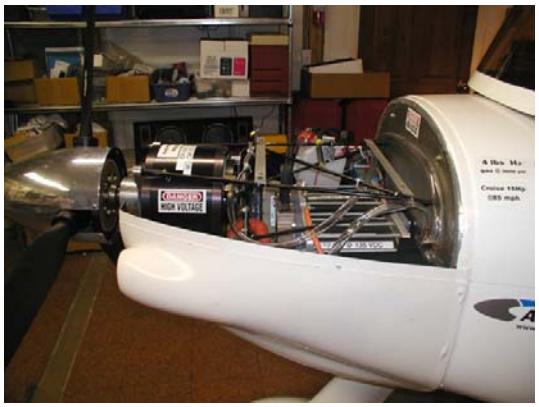

Figure 10-4 and 10-5 – The FASTec/ATP fuel cell E-plane [Ref Unknown]

10.5.3 ENFICA Rapid 200-FC fuel cell hybrid airplane

This aircraft was developed by the ENFICA-FC (ENvironmentally Friendly Inter City Aircraft powered by Fuel Cells) research consortium which consists of 9 industrial and academic partners. The objective of this 4.5M€, 3 year program was aimed at investigating the use of fuel cells as a means of propulsion for more/all electric aircraft. Such work is aimed at the development of the next generation of commuter airplanes which are characterised by low noise and low emissions which will make them more

desirable for operation from urban airfields. This would involve the development and evaluation of a fuel cell system within an aerospace environment. Specifically this project will bring together the experience of the partners in the fields of fuel cell systems and hydrogen storage systems in the development of this demonstrator aircraft.

The baseline production aircraft selected for this project was the two seater Rapid 200 manufactured by Jihlavan Aircraft. This light sport aircraft, with a wingspan of 10m and weight of 500kg, was selected for its low power requirement at low speed flight. Partners Intelligent Energy developed the 20kW fuel cell system which uses centrifugal compressors to enable it to operate at elevated pressures. Hydrogen for the fuel cells is stored at 350 bars within two 26 litre Dynatec L026 tanks which are installed in the baggage compartment behind the pilot. The power from the fuel cell is supplemented with two Lithium Polymer battery packs which are able to deliver an additional 20kW for take-off and climb. This battery/fuel cell combination was selected to minimise the weight of the fuel cell system. In order to preserve battery life, the fuel cell has priority as the primary power source and as a result it serves as the sole power source during the cruise and descent flight phases. A complex control system is used to switch between the power sources and then deliver the power to a 46kW commercial air cooled brushless motor manufactured by Phase Motion Control.

The fuel cell system was continually tested for more than 6 hours by the manufacturer to assert its reliability, within which time it showed no degradation in performance. The system was then installed on the aircraft and extensively tested before the aircraft made its maiden flight in May 2010. The completed aircraft was flight tested as proof of functionality of fuel cell systems for the next generation of inter-city aircraft. During this in-flight testing, an endurance of 40 minutes was obtained which was limited by the water consumption and the size of the water tank (not the hydrogen tank). The results showed the performance of the fuel cell aircraft to be inferior to the original aircraft along with a reduction in payload capacity. A recommendation was made for further development work to reduce the weight of the systems to improve its performance. For example, to be able to carry 1.2kg of hydrogen currently requires a 52kg storage system.

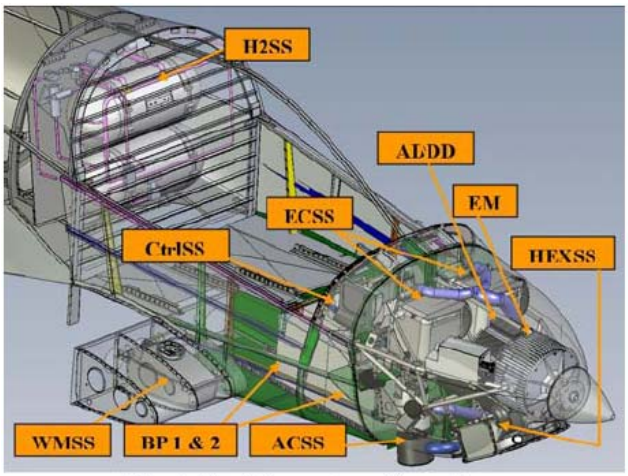

Fig 4. Final lay-out configuration.

Component	Mass [kg]
Empty Aircraft [EA]*	221
Electro-Chemical Sun-System [ECSS]	103
Water Management Sub-System [WMSS]	
Heat Exchanger [HEXX]	
Control Sub-System [CtrlSS]	
Pressurized Hydrogen Sub System [H2SS]	51
Electric Motor [EM]	38
AC/DC+DC/DC Sub-System [ADDD]	14
Battery Pack 1 [BP1]	26
Battery Pack 2 [BP2]	26
Pilot [Pil]**	75
TOTAL	554

Figure 10-6 and 10-7 – The ENFICA fuel cell airplane [52]

10.5.4 Boeing fuel cell demonstrator airplane

The aim of the fuel cell demonstrator airplane was to provide an insight into fuel cell technology with a view to using fuel cells to replace large aircraft APUs. This work is coincident with the significant amount of work already being carried out to reduce the emissions and improve the fuel economy of commercial aircraft engines. Although the APU is not the largest contributor of emissions it is still an area which needs to be addressed. The 20kW fuel cell used for this project will give valuable insight into the use of larger 130kW to 600kW fuel cells to replace the APU in the tail of large commercial aircraft. The experience gained from this project will highlight any potential problems which will need to be addressed if fuel cells are to be used in aerospace applications. This case study will also help new airworthiness regulations to be defined and will give valuable insight into the problems of hydrogen fuel handling.

The airplane used was a refitted commercially available two seater Diamond Dimona powered glider. The low cruise speed of this aircraft implied low power requirements (high glide ratio) which were a particularly attractive feature to keep the fuel cell system to a sensible size. The existing engine was replaced with a PEM fuel cell, batteries and an electric motor which was used to drive a conventional propeller. The fuel cell was sized for cruise with the power required being a function of the cruise speed. This resulted in a power of 15kW being required to achieve a cruise speed of 60kts. During cruise, the electric motor is powered solely by the fuel cell but this has insufficient power for the take-off and climb phases. For the needs of these more demanding short period flight phases, the fuel cell power output was supplemented by a bank of batteries, which keeps the fuel cell to a sensible size. The batteries will also be used to supply start-up power for the fuel cell as well as begin able to provide emergency power in the event of failure of the fuel cell.

Since the range of the aircraft is small (100nmi typically), the hydrogen and air required by the fuel cell were supplied in gaseous form. For this purpose, a number of on-board composite filament wound fuel tanks were connected together and used to supply low pressure hydrogen to the fuel cell, via a regulator. The motors and controllers used in electric powered cars were shown to be able to meet these requirements and were adapted for this project. An efficient low speed motor was envisioned to provide 50kW peak power and a continuous speed range of 2200-2500 rpm during cruise, rising to 2500-2800 rpm during take-off and climb. A large heat exchanger was also required to be installed in order to disperse the heat generated by the fuel cell, motor and controller. The most efficient location for this is just aft of the propeller where it is able to make use of the higher velocity air, as shown in the figure below.

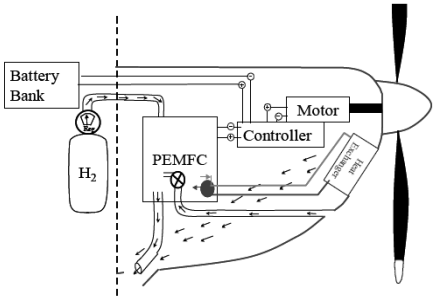

Figure 10-8 – The Boeing fuel cell demonstrator fuel cell installation [48]

A mass budget of 247kg was available which was made up of the mass of the conventional engine and fuel system which have been removed and that which would normally be available for gasoline, a passenger and any baggage. The majority of this mass budget is taken up by the fuel cell, batteries and motor. The remainder is taken up by the controller, fuel tanks, hydrogen fuel, heat exchanger and balance of plant. The PEM fuel cells which are supplied by the UK manufacturer Intelligent Energy function at higher than atmospheric pressures to improve their efficiency. The controller and power conditioner used to regulate the power delivery from the batteries and fuel cell was developed by Boeing. The initial layout of the aircraft as of 2003 is shown in the figure below.

Figure 10-9 [Ref Unknown]

At the time of the initial study for this project, it was felt that fuel cells were still too immature for them to be feasible to replace the APU. This study suggested a further development time of 10-15 years from year 2003 was before they become feasible.

10.5.5 Design study of a fuel cell powered aircraft – Menard

This was a Cranfield University MSc project [53], whose aim was to investigate the feasibility of using a fuel cell to power a light reconnaissance aircraft. The project gave an overview of the use of fuel cells and the problems associated with the storage of large quantities of hydrogen onboard the aircraft. The project initially investigated the implications of installing a fuel cell into two different aircraft types. These were:

1. Reconnaissance airplane - This was based around the 1970s ducted fan Edgley Optica which is low powered and quiet. The powerplant was to be replaced with a DC fuel cell, converter and AC motor. Three different fuel cell types were investigated for this aircraft, scaled-up Ballard Mark 902, modular Ballard Mark 9 SSL and a high power non-commercial research unit
2. 4 seat general aviation aircraft - This was based around the Cessna 172 Skyhawk. Again three different fuel cell options were investigated, 6x Ballard Mark 9 SSL stacks, a GM designed fuel cell stack and a high power non-commercial research unit

This initial study showed fuel cells to be less able than piston engines to meet the performance demands of these aircraft. The four seat high wing reconnaissance aircraft was selected as the final aircraft configuration for further analysis due to its lower thrust requirements. This configuration also had plenty of space available in the fuselage for the fuel cell system and extra fuel in addition to that already stored in the wings. It used two pusher propellers which were driven by motor located in under-wing nacelles. The layout of the aircraft and the various internal components is shown in the figure below. This also shows a cross-section through the wing and wing fuel tanks as will be discussed below.

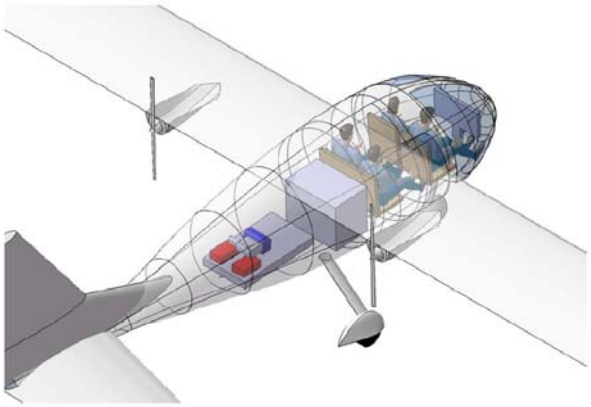

Figure 38 : Power plant location

Figure 44 : detailed hydrogen storage concept

Figure 10-10 and 10-11 – MSc design study of a fuel cell powered aircraft [53]

The unconventional nature of the powerplant installation meant that the aircraft had to be designed from scratch to ensure it was able to meet all of the design requirements. A spreadsheet approach was used for this task which was able to be adapted to take account of the output power and weight of the fuel cell propulsion system. This identified the need for 8x water cooled 21kW Ballard Mark 9 SSL PEM fuel cell stacks in order to meet the design requirements.

To meet the requirements of an 800 km range at 190km/h, the amount of hydrogen that needed to be carried onboard the aircraft was determined as 55kg. Due to the low density of hydrogen, liquid hydrogen was considered the only viable storage option. This would consist of integral wing tanks situated between front and rear spars at 15% and 60% respectively, which would be wrapped in aluminium foil based insulation to minimise boil off. The actual thickness of the insulation was determined from a trade-off study of weight penalty, volume stored and hydrogen losses. The fuel tanks were designed as a series of overlapping cylinders which were intended to be the optimal configuration to withstand the 20 PSI pressure of the hydrogen. When extended to the full span, the tanks have the potential to carry 132kg of hydrogen. The tanks were perceived as being constructed as either a one piece unit or from upper and lower shells which can be accessed by removing the wing skins.

A schematic of the propulsion system is shown below.

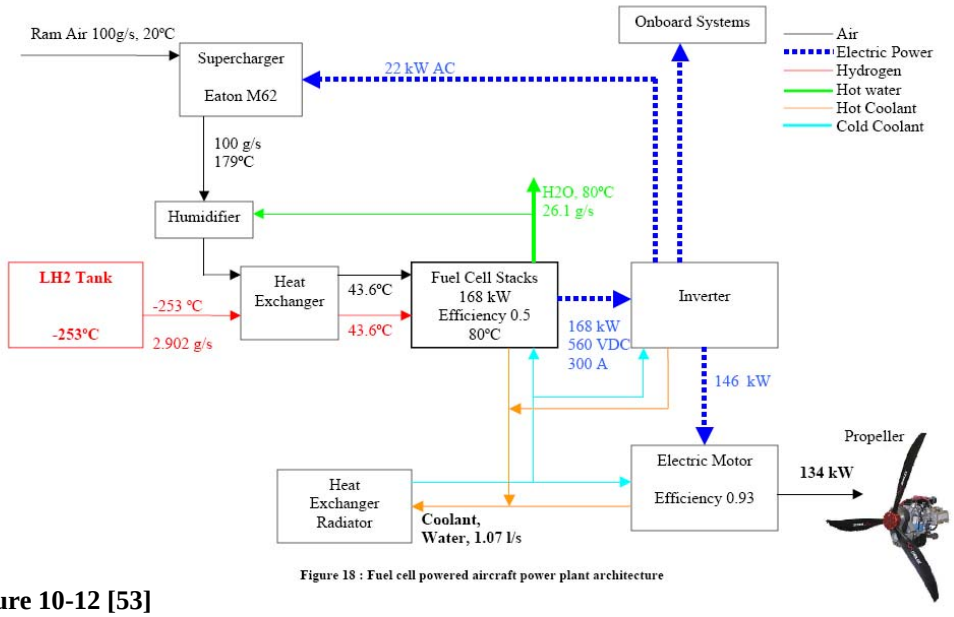

Figure 18 : Fuel cell powered aircraft power plant architecture

Figure 10-12 [53]

The components selected for the system are:

- A scaled up TIM-600 inverter capable of handling 168kW for a weight of 16.8kg.
- A Zytec motor capable of handling 100kW for a weight of 21kg with an efficiency of 93%..
- A 58.6 litre/min water pump which uses 400W and weighs 6.8kg. A total figure of 12kg was assumed for the complete cooling system including heat exchanger and cooling fluids.
- A Eaton M62 supercharger which requires 22kW to operate at 8600 rpm for a weight of 21kg.
- Batteries manufactured by aircraft battery specialists SAFT, which are used to provide additional power for take-off and power in an emergency.

The validity of the results obtained are however dependant on the initial assumptions which had to be made about certain parameters (such as fuel cell efficiency, whose exact values were not available at the time of the project). As a result, although this project forms gave a reasonable introduction, the results obtained should not be relied upon and future work should strive to obtain more accurate predictions.

10.5.6 Conceptual design of a Fuel Cell Powered Aircraft – Bekiaris

This was another Cranfield University MSc project [54] aimed at investigating the feasibility of using a fuel cell to power a light aircraft. Time constraints meant that a conventional baseline configuration designed to meet VLA requirements was opted for. This was a low wing monoplane with 2 seats in tandem and a conventional tail. An Xcellsis PEM fuel cell engine was selected for the aircraft which was predicted to occupy a large part of the total volume of the fuselage. Data relating to the operating performance of such a unit was scarce but necessary to predict its performance over a range of operating conditions. Bekiaris therefore opted to define a basic system

schematic using what data could be collected for the Xcellsis HY-75. The remaining data came from its relative the Ballard Mark 902 fuel cell.

The basic schematic was used to construct a basic analytical model which could be used to predict the performance of the fuel cell aircraft throughout the aircraft flight. This involved defining analytical and empirical performance models to estimate the performance and efficiency of the various components and the interaction between them. Collectively, these would then used to build a very basic overall fuel cell engine performance model. The objective was to create a simple black box representation of the complete system which can be easily incorporated into an aircraft conceptual design process. Bekiaris was however only able to build an engine specific fuel consumption model within the time allocated. This model was developed directly from theory. This made use of expressions for the ideal voltage which was corrected to take account of loses such as polarisations. The effect of non-standard pressures was then accounted for with a simplified form of the Nernst equation. When compared with experimental data, it was evident that better theoretical correlations between the pressure and temperature conditions at the various voltage losses are required as a result of discrepancies.

Liquid hydrogen storage within integral wing tanks was favoured over compressed hydrogen for this project since it would offer the same amount of energy for a smaller volume. The use of liquid hydrogen was however shown to be accompanied by its own set of problems. Two options were proposed for the construction of the tanks. The first option was the vaulted composite panel construction used on the multi-lobed hydrogen tanks of the Lockheed Martin X-33 which would be wrapped with insulation. The second option was a system proposed by Linde AG to reduce hydrogen boil-off and enables liquid hydrogen to be stored for a period of two weeks without significant vapour loss. In this system, a heat exchanger transfers heat from the hydrogen being drained to air to be fed into a cavity making up the inner and outer skins of a hydrogen tank. The use of liquid hydrogen means that fuel pre-heaters are required. Its high pressure means that no fuel pump is required; an ejector pump is still however required to re-circulate the hydrogen.

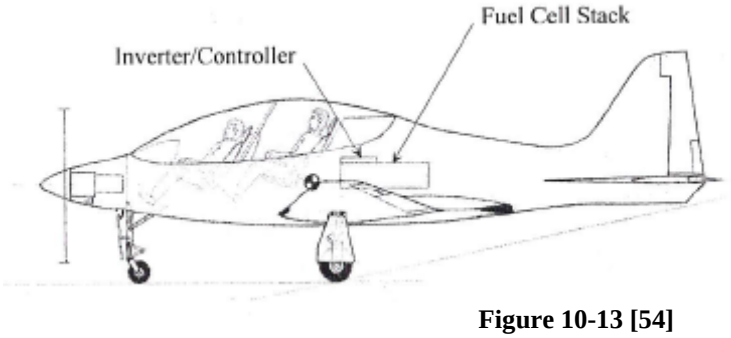

Figure 10-13 [54]

Within the aircraft, the fuel cell is located aft of the cockpit along with its associated equipment. Its DC power output is converted to AC through and inverter/controller and then fed to an electrical motor and gearbox located ahead of the cockpit. A liquid cooled brushless AC racing motor by Zytec was considered to be the best for this application with a specific power rating of 4.76kW/kg. A matching liquid cooled Zytec inverter/controller was scaled up to match the motor with a specific power rating of 14.58kW/kg. A reduction gearbox is a necessity to enable the high motor speeds (necessary for high efficency) to be reduced to 1000-2000 rpm suitable for the propeller. An inline split path planetary gearbox was selected as the best for this application in terms of its specific power requirements, efficiency and external

aerodynamic drag profile. Compared to other designs, this offers an efficiency of about 98% at cruise and weight savings of up to 40%. Separate liquid cooling systems were proposed for the fuel cell and motor/gearbox to remove waste heat. Some of the waste heat from the fuel cell is recycled within the pre-heater and humidifier with the remainder being disposed of.

A significant lack of information of the various engine parameters resulted in only a simplified specific fuel consumption model being possible and therefore its accuracy was in doubt. The SFC figures from the Xcellesis data were therefore considered the most accurate and were used for the rest of the analysis. These figures did not however include any allowance for altitude and throttle setting. The final aircraft design was optimised using a modified design spreadsheet whereby the semi-empirical piston engine performance relations were replaced by these representations for the fuel cell. In addition, the wing mass was predicted to be 50% greater than an equivalent conventional fuel wing to allow for the integral liquid hydrogen fuel tank double wall construction and insulation materials. When accounting for the mass of liquid hydrogen contained in the tanks, the appropriate density figures were required.

Bekiaris concluded that fuel cells were not viable at the time of the project due to their low power and high weight. Although Bekiaris made the best use of the data available at that time, the accuracy of the results obtained are questionable. The results of an analysis carried out to examine the benefits of using a compressor showed there to be little benefit in using a compressor on a fuel cell engine at altitude. Different electric motor driven compressor configurations were discussed including, positive displacement, centrifugal and axial but a compressor was finally deemed as not being required. These results are however contrary to what is experienced in practice and it is believed that there was probably an omission or over simplification in the analysis. Bekiaris was also able to obtain estimates for the mass and volume of the fuel cell stack but these were quite basic. A better approach would have been to sum the mass and volume of all these components (including allowance for miscellaneous items) to give an overall figure for mass and space requirements.

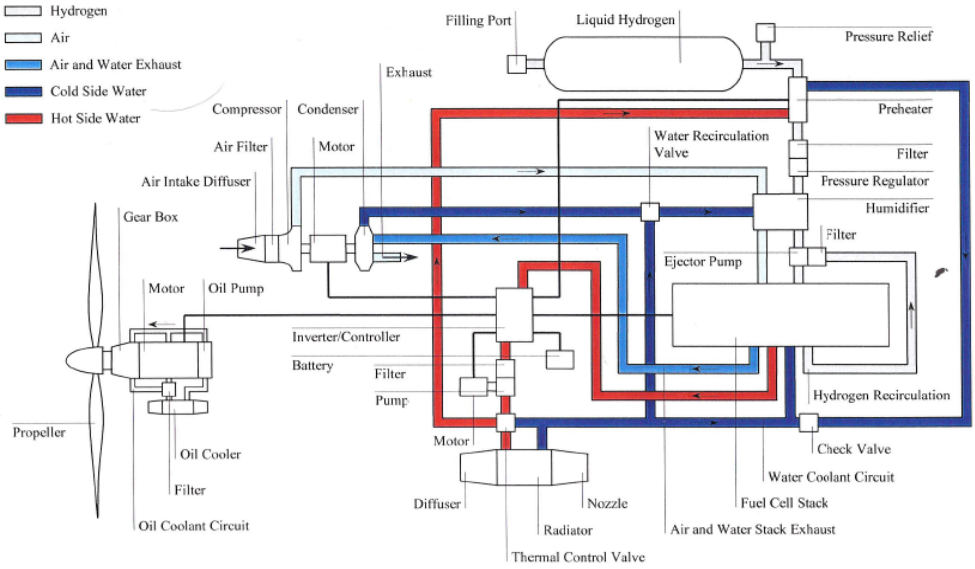

Figure 14 – Polymer Electrolyte Fuel Cell Engine Operating on Liquid Hydrogen and Air

Figure 10-14 [54]

11 Alternative fuels literature review

11.1 The need for alternative fuels

Any fuel can be simply regarded as an energy carrier, currently the majority of which are hydrocarbon based and obtained from fossil sources. Although they have been in widespread use for many years, there are a number of drawbacks associated with their use and as a result alternative fuels are actively being sought. This section will firstly present an overview of the different fuels that are currently available before discussing their availability and the impacts associated with their use.

11.1.1 An overview of current fossil fuels

The majority of current fossil fuels are hydrocarbon based and are categorised according to their hydrocarbon composition, which includes,

11.1.1.1 Petroleum based fuels

Petroleum based fuels (kerosene, diesel, gasoline etc) currently make up about one half of the global energy supply. These are obtained from hydrocarbon based chemical compounds from sedimentary rock deposits such as wells, tar sands and oil shale which are refined through various stages into petroleum based fuels and other products by means of distillation processes. The quantity of fuel obtained (per unit of crude oil) is dependant on the origin of the crude oil. Gasoline is normally blended with other compounds to achieve the different octane rating blends as well as including various additives to improve combustion and engine life etc.

11.1.1.2 Liquefied petroleum gas (LPG)

This is a by-product of the refining of petroleum derived fuels and is suitable as a fuel for both IC engines and fuel cells. This will be discussed in more detail later.

11.1.1.3 Coal

This is the most abundant of all the fossil fuels and is graded according to its composition and the degree of impurities present. It can be processed to obtain various liquids, gases and other compounds (carbonisation processing and later gasification processes were used to obtain town gas in the nineteenth century). Such processing requires temperatures of over 1200˚C and additional clean-up stages due to the number of contaminants. Numerous research studies have been carried out to investigate the benefits of operating a fuel cell on such gases.

11.1.1.4 Natural gas

Natural gas is a mixture of hydrocarbons including methane, ethane, propane as well as other gases such as nitrogen, CO_2, helium and sulphur compounds. It is typically found in porous rocks and more commonly in the vicinity of oil reservoirs and its composition can vary from source to source as well as being dependant on the seasonal climate. It can however be blended to achieve a desired composition to meet specified

requirements. Its variable composition makes it difficult to be able to use within fuel cell systems since the catalyst used can be severely affected by such variations.

11.1.1.5 The limitations of fossil fuels for fuel cell systems

It is possible to use fossil fuel fuels to power fuel cells but the fuel processing required to extract the hydrogen can make this uneconomical. Since high temperatures can be required along with various additional clean up stages to remove traces of other unwanted compounds (such as sulphur and nitrogen which may affect the performance or life of a fuel cell). They are therefore not really suitable for mobile applications.

11.1.2 Diminishing fuel supplies

If examine the world's predicted fuel demands and the viability of meeting these demands with existing fossil fuel sources, the need for alternative fuels is apparent. Since this study is biased towards transportation fuels, this discussion will be limited to oil which is the primary source. Although the transportation is the largest user of the world oil (60.3% - 2007 Key world energy statistics [55]) it is not the only consumer.

An increasing world population along with an increasing demand for fuel, as a result of increases in standards of living and energy demands is putting considerable demands on the world's few existing finite oil reserves. This has resulted in cost increases, not only for transportation but also for domestic tasks such as heating and cooking. Whereas coal reserves are estimated to be sufficient for another 200-300 years, the oil and gas reserves are however only sufficient for about the next 100 years (assuming that we are able to tap into new oil reserves). At our current rate of consumption, our easy to access oil reserves will only be sufficient for 70 years, which does not take into account our ever increasing population. Natural gas reserves on the other hard will give us between 80 and 100 years. The demand for oil is predicted to increase even more over the coming years and our diminishing oil reserves may not even last this long. Alternative hydrocarbon fuel sources are available such as heavy oil deposits, oil shale or tar sand deposits but the extraction of fuel from these sources is difficult, costly and limited.

With time oil is proving harder to obtain with new techniques and technologies being developed to enable oil wells to be utilised which were previously inaccessible. This includes deep sea oil drilling techniques, which have in recent times shown to have significant difficulties and risks associated with them. Another difficulty is that 61.5% of the world's existing oil sources are reportedly located in the Middle East with the rest coming from US, Africa, Europe and Asia. Mans thirst for energy and oil puts pressure on international relations, possibly being one of the driving forces for recent conflicts (the next generation of beasts wild with hunger? [Nostradamus quatrain]). It is evident that we need to be concentrating on finding alternative energy sources in preparation for the inevitable.

11.1.3 What about natural and nuclear energy sources?

The use of natural energy sources such as hydro, geothermal, solar, wind, tidal and waves are slowly being exploited but are facing obstacles such as public opposition. This is to be expected however since it is unfair to expect a quaint village to redevelop

its landscape in order to find ways to meet the power demands of adjacent towns. A better solution would be to put the responsibility on individuals to meet their own power demands. No solar panels or wind turbines equals no energy. Alternative energy sources are however unlikely to be able to fulfil all our energy needs and are unlikely to be suitable for transportation which means that fossil fuels may still remain in the loop for a while longer. The progressive increase in the use of alternative fuels will however lead to them being phased out with time. The manufacture of numerous chemical and materials is also reliant on oil and gas and so alternative sources must be sought for these as well.

Atomic energy has been explored for some time but has proven to have catastrophic impacts in the event of a failure as was evident in the melt down of the power station in Chernobyl Russia. This disaster saw the atomic reactions running away uncontrollably, with many lives being sacrificed and radioactive clouds coving the whole of Europe. The reactor was eventually entombed in concrete but is predicted to take many years to cool down. This disaster has made the surrounding environment inhabitable since and people and animals still have to deal with the impact of the radiation. The disposal of radioactive waste is an additional problem with high risk waste currently being entombed in concrete deep within purpose built landfill sites. Atomic energy has too many drawbacks for its use to be further widespread.

Either of these energy sources is particularly well suited to the generation of electricity. The transformation of an energy source into electrical energy does enable the efficient transportation of energy but the problem of the storage of large quantities of electric makes this form of energy less attractive. For this reason, they are not well suited to mobile applications.

11.1.4 Pollution factors associated with existing fossil fuels

As will be discussed, the use of fossil fuel fuels has serious pollution implications. The combustion of hydrocarbon based fossil fuels results in the carbon being converted to carbon dioxide and the hydrogen to water. Of concern is the 24% increase in CO_2 in the environment in the last 50 years which has been shown to be directly related to the increase in oil usage. CO_2 is not solely responsible but has been shown to be the major contributing (63% - IPCC Fourth Assessment Report Climate Change 2007 [55]) greenhouse gas responsible for global warming. A 2007 study to determine the CO_2 emissions in grams output per tonne carried and kilometre travelled showed aviation to be the worst of all the forms of transport (673-867g tkm). But in actual fact 90% of the world's trade is moved by shipping which amounts to 3% of the total global CO_2 production the lack of emission regulations for shipping is a particular concern.

11.1.5 What is the contribution of transportation to these problems?

It is a common myth that aviation is one of the biggest energy consumers within the transportation sectors. In-fact the world cars and trucks are the collectively the largest at about 80% with the remaining 20% being consumed by rail, sea and air transport. It is sensible to target the biggest energy consumers but any additional improvements made by other consumers will definitely help and pave the way for others.

11.1.6 Existing fuel infrastructures

The current fuel infrastructure has seen continual growth since the widespread introduction of the internal combustion engine at the turn of the 20th century when petroleum fuels were supplied by local chemist shops. Prior to this, the distribution of fossil fuels was predominantly intended for heating homes etc. Our modern dependence on fuels means that a fuel distribution infrastructure is a necessity which is applicable to the alternative fuels being used. Ideally the current petroleum fuel infrastructure could be adapted to cater for an alternative fuel but where this is not possible, a new infrastructure will have to be put in place, but at what cost?

11.2 An overview of alternative fuels

There are numerous alternative fuels available which include Hydrogen, Alcohol fuels and Bio fuels which will be introduced below. Hydrogen will be covered in depth in a later section and a brief overview of Bio and Alcohol fuels will be presented below.

11.2.1 Bio-fuels

These are derived from natural organic material, which includes a wide range of living organisms from algae, plants and trees through to animal flesh and waste. It has high energy content and can be utilised as a fuel by either direct combustion or conversion to biogas, ethanol, syngas, methanol, ammonia or other liquid hydrocarbon fuels. Potential sources are the 150 giga-tonnes of vegetable bio matter generated worldwide on an annual basis or the refuse digestion within landfill sites. Such bio-gases will contain high levels of nitrogen and carbon oxides which make them undesirable for typical gas fuelled engines but are less of a problem for a number of fuel cells. Bio-fuels can also be used to obtain alcohol fuels. Methanol can be synthesised from syngas, which itself can be obtained from biomass (in addition to natural gas) and ethanol can be obtained by fermentation of biomass.

11.2.2 Alcohol fuels

Alcohol fuels were the first fuels to be used within IC engines but lost their popularity due to the advent of cheap post-war oil. Since they are able to be distilled from crops, they are however still used within countries which with no oil reserves. They are well suited for use within modern IC engines and have been shown to be less polluting than gasoline. Ethanol and Methanol are the most popular of these fuels. Methanol is available at a lower cost than Ethanol since it is able to be manufactured from a number of sources and has a greater flexibility within IC engines. The octane of gasoline can be increased by blending it with methanol and ethanol to improve the performance of an IC engine.

Ethanol is probably the best known of the alcohol fuels and is available from a number of sources such as fermented corn, sugarcane or the bio-conversion of other natural materials. Ethanol is less toxic and less aggressive to metals and polymers than methanol and has slightly higher hydrogen content. Ethanol is however only suitable in countries where its production is not likely to be detrimental to food supply and even in

these cases, it is only able to meet a small fraction of fuel demands. Other fuels such as methanol are better suited in this case since they are not dependant on these agricultural sources.

Alcohol fuels continue to receive renewed interest during times of high oil prices and as a result of pollution concerns. The 1975 National Alcohol Program (NPA) of Brazil, lead to the widespread use of sugarcane derived ethanol alcohol vehicles. In the early-mid 80s the Bank of America who converted their 200+ fleet to pure methanol, which showed benefits of reduced engine wear, pollution and cost compared to the use of gasoline. Since the end of the 80's concerns about air pollution have led to the development of cars (20,000 in 1997) able to utilise such fuels. The majority of these are in California which use an 85/15 methanol/gasoline fuel blend called M85. To overcome concerns about fuel availability, these vehicles were also fuel flexible. More recently, a number of car manufacturers have still been actively perusing methanol and this has led to developments such as the Exige 270E 'tri-flex-fuel' car from Lotus, which is capable of using any mixture of methanol, gasoline or ethanol.

11.3 Hydrogen as a fuel

Hydrogen has recently received considerable interest and research effort recently as a clean fuel which has led to proposals for a 'Hydrogen Economy'. Hydrogen has significant environmental benefits with water being the only by-product of a combustion process. Although it has a significantly high value of energy per kilogram (or specific energy) it has the lowest molecular weight of all the gases making it more likely to leak and therefore requires careful handling and costly specialised fuel tanks. As shown in the chart below, the energy content per unit volume of hydrogen is considerably less than for other fuels which means that considerably larger fuel tanks are also required in order to carry the same total energy content.

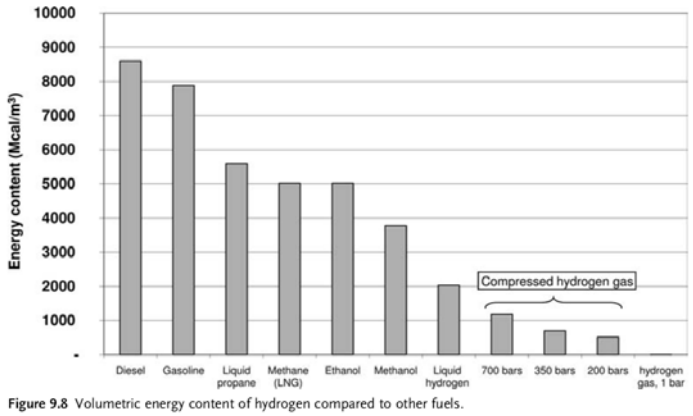

Figure 9.8 Volumetric energy content of hydrogen compared to other fuels.

Figure 11-1 – Volumetric energy content of hydrogen compared to other fuels [55]

It has very low ignition temperatures and is therefore extremely volatile. Although a hydrogen and air mixture is able to detonate, a high fuel concentration of about 18% is required. It is safer than similar alternatives such as Methane and Propane but its higher proneness to leaking means that systems should be designed and monitored accordingly.

11.3.1 The current availability of hydrogen

Hydrogen is already used in large quantities in the order of 50 million tons, 35% of which is used as a chemical reagent (mainly for oil refining and petroleum processing) and 51% being used for the manufacture of ammonia (as used for the manufacture of fertiliser). 8% is also used for the production of methanol. It is therefore already produced on a mass scale in order to be able to meet these demands

11.3.2 Hydrogen fuel infrastructures

The hydrogen fuel infrastructure currently in place is to meet the needs of the refining and ammonia production industries. Presently, the only hydrogen vehicles in regular use are buses with a number of dedicated hydrogen refilling stations located in various cities worldwide (47 in 2004 [55]). Recommendations were made to put more in place by a number of countries to extend the use of such vehicles, of which Iceland appears to be the most committed with deadlines being put in place. There is however significant cost penalties associated with the development of an accompanying infrastructure. In the short term, fuel reformers could be used on-board hydrogen powered vehicles to enable them to extract the hydrogen from existing fuels such as petrol and kerosene. The aviation industry is unlikely to adapt hydrogen as a fuel until dedicated hydrogen infrastructures have reached sufficient maturity.

Local filling stations can utilise hydrogen manufactured by present production methods but this requires the large scale storage of hydrogen either directly in compressed or liquefied form or retained in a hydrogen absorber. Alternatively, man-made hydrogen rich carrier fuels can be used (such as methanol and ammonia) which are made from mass produced hydrogen and can be reformed as required. Alternatively, the hydrogen can be manufactured on site. The volatile nature of hydrogen means it must be kept separate from oxygen at all times which means that nitrogen must also be readily available at all times at any refuelling station to take the place of air in any system.

11.3.3 Hydrogen production

Hydrogen is not a naturally occurring gas and therefore must be extracted from other fuels (such as fossil or bio fuels) or from the electrolysis of water. Electrolysis requires a considerable amount of electricity from the national grid and is therefore reliant on fossil fuels. Such a process could however become carbon dioxide neutral if electricity from renewable sources or other similar processes was used instead. The extraction of hydrogen from fossil fuels tends to result in a large amount of unwanted residual carbon dioxide greenhouse gas as a by-product. Novel hydrogen production methods are being explored which involve the use of biological methods such as enzymes, bacteria or even light to break down fuels. These are applicable to both fossil and bio fuels but as yet these they are still in their infancy and are not commercially available.

The manufacture of hydrogen is currently heavily reliant on fossil fuels with natural gas accounting for 48%, liquid hydrocarbons 30%, coal 18% and only 4% from water electrolysis. This is contrary to our goal to reduce our dependence on the use of fossil fuels. The processing of these also requires energy intensive reforming processes which offset the benefit of the clean burning hydrogen fuel. Future manufacturing processes

are predicted to rely on the increased use of water electrolysis and a process known as thermo-chemical water dissociation. When powered by renewable energy sources hydrogen will be more viable as a replacement fuel.

11.3.4 Liquefied hydrogen

To liquefy it, hydrogen has to be cooled to about 22K which can require a considerable external energy input equivalent to at least 25 - 45% of the hydrogen's heating value. This is normally carried out over three stages, initial compression, cooling to about 78K with liquid nitrogen and final cooling by expansion through a turbine. When the energy of manufacture is taken into account, liquefied hydrogen proves to be an inefficient means of storage. The low temperatures involved also present their own problems not only due to risks of frostbite but also due to air condensing to a liquid on exposed surfaces which can ignite certain materials. Any equipment must therefore be sufficiently insulated. The use of liquid hydrogen would not only have implications on fuel infrastructures but also on the refuelling procedures which must prevent the cryogenic fluids coming into contact with the skin or other disasters. Re-education of the public may be required to be able to use such specialised refuelling systems.

11.3.5 The outlook for using hydrogen as a fuel

This review has shown hydrogen to be less desirable than initially thought when the energy required during its manufacture is taken into account. Alternative manufacturing processes are being investigated but these are still in the early stages of development. Since the Hindenburg disaster, the public has a negative view of hydrogen but subsequent research has shown it to be no more dangerous than methane and propane which are already being widely used. Public opinion is therefore an obstacle which must be overcome if hydrogen is going to receive serious consideration for use as a fuel. The widespread introduction of hydrogen as a fuel requires a significant investment in a dedicated fuel infrastructure which has cost implications. In the US, the DOE made the decision in May 2009 to cut funding for research into the use of hydrogen for automotive fuel cells as a result of it bleak outlook.

11.4 Hydrogen storage considerations

A major drawback of using hydrogen as a fuel is its low density ($0.084 kgm^{-3}$ STP) which makes it difficult to efficiently store. To store it directly its energy density must therefore be increased by either compressing or liquefying the gas. More efficiently it can be used to manufacture hydrogen rich man made fuels or chemicals. Novel methods such as carbon nano-fibres and metal hydrides have also been receiving considerable interest recently. The most appropriate hydrogen storage solution is a trade-off of efficiency, mass, practicality, cost and safety. The storage of gaseous hydrogen on-board vehicles is a particular problem since its low energy density per unit volume means that very large storage tanks are required. It can be stored in a liquid form but the low temperatures required bring about its own set of problems.

The very small size of hydrogen molecules mean that it will leak 3.3 times faster than air. This is particularly concerning when we consider the ease of which hydrogen can be

easily ignited and the difficulty of detecting it when alight as a result of it burning with a clear flame. Fortunately its low density means that any leaking fuel can also quickly dissipate into the environment. Even so, any system will require high integrity seals in order to safely contain the fuel. The volatile nature of hydrogen/air mixtures means that any storage tank must also remain air free at all times and should be purged with nitrogen when empty.

11.4.1 Compressed storage

If stored in its gaseous format, the low density of hydrogen implies that it must be stored at very high pressures to make its use viable. Pressurised cylinders are favourable when hydrogen is required in small quantities due to its simplicity. In such cases, steel alloy cylinders may be sufficient but they do have significant weight penalties associated with them. Composite tanks are a lighter alternative and have already seen use on vehicles. An example of such was the composite tanks fitted in the roof of a bus which consisted of a aramide and epoxy composite outer shell which encompassed a 6mm aluminium inner shell. This combination gave an efficient cylinder with good burst characteristics although the cylinder was only operating with a maximum working pressure of a quarter of its design value. An example of a high pressure cylinder used onboard a hydrogen powered car is shown in the figure below.

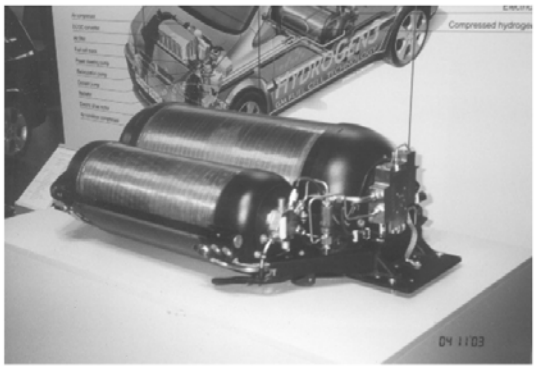

Figure 5.4 General Motors very high pressure hydrogen gas cylinder

Figure 11-2 – Typical high pressure hydrogen storage cylinder for vehicles [49]

The shape of high pressure tanks also makes them good candidates for aircraft external fuel tanks. When the full extent of the weight of such a hydrogen storage system is taken into account the hydrogen stored typically amounts to less than 2% of the total mass. Of high importance are the burst characteristics of such a compressed cylinder. The occurrence of a leak, leading to fracture can lead to large forces being generated in the vicinity of the defect. Any sudden decompression will result in highly explosive volatile gas regions as the gas mixes with the surrounding air. Safety devices such as burst disks (to safely vent the gas in a controlled manner) and flame traps (fitted to pressure regulators to prevent flame back-flow into a cylinder) must therefore be used.

11.4.2 Liquefied storage

The very low density of hydrogen means that it is not practical to liquefy it just by compressing it, as it down with other gases (kinetic theory). Instead its temperature has

to be reduced instead to about -253ºC to store it as a cryogenic liquid, known as LH_2. This method is the most common method of storing large amounts of hydrogen for industrial applications but after liquefaction the density is still only 71kgm^{-3}. Smaller scale LH_2 tanks have already been approved for vehicular use with two types being common, vacuum wall and solid insulated wall. These are considered safer than compressed gas alternatives, since failure of the tank does not result in sudden decompression. In the event of failure, the liquid fuel will remain in place and slowly evaporate. It should be noted that the liquid fuel from a LH_2 tank will need to be preheated to convert it to a gas before it can be used in a fuel cell. Waste heat can be used for this purpose but a heat exchanger is still required.

Reinforced cylindrical vacuum wall tanks are the most effective cryogenic tanks. These typically consist of two 3cm thick walls, each with 70 aluminium foil/fibre glass layers. An alternative is solid insulated wall tanks which use solid insulation materials combined with a reflective layer. Solid insulation materials used include, foam, glass and aluminium mixtures. The results of a study carried out into the effectiveness of a number of these materials for cryogenic tanks are presented below.

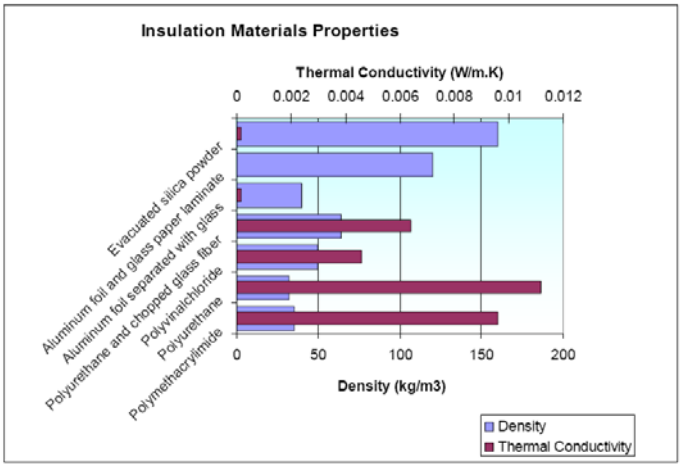

Figure 19: Material Properties, from Colozza (2002)

Figure 11-3 – Insulation material properties [54]

The temperature of liquid hydrogen needs to be maintained at about -253ºC to keep it in its liquid state which is difficult with even the best insulation materials. When not in use, LH_2 will still slowly evaporate and any tank will need to be fitted with a pressure release to prevent the pressure exceeding a specified level (typically 3 bar). This not only wastes fuel but also creates a dangerous situation due to the escaping volatile vapours. It is therefore unsafe to allow a liquid hydrogen tank to stand for long periods (a limit of 5 hours has been estimated for a full tank). This is not an issue when in use since this hydrogen vapour would normally be consumed by the fuel cell. This reduces the practicality of liquid hydrogen fuelled vehicles since they must be de-fuelled after use and then refuelled before the next trip.

11.4.3 Metallurgical considerations

The design of suitable storage devices is further complicated by the fact that hydrogen is known to react with certain metals. The small molecular nature of hydrogen means that

it is able to diffuse into certain normally impermeable materials and can even pass through microscopically porous materials. This includes carbon composite materials which are not hydrogen proof. The dissociation of the hydrogen molecules in close contact with the materials surface can also severely affect the mechanical properties of the material which can result in blistering and cracking of the material. Another phenomenon that a designer needs to be aware of is hydrogen embitterment in which the carbon in carbon based materials reacts with hydrogen to form voids of CH_4 in the material. Gas pressure within the voids then leads to internal stresses in the blisters and cracks. Hydrogen damage is therefore more likely to occur for materials with high carbon content. Non-ferrous metals are less susceptible and certain chromium based steels and alloys are known to be resistant to this phenomenon.

Cryogenic fuels present their own problems due to the extremely low temperatures involved, which can seriously affect the strength and fatigue properties of materials. The varying thermal stresses due to fuelling/de-fuelling temperature changes can lead to fatigue problems and stresses in tank mounting etc. As a result, only materials than remain ductile at low temperatures can be used which includes, aluminium, titanium, nickel alloys and austenitic stainless steels. The tensile properties of alloys are known to improve at cryogenic temperatures whereas the properties of a quasi-isotropic laminate get worse. The magnesium based alloys tend to see an improvement in their fatigue properties with opposite being true for steel. The fatigue properties of plastics are dependant on weather they are thermoplastic (improved properties) or thermosetting (degraded properties). The lower molecular kinetic energy of the substance means that hydrogen embrittlement is also less of a problem.

11.4.4 Other storage methods

11.4.4.1 Reversible metal hydrides

Certain metals and alloys known as reversible metal hydrides are able to easily react with hydrogen to create a storage solution. Due to their small size, the hydrogen molecules are able to be absorbed in-between the molecules of these hydrogen absorbers. The exothermic hydride formation process can be easily reversed by supplying heat to the hydride. The exact nature of the reaction is dependant on the material involved as well as its operating temperature and pressure. Since the rate of hydrogen release is dependant on the heat supplied, the process is easy to control. The volumetric efficacy of such a system is comparable to liquid hydrogen but at a less attractive gravitational efficiency. Only hydrogen with a very high purity can be used (otherwise the material will be damaged by impurities) and a refill time of 1 hour is currently typically required for a 5kg system. These systems exhibit good safety characteristics since any leak will be accompanied by a temperature drop which will inhibit the hydrogen release reaction.

11.4.4.2 Carbon nanofibres

A revolutionary hydrogen storage method is carbon nanofibres. These are reported to be able to store 67% of their own weight in hydrogen though the results are in question. This system is still in its infancy and therefore not a practical consideration at present.

11.4.4.3 Hydrogen carrier fuels

These are man-made fuels which are manufactured to hold large quantities of hydrogen in comparison to their mass. A number of criteria exist for these fuels,

1. It must be easy to extract the hydrogen from the fuel.
2. Manufacture of the fuel must be easy and efficient.
3. The fuel must pass certain safety consideration.

These most promising of these are Methanol and Ethanol which are discussed in a dedicated separate section.

11.4.4.4 Alkali metal hybrids

Alkali metal hybrids are chemical hydrogen absorbers which are similar to reversible metal hydrides but water instead of heat is used to promote the release of hydrogen. Such a substance is calcium hydride which when reacted with water it reverts to calcium hydroxide and hydrogen. This is already available commercially as polythene Powerballs which are held under water and simply cut open as required. A control system regulates the frequency that the balls are cut open and therefore the hydrogen supply. This system is heavier than the reversible metal hydrides since allowance must also be made to carry a large quantity of water (typically 3 times as much as is required for the reaction) and the waste sodium hydroxide/water solution. Manufacture of the hydride is energy intensive and certain batteries are preferable.

11.4.4.5 Sodium borohydride

Sodium borohydride is a stable hydrogen carrier which has been around since 1943 and is currently manufactured from borax in quantities of 5000 tonnes per year. With the aid of a suitable catalyst, it controllably reacts with water to generate hydrogen. Only pure hydrogen is produced which is diluted with water vapour. This has shown promising results and a number of hydrogen powered vehicles have already been built by Millennium Cell Corporation utilising this.

This is also available as solid form which is formed from sodium borohydride and a suitable catalyst and only needs water to generate hydrogen. A more practical derivative is sodium borohydride in solution form which does not require a separate water supply and only needs to be bought into contact with a suitable catalyst and is easy to control. Recirculation systems are the most common but the solution cannot be replaced or replenished until all the sodium borohydride has been used up and then it must be completely renewed. The Hydrogen on Demand System developed by Millennium Cell Corporation is more refined single pass concept. Solution based sodium borohydride is safe to transport, generates only pure hydrogen and no extra energy is required to promote the reaction. The fuel solution is upto100 times more expensive than hydrogen produced by other means due to the extreme manufacturing energy requirements required which far exceed those of methanol.

11.4.4.6 Ammonia

Ammonia is a toxic gas with high hydrogen content. It is currently produced at a rate of 100 million tonnes (by energy intensive steam reforming of methane) for the

manufacture of fertiliser and explosives and is competitively priced and readily available. It is easy to liquefy by either cooling it to -33ºC or compressing it to 8 bar but requires large amounts of energy to enable it to vaporise back into a gas. Its dissociation back to hydrogen is energy intensive and requires an inexpensive catalyst and reaction temperatures of 800-900ºC. Ammonia based fuels can cause permanent damage to PEM fuel cells (is only suitable for alkaline fuel cells) and generate a corrosive mixture when dissolved in water.

11.5 Methanol in depth review

11.5.1 Methanol as a fuel

Methanol (methyl alcohol) is a liquid oxygenated hydrocarbon fuel which was first discovered in 1661 by Robert Boyle. It is colourless and water soluble with a mild alcoholic odour. It has a simple chemical composition and is the simplest of all alcohols containing only one carbon atom. It has a freezing to boiling temperature range of 97.6 to 64.4 ºC and a typical density of 791 kgm^{-3} (20 ºC). A downside is that it contains only about half the energy density of gasoline. The attractiveness and low cost of this fuel has however led to the proposal of a 'Methanol Economy'.

Methanol is regarded as a safe and efficient hydrogen carrier and energy storage medium. When conventional transportation means are unavailable, other fuels such as natural gas can be safely and easily transported by converting them into methanol. Volatile hydrogen can also be effectively tamed by combining it with CO_2 into easy to handle and store liquid methanol. As a transportation fuel it does not need to be pressurised or liquefied (in contrast to hydrogen) and can be easily distributed, handled and stored (especially on-board vehicles). It also already has a proven track record of being able to be safely carried on-board vehicles as it is currently already used in a number of IC engined vehicles.

Low cost fuel grade methanol can also be used within existing natural gas powered turbines for power generation. Only minor modifications are required and a higher power output can be achieved along with lower NO_X and zero SO_X emissions (since methanol is sulphur free). Methanol and DME can also be used as household fuels and methanol cooking stoves have already been developed.

11.5.2 The manufacture of methanol

Methanol first obtained as a by-product from the charcoal manufacturing process. This was later replaced by the use of coal based processes during the industrial revolution and then much later by synthetic processes. It can be manufactured from a number of sources including fossil fuels but at present, syn-gas is the worldwide adopted approach. Research has however been invested in the low-pressure synthesis of carbon oxides and hydrogen which have been refined to produce a selectivity of 99.8% at a process efficiency of 75%. It is however the intention that methanol will eventually become the ultimate green fuel with the carbon coming from the chemical conversion of atmospheric CO2 and the hydrogen being obtained by the electrolysis of water (using renewable energies for the process). The demand for methanol has progressively

increased over the years which have led to a number of mega methanol production plants being created. Methanol is manufactured worldwide but China is currently the largest methanol producer. Unfortunately, they rely on coal for its manufacture as a result of its availability and low cost which not environmentally friendly.

11.5.3 The use of methanol within traditional IC engines

The excellent combustion characteristics of Methanol (octane rating of 100) and its Dimethyl Ether (DME) derivative have drawn particular attention to their use as fuels in IC engines. Conventional IC engines can easily be adapted to use this fuel. As a fuel, methanol can be used either neat or blended with conventional fuels as an oxygenated additive. Typically twice as much methanol is however required to achieve the same quantity of stored energy as gasoline due to its lower energy density. This is however offset by the fact that the higher octane rating of methanol allows an engine to be operated at higher compression ratios (10-11:1 vs 8-9:1 for a gasoline engine) making them more efficient. Methanol also has higher flame speed and therefore the combustion process will be more complete. As a result, less than double the amount methanol is actually required to achieve the same power output. The low volatility of pure methanol makes the fuel much safer than gasoline but can lead to cold start problems and the need to use volatile additives or blend it with gasoline (as with M85 blends). Its lower volatility and improved performance have made methanol the fuel of choice for the Indianapolis races since the 1960's.

Methanol can be used directly within a diesel engine but its cetane number of 3 (the ability of a fuel to self ignite at high pressures which is 40-55 for diesel) necessitates the need to adapt the engines. Nitrogen based ignition improving additives are also used to increase the cetane number. The use of methanol as opposed to diesel is able to reduce the two main sources of pollution commonly associated with diesel engines. There are no particulates and the amount of NO_x generated is minimal because of its lower combustion temperature. The energy content of diesel is about 2.2 times greater than methanol meaning a much greater fuel tank is required.

The dehydration of methanol results in a fuel more suitable for use within diesel engines due to its much higher cetane number of 55-60, known as Dimethyl Ether. DME shares the same benefits as methanol of zero particulates and low NO_x along with a reduction in engine noise. The low energy density of DME means that the fuel tank must be twice the size of a diesel tank. DME has a low lubricity and lower viscosity making the fuel system more susceptible to leakage and wear. DME is also known to be incompatible with a number of plastics and rubbers and PTFE and Buna-N are often used. DME is already produced in large quantities (4 million tonnes a year in China in 2008) and is regarded as the most attractive contender for the replacement of diesel fuel. Refined DME engines and vehicles are currently being developed. Research has shown that DME can also be used as a substitute for LPG and is comparable to natural gas, for use within power generation gas turbines. The low octane number of 35 RON of DME means it can not be used within spark ignition engines. This can be improved by mixing it with 20% LPG.

11.5.4 Material compatibility issues

Care needs to be taken when designing new systems or adapting existing systems to use methanol since it is the worst of the pure alcohols for attacking metals and polymers. Such design precautions are not expected to have any serious cost implications. Methanol vapour is reported to be worse than methanol liquid for corrosion with a high electrical conductivity which promotes a corrosive reaction. Magnesium is the worst corroded with aluminium, copper, brass, zinc and bronze also being affected. Aluminium is also rapidly corroded this has the added complication that the resultant products (gelatinous precipitates) are known to be sufficient to clog filters etc. Stainless steel is more resistant to methanol than some of the other metals but incurs a weight penalty. Nickel coatings are reported to be the most effective of the metallic coatings to resist methanol. This can be applied to the inside surface of an aluminium fuel tank to provide a light weight solution but joints would still present a sealing problem.

The molecular nature of methanol is also known to cause problems with certain polymers resulting in swelling/shrinking, hardening/softening or cracking of the material. The polymers offering the best methanol resistance are those with high fluorine content (such as Teflon) and it may be possible to use these as a barrier coating. Since traditional fibre reinforced polymers can soften and delaminate, a group of methanol resistant polymers have be developed but their use is limited to static storage tanks at this stage. Methanol incompatibility also extends to engine lubricants and specific formulations must be used.

11.5.5 Methanol and DME storage and distribution

Significant progress has already been made in the development of methanol fuelled vehicles but for these to become more widespread they need to be accompanied by an increase in the distribution of the fuel. 100 or so methanol refilling stations have already been built in California to satisfy the needs of the many flexible fuel vehicles already in service. These distribute either M100 (100% methanol) or M85 (85% methanol/15% gasoline), or both. These are similar to conventional fuel refilling stations with similar handling precautions. Although the construction of dedicated methanol refilling stations is straightforward, the conversion of existing refilling stations to cater for methanol is the most cost effective solution. In such cases, a small number of modifications are required to make the equipment compatible with methanol. In comparison, the costs of developing a hydrogen refilling station are considerably more than for methanol as a result of the much more specialised equipment which is required (both for high pressure and cryogenic systems).

The liquid state of methanol allows it to be easily distributed by rail, road and sea as is the case already for 500,000 tons per year in the US. Distribution by pipeline has also been demonstrated and the storage of large quantities is also viable. DME on the other hand has similar physical properties to LPG and therefore the existing LPG infrastructure and refilling stations can be used with minor modifications.

11.5.6 Methanol price and availability

Methanol is currently manufactured in the order of 40 million tonnes (2007 figures) as an ingredient for the production of various chemicals and products either in its direct form or following conversion into synthetic hydrocarbons. Only 7% of this methanol was destined for fuel use. Methanol production from natural gas is at present the most cost effective approach as production from other sources often requires further processing stages. The cost of DME is slightly higher since further methanol refining stages a required in its manufacture but is still considerably less than diesel. Since natural gas is the main ingredient of methanol, the price of methanol is dependant on the price of this. The 2007 mass production cost of methanol was estimated to be below 30 cents per gallon and even taking into account its lower energy content, it is still competitive with gasoline and diesel.

11.5.7 Methanol safe handling practices

Methanol is non-toxic and is actually already present in small quantities in a number of consumer products such as windscreen washer fluid, de-icer, antifreeze and many more. It also occurs in very small quantities naturally in our bodies and in our food and a daily intake of up to 500mg, taken in this way is considered perfectly safe. Methanol can be difficult to detect due to it being colourless and only having a mild alcoholic odour but with the correct precautions in place, it is not any more dangerous than any of the existing fuels. The same handling precautions as gasoline have been shown to be sufficient. In the long term, methanol is better than gasoline as it does not present the same carcinogenic risk. DME is similar to methanol, being non-toxic and non-carcinogenic having a mild odour and burning with a visible blue flame. As for similar fuels, a certain amount of careful handling is required.

Fuel refilling carries the greatest risk of methanol being absorbed into the body by ingestion, inhalation or skin contact. The fatal limit for ingestion of methanol is about 1g per kg of body mass which is 25-90mL as opposed to 120-300mL for gasoline but antidotes are available to treat cases of methanol poisoning. The inclusion if dyes and odour/taste agents in the fuel and anti-siphoning measures on vehicles will all help prevent the accidental ingestion of methanol. The levels of methanol inhalation during normal refuelling present no risk but as an added precaution, vapour recover systems can be used. The risk of skin contact can be significantly reduced with the use of spill-free nozzles.

Fire risk for methanol is significantly less than for gasoline as a result of its lower volatility and the vapour concentration must be four times as much to be ignitable. In the event of a methanol fire, it burn with a visible light blue flame, produces little smoke (improving visibility and reducing smoke inhalation) and can be easily extinguished (even with water). Since methanol burn at an eighth of the heat output and at a quarter of the speed of gasoline, fires are considerably safer as they less eagerly spread to surrounding combustible materials. It is estimated that gasoline based fires could be reduced by 90% with the use of methanol which is one of the reasons why methanol is regarded as one of the safest fuels and has been used for Indianapolis-type race cars since the 1960s (as well as the superior performance benefits).

11.5.8 Environmental considerations

The continual development of IC engines has lead to a significant reduction in their emissions which has made them competitive with alternative fuelled vehicles. However they are susceptible to an increase in emissions as a result of age and poor maintenance, whereas the emissions from a methanol fuelled IC engine will continue to be low throughout its life. The incomplete combustion of methanol in IC engines can result in formaldehyde production, which can however be treated with a catalytic muffler. DME fuelled CI engines will also benefit from significantly reduced exhaust emissions and significantly less complicated exhaust after treatment systems are required. The absence of sulphur from DME means that no emissions are produced and since there are no C-C bonds in the make up of DME, particulates are also virtually eliminated.

Methanol spills do not present any risk to the environment as it is easily degraded by photo-oxidation and biodegradation and is used in windscreen washer fluids for this very reason. Methanol is already currently used within sewerage plants to accelerate the bacterial treatment process and so there is little risk to water treatment either. Since methanol is miscible with water, any major spill would be conveniently diluted and biodegraded by micro-organisms in just a few days. This is in contrast to the scale of disaster experienced with crude oil spills. A similar situation exists for DME, which is non-toxic, water soluble and easily broken down by micro-organisms.

11.5.9 The prospect of the manufacture of methanol by CO_2 recycling

At present fossil fuels are used for the manufacture of syn-gas and methanol. Natural gas is preferred in terms of efficiency, cost and emissions, while coal is noted to be the most unfriendly in terms of CO_2 production. If we take into account the CO_2 generated from the manufacture of methanol, the CO_2 emissions from methanol fuelled vehicles will only be slightly lower than their gasoline counterparts. This can be significantly improved if we are able to manufacture methanol with renewable sources instead. The manufacture of methanol from chemically recycled CO_2, obtained from chimneys of power and manufacturing plants has been proposed. When this CO_2 is combined with hydrogen generated from water by renewable energy sources these fuels can become environmentally CO_2 neutral. In such cases, fossil fuels may not longer be required.

11.6 Fuel study conclusion

This study highlighted the limitations of conventional fuels before investigating a number of alternative fuels which have the potential to eventually cut our ties with the almost exhausted fossil fuels. Hydrogen and the hydrogen carrier fuel methanol were identified as the best contenders as fuels most suitable for a fuel cell vehicle. Hydrogen was however shown to have significant difficulties in terms of its storage and distribution due to its volatile nature. Methanol on the other hand, is in a normally liquid state at standard conditions and much safer to handle. Compared to gasoline, methanol has only half the energy density but liquid hydrogen has half that of methanol and gaseous hydrogen only a sixth. The low energy density of these fuels is offset to some extent by the fact that the fuel consumption of a fuel cell engine is only a third of a

gasoline engine. If we also take into account the total cost of hydrogen and methanol after production, transportation and storage, methanol wins again. The manufacture of methanol by CO_2 recycling also has the potential to alleviate the problems of global warming. Methanol is not limited to use as a fuel and can also replace oil and gas as a vital ingredient for the manufacture of synthetic hydrocarbons and their products.

In this study methanol has been shown to be the best substitute for non-renewable fossil fuels and is already mass produced in large quantities. With only a few years supply of fossil fuels still remaining, the time to implement such a change is now. The switch to alternative fuels will however be progressive, with alternative fuels supplementing fossil fuels initially before eventually completely replacing them. This has been shown to be straightforward with conventional gasoline and diesel engine being easily adapted to use methanol with a number of minor modifications. A more long term challenge will be the introduction of fuel cell vehicles. In the short term, hydrocarbon based fuels can be utilised within such a vehicle by means of a fuel processor but alcohol fuels are more attractive even for this due to their lower energy requirement for such a process. Methanol reformer equipped fuel cell powered vehicles, have already been shown to have emissions which are considerably less than the very strict limits laid down for SULEV (super ultra low emission vehicles) vehicles in California. The methanol derivative DME is expected to be similar.

In order for a fuel to be able to become widespread, as well as having the backing of sufficiently large manufacturing plants, it must also have a suitable distribution infrastructure. At the end of the distribution network, there must be refilling stations which can be easily and safely used by the customer. Existing fuels have always benefited from being sufficiently safe and easy to distribute with a vast distribution infrastructure already in existence. Although past experience has shown the general public to be more than capable of handling specialised fuels such as LPG, the ideal replacement fuel will be similar to existing fuels. Methanol has a distinct benefit in this area of being able to utilise existing refilling stations with a number of modifications.

Since hydrogen is significantly different to conventional fuels a new fuel infrastructure would be required. A small number of hydrogen outlets already exist but a new and costly infrastructure would have to be developed for hydrogen to be widespread as a fuel. A number of regulations would also have to be overcome for such an infrastructure to become reality. In particular, a US NFPA regulation prohibits a hydrogen pump from being installed within 25m of gasoline pumps, making the integration of hydrogen pumps into existing refilling stations difficult. From a financial perspective, hydrogen an unviable option due to the cost of developing such a new infrastructure and a number of hydrogen fuel studies have recently been abandoned for this reason. Hydrogen is still attractive as a fuel but only for specialised applications requiring a limited distribution infrastructure.

12 Fuel processing

12.1 An overview of fuel processing

Since hydrogen rich fuels contain more hydrogen per volume than pure hydrogen in its most dense liquid state they are becoming increasingly attractive for fuel cell systems. The use of such fuels also has other practical benefits over hydrogen such as storage and distribution. It is however necessary to use a fuel processor to extract the hydrogen from them as required by a fuel cell. This way, fuel cell vehicles are able to utilise existing fuels in the short term until pure hydrogen becomes more viable. In this way, hydrogen is able to be extracted from a range of fuels such as petrol, kerosene, propane and methanol but the exact process used is specific to the fuel. The reaction temperatures required for theses chemical conversion processes can be high and therefore catalysts are often used. The three main fuel reforming approaches are steam, partial oxidation and autothermal, each of which will be discussed below.

The hydrogen output from the main reformer is however typically polluted with other unwanted substances such as CO, CO_2 and H_2O. Some of which act as mere dilutants with a fuel cell but others must be removed by additional clean-up stages such as desulphurisation, shift reaction and gas clean-up. The exact nature of the process is dependant on the type if fuel cell used. Other stages required are those to vaporise liquid fuels into the required gaseous form and preheat the reactants (fuel and air) before they enter the fuel reformer. These normally require additional heat input which must be allowed for. The numerous stages involved each have their own optimal operating conditions as well as being dependant on the composition of the gasses, reactor operating temperature and supply feeds. Collectively, control of the complete process can be complex.

12.2 Steam reforming

Steam reforming is widely used and is the most common fuel reforming approach. The process involves two reforming (oxygenolysis) reactions and a water-gas shift reaction as given in the example below for methane.

$$CH_4 + H_2O \longrightarrow CO + 3H_2 \qquad \text{Eq 12-1}$$

$$C_8H_{18} + 8H_2O \longrightarrow 8CO + 17H_2 \qquad \text{Eq 12-2}$$

$$CO + H_2O \longrightarrow CO_2 + H_2 \qquad \text{Eq 12-3}$$

The two reforming reactions indicate that the output from the reformer is a mix of CO, CO_2 and H_2 as well as fuel and steam. The exact output from the reformer is governed by operating conditions such as temperature, pressure, fuel and steam content. As shown in the figure below, the reaction temperature needs to be high enough to achieve full conversion of the fuel for all hydrocarbon and alcohol fuels with temperatures of up to 700ºC being the most desirable for the production of hydrogen. These can be reduced with the use of a catalyst and temperatures of about 500ºC are typically used in conjunction with a Nickel catalyst.

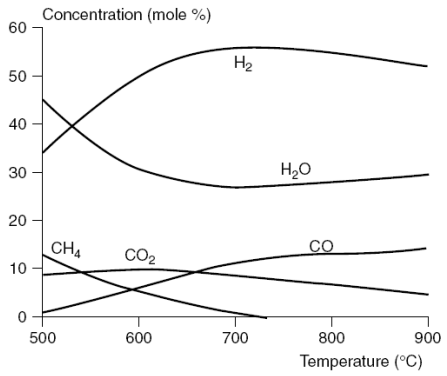

Figure 8.2 Equilibrium concentrations of steam reformation reactant gases as a function of temperature.

Figure 12-1 Output concentrations from a steam reformer as a function of temperature [56]

This process is endothermic and an external heat source is required to sustain the reaction. This is typically achieved by the combustion of an additional amount of fuel within a burner which is thermally coupled to the reformer. The steam reforming reactions are separate from the combustion reactions in the burner, except for thermal conduction between the two and thus will be reversible and not include any nitrogen. The steam reforming of Naphtha is a special case which is initially endothermic but becomes exothermic as the temperature is lowered but these lower temperatures will favour the production of methane as opposed to hydrogen.

Other fuels such as alcohols can be reformed in a similar way as for the example given for methane above. The reaction for methanol is given below.

$$CH_3OH + H_2O \longrightarrow 3H_2 + CO_2 \qquad \text{Eq 12-4}$$

Methanol has the distinct advantage over other fuels in that much lower temperatures are required. Since a certain amount of unconverted methanol within the reformate is also tolerable within phosphoric and PEM fuel cells lower temperatures can be used. High operating temperatures are however still desirable to prevent carbon formation. With the aid of copper and zinc oxide catalysts, temperatures of the order of 250ºC are typically used. A distinct advantage for PEM fuel cells is than CO is not shown as a product of the process. Although not shown, traces of CO are still present.

The theoretical efficiency which is taken as the ratio of the heating value of hydrogen produced to the total fuel consumed in both of the reactions is 100% for a steam reforming process. The actual efficiency will be less than this as a result of heat losses and incomplete reactions. A certain amount of CO will also be included in the output from the reactor and further processing will be required when it is destined for use in certain fuel cells such as the PEM. Two of the most common methods used will be discussed in the sections which follow.

12.2.1.1 Steam reforming and shift reactions

This process involves an additional shift reactor stage in which the CO in the reformate reacts with extra steam to produce additional hydrogen and CO2. More than one shift reactor may be required and both high temperature and low temperature reactors can be used. As shown in the schematic below, these are typically followed by a preferential oxidation stage in which any remaining CO is oxidised with oxygen (usually with the aid of a suitable catalyst).

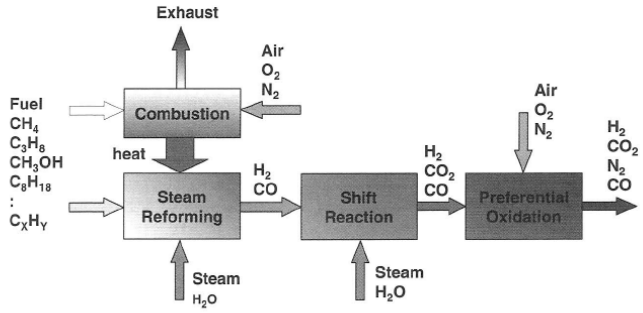

FIGURE 9-24. Schematic representation of a steam reforming process.

Figure 12-2 – Steam reforming process [57]

12.2.1.2 Steam reforming and membrane separation

This uses a metal membrane which will only allow hydrogen to pass through, with the result being a product gas consisting of mainly high purity hydrogen. The reformate products that were unable to pass through the membrane are combusted within the burner instead. This process has proven to be very efficient, but large pressure differentials are required across the metal membrane in order to make it work. As a result it is better suited to compressed and liquid fuels (such as methanol) which do not require significant additional compression. The schematic is shown below.

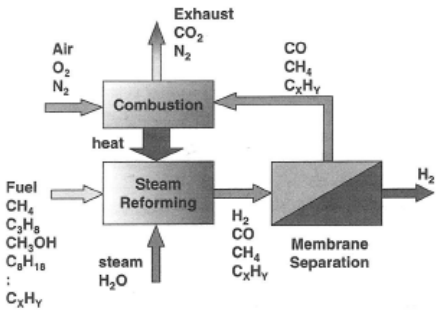

FIGURE 9-26. Schematic representation of the steam reforming process with metal membrane separation.

Figure 12-3 –Steam reforming with membrane separation [57]

12.2.1.3 Variants of steam reforming

Dry reforming (also known as CO_2 reforming), as defined by the following reaction can be used when there is no available steam source. Such systems rely on the recirculation of water and CO_2 from the exhaust into the inlet.

$$CH_4 + CO_2 \longrightarrow 2CO + 2H_2 \qquad \text{Eq 12-5}$$

A hybrid approach between the steam and dry reforming methods which uses both steam and CO_2 is also possible. In either approach care needs to be taken since the nickel catalysts are easily damaged by carbon formation.

When high temperature fuel cells are used, the heat required to maintain an endothermic reforming process can be supplied by heat generated by the fuel cell stack instead of being supplied by an external source. The heat generated by the fuel cell is typically twice that required to sustain the steam reforming reactions. Such systems also reduce the cooling requirements, increase the overall efficiency of the system and reduce the system cost. The are two variants of this system. In the direct arrangement, the reforming is performed within the anode chamber and therefore is able to utilise the already available steam. In the indirect arrangement, the reformer is placed in close thermal contact with the fuel cell.

12.3 Partial oxidation reforming

Partial oxidation is effectively a less than stoichiometric combustion process, in which CO and hydrogen are produced instead of the products normally associated with a typical combustion process. It is an exothermic reforming process which is faster than steam reforming but operates at temperatures of 1200 - 1500ºC (without a catalyst) and is therefore impractical for mobile applications. These systems are much simpler than steam reformers since they do not require an external heat or steam supply. The reaction can however be difficult to control and the process is less efficient than steam reforming and therefore produces less hydrogen per mole of fuel. This is made worse by the use of air instead of pure oxygen. The reformate gas also contains a large amount of nitrogen, which reduces the hydrogen content of the gas. As with a steam reformer, shift reactor and partial oxidation stages are required to complete the process. An example reaction for methane and schematic of the process is given below.

$$CH_4 + \tfrac{1}{2}O_2 \longrightarrow CO + 2H_2 \qquad \text{Eq 12-6}$$

$$C_8H_{18} + 4O_2 \longrightarrow 8CO + 9H_2 \qquad \text{Eq 12-7}$$

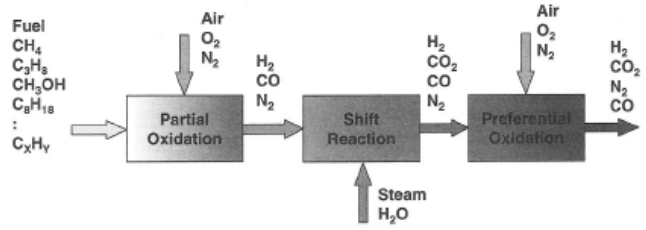

FIGURE 9-27. Schematic representation of the partial oxidation process.

Figure 12-4 – Partial oxidation reforming process [57]

A derivative of this is known as Catalytic Partial Oxidation which enables the temperature requirements to be reduced with a catalyst such as platinum or nickel. There are numerous CPO reactors in development which are applicable to both stationary and mobile applications. The best know of these is the Johnson Matthey HotSpot reactor which will be discussed in more detail in a later section. As with other reformers, methanol has a distinct advantage over other fuels in that the reactions are able to proceed at much lower temperatures, which results in a much simpler design. An experimental unit has been developed which uses a methanol/water mix and controlled air flow in an ignitor. This arrangement means that only a small fraction of the methanol is burnt and the heat produced is sufficient to vaporise the remaining water and methanol, which is then fed to a catalyst (supported on a honeycomb monolith) reactor.

12.4 Autothermal reforming

Autothermal reforming is a hybrid between partial oxidation and steam reforming in which the endothermic steam reforming and exothermic partial oxidation reactions occur simultaneously. Both steam and an oxidant are used along with a catalyst to react with the fuel. Depending on the amount of oxygen which is introduced to the system the process can be endothermic, exothermic or neutral. An autothermal process has a theoretical efficiency of 100% and exists when the system is neutral and there is no net heat transfer. The amount of oxygen required to achieve such a situation is different for every fuel (X=0.23 in the case of methanol). In practice however, it is typical to use slightly more oxygen than is theoretically required along with additional steam (to give a steam to carbon ratio of approx. 2-3), in order to reduce the risk of carbon formation within the fuel processor. Although this results in a reduction in efficiency the service life of the fuel processor is increased. The amount of steam required is less than with a standard steam reformer since the heat required is generated by partial combustion of the fuel. A schematic of the process is given below.

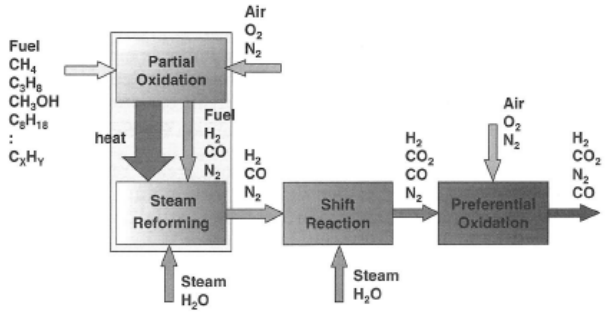

FIGURE 9-28. Schematic representation of an autothermal reforming process.

Figure 12-5 – Autothermal reforming process [57]

As with other fuel processors, additional processing is required to remove unwanted elements. The shift reactor used consists of a high temperature (400-500˚C) and low temperature stage (200-250˚C) which allows each stage to utilise a catalyst optimised for that particular temperature range. The output still has a CO content of about 1% which must be further reduced by either preferential or selective oxidation.

12.5 Electrolysers

Although not strictly a fuel reforming process, water can be divided into hydrogen and oxygen by passing electricity through it. The reaction is reverse to that encountered in a fuel cell. Efficiencies of 60 to 70% have been reported for such units and they can be operated at higher pressures if so desired. Pure forms of hydrogen are generated but with the presence of significant amounts of water vapour. Such a system can also be used to store surplus electrical energy as was successfully demonstrated on the NASA Helios hybrid UAV project. This aircraft was equipped with solar panels to provide power during the day as well as generate hydrogen to power fuel cells at night.

12.6 Additional clean-up phases

Any fuel processor typically relies on additional processing stages to support the reformer. The stages required are dependent on the reformer and fuel used and the reformate composition required by the fuel cell.

Desulphurisation is the first stage of a fuel processor. It is used to remove the traces of sulphur that are commonly found in a number of fuels such as natural gas, gasoline and diesel. This is necessary to prevent premature degradation of the catalysts used and poisoning of PEM fuel cell anodes. The sulphur content will vary from fuel to fuel and this stage may not be required in all cases. A hydrodesulpharisation (HDS) reactor is typically used for this stage which operates on recirculated hydrogen gas. These use nickel-molybdenum or cobalt-molybdenum catalysts to convert any sulphur compounds into hydrogen sulphide which is followed by the conversion to zinc sulphide, by absorbing this into a bed of zinc oxide. Alternatives to the HDS are absorbents such as activated carbon and molecular sieves. The output from such devices is however very low and regular maintenance is required.

Pre-reforming to prevent carbon formation. Carbon formation is a problem in areas where hot fuel gases are present or when nickel based catalysts and materials are used. Higher hydrocarbons are at a greater risk and thus liquid petroleum fuels are particularly vulnerable. This can be minimised by adding steam to the fuel stream, which promotes reactions to counteract this effect with a steam/carbon ratio of 2-3 being typical. Careful control of a fuel processor is also required to prevent the sometimes very rapid growth of carbon deposits. The use of a low temperature steam reforming phase (250-500˚C) prior to the main reforming phase can be used as a further preventative step.

Shift reaction is a post-reformer stage. This used to reduce the CO content of the reformate and depending on the process involved, more than one stage may be used. In the case of a normal steam reformer, higher reaction temperatures not only favour the production of hydrogen but also increase the CO content. One way of dealing with the CO is to convert it into CO_2. This is done by cooling the reformer output gases and then using one or more catalyst reactors to invoke a shift reaction. These units are however excessively large, have a number of safety hazards and the catalysts are easily poisoned by sulphur. Methanol reformers have the advantage of being able to dispense with the extra shift reactors.

Gas clean-up is the final gas processing stage. This is used to further reduce the CO content which can cause a drop in performance or even permanently damage a fuel cell. Methanol reformers have a low CO output of only about 0.1% (when operating at 200˚C), but this is still too high for PEM fuel cells. The output from shift reactors is also far too high. One of a number of different methods can be adopted for this stage which includes preferential oxidation, CO methanation, palladium/platinum membrane separation, selective oxidation, or pressure swing absorption. Each of these suffers from the same cost, complexity and volumetric penalties. However, preferential oxidation seems to be receiving considerable interest. This involves the controlled combustion of CO and excess oxygen (a stiochiometric ratio of 2-3.5 is typically used) on a noble metal catalyst which is biased towards CO. As the excess oxygen also reacts with some of the hydrogen, a reduction is efficiency is experienced (which is dependant on the stoiciometric ratio) and careful control is required to prevent combustion of the hydrogen.

12.7 Fuel processor requirements and selection

The required output from a fuel processor is dependant on the fuel cell type and its operating conditions. Low temperature fuel cells are for example intolerant of a number of fuel contaminants and therefore have stricter fuel processor requirements associated with them. As shown in the table below, the gas species typically found in a reformate can act as either a fuel, diluent or poison depending on the type of fuel cell being used.

Table 8.6 The fuel requirements for the principal types of fuel cells

Gas species	PEM fuel cell	AFC	PAFC	MCFC	SOFC
H_2	Fuel	Fuel	Fuel	Fuel	Fuel
CO	Poison (>10 ppm)	Poison	Poison (>0.5%)	Fuel[a]	Fuel[a]
CH_4	Diluent	Diluent	Diluent	Diluent[b]	Diluent[b]
CO_2 and H_2O	Diluent	Poison[c]	Diluent	Diluent	Diluent
S (as H_2S and COS)	Few studies, to date	Unknown	Poison (>50 ppm)	Poison (>0.5 ppm)	Poison (>1.0 ppm)

[a]In reality CO reacts with H_2O producing H_2 and CO_2 via the shift reaction 8.3 and CH_4 with H_2O reforms to H_2 and CO faster than reacting as a fuel at the electrode.
[b]A fuel in the internal reforming MCFC and SOFC.
[c]The fact that CO_2 is a poison for the alkaline fuel cell more or less rules out its use with reformed fuels.

Table 12-1 – Fuel requirements for the different fuel cell types [56]

It is important that any poisons in the reformate are reduced to permitable levels since they can cause considerable damage to the fuel cell. CO in particular must be kept below 10ppm otherwise it can ruin the catalyst on the electrodes of the fuel cell. This is less of a problem for fuel cells operating at higher temperatures (>120-130˚C in the case of a PEM fuel cell) but certain fuel cell membranes are temperature limited. The use of PtRu catalysts and a process known as air bleed can also help. Diluents such as CO2, will not damage a fuel cell but their presence will dilute the hydrogen content in the fuel and therefore reduce its performance. Although not listed in the table above, the reformate will also contain concentrations of steam. Although this is a diluent, it is however actually beneficial to the fuel cell by keeping it hydrated. Since variations in reformate composition can affect a fuel cells output potential as well as its lifespan and performance, careful control of the fuel processor is required.

The actual reformate composition from the fuel processor is dependant on a number of factors such as fuel type, reformer type and fuel processor efficiency. Typical reformate compositions for a number of combinations of fuel and reformer types are given in the following table for reference.

TABLE 9-6
Typical Reformate Compositions for Various Fuels and Various Reforming Processes (It Includes Preferential Oxidation as Well)

	H_2	CO_2	N_2
Natural gas Autothermal	0.42	0.16	0.42
Gasoline Autothermal	0.40	0.20	0.40
Methanol Autothermal	0.50	0.20	0.30
Natural gas Steam reforming	0.75	0.24	0.01
Methanol Steam reforming	0.70	0.29	0.01

Table 12-2 – Typical reformate compositions for the different fuel reformers [57]

Since the energy requirements of the reforming processes are affected by fuel choice, this is the basis of the primary selection of the most appropriate fuel reforming process. The total energy of the fuel processor including energy for steam generation and fuel evaporation processes must however be taken into account, especially where reformate is used to meet this demand. In some cases however, the hydrogen is not completely consumed with the fuel cell and can be fed back to the processor to provide this energy. High temperature fuel cells may be able to meet some of the energy demand by utilising excess heat from the fuel cell. It is worth noting that methanol reformers have the lowest energy demands of all the reformers. Additional consideration must also be given to other factors such as, reformate requirements, application, physical constraints, complexity, costs, operation and maintenance. For instance, partial oxidation offers the benefit of simplicity while steam reformers offer a higher level of efficiency.

12.8 Fuel processor performance prediction

Fuel conversion efficiency is one of the most important measures of the performance of a fuel processor, which is defined as the ratio of the output and input products. This can be determined by the expression below which takes into account the effect of all the compounds as well as any reformate which is re-circulated back to the fuel processor.

$$\eta_{Fuel\,\mathrm{Pr}\,ocessor} = \frac{LHV(H_2)n_{H_2} + LHV(CO)n_{CO} + LHV(CH_4)n_{CH_4}}{LHV(Fuel)n_{Fuel} + \left[LHV(H_2)n_{H_2} + LHV(CO)n_{CO} + LHV(CH_4)n_{CH_4}\right]_{\mathrm{Re}\,circulated}}$$

Eq 12-8

In the case of a PEM fuel cell, CO and methane are not utilised by the fuel cell and therefore these terms are eliminated from the above equation. In addition to this, the total efficiency must account for operational factors which affect the performance of the fuel processor. These include heat losses and the heat generated by the condensation of steam. These can be used to give an expression for operational efficiency as below.

$$\eta_{Fuel\,\mathrm{Pr}ocessor(Operation)} = 1 - \frac{\dot{Q}_{CondFP} - \dot{Q}_{Losses}}{LHV(Fuel)n_{Fuel}} \qquad \text{Eq 12-9}$$

The total efficiency of the fuel processor will then be the product of these as below.

$$\eta_{Fuel\,\mathrm{Pr}ocessor(Total)} = \eta_{Fuel\,\mathrm{Pr}ocessor} \cdot \eta_{Fuel\,\mathrm{Pr}ocessor(Operation)} \qquad \text{Eq 12-10}$$

The total efficiency of a fuel processor-fuel cell combination will be the ratio of the fuel cell power output to the fuel input into the fuel processor.

12.9 Methanol and DME reforming for hydrogen fuel cells

Of all the liquid fuels, methanol is the safest and is showing the most promise for transportation fuel cells and is the only fuel which has been developed for such purpose. Methanol reformers are not limited to on-board applications and can be used for the generation of hydrogen at refilling stations via methanol-to-hydrogen units (MTH) for hydrogen powered vehicles. Although still costly, Methanol and DME steam reformers typically operate at efficiencies of 80-90% and at temperatures of 250-350ºC and are therefore well suited to on-board applications. A typical steam reformer has an output of 0.14kg of hydrogen for each kg of methanol can be assumed for a hydrogen utilisation of 75%. The lower reformer temperatures mean that less CO is produced and no nitrogen oxides are produced. This means that only 1 CO processing stage is required compared to the 4 stages typically used for reforming other fuels. Autothermal reformers as being developed by Johnson-Matthey are also becoming popular and are currently showing the most promise for on-board applications due to their size. A DME reformer involves two stages. In the first stage, the DME is hydrolyzed to methanol with the aid of a catalyst (mildly acidic). The second stage then utilizes a typical methanol reformer.

13 A review of existing fuel processors

The majority of commercially available fuel processors are aimed at stationary systems. Steam reformers have been in service for many years in an industrial context as a means of generating hydrogen on a large scale. Such units have however typically been burdened with problems such as cost, size, weight and operating requirements. Natural gas is fuel of choice for these systems because of its availability and ease of processing. Alternatively, partial oxidation systems can be used such as compact regenerative, plate, membrane, plasma reformers.

The requirements of vehicles (especially their range), indicates that on-board fuel processing is the only really viable solution to supply hydrogen. Such vehicular based reformers are currently being investigated to generate hydrogen for both fuel cell and IC engine applications. The difference between the systems is relative to the fuel being used and the level of purity of hydrogen required. These have more stringent requirements than their stationary counterparts such as, mass, volume, efficiency, cost, start-up, transient behaviour and low levels of CO and other pollutants. Mobile fuel processors are not limited to vehicular use and are also used for portable power generation. Steam, CPO or autothermal are typically reforming approaches. Methanol, gasoline, diesel, kerosene and multi-fuel fuel processors are receiving the most interest.

13.1 Methanol fuel processors

These have undergone a significant amount of development work recently and are now more realistic compared to what they used to be. The key developers are, Excellsis (DaimlerChrysler), GM, Honda, International fuel cells, Mitsubishi, Nissan, Toyota and Johnson Matthey. Steam reforming seems to be the preferred approach but partial oxidation is also received significant interest. Research has also shown the emissions from methanol reformer equipped fuel cell powered vehicles to be considerably less than the very strict limits laid down for SULEV (super ultra low emission vehicles) vehicles in California. Some of these fuel processors will be discussed below.

13.1.1 Xcellsis-Ballard fuel processors

This is an integrated autothermal fuel processor which is able to provide a hydrogen output of $1.2m^3h^{-1}$ for a weight of 1.8kg and a volume of 0.5L, as shown below. Reactions take place through a porous copper/zinc catalyst based sintered reactor. After which, the reformate passes through a mixing zone (where air was added) before it was treated in a preferential oxidation zone. The pressure drop over the complete unit at full load was 200mbar. Almost complete conversion was shown at an operating temperature of 280˚C and a methanol feed rate of 15molh-1 with just 0.9% (vol.) methanol remaining and a CO content of 0.1% (vol.). During start-up an excess amount of air is supplied to the fuel processor to achieve total combustion of the methanol within the preferential oxidation stage which provides the start-up energy required. A start-up time of 10mins is typical.

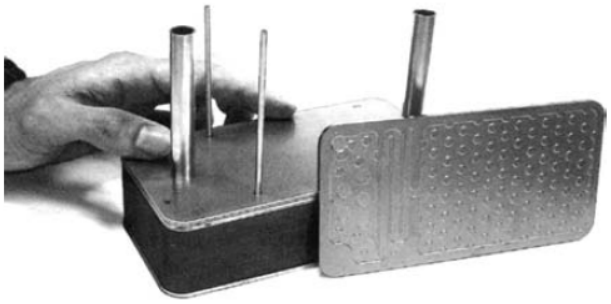

Figure 9.6 Single plate and complete integrated fuel processor for 20 L min^{-1} hydrogen output as developed by Schuessler from Ballard Power systems [398].

Figure 13-1 – Internal components within a Ballard fuel processor [58]

13.1.2 DaimlerChrysler methanol vehicles

The biggest breakthrough in vehicle methanol reformers came from the 50kW NeCar 3 and the more advanced 75kW NeCar 5 projects. A catalytic afterburner and thermal oil cycle was used to meet the energy requirements as well as heating a micro structured heat–exchanger evaporator. A water cooled preferential oxidation unit was used for CO removal. Two of these processors were later incorporated into a methanol fuelled bus. They were switched in parallel to supply six Ballard Mark 7 stacks, which gave a net continuous power output of 100kW. Air was supplied from a two stage air compressor with heat and pressure energy recovery. The characteristics of the fuel processor are given below along with a representation of its space requirements within the NeCar3.

Table 8.8 Characteristics of the methanol processor for NeCar 3 (Kalhammer et al., 1998)

Maximum unit size	50 kWe
Power density	1.1 $kW_e L^{-1}$ (reformer = 20 L, combustor = 5 L, CO selective oxidiser 20 L)
Specific power	0.44 $kW_e kg^{-1}$ (reformer = 34 kg, combustor = 20 kg, CO selective oxidiser = 40 kg)
Energy efficiency	not determined
Methanol conversion	98–100%
Efficiency	
Turn-down ratio	20 to 1
Transient response	<2 s

Figure 8.13 NeCar 3 packaging of stack and fuel processor.

Figure 13-2 and 13-3 NeCar 3 specifications [56]

Following the success of the NeCar3, DaimlerChrysler and Excellsis joined forces with BASF to develop the ME 75-5 advanced fuel processor. The catalytic reformer and preferential oxidation reactions were combined into one and the evaporator was integrated into the catalytic afterburner. System start-up was aided by the novel reactor which could be operated either in combustion mode, autothermal or steam reforming mode. This complete fuel processor package was used in the NeCar5 (with a 75kW Ballard Mk9 stack) and Jeep Commander research projects. The NeCar5 eventually became famous for being the first methanol fuelled car to cross the US. The complete fuel cell drive system of the NeCar5 has the same space requirements as the drive assembly of a conventional gasoline vehicle. In contrast to the much larger system used

in the NeCar3, all of the interior space of the car was able to be retained. The ME 75-5 fuel processor is shown below along with a picture of it installed in the NeCar5.

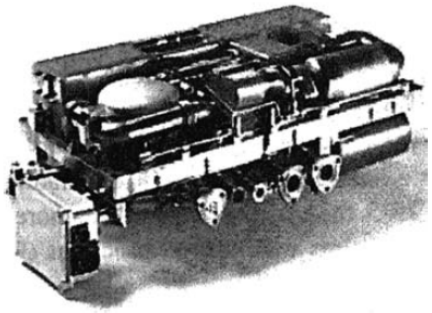

Figure 9.10 The ME 75-5 methanol fuel processor developed by XCellsis for NECAR 5 and other fuel cell vehicles [70].

Figure 5.6 Packaging of the NeCar 5 methanol fuel processor

Figure 13-4 [58] and 13-5 [49] – The NeCar 5 fuel processor

13.1.3 Hyundai "Santa Fe" project

This project used a 25kW fuel processor which was developed by SK Corp and designed to fit in a Hyundai "Santa Fe" car. It consisted of a steam reformer with membrane separation technology and was reported to be able to deliver very pure hydrogen. Instead of a compressor/expander unit, this used a high performance blower to supply air to the system. The only feeds to the system were water and methanol, which were pre-heated and evaporated with heat from the catalytic burner. A 300-350˚C membrane separator was then used to purify the reformate, in which 70-75% (vol.) of hydrogen permeated through the membrane. The remaining reformate products were combusted in the burner to supply the energy for the steam reforming and membrane separation processes. The final fuel processor, as shown below had an efficiency of 75% and a start-up time of 15 mins.

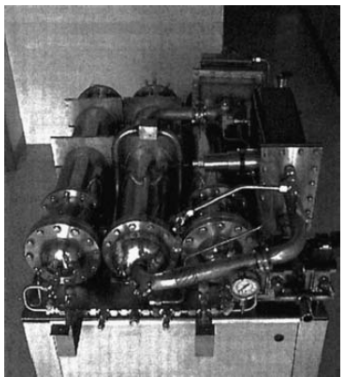

Figure 9.15 25-kW methanol fuel processor developed by Han *et al.* [587].

Figure 13-6 – Early development of the Hyundai fuel processor [58]

13.1.4 Other mobile methanol fuel processor projects

A number of other car manufacturers developed their own methanol fuelled fuel cell vehicles, although little is known about these projects. Toyota developed a 50kW vehicle with a methanol steam reformer and water-gas shift/preferential oxidation

catalytic clean up. GM developed a 30kW methanol vehicle in the 1990's which used their own methanol reformer. This had a specific power of 0.44kWeL-1, a power density of 0.5kWekg-1, an efficiency of 82-85% and a conversion rate of >99%. On a slightly larger scale, a 75kW methanol fuel processor/fuel cell combination was developed by Yan. This used an autothermal fuel processor along with a catalytic CO clean-up unit (water-gas shift/preferential oxidation) to generate $120m^3h^{-1}$ of reformate which contained 53% (vol.) hydrogen and less than 30ppm of CO during stationary operation (which peaked to in excess of 100ppm during peak operation).

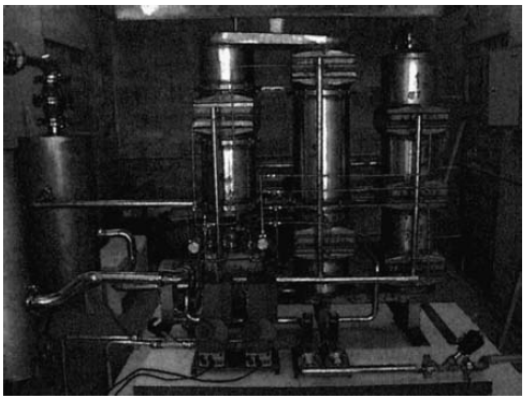

Figure 9.12 75 kW_{el} methanol fuel processor developed by Yan *et al.* [584].

Figure 13-7 – A 75kW fuel processor developed by Yan [58]

The UK 'Mercatox' project aimed to develop an on-board methanol steam reformer specifically for automotive use. The concept was similar to that of a plate reformer in a compact aluminium heat exchanger arrangement, with a separate gas clean-up unit of a similar arrangement. The design targets were, suitable for a 50-kWe, volume of 49L, mass of 50kg and a warm-up and response times of less than 5s.

At the top end of the scale, a 240kW methanol system has been developed for naval applications. While at the other end of the scale miniature reformers are being developed to replace batteries in portable electronic equipment such as the 2.5W reformer by CASIO. The smallest methanol steam reformer is suitable for 50-500mW applications and fits two evaporators/pre-heaters, a reformer and a burner into a volume of less than $0.2cm^3$.

Figure 9.20 500-mW methanol fuel processor developed by Holladay *et al.* [601].

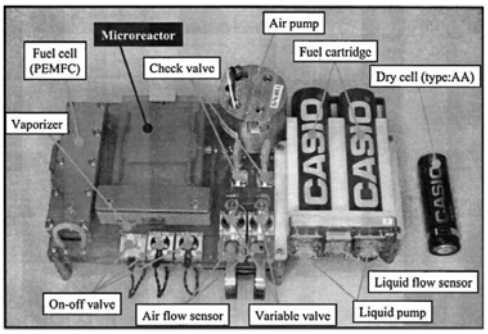

Figure 9.18 2.5-W methanol fuel processor/fuel cell system developed by CASIO [568].

Figure 13-8 and 13-9 – Small scale fuel processors [58]

13.1.5 Johnson Matthey HotSpot reactor

This originated in the 1980's as a form of catalytic partial oxidation reforming. The reactor consisted of a platinum/chromium oxide catalyst within a ceramic support. It received its name because of the 600˚C hot spot generated by the injection of the air and hydrocarbon mixture into the centre of the reactor. This early design took 25-30mins to become fully operational and the hydrogen output was only 12L. A later development of the HotSpot reactor saw it move over to autothermal reforming (although partial oxidation was still used for system start-up) which enabled it to handle the reforming of methanol for both residential and automotive applications. This reactor provided an output of 2.4mol of hydrogen per mol of methanol at a much lower maximum temperature of 400˚C. The power density of the complete system was 0.75kWL^{-1} (including manifolds and CO clean-up).

The latest development saw it expanded to an eight unit device which is able to produce more than 6000L of hydrogen per hour while weighing 8.8kg and occupying a volume of 6L. It works in partial oxidation mode for start-up before switching to autothermal reforming. The unit is fully operational after 50-170s and has an overall efficiency of 95.4%. Its modularity allows it to be easily adapted to different sizes and enables units to be switched off when not required. An add-on known as the Demonox system was developed to reduce the CO content in the reformate but a PROX can also be used..

Figure 8.15 The Johnson Matthey HotSpot™ reactor. These can be made in different forms suitable for methanol, methane, or gasoline processing. (Picture by kind permission of Johnson Matthey plc.)

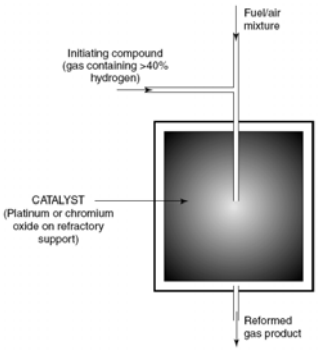

Figure 8.12 Simplified schematic of Johnson Matthey HotSpot reactor. Current versions of these devices have proprietary features not shown here. See also the photograph shown in Figure 8.15.

Figure 13-10 and 13-11 – The HotSpot fuel processor [56]

The HotSpot fuel processor is not limited to methanol and can be made in a number of different forms to cater for other fuels such as methane and gasoline.

13.2 Gasoline fuel processors

There has been considerable interest in gasoline fuel processors especially in the automotive industry for supplementing the power of electric vehicles. The use of gasoline fuel processors also allows fuel cell vehicles to take advantage of conventional fuels and therefore be introduced into the market place sooner. The onboard reforming of gasoline is capable of achieving efficiencies of 80%, its drawbacks being start-up time, cost and the high temperatures involved. In order for gasoline reforming to become viable development work is required in these areas. These include start-up and transient behaviour, afterburner design, tolerance to fuel additives and sulphur removal techniques. Additional CO removal and desulphurisation stages are also required if they

are to be applied to PEM fuel cells. GM and Renault have been the most active in developments in this area as will be discussed in the following sections. Toyota has also developed a gasoline processor as shown below and Johnson Matthey is also reported to be developing their own gasoline fuel processor.

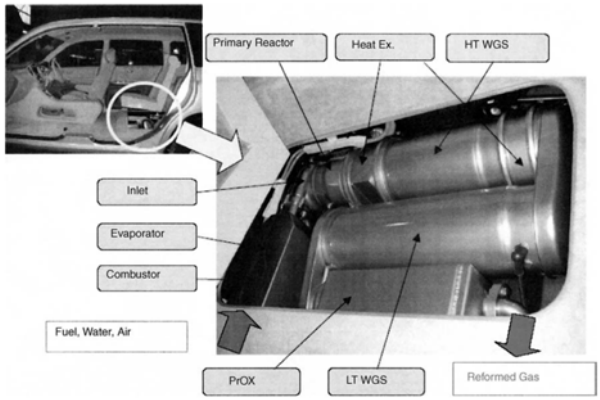

Figure 9.48 Fuel cell vehicle with on-board fuel processor developed by Toyota [447].

Figure 13-12 – An example gasoline fuel processor [58]

13.2.1 General motors research efforts

The first gasoline fuel processor developed by GM had an autothermal reformer, two water-gas shift stages and a PROX. It had a power output of 68kW an efficiency of 78% and weighed 34kg in its entirety. This early design was eventually abandoned due to a problem with uneven temperature distributions within the reformer. In 2001 GM revealed the world's first vehicle supplied by a gasoline fuel processor. This had a system power of 25kW, a peak efficiency of 80% and a start-up time of 3mins.

13.2.2 Renault research efforts

The fuel processor developed for Renault by Nuvera Fuel Cells has been reported to be the most promising of all the gasoline fuel processors for automotive use. It design targets were to meet the requirements of a 70kW fuel cell system (200kW thermal power output) at an efficiency of 40%. This first generation fuel processor utilised autothermal reforming with water-gas shift and preferential oxidation CO clean-up. It had a start-up time of 4mins (during which time batteries were used), a transient response time of 7 seconds, a volume of 280L and weight of 235kg. The third generation fuel processor as shown below had a thermal output of 215-33 kW and occupied a volume of 150L (which included the balance-of-plant). It had and a start-up time of less than 4 seconds but full power was not available for 15 minutes.

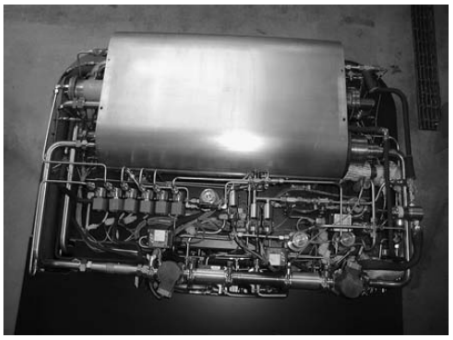

Figure 9.50 3A generation fuel processor developed by Nuvera [620].

Figure 13-13 – A gasoline fuel processor developed by Nuvera for Renault [58]

13.3 Diesel and Kerosene fuel processors

The reforming of jet fuel (kerosene) results in unwanted CO and sulphur by-products which necessitates additional fuel reforming stages which add cost, complexity, mass etc to the overall system. Diesel fuel processors are currently receiving interest for cars and auxiliary power sources in trucks. The catalytic partial oxidation and autothermal reforming of diesel (as well as JP-8, natural gas and gasoline) is being investigated by Delphi for use with their range of solid oxide fuel cells. Volkswagen has also joined forces with IdaTech to develop a diesel fuel processor/fuel cell system. Both Airbus and Boeing are investing the use of fuel cells to replace APU's. These would consist of a solid oxide fuel cell fed by a kerosene fuel processor (using either partial oxidation or autothermal reforming). The anode waste gases would then be fed to an afterburner to generate power for the compressor. On a very large scale, studies are also being carried out with regards the development of 2.5MW fuel processor/fuel cell system for submarines.

13.4 Multi-fuel processors

The ideal fuel processor would be one which is able to cater for a number of different fuels. This would make it not only future safe but also operationally flexible. Research is underway to develop such a system, which is able to provide the level of efficiency and reliability found in fuel processors which have been tailored to specific fuels. The fuel processor developed by Nuvera (already listed in the gasoline reformer section) is able to meet such requirements and able to handle gasoline, alcohols, natural gas, diesel and jet fuel. So far this has demonstrated a good efficiency and low CO content. Another key player in this area is International Fuel Cells who been developing a fuel processor which has a power equivalent to 50kW. This unit used an autothermal reformer, catalytic CO removal and feed desulphurisation and is able to cater for both methanol and gasoline.

14 Design and integration considerations for fuel cell systems

14.1 Introduction

There are still a number of problems which have to be overcome before fuel cells can become commercially widespread within vehicles. Some of these which are associated with their start-up and shut-down and the onboard storage for fuels for long periods have proven to be less of an issue for vehicles such as buses. Since aircraft are characterised by similar steady operation over long periods, fuel cells are also expected to be well suited to operation within aircraft. This section will give an overview of what makes a complete fuel cell system and some the factors which need to be considered when integrating such systems.

14.2 What is balance of plant?

The balance of plant is the significant amount of additional ancillaries which are required to enable a fuel cell to function. A complete fuel cell system including all ancillaries is a complex and difficult to manufacture system which must include the following sub-systems.

- Fuel supply – As will be discussed later, the fuel system can take a number of different forms depending on the fuel used. Pumps and regulators will generally be required to maintain a continual supply of fuel. Fuel pre-heaters and humidifiers may also be required to condition the fuel before it enters the fuel cell. Depending on the system, some form or recirculation may also be used.
- Air supply – This must be sufficient to maintain a continuous supply of air to the fuel cell. Systems can range from blowers for smaller fuel cells to compressors for larger systems typically found on vehicles or in some cases even bottled oxygen is used. This is usually linked with the humidification system.
- Humidification system – This is a necessity to keep the fuel cell sufficiently hydrated. A certain amount of product water from the fuel cell outlet is usually recovered and injected back into the fuel cell inlet for this purpose.
- Cooling system – This is necessary to maintain the heat balance of the plant.
- Fuel cell operation - Various miscellaneous monitoring and control systems are required in order to maintain the correct operation of the fuel cell. This includes systems to maintain the correct water balance and temperature etc.
- Power conditioning - Simple voltage regulators or DC/DC converters are used for this task to transform the DC output into a useable form.
- Electronic control system – This is required to monitor numerous sensors and maintain the fuel cell operating conditions via a numerous pressure regulators, control valves and pumps.
- Fuel cell start-up and shut-down systems - Additional valves and heaters may be required for these stages along with additional controller stages.

The balance of plant can add a significant amount of extra weight and occupy a considerable volume and as shown in the figure below which shows the complete Xcellsis HY-80 80kW fuel cell system used for the Ford Focus FCV. In this figure, the fuel cell is the box in the centre with the remainder being the balance of plant and PDU.

Figure 14-1 – Complete Ballard fuel cell system (including balance of plant) [59]

The balance of plant can consume an appreciable amount of power from the fuel cell output which reduces the overall efficiency of the complete fuel cell system and therefore careful integration of the different systems is required. Isolated fuel cells can be seen to be most efficient at the lower end of their operating range but when the power requirements of the ancillaries are taken into account a more constant efficiency over a wide operating range is apparent. An overview of a number of these sub-systems will be given in the sections below.

14.3 Fuel cell system design considerations and requirements

As with any other more traditional propulsion system, fuel cell systems will be designed to meet design requirements laid down by the airworthiness regulations, customer and other internal design groups. Design considerations of particular relevance for fuel cell systems include:

- Fuel cell volume and mass – Which is usually expressed in terms of specific power and power density which are measures of the volume and mass respectively as a function of the fuel cell power output.
- Fuel processor mass and volume – Which are usually expressed as a function of either the hydrogen output or the power output of a fuel cell which it is sufficient to supply.
- Operating conditions – Consideration needs to be given to the temperature and pressure of the fuel cell operating environment. These will have a notable impact on the performance of the fuel cell, fuel processor and compressor as well as other systems such as the cooling.
- Compressor requirements – Consideration needs to be given to its mass, volume, input power requirements and efficiency which are normally derived as a function of its pressure ratio and flow rate.

- Reactant consumption of the fuel cell – Where hydrogen is used as the fuel, this will dictate the quantity which needs to be carried on-board the vehicle. When oxygen is used instead of air, this will also need to be carried on-board.
- Fuel consumption of the fuel processor – Where a fuel processor is used, its consumption dictates the quantity of fuel required to produce the desired quantity of hydrogen.
- Cooling system heat exchanger requirements – Its frontal area will not only dictate its heat removal capacity but since it interacts with the free-stream air, it will also contribute to the drag f the vehicle.
- Manoeuvring loads – The effect of g-loads could have a significant impact on the performance of a fuel cell. Such loads may result in a displacement of water within the fuel cell significant enough to locally dehydrate the cell and could thus result in degradation in performance or even permanent damage.
- Cost – The acquisition and operating costs need to be competitive with traditional propulsion systems to avoid their dismal on the basis of cost.
- Technology readiness – A limiting factor in fuel cell development is financial investment. Fuel cell systems need to be implemented at the early stage in order to generate a return on the existing developments.
- Start-up and shut-down – Certain fuel cell systems make take a long time to become fully operational and in such conditions, power from an alternative source is required.
- Transient performance – The response time of some fuel cell systems may be unsuitable for certain vehicles but this is less of a problem for continual operation vehicles such as aircraft, trains and buses.
- Lifespan and Maintenance – The lack of moving parts in a fuel cell gives them a competitive edge compared to IC engines. There is however a significant number of seals between the different fuel cell layers which will require careful inspection. The delicate construction of the fuel cell stack will require specialist tools and processes in order to carry out any repairs. In the event of any problems, maintenance engineers are not likely to be able to carry out such repairs and exchange units are likely to be used instead.
- Safety – The construction of a fuel cell stack means that failure of a single cell will not result in complete failure of a stack and will only result in degradation in performance. Since hydrogen fires burn with a virtually invisible flame, hydrogen leaks from seals are of particular concern. Suitable hydrogen leak detection and fire extinguisher systems are therefore required to reduce the risk.

14.4 Fuel supply

The hydrogen and oxidant reactants which enter the fuel cell are distributed over the surface of the electrodes by means of a large number of passages in the backing plates. A number of different passage patterns have been explored to distribute the reactants as evenly as possible over the surfaces but it is inevitable that concentration gradients will still exist. It is typical for there to be a high concentration of reactants at the centre of the fuel cell which diminishes towards the edges. This also results in voltage gradients within the fuel cell plates but this subject is beyond the extent of this study. If we consider a simple straight channel with a reactant fed at one end as an example, as the

reactant travels along the channel it is also slowly absorbed into the fuel cell electrodes. By the time the reactant reaches the end of the channel, its concentration is considerably diminished. At these extremities, there is also likely to be a significant build up of impurities in the remaining reactants. It is therefore necessary to supply the reactants to the fuel cell in excess of what is actually required. In this context we are able to define an utilisation factor, which is a measure of the amount of hydrogen or oxidant which is actually converted within a fuel cell to that which is actually supplied.

Fuel cells generally use hydrogen as their fuel which can be supplied directly from an onboard hydrogen source or extracted from another fuel such as methanol. An overview of each of these approaches will be given in the sections which follow.

14.4.1 Direct hydrogen fuel supply

This is the simplest means of fuel supply in which hydrogen is held onboard the vehicle directly by means of some form of hydrogen storage. The most common approaches are compressed or liquefied tanks but other approaches such as hydrogen absorbers are also receiving considerable interest. In a typical system utilising compressed hydrogen from a high pressure cylinder, a pressure regulator is used to control the pressure of the hydrogen entering the fuel cell. Incidentally, the pressure of the hydrogen must balance that of the oxidant as a pressure differential across the membrane will result in its damage. As already discussed, the hydrogen is supplied to the fuel cell in excess of what is actually required and one of the three approaches below is typically used to utilise as much of this as possible to maintain a high economy.

- Dead end with purge – In this system, the fuel cell hydrogen exit is blocked off so that the hydrogen is retained within the stack until it is consumed by the fuel cell. Even bottled hydrogen is not 100% pure and impurities can build up within the fuel cell which is in addition to the water vapour which the hydrogen can collect. These dilatants can decrease its performance and it is necessary to purge such a system at regular intervals. For such purposes a purge valve at the fuel cell exit which is regularly opened. The downside of this being that hydrogen is wasted each time the system is purged.
- Closed loop with purge – This is an improvement over the previous system in which the hydrogen is able to freely pass through the stack. Upon its exit from the stack, it passes through a water separator to remove the excess water. The remaining dry hydrogen is then returned to the fuel cell inlet via a circulation pump or ejector pump. Such a system will still require purging but at less frequent intervals and is thus more economical.
- Straight through with a tail gas burner – In this system, the hydrogen passes through the stack just once. Upon its exit from the fuel cell, the remaining hydrogen passes through a water separator before being burnt in a tail gas burner. The pressure and temperature gases from the burner can be used to drive a compressor or heat another system. In such a system, the flow rate of hydrogen fed to the stack requires careful control to prevent wastage.

14.4.2 Hydrogen fuel supply via a fuel processor

Instead of having to store large quantities of hydrogen, it is sometime more efficient to extract hydrogen from a hydrogen rich fuel instead. Such a process requires the integration of a fuel processor into the fuel cell system. The exact nature of each fuel processor is different but they typically include a reforming stage followed by several gas clean-up stages. When we consider that each stage has its own air, steam and heat requirements, the complexity of the integration of such a system soon becomes apparent. Fuel processors are complex in their own right and their design involves careful planning of the layout of the different components and the flows between them. In addition to this, the design of a fuel processor needs to also encompass the fuel cell system with a view to providing some commonality between the two systems. This would enable heat, air, water and coolant to be shared between the systems and thus reduce the number of components required. The design target for such a system is a high efficiency, minimal content of CO and other by-products and sufficient flexibility to meet its demands. Due to their complexity, it is typical for a fuel processor to use a dedicated control system for control of the temperature and all the air, fuel and steam supplies. An example of an integrated fuel cell/fuel processor system is shown below.

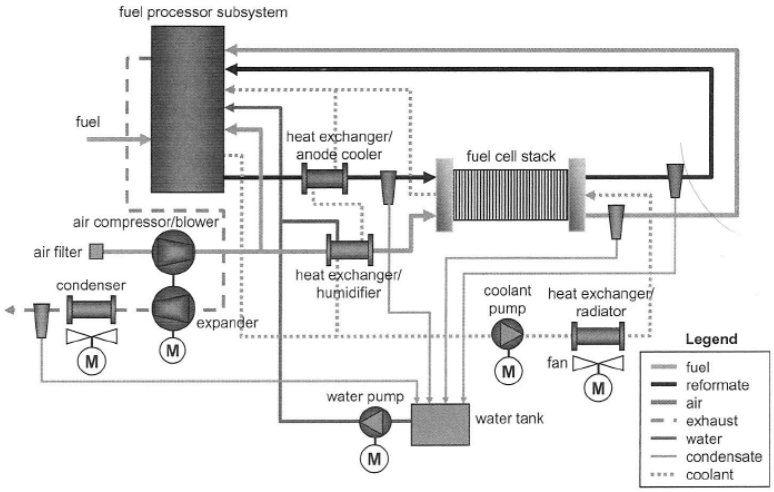

FIGURE 9-38. A complete fuel cell system integrated with fuel processor.

Figure 14-2 – An example complete fuel cell system with integrated fuel processor [57]

The reformate from a fuel processor typically contains significant proportions of carbon dioxide and nitrogen in addition to hydrogen which act as dilutants in the fuel cell. In such systems, any unused reformate which leaves the fuel cell is typically burnt within a tail gas burner to generate heat for the fuel processor. Since the reformate already leaves the fuel processor in a hot and saturated state, there is no need for an anode humidifier as used on direct hydrogen systems. A cooler and water separator is still required however to reduce the temperature and water content of the reformate.

14.5 Oxidant supply

The oxidant used with a fuel cell is either oxygen from a compressed source or atmospheric air. As with the fuel supply, the oxidant must be supplied to the fuel cell in

excess of that required to ensure there is a sufficient concentration across the surface of the fuel cell. This is defined by the stoichiometric ratio with a value of 2 or above being typical. Where oxygen is used, it is typical to use a closed loop with purge system as for the hydrogen supply. When air is used, there is no need to re-circulate the oxidant and a straight through system can be used. In such systems, the air is driven through the fuel cell with the aid of a blower or air compressor. The oxygen depleted air leaving the fuel cell has a high water content which is usually recovered with a water separator to be used elsewhere within the fuel cell system. Where the air is compressed before entering the fuel cell, an expander can be used at the fuel cell exit to recover some of this energy. In systems where a burner is employed, the excess oxidant is used in the burner to compliment the excess hydrogen from the fuel supply.

14.5.1 Using air instead of oxygen

Systems using air are less efficient that those using oxygen since only 21% of air is oxygen. This means that considerably more air needs to be delivered to the fuel cell to supply the same quantity of oxygen. When we take into account the excess defined by the stoichiometric ratio, the quantity of air must be ratioed by the same amount and thus the quantity of air required can be considerable. Supplying too much air to the fuel cell is however not only a waste of energy required for the compressor or blower but can also carry too much heat away from the fuel cell. In small systems, air can be supplied at higher stoichiometric ratios to cool the fuel cell. Although such an approach is insufficient to completely cool a larger fuel cell, it could bring the temperature down below what is required. Where air is used, some form of air cleaner must also be incorporated into the air supply to remove particles and other unwanted substances.

14.5.2 Air compressors

As already discussed fuel cells are typically operated at higher than ambient pressures to increase performance and improve water balance (1.5 bar being a typical figure). This thus necessitates the need for some form of air compressor. The incorporation of an air compressor into the system does however increase the cost and complexity of the system. Allowance must also be made for the power-off take required to drive the compressor which can have a considerable impact on the actual fuel cell output. It is possible to run a fuel cell at near atmospheric pressures but some level of compression is still required to overcome the pressure drop within the fuel cell. The type of compressors used is however relative to the application and larger fuel cells may require an extensive device while a simple blower may be sufficient for smaller fuel cells. Blowers are only suitable for small to medium sized fuel cells which require low pressures. No single type of compressor can thus cater for the range of fuel cell sizes encountered in practice.

The selection of a suitable compressor is based on the following requirements. Although it will not be possible to fulfil all of these, the ideal is device is one which offers the best balance of all of these parameters.

- Desired pressure ratio and mass flow rate – As required by the fuel cell.
- Good efficiency - Over the operating range encountered from partial to full load.

- Heating effect of the compressor – This is related to the efficiency of the compressor. Higher heating dictates the need for additional cooling stages to bring the temperature of the air down to a level suitable for entry to the fuel cell.
- Noise and vibration – Important for any aircraft. The compressor is the major source of noise within a fuel cell system and can be influenced by other system components.
- Low mass and volume – Important for any aircraft.
- Low cost – Including initial outlay and subsequent maintenance costs.
- Durability and lifespan – Crucial for the safety and reliability of any system.
- Outlet air purity – The outlet air must be free from contaminants such as oil
- Transient response – The device must be able to meet the fuel cell demands.

There are four main types of compressor commonly encountered in reasonable sized fuel cell systems dictating the need for a high mass flow rate. These are given below and can be categorised as positive displacement or aerodynamic compressors.

- Roots compressor – These are cheap and work over a wide range of flow rates but only achieve reasonable efficiencies for small pressure differentials.
- Lysholm (screw) compressor – These provide good efficiency over a wide range of flow rates but are expensive to manufacture. By changing the length and pitch of the screws, these can be designed to provide a wide range of compression ratios.
- Centrifugal (radial) compressor – These are common, inexpensive, reliable and a wide range of units are available to suit a variety of flow rates. They offer good efficiency but only within well defined pressure and flow rate limits and are not suitable for low flow rates. These units also require careful lubrication due to the high rotor speeds of typically 80,000rpm. Care must be taken during their operation to avoid surge, a condition where the compressor becomes unstable. To achieve optimum efficency, the operating pressure must increase/decrease in accordance with increases/decreases in flow rate.
- Axial compressor – These offer good efficiency but only over a narrow range of flow rates and are expensive to manufacture.

The selection of a suitable air compressor has traditionally been made from existing units. Although these units are mature, they were however designed specifically for other applications. For example, the majority of compressors which operate with pressure ratios between 1.4 and 3 have been designed for IC engines. An example of such a unit this is the Eaton supercharger which is well suited for applications with a pressure ratio between 1.35 and 1.7. The smallest unit in this range is able to deliver flow rates of 50 to $100Ls^{-1}$ and thus these are only suitable for large fuel cell systems over 50kW. Compressors for systems of less than 50kW are significantly more difficult to obtain. Systems operating at higher pressures ratios between 1.6 and 3 also experience difficulties in finding a suitable unit. The Lysholm compressor is the most suitable in this case but these are designed for high flow rates. The smallest unit corresponds to mass flow rates up to $0.12kgs^{-1}$ which corresponding to systems of about 100kW.

More recently, a number of companies such as Opcon Autorotor, Eaton and Rotrex have started to develop air compressors specifically aimed at fuel cell systems. The correct selection of such devices does however require the use of manufacturer's performance charts in terms of the 'non-dimensional' mass flow and rotational speed factors. These can however be difficult to obtain and in some cases custom compressor units may have to be developed to meet the needs of a particular application.

A characteristic of any compression process is that the air is heated as a result of the process and thus the air may need to be cooled before it can be safely used within the fuel cell. An intercooler (using free-stream air) can be used for this task or alternatively a heat exchanger can be used to transfer the heat to the incoming hydrogen flow. If the fuel cell and fuel processor are designed to operate at similar pressures, then the same compressor unit can be used to deliver air to both.

14.5.3 Turbines and expanders

These are used for the recovery of power from high pressure air leaving the fuel cell or hot exhaust gases leaving a burner. Although these are not used for oxidant supply, they are relatives of the air compression devices and thus worth a mention here. Because of the nature of the expansion process, these units also enable the exhaust gases to be cooled sufficient for later water recovery stages. The preferred choice of turbine for use in fuel cell systems is the centripetal (radial) turbine which can be likened to the centrifugal compressor. These do however operate at extremely high speeds which means that they are unsuitable for driving lower speed compressors such as the screw compressor. Their speed is thus well matched to driving centrifugal compressors as is done in a turbocharger. Such turbocharger units are readily available in a range of sizes but are only suitable for fuel cells over 50kW. It is however possible to combine two positive displacement devices in the same way.

In such turbocharger units, the energy of the exhaust gases must be increased with the use of a tail gas burner which uses either an additional supply of hydrogen or the excess from the fuel cell. Compared to turbochargers, mechanical superchargers offer benefits of an improved transient response but at the expense of NHV behaviour, power demands and efficiency. Waste gates, variable turbine geometries and turbine inlet throttles can be used to balance the compressor and turbine power requirements and demands respectively. The advent of fuel cells has promoted the development of compressor/expander units specifically for fuel cells. Key players in this field are Honeywell and Vairex. These units are however currently only aimed at 50kW fuel cell vehicles. For larger systems, automotive turbochargers remain the best option.

14.6 Humidification requirements and water management

A criterion for a PEM fuel cell is that its electrolyte membrane is kept sufficiently hydrated. Failure to do so will result in the electrolyte drying out which is accompanied by a degradation in fuel cell performance and the risk of permanent damage to the fuel cell. The flow of air entering the fuel cell has a drying effect on the membrane, which is another reason why air cooling is not used in larger fuel cells. Although the atmospheric air entering the fuel cell will have some humidity, this will be insufficient to meet the

needs of the fuel cell. To overcome this, the intake air must be maintained at a high level of humidity which is typically achieved by means of injection of water under high pressure into a cathode air supply humidifier. An additional complexity when fuel cells are used in vehicles is the influence of external forges which can cause movement of the water within the fuel cell leading to humidity gradients within the membrane. It is also usual to hydrate the hydrogen entering the system as well but this is usually less than for the air side of the fuel cell.

The water used for hydration must be of high purity to prevent the fuel cell from being contaminated and water obtained from the fuel cell exit as a by-product of the reaction is used for this purpose The water captured at the fuel cell exit is not only used for hydration but is also required for other systems such as the fuel processor (to generate steam for the reformer and shift reactors). The total balance of water within the system is more complex than this in reality since water is also generated by the tail gas combustor and preferential oxidation units. In addition, the quantity of water that initially enters the fuel cell along with the air is also dependent on environmental conditions. Any unused water can either be dumped or left to exit the system in its vapour state (which can be beneficial to increase the mass flow rate through any expander such as a turbine).

14.7 Thermal management and the cooling system

In any fuel cell system it is necessary to make provision for adequate cooling of the system. This needs to be sufficient to not only cool the fuel cell but also all the associated ancillaries such as the fuel processor. Fortunately, some of this waste heat can be reused within other components such as fuel pre-heaters and vaporisers. Drive components such as traction motors and controllers also require cooling but they typically use their own cooling circuit. In small systems, the power is usually low enough that air cooling is sufficient in which excess air is supplied to the fuel cell to remove the waste heat. This is however insufficient for higher powered systems and a liquid cooling system is typically used instead.

Although IC engines operate at higher temperatures than fuel cells, the heat load on their cooling system is less since a significant proportion of their waste heat is carried out the engine by the hot exhaust gases. The cooler exhaust gases of a fuel cell means that the proportion of heat retained within the fuel cell which must be removed by the cooling system is higher. Within a fuel cell system, surplus heat is typically removed by a combination of an exhaust gas condenser and a radiator type heat exchanger. The actual ratio of heat removed by the condenser to that removed by the radiator is however dependant on the operating temperature and pressure of the system. Heat removal by the condenser is more favourable at higher temperatures and lower pressures with the radiator being more favourable in the opposite sense.

The working principle of using a condenser for cooling is that a portion of the waste heat is consumed by the phase change that takes place (the condensation of steam into water). Such units do however have lower heat transfer coefficients that their radiator counterparts which imply the need for larger heat exchange areas and thus a large unit when subject to the same heat load. The dependency of the effectiveness of a radiator on

temperature means that at low operating temperatures (as encountered with PEM fuel cells) larger radiators are required in order to be able to remove sufficient heat. Automotive radiators are typically used for this purpose because of their compactness (producing heat exchange areas of greater that $1000m^2/m^3$) but even this may prove to be insufficient in some cases the size of fuel cell may be limited by the cooling system.

Although the cooling system could utilise water recovered from the fuel cell, a separate water circuit is typically used to cool both the fuel cell stack and fuel processor. The cooling circuit encompasses many components within the fuel cell system as some of these have also have cooling needs while it is possible to utilise some of the waste heat elsewhere within others (such as the air humidifiers). This allows antifreeze and coolant additives to be used which prevent freezing and offer improved heat capacity. The figure included in the hydrogen supply section gives and example of such a system.

14.8 Electrical energy storage

It is necessary to provide some means of energy storage onboard a fuel cell powered vehicle to provide an alternative source of energy to meet the following requirements.

- Start-up – It may take a few minutes for a fuel cell to become fully operational during which time power is required for pre-heaters, pumps, sensors, control systems. This is however less of a concern for a aircraft as a ground cart could be used as for the start-up of a conventional aircraft.
- Short term high power demands – In the case of an aircraft, such instances will be experienced during take-off and acceleration. For continual high power operation, it will be necessary to use a larger fuel cell but for short periods, an additional energy supply can be used to boost the power from the fuel cell.
- Transient operation – Fuel cells will not be as responsive as IC engines and therefore a means of smoothing out the power distribution is required.
- Back-up power – In the event of failure of the fuel cell, there must be sufficient power available to be able to safely bring the vehicle to rest.

Batteries are the commonest way to provide additional electrical power but super capacitors have also been receiving considerable interest. A pack of super capacitors has been shown to be an efficient means of storing a large quantity of energy for a short period of time. Tests on such a pack of 90 super capacitors showed it was able to provide 50kW over a 15 second period for a weight penalty of 168kg. The short duration of such units is however less likely to be sufficient for providing back-up power and batteries may still be required for such needs.

14.9 Costs

At their current level of technology, fuel cells are considerably more expensive than a comparable IC engine. The main cost drivers for fuel cells are the fuel cell manufacturing processes and the system ancillary equipment required. Cost will unfortunately be one of the main deciding factors as to the initial success of a fuel cell powered aircraft and we are unlikely to see such aircraft entering production in the short term as a result. Such units are more likely to be realised in the automotive industry first

which and their costs are expected to come down as a result of the increases in production. The US DOE set a target price of 45$/kW for a fuel cell in the year 2010 which was backed by a Ballard's 2010 predictions of 45$/kW.

Although system costs will be higher, fuel costs will during our time of rising fuel costs, makes fuel cell powered aircraft a significant long term investment. As an example, a study carried out in 2006 predicted the cost of fuel for a Cessna 172 in 2010-2015 to be 50.56$/h (assuming a price of 5$/gallon). Oil prices have however risen considerably greater than these predictions in recent years and they are expected to continue to do so in the next few years. An equivalent fuel cell with an assumed hydrogen consumption of 9kg/h (with a predicted hydrogen price for the 2012-2015 period of between 2.35$/kg to 6.97$/kg) is expected to have a fuel cost of between 18$/h and 63$/h. The maintenance costs are expected to be slightly higher due to the complexity and specialist nature of the systems but the US DOE has set a service life target of 5000 hours by the year 2010.

14.10 Safety considerations

The greatest risk within a fuel cell system is that of hydrogen leaks which can result in a dangerous hydrogen/oxygen gas mixture. The dangerous nature of a leaked gas mixture means that the fault tolerance of such a system is low and careful manufacture, assembly, testing and maintenance is necessary. Problematic areas within a fuel cell are couplings, joints and the mating faces between plates and electrodes. Although bi-polar plates are designed with a layout to reduce the risk of leaks at the edges, leaks are still problematic. The porous nature of the electrodes is also an area of concern especially its edges, where a gasket is normally used. Adequate means of detecting hydrogen leaks must be incorporated into a fuel cell system to prevent a disaster. Another concern for any propulsion system is that of loss of power in the event of a failure. As discussed, the construction of a fuel cell stack means that failure of a single cell will not result in complete failure of a stack. In such cases, the loss of an individual cell will only result in degradation in performance which is in contrast to an IC engine.

14.11 Fuel cell durability and reliability

The lifespan of a fuel cell is an important consideration which must be thoroughly evaluated if fuel cells are to be accepted as primary sources of power for propulsion. A significant amount of experimental testing is required to determine the lifetime of a fuel cell system. Such testing is costly and is sometimes impractical. Typical figures suggest an operating lifetime of between 3000 and 5000 for automotive applications and up to 20,000 hours for buses. Such studies are however are carried out for the use of air and pure hydrogen with little information being available for the use of reformed fuels. In such studies water management and been shown to be a major contributor to the lifespan and performance of a fuel cell. Excess water can lead to impurities being deposited on the catalysts or membrane and thus poisoning of the fuel cell. In the case of methanol reformer systems, it is important to keep the quantity of unreacted methanol to a minimum as this can diffuse to the cathode and contaminate the catalyst.

A number of preventative measures can be used to preserve the life of a fuel cell. Such measures include, the injection of oxygen into the fuel stream to remove contaminants

by oxidation and regular reactant chamber purging with an inert gas. Other measures include the operation at lower pressures and temperatures and the maintenance of a correct water balance. The performance of any fuel cell in a stack can be carefully monitored by assessing its electrical or thermal response. Such data can be fed back to the fuel cell control unit to adjust the flow rate of reactants or humidity to that cell. The reader is advised to refer to 'Failure Analysis of Polymer Electrolyte Fuel Cells' by Pratap Rama et al [60] for a theoretical analysis of fuel cell failure.

14.12 Future outlook and challenges for fuel cells

There is a definite market for fuel cell powered aircraft but there are a number of barriers preventing the realisation of such an aircraft in the short term. These have already been mentioned in the discussion above but to summarise, these are, cost, specific power and power density, fuel choice and safety. These areas have already been highlighted as long term goals for further development of fuel cell system and so improvements are expected within the next few years.

14.13 Traction motors for electric vehicles

Electric motors are a key component within any electric vehicle and selection of the correct motor is vital to the performance and efficiency of the vehicle. There are many different types of motors available with the best one to use being dependent on the application. A high efficiency motor is desirable to ensure that its power demands and thus the size of the accompanying batteries or fuel cell and ultimately the weight of the vehicle are kept to a minimum. Since a reduction in the weight of the vehicle will result in a reduction in the power demands, a converging design spiral results. Selection of the best motor will however involve a trade-off of a range of requirements such as efficiency, power output, operating range, weight, size, cooling requirements, maintenance and cost.

14.13.1 An overview of electric traction motors

Selection of the right motor does require some knowledge of the characteristics of the different motors. An overview of the most common motor types is given below, each of which works in a slightly different way.

- Permanent magnet brushed DC motor – These traditional motors use fixed permanent magnets, a multiple coil wound rotating core and brushes. The torque is dependant on the current, which is dependent on the supply voltage and the resistance of the armature. The presence of back EMF results in maximum torque when the armature is stationary with a progressive drop in current and thus torque with increasing motor speeds. A controller is required at low speeds to limit the current and thus prevent damage to the motor. These motors have been replaced by more sophisticated types for vehicle traction applications but are still very popular for general purpose applications.

- Electro-magnet brushed DC motor – These are a more sophisticated form of the motor above whereby the magnetic field is generated by electro-magnets (field windings) instead. Field windings are more efficient and cheaper way to generate a strong magnetic field and also enable the magnetic field strength to be varied for better motor control. Such motors do however generate additional heat and thus require improved cooling. The field windings in the series and shunt wound variants are fitted in series and parallel to the motor core and are thus dependent on the operating characteristics of the core, resulting in limited control of the motors speed and torque. The field windings in the separately excited motor are part of a separately controlled circuit which allows independent control of the magnetic flux and thus allows greater control of the motor torque at any speed. As a result, these motors are a popular choice for electric vehicles.

Brushless motor were envisioned to overcome the problems of friction, heat and wear associated with the contact between brushes and the commutator in traditional motors. They are also typically arranged so that the majority of heat is generated in the outer part of the motor and is therefore easier to dispense. The three most common types of brushless motors used in electric vehicles are briefly discussed below.

- Brushless DC motor (self-synchronous AC motor) – This is an AC motor which consists of a permanent magnet rotor which is surrounded by a number of stator coils. The stator coils are successively energised to induce magnetic fields in the stator which interact with the magnetic field of the rotor and generate a torque. They use DC power which is converted to AC by the motor controller but have operating characteristics similar to that of a traditional DC motor. Back EMF in the stator coils reduces the magnetic field strength and thus torque as the speed increases. Sophisticated versions of this motor are well suited for high power and traction applications. Compared to similar motors, the permanent magnet rotor does increase the cost of the motor but it also increases its efficiency and specific power.

- Switched reluctance motor – This consists of a cheap plain iron rotor which is surrounded by a number of stator lobes which are successively magnetised by coils. Induced magnetic fields in the rotor and stator generate a force of attraction between the two components to bring them in-line. Successive switching of the stator coils enables an angular momentum of the rotor to be maintained. The speed is controlled by the duration that each stator coil is switched on for and thus a microcontroller is required. The elimination of permanent magnets and back EMF means that higher speeds can be achieved. These motors offer benefits of higher torque per unit volume and higher speeds and thus higher power densities. Their peak efficiency is lower but more desirable efficiencies can be obtained over much wider operating band.

- Induction motors – These consist of a linked rod rotor which is surrounded by a number of equally spaced stator coils. When connected to a three phase AC supply, an anti-clockwise rotating magnetic field is generated by the stator coils. A corresponding current is generated in the rotor rods and force which prompts

the rotor to follow the rotating field. The maximum torque that can be obtained is dependent on the strength of the magnetic field from the coils. The number of stator coils (poles) defines the design speed of the motor but variation of the frequency of the three phase supply enables the speed of the motor to be controlled. An inverter is required in order to be able to connect these motor to a DC system. These motors are very slightly less efficient than similar types but have a number of advantages which has resulted in their widespread use.

14.13.2 Motor cooling requirements

There are four main sources of loses within a motor, copper losses, iron losses, friction and windage and constant losses. These motor losses are dependent on its torque and speed and thus its efficiency is also dependent on these. Such losses are accompanied by a generation of heat and sufficient heat removal methods are required to prevent an excess build up of heat which can lead to its failure. Motors are able to safely exceed their rated power output for transient short periods but should not do so for extended periods when they are likely to overheat. The power output of the motor is thus limited as a result of its cooling effectiveness. Configurations in which the losses and heat are generated in the outer components instead of the core have proven to be easier to cool due to their greater surface area. Air cooling is generally the preferred method of heat removal but liquid cooling can be used for high power motors where this is insufficient.

14.13.3 Motor requirements and selection

Size and mass are particularly important requirements for traction motors and typical measured in terms of power density (power per unit volume) and specific power (power per kilogram mass). For DC systems, AC motors are generally lighter than their DC counterparts but an inverter is required. The method of cooling can be seen to have a significant impact on its specific power with liquid cooling enabling an equivalent power to be extracted from a much smaller motor. These motors do however have the additional weight of the cooling system. Efficiency is also a particularly important parameter which is influenced by,

- The type of motor - Brushless motor types can achieve slightly higher efficiencies due to lower losses in the rotor.
- Operating speed - Motor losses are related to its torque and thus speed, with high speed low torque motors being the most efficient.
- Cooling - Since the resistance of the motor windings increases with temperature.
- Size of the motor – The efficiency can be seen to increase with size for induction motors.
- Operating conditions – A wide operating efficiency band is important for motors which are subject to variable speed/torque conditions as with reluctance motors.

It is worth noting that the size of a motor can be shown to be governed by its torque requirements and not power requirements. This means that high speed low torque requirements will only require a small motor. A high speed motor/gearbox combination will thus sometimes be more compact and lighter than an equivalent low speed motor for low speed applications. A next generation improved motor has been proposed called the HTS motor (High Temperature Superconductor) which uses superconductor alloys

instead of traditional copper windings. Their main drawback is the need for a complex cooling system to maintain low operating temperatures of about 50ºK.

14.13.4 Associated regulators and controllers

The voltage output from sources such as fuel cells can vary with respect to time, temperature and current leading to an impractical very wide voltage range. The first stage in such a circuit is thus a voltage regulator, which is used to transform unsteady voltages into a more practical and regulated form. Batteries are able to deliver a well regulated voltage output but even this has to be varied when controlling equipment such as motors. It is typical to incorporate electronic switching circuits for such purposes to either drop or boost the voltage output to achieve either a fixed or variable voltage as desired. The requirements of electric vehicles mean that custom DC/DC converters and step-up/step-down chopper circuits may be required. When a AC motor is to be driven from a DC supply an inverter is also required.

Motor controllers are vital to the efficient operation of any motor. In the case of basic DC motors, these may be simple units which use step-up and step-down regulators to vary the supply voltage and thus torque. In the case of more sophisticated motors, an additional control is achieved by varying the magnetic field via field windings. A combination of both flux and voltage control enable a motor to work over a wider range of torque and speed conditions but requires a complex electronic control system.

15 Sizing and integration of the fuel reformer based MALE fuel cell system

This section gives an overview of the selection, sizing and integration of the fuel cell propulsion system which is being investigated to replace the conventional turboprop engine of the MALE UAV. The enormity of the system selection and sizing work meant that it was necessary to incorporate as much as possible of this work into the accompanying appendices and other thesis sections. This section will thus only give an overview of each of these stages and point the reader to the relevant sections for further information. The main focus of the discussion contained in this section will thus be on the integration of the system into the aircraft.

15.1 Selection of the fuel cell type and candidate fuel

The study into different fuel cell types showed the PEM fuel cell to have benefits of low operational temperatures, short transient and start-up periods and respectable efficiencies. They are thus regarded as the fuel cell of choice for use in the majority of other fuel cell powered vehicles. As a result, they have received considerable investment from developers and are thus currently the most technically advanced. The PEM fuel cell has thus been highlighted as being most appropriate for this project.

The study into alternative fuels has focused on an in-depth review of hydrogen and methanol. Hydrogen is the most appropriate fuel for use in fuel cells with its pure form currently regarded by many as the fuel of choice for fuel cell vehicles. Hydrogen is however accompanied with storage and operational problems which have proven to be one of the bottle necks in the development of fuel cell vehicles. An alternative approach to the use of pure hydrogen is to extract it on-demand from a hydrogen rich fuel which can be more likened to conventional fuels. Such a process does however necessitate the need for additional equipment to reform the fuel which adds cost, weight and complexity to the system. This is however offset by the fact that more conventional fuel tanks and fuel delivery equipment can be used. In this study methanol was shown to be the best synthetic hydrogen carrier fuel for this purpose. Its benefits include the requirement of a low reforming temperature, already being mass produced in large quantities and the potential to adapt existing fuel infrastructures for its use.

15.2 An overview of the all-electric propulsion system

The all-electric propulsion system which was devised for this project can be broken down into two sub-systems as given below.

- The fuel reformer based fuel cell system – This system utilises a fuel cell and its associated balance of plant to generate DC electrical power for the electric powertrain. This is accompanied by a fuel processor which is integrated into the system and used to extract hydrogen on-demand from the methanol fuel. The system also incorporates an air compressor which is used to improve the performance of the system. The power demands of the compressor are met by

burning excess hydrogen in a tail-gas burner to generate hot gases to drive a turbine which is directly coupled to the compressor.

- The all-electric power train – This system utilises 2 large traction motors and their associated controllers to transform electrical power into mechanical shaft power. The traction motors are linked via a 2 into one reduction gearbox, the output from which drives the aircraft propeller. Also incorporated into the system are regulators and inverters which are used to stabilise and transform the output voltage from the fuel cell system.

A more in-depth description of these systems is given in Appendix E and the reader is advised to refer to this section for further details.

15.3 The influence of fuel cell operating parameters

The performance and efficiency of the fuel cell system is directly related to the numerous system variables. This includes a range of parameters such as operating temperature and pressure, fuel and air flow, system humidity, output current, reformate composition and many more. It can be shown however that many of these parameters are inter-related and the number of actual independent variables is significantly reduced. For the purpose of this work, an extensive spreadsheet was developed to analyse the complete fuel reformer based fuel cell system. This was able to automate the optimisation of the majority of the variables with the only unknowns being operating pressure ratio and desired output power.

A breakdown of the different stages that make up the complete analysis spreadsheet is given in Appendix H with the accompanying equation derivations given in Appendix G. These sections also include a thorough discussion of the relationships that exist between the different operating parameters. The reader is thus advised to review these sections for a better understanding of the function of the different fuel cell operating parameters.

The hydrogen and oxygen stoichiometric ratios are particularly important as these have a strong influence on the fuel consumption of the system. The stoichiometric ratio is by definition the ratio of the actual quantity of hydrogen or oxygen delivered to the theoretically required quantity. In this particular system, the excess hydrogen leaving the fuel cell is utilised in the burner to generate hot gases to drive the turbine. Thus the careful control of the hydrogen stoichiometric ratio enables the power out of the turbine to be regulated to match power requirement of the compressor. In a similar way, the oxygen stoichiometric ratio is regulated according to the water content of the air. Too much air not only requires excess fuel to drive the compressor but also has a drying effect on the fuel cell and thus should be avoided. Too little air can result in their being either insufficient air in the burner or the fuel cell becoming flooded.

The operating temperature of the fuel cell can be shown to be directly related to the pressure by the requirement to keep the fuel cell exit gases in a two phase state. This implies that the exit gases must be kept within the thermodynamic vapour dome. The final operating parameter is the compressor pressure ratio, which can be shown to be an independent design variable. As a result, it is not influenced by other parameters but does have a considerable impact on the performance of the whole system. In particular, this affects the operating pressure and thus the performance of the fuel cell and fuel

processor over the range of altitudes experienced. To determine the best pressure ratio, the system was tested at two different values to arrive at the results below.

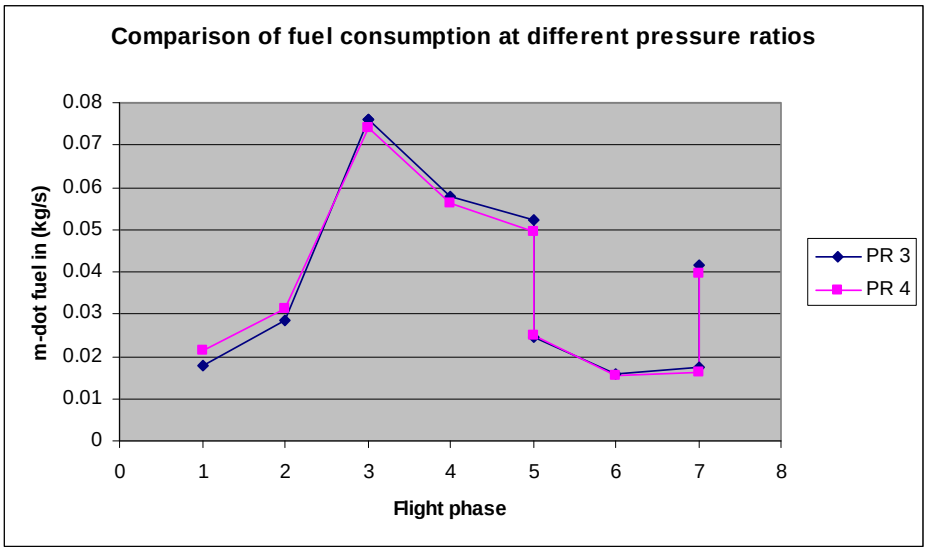

Chart 15-1 – Fuel consumption at different pressure ratios

Flight phase points 1-3 is climb start to end, 3-5 is cruise outbound start to end and 5-7 is loiter start to end. Point 7 also represents the start of cruise inbound. These trends show us that there is a slight fuel consumption advantage at loiter in terms of using a pressure ratio of 4 as opposed to 3. The reverse can be seen to be true at start-mid cruise but since the aircraft spends the majority of its time at loiter it makes sense to optimise the fuel consumption for this phase. Although it is possible to use even higher values of pressure ratio, to do so would require a significantly more demanding compressor unit. The pressure ratio has thus been fixed at a value of 4 for this system. As will be discussed elsewhere, operation at a higher pressure ratio also results in a smaller required radiator size. This has the added benefits of reductions in mass and drag.

15.4 The influence of the fuel processor

In this analysis we are considering two types of fuel processor, the autothermal reformer based unit and the steam reformer based unit. As is discussed in a different section, each unit has its own advantages and disadvantages and thus it is worth assessing the performance of each one. Values of typical reformate compositions for each unit are given in the table below.

Typical reformate compositions

	H2	CO2	N2
Methanol autothermal reformer	0.50	0.20	0.30
Methanol steam reformer	0.70	0.29	0.01

Table 15-1

15.5 Overall sizing of the all-electric propulsion system

The fuel cell system and powertrain must be sized to be able to deliver sufficient power to the propeller at the most demanding flight phase. There will however be a number of losses in the components that make up the powertrain which must be taken into account.

To compensate, the power delivered by the fuel cell must therefore be more than that required at the propeller shaft. The methodology used to size the fuel cell system was a propeller back approach, whereby our starting point is the propeller thrust requirements. The overall efficiency of our powertrain is thus taken to include the efficiency of the propeller, gearbox, motors and motor controllers. Additional losses due to other components within the powertrain are considered negligible compared to these. The reader is advised to refer to Appendix E for further details of the derivation of the fuel cell system power requirements.

It can be shown that the propeller is the source of the greatest loss within the powertrain. Its efficiency is dependent on its size, operating speed, power input and location on the aircraft. The importance of correct propeller matching can thus not be underestimated. A detailed description of the determination of the propeller efficiency is given in the baseline design section of the main text of this thesis.

15.6 The analysis of the final system

For the purpose of this feasibility study we are primarily interested in evaluating the specific fuel consumption of the installed system throughout the flight profile of the aircraft. This required the construction of an analytical model of the fuel cell system which gives the fuel consumption as a function of power output and operating altitude. This model was based on test data obtained from the fuel cell design and analysis spreadsheet described in Appendix H. Using this spreadsheet, the system was tested over a range of combinations of fuel cell power output and altitude to generate an extensive database of results. This raw data can then be converted more manageable but complex analytical expression with the aid of various stages of numerical analysis. The result is a polynomial expression to determine the fuel consumption as a function of the fuel cell power output. The constants of this expression are themselves determined by expressions which are functions of the operating altitude. This process is repeated to obtain two expressions, one for an autothermal based fuel cell system and the other for a steam reformer based system. A more detailed description of this procedure and the resulting expressions are given in Appendix J.

The analytical expressions discussed above were shown to give very good results for medium to high power settings as encountered in the take-off to descent flight phase. These were however less satisfactory for low power settings as encountered in the sea level loiter and landing phases. An alternative low power expression was thus derived for these phases following a similar process as above utilising low power data at sea level conditions from the design and analysis spreadsheet. Since these low power flight phases are at sea level conditions, the resulting quadratic expressions are much simpler that before with fixed constants. These analytical models can finally integrated into the existing performance analysis spreadsheets used for the baseline aircraft as discussed in the evaluation section and Appendix J.

15.7 The selection of a suitable compressor-turbine unit

An overview of the different compressor types and their suitability for fuel cell systems was given in the integration consideration section. The analysis of the reformer based

fuel cell system at different conditions showed the maximum required mass flow rate of air to be 0.6397 kg/s at the top of climb. Using the density of air at this condition, this gives a required volumetric flow rate of 829.94 litres/s. Since our system utilises four independently controlled reformer-fuel cell units, it makes sense to use a separate compressor-turbine unit for each. If we were to use a single compressor to supply air to all four fuel cells then a wide variation in the flow rate would be experienced if any of the fuel cell units were shut down. Thus the use of a dedicated compressor for each fuel cell enables each compressor to operate in the highest efficiency regime. The required mass flow rate through compressor will then be 207.49 litres/s.

From the earlier discussion, a centrifugal compressor–radial turbine turbo-compressor arrangement is clearly the best solution to meet the desired mass flow rates and pressure ratios. Compared to other types, the centrifugal compressor is also well suited to meeting the required compressor ratio value of 4. The Autorotor twin screw compressors would also provide a good solution for the air compressor side of the system but would be difficult to link to a suitable turbine. The selection of an off the shelf compressor-turbine unit is however fraught with difficulty due to the lack of available manufacturers data. The analysis for such a unit needs to take into account power requirements, efficiency and the impact of altitude and is thus clearly not possible within the timeframe of this project.

15.8 Sizing and integration of the fuel cell system components

In this study it was sufficient to represent the main components of the reformer based fuel cell system as boxes. The main purpose of this work being to ensure that there is sufficient space available within the aircraft and to determine the best location of each component with respect to the centre of gravity of the aircraft. The mass of each component must thus also be determined. For the purpose of this work it is sufficient to concentrate on the fuel cell and reformer modules with other components being less critical in comparison. The mass and volume of each is determined from statistical estimates of the specific power and power density as is discussed in Appendix E.

An example of a modern methanol reformer module, the ME-75-6 (typical of that used in this project) is shown in the figure below. The accompanying figure shows it in situ in the Xcellsis ME-75-6 fuel cell engine.

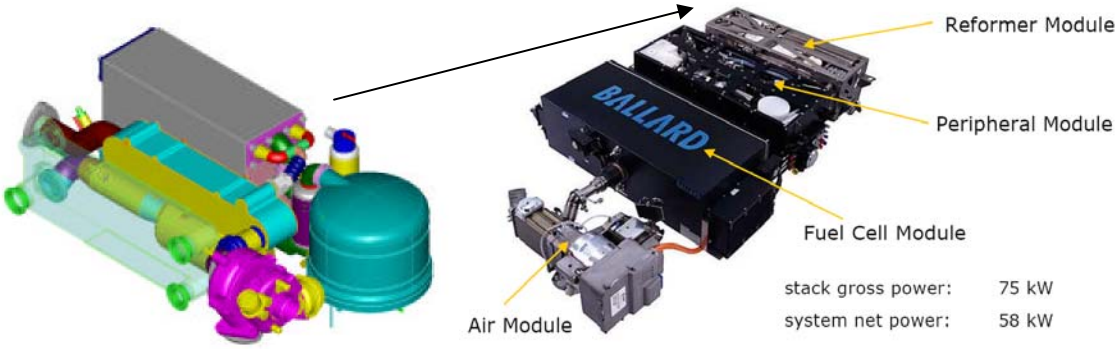

Figures 15-1 and 15-2 – The Xcellsis fuel processor in situ [59]

The fuel cell system air intake and exhaust must also be given careful consideration for the integration of the system. These are sized according to the methods of Appendix I. The final routing and layout of these is decided by designer's eye.

15.9 Sizing and integration of the cooling system

The design and sizing of the cooling system involved an extensive analysis of the complete system based on the first law of thermodynamics. Due to its close relationship with the fuel cell operating conditions, the cooling system analysis was incorporated into the fuel cell system design and analysis spreadsheet. Due to the scale of the task, the description of the selection, sizing and integration of the cooling system is given in Appendix I. The final system consists of a large 3-row air-liquid heat exchanger located in the aft fuselage which is used to dispense 65% of the waste heat. The remaining heat is dispensed of predominantly by smaller 3-row air-liquid heat exchangers located in each tailboom. These are supplemented with a liquid-liquid heat exchanger which is located in the fuselage and used to transfer some of the waste heat to the fuel held in the wing fuel tanks and thus also prevent the fuel from freezing.

Each air-liquid heat exchanger must be accompanied by an intake and exhaust which were sized according to the following guidelines.

- Duct entrance area = One third of the heat exchanger matrix frontal area.
- Duct exit area = 115% of the duct entrance area.
- Length of the entrance and exit ducts = Equivalent to the radiator height.

The boom radiators utilise a pitot type intake located at the front of the boom and a straight-out exit underneath the boom. The fuselage radiator utilises a flush NACA inlet on each side of the aft fuselage and an exit aperture located at the very rear of the fuselage just below the propeller shaft. In each case, fairly complex ducting is used to channel the flow to and from the internal heat exchanger housing. Time constraints have meant that it has not been possible to determine the component of the aircraft drag due to the presence of the heat exchanger inlets and exhausts. This is however a important consideration for any design incorporating such units and is thus left by the author as an area for further research investigation.

Not included in this work are the cooling requirements of the vaporiser, fuel processor and other components. These are however expected to balance the heat requirements of components such as fuel pre-heaters and such like. An extensive analysis would be required to predict the cooling/heat transfer requirements of such units and is beyond the scope of this work. There effect is however expected to be negligible in comparison with the main cooling system components such as the fuel cell and heat exchangers.

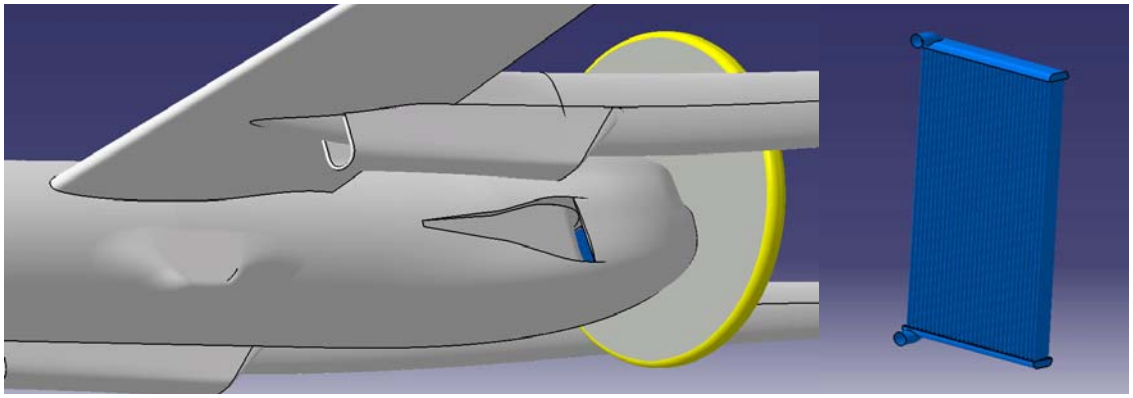

Figure 15-3 and 15-4 – The location and configuration of the tail boom and fuselage heat exchanger inlets and exhausts and an uninstalled view of a heat exchanger

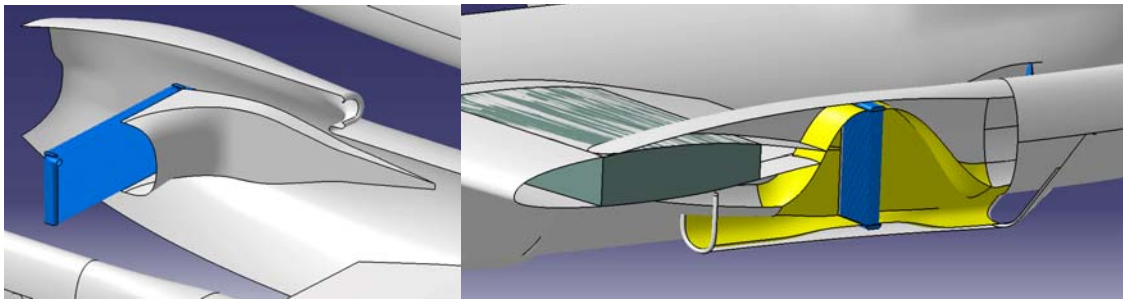

Figure 15-5 and 15-6 – Views of the internal positioning and ducting for the fuselage and tail boom heat exchangers

15.10 Selection, sizing and integration of the electric powertrain

For the purpose of this study, it was preferential to select the powertrain components from current off the shelf components. This not only simplified task but also enabled us to obtain the best possible estimates of size and weight. As discussed in Appendix E, an extensive review of commercially available traction motors and motor controllers was carried out. The motor deemed the most suitable for this project was the AC Propulsion AC-200. This motor was selected in preference to other designs for its long and narrow geometry which enabled it to be easily integrated into the aft fuselage. An additional benefit was that it was air cooled and thus offered a reduction in weight, cost and complexity. The motor controllers used were the accompanying AC Propulsion AC-200 controllers which were designed specifically for the AC-200 motor. Power requirements dictate the use of a dedicated controller for each motor and thus two are required.

The final stage of the powertrain is a 2 into 1 reduction gearbox which couples the two parallel motors to the propeller shaft and reduces the speed of the output shaft to a value suitable for the propeller. A review of such gearboxes showed there to be no existing unit which is capable of meet the needs of this project. Consideration was giving to making an statistical estimate from existing units. The only existing units were however primarily aimed at heavy duty applications which were not weight critical and thus were not representative of gearboxes for aerospace applications. The best approach was thus to produce a conceptual design of such a unit which could be used to determine the

volume and mass of each component and the complete assembly. The resulting gearbox assembly is shown below which is accompanied by a table giving a mass breakdown.

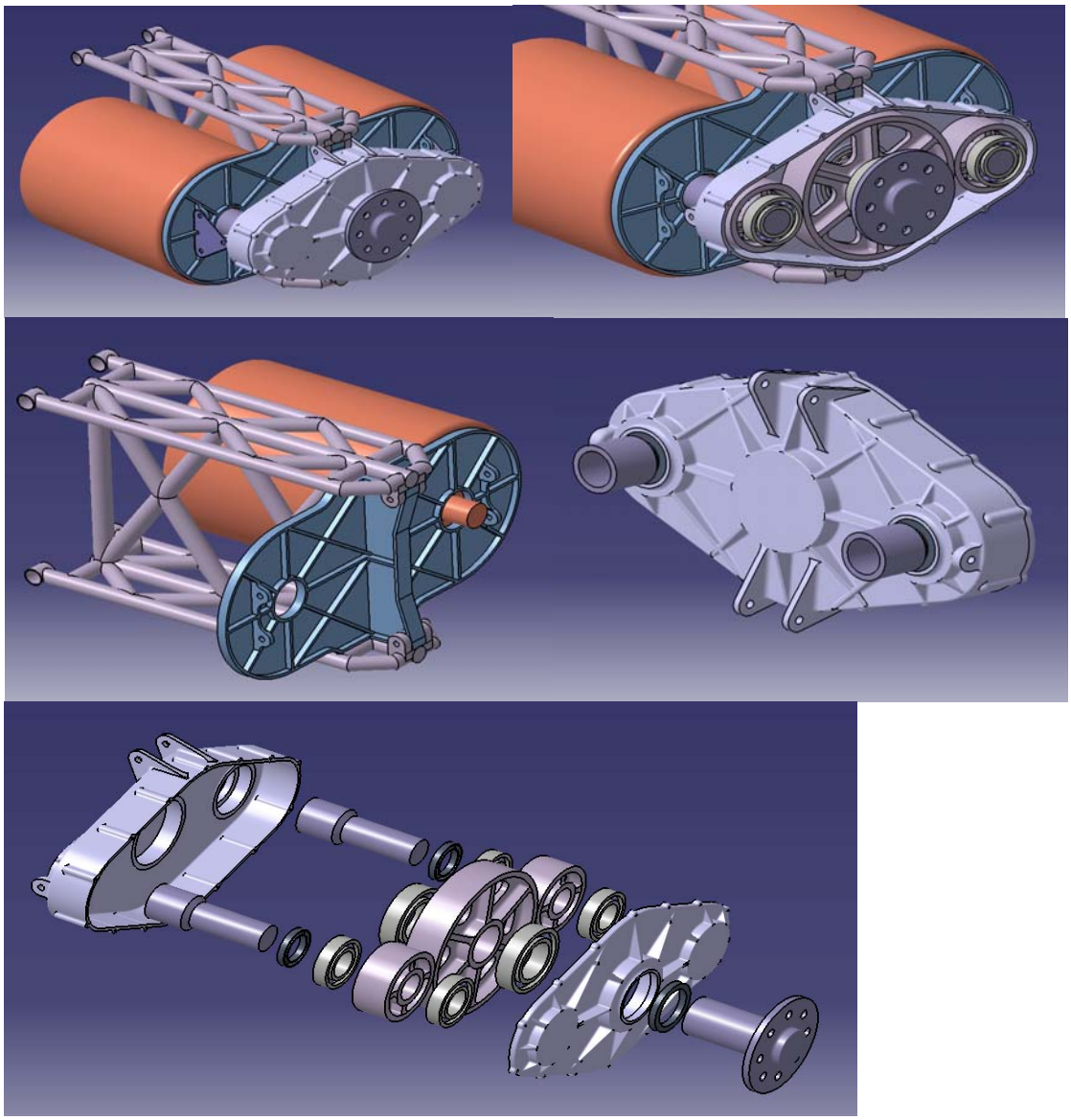

Figure 15-7 to 15-11 – Views of the electric powertrain assembly

Gearbox assembly item	Quantity	Volume (m3)	Material	Density (kg/m3)	Mass (kg)
Prop gear	1	9.215E-04	Alloy Steel	7750	7.1
Motor gear	2	3.182E-04	Alloy Steel	7750	4.9
Motor shaft	2	2.636E-04	Medium Steel	7860	4.1
Motor gear bearings	4	5.519E-05	Chromium Steel	7800	1.7
Prop shaft	1	6.663E-04	Medium Steel	7860	5.2
Prop gear bearings	2	1.119E-04	Chromium Steel	7800	1.7
Motor shaft oil seals	2	8.985E-06	Fluoroelastomer	1840	0.0
Prop shaft oil seal	1	1.225E-05	Fluoroelastomer	1840	0.0
Gear box end mount	2	1.026E-05	Mild Steel	7860	0.2
Gearbox front casing	1	7.903E-04	Magnesium RZ5	1840	1.5
Gearbox rear casing	1	1.235E-03	Magnesium RZ5	1840	2.3
Assembly backing plate	1	1.315E-03	Magnesium RZ5	1840	2.4
Top and bottom mountings	1	6.255E-05	Mild Steel	7860	0.5
Mounting structure	1	1.014E-03	Mild Steel	7860	8.0
Drive motor	2	N/A	N/A	N/A	100.0
				Total mass (kg)	139.7

Table 15-2 – Gearbox mass estimate

15.11 Design considerations for the use of methanol

The use of methanol as a fuel requires certain design modifications to prevent components of the aircraft being attacked by the methanol. In particular, fuel system components must be manufactured from metals, plastics and rubbers which are resistant to the fuel. Such modifications are however not expected to have a significant effect on the overall aircraft. Of greater concern are composite materials which can be attacked by methanol if they come into direct contact with the fuel. A particular problem with respect to this phenomenon is the storage of methanol within our composite wing-box. Research into this identified the best solution to be the use of a fuel bladder material within the tank which is resistant to methanol. The lightest and thinnest material capable of this task is manufactured by Aero Tech Laboratories, which is 1.2mm thick and has a density of 0.8kgm^2. The volume reduction due to this material is thus negligible but the additional weight penalty will need to be taken into account. A fuel tank liner for both wing fuel tanks with a total surface area of 23.913m^2 has a mass of 0.023kg. A liner for the fuselage tank with a surface area of 6.833m^2 will have a mass of 0.007kg.

A final consideration for the use of methanol is the freezing and flash points of the fuel in comparison with traditional Jet A fuel. In the case of methanol, these are -97.7°C and 12°C while for Jet A, these are -40°C and 38°C. From these figures we can seen that methanol is more suitable for low temperature applications such as high altitude flight. Its lower flash point however necessitates the need for additional safety precautions.

15.12 The impact of the systems on the aircraft configuration

The final mass breakdown for the MALE configuration with the fuel cell system integrated is given in the table below. Integration of the fuel cell propulsion system into the MALE configuration did however require a wing shift of 620mm towards the nose of the aircraft in order to keep the centre of gravity within acceptable limits. Analysis of this modified configuration gave the longitudinal static stability results presented in the table below for a number of different points throughout the flight profile.

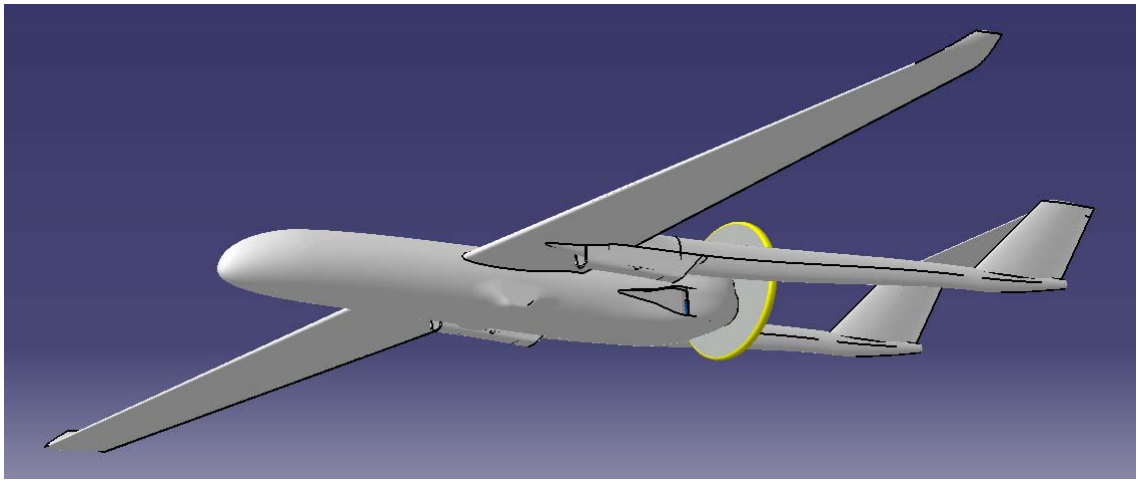

Figure 15-12 View of the fuel cell powered MALE

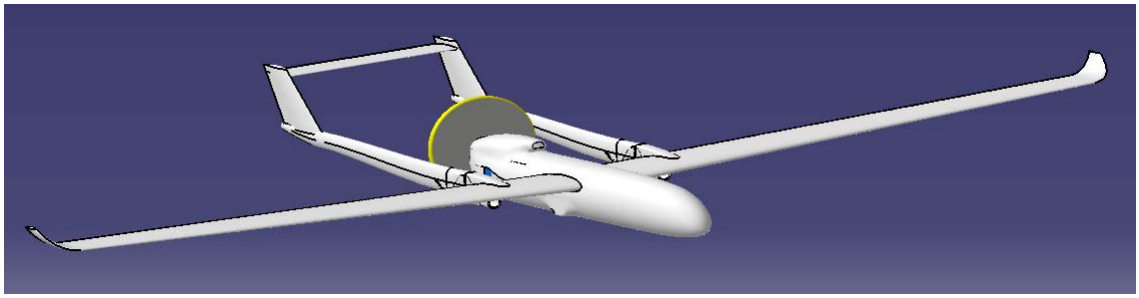

Figure 15-3 – View of the fuel cell powered MALE configuration

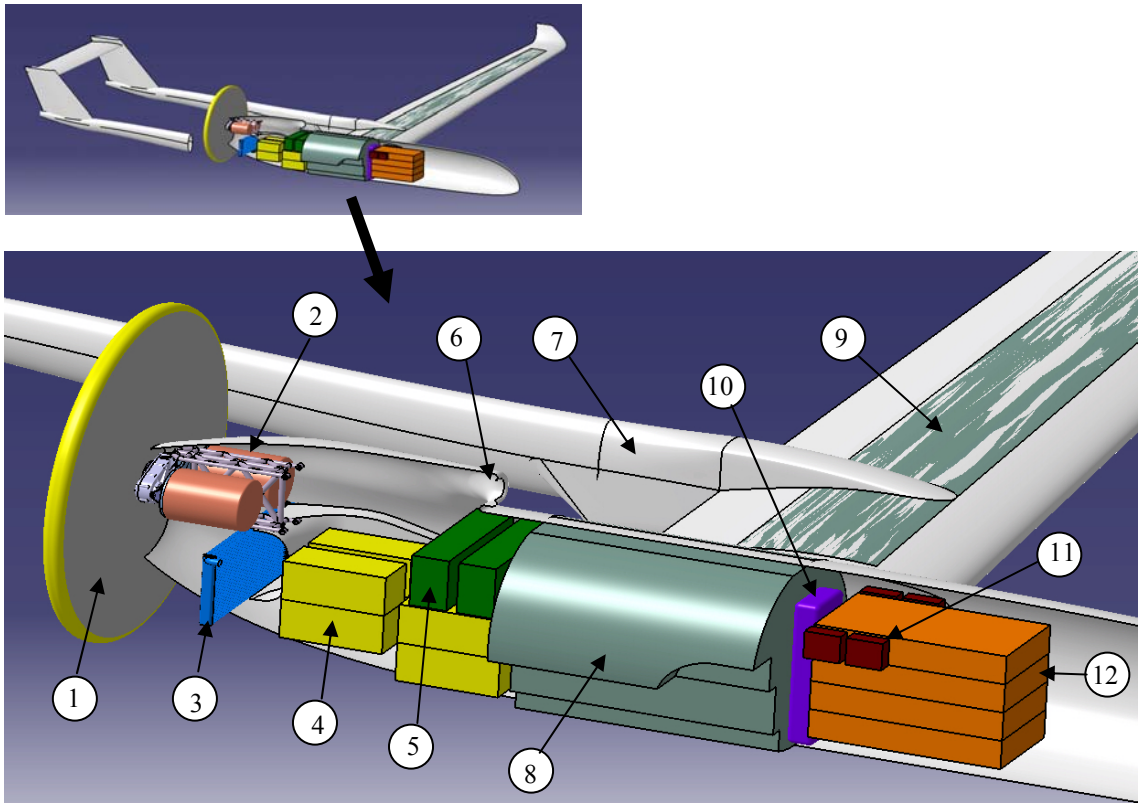

Figure 15-14 – Internal view of the fuel cell powered MALE configuration

Fuel cell powered MALE component breakdown

Item	Description
1	Propellor
2	Electric power train (including motor, gearbox and frame)
3	Fuselage heat exchanger
4	Fuel cell stacks (4 off)
5	Motor controllers (2 off)
6	Fuel cell pitot air inlet
7	Tail boom heat exchanger (2 off)
8	Fuselage fuel tank
9	Wing fuel tanks
10	Fuel system liquid-liquid heat exchanger
11	Fuel cell stack control unit (4 off)
12	Fuel processor (4 off)

Table 15-3 – Breakdown of fuel cell components

Component level mass estimation - Conceptual estimates

Genral items relative to both configurations	Mass (kg)
Wing	208.7
Fuselage (including emenage and undercariage)	246.7
Systems	377.2
Payload for primary mission	362.9
Fuel (including allowance and reserve)	2011.4

Items specific to the turboprop configuration	Mass (kg)
Installed powerplant	222.0
Total all-up mass	3428.7

Items specific to the fuel cell configuration	Mass (kg)
Electric powertrain assembly	139.8
Fuselage radiator	8.3
Tail boom radiators - 2 off (total)	5.4
Fuel cell stack - 4 off (total)	333.2
Methanol fuel processor - 4 off (total)	353.7
Motor controller - 2 off (total)	60.0
Fuel cell control unit - 4 off (total)	4.0
Fuel tank liner - wings and fuselage	0.0
Total all-up mass	4111.2

Static stability results

MALE - Fuel Cell	Kn (%)
End of take-off	5.6
Start of cruise 1	5.5
Start of loiter	6.4
End of loiter	12.1
End of cruise 2	13.1
Start of landing	13.7

MALE - Original	Kn (%)
End of take-off	7.3
Start of cruise 1	7.0
Start of loiter	7.1
End of loiter	6.5
End of cruise 2	6.2
Start of landing	6.4

Table 15-4 – Component level mass estimation and static stability results for the fuel cell powered MALE configuration

15.13 Sizing and integration of the hybrid systems

The hybrid propulsion system was envisioned as a means of reducing the fuel consumption of the fuel cell powered aircraft. Such a configuration utilises a turboprop/fuel cell propulsion system combination. The turboprop engine is retained for all but the loiter phase and thus retains its original size. During loiter, power for propulsion comes solely from the electric powertrain and fuel cell system combination. In this case, the fuel cell system will thus be sized to meet the demands of the loiter phase only. An estimate of the mass for this configuration is given in the table below. This was obtained by scaling the mass of each of the all-electric components by the ratio of required power output of each system. This ratio of 414.55/156.16 gives us a scale factor of 37.67%.

Component level mass estimation - Conceptual estimates

Genral items relative to all MALE configurations	Mass (kg)
Sum of wing/fueselage/systems/payload/fuel	3206.8

Items specific to the hybrid fuel cell configuration	Mass (kg)
Installed turboprop powerplant	222.0
Electric powertrain assembly - excluding motors	139.8
Traction motor	37.7
Fuselage radiator	5.2
Tail boom radiators	0.0
Fuel cell stack - 1 off	125.5
Methanol fuel processor - 1 off	133.3
Motor controller - 1 off	22.6
Fuel cell control unit - 1 off	1.5
Fuel tank liner - wings and fuselage	0.0
Total all-up mass (kg)	3672.3

Table 15-5

16 Evaluation of the technologies

This section contains a brief overview of the procedures used to analyse the thrust vectoring and fuel cell systems along with a summary of the most results obtained. References will be given in the text to more detailed description of the analysis procedures which are included in the appendices. Where required, the benchmark figures for this work are those determined for the baseline aircraft.

16.1 Thrust vectoring take-off performance analysis

The purpose of this analysis is to determine the point during the take-off ground run when there is sufficient lift and control authority to be able to safely rotate the nose of the aircraft. It would have been preferable to analyse the complete take-off phase encompassing the rotation, transition and climb-out segments but it was only possible to analyse the ground run within the time available. The error in doing so is however small since the ground run segment can be seen to be the biggest contributor to the total take-off distance.

The main focus of this work was to identify a trend between the exhaust plume deflection angle and the ground run required which can be used to asses the viability of the system. A similar analysis was also carried out for a conventional configuration utilising elevons, which was more detailed than that encountered in the baseline performance analysis. These results enable us to make a more accurate assessment between the two systems. The work carried out up to this point had identified the landing gear setting angle as being an important parameter which could potentially also have a considerable impact on take-off performance. An analysis was therefore carried out to assess the influence of landing gear setting angle. Since the vectored thrust can be seen to contribute to the lift of the aircraft, a final analysis was carried out to investigate the potential of reducing the size of the wing. Each stage of this work will be discussed in the sections which follow which will also include a summary of the results obtained.

16.1.1 An overview of the analysis procedure

The thrust vectored take-off performance study utilises two analyses, the first of which is to determines the point during the ground run where there is sufficient speed and thus life to commence the rotation phase. The other analysis is used to determine the point where there is sufficient control authority to safely control the aircraft. This process is repeated for a number of plume deflection angles and engine bleed settings to arrive at a set of curves as shown in the figure below, which form the boundaries of the solution space. The point of intersection between these two curves gives us the optimal engine bleed setting when there is just enough lift and control authority to be able to rotate the nose of the aircraft. Although it is possible to operate the aircraft at any other point within the solution space, a performance penalty will occur due the degradation in engine performance and thus thrust due to excessive engine bleed. The procedure to derive each data point used to construct the boundaries is beyond the scope of this discussion and the reader is advised to refer to Appendix D for further details.

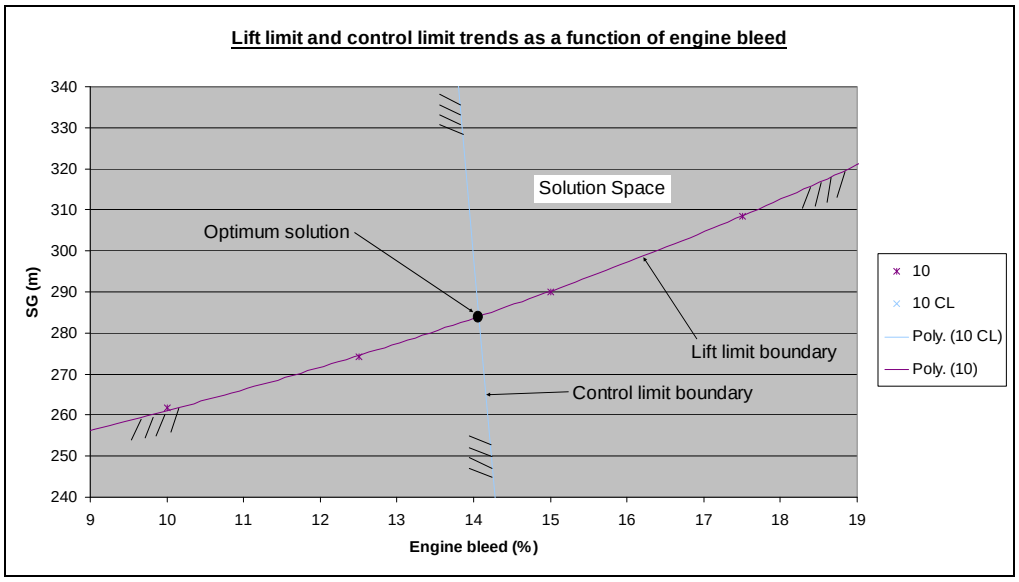

Chart 16-1

16.1.2 Final results for the thrust vectored aircraft configuration

The final lift boundary and control boundary results for a range of plume deflection angles from 0 to 20º in 2.5º steps are given in the figure below. A further analysis was carried out to determine the intersection of each of the curves, the results of which are presented in the influence of the landing gear setting angle section below.

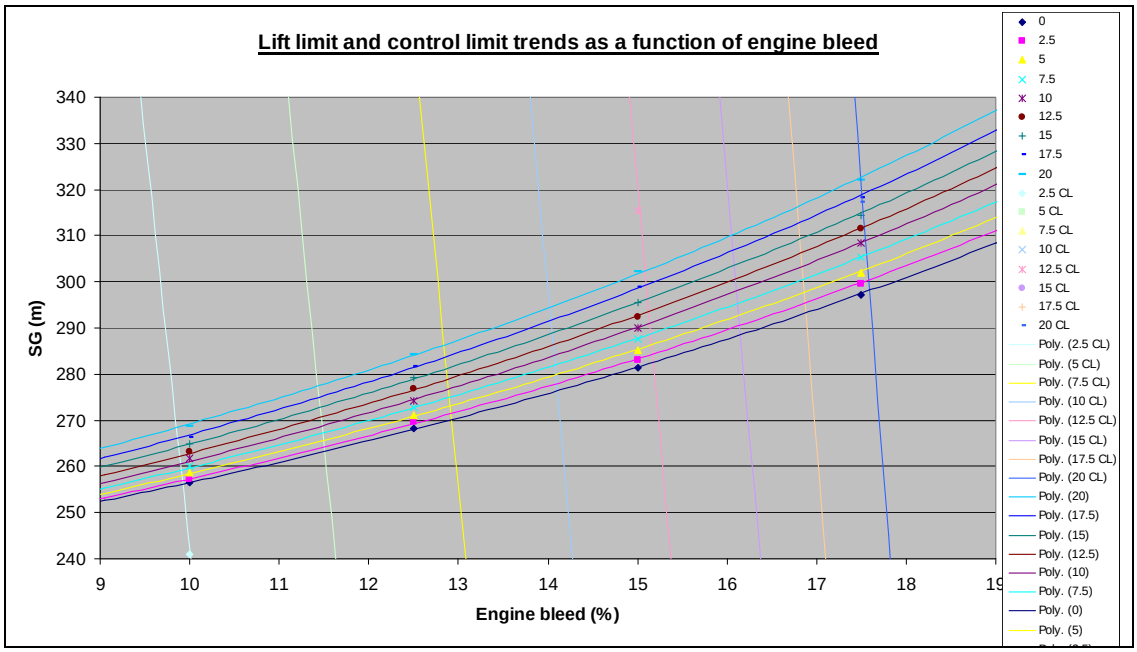

Chart 16-2

16.1.3 Comparison with conventional elevons

An analysis similar to that for the thrust vectoring system was carried out for a more conventional configuration utilising elevons for control instead of the nose jet control system. As before, this analysis was carried out for a range of plume deflection angles

from 0 to 20º in 2.5º steps, as given in the figure below. The advantage of such a system is that since there is no additional engine bleed as before then there is no accompanying degradation in engine performance. The procedure to derive each data point used to construct the boundaries is beyond the scope of this discussion and the reader is advised to refer to Appendix D for further details.

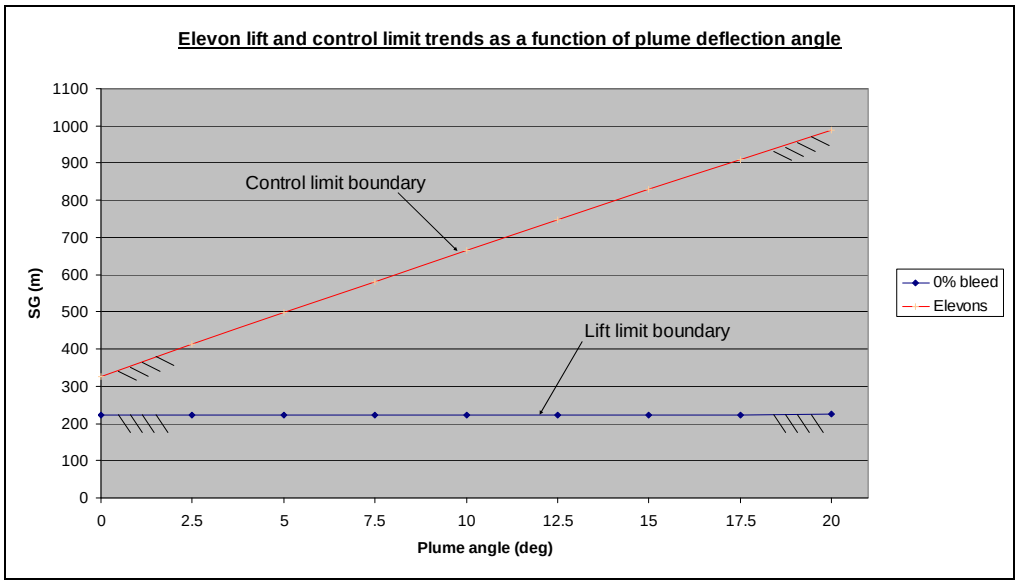

Chart 16-3

16.1.4 The influence of landing gear setting angle

In our work so far, the setting angle was assumed to be 5º. The purpose of this work was to investigate the influence of landing gear setting angle on the take-off performance of the thrust vectored aircraft. The analysis follows exactly the same procedure as given above for the thrust vectored configuration with the only difference being the landing gear setting angle. During this work, a range of values were explored from 4 to 10º.

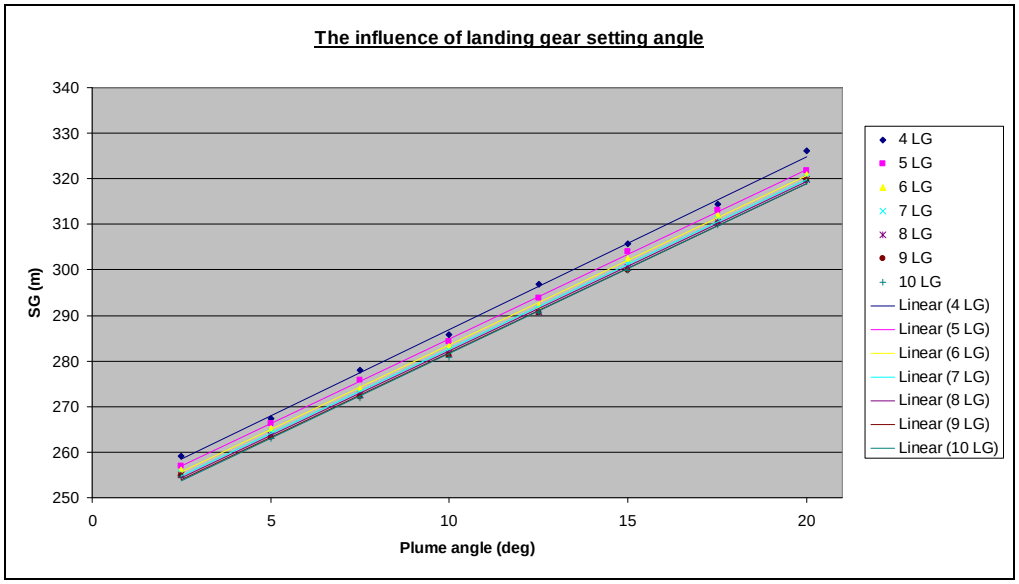

Chart 16-4

16.1.5 Investigation into possible wing size reduction

As course of the studies of take-off performance, the question was raised whether the incorporation of a thrust vectoring system would enable a smaller wing to be used. The rationale was that the vertical component of vectored thrust along with the thrust from the nose jet will contribute to the lift of the wing. The purpose of this work is therefore to examine the impact of reducing the size of the wing on the take-off performance. The approach adopted in this study was to test a number of variants of the thrust vectored aircraft by the same procedure as before, each with a different wing size. This gives us similar results as before with results for the 80% wing presented below. The reader is advised to refer to Appendix D for further details of the analysis procedure.

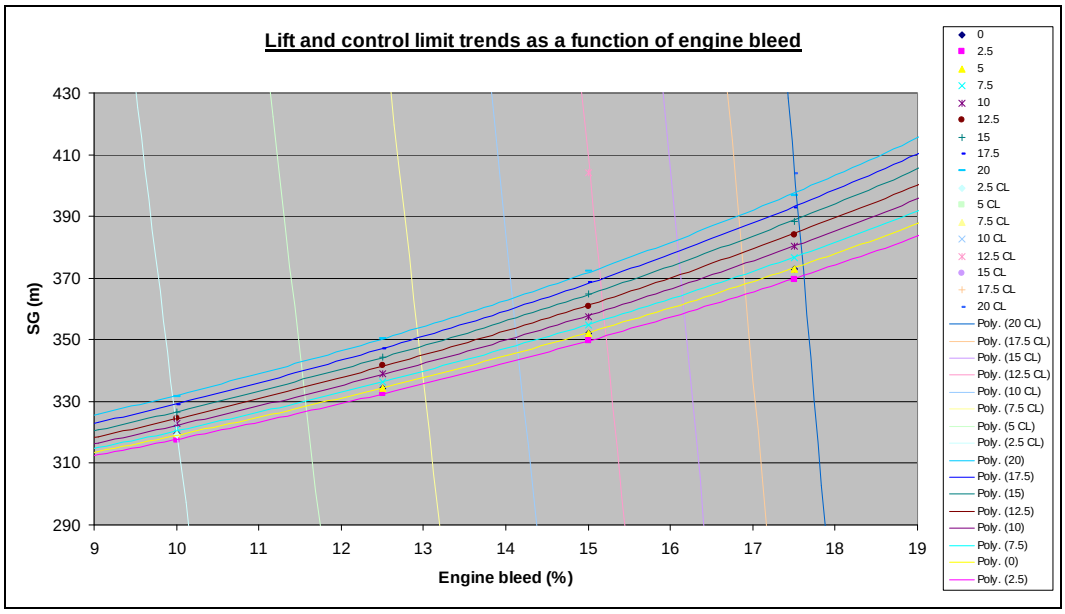

Chart 16-5

As before, the intersection between the curves gives us the optimal solution, from which we can generate the set of optimal solution curves as presented below for a range of wing sizes from 50 to 100% in 10% steps.

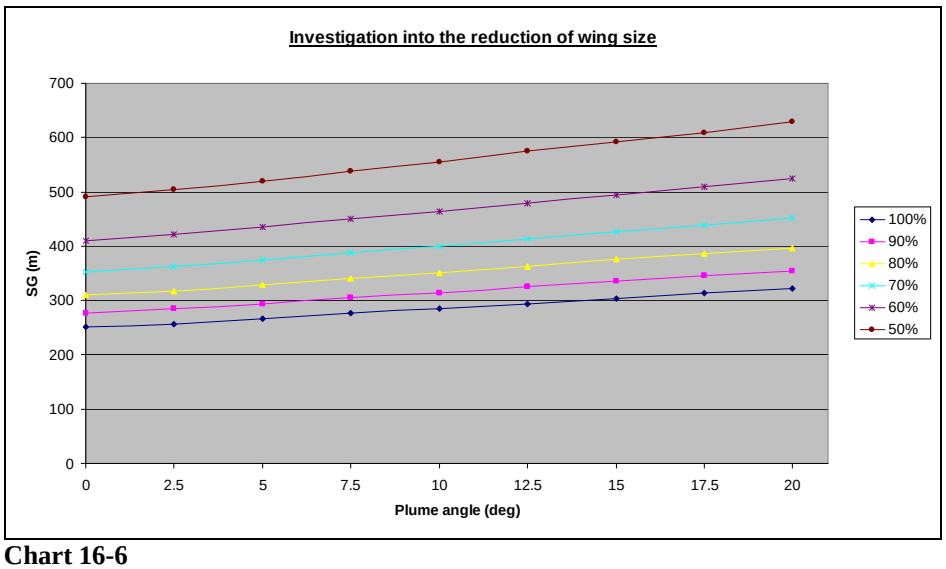

Chart 16-6

These results show the take-off distance of the aircraft to be significantly hindered by a reduction in the size of wing. This is a situation which can be seen to be made worse with the use of vectored thrust, with the best results being obtained for zero nozzle deflection. There are however still a number of benefits to be realised with a reduction in wing size during other flight phases. This thrust vectoring system has however proven to be incapable of compensating for the reduction in wing lift as a result of this reduction in wing size. The main difficult can be shown to lie in generating a control moment which is sufficient to counteract the additional moment due to the deflected exhaust thrust. This is a problem which is inherent to all aft located thrust vectoring systems, with a thrust vectoring system located at the centre of gravity expected to give more desirable results.

16.2 Thrust vectoring cruise performance analysis

The purpose of this analysis is to asses the benefits of using a low cost thrust vectoring system to trim the aircraft during cruise as opposed to the conventional elevons. The cruise phase is particularly important as this has the largest fuel demands. It was proposed that the efficiency of an aircraft can be increased by eliminating conventional aerodynamic control surfaces and thus the additional drag penalty associated with their use. The purpose of this analysis is thus to make a comparison between the fuel consumption at cruise of the thrust vectored and conventional elevon configurations.

It was therefore necessary to carry out two analyses, one for the thrust vectored proposal and the other for a conventional aircraft configuration utilising elevons. Compared to those used for the baseline aircraft, these analyses are considerably more detailed and need to take into account the plume angle or elevon deflection required to trim the aircraft. The reader is advised to refer to Appendix D for further details of the analysis procedure. The results for fuel consumption are given below along with the range of plume angle or elevon deflection required to trim throughout the flight phase and the resulting range of thrust specific fuel consumption.

Cruise results - thrust vectored aircraft

	Fuel used - m_f (kg)	Plume angle range (deg)	TSFC range (mg/Ns)
Outbound	966.5	-4.2 to -0.1	24.5 to 23.1
Inbound	913.3	-0.1 to 4.2	23.1 to 24.6

Cruise results - conventional elevon aircraft

	Fuel used - m_f (kg)	Elevon angle range (deg)	TSFC range (mg/Ns)
Outbound	946.3	-0.2 to -0.0	23.2 to 23.2
Inbound	895.5	-0.0 to 0.2	23.2 to 23.1

Table 16-1

16.3 Thrust vectoring landing performance analysis

Since the landing approach and ground run are both significant contributors to the total landing distance, it was necessary to analyse the performance of the aircraft throughout the complete landing phase. This analysis was broken down in two stages as follows.

- Approach and flare – This covers the flight path from the screen height to the point where the vertical velocity is zero and the aircraft is firmly on the ground. This complex analysis involves finding the simultaneous solutions to the balance of the forces and moments acting on the aircraft for a range of vectoring angles.
- Ground run – This is a continuation of the last stage and covers the ground distance required to bring the aircraft to rest. This analysis is a less complex balance of the deceleration forces acting on the aircraft.

The reader is advised to refer to Appendix D for further details of the analysis procedures.

A variant of the landing analysis was carried out to investigate the potential of landing the aircraft on an aircraft carrier. This analysis follows the same procedure as above with the only difference being a lower landing approach speed which became $V_{Approach} = 1.15 \cdot V_{Stall}$. In reality however, a carrier aircraft is likely to be subject to an additional braking force due to an arresting hook. We have however assumed that an arresting hook is not used and are thus assessing the viability of landing an unmodified land based aircraft on an aircraft carrier.

16.3.1 Results

The final results for the approach, flare and ground run stages of the landing phase are given in the table below for the baseline case which has an initial descent speed of 5m/s.

Landing results - Descent speed 5m/s

	Landing approach				Flare out			Ground run	Total
Phi	Lift wing (N)	Lift thrust (N)	Lift nose jet (N)	Distance (m)	V-td (m/s)	time (s)	Distance (m)	Distance (m)	Distance (m)
30	49625.7	16367.5	10810.4	269.1	40.7	2	81.3	221.8	572.2
25	50350.6	13008.3	8174.6	270.6	41.0	2	81.9	224.7	577.1
20	50921.6	10424.2	6160.3	271.9	41.2	2	82.4	226.9	581.1
15	51389.9	8357.4	4560.8	273.1	41.4	2	82.7	228.7	584.5
10	51786.2	6652.9	3251.9	274.2	41.5	2	83.1	230.2	587.5
5	52130.0	5211.6	2153.8	275.3	41.7	2	83.3	231.6	590.2
0	52434.2	3967.0	1212.9	276.3	41.8	2	83.6	232.7	592.6

Table 16-2

16.3.2 The influence of initial vertical descent velocity

To investigate the influence of initial vertical descent velocity, the process above was repeated for a range values to generate the results presented below for the total landing distance.

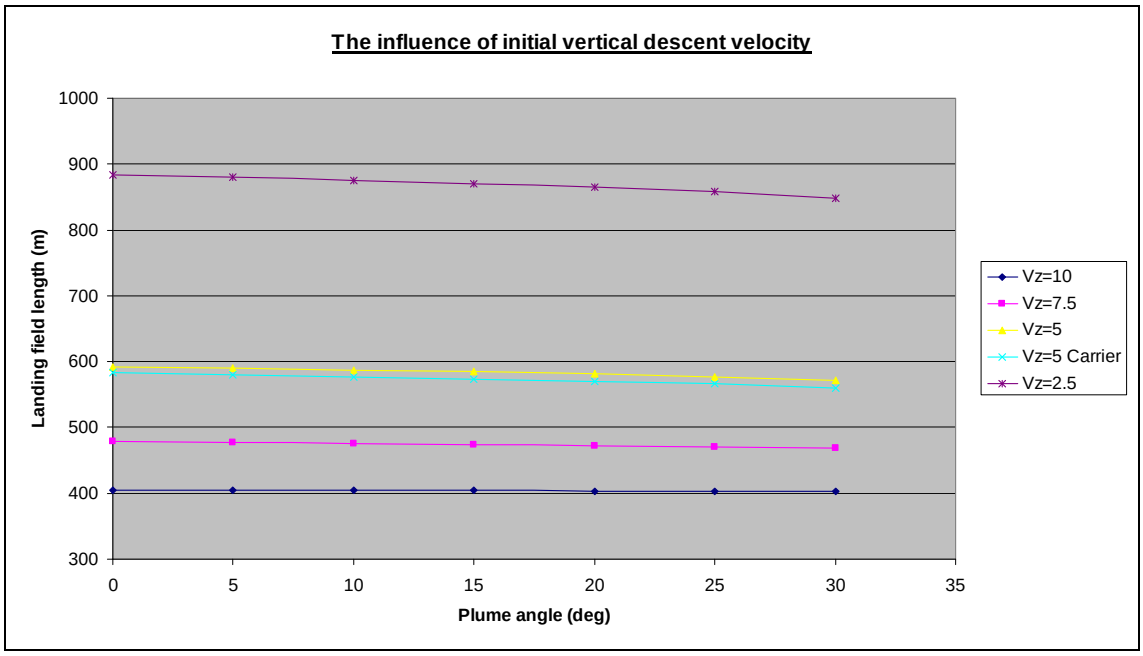

Chart 16-7

16.4 Fuel cell powered MALE performance analysis

The purpose of this analysis is to evaluate the performance of a fuel cell powered variant of the MALE in comparison to the conventional turboprop configuration. As course of this study, five different fuel cell system variants were considered as follows. This included autothermal and steam reformer based variants of an all-electric system, autothermal and steam reformer based variants of a hybrid system and a hybrid system with oxygen injection. A detailed discussion of each of the systems above is beyond the scope of this discussion and the reader is advised to refer to Appendix J for further details. An overview of the methodology used to evaluate the performance of each of the system variants above will be given below, but the reader is advised to refer to Appendix J for further details. For each system, an analytical model had to be created which could be used to predict the fuel consumption with respect to power output and operating altitude. This analytical model was then integrated into the existing performance analyses used for the baseline aircraft to enable us to predict the performance of such a system in contrast to the baseline turboprop configuration.

The analyses of the all-electric fuel cell systems revealed that the fuel consumption of these systems was significantly higher than that of a turboprop engine. This means that the range of our baseline aircraft would be significantly reduced as a result. As expected this was seen to be most evident at the most power demanding phases. As a result, it was decided to investigate the potential of retaining the turboprop engine for the entire flight except the loiter phase. In such a hybrid system the turboprop engine is disengaged for the loiter phase and the propeller is instead driven by a motor which is powered by the fuel cell system. For all other flight phases the fuel cell system is disengaged and the propeller power is delivered entirely by the turboprop. The only difference between the two hybrid systems is the fuel processor used.

16.4.1 Analysis of the autothermal and steam reformer based fuel cell systems

The performance analysis for the all-electric autothermal and steam reformer based systems followed the same procedure as for the conventional turboprop engined aircraft configuration. The only difference being that the spreadsheets are modified to include the new expressions for fuel consumption. The results of these analyses are given below alongside the results for the original turboprop configuration, for comparison.

To provide a 'like for like' comparison, the fuel tanks have been assumed to retain their original size as determined for the baseline turboprop configuration. It has therefore been necessary to reduce the loiter time of the aircraft for each variant accordingly in order to meet this constraint. Since the density of methanol of 0.796kg/m^3 at 15ºC lies within the range 775 to 840kg/m^3 for Jet A fuel at 15ºC the weight of the two fuels is thus comparable. In the case of the autothermal reformer, this meant that the loiter time had to be reduced from 35 hours to 9.15 hours. Likewise for the steam reformer, the loiter time was reduced to 18.03 hours.

16.4.2 Analysis of the hybrid autothermal and steam reformer based fuel cell systems

In the case of the analysis of the hybrid systems, only the loiter phase of the baseline turboprop performance analysis is modified to incorporate the characteristics of the fuel cell system. The remainder of the baseline performance analysis is retained. The results of these analyses are given below alongside the results for the original turboprop configuration, for comparison. As before, the total volume of the fuel tanks is assumed to be fixed at the value determined for the baseline aircraft design. As a result, the loiter time has been reduced accordingly. In the case of the autothermal reformer, the loiter time had to be reduced from 35 hours to 17.96 hours while that of the steam reformer was reduced to 26.45 hours.

In the analysis of these hybrid systems we have assumed that the turboprop engine is the sole means of propulsion at all flight phases other than the loiter phase. During these flight phases the fuel cell system is assumed to be switched off. The turboprop engine is thus sized to meet the most critical thrust requirements which were at the end of cruise outbound and the start of cruise inbound. A possibility would be to operate the fuel cell system in conjunction with the turboprop engine at these most demanding phases. The power output from the traction motor (connected to the fuel cell) would thus be used to supplement that from the turboprop engine. The result would be that a smaller and lighter turboprop engine could be utilised which would result in a reduction in the weight of the aircraft and thus a reduction in the mission fuel consumption. There was unfortunately insufficient time to investigate this proposal and this task is thus reserved for future work.

16.4.3 Final results

The results in the table below include the increase in the mass of the aircraft due to the additional mass of the fuel cell system. If it were possible to reduce the weight of the

fuel cell systems so that the mass of the aircraft were to retain its same value as the original estimate of 3428.7kg then an improvement in the loiter time could be realised. For the autothermal and steam reformer systems, loiter times of 13.99 and 24.21 hours could be achieved respectively. In the case of the hybrid autothermal and steam reformer based systems, loiter times of 19.19 and 28.20 hours could be respectively. Also included in this table are the initial and refined baseline fuel consumption figures. The difference between these two sets is due to the vagueness of fuel consumption predictions with weight fractions, especially for unconventional aircraft like UAVs.

Fuel mass used for the different variants of the MALE UAV

Segment fuel consumption (kg) Flight phase	Conceptual design	Refined baseline	Autothermal reformer	Steam reformer	Hybrid autothermal	Hybrid steam
Take-off ground roll	17.1	1.1	1.2	0.9	1.1	1.1
Take-off rotation	17.1	0.4	0.6	0.5	0.4	0.4
Take-off climb out	17.1	0.4	0.6	0.5	0.4	0.4
Second segment climb	17.1	0.0	0.1	0.1	0.0	0.0
Climb	16.3	50.4	92.7	67.3	50.6	50.6
Cruise egress	151.2	237.6	680.3	509.5	253.5	253.5
Loiter at altitude	1555.0	1417.3	680.2	996.1	1344.8	1356.9
Cruise ingress	74.1	196.1	381.4	279.4	197.6	197.6
Descent	7.8	14.4	11.2	8.4	12.9	12.9
Loiter sea level	13.8	16.1	49.1	35.1	36.2	24.0
Landing approach and flare	5.4	0.0	0.0	0.0	0.0	0.0
Landing ground roll	5.4	0.0	0.0	0.0	0.0	0.0
Total fuel used for the mission	1897.5	1933.6	1897.5	1897.5	1897.5	1897.5
Reserve (6% of the total)	113.9	116.0	113.9	113.9	113.9	113.9
Total fuel (mission and reserve)	2011.4	2049.6	2011.4	2011.4	2011.4	2011.4
Loiter time at altitude (hours)	35.00	35.00	9.15	18.03	17.96	26.45

Table 16-3

16.4.4 Investigation into the use of oxygen injection

In all of the systems above, we have to supply an excess amount of hydrogen to the fuel cell so that the waste leaving the fuel cell can be burned to generate the power needed for the air compressor. An additional quantity of fuel is therefore consumed in order to be able to deliver oxygen at the desired quantity and pressure for the fuel cell. Taking into consideration that air is made up of approximately only 21% oxygen, then a significant amount of energy is being wasted to deliver the remaining 79% which is predominantly nitrogen and serves no other purpose than to act as a dilutant. We are therefore expending work and fuel to deliver it to the fuel cell in order to throw it away!

It was therefore proposed that the use of oxygen from a purer source would give rise to a reduction in the fuel consumption of the system. The only realistic means of achieving this would be to carry a compressed or liquefied source of oxygen on-board the aircraft. The oxygen demands of the fuel cell system meant that it was unlikely that sufficient oxygen can be carried on-board the aircraft to meet our needs. Such a system would therefore supplement the oxygen obtained from the air. A liquefied oxygen source was considered to be the only practical means of meeting our needs for this application. The feasibility of such a system is considered in detail in Appendix J. This showed that the mass of the liquid oxygen which must be carried on-board the aircraft far exceeds the fuel mass saved with the use of such a system. Such a system is therefore not viable.

17 Discussion

17.1 A review of the MALE and UCAV baseline designs

The MALE and UCAV configurations selected for use as baseline designs for this study are in-line with current UAV designs. Each design was only developed to a level sufficient for this work and further refinements are to be expected for such designs to become more realistic. They did however prove to be more than satisfactory for the needs of this project without devoting too much time to their design and development.

The main difficulty with the MALE was the provision of fuel tanks of sufficient size to be able to hold sufficient fuel to meet the mission requirements. This necessitated the need for a large fuselage fuel tank and thus a fuselage which is larger than desired. In the case of the UCAV, a large amount of sweep was required to get the centre of gravity in the desired location for stable flight. The desired slenderness of the configuration also presented its own problems with undesirable blisters in the wing surface being incorporated to accommodate the landing gear and lethal payload. A simplistic means of landing gear retraction was opted for to keep in-line with the theme of reduced cost UAVs but a better option would be increase the complexity of this slightly so that the associated blisters can be eliminated.

17.2 The identification and selection of the technologies

At this point in the project, the questions which looms is, 'Did we select the best possible candidate technologies to make the best possible contribution to knowledge?' The choice of technologies was vast and a real engineer only has to open his eyes to find possible technologies. Examples can be found everywhere from other engineering streams, our natural environment and even in the minds of a science fiction writer. For example, 30 years ago it was laughable that the James Bond movies depicted mobile communication devices small enough to fit in wrist watches, but now? The children's toy cars the 'Hot Wheels Colour Shifters' are another excellent example. These toys change colour by simply immersing them in hot or cold water respectively. What benefit would such paint have to a stealth aircraft which can change the colour of the aircraft from white on a hot day to black on a cold night? The recognition of future concepts and how to apply them in an engineering concept has been the ultimate test for centenaries to distinguish the notable scientists and engineers from the rest. Something as simple as watching a pot boiling led to the development of the IC engine. The really worthy engineers and scientists will only see a world full of possibilities.

As the focus of this project is on the integration and not the development of technologies then we are restricted to utilising existing technologies. Our goal here is thus to identify new openings and opportunities for these systems. The technologies selected for this project were low cost mechanical thrust vectoring and fuel cell systems. The thrust vectoring system was selected to keep in-line with the focus of Flaviir project and to evaluate an alternative to the fluidic devices being proposed. The fuel cell system was selected to explore the viability of fuel cells in aerospace applications. Currently,

anybody who is anybody in engineering has got a fuel cell development project. These have already seen use in a range of applications from golf karts to ships with minimal progress being made for aircraft. The best technologies were therefore selected in-line with the theme of this PhD.

17.3 The feasibility of low cost mechanical thrust vectoring

This study investigated the feasibility of using a low cost thrust vectoring system utilising post exit paddles for the trim and control of a large UAV. The system used was that originally investigated by NASA for their X-31 and F/A-18 aircraft, which was rescaled to suit our application. This system was analysed at a number of different flight phases to assess the benefits of the system under a number of different conditions. The results of this work, as presented in the evaluation section, will be now discussed in the sections which follow.

During the performance evaluation work, the mass of the thrust vectoring system was assumed to be negligible in comparison with the mass of the aircraft. This is probably an over-simplification but to be able to make an reasonable estimate of the complete thrust vectoring system would have required more detailed knowledge of the different components. This would have involved a lengthy process to size the actuators and nose jet pneumatic system components, a process we did not have sufficient time for. It is however the trends which we are most concerned with and thus these differences are not critical for the purpose of this study.

As will be discussed in the following section, the main difficulty with this system for take-off is its location on the aft fuselage. The result is that a downward deflection of the nozzle is accompanied by a large increase in the nose down pitching moment of the aircraft. This moment must be counteracted by either the pneumatic pitch control system or the elevons and the take-off must be delayed until there is sufficient control power available. As a minimum, the solution to this problem would be to relocate the vertical component of vectored thrust to the same location at the main gear wheels. Any possibility to locate the vectored thrust forward of this point would contribute to the nose up pitching moment and thus reduce the control power for rotation. A similar situation exists for landing. Examples of this design practice can clearly be seen on the Harrier Jump Jet and similar STOL/VTOL designs. These systems are however not without their own penalties with weight being a particular problem.

17.3.1 Thrust vectoring for take-off

During this part of the study, an investigation was carried out into the use of vectored thrust to contribute to the lift of the aircraft during the take-off phase and thus reduce the take-off distance. An additional component of vertical thrust from the nose jet control system not only provided pitch control but also contributed to the lift of the aircraft. The analysis described in the evaluation section is used to determine the optimal engine bleed setting and point during the ground run when there is just enough lift and control power available to be able to rotate the nose of the aircraft. At this optimal condition the ground run distance is at its minima. By collating these points for a number of plume angles we are able to obtain a single curve for the optimal ground

run as a function of plume deflection angle. This process was repeated for a number of different landing gear setting angles to test the influence of this parameter. The results are presented in the 'influence of landing gear setting angle' chart, where the baseline landing gear setting angle is taken to be 5º.

Inspection of the results shows us that that the ground run distance required increases with exhaust plume deflection angle. Although the lift due to the vertical component of thrust increases with vectoring angle, a number of other factors also increase in relation to the vectoring angle, which are detrimental to the performance. As is discussed in the appendices, each nozzle deflection angle corresponds to a different exhaust nozzle configuration which gives rise to a different engine operating condition. Deflection of the nozzle thus moves the operating point of the engine away from its design condition resulting in a reduction in available thrust. This is combined with the fact the horizontal component of thrust reduces in proportion to the cosine of the deflection angle. Collectively, this means that the propulsive thrust is reduced as the vectoring angle is increased, which results in a decrease in the acceleration and thus the speed of the aircraft. Since the lift of the wing is proportional to the square of the speed then for the same point along the runway, the wing lift will decrease as the vectoring angle increases. The additional components of lift from the nose jet and vectored thrust have proven to be insufficient to meet this shortfall.

If we now review the results from a control perspective, it was seen that the control force required to rotate the nose of the aircraft increases with plume deflection angle. The reasoning is that as the vertical component of vectored thrust increases, the aircraft experiences an increase in the nose down pitching moment about the main landing gear. Although the horizontal component of thrust reduces in relation, the moment arm due to the vertical component of thrust is greater than the horizontal component and thus has a greater influence. As a result, an increase in control force is required for an increase in the plume deflection angle. Considering the moments acting on the aircraft, we arrive at another important consideration. It can be seen that the lift from the wing contributes in a positive way to the rotation of the nose of the aircraft about the main wheels. Thus, the control power requirements of the nose jet or the elevons are reduced as the aircraft gains speed. This highlights the importance of speed and wing lift during take-off.

A further investigation was carried out to explore the influence of landing gear setting angle on the take-off ground run. For a plume deflection angle of 10º, this showed a decrease in the ground run from 284.3m at a landing gear setting angle of 5º to 280.9m at 10º. The effect is thus marginal and would be insignificant if we were to take into account the increase in drag due to the higher angle of attack.

The final stage of work involved an investigation into a possible reduction in wing size. The results of this study showed a considerable increase in the take-off field length as a result of a reduction in wing size. As can be seen, for a 50% reduction in wing size at 0º plume angle, the take-off ground run required increases from 250.9m to 480.1m corresponding to a 91% increase. At 10º plume angle, the distance increases by 95% and at 20º also by 95%. Thus the lift from the thrust vectoring system has been shown to be unable to match the lift generated by the wing and in this case there appears to be no substitute for wing size.

At this point we can ask the question, 'how does this compare to the conventional configuration with elevons?'. If we first examine the trends for the control and lift limit boundaries of the elevons, we can see that the ground run distance is dictated by the control limit. This can however also be seen to increase with deflection in plume angle and thus there is no benefit in using deflected thrust for this configuration. At 0º plume angle this gives us a ground run distance of 324.9m. The configuration using the nose jet shows a similar trend with 0º plume angle giving the best figure of 250.9m, in which case the nose jet is replacing the function of the elevons. Thus a 22.8% reduction in the ground run distance can be achieved with the use of just the nose jet system as opposed to the conventional elevons. We could improve the conventional elevons by increasing their size until we match the lift limit boundary of 223.7m but this would result in performance problems at other flight phases. In this study, the two systems have been considered in isolation but the take-off performance could be further improved by using the nose jet system to supplement the conventional elevons. Such a system would require less engine bleed for the nose jet (the current figure being 8.2%) and thus further improve the acceleration of the aircraft and the point at which rotation can be initiated.

To summarise, for this particular aircraft and thrust vectoring system, the best take-off performance can be achieved with the nose jet alone. The thrust vectoring nozzle would thus remain in its undeflected state and the nose control jet used to supplement the control power of the elevons. If it is necessary to eliminate the elevons completely then the thrust vectoring nozzle should remain in its undeflected state during take-off.

17.3.2 Thrust vectoring for cruise

During this part of the study, an investigation was carried out into the use of vectored thrust to trim the aircraft at cruise as opposed to using conventional elevons. The intention being to reduce the trim drag. This study utilised the performance analysis spreadsheets used for the baseline study which were extended to include aircraft control terms. In the case of the conventional elevons, additional terms were added to determine the elevon deflection angle required to balance the moments acting on the aircraft and thus trim the aircraft. This analysis also had to take into account the variations in lift and drag of the aircraft due to the deflection of the elevons. A similar analysis for the thrust vectoring system was used to determine the plume deflection angle required to trim the aircraft. In this case, the analysis had to account for the variations in lift and thrust due to deflection of the exhaust plume.

It was hoped that the thrust vectoring system would give rise to a reduction in the fuel consumption at cruise as a result of the elimination of the drag component due to the elevons. In actual fact, for the complete cruise phase we saw a 2% increase from 1841.8 to 1879.9kg. In the case of the conventional elevons, we require an elevon deflection range between -0.18 and 0.16 deg to trim the aircraft, in which case the component of drag due to their deflection is small. In the case of the thrust vectoring system however, the plume deflection range is between -4.18 and 4.23 deg, which is sufficient enough to have a knock on effect on the performance and thus the fuel consumption of the engine. The decrease in fuel consumption at cruise is however only 2% and could be easily catered for if required.

17.3.3 Thrust vectoring for landing

During this part of the study, an investigation was carried out into the use of vectored thrust to contribute to the lift of the aircraft during the landing phase and thus reduce the landing distance. As for the take-off case, the lift from the wing is supplemented by additional components of lift from the vectored thrust and the pitch control nose jet. The actual analysis was a very complex balance of the forces and moment acting on the aircraft over the landing approach, flare out and ground run phases. Although the baseline vertical descent velocity was taken to be 5m/s, a range of other values were explored to examine the influence of this parameter. In addition, an aircraft carrier variant was explored with a slightly slower approach speed. The results showed the vertical descent velocity to have considerable impact on the on the total landing field length with a 16.0% reduction being achieved for an increase from 5 to 7.5m/s and a 31.7% reduction for an increase from 5 to 10m/s. The effect of a reduction in approach speed was however less pronounced with only a 1.7% reduction in the landing field length.

The results for the effect of thrust vectoring showed less promise with only a 1.6% reduction being achieved between a vectoring angle of 0 and 15deg and 3.4% being achieved between 0 and 30deg.

This analysis does however assume that we are utilising the nose jet system for pitch control, in which case the engine needs to be spooled up to generate the engine bleed required. This means that some form deflector is required to reverse the thrust. Our original control analysis work showed there to be sufficient control authority available throughout the landing phase with a required landing field length of 577.86m. The conventional configuration utilising elevons is thus comparable to the thrust vectored system with there being little benefit in using such a system.

17.3.4 Significant integration considerations for this system

As with any thrust vectoring nozzle, we have to take into account the impact which the nozzle has on the operating characteristics of the engine. We also need to take into account the effect of variations in the mass, centre of gravity, lift and drag of the whole aircraft. Of particular importance to this system however is the need to provide structural attachment points for the paddles and the accompanying hydraulic rams. As any aircraft structure can be seen to deflect when a load is applied, the elastic deformation of the structure needs to be accounted for in the design and in the flight control system commands. From a more general design perspective, allowance needs to be made for the additional length of the vectoring paddles. In particular the designer needs to ensure that they do not come into contact with the ground during the high angle of attack take-off rotation and landing approach flare phases. As this is often a critical consideration in the design of the tail of many aircraft, the integration of such a system on an existing aircraft may prove troublesome.

17.3.5 Comparison with other thrust vectoring systems

How does this system compare to other thrust vectoring systems? No analysis was carried out of other thrust vectoring systems but we are able to draw up some

conclusions on the lessons learnt in this project. Inspection of published data for other systems showed the internal vectoring concepts to have lower flow turning thrust losses associated with them. These systems are thus expected to offer better performance but at the expense of mass, cost and complexity. Fluidic devices are another form of thrust vectoring which is considered to offer great potential. These devices do however require large amounts of engine bleed air to operate, which would result in a considerable reduction in engine performance and increase in fuel consumption. Thus similar results to those found in this analysis are expected for such fluidic devices.

17.4 The feasibility of fuel cell systems for propulsion

This study investigated the feasibility of using a fuel cell system as the primary propulsion system of a MALE UAV in contrast to a more conventional turboprop. As course of this study, five different fuel cell system variants were considered as follows.

- Autothermal reformer based fuel cell system – In this system, the turboprop engine has been replaced with an all electric powertrain which was powered by an autothermal reformer based fuel cell system.
- Steam reformer based fuel cell system - In this system, the turboprop engine has been replaced with an all electric powertrain which is powered by the steam reformer based fuel cell system.
- Hybrid autothermal reformer based fuel cell system – In this system, the aircraft has been retrofitted with a hybrid electric/turboprop powertrain. During the most demanding flight phases, the turboprop is responsible for delivering the required power. Whilst during the loiter phase, the turboprop is switched off and the fuel cell system has sole responsibility for meeting the power demands.
- Hybrid steam reformer based fuel cell system – This system adopts the same approach as the hybrid autothermal system with the exception that a steam reformer is used instead.
- Hybrid fuel cell system with oxygen injection – This system adopts the same approach as the two other hybrid systems above with the exception that the oxygen in the air is supplemented with additional oxygen.

A detailed discussion of each of the systems above is beyond the scope of this discussion and the reader is advised to refer to Appendix J for further details. This work involved the development of an analytical model representative of each system which could be used to predict the fuel consumption with respect to its operating conditions. The integration of these analytical models into the baseline performance analyses enabled the performance of an aircraft incorporating such a system to be evaluated in contrast to the baseline turboprop configuration.

17.4.1 Fuel choices

Fuel cells need a ready supply of hydrogen and oxygen in order to complete the associated electro-chemical reaction. For short duration vehicles, it is sufficient to use bottled supplies of hydrogen and oxygen, as is the case with a number of existing research vehicles. More practical systems however require larger quantities of the reactants and thus alternative sources are required. Fortunately, a ready supply of oxygen is available from the atmospheric air, although a decrease in performance is

experienced as a result of the presence of nitrogen. A ready supply of hydrogen on the other hand is more problematic due to its low density which has traditionally necessitated the need for large compressed hydrogen storage tanks. Cryogenic storage tanks have also received considerable interest for the direct storage of hydrogen but these have proven to present their own set of problems.

The problem of sufficient hydrogen storage has thus been one of the bottle necks in the development of fuel cell powered vehicles. An alternative solution to this problem is to extract the hydrogen on demand from a hydrogen rich fuel such as methanol. Such an approach does however necessitate the need for additional equipment to process the fuel in situ. The advantage of such an approach is that a liquid hydrogen carrier such as methanol is easier to store and provides a good hydrogen yield. Studies into such fuel reformer based fuel cell systems for automotive applications have highlighted problems with transient performance and start-up times. Such system behaviour is however less likely to be such of a problem for steady state applications such as aircraft propulsion. Although it is possible to extract hydrogen from any hydrogen based fuel such as the natural hydrocarbon based fuels, the more synthetic fuels such as methanol are easier.

The criteria for the selection of a suitable fuel for a reformer based system is based on a number of considerations including, availability, ease of storage, required reforming temperature, the content of impurities and the hydrogen yield of the fuel. Of all the fuels considered, methanol has proven to be the most suitable for this application with all the desired qualities of yield, availability, storage and low reforming temperature.

17.4.2 Fuel processors

Mobile fuel processing is an area which has been receiving considerable interest recently, especially for fuel cell systems. Such fuel processors would have once filled the entire boot of a car but there now exists units which take up virtually no space at all. Two fuel processing approaches have almost dominated the market for mobile applications, these being steam and autothermal reforming. Each of these has their own benefits and drawbacks and thus it was necessary to explore each approach to determine the best system for this application.

Steam reformers are the most efficient of all the fuel processors but are generally heavier and bulkier due to the additional accompanying equipment. These units also require external sources of heat and steam, which are required to promote the reforming reactions. The main problem with these is the generation of the required heat. This is typically achieved with the combustion of an additional amount of fuel but this reduces the overall efficiency of the system. In the case of this particular system, we are already burning excess fuel to generate the power required to drive the compressor. Thus, if we are able to locate this burner in close proximity to the fuel processor we can utilise the waste heat from the external surface of the burner within the fuel processor. The result is a fuel processor which is capable of achieving a high level of efficiency.

Autothermal reformers generate the heat required for reforming internally by the partial combustion of a small amount of the fuel being reformed. Such units do not require any additional steam or heat inputs and are generally lighter and smaller than their steam

reformer relatives. These units are however less efficient than the steam reformer counterparts. Their ability to function as a self contained compact unit is however an extremely attractive feature which offsets some of the other problems.

17.4.3 All-electric propulsion systems

In the all-electric propulsion systems, the turboprop engine has been completely removed and replaced with two powerful traction motors which are used to drive the propeller instead. The power to drive the motors is generated by a fuel cell system which utilises hydrogen from either a steam reformer based or autothermal reformer based fuel processor. To enable a equal comparison to be made between the systems, it was assumed that the aircraft fuel tanks have been retained at their original size determined for the turboprop engine and thus the loiter time was reduced accordingly from the original figure of 35 hours. In the case of the autothermal reformer, the loiter time of the aircraft was reduced by 73.9% to 9.15 hours, while that of the steam reformer based aircraft was reduced by 48.5% to 18.03 hours.

17.4.4 Hybrid propulsion systems

The hybrid propulsion system was envisioned to improve the fuel consumption of the aircraft propulsion system by retaining the turboprop engine for all but the loiter phase. During loiter, the turboprop is disengaged and power is delivered by a smaller variant of the fuel cell systems above. Such a system retains a reasonable fuel consumption figure while enjoying the benefits of a quiet and environmentally friendly propulsion system for its lengthy loiter phase. Following the same procedure as before, the loiter time of the aircraft utilising an hybrid autothermal system is reduced by 48.7% to 17.96 hours, while that of the hybrid steam reformer system was reduced by 24.4% to 26.45 hours. The hybrid steam reformer based system is thus the best choice for our application. A loiter of 28.20 hours can however be achieved if the system mass could be reduced

17.4.5 Significant integration considerations for this system

The integration of the fuel cell system has to take in to account usual considerations such as centre of gravity, space allocation and the provision of inlet and exhaust apertures. The main difficulty in the integration of this system was the provision of sufficiently large heat exchangers for cooling. A number of locations were explored for these units with the final configuration being a large unit in the aft fuselage and two smaller units located in the tailbooms. Each unit requires its own inlet an exhaust which contributes to the drag of the aircraft. This is however less of a problem for the smaller hybrid system, in which a single heat exchanger located in the aft fuselage, will be sufficient.

17.4.6 Evaluation of the overall system propulsive efficiency

The overall efficiency of a system is typically used as a means of comparing the overall performance of a number of different systems which are intended to fulfil the same task. The efficiency of the system cannot however be considered in isolation when selecting a system and other factors must be taken into consideration. In this section, the efficiency

of the turboprop and fuel cell system variants is calculated at a number of key points throughout the flight profile. The results of this analysis will then form a means of evaluating each system in addition to the other factors being considered such as loiter time, practicality and cost.

The efficiency of any system is defined as the ratio of the useful energy output to the total energy input required, as follows.

$$\eta = \frac{Desired\_Output}{\mathrm{Re}quired\_Input} \qquad \text{Eq 17-1}$$

In this particular study, this equates to the ratio of the propulsive power output of the propulsion device to the energy input of the fuel consumed by the system. In this study we have assumed that each system shares a common propeller and therefore it is justified to determine the efficiency of each system in terms of the propeller shaft input power. This assumption holds true as long as the speed and therefore the efficiency of the propeller remains the same, which will be pre-set by the gearbox in each system. In each case, any error due to any small deviations is however expected to be negligible.

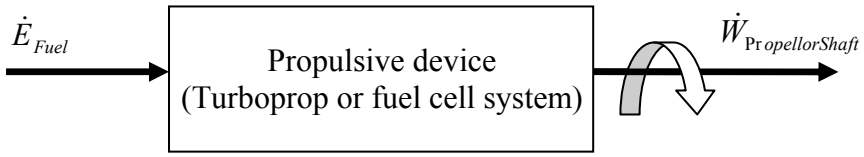

The efficiency of the propulsion system can then be determined from the expression.

$$\eta = \frac{\mathrm{Pr}opellorShaft\_input\_power}{Rate\_of\_fuel\_energy\_input} \qquad \text{Eq 17-2}$$

In cases where a combustion process takes place, the energy of the fuel is based on the heating value of the fuel (HV), which is a measure of the amount of the total quantity of heat released when a unit quantity of the fuel is burned under controlled conditions. This is also known as the enthalpy of combustion reaction. Two versions of the HV value exist, a higher heating value (HHV) and a lower heating value (LHV), dependent on whether the by-product water leaves the system as liquid or vapour. The difference between the two values is thus the product of the quantity of water and the enthalpy of vaporisation of water. The efficiency of IC engines for example is determined using the LHV since the water exists as a vapour in the exhaust gases.

In the case of fuel cells however, where no combustion process takes place, the overall reaction of hydrogen within the fuel cell is the same as a that for a hydrogen combustion process ($H_2 + \frac{1}{2}O_2 \rightarrow H_2O$). In this case, the heating value of the fuel is therefore still a valid measure of the energy of the fuel entering the system. For a PEM fuel cell on its own, its low temperature means that either the LHV or HHV values can be used. Since the system proposed in this study incorporates a tail-gas burner then the water will leave the system as a vapour and thus the LHV should be used. The efficiency of both the turboprop and fuel cell systems can then be determined from the expression.

$$\eta = \frac{\dot{W}_{\mathrm{Pr}opShaft}}{\dot{m}_{Fuel} \cdot LHV} \qquad \text{Eq 17-3}$$

The terms $\dot{W}_{\mathrm{Pr}\,opShaft}$ and $\dot{m}_{Fuel}$ have already been determined for the complete flight profile from our analysis work on each system. The remaining term LHV for the two different fuels used is then,

- Methanol = 20.07 MJ/kg
- Jet A = 42.80 MJ/kg

In this analysis, it was only deemed necessary to concentrate on those flight phases with the highest fuel burn which includes climb, cruise egress, high altitude loiter, cruise ingress, descent and sea level loiter. With start, mid and end points of each phase being considered to get a full appreciation of the conditions at each stage, the results of which are presented in the table below.

A comparision between the efficency of the baseline turboprop and fuel cell system variants at a number of different flight points

	Flight point	Start climb	Mid climb	End climb	Start cruise egress	Mid cruise egress	End cruise egress	Start loiter at altitude	Mid loiter at altitude	End loiter at altitude	Start cruise ingress	Mid cruise ingress	End cruise ingress	Start descent	Mid descent	End descent	Start loiter sea level	Mid loiter sea level	End loiter loiter
Refined turboprop	mf (g/s)	53.97	36.50	30.74	35.12	27.55	23.02	13.30	11.09	9.69	18.94	23.56	29.31	22.34	7.91	0.17	4.49	4.48	4.46
	Prop Shaft Pwr (kW)	516.62	355.89	340.66	389.19	306.80	255.25	127.26	104.87	91.76	205.25	257.51	321.02	244.68	72.44	1.25	35.23	35.08	34.93
	Fuel Type	Jet A																	
	LHV (MJ/kg)	42.80																	
	Efficency (%)	**22.36**	**22.78**	**25.89**	**25.89**	**26.02**	**25.90**	**22.35**	**22.09**	**22.12**	**25.32**	**25.54**	**25.59**	**25.59**	**21.39**	**16.96**	**18.31**	**18.31**	**18.31**
Autothermal reformer	mf (g/s)	80.09	65.54	62.67	192.63	64.89	50.83	22.47	20.51	19.16	37.77	45.86	56.04	35.91	7.72	18.10	13.77	13.63	13.50
	Prop Shaft Pwr (kW)	344.82	344.82	344.82	461.22	356.43	292.88	133.65	120.99	112.05	215.86	264.27	324.80	211.00	49.66	3.25	64.35	63.80	63.26
	Fuel Type	Methanol (CH_3OH)																	
	LHV (MJ/kg)	20.07																	
	Efficency (%)	**21.45**	**26.22**	**27.42**	**11.93**	**27.37**	**28.71**	**29.64**	**29.40**	**29.13**	**28.48**	**28.72**	**28.88**	**29.28**	**32.05**	**0.89**	**23.29**	**23.32**	**23.35**
Steam reformer	mf (g/s)	57.72	47.65	45.69	143.37	48.70	38.21	17.36	15.18	13.77	27.64	33.61	40.96	26.27	5.70	12.96	9.81	9.74	9.68
	Prop Shaft Pwr (kW)	344.82	344.82	344.82	462.95	360.43	298.60	140.42	121.70	108.98	214.16	263.52	324.69	211.73	50.02	3.27	63.76	63.37	62.98
	Fuel Type	Methanol (CH_3OH)																	
	LHV (MJ/kg)	20.07																	
	Efficency (%)	**29.77**	**36.05**	**37.60**	**16.09**	**36.88**	**38.94**	**40.30**	**39.94**	**39.42**	**38.61**	**39.07**	**39.50**	**40.16**	**43.71**	**1.26**	**32.37**	**32.40**	**32.43**
Hybrid autothermal	mf (g/s)	54.20	36.53	30.74	37.43	29.40	24.62	24.31	20.50	18.20	19.19	23.73	29.42	21.08	6.87	0.39	10.14	10.05	9.96
	Prop Shaft Pwr (kW)	516.14	355.67	340.66	414.71	327.36	272.85	134.67	111.61	97.33	207.98	259.40	322.20	230.93	62.89	2.85	46.15	45.79	45.43
	Fuel Type	Jet A						Methanol (CH_3OH)						Jet A					
	LHV (MJ/kg)	42.80						20.07						42.80					
	Efficency (%)	**22.25**	**22.75**	**25.89**	**25.89**	**26.02**	**25.90**	**27.61**	**27.12**	**26.65**	**25.32**	**25.54**	**25.59**	**25.59**	**21.39**	**16.96**	**10.63**	**10.64**	**10.65**
Hybrid steam	mf (g/s)	54.20	36.53	30.74	37.43	29.40	24.62	16.67	14.04	12.45	19.18	23.72	29.41	21.13	6.91	0.39	6.71	6.67	6.63
	Prop Shaft Pwr (kW)	516.14	355.67	340.66	414.71	327.36	272.85	134.67	111.43	97.08	207.86	259.32	322.14	231.48	63.27	2.80	45.69	45.45	45.21
	Fuel Type	Jet A						Methanol (CH_3OH)						Jet A					
	LHV (MJ/kg)	42.80						20.07						42.80					
	Efficency (%)	**22.25**	**22.75**	**25.89**	**25.89**	**26.02**	**25.90**	**40.25**	**39.54**	**38.85**	**25.32**	**25.54**	**25.59**	**25.59**	**21.39**	**16.96**	**15.90**	**15.91**	**15.92**

Table 17-1

From the results above, the fuel cell systems can be seen to have a much better efficiency compared to the baseline turboprop engine. The high altitude loiter flight phase in particular has proven to be the most fuel demeaning in all cases and thus it is desirable to achieve the highest propulsive efficiency at this stage when designing a system. The mid-loiter at altitude results in the table above showed a definitive increase in efficiency of 17.4% (from 22.1% to 39.5%) between the baseline turboprop and the hybrid steam reformer. Similarly, attractive increases in efficiency of 5.1%, 17.9% and 7.0% were shown for the hybrid autothermal, all-electric steam reformer and all-electric autothermal systems respectively at the same mid-loiter point. Although a similar comparison could be made at other flight phases, the results are less comparative for the hybrid systems at these phase since the fuel cell system is only utilised during the loiter phase on these systems.

The rationale for the higher efficiencies encountered with the fuel cell systems is that more of the energy of the fuel is utilised within the system as opposed to being ejected out of the exhaust as hot gases, as with the turboprop. The main downside of methanol based propulsion systems however, is the low energy content of the fuel, which, as can be seen from above, is roughly half of that of conventional fuels. This means that a higher mass flow rate of fuel is required to achieve the same energy content of fuel. This is unfortunately only partly offset by higher efficiency of the fuel cell systems compared to the turboprop engine. As a result, even though the fuel cell systems have a higher efficiency, a higher fuel flow rate will be required for thee systems because of their fuel.

17.4.7 Evaluation of the direct operating costs

The direct operating cost of an unmanned aircraft are defined as those costs which are incurred for each hour that the aircraft flies and will typically consist of,

- Fuel costs
- Maintenance and repair costs (labour and parts)
- Flight related charges (landing fees etc)

Due to the relative newness of fuel cell vehicles, it is unfortunately not possible to make an accurate prediction of the maintenance and repair costs for such a propulsion system. These are however expected to be significantly lower than its IC engine competitor due to the lack of moving parts which would otherwise be susceptible to wear. Here, we are therefore only able to make a realistic comparison of fuel costs.

As of December 2011, the US trade prices of methanol and jet fuel were,

- Jet fuel – $2.87/gallon
- Methanol - $1.38/gallon

As can be seen from these figures, there is a considerable cost saving associated with the use of methanol instead of jet fuel. This equates to a 51.9% saving on the trade price of fuel.

As a first pass approximation, the densities of methanol and jet fuel are roughly comparable at about 800kg/m3. In such case, the fixed total mission fuel mass of 2011.3kg equates to a volumetric quantity of 664.2 US Gallons (where, $1m^3$ = 264.2 US Gallons). A tank full of methanol for an all-electric propulsion system would thus cost $916.6 as opposed to $1906.2 for a tank full of jet fuel for the baseline turboprop. In the case of the hybrid steam reformer system, 1356.9kg of methanol would be required for the fuel cell system (for the loiter phase) and 654.4kg of jet fuel for the turboprop (for all other flight phases). This equates to 216.1 US Gallons of jet fuel at a cost of $620.2 and 448.1 US Gallons of methanol at a cost of $618.4, which gives a total fuel cost of $1238.6. There is thus a significant cost saving to be made with both the all-electric and hybrid propulsion systems in comparison with the baseline turboprop configuration. It should however be re-emphasised that the fuel prices quoted are trade prices and are thus subject to additional cost factors.

18 Conclusions and recommendations

This project aims to contribute to knowledge in two gaps in current aerospace technology. The technology areas identified for study were;

- Low cost mechanical thrust vectoring systems - To investigate the feasibility of using low cost mechanical thrust vectoring systems to replace conventional control surfaces. This is also an alternative to the fluidic thrust vectoring devices proposed by the Flaviir project.
- Fuel reformer based fuel cell propulsion systems - To investigate the use of a fuel reformer based fuel cell system to supply power to an all-electric power train which will be a means of primary propulsion.

The main conclusions for each of these studies will be given below but the reader is advised to refer to preceding sections for more in-depth details. Each of these technologies was integrated onto a baseline aircraft configuration which was identified as the configuration most suitable to each technology.

- A UCAV configuration - For the thrust vectoring system
- A MALE configuration - For the fuel cell propulsion system.

Each aircraft was a new design, which was sized and developed from a blank sheet of paper to a level of detail sufficient for the needs of this project. Each design is therefore not fully developed in areas not required for this project.

18.1 Thrust vectoring conclusions and recommendations

18.1.1 The thrust vectoring technology gap and contribution to knowledge

Thrust vectoring has traditionally been achieved with the use of mechanical thrust vectoring nozzles. Although a variety of concepts have evolved over time, these have however proven to be heavy and complex devices. As a result, alternative thrust vectoring concepts such as fluidic devices have been receiving considerable interest lately. These fluidic devices are however not without their own problems and have proven to suffer with unstable operating regimes and require large amounts of engine bleed to operate. A few years ago, NASA was carrying out investigations into a low cost mechanical thrust vectoring system which used post-exit paddles that deflected into the exhaust flow to change the direction of the flow. Although this system was tested extensively on the X-31 and F/A-18, the concept was later abandoned, probably because of the advent of fluidic devices. This system has however recently been receiving renewed interest on the Mitsubishi ATD-X.

Thrust vectoring originated as a means of providing vertical lift capability and more recently as a means of increasing the manoeuvrability of aircraft. Even more recently however, interest has been expressed in its use as a means to trim an aircraft and thus reduce the trim drag associated with conventional control surfaces. Such work has until now primarily been biased towards the use of fluidic devices because of the weight and

complexity penalties associated with traditional mechanical devices. As already mentioned however, these fluidic devices are not without their own problems and thus the purpose of this study was to review alternative mechanical thrust vectoring concepts to assess their viability to control and trim an aircraft. The system of particular interest in this study is the paddles vectoring system as used on the X-31. To-date, nobody else has investigated the use of this system to trim an aircraft or even considered the application of this system to a UAV.

18.1.2 Project outcome and lessons learnt for low cost mechanical thrust vectoring

Three flight phases were investigated as part of this analysis work, these being;

- Take-off and landing - During these phases we are interested in verifying that the system has sufficient control power to rotate the nose of the aircraft. We are also interested in finding the optimal combination of operating parameters to achieve the shortest possible take-off or landing field length.
- Cruise - During the cruise phase, our objective is to use the thrust vectoring system to replace the conventional elevons and thus improve the efficiency of the aircraft by reducing the trim drag.

18.1.2.1 Conclusion for the take-off analysis

The important points noted from the analysis of the take-off phase are;

- This thrust vectoring system is not able to reduce to the ground run distance required to rotate the nose of the aircraft.
- Although the thrust vectoring system did provide two additional components of lift from the nose jet and the vertical component of vectored thrust, the overall lift of the aircraft was reduced as a result. The reasoning being that deflection of the thrust vectoring nozzle was seen to result in a reduction in engine thrust as a result of engine bleed, nozzle deflection and engine operating characteristics. The result is that the acceleration and thus the forward speed of the aircraft are reduced. Since the lift of the wing is proportional to the square of the speed, the loss in lift can be seen to quite substantial and the lift from the nose jet and thrust vectoring nozzle was insufficient to compensate.
- The amount of engine bleed must also be increased relative to the nozzle deflection angle. This is in order to generate the control power required to counteract the additional moments about the main wheels and thus enable the nose wheel to be rotated. This further worsens the take-off performance as a result of a further loss in engine performance.
- The best take-off performance was obtained for zero nozzle deflection angle with just the nose jet part of the system in use.

The analysis of a configuration utilising elevons showed the required ground run to be dictated by the control power requirements with the lift limit boundary far exceeded. As before, the best take-off performance was obtained for zero nozzle deflection angle with a distance of 324.9m being achieved. The optimal system would thus be one in which

the nozzle has a deflection angle of zero and the nose jet is used on conjunction with the elevons to match the lift limit boundary figure of 223.7m.

It was also proven in a further analysis that the thrust vectoring system was insufficient to enable the wing size to be reduced. The final conclusion from this analysis is thus;

- There is no gain to be made in using the thrust vectoring nozzle during take-off.
- The nose jet system on its own however has the greatest potential to reduce the take-off distance when used in conjunction with the elevons.

18.1.2.2 Conclusion for the landing analysis

The important points noted from the analysis of the landing phase are;

- This thrust vectoring system is not able to reduce the landing field length.
- Because the analysis is a complex balance of forces and moments it is difficult to pin-point the exact cause of the characteristics responsible for the landing performance associated with this system.
- It was evident from the analysis that that the engine had to be spooled up in order to generate the engine bleed mass flow rate required by the nose jet system. This meant that an additional unit would be required to dispose of the engine thrust, which would prevent the aircraft from being slowed.
- The final conclusion is therefore that there is no benefit to be gained in the use of this thrust vectoring system during landing.
- It was however shown that that there was a potential benefit of landing the aircraft at an higher initial vertical descent velocity but such a result is however independent on whether a thrust vectoring system in employed or not.

18.1.2.3 Conclusion for the cruise analysis

The important points noted from the analysis of the cruise phase are;

- The aircraft configuration utilising thrust vectoring for trim will have comparable performance with a conventional configuration utilising elevons.
- Whereas the elevons only required minimal deflection to generate the trim forces required, the required deflection of the exhaust plume was a more significant ± 4.2º.
- The main drawback of this thrust vectoring system is that a deflection of the nozzle is accompanied by a reduction in engine performance and an increase in specific fuel consumption. Thus, although the drag of the aircraft is reduced, the engine experiences an overall reduction in performance.
- The final conclusion was that the benefit of using such a system at cruise was questionable.

18.1.2.4 The overall viability of this thrust vectoring system

The final conclusion for this thrust vectoring system is thus;

- This system has been shown to offer no benefit during take-off and landing
- The added cost and complexity of the system for trim at cruise is not viable for a conventional aircraft configuration.

- Such a system would however offer a number of IR reduction benefits to reconnaissance, bomber and attack aircraft. The large external thrust vectoring paddles would act as a shield to conceal the engine exhaust as would normally be seen by an observer on the ground.
- The use of the thrust vectoring system does however also offer the potential to reduce the size of or even eliminate the conventional control surface. Such an action would have the benefit of reducing the number of and size of the free edges and thus increasing the stealth characteristics of the aircraft by reducing its RCS signature.
- If utilised on an attack aircraft, such a system would also offer the additional benefit of improved manoeuvrability.

18.2 Fuel cells conclusions and recommendations

18.2.1 The fuel cell propulsion system technology gap and contribution to knowledge

Recently, fuel cells have been receiving considerable interest as a means of generating electrical power for numerous applications ranging from portable electrical power to propulsion. In order for a fuel cell to operate, a ready supply of hydrogen and oxygen is however required to complete the electro-chemical reaction. Bottled supplies of the reactants have proven to be sufficient for demonstration systems but more practical systems require more substantial supplies. Although oxygen is readily available from the atmospheric air, a sufficient supply hydrogen must however be carried on board the aircraft. In previous research efforts, the mass storage of hydrogen has proven to be problematic due to its low density and thus large compressed hydrogen or cryogenic storage tanks have traditionally been required, each of which however have their own set of problems.

An alternative source of hydrogen, as studied here, is its extraction on demand from hydrogen rich fuels. Although this necessitates the need for additional equipment, the carrier fuels are typically much easier to handle and store. Such systems have however to-date proven to be burdened with problems such as poor transient performance and long start-up times making them less desirable for automotive applications. This is however less likely to be such of a problem for more steady state applications such as aircraft propulsion. This project thus aimed to try to utilise the automotive research effort in this field in a more applicable application.

To-date, only a small number of light aircraft and small UAV demonstrator vehicles have been built to study the viability of using fuel cells as a means of generating power for the primary propulsion of such craft. These demonstrator vehicles have however been reliant upon bottled sources of hydrogen and oxygen. To-date nobody else has;

- Investigated the use of a methanol reformer based primary propulsion fuel cell system for a light aircraft or large UAV.
- Investigated for use of a methanol reformer based fuel cell system at high altitude conditions.

18.2.2 Project outcome and lessons learnt for fuel reformer based fuel cell systems for primary propulsion

The systems studied can be categorised as either all-electric or hybrid and further categorised as autothermal or steam reformer based. In the all-electric systems, the turboprop engine was replaced with two large traction motors which are powered by a fuel reformer based fuel cell system. The hybrid system was conceived as a means to improve the fuel economy of the all-electric systems. This system configuration utilises the fuel cell system for loiter and the turboprop engine for all other flight phases.

The important points noted from the analysis of the different fuel cell system variants studied here are;

- All of the systems studied showed there to be a performance penalty in comparison with conventional turboprop propulsion.
- The hybrid fuel cell/turboprop propulsion system was conceived as a means to be able to utilise the best benefits of each system while keeping the fuel economy to a reasonable level.

As course of this work, two fuel processor variants were studied, each of which has their own benefits and drawbacks. These being;

- A steam reformer base system – This is generally the more efficient of the two but requires an external source of heat. The need for an external heat source is a considerable drawback of the steam reformer and sometimes required the combustion of an additional amount of fuel. In the systems studied here however it was proposed to utilise the waste heat from the burner, which itself is used to generate power for the turbine.
- An autothermal reformer based system – This is a more self contained unit which generates its own heat by means of partial internal combustion. The result is that it has a lower overall efficiency.

A further study was carried out to investigate potential candidate fuels, the important points from the study being;

- The traditional fuel of choice for fuel cells has been hydrogen which has proven to be difficult to store in sufficient quantities.
- Although hydrogen carrier fuels such as methanol do require a fuel reformer to extract the hydrogen, they offer distinct benefits of being considerably easier to handle and store
- Of the carrier fuel studied, methanol has the distinct advantage of being able to be reformed at relatively low temperatures and has the lowest content of CO in the reformate.
- The additional benefits of widespread availability and cost were prompted methanol to be selected as the fuel of choice for this project.

The final system of choice was a hybrid fuel cell system which utilises methanol and a steam reformer. Although this system results in a reduction in the loiter time from 35 to 26.45 hours, such a system does offer a number of benefits such as;

- Since we are solely reliant on the fuel cell system at high altitude loiter, we are able to reduce the quantity of greenhouse gases which are emitted directly into the higher layers of the atmosphere.
- Other benefits offered by this system are a reduction in noise, IR signature and the ability to utilise a range of alternative fuels.

It is this author's opinion that utilising today's technology methanol and fuel cells are the best way forward to meet the need of our future energy demands for transportation.

18.3 Fulfilment of project objectives

At the end of this project, the success of the ultimate project can only be assessed by answering the questions;

- 'Have we achieved what we set out to achieve?' -
- 'Has the project been worthwhile?'

At the start of this project we set out to identify and investigate a number of novel technologies which could be utilised on the next generation of UAVs. As course of this project, two technologies have been identified and evaluated which fit this criterion and show potential for use on future aircraft. We are therefore able to say without doubt that the project objectives have been met and the project has proven worthwhile to the advancement of aerospace technology.

18.4 Recommendations for future work

The analysis of the thrust vectoring system utilised the best analytical methods which were available within the time constraints of this project. More accurate results can however be obtained with the use of more refined methods such as more refined experimental models or CFD analysis tools. Although conventional mechanical thrust vectoring systems are nowadays regarded as being too heavy and complex, it would also be worthwhile analysing these existing systems in order to obtain a baseline for comparison. The original NASA work, upon which this study was based, not only investigated the 3 vane system studied here but also proposed a 4 vane system. The 4 vane system was however later abandoned in favour of the 3 vane system, primarily due to its reduction in weight and complexity. It would however be interesting to revisit the 4 vane system in greater depth in a future study to make a more refined evaluation of its performance in comparison to the 3 vane system. This study would not only be key to ensuring ourselves that we are not overlooking a potentially good thrust vectoring system but may also further our understanding of the 3 vane system and how it could be refined.

At the end of this feasibility study for the thrust vectoring system we are faced with the decision whether to continue to peruse this thrust vectoring system or not in further studies. Based on what learnt in this study, it is in this author's opinion that the paddles thrust vectoring system does show significant promise as a simplistic, light weight and cost effective means of enhancing the manoeuvrability of an aircraft. In earlier studies, it has already proven itself to be very effective when used for short periods such as to gain a manoeuvring advantage over an opponent. This study has however shown it to less desirable for use for longer periods such as for trimming an aircraft, due to its

detrimental effect on engine thrust and engine performance. The system does however offer the potential of being a simplistic addition to any combat aircraft for which a complex conventional thrust vectoring nozzle would not be cost effective or viable. A potential future development of the system could even be retractable thrust vectoring vanes which could be retracted into the airframe when not required. Such a solution would have the benefit of reducing the additional afterbody drag of the aircraft associated with these normally exposed thrust vectoring vanes and thus improve the performance, efficiency and range of the aircraft for all other flight phases.

Of all the fuel cell system variants studied, the hybrid fuel cell system showed the most promise as an alternative propulsion system. This system still however utilises a conventional IC engine in conjunction with the fuel cell system and thus is still dependent on traditional hydrocarbon based fuels. The hybrid system is thus still one step away from the idealistic propulsion system which is able to completely dispense with these fossil based fuels. Although the all-electric variants of the fuel cell system fall under this idealistic umbrella, they are however burdened with other problems such as inferior fuel consumption. Therefore, although the hybrid system has proven to be a good step in the right direction, it is however only a foundation upon which further development work should be carried out in our quest for the ideal all-electric system. This further development work is however not restricted to improving the efficiency of the fuel cell system as a new fuel (such as a blend of methanol) which yields an higher energy content (more comparable with that of conventional fuels) would also have great benefit in reducing the fuel consumption of the fuel cell system.

Any such fuel cell system variant would however require significantly more research and development to gain a better understanding of the real-world characteristics of the many components which make up the system. Such work would also necessitate the development of an experimental test rig which would not only verify the results obtained as part of analytical studies but also gain some insight into how the different components interact with each other in a real-world system. At present, there is also a significant lack of good quality data which is able to help us better understand the behaviour of fuel cell systems which operate for long periods at high altitude conditions. The development of such a system to safely operate under these conditions would therefore necessitate the need for further good quality studies in this area.
On a component level, there are also a number of obstacles which would need to be overcome for such a fuel cell system to become reality. Many of these are associated with the lack of availability of purpose built components and the lack of understanding of the characteristics of off the shelf components operating within these environments. An example of this being the potential risk of ice formation within existing air supply components which have be utilised from a conventional internal combustion engine and ultimately exposed to high altitude conditions. One particular hurdle in this context is the availability of a suitable air compressor which is able to deliver air at the desired pressure and mass flow rate. Such a unit would probably have to be purposely developed for this purpose.

Although fuel cells have seen significant advancements in the past few years, there is still some way to go before they evolve to a level which makes them more viable for many more general roles. The main burdens in the widespread realisation of fuel cells

are, cost, manufacturability, maintenance, mass, volume, fuels and availability. These are all areas which also present opportunities for future fuel cell development work. As with any system, there will always be on-going work to increase the efficiency of the system. In a fuel cell, although the theoretical cell potential decreases with increasing operating temperatures, the operation cell potential actually increases with temperature. This is a result of internal voltage losses within the fuel cell which decrease at higher temperatures. Thus if we could find a way to decrease these losses at lower temperatures then we could see a further improvement in its efficiency.

With respect to this particular fuel cell system, hydrogen is being accurately fed to the fuel cell in excess of that required by the fuel cell in order to supply sufficient fuel to a tail gas burner. The hot gases from which, drive a turbine which is directly linked to a compressor which supplies air to the fuel cell. Therefore, the fuel efficiency of the system is directly related to the quantity of air demanded by the fuel cell. This in itself is fixed by the need to achieve a sufficient concentration of oxygen over the face of each fuel cell membrane in the stack. As well as this, there also needs to be a sufficient excess of oxygen leaving the fuel cell to achieve complete combustion in the tail gas burner. A major difficulty is this study was the prediction of the actual oxygen stoichiometric ration required by the fuel cell to meet these conditions. This is however an area which required a more detailed analysis of the flow conditions within each bi-polar plate and is thus a definite area for future work. Optimisation of the oxygen stoichiometric ratio would thus ultimately lead to a significant improvement in the fuel efficiency of the complete system as a whole.

On a final note, the reliability of current fuel cell systems also needs to be thoroughly investigated if fuel cell systems are to be proved that they are capable of meeting airworthiness requirements. This work would require significant research effort not only into the endurance of these systems but would also require a thorough reliability and failure analysis to ensure that any power loss due to failure would be partial and not total.

References

1. Howe, D. (2000), *Aircraft conceptual design synthesis,* Professional Engineering Publishing, London.
2. Jenkinson, L.R. et al. (1999), *Civil jet aircraft design*, Arnold, London
3. Raymer, D.P. (1999), *Aircraft design: a conceptual approach*, third edition, AIAA education series, Reston
4. Stinton, D. (2001), *The design of the aeroplane*, second edition, Blackwell science, Oxford.
5. Loftin, L.K. (1980), *Subsonic aircraft: Evolution and the matching of size to performance*, NASA-RP-1060.
6. Roskam, J. (1990), *Airplane Design Part I: Preliminary Sizing or Airplanes,* Roskam Aviation and Engineering Corporation, Ottawa, Kansas.
7. Roskam, J. (1990), *Airplane Design Part II: Preliminary Configuration Design and Integration of the Propulsion System,* Roskam Aviation and Engineering Corporation, Ottawa, Kansas.
8. Roskam, J. (1990), *Airplane Design Part III: Layout Design of Cockpit, Fuselage, Wing and Empennage,* Roskam Aviation and Engineering Corporation, Ottawa, Kansas.
9. Roskam, J. (1990), *Airplane Design Part IV: Layout Design of Landing Gear and Systems,* Roskam Aviation and Engineering Corporation, Ottawa, Kansas.
10. Roskam, J. (1990), *Airplane Design Part V: Component Weight Estimation,* Roskam Aviation and Engineering Corporation, Ottawa, Kansas.
11. Roskam, J. (1990), *Airplane Design Part VI: Preliminary Calculation of Aerodynamic, Thrust and Power Characteristics,* Roskam Aviation and Engineering Corporation, Ottawa, Kansas.
12. Roskam, J. (1990), *Airplane Design Part VII: Determination of Stability, Control and Performance Characteristics,* Roskam Aviation and Engineering Corporation, Ottawa, Kansas.
13. Roskam, J. (1990), *Airplane Design Part VIII: Airplane Cost Estimation,* Roskam Aviation and Engineering Corporation, Ottawa, Kansas.
14. Torenbeek, E. (1982), *Synthesis of subsonic airplane design*, Martinus Nijhoff Publishers, Holland.
15. *U-99 Cranfield GDP project specifications report*.
16. Mattingly, J.D. et al. (2002), *Aircraft engine design,* 2nd ed., American Institute of Aeronautics and Astronautics, Reston, VA.
17. *Method for the rapid estimation of spanwise loading of wings with camber and twist in subsonic attached flow*, ESDU 83040.
18. *Lift-curve slope and aerodynamic centre position of wings in inviscid subsonic flow*, ESDU 70011.
19. *Increments in aerofoil lift coefficient at zero angle of attack and in maximum lift coefficient due to deployment of various leading-edge high-lift devices at low speeds*, ESDU 94027.
20. Hoak, D. E., et al., *The USAF Stability and Control DATCOM*, Air Force Wright Aeronautical Laboratories, Oct. 1960 (Revised 1978).
21. Roskam, J. (1979), *Airplane flight dynamics and automatic flight controls,* Roskam Aviation and Engineering Corporation, Ottawa, Kansas.
22. *Stability derivative L_P, rolling moment due to rolling for swept and tapered wing*, ESDU Aircraft 06.01.01.
23. *Rolling moment derivative, L_ξ for plain ailerons at subsonic speeds*, ESDU 88013.
24. Cook, M. V. (2007), *Flight dynamics principles: a linear systems approach to aircraft stability and control,* Elsevier, Amsterdam.
25. Lan, C. E. (1981), *Airplane aerodynamics and performance,* Roskam Aviation and Engineering, Ottawa, Kansas.
26. Cupstid, J. (1999), *Future aircraft technology enhancements – Block 1, Air Force Research Laboratory*, Report No. AFRL-VA-WP-TR-1999-3061.
27. Rolls Royce plc (1996), *The jet engine,* 5th ed, Rolls Royce plc, Derby.
28. Mason, M.S. (2002), "Fluidic thrust vectoring of low observable aircraft", *CEAS Aerospace Research Conference*, 10-12 June 2002, Cambridge.
29. Mason, M.S. (2004), *Fluidic thrust vectoring of low observable air vehicles*, AIAA 2004-2210.
30. Joslin, R. D. and Miller, D. N. (2009), *Fundamentals and applications of modern flow control,* American Institute of Aeronautics and Astronautics, Reston, Va.

31. http://www.dfrc.nasa.gov/PAO/PIAS/HTML/FS-048-DFRC.html
32. Mishler, R. & Wilkinson, T. (1992), *Emerging airframe/propulsion integration technologies at General Electric*, AIAA 92-3335.
33. Klafin, J.F. (1988), *Integrated thrust vectoring on the X-29A*, AIAA 88-4499.
34. http://vayu-sena.tripod.com/info-su30mki.html#11
35. http://www.nasa.gov/centers/dryden/news/FactSheets/FS-002-DFRC.html
36. http://www.nasa.gov/centers/dryden/news/FactSheets/FS-009-DFRC.html
37. http://oea.larc.nasa.gov/PAIS/Partners/X_31.html
38. http://www.globalsecurity.org/military/systems/aircraft/x-32.htm
39. http://www.aerospaceweb.org/question/planes/q0042.shtml
40. http://www.fas.org/man/dod-101/sys/ac/jsf.htm
41. http://en.wikipedia.org/wiki/McDonnell_Douglas_X-36
42. http://www.youtube.com/watch?v=495b5SVXJUA
43. http://www.kbvp.com/photo/f-22-thrust-vectoring-nozzles-california-capital-airshow-photo-gallery
44. http://science.howstuffworks.com/f-22-raptor5.htm
45. .Ikaza, D. (2001), "Thrust Vectoring Nozzle for Modern Military Aircraft", *Active Control Technology for Enhanced Performance Operational Capabilities of Military Aircraft, Land Vehicles and Sea Vehicles; 01 June 2001*.
46. Black, G. (2010), *Cirrus Vision Update: October 2010*. Available from: www.cirrusaircraft.com.
47. Gal-Or, B. (1990), *Vectored propulsion, supermaneuverability and robot aircraft,* Springer, New York.
48. Friend, M.G. and Daggett, D.L. (2003), *Fuel cell demonstrator airplane*, AIAA 2003-2868.
49. Larminie, J. and Lowry, J. (2003), *Electric vehicle technology explained*, Wiley, New York.
50. Pratt, J. W. et al. (2007), "Performance of proton exchange membrane fuel cell at high-altitude conditions", *Journal of Propulsion and Power,* vol. 23, no. 2, pp. 437-444.
51. Unknown. (2008), *Antares DLR-H2: New DLR research aircraft takes off using fuel cell propulsion*, available at: www.dir.de (accessed 02/10/2009).
52. Romeo, G. et al. (2010), *ENFICA-FC: Design, realization and flight test of all electric 2-seat aircraft powered by fuel cells*, 27th ICAS 2010.
53. Menard, E. (2006), *Design study of a fuel cell - powered aircraft,* MSc thesis, Cranfield University.
54. Bekiaris, N. (2002), *Conceptual design of a fuel cell powered aircraft,* MSc thesis, Cranfield University.
55. Olah, G.A. et al. (2009), *Beyond oil and gas: the methanol economy,* 2nd ed, Wiley-VCH, Weinheim.
56. Larminie, J. and Dicks, A. (2003), *Fuel cell systems explained,* 2nd edition, Wiley, Chichester.
57. Barbir, F. (2005), *PEM fuel cells: theory and practice,* Elsevier, Amsterdam.
58. Kolb, G. (2008), *Fuel processing for fuel cells,* Wiley-VCH, New York.
59. Ballard Power Systems (2006), *CUTE – A fuel cell bus project for Europe: lessons learnt from a fuel cell perspective*, Power to change the world presentation May 10-11th 2006.
60. Rama, P. et al. (2008), *Failure analysis of polymer electrolyte fuel cells*, SAE 2008-01-0634.
61. Mason, M.L. et al. (1992), *A static investigation of the thrust vectoring system of the F /A-18 high-alpha research vehicle*, NASA-TM-4359.
62. Bowers, A. and Pahle, J. (1996), *Thrust vectoring on the NASA F-18 high alpha research vehicle*, NASA TM 4771.
63. Bowers, A. et al. (1991), *Multiaxis thrust vectoring using axisymmetric nozzles and postexit vanes on an F/A-18 configuration vehicle*, NASA TM 101741.
64. Asbury, S.C. and Capone, F.J. (1995), *Multiaxis Thrust-Vectoring Characteristics of a Model Representative of the F-18 High-Alpha Research Vehicle at Angles of Attack from 0 deg to 70 deg*, NASA-TP-3531.
65. Johnson, S.A. (1992), *Aircraft ground test and subscale model results of axial thrust loss caused by thrust vectoring using turning vanes*, NASA-TM-4341.
66. *Introductory memorandum on the pressure losses in internal flow systems*, ESDU FMI1.
67. *One-dimensional compressible gas flow in ducts*, ESDU 74028.
68. *Properties of a standard atmosphere*, ESDU 77021.
69. *Pressure losses in curved ducts: single bends*, ESDU 83037.
70. *Friction losses for fully-developed flow in straight pipes*, ESDU 66027.

71. *Pressure losses in valves*, ESDU 69022.
72. *Jet flow parameters*, ESDU 67035.
73. Mattingly, J.D. (2002), *ONX Program User Guide*.
74. Mattingly, J.D. (2002), *AEDsys Program User Guide*.
75. Mattingly, J.D. (2002), *Nozzle Program User Guide*.
76. Wilkinson, D.P. et al. (2009), *Proton exchange membrane fuel cells: materials properties and performance,* CRC Press.
77. Hoogers, G. (2003), *Fuel cell technology handbook,* Crc, Boca Raton, FL.
78. Spiegel, C. (2008), *PEM fuel cell modeling and simulation using Matlab,* Academic Press/Elsevier, Amsterdam/Boston.
79. Bagotsky, V.S. (2009), *Fuel cells: problems and solutions,* Wiley, New York.
80. Kays, W. M. and London, A. L. (1998), *Compact heat exchangers,* 3rd edition, Kreiger Publishing Company, Malabar.
81. ESDU 92013. *Selection and costing of heat exchangers*.
82. ESDU 94042. *Selection and costing of heat exchangers – Shell and tube type*.

Bibliography

Bibliography for baseline aircraft design study

Tailless aircraft design considerations

1. Lee, G.H. (1947), "Tailless aircraft design problems", *J. of the Royal Aero Soc.*, 1947.
2. Lippisch, A. (1981), *The delta wing*, IOWA State University Press.
3. Nickel, K. (1994), *Tailless aircraft: in theory and practice,* Edward Arnold, London.
4. Valiyff, A. and Arjomandi, M. (2009), *An investigation into the aerodynamic efficency of tailless aircraft*, AIAA 2009-1436.
5. Weyl, A.R. (1945), "Tailless aircraft and flying wings", *Aircraft engineering*, February 1945.

Stability and control considerations

6. Altman, A. (2002), *A comparative study to identify the propeller-driven MALE UAV configuration with the maximum endurance performance*, AIAA 2002-3468.
7. Castro, H. V. (2001), *The longitudinal static stability of tailless aircraft,* College of Aeronautics Report. Cranfield University.
8. Esteban, A. (2001), *Static and dynamic analysis of an unconventional plane: flying wing*, AIAA 2001-4010.
9. Joubert, J. W. J. (1996), *Flying qualities of an advanced combat wing fighter aircraft,* MSc thesis, Cranfield University.
10. Mennicken, P. (2001), *The stability control and flying qualities of the small scale tailless aircraft for UAV application*, Thesis, Cranfield University.
11. *Notation for aircraft dynamics*, ESDU 67022.
12. Pamadi, B. N. (2004), *Performance, stability, dynamics, and control of airplanes,* 2nd edition, American Institute of Aeronautics and Astronautics, Reston, VA.
13. Perkins, C. D. and Hage, R. E. (1949), *Airplane performance stability and control,* Wiley, New York.

Aircraft configuration considerations

14. Goraj, Z. and Frydrychewicz, A. (2004), *Development approach of the PW 103 – an increased reliability MALE UAV*, 24th ICAS 2004.
15. Nangia, R.K. and Palmer, M.E. (2005), *A comparative study of UCAV type wing planforms – aero performance & stability considerations*, AIAA 2005-5078.
16. Nickol, C.L. et al. (2007), *High altitude long endurance UAV analysis of alternatives and technology requirements development*, NASA TP-2007-214861.
17. Tsach, S. et al. (2004), *History of UAV development in IAI & road ahead*, 24th ICAS 2004.

18. Yenne, B. (2004), *Attack of the drones – a history of unmanned aerial combat*, Zenith Press, St. Paul USA.

Weight estimation for next generation technology

19. Eustance, P.A. (2000), *Predicting the effects of new technologies on aircraft structural mass: UCAV case study*, ICAS 2000.
20. Zhang, Y. and Heping, W (2006), *A study of structure weight estimating for high altitude long endurance (HALE) unmanned aerial vehicle (UAV)*, 25th ICAS 2006.

Propulsion systems

21. Campbell, D.J. (2003), *Revolutionary propulsion and power for 21st century aviation*, AIAA 2003-2561.
22. Kong, C. (2000), "Propulsion system integration of turboprop aircraft for basic trainer", *Aircraft engineering and aerospace technology*, Vol. 72, No. 6, Pg. 524-536.
23. Sehra, A.K. and Shin, J. (2003), *Revolutionary propulsion systems for 21st century aviation*, NASA TM-2003-212615.
24. Snyder, C.A. et al. (2009), *Propulsion investigation for zero and near-zero emissions aircraft*, NASA TM-2009-215487.

Operational considerations

25. Dollmayer, J. and Carl, U.B. (2006), *Consideration of fuel consumption caused by aircraft systems in aircraft design*, 25th ICAS 2006.

On-board systems and their requirements

26. Atreya, S et al. (2005), *Power system comparisons for a high altitude long endurance (HALE) remotely operated aircraft (ROA)*, AIAA 2005-7401.
27. Colozza, A.J., *Effect of power system technology and mission requirements on high altitude long endurance aircraft*, NASA CR-194455.

Aircraft conceptual design

28. Abbott, I. H. and Von Doenhoff, A. E. (1959), *Theory of wing sections, including a summary of airfoil data,* corrected version edition, Dover Publications, New York.
29. *Aerofoil and wing pitching moment coefficient at zero angle of attack due to deployment of leading-edge high-lift devices*, ESDU 00029.
30. Altman, A. (2000), *A conceptual design methodology for low speed HALE UAVs*, PhD thesis, Cranfield University.
31. Clarke, A. (2006), *Nine month review*, Cranfield University.
32. Clarke, A. (2007), *Twenty one month review*, Cranfield University
33. Fielding, J.P. (1999), *Introduction to aircraft design*, Cambridge University Press, Cambridge.
34. *Information on the use of data items on high-lift devices*, ESDU 97002.
35. *Maximum lift of wings with leading-edge devices and trailing-edge flaps deployed*, ESDU 92031.
36. *Pitching moment of low-aspect-ratio cropped-delta wings up to high angles of attack at subsonic speeds*, ESDU 95022.
37. *Properties of a standard atmosphere*, ESDU 77021.
38. *Take-off performance of vectored-jet-thrust V/STOL aircraft*, ESDU 87037.
39. *The maximum lift coefficient of plain wings at subsonic speeds*, ESDU 89034.
40. Thomas, F. (1999), *Fundamentals of sailplane design,* 3rd Ed, College Park Press.
41. *Wing angle of attack for zero lift at subcritical Mach number*, ESDU 87031.

Additional bibliography for thrust vectoring study

Engine design

42. Mattingly, J.D. (1992), *Improvements in teaching aircraft engine design*, AIAA 92-3758.
43. Mattingly, J.D. (1999), *New software to support systems approach to conceptual design of aircraft engines*, AIAA 99-2849.
44. Stricker, J. M. (1999), "*The Gas Turbine Engine Conceptual Design Process: An Integrated Approach*", NASA Center for AeroSpace Information, 7121 Standard Dr , Hanover, Maryland, 21076-1320, USA.
45. Woodford, S. (1999), *The minimisation of combat aircraft life cycle cost through conceptual design optimisation,* PhD thesis, Cranfield University.

Additional nozzle design references

46. Crown, J.C. (1948), *Supersonic nozzle design*, NACA TN 1651.
47. Viets, H. (1977), "Thrust augmenting ejector analogy", *J. of Aircraft*, Vol. 14, No. 4, pg. 409-411.

Gas turbine and thrust vectoring books

48. Boyce, M.P. (2006), *Gas turbine engineering handbook*, 3rd ed., Gulf Professional Pub., Boston.
49. Covert, E. E. (1985), *Thrust and drag: its prediction and verification,* American Institute of Aeronautics and Astronautics, New York.
50. Flack, R. D. (2005), *Fundamentals of jet propulsion with applications,* Cambridge University Press, Cambridge.
51. Hüenecke, K. (1997), *Jet engines: fundamentals of theory, design and operation,* Airlife Publications, Shrewsbury.
52. Kerrebrock, J. L. (1992), *Aircraft engines and gas turbines,* 2nd ed, MIT Press, Cambridge, MAs.
53. Mattingly, J. D. (1996), *Elements of gas turbine propulsion,* McGraw-Hill, New York.
54. Mattingly, J. D. (2006), *Elements of propulsion: gas turbines and rockets,* American Institute of Aeronautics and Astronautics, Reston, VA.
55. Mattingly, J.D. (2006), *Elements of propulsion*, American Institute of Aeronautics and Astronautics, Reston, Va.
56. Oates, G. C. (1997), *Aerothermodynamics of gas turbine and rocket propulsion,* 3rd ed, American Institute of Aeronautics and Astronautics, Reston, PA.
57. Oates, G.C. (1989), *Aircraft propulsion systems technology and design*, American Institute of Aeronautics and Astronautics, Washington, DC.
58. Saravanamuttoo, H. I. H. et al. (2001), *Gas turbine theory,* 5th ed, Prentice Hall, Harlow.
59. Treager, I. E. (1994), *Aircraft gas turbine engine technology,* 2nd ed, Glencoe, New York.
60. Walsh, P. P. and Fletcher, P. (2004), *Gas turbine performance,* 2nd edition, Blackwell Science, Oxford.
61. Zucrow, M. J. (1958), *Aircraft and missile propulsion,* Wiley, New York.

Thrust vectoring system benefits

62. Alexander, M.G. et al. (1992), *Maneuvering technology for advanced fighter aircraft*, SAE 921984.
63. Geidel, H. A. (1987), "Improved agility for modern fighter aircraft. II - Thrust vectoring engine nozzles", *International Symposium on Air Breathing Engines, 8th, Cincinnati, OH, Proceedings; UNITED STATES; 14-19 June 1987.* ISABE 87-7062.
64. Ghosh, K. et al. (2006), *Effect of thrust vectoring on aircraft post-stall trims, stability and manoeuvre*, AIAA 2006-6486.
65. Gilyard, G.B. and Bolonkin, A. (2000), *Optimal pitch thrust-vector angle and benefits for all flight regimes*, NASA TM-2000-209021.
66. Herrick, P.W. (1992), "Fighter aircraft affordability, survivability and effectiveness through multi-function thrust-vectoring nozzles", *Int. J. of Turbo and Jet Engines*, 9, 29-48.
67. Horinouchi, S. (2008), *Noise reduction by thrust vectoring for supersonic business jet*, 26th ICAS 2008.
68. Hreha, M. et al. (1994), *An approach to aircraft performance optimisation using thrust vectoring*, AIAA 94-3361.
69. Wang, Z. et al. (2007), "Effect of thrust-vectoring jet on delta wing aerodynamics", *J. of Aircraft*, Vol. 44, No. 6, Pg. 1877-1888.

Thrust vectored aircraft and research projects – General

70. Bare, E. and Reubush, D.E. (1987), *Static internal performance of a two-dimensional convergent-divergent nozzle with thrust vectoring*, NASA-TP-2721.
71. Capone, F. et al. (1992), *Comparative investigation of multiplane thrust vectoring nozzles*, AIAA 92-3263.
72. Capone, F.J. (1978), *Static performance of five twin-engine nonaxisymmetric nozzles with vectoring and reversing capability*, NASA-TP-1224.
73. Carson, G.J. and Capone, F.J. (1991), *Static internal performance of an axisymmetric nozzle with multiaxis thrust-vectoring capability*, NASA-TM-4237.
74. http://en.wikipedia.org/wiki/Thrust_vectoring, (accessed 04/12/2008).
75. Jie, J. et al. (2000), *Experimental investigation of static internal performance for an axisymetric vectoring exhaust nozzle*, ICAS 2000.

76. Lamb, M. (1995), *Internal performance characteristics of thrust-vectored axisymmetric ejector nozzles*, NASA-TM-4610.
77. Unknown (1994), "Thrust vectoring trio", *Air international journal*, July 1994, pg. 22-24.
78. Unknown, "New nozzle design aimed at F-15, F-16 aircraft", *AW&ST*, Sept. 13th 1982. Pg. 70-73.
79. Wing, D.J. and Capone, F.J. (1993), *Performance characteristics of two multiaxis thrust-vectoring nozzles at Mach numbers up to 1.28*, NASA-TP-3313.

Thrust vectoring – post exit vanes

80. Berrier, B.L. and Mason, M.L. (1988), *Static performance of an axisymmetric nozzle with post-exit vanes for multiaxis thrust vectoring*, NASA-TP-2800.
81. Bowers, A.H. et al. (1991), *Multiaxis thrust vectoring using axisymmetric nozzles and postexit vanes on an F/A-18 configuration vehicle*, NASA-TM-101741.

Thrust vectoring - Eurofighter

82. Ikaza, D. and Rausch, C. (2000), "Thrust vectoring for eurofighter - the first steps", *Air & Space Europe,* vol. 2, no. 1, pp. 92-95.
83. Jimenez, A. (2001), *Thrust vectoring for advance fighter aircraft, propulsion package development*, ITP Spain, AIAA 2001-3991.

Thrust vectoring – F-15 ACTIVE

84. Doane, P. et al. (1994), *F-15 Active: A flexible propulsion integration testbed*, AIAA 94-3360.
85. Orme, J.S. and Sims, R.L. (1999), "Selected performance measurements of the F-15 active axisymmetric thrust-vectoring nozzle", ISABE - International Symposium on Air Breathing Engines, 14th, Florence, Italy, 5-10 Sept. 1999.
86. Orme, J.S. et al. (1998), *Initial Flight Test Evaluation of the F-15 ACTIVE Axisymmetric Vectoring Nozzle Performance*, NASA/TM-1998-206558.
87. Smolka, J. W. et al. (1996), "F-15 ACTIVE flight research program", *1996 report to the aerospace profession; SETP Symposium, 40th, Beverly Hills, CA; UNITED STATES; Sept. 1996.*

Thrust vectoring – Su-27

88. www.sci.fi/~fta/Su-27.htm, (accessed 09/12/2008).

Thrust vectoring – F-15 SMTD

89. Bursey, R. and Dickinson, R. (1990), *Flight test results of the F-15 SMTD thrust vectoring/thrust reversing exhaust nozzle*, AIAA 90-1906.
90. Laughreu, J.A. (1991), *Use of thrust vectoring and reversing on the S/MTD,* SAE 911173.
91. Moorhouse, D.J. and Laughrey J.A. (1991), *Results and lessons learned from the STOL & maneuver demonstration program*, SAE 912005.

Thrust vectoring - F-18 high alpha research vehicle

92. Asbury, S. C. and Capone, F. J. (1994), *High-alpha vectoring characteristics of the F-18/HARV*, AIAA 92-3095
93. Ashby, S.C. and Capone, F.J. (1992), *Thrust vectoring characteristics of the F-18 high alpha research vehicle at angles of attack from 0° to 70°.* AIAA 92-3095.
94. Bowers, A.H. et al. (1996), *An overview of the NASA F-18 high alpha research vehicle*, NASA TM 4772.
95. Capone, F.J. and Berrier, B.L. (1980), *Investigation of axisymmetric and nonaxisymmetric nozzles installed on a 0.10 scale F-18 prototype airplane model*, NASA-TP-1638
96. http://en.wikipedia.org/wiki/High_Alpha_Research_Vehicle
97. http://www.nasa.gov/centers/dryden/history/pastprojects/HARV/index.html

Thrust vectoring – F-16 MATV

98. Anna, P.D. and Kidman, D.S. (1994), "Flight test results of the F-16 aircraft modified with the axisymmetric vectoring exhaust nozzle", NASA Dryden Flight Research Center, *Fourth High Alpha Conference*, Volume 2 (SEE N95-14239 03-02).
99. http://en.wikipedia.org/wiki/F-16_VISTA
100. http://www.f-16.net/f-16_versions_article19.html
101. Sweeney, J. E. and Gerzanics, M. A. (1994), "F-16 multi-axis thrust vectoring program", *Israel Annual Conference on Aerospace Sciences, 34th, Tel Aviv, Proceedings; ISRAEL; 16-17 Feb. 1994.*
102. www.acesaero.com/dreammachine.pdf *(details of MATV project)*
103. Zwerneman, W.D. and Eller, B.G. (1994), "Vista/F-16 Multi-Axis Thrust Vectoring (MATV) control law design and evaluation", NASA. Dryden Flight Research Center, *Fourth High Alpha Conference*, Volume 2 19 p (SEE N95-14239 03-02); UNITED STATES.

Thrust vectoring - X-31

104. http://en.wikipedia.org/wiki/Rockwell-MBB_X-31

Thrust vectoring - X-32

105. http://en.wikipedia.org/wiki/Boeing_X-32

Thrust vectoring - X-35

106. http://en.wikipedia.org/wiki/Lockheed_Martin_X-35
107. http://www.aeroflight.co.uk/types/usa/lockheed_martin/x-35/X-35.htm

Thrust vectoring - X-36

108. http://www.nasa.gov/centers/dryden/news/FactSheets/FS-065-DFRC.html
109. http://www.nationalmuseum.af.mil/factsheets/factsheet.asp?id=358

Thrust vectoring - ATD-X

110. http://en.wikipedia.org/wiki/Mitsubishi_ATD-X

Thrust vectoring - ADEN Nozzle

111. Mishler, R. and Wilkinson, T. (1992), *Emerging Airframe/Propulsion Integration Technologies at General Electric*, AIAA 92-3335.

Thrust vectoring - STOLEN Project

112. Barnes, G.R. (1984), *Vectoring exhaust nozzle technology*, AIAA 84-1175.
113. Curry, S.G. (1983), *Exhaust Nozzle concepts for STOL Tactical Aircraft*, AIAA 83-1226.

Thrust vectoring - Saturn AL-31

114. http://en.klimov.ru/production/aircraft/tvn/
115. http://en.wikipedia.org/wiki/AL-31
116. http://warfare.ru/?catid=341&linkid=2493
117. http://www.airforce-technology.com/projects/su37/

X-31 thrust vectoring system

118. Berrier, B.L. and Mason, M.L. (1987), *Static investigation of post-exit vanes for multiaxis thrust vectoring*, AIAA 87-1834.
119. Georg, H. (1994), "Aerodynamic development and effectiveness evaluation of the X-31A thrust vectoring system", *Fourth high alpha conference*, NASA Dryden Flight Research Centre, Edwards, California, July 12-14 1994.
120. Powers, S. and Schellenger, H. (1989), *The X-31: High performance at low cost*, AIAA 89-2122.
121. Robinson, M.R. and Herbst, W.B. (1990), *The X-31A an advanced maneuverability aircraft*, ICAS-90-0.4.

Thrust vectoring for VTOL/STOL

122. Curry, S.G. et al. (1983), *Exhaust nozzle concepts for STOL tactical aircraft*, AIAA 83-1226.
123. Eckard, G.J. and Poth, G.E. (1983), *Innovative concepts for tactical STOL*, AIAA 83-2129.
124. Flethcher, J. (1984), "Layout considerations and types of V/STOL aircraft", *AGARD Spec. Course on V/STOL Aerodyn. 36 p (SEE N84-25625 16-01).*
125. Hutchinson, J. (2004), "Going vertical – developing a short take-off, vertical landing system", *Ingenia* - Issue 20, Aug 2004, pg. 25-30.
126. Kentfield, J.A.C, (1967), "Nozzles for jet lift V/STOL aircraft", *J. of aircraft*, July/Aug 1967.
127. Miller, D.P. and Clark, J.W. (1965), *Investigation into the use of vectored thrust during carrier landings*, AIAA 65-792.
128. Nelms, W. P. and Anderson, S. B. (1984), "V/STOL concepts in the United States: Past, present, and future", *AGARD Spec. Course on V/STOL Aerodyn. 44 p (SEE N84-25625 16-01).*
129. Probert, B. (1998), *Aspects of Wing Design for Transonic and Supersonic Combat Aircraft,* NASA no. 19990036209.
130. Raymer, D. P. (1988), *The impact of VTOL on the conceptual design process,* AIAA 88-4479.
131. Tape, R. F. et al. (1983), "Vectoring exhaust systems for STOL tactical aircraft".
132. Tape, R.F. et al. (1987), *STOL characteristics of a tactical aircraft with thrust vectoring nozzles*, AIAA 87-1835.
133. Wood, C. B. and Berger, C. W. (1999), "Pratt & Whitney's multi-axis thrust vectoring engine exhaust nozzle design, development, flight test techniques and results", *International Society for Air Breathing Engines - ISOABE, ISABE - International Symposium on Air Breathing Engines, 14th, Florence, Italy, 5-10 Sept. 1999.*

Engine and nozzle integration

134. Henderson, W. P. (1991), *Airframe propulsion integration at transonic speeds*.
135. Henderson, W.P. (1989), *Propulsion integration for military aircraft*, SAE 892234.

136. Henderson, W.P. and Berrier, B.L. (1989), *Airframe/propulsion integration characteristics at transonic speeds, Transonic Symposium: Theory, Application, and Experiment*, Volume 1, Part 1 (SEE N89-20925 14-02).
137. Kitowski, J.V. (1992), *Fighter airframe/propulsion integration – A General Dynamics perspective*, AIAA 92-3332.
138. Liston, G.W. and Small, L.L. (1992), *Fighter airframe/propulsion integration – A Wright Laboratory perspective*, AIAA 92-3337.
139. Mace, J. and Nyberg, G. (1992), *Fighter airframe/propulsion integration – a McDonnell aircraft perspective*, AIAA 92-3333.
140. Powers, S.A. and Robinson, M.R. (1992), *Fighter airframe/propulsion integration – A Rockwell perspective*, AIAA 92-3334.
141. Richey, G.K. et al. (1977), *Two-dimensional nozzle/airframe integration technology an overview*, AIAA 77-839.
142. Sanghi, V. et al. (1998), "Engine-airframe integration during conceptual design for military application", *J. of Aircraft*, Vol. 35, No. 3, Pg. 380-386.

Engine performance considerations

143. Yuhas, A. (1992), *Effects of bleed air extraction on thrust levels of the F404-GE-400 turbofan engine*, AIAA 92-3092.

Thrust vectoring system design and selection

144. Gamble, E. et al. (2004), *Nozzle selection and design criteria*, AIAA 2004-3923.
145. Glenet, S. J. (2006), *Preliminary design of a distributed propulsion thrust vectoring system,* MSc thesis, Cranfield University.
146. Lewis, R. (2004), *Optimisation of a thrust vectoring system for a next generation fighter aircraft,* MSc thesis, Cranfield University.
147. Moron, L. et al. (2007), *Design and analysis of a planar 2-d nozzle for a small jet engine*, GT 2007-28115.

Thrust vectoring control

148. Cornelius, K.C. and Lucius, G.A. (1995), "Thrust vectoring control from convergent nozzles with translating side walls", *J. of Propulsion and Power*, Vol. 11, No. 3, Pg. 427-432.
149. Curtin, R.J. (1997), *Thrust vectoring for longitudinal flight control*, MSc thesis, Cranfield University.
150. Gal-Or, B. (2003), "Jet engines as prime flight effectors in future tailless, vectored, stealthy air vehicles: the first key design rules", *International journal of turbo and jet engines*, 20, 297-305.
151. Simon, J.M. et al. (1993), *Control concepts for a vertical tailless fighter*, AIAA 93-4000.
152. Snow, B.H. (1990), *Thrust vectoring control concepts and issues*, SAE 901848
153. Snow, B.H. (1991), "The key thrust vectoring issue: control", *Aerospace Engineering Journal*, August 1991.
154. Vinelli, G. (2000), *Modelling of the control of a thrust vectored aircraft*, ICAS 2000.

Thrust vectoring and pitch control system general design references

155. *Flow through sudden contractions of duct area: pressure losses and flow characteristics*, ESDU 05024.
156. *Friction losses for fully-developed flow in straight pipes of constant cross section – subsonic compressible flow of gases*, ESDU 74029.
157. Munson, B. R. et al. (1998), *Fundamentals of fluid mechanics,* 3rd ed, Wiley, New York.
158. *One-dimensional isentropic gas flow*, ESDU S.00.03.07.
159. *Pressure losses in flowmetering devices*, ESDU 66030.
160. Scott, M. L. (1981), *S80 Roll control and remote augmented lift systems,* MSc thesis, Cranfield University.
161. *Specific heat capacities and their ratio as functions of temperature for several common gases*, ESDU 00.01.08.

Thrust vectoring general

162. Barnes, G.R. et al. (1984), *Vectoring exhaust nozzle technology*, AIAA 84-1175.
163. Friehmelt, H. (1996), *Thrust vectoring and tailless aircraft design – review and outlook*, AIAA 96-3412-CP.
164. Gal-Or, B. (1990), "Fundamental concepts of vectored propulsion", *J. of Propulsion*, Vol. 6, No. 6, Pg. 747-757.
165. Gal-Or, B. and Sherbaum, V. (1993), "Thrust vectoring: theory, laboratory and flight tests", *J. of Propulsion and Power*, Vol. 9, No. 1. Pg. 51-58.

166. Gill, J.C. (1974), "Advanced technology thrust vectoring exhaust systems", *J. of Aircraft*, Vol. 11, No. 12, Pg. 764-770.
167. Herbst, W.B. (1980), "Future fighter technologies", *J. of Aircraft*, Vol. 17, No. 8, Pg. 561-566.
168. Sherbaum, V. and Lichtsinder, M. (1998), "Jet deflection angles in military, civil and RPVthrust vectoring aircraft", *International journal of turbo and jet engines*, 15, 91-94.

Fluidic thrust vectoring concepts

169. Alvi, F.S. et al. (2000), "Vectoring thrust in multiaxes using confined shear layers", *ASME J. of Fluids Engineering*, Vol. 122.
170. Banazadeh, A. et al. (2007), *Multi-directional Co-flow fluidic thrust vectoring intended for a small gas turbine*, AIAA 2007-2940.
171. Bettridge, M.W. et al. (2004), *Aerodynamic jet vectoring using steady blowing and suction*, AIAA 2004-0921.
172. Deere, K.A. (2003), Summary of fluidic thrust vectoring research conducted at NASA Langley Research Centre, AIAA 2003-3800.
173. Deere, K.A. et al. (2005), *A computational study of a new dual throat fluidic thrust vectoring nozzle concept*, AIAA 2005-3502.
174. Dores, D. et al. (2006), *Characterization of a counterflow thrust vectoring scheme on a gas turbine engine exhaust jet*, AIAA 2006-3516.
175. Flamm, J.D. et al. (2005), *Experimental study of a dual- throat fluidic thrust-vectoring nozzle concept*, AIAA 2005-3503.
176. Flamm, J.D. et al. (2006), *Design enhancements of the two-dimensional, dual throat fluidic vectoring nozzle concept*, AIAA 2006-3701.
177. Forliti, D.J. and Diaz-Guardamino, I.E. (2008), *Thrust vector control using trasverse injection and countercurrent shear*, AIAA 2008-3879.
178. Gill, K. et al. (2007), *Development of an integrated propulsion and pneumatic power supply system for flapless UAVs*, AIAA 2007-7726.
179. Gu, D. et al. (2008), "Modelling and robust control of fluidic thrust vectoring and circulation control for unmanned air vehicles", University of Leicester, *Special issue paper 333, Proc. IMechE Vol. 222 Part I: J. Systems and Control Engineering*.
180. Kowal, H.J (2002), "Advances in thrust vectoring and the application of flow-control technology", *Canadian aeronautics and space journal*, Vol 48, No. 2, June 2002.
181. Lim, C. et al. (2006), *Studies on thrust vector control using a fluidic counter-flow concept*, AIAA 2006-5204.
182. Lord, W.K. (2000*), Flow control opportunities in gas turbine engines*, AIAA 2000-2234.
183. Nabavi, Y. and Calisal, S.M. (2006), *An innovative design for fluidic thrust vectoring using smart structure materials*, AIAA 2006-4978.
184. Neely, A.J. et al. (2007), *Performance studies of shock vector control fluidic thrust vectoring*, AIAA 2007-5086.
185. Panitz, T. and Wasan, D.T. (1972), "Flow attachment to solid surfaces: the coanda effect", *AIChE Journal*, Vol. 18, No. 1, Pg. 51-57.
186. Pilmoor, M. et al. (2006), *Development of a dynamic wind tunnel model for demonstration of flow control manoeuvre effectors*, AIAA 2006-3507.
187. Saghafi, F. and Banazadeh, A. (2006), *Co-flow fluidic thrust vectoring requirements for longitudinal and lateral trim purposes*, AIAA 2006-4980.
188. Santos, M.M. (2005), *Experimental study on counter-flow thrust vectoring of a gas turbine*, PhD thesis, Florida State University.
189. Sobester, A. and Keane, A.J. (2006), *Multi-objective optimal design of a fluidic thrust vectoring nozzle*, AIAA 2006-6916.
190. Sparks, R. et al. (2005), *Development of an integrated circulation control/fluidic thrust vectoring flight test demonstrator*, CEIAT 2005-xxxx.
191. Waithe, K.A. and Deree, K.A. (2003), *Experimental and computational investigations of multiple injection ports in a convergent-divergent nozzle for fluidic thrust vectoring*, AIAA 2003-3802.
192. Wilde, P.I.A. et al. (2007), *Integrated design of a model-scale gas turbine powered flapless demonstrator aircraft: a case study*, AIAA 2007-7727.
193. Williams, R.G. and Vittal, B.R. (2002), *Fluidic thrust vectoring and throat control exhaust nozzle*, AIAA 2002-4060.

Additional bibliography for fuel cell system study

Fuel cells - introduction and general concepts

194. *Ballard PEM fuel cell product portfolio*, www.ballard.com.
195. Barbir, F. (2007), *Fuel cells for clean power generation: Status and perspectives*.
196. Barbir, F. and Yazici, S. (2008), "Status and development of PEM fuel cell technology", *International Journal of Energy Research,* vol. 32, no. 5, pp. 369-378.
197. Burke, K.A. (2003), *Fuel cells for science applications*, AIAA 2003-5938.
198. Cook, B. (2002), "Introduction to fuel cells and hydrogen technology", *Engineering science and education journal*, December 2002, Pg. 205-216.
199. Isbii, R.K. (2008), "Stationary and transportation fuel cell applications", *First international conference on energy efficiency and conservation*, Hong Kong, 15-17 January 2003.
200. Schneider, M. T. et al. (2004), "Innovation process 'fuel cell vehicle': What strategy promises to be most successful?", *Technology Analysis and Strategic Management,* vol. 16, no. 2, pp. 147-172.
201. Stumper, J. and Stone, C. (2008), "Recent advances in fuel cell technology at Ballard", *Journal of Power Sources,* vol. 176, no. 2, pp. 468-476.
202. Thomas, C. E. (2009), "Fuel cell and battery electric vehicles compared", *International Journal of Hydrogen Energy,* vol. 34, no. 15, pp. 6005-6020.
203. U.S. Department of Energy (2004), *Fuel cell handbook*, 7th Edition, EG&G Technical Services Inc, Office of Fossil Energy, National Energy Technology Laboratory.

Fuel processing and reformer based fuel cell systems

204. Amphlett, J.C. et al. (1995), *Predicted emissions from a methanol-fueled "electrochemical automobile engine" based on a PEM fuel cell*, SAE 952374.
205. Avci, A. K. et al. (2003), "On-board hydrogen generation for fuel cell-powered vehicles: The use of methanol and propane", *Topics in Catalysis,* vol. 22, no. 3-4, pp. 359-367.
206. Barbir, F. et al. (1999), "*Development of advanced low-cost PEM fuel cell stack and system design for operation on reformate used in vehicle power systems"*, Fuel cells for transportation, FY 1999 progress report.
207. Bhatia, K.K. (2004), *Study of a methanol reforming polymer electrolyte fuel cell system*, Pennsylvania State University PhD Thesis.
208. Boettner, D. D. and Moran, M. J. (2004), "Proton exchange membrane (PEM) fuel cell-powered vehicle performance using direct-hydrogen fueling and on-board methanol reforming", *Energy,* vol. 29, no. 12-15, pp. 2317-2330.
209. Boettner, D.D. et al. (2002), "On-board reforming effects on the performance of proton exchange membrane (PEM) fuel cell vehicles", *Journal of Energy Resources Technology, Transactions of the ASME,* vol. 124, no. 3, pp. 191-196.
210. Bowers, B.J. et al. (2004), *Development of an onboard fuel processor for PEM fuel cell vehicles*, SAE 2004-01-1473.
211. Bowers, B.J. et al. (2007), *Multi-fuel fuel processor and PEM fuel cell system for vehicles*, SAE 2007-01-0692.
212. Carpenter, I. et al. (1999), *On-board hydrogen generation for PEM fuel cells in automotive applications*, SAE 1999-01-1320.
213. Chuang, C. et al. (2008), "Optimal design of an experimental methanol fuel reformer", *International Journal of Hydrogen Energy,* vol. 33, no. 23, pp. 7062-7073.
214. Danial, D.E. et al. (2001), "Fuel processors for automotive fuel cell systems: a parametric analysis", *Journal of Power Sources,* vol. 102, no. 1-2, pp. 1-15.
215. Doss, E. et al. (2001), "Fuel processors for automotive fuel cell systems: a parametric analysis", *Journal of Power Sources,* vol. 102, no. 1-2, pp. 1-15.
216. Edwards, N. et al. (1998), "On-board hydrogen generation for transport applications: the HotSpot™ methanol processor", *Journal of Power Sources,* vol. 71, no. 1-2, pp. 123-128.
217. Eggert, A.R. et al. (2000), *Characteristics of an indirect-methanol fuel cell system*, AIAA 2000-3040.
218. Ellis, S.R. et al. (2001), *Hotspot processor for reformulated gasoline*, Johnson Matthey Technology Centre, ETSU F/02/00143/REP, DTI/Pub URN 01/958.
219. Emonts, B. et al. (1998), "Compact methanol reformer test for fuel-cell powered light-duty vehicles", *Journal of Power Sources,* vol. 71, no. 1-2, pp. 288-293.

220. Ersoz, A. et al. (2006), “Reforming options for hydrogen production from fossil fuels for PEM fuel cells”, *Journal of Power Sources,* vol. 154, no. 1, pp. 67-73.
221. European commission, *On-board gasoline reforming for fuel cell vehicles (PROFUEL)*, FP5 – energy, environment and sustainable development research programme.
222. Fischer, K. et al. (2005), "Performance of gasoline fuel cell cars - a simulation study", *Proceedings of the Institution of Mechanical Engineers D, Journal of Automobile Engineering,* vol. 219, no. D7, pp. 889-896.
223. Garland, N. L. et al. (2002), “Recent development of automotive fuel processor technologies”, *ACS Division of Fuel Chemistry, Preprints,* Vol. 47, pp. 538.
224. Golunski, S. (1998), “HotSpot™ fuel processor: Advancing the case for fuel cell powered cars”, *Platinum Metals Review,* vol. 42, no. 1, pp. 2-7.
225. Hagan, M. et al. (2000), *Automotive fuel processing systems for PEM fuel cells*, SAE 2000-01-0007.
226. Hung, T.C. (2006), *Fuel reforming for fuel cell application*, Hong Kong University Thesis.
227. Hwang, I. et al. (2003), *Development of fuel cell hybrid electric vehicle fueled by methanol*, SAE 2003-01-0421.
228. Lattner, J. R. and Harold, M. P. (2005), "Comparison of methanol-based fuel processors for PEM fuel cell systems", *Applied Catalysis B: Environmental,* vol. 56, no. 1-2, pp. 149-169
229. Megede, D. (2002), “Fuel processors for fuel cell vehicles”, *Journal of Power Sources,* vol. 106, no. 1-2, pp. 35-41.
230. Moore, R.M. (2000), *Indirect-methanol and direct-methanol fuel cell vehicles*, AIAA 2000-3038.
231. Ogden, J.M. (2001), “Review of small stationary reformers for hydrogen production”, *Report to the international energy agency*, Centre for energy and environmental studies, Princeton University.
232. Panik, F. et al. (2002), *Concept study of a methanol fuel cell vehicle*, SAE 2002-21-0069.
233. Park, J. et al. (2005), "PEMFC operation with methanol reforming process", *Proceedings of the 3rd International Conference on Fuel Cell Science, Engineering, and Technology, 2005,* pp. 767.
234. Prigent, M. (1997), “On board hydrogen generation for fuel cell powered electric cars: A review of various available techniques”, *Revue de l'Institut Francais du Petrole,* vol. 52, no. 3, pp. 349-360.
235. Privette, R. M. et al. (1999), *Compact Fuel Processor for Fuel Cell-Powered Vehicles*, SAE 1999-01-0536.
236. Qi, A. et al. (2007), "Integrated fuel processors for fuel cell application: A review", *Fuel Processing Technology,* vol. 88, no. 1, pp. 3-22.
237. Ramaswamy, S. et al. (2003), “On-board hydrocarbon fuel processors for fuel cell vehicles: Performance and system interactions”, *ACS Division of Fuel Chemistry, Preprints,* Vol. 48, pp. 697.
238. Sadler, M. et al. (2000), *Warm-up strategies for a methanol reformer fuel cell vehicle*, SAE 2000-01-0371.
239. Sandhu, S. S. et al. (2005), "A reformer performance model for fuel cell applications", *Journal of Power Sources,* vol. 140, no. 1, pp. 88-102.
240. Severin, C. et al. (2005), "Compact gasoline fuel processor for passenger vehicle APU", *Journal of Power Sources,* vol. 145, no. 2, pp. 675-682.
241. Sundaresan, M. et al. (2003), "Catalytic burner for an indirect methanol fuel cell vehicle fuel processor", *Journal of Power Sources,* vol. 113, no. 1, pp. 19-36.
242. Unknown, *Specifications for InnovaGen 5 fuel processor*, www.innovatek.com.
243. Virji, M. B. V. and Thring, R. H. (2005), “Analysis of a 50 kWe indirect methanol proton exchange membrane fuel cell (PEMFC) system for transportation applications”, *Proceedings of the Institution of Mechanical Engineers, Part D: Journal of Automobile Engineering,* vol. 219, no. 8, pp. 937-950.
244. Yan, X. et al. (2006), “A 75-kW methanol reforming fuel cell system”, *Journal of Power Sources,* vol. 162, no. 2, pp. 1265-1269.

Alternative fuels general overview

245. Bechtold, R. L. (1997), *Alternative fuels guidebook: properties, storage, dispensing and vehicle facility modifications,* Society of Automotive Engineers, Warrendale, PA.

246. Berlowitz, P.J. and Darnell, C.P. (2000), *Fuel choices for fuel cell powered vehicles*, SAE 2000-01-003.
247. Daggett, D. et al. (2006), *Alternative fuels and their potential impact on aviation*, 25th ICAS 2006.
248. Ogden, J. M. et al. (1999), "A comparison of hydrogen, methanol and gasoline as fuels for fuel cell vehicles: implications for vehicle design and infrastructure development", *Journal of Power Sources,* vol. 79, no. 2, pp. 143-168.
249. Thomas, C. E. et al. (2000), "Fuel options for the fuel cell vehicle: hydrogen, methanol or gasoline?", *International Journal of Hydrogen Energy,* vol. 25, no. 6, pp. 551-567.
250. Thomas, C.E. et al. (1998), *Societal impacts of fuel options for fuel cell vehicles*, SAE 982496.

Hydrogen fuel considerations

251. Ball, M. (2009), *The hydrogen economy: opportunities and challenges,* Cambridge University Press, Cambridge.
252. Battipede, M. et al. (2008)*, Innovative hydrogen storage tank for flying fuel cell power system*, AIAA 2008-5730.
253. Carvalho, L. et al. (2008), *An overview of hydrogen fuel for vehicular application*, SAE 2008-36-0322.
254. Colozza, A.J. (2002), *Hydrogen storage for aircraft applications overview*, NASA CR-2002-211867.
255. James, B.D. et al. (1996), *Comparison of onboard hydrogen storage for fuel cell vehicles*, Final report, prepared for Ford Motor Company.
256. Klein, G. (2006), *Hydrogen technology – ready for take-off – hydrogen applications in the aerospace industry*, 25th ICAS 2006.
257. Mercuri, R. et al. (2002), "Options for refuelling hydrogen fuel cell vehicles in Italy", *Journal of Power Sources,* vol. 106, no. 1-2, pp. 353-363.
258. Millis, M.G. et al. (2009), *Hydrogen fuel system design trades for high-altitude long-endurance remotely-operated aircraft*, NASA TM 2009-215521.
259. Raman, V. (1999), *The hydrogen fuel option for fuel cell vehicle fleets*, SAE 1999-01-0529.
260. Sefain, M.J. (2005), *Hydrogen aircraft concepts & ground support*, PhD thesis, Cranfield University.
261. Smith, T.D., *Hydrogen-powered flight*, NASA report, Source unknown.
262. U.S. Department of Transportation (2007), *Guidelines for use of hydrogen fuel in commercial vehicles*, Final Report, Federal Motor Carrier Safety Administration.
263. Unknown (2003), *Fuel cells and hydrogen: the path forward – a comprehensive strategy for federal investment in fuel cell technology and fuel infrastructure*, available at: www.fuelcellpath.org.
264. Unknown (2009), *Worldwide hydrogen fueling stations, fuel cells 2000*, available at: www.fuelcells.org.
265. Verstraete, D. (2009), *The potential of liquid hydrogen for long range aircraft propulsion*, PhD thesis, Cranfield University.
266. Wentz, W.H. et al. (2005), *Hydrogen fuelled general aviation airplanes*, AIAA 2005-7324.
267. Wyczalek, F.A. (2004), *Hydrogen fuel – defining the future*, AIAA 2004-5606.

Fuel cell books

268. Barclay, F.J. (2006), *Fuel cells, engines and hydrogen – an exergy approach*, Wiley.
269. Ehsani, M. et al. (2009), *Modern electric, hybrid electric and fuel cell vehicles: fundamentals*, theory and design, 2nd Edition, CRC Press.
270. Emadi, A. et al. (2004), *Vehicular electric power systems – land, sea, air and space vehicles*, Marcel Dekker Inc, New York.
271. Gou, B. et al. (2009), *Fuel cells: modeling, control and applications*, CRC Press.
272. Hodkinson, R. and Fenton, J. (2001), *Lightweight electric/hybrid vehicle design*, Butterworth Heinemann.
273. Husain, I. (2003), *Electric and hybrid vehicles: design fundamentals*, CRC Press.
274. Sammes, N. (2006), *Fuel cell technology: reaching towards commercialization*, Springer.
275. Sorensen, B. (2005), *Hydrogen and fuel cells: emerging technologies and applications,* Elsevier, 2005, Amsterdam.
276. Westbook, M.H. (2001), *The electric and hybrid electric car*, Society of Automotive Engineers.

Balance of plant

277. Fuber, R. and Weber, O. (2000), *Air intake and exhaust systems in fuel cell engines*, SAE 2000-01-0381.
278. He, X. et al. (2004), *Peripheral systems for a fuel cell powered vehicle*, SAE 2004-01-1010.
279. Pischinger, S. and Lang, O. (2003), "Air-supply components", in: *Handbook of fuel cells – fundamentals, technology and applications, Volume 4: Fuel cell technology and applications*, Edited by Vielstich, W.
280. Semenov, S.Y. (2009), *Lightweight planar heat pipe for fuel cell cooling*, AIAA 2009-4654.
281. Wiartalla, A et al. (2000), *Compressor expander units for fuel cell systems*, SAE 2000-01-0380.

Operational aspects

282. Wilkinson, D.P. and St-Pierre, J. (2003), Durability, in: *Handbook of fuel cells – fundamentals, technology and applications, Volume 3: Fuel cell technology and applications*, Edited by Vielstich, W.

Fuel cell costs

283. Carlson, E.J. et al. (2002), *Cost modeling of PEM fuel cell systems for automobiles*, SAE 2002-01-1930.
284. James, B. and Kalinoski, J. (2009), *Automotive fuel cell system cost trends and predictions, Fuel cell seminar 2009 presentation*, GHT 41, Directed technologies.
285. James, B. and Kalinoski, J. (2009), *Mass production cost estimation for direct H_2 PEM fuel cell systems for automotive applications: 2008 update*, Directed technologies, Report for the U.S. Dept. of energy.
286. James, B.D. et al. (2002), "DFMA cost estimates of fuel-cell/reformer systems at low/medium/high production rates", Directed technologies, *Future car congress 2002*, 4 June 2002.
287. Lomax, F.D. et al. (1998), *Detailed manufacturing cost estimates for polymer electrolyte membrane (PEM) fuel cells for light duty vehicles*, Directed technologies, Report for Ford Motor Company.

High altitude fuel cell operation

288. Chang, V. and Gallman, J. (2004), *Altitude testing of fuel cell systems for aircraft applications*, SAE 2004-01-3200.
289. Himansu, A. et al. (2006), "Hybrid solid oxide fuel cell/gas turbine system design for high altitude long endurance aerospace missions", *Star,* vol. 44, no. 15.
290. Pratt, J. et al. (2005), *Experimental evaluation and computer simulation of an air-breathing PEM fuel cell at aircraft flight altitudes*, AIAA 2005-953.
291. Pratt, J. W. et al. (2005), "Experimental performance of an air-breathing PEM fuel cell at high altitude conditions", *43rd AIAA Aerospace Sciences Meeting and Exhibit - Meeting Papers,* pp. 9363.
292. Spiegel, R. J. et al. (1999), "Fuel cell bus operation at high altitude", *Proceedings of the Institution of Mechanical Engineers, Part A: Journal of Power and Energy,* vol. 213, no. A1, pp. 57-68.
293. Tarroja, B. et al. (2009), *Thermodynamic design analysis of a solid oxide fuel cell gas turbine hybrid system for high-altitude applications*, AIAA 2009-4526.

General vehicle applications of fuel cells

294. Ahluwalia, R. K. et al. (2004), "Fuel economy of hydrogen fuel cell vehicles", *Journal of Power Sources,* vol. 130, no. 1-2, pp. 192-201.
295. Ahn, B.K. et al. (2006), "Fuel cell vehicle development at Hyundai-Kia Motors", *IEEE*, 2006.
296. Aso, S. et al. (2007), "Development of fuel cell hybrid vehicles in Toyota", *IEEE*, 2007.
297. Bernay, C. et al. (2002), "Prospects of different fuel cell technologies for vehicle applications", *Journal of power sources*, 108 (2002) 139-152.
298. Bork, C. (2009), *Development and testing of a PEM fuel cell system for an electric land speed vehicle*, Thesis, Ohio State University.
299. Bosco, A, *Hy-Wire – General motors fuel cell research*, Source unknown.
300. Cantemir, C. et al. (2004), *High performance fuel cell sedan*, SAE 2004-01-1003.
301. Chan, C.C. (2007), "The state of the airt of electric, hybrid and fuel cell vehicles", *Proceedings of the IEEE*, Vol. 95 No.4 April 2007, Pg. 704-718.
302. Eichenberg, D.J. (2005), *The fuel cell powered club car carryall*, NASA TM-2005-214024.
303. Fuel cells 2000 (2011), *Fuel cell specialty vehicles*, available at: www.fuelcells.org.

304. Fuel cells 2000 (2011), *Fuel cell vehicles (from Auto Manufacturers)*, available at: www.fuelcells.org.
305. Georgetown University, *Advanced vehicle development – The fuel cell bus program*, http://fuelcellbus.georgetown.edu/.
306. Gurski, S. and Nelson, D.J. (2002), *Design and integration challenges for a fuel cell hybrid electric sport utility vehicle*, SAE 2002-01-0095.
307. Haraldsson, K. et al. (2005), "Fuel cell buses in the Stockholm CUTE project – first experiences from a climate perspective", *Journal of power sources*, 145 (2005) 620-631.
308. Kohler, H. (2006), "Making sustainable transport a reality – a carmaker's view", *Cute conference*, Hamburg, May 10th 2006.
309. Kohout, L.L. (2002), "Fuel cell activities at the NASA Glann Research Centre", *Presentation at the Ohio Technical College*, July 10, 2002.
310. Lin, B. (2000), "Conceptual design and modeling of a fuel cell scooter for urban Asia", *Journal of power sources*, 86 (2000) 202-213.
311. Matsuo, S. (2003), "Honda fuel cell activities", in: *Handbook of fuel cells – fundamentals, technology and applications, Volume 4: Fuel cell technology and applications*, Edited by Vielstich, W.
312. Panik, F. (1998), "Fuel cells for vehicle applications in cars - bringing the future closer", *Journal of Power Sources,* vol. 71, no. 1-2, pp. 36-38.
313. Perez-Davis, M.A. (2002), *Fuel cell research at NASA GRC*, Report prepared for OakRidge National Laboratories (ORNL).
314. Rajashekara, K. (2000), *Propulsion system strategies for fuel cell vehicles*, SAE 2000-01-0369.
315. Rodrigues, A. et al. (2003), "General Motors/OPEL fuel cell activities – driving towards a successful future", in: *Handbook of fuel cells – fundamentals, technology and applications, Volume 4: Fuel cell technology and applications*, Edited by Vielstich, W.
316. Schmid, H.P. and Ebner, J. (2003), "Daimler-Chrysler fuel cell activities", in: *Handbook of fuel cells – fundamentals, technology and applications, Volume 4: Fuel cell technology and applications*, Edited by Vielstich, W.
317. Tran, D. and Cummins, M. (2001), *Development of the jeep commander 2 fuel cell hybrid electric vehicle*, SAE 2001-01-2508.
318. Truckenbrodt, A. (2004), *Fuel cell vehicles for future car concepts*, SAE 2004-21-0081.
319. U.S. Department of Energy (2004), *Fuel cell vehicle world survey 2003*.
320. US fuel cell council (2001), *Fuel cell power for vehicles*, www.usfcc.com.

Methanol fuel considerations

321. Allard, M. (2000), *Issues associated with widespread utilization of methanol*, SAE 2000-01-0005.
322. American Methanol Institute, *Beyond the internal combustion engine – the promise of methanol fuel cell vehicles,* www.methanol.org.
323. American Methanol Institute, *Methanol: an ideal hydrogen carrier*, www.methanol.org.
324. Lynn, J. (2009), Can methanol really make a dent in US oil demand?, available at: www.energy tribune.com/articles.cfm?aid=2131, (accessed 07/04/2010).
325. Methanol institute (2008), *Methanol safe handling manual*, prepared by Alliance Consulting International.
326. Nichols, R. J. (2003), "The methanol story: A sustainable fuel for the future", *Journal of Scientific and Industrial Research,* vol. 62, no. 1, pp. 97-105.
327. Nowell, G.P., *The promise of methanol fuel cell vehicles*, American Methanol Institute.
328. Panik, F. (2002), *Concept study of a methanol fuel cell vehicle*, SAE 2002-21-0069.
329. The American Methanol Institute, *Methanol fuel cell vehicles*, www.methanol.org.
330. Unknown, *Alcohol fuel*, available at: http://en.wikipedia.org/wiki/Alcohol_fuel, (accessed 07/04/2010).
331. Unknown, *Methanol*, available at: http://en.wikipedia.org/wiki/Methanol. (accessed 16/03/2010).
332. Unknown, *Spill free and secure refueling by Identic*.

Fuel cell system mass and volume considerations

333. Das, S. (2005), *Lightweight opportunities for fuel cell vehicles*, SAE 2005-01-0007.
334. Fluiter, T. (2008), *Design of lightweight electric vehicles*, Masters Thesis, University of Waikato.
335. Guinea, D.M. et al. (2007), "Specific weight: A challenge for a fuel-cell-powered electric helicopter", *Journal of aircraft*, 2007, Vol. 44 No. 6.

Fuel cell system design, simulation, operation and integration

336. Abul-Hawa, A.A. et al., *Control strategy for polymer electrolyte membrane fuel cell systems*, Source unknown.
337. Al-Baghdadi, M. A. R. S. (2005), "Modelling of proton exchange membrane fuel cell performance based on semi-empirical equations", *Renewable Energy,* vol. 30, no. 10, pp. 1587-1599.
338. Amphlett, J. C. et al. (1995), "A practical PEM fuel cell model for simulating vehicle power sources", *Annual Battery Conference on Applications and Advances, 10th, California State Univ , Long Beach, CA*.
339. Amphlett, J. C. et al. (1998), "Simulation of a 250 kW diesel fuel processor/PEM fuel cell system", *Journal of Power Sources,* vol. 71, no. 1-2, pp. 179-184.
340. Amphlett, J. et al. (1995), "Performance modeling of the Ballard Mark IV solid polymer electrolyte fuel cell I. Mechanistic model development", *Journal of the Electrochemical Society,* vol. 142, no. 1, pp. 1-8.
341. Amphlett, J. et al. (1995), "Performance modeling of the Ballard Mark IV solid polymer electrolyte fuel cell II. Empirical model development", *Journal of the Electrochemical Society,* vol. 142, no. 1, pp. 9-15.
342. Balasubramanian, B. et al. (1999), "Optimal operating temperature and pressure of PEM fuel cell systems in automotive applications", *ACS Division of Fuel Chemistry, Preprints,* vol. 44, no. 4, pp. 977-981.
343. Barbir, F. (2002), "PEM fuel cell stack design considerations", *AICHE spring national meeting*, March 2002, New Orleans, pg 520-530.
344. Barbir, F. et al. (1999), "Trade-off design analysis of operating pressure and temperature in PEM fuel cell systems", *Proceedings of the ASME*, Advanced energy systems division, 1999, Vol. 39.
345. Barbir, F. et al. (2000), *Design and operational characteristics of automotive PEM fuel cell stacks*. SAE 2000-01-0011.
346. Benziger, J. B. et al. (2006), "The power performance curve for engineering analysis of fuel cells", *Journal of Power Sources,* vol. 155, no. 2, pp. 272-285.
347. Boettner, D. D. et al. (2002), "Proton exchange membrane fuel cell system model for automotive vehicle simulation and control", *Journal of Energy Resources Technology, Transactions of the ASME,* vol. 124, no. 1, pp. 20-27.
348. Cunningham, J.M. et al. (2001), *A comparison of high-pressure and low-pressure operation of PEM fuel cell systems*, SAE 2001-01-0538.
349. Gummalla, M. et al. (2006), "Fuel cell airframe integration study for short-range aircraft, volume 1, aircraft propulsion and subsystems integration evaluation", *Star,* vol. 44, no. 23.
350. Haraldsson, K. and Alvfors, P. (2005), "Effects of ambient conditions on fuel cell vehicle performance", *Journal of Power Sources,* vol. 145, no. 2, pp. 298-306.
351. Hauer, K. et al. (2000), *Dynamic response of an indirect-methanol fuel cell vehicle*, SAE 2000-01-0370.
352. Heinzel, A. et al. (1998), "Membrane fuel cells - concepts and system design", *Electrochimica Acta,* vol. 43, no. 24, pp. 3817-3820.
353. Kazim, A. and Lund, P. (2006), "Basic parametric study of a proton exchange membrane fuel cell", *Proceedings of the Institution of Mechanical Engineers, Journal of Power and Energy,* vol. 220, no. A8, pp. 847-854.
354. Khater, H.A. et al. (2009), *Modeling of a methane fuelled proton exchange membrane fuel cell system*, AIAA 2009-4589.
355. Kolavennu, P. K. et al. (2006), "Design of a Fuel Cell Power System for Automotive Applications", *International Journal of Chemical and Reactor Engineering,* vol. 4, no. 4, pp. 1310.
356. Konrad, G. et al. (2003), "System design for vehicle applications: DaimlerChrysler", in: *Handbook of fuel cells – fundamentals, technology and applications, Volume 4: Fuel cell technology and applications*, Edited by Vielstich, W.
357. Kulikovsky, A. A. (2004), "The effect of stoichiometric ratio λ on the performance of a polymer electrolyte fuel cell", *Electrochimica Acta,* vol. 49, no. 4, pp. 617-625.
358. Masten, D.A. and Bosco, A.D. (2003), "System design for vehicle applications: GM/Opel", in: *Handbook of fuel cells – fundamentals, technology and applications, Volume 4: Fuel cell technology and applications*, Edited by Vielstich, W.

359. Miller, A. R. et al. (2007), "System design of a large fuel cell hybrid locomotive", *Journal of Power Sources,* vol. 173, no. 2, pp. 935-942.
360. Ogburn, M.J. (2000), *Systems integration, modeling and validation of a fuel cell hybrid electric vehicle*, Masters Thesis, Virginia Polytechnic and State University.
361. Perez-herranz, V. et al., *Effect of stoichiometric ratio on the performance of a 3kW PEM fuel cell stack*, source unknown.
362. Sharma, R.et al. (2004), *Water balance limitations in transportation PEM fuel cell systems*, AIAA 2004-5608.
363. Yang, W. et al. (1998), *Control challenges and methodologies in fuel cell vehicle development*, SAE 98C054.

Fuel cell opportunities and challenges

364. Emadi, A. and Williamson, S.S., *Fuel cell vehicles: Opportunities and challenges*, IEEE paper.
365. Stobart, R. (2008), *Fuel cell systems: a review of current issues*, Presentation to IET/IMechE seminar, 3rd December 2008.

Aerospace applications of fuel cells – general

366. Bradley, T. H. et al. (2007), "Development and experimental characterization of a fuel cell powered aircraft", *Journal of Power Sources,* vol. 171, no. 2, pp. 793-801.
367. Bradley, T.H. (2008), *Modeling, design and energy management of fuel cell systems for aircraft*, PhD thesis, Georgia Institute of Technology.
368. Breit, J. and Szydlo-Moore, J (2007), *Fuel cells for commercial transport airplanes needs and opportunities*, AIAA 2007-1390.
369. Fenton, J. et al. (2009), *Compact, lightweight and optimized fuel cells for space and aircraft power*, NASA CR-2009-215441.
370. Galvao, F.L. (2007), *Long range aircraft, an ideal case for fuel cell power*, SAE 2007-01-2957.
371. Gummalla, M. (2006), *Fuel cell airframe integratrion study for short-range aircraft – Volume 1: Aircraft propulsion and subsystems integration evaluation*, NASA CR-2006-214457/VOL1.
372. Hiebel, V. (2006), *Fuel cell systems for aeronautic applications – a clean way from kerosene to energy*, Airbus, ICAS 2006.
373. Himansu, A. (2006), *Hybrid solid oxide fuel cell/gas turbine system design for high altitude long endurance aerospace missions*, NASA TM-2006-214328.
374. Kohout, L.L. and Schmitz, P.C. (2007), *An analysis of fuel cell options for an all-electric unmanned aerial vehicle*, NASA TM-2007-214699.
375. Liang, A., *Emerging fuel cell developments at NASA for aircraft applications*, Source unknown.
376. Oman, H. (2004), "Fuel-cell powered airplane propulsion", *IEEE AESS Systems magazine*, January 2004.
377. Ordonez, J. and Luongo, C. (2009), *Modeling and optimization of fuel cell systems for aircraft applications*, NASA CR-2009-215441.
378. Rajashekara, K. et al. (2008), "Hybrid fuel cell power in aircraft", *IEEE industry applications magazine*, July/Aug 2008.
379. Santin, M. et al. (2008), "Technological aspects of gas turbine and fuel cell hybrid systems for aircraft: A review", *Aeronautical Journal,* vol. 112, no. 1134, pp. 459-467.
380. Upton, E. and Mavris, E. (2006), *Quiet, clean and efficient, but heavy – concerns for future fuel cell powered personal air vehicles*, SAE 2006-01-2436.
381. Wentz, W.H. and Mohamed, A.S. (2004), *Preliminary design considerations for zero greenhouse gas emission airplanes*, SAE 2004-01-1803.

Aerospace applications of fuel cells - small UAV research effort

382. Bradley, T.H. et al. (2007), *Flight test results for a fuel cell unmanned aerial vehicle*, AIAA 2007-32.
383. Bradley, T.H. et al. (2008), *Design studies for hydrogen fuel cell powered unmanned aerial vehicles*, AIAA 2008-6413.
384. Chiang, C. et al. (2008), *Systems integration of a hybrid PEM fuel cell/battery powered endurance UAV*, AIAA 2008-151.
385. Herweth, C. et al. (2006), *Development of a fuel cell powered UAV for environmental research*, AIAA 2006-237.
386. Moffitt, B.A. et al. (2006), *Design and performance validation of a fuel cell unmanned aerial vehicle*, AIAA 2006-823.
387. Moffitt, B.A. et al. (2006), *Design space exploration of small-scale PEM fuel cell long endurance aircraft*, AIAA 2006-7701.

388. Ofoma, U.C. and Wu, C.C. (2005), *Design of a fuel cell powered UAV for environmental research*, AIAA 2004-6384.
389. Soban, D.S. and Upton, E. (2005), *Design of a UAV to optimize use of fuel cell propulsion technology*, AIAA 2005-7135.

Aerospace applications of fuel cells – general aviation and larger UAVs

390. Balaba, D. et al. (2008), *A general aiviation aircraft retrofit with a PEM fuel cell*, SAE 2008-01-2914.
391. Bentz, J.C. (1992), *Fuel cell powered electric propulsion for HALE aircraft*, ASME 92-GT-404.
392. Dornheim, M.A. (2005), "Fuel-cell flier", *Aviation week and space technology*, June 27th 2005.
393. Kohout, L.L. and Schmitz, P.C. (2003), *Fuel cell propulsion systems for an all-electric personal air vehicle*, AIAA-2003-2867
394. Lapena-Rey, N. et al. (2007), *The Boeing fuel cell demonstrator airplane*, SAE 2007-01-3906.
395. Romeo, D et al. (2005), "ENFICA-FC: Environmental friendly inter-city aircraft and 2-seat aircraft powered by fuel cells electric propulsion", *AIRTEC 2nd Int. Conf. "Supply on the wings"*, 24-25 October 2005, Frankfurt/Main, Germany.
396. Romeo, G. et al. (2007), *ENFICA-FC: Preliminary survey & design of 2-seat aircraft powered by fuel cells electric propulsion*, AIAA 2007-7754.
397. Unknown (2009), "Fuel cells take off", *Eureka on campus magazine*, Summer 2009, Pg. 12-13.
398. Youngblood, J.W. et al. (1984), *Design of long-endurance unmanned airplanes incorporating solar and fuel cell propulsion*, AIAA 84-1430.

Aerospace applications of fuel cells – APU replacement

399. Daggett, D.L. et al. (2003), *Fuel cell APU for commercial aircraft*, AIAA 2003-2660.
400. Eelman, S. et al. (2004), *Fuel cell APU's in commercial aircraft – an assessment of SOFC and PEMFC concepts*, 24th ICAS 2004.
401. Pachidis, V. (2001), *Cryoplane-Parts 1 and 2: investigation of a fuel cell as an aircraft APU,* MSc thesis, Cranfield University.

Cooling system design and analysis

402. Ahn, J. and Choe, S. (2008), "Coolant controls of a PEM fuel cell system", *Journal of Power Sources,* vol. 179, no. 1, pp. 252-264.
403. Brevoort, M. J. and Naca (1941), *Radiator design,* NACA report, Washington, D.C.
404. Callister, J.R. et al. (1997), *The design of automobile and racing car cooling systems*, SAE 971835.
405. Dong, J. et al. (2007), "Heat transfer and pressure drop correlations for the multi-louvered fin compact heat exchangers", *Energy Conversion and Management,* vol. 48, no. 5, pp. 1506-1515.
406. Emmenthal, K.D. and Hucho W.H. (1974), *A rational approach to automotive radiator systems design*, SAE 740088.
407. Hager, J. and Schickmair, L. (2005), *Fuel cell vehicle thermal management system simulation in contrast to conventional vehicle concepts*, SAE 2005-01-2050.
408. Hartshorn, A. S., Seddon, J. (1944), *Note on the radiator requirements for high powered liquid-cooled engines.* RAE TN Aero 1418
409. Kern, J. and Eitel, J. (1993), *State of the art and future developments of aluminum radiators for cars and trucks*, SAE 931092.
410. Kroger, D.G. (1984), *Radiator characterization and optimization*, SAE 840380.
411. Mayer, H., *Cooling systems for automotive conversions*, available at: www.ch601.org/resources/cooling_systems1.htm. (accessed 06/05/2010).
412. Meredith, F. W. (1935), *Note on the cooling of aircraft engines with special reference to ethylene glycol radiators enclosed in ducts. R&M No. 1683*
413. Miley, S. J. "A review of liquid cooled aircraft engine installation aerodynamics", *1986 AIAA General Aviation Technology Conference; Anaheim, CA; Sep 29-Oct 1.*
414. Morse, J.D. (1967), *Engine cooling radiators*, SAE 670525.
415. Nenden, J. and Sunden B. (1999), *A method to determine the thermal characteristics of radiators*, IMechE Report C543/102/99.
416. Nolan, J. and Kolodziej, J. (2010), "Modeling of an automotive fuel cell thermal system", *Journal of Power Sources,* vol. 195, no. 15, pp. 4743-4752.
417. Oliet, C. et al. (2007), "Parametric studies on automotive radiators", *Applied Thermal Engineering,* vol. 27, no. 11-12, pp. 2033-2043.
418. Renn, V. and Gilhaus, A. (1986), "Aerodynamics of vehicle cooling systems", *J.Wind Eng.Ind.Aerodynamics,* vol. 22, no. 2-3, pp. 339-346.

419. Rubert, K. F., Knopf, G. S. (1942), *A method for the design of cooling systems for aircraft power-plant installations; NACA ARC 5842*
420. Srun, N. (1999), *A simple engine cooling system simulation model*, SAE 1999-01-0237.
421. Tifford, A. N. (1942), *Radiator design and installation - 2,* NACA report.
422. Tifford, A. N. and Wood, G. P. (1942), *Generalized equations for selection charts for heat exchangers in aircraft, NACA ACR 5953.*
423. Wood, G. P. and Brevoort, M. J. (1943), *Design, selection, and installation of aircraft heat exchangers,* NACA report.

General reference data for fuel cell system design and integration

424. Brooks, C. and Huff, I. (2006), *The effect of altitude in relative humidity*. Source unknown.
425. Carvill, J. (1994), *Mechanical engineer's data handbook*, Butterworth-Heinemann, Boston.
426. Dorf, R.C. (2004), *Handbook of engineering tables*, CRC Press, Washington.
427. Dudley, D. (1994), *Handbook of practical gear design,* CRC Press, Boca Raton, Fl.
428. Garrett, D. F. (1992), *Aircraft systems and components,* Iap, Casper,WY.
429. Gülich, J.F. (2010), *Centrifugal pumps*, 2nd ed., Springer-Verlag, Berlin, Heidelberg.
430. Hoerner, S. F. (1965), *Fluid-dynamic drag: practical information on aerodynamic drag and hydrodynamic resistance,* 1965 edition, The Author, Midland Park, N.J.
431. Incropera, F.P. and DeWitt, D.P. (2001), *Fundamentals of heat and mass transfer,* 5th ed, Wiley, New York.
432. Labajo, J.L. et al. (1991), "An equation relating temporal changes of relative humidity and temperature: case of variable intervals in time", *Atmosfera*, 1991, pg. 257-264.
433. Lombardo, D. A. (1993), *Advanced aircraft systems,* Tab Books, Blue Ridge Summit.
434. Ozisik, M.N. (1985), *Heat transfer a basic approach,* McGraw-Hill, New York.
435. *Radial, mixed and axial-flow pumps – Introduction*, ESDU 80030.

Electric vehicle design background

436. Choi, T.P. et al. (2005), *Creation of a design framework for all-electric aircraft propulsion architectures*, AIAA 2005-5549.
437. Gur, O. and Rosen, A. (2009), "Optimising electric propulsion systems for unmanned aerial vehicles", *J. of Aircraft*, Vol. 46, No. 4, Pg. 1340-1353.
438. Hodkinson, R. and Fenton, J. (2001), *Lightweight electric/hybrid vehicle design,* Butterworth-Heinemann, Oxford.
439. Husain, I. (2003), *Electric and hybrid vehicles: design fundamentals,* CRC Press, Boca Raton Fl.
440. Nam, T. et al. (2005), *A generalized aircraft sizing method and application to electric aircraft*, AIAA 2005-5574.
441. Westbrook, M. H. (2001), *The electric and hybrid electric car,* Institute of Electrical Engineers and Society of Automotive Engineers, London.

Traction components an overview and selection

442. Burke, A.F. (2007), "Batteries and ultracapacitors for electric, hybrid and fuel cell vehicles", *Proceedings of the IEEE*, Vol. 95, No. 4, April 2007.
443. Hashemnia, N. and Asaei, B. (2008), "Comparative study of using different electric motors in the electric vehicles", *Proceedings of the 2008 International conference on electrical machines*.
444. Krishnan, R. and Bharadwaj, A.S. (1991), *A comparative study of various motor drive systems for aircraft applications*, IEEE paper.
445. Nanda, G. and Kar, N.C. (2006), "A survey and comparison of characteristics of motor drives used in electric vehicles", *IEEE CCECE/CCGEI*, Ottawa, May 2006.
446. Perez-Davis, M.A. et al. (2001), *Energy storage for aerospace applications*, NASA TM-2001-211068.
447. Posma, B.W. (2002), "Saminco 220 kW traction drive for fuel cell and diesel electric vehicles", *Presented at: HEV market TOPTEC: Challenges and opportunities for trucks, buses and cars*, June 26-27 2002, Florida.
448. Satoh, H. et al. (2004), *Development of traction motor for fuel cell vehicle*, SAE 2004-01-0567.
449. West, J.G.W. (1994), "DC, induction, reluctance and PM motors for electric vehicles", *Power Engineering Journal 1994*, Pg. 77-88.
450. Xue, X.D. et al. (2008), "Selection of electric motor drives for electric vehicles", *2008 AUPEC Conference*.
451. Zenith, F. and Skogestad, S. (2005), "Control of a fuel-cell powered DC electric vehicle motor", *AiChE Annual Meeting 2005*.

Solid oxide fuel cells

452. Bundschuh, N. et al. (2006), *A comparison of solid oxide fuel cell designs as energy source for the all-electric aircraft*, 25th ICAS 2006.
453. Cable, T.L. and Sofie, S.W. (2007), *A symmetrical planar SOFC design for NASA's high specific power density requirements*. Source unknown.
454. Mehdi, I. S. et al. (2005), "Application of solid oxide fuel cells to aircraft", *Proceedings - Electrochemical Society,* Vol. PV 2005-07, pp. 249.
455. Sun, C. and Stimming, U. (2007), "Recent anode advances in solid oxide fuel cells", *Journal of Power Sources,* vol. 171, no. 2, pp. 247-260.

Regenerative fuel cells and solar power

456. Bents, D.J. (2006), "Hydrogen-oxygen PEM regenerative fuel cell development at NASA Glenn Research Centre", *Prepared for 2006 fuel cell seminar*, Honolulu.
457. Bents, D.J. (2007), "Solar airplanes and regenerative fuel cells", *NASA presentation to 43rd annual I.R.I.S. show*, Mayfield, Oct 9th 2007.
458. Dornheim, M.A. (2005), "Perpetual motion", *AW&ST*, June 27th 2005, Pg 48-50.
459. Fellner, J.P. (2000), *Primary and regerative fuel cells for UAV applications*, SAE 2000-01-3660.
460. Hall, D.W. et al. (1983), *A preliminary study of solar powered aircraft and associated power trains*, NASA CR-3699.
461. Oman, H. (2002), "Fuel cells power aerospace vehicles", *IEEE AESS Systems magazine*, February 2002.
462. Ross, H. (2008), *Fly around the world with a solar powered airplane*, AIAA 2008-8954.
463. Unknown, *Solar powered multipurpose remotely powered aircraft*, NASA N93-29722.

Direct methanol fuel cells

464. Apanel, G. and Johnson, E. (2004), "Direct methanol fuel cells – ready to go commercial?", *Fuel Cells Bulletin,* vol. 2004, no. 11, pp. 12-17.
465. Halpert, G. et al. (1997), "An update of direct methanol fuel cell technology", JPL, *Windsor workshop of transportation fuels*, Canada, June 10th 1997.
466. Halpert, G. et al. (1999), "Direct methanol, liquid-feed fuel cell progress and prospects", *Presented at IMTOF '99*, Colorado, June 21st 1999.
467. Narayanan, S.R. et al. (2003), *Status of direct methanol fuel cells*, AIAA 2003-5943.

A1 Baseline UCAV and MALE performance

This section gives an overview of the methods used to analyse the performance of the baseline UCAV and MALE designs. The analysis methods presented enable the optimal thrust requirements to be determined at each stage in the flight, which in turn is used to determine the engine fuel consumption. These results can also be used to determine that there is sufficient thrust available from the engine at all phases throughout the flight.

A1.1 Baseline aircraft performance analysis an overview

The performance analysis for the baseline UCAV is broken down into the following stages corresponding to its design flight profile.

1. Take-off ground roll
2. Take-off rotation
3. Take-off climb out – To clear a screen height of 10.668m.
4. Take-off second segment climb – To achieve a vertical velocity of 12.5m/s.
5. Climb – Climb and accelerate to an altitude of 12.192km and speed of Mach 0.9. at a constant vertical velocity of 12.5m/s.
6. Cruise outbound – Cruise at Mach 0.9 and 12.192km over a distance of 1389km.
7. Cruise inbound – Cruise Mach 0.9 and 12.192km over a distance of 1389km.
8. Descent - Descend to an altitude of 15.24m and decelerate to a speed of Mach 0.1764 at a constant vertical descent speed of 10m/s.
9. Landing approach and flare - Descend from a screen height of 15.24m.
10. Landing ground run – To bring the aircraft to rest.

In a similar way, the performance analysis for the baseline MALE is broken down into the following stages corresponding to its design flight profile.

1. Take-off ground roll
2. Take-off rotation
3. Take-off climb out – To clear a screen height of 10.668m.
4. Take-off second segment climb – To achieve a vertical velocity of 6.1m/s.
5. Climb phase 1 – Climb and accelerate to an altitude of 4.572km and speed of Mach 0.3488 over a distance of 111.12km.
6. Climb phase 2 – Climb to 7.620km at Mach 0.3488 over a distance of 926km.
7. Loiter – Loiter for 35 hours at an altitude of 7.620km and speed of Mach 0.2507.
8. Descent phase 1 – Descend to 4.572km at Mach 0.3488 over a distance 926km.
9. Descent phase 2 – Descend to sea level and decelerate to a speed of Mach 0.1073 over a distance of 111.12km.
10. Loiter (reserve) – Loiter for 1 hour at sea level and a speed of Mach 0.1046.
11. Landing approach and flare – Descend from a screen height of 10.668m.
12. Landing ground run – To bring the aircraft to rest.

The different performance conditions of each flight phase necessitate the need for a different analysis for each phase as will be discussed in the sections that follow. At the heart of each analysis is fundamental equations derived from Newton’s second law for the resultant forces acting in the aircraft in the X and Z directions respectively. To

improve the accuracy of the results, the flight phase is broken down into a number of smaller steps which can be analysed sequentially.

A1.2 Take-off performance analysis

The analysis procedure for take-off performance is generic to both the UCAV and MALE, the difference being the field performance and regulatory clearance screen height. The take-off phase is taken to include, ground roll, rotation, climb-out and second segment climb, each of which will be presented in the sections which follow.

A1.2.1 Take-off ground roll

During the take-off ground roll phase the aircraft accelerates along the runway until it reaches its specified take-off rotation speed. In this analysis, the engine is held at its maximum thrust and the time and ground distance determined when the velocity of the aircraft reaches the desired value for rotation. The only difference between the analyses of the UCAV and MALE is the target speed V_1, as given in the flowchart below.

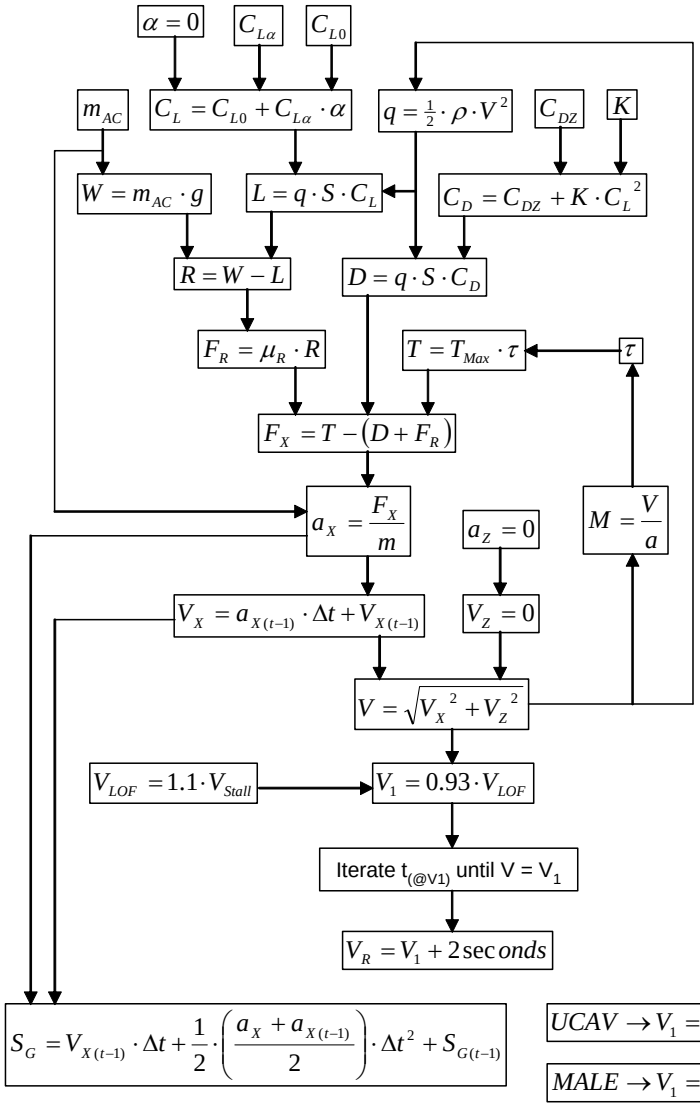

Figure A-1

A1.2.2 Take-off rotation

During the take-off rotation phase, the aircraft gradually rotates about its main wheels to raise the nose of the aircraft. During this time, the angle of attack of the wings and thus the lift gradually increases until the entire weight of the aircraft is supported by the wings. In this analysis, the aircraft angle of attack is assumed to increase by 1 degree per second until the weight of the aircraft is supported by the wings. The time and ground distance covered until this condition is satisfied can be determined respectively. This analysis is identical for the MALE and UCAV as presented in the flowchart below.

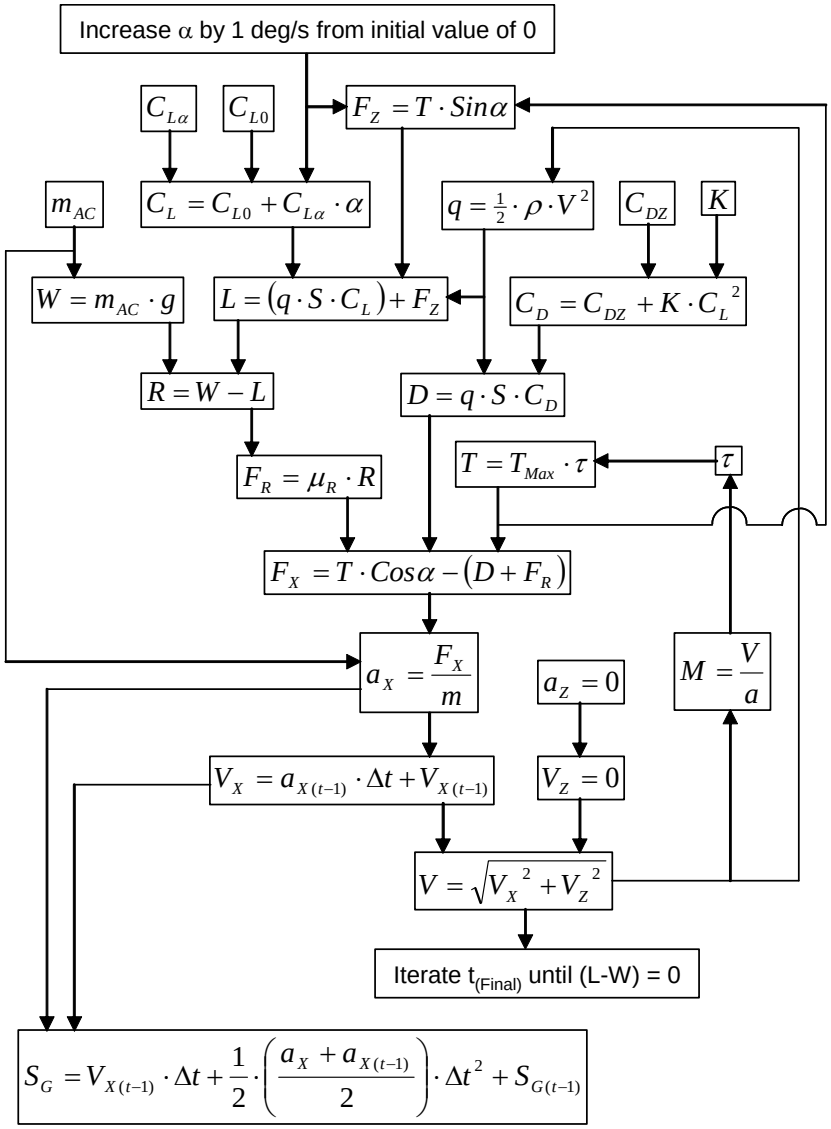

Figure A-2

A1.2.3 Take-off climb out

During the take-off climb out phase the aircraft initially climbs to a height sufficient to clear a screen height specified by the airworthiness regulations. In this analysis, the aircraft is assumed to maintain the angle of attack attained at the end of the take-off rotation. The time and ground distance covered until the aircraft reaches the screen

height can then be determined. This analysis is identical for the MALE and UCAV as presented in the flowchart below.

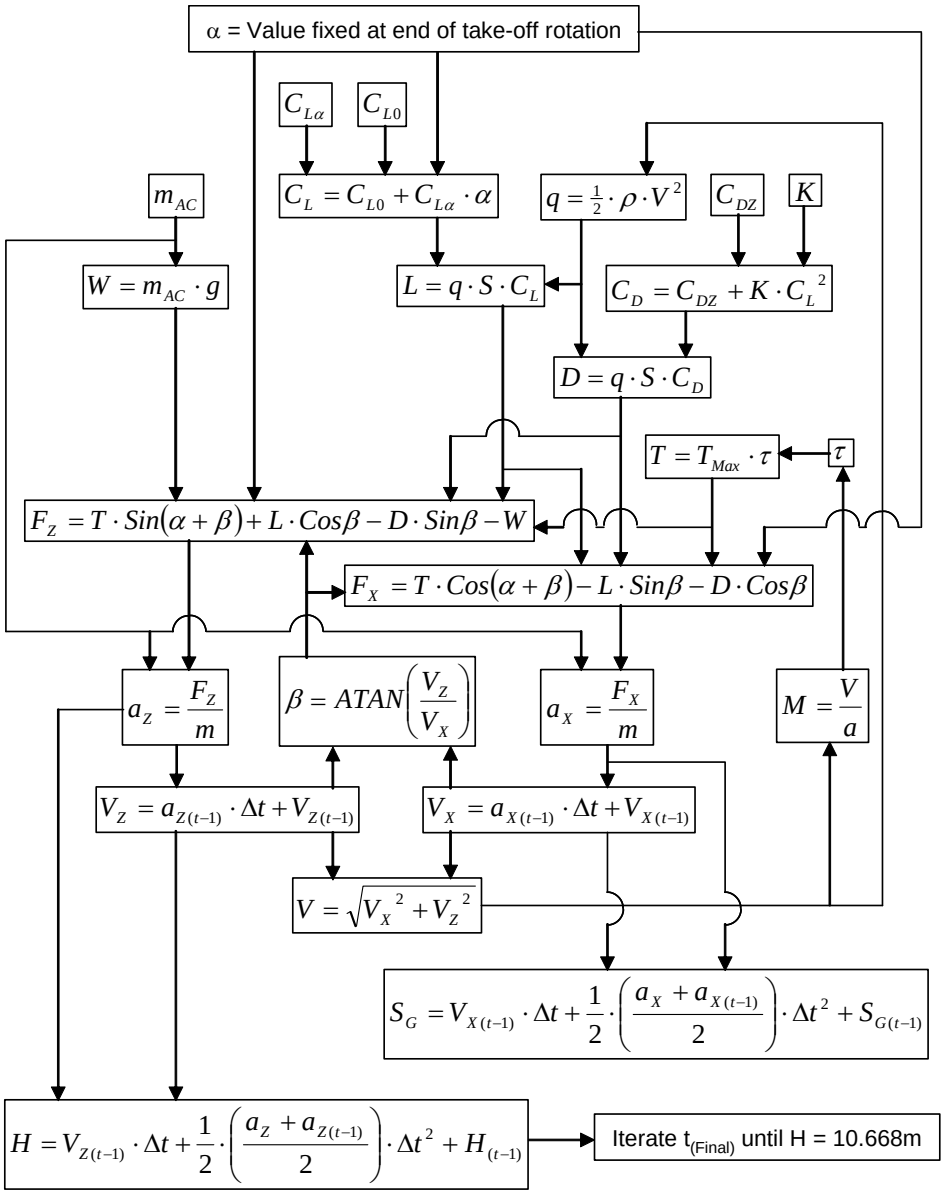

Figure A-3

A1.2.4 Second segment climb

The second segment climb phase is the final take-off stage, during which the aircraft attains a desired aircraft vertical velocity in preparation for the main climb phase. In this analysis, the aircraft is assumed to maintain the angle of attack attained during the initial take-off climb out phase. The time and ground distance covered to complete this phase can then be determined as the condition when the desired vertical velocity is met. The only difference between the analyses of the UCAV and MALE is the target vertical velocity V_Z as given in the flowchart below.

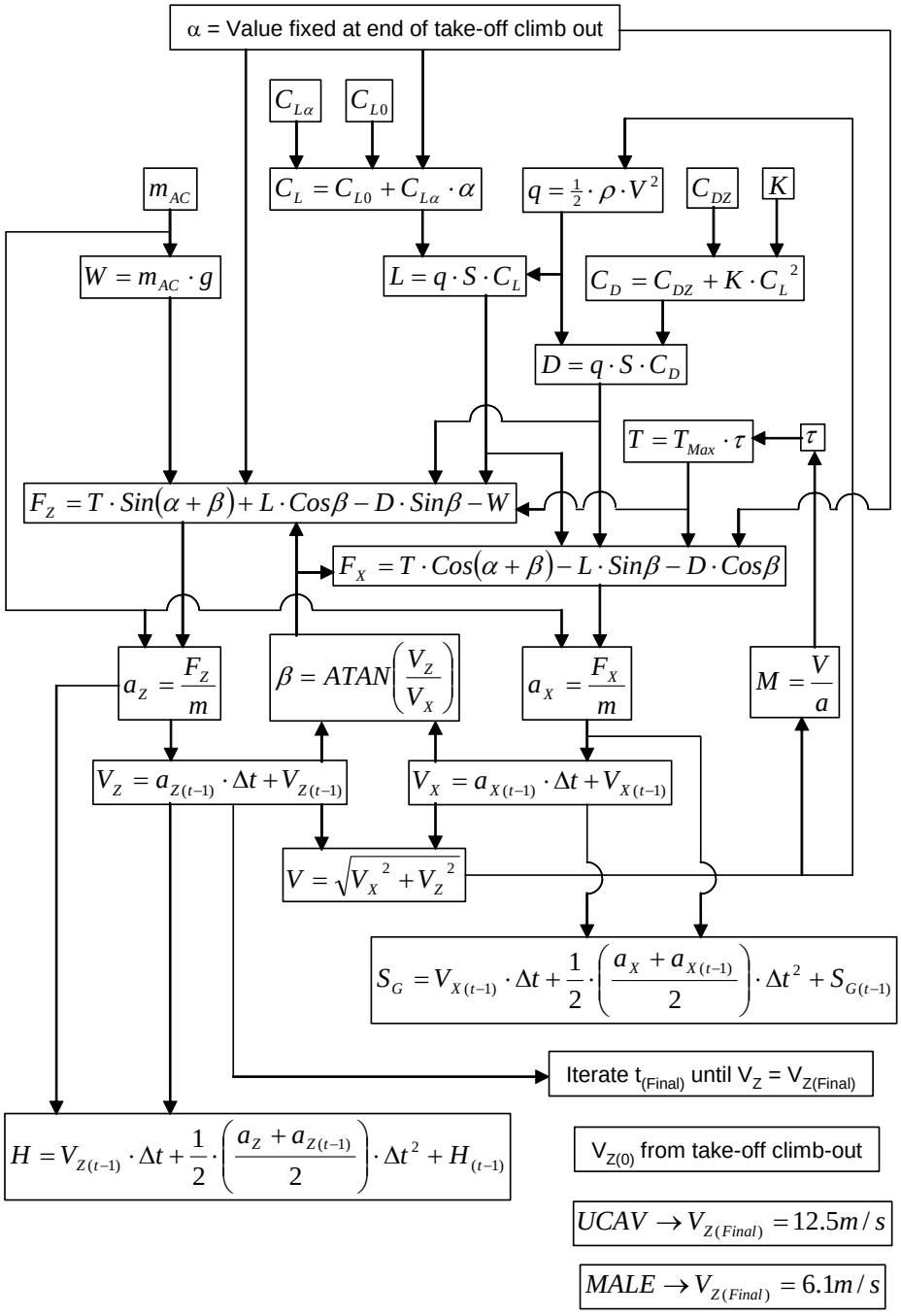

Figure A-4

A1.3 Climb performance analysis

The analysis procedure is different for the climb performance of the UCAV and MALE configurations. In the case of the UCAV, the aircraft not only climbs to the desired cruise altitude but also accelerates to the desired cruise speed. In the case of the MALE, the climb phase is broken down into 2 stages. During the first stage the aircraft climbs to an intermediate altitude and accelerates to its cruise speed. In the second stage, the aircraft climbs at a constant speed climb to its final loiter altitude. The analysis procedure for each of these will be discussed in the sections which follow.

A1.3.1 UCAV climb

During the climb phase, the UCAV climbs and accelerates to its cruise altitude and speed of 12.192km and Mach 0.9 respectively. During this analysis, the flight path of the aircraft is fixed and the angle of attack of the aircraft is treated as a variable which is iterated to find the optimal solution corresponding to minimum thrust. The total altitude attained and distance covered can also be determined for each step to verify the results. The accuracy of the solution can be seen to be dependent on the number of steps used and the corresponding time interval of each step. The analysis is presented in the flowchart below.

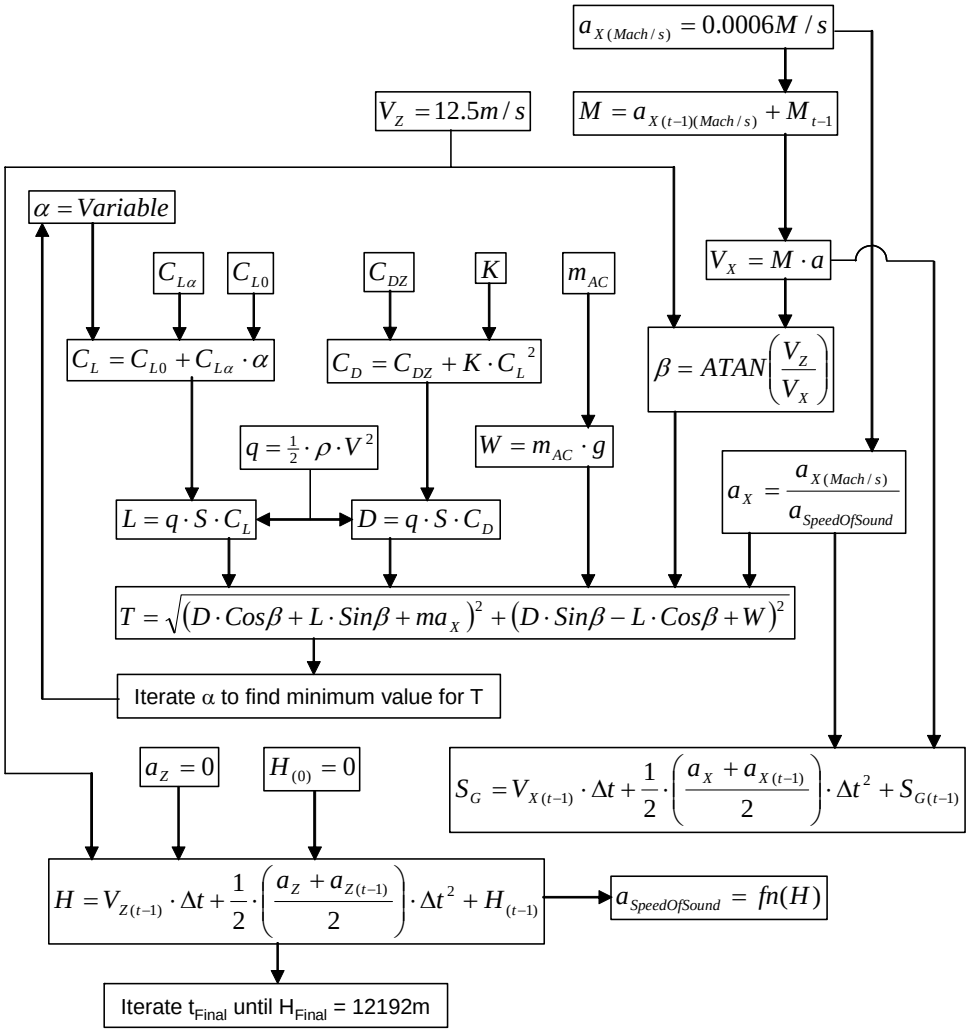

Figure A-5

A1.3.2 MALE first climb stage

During the first climb phase, the MALE climbs to an intermediate altitude of 4.572km and accelerates to the desired second climb phase speed of Mach 0.3488. During this analysis, the angle of attack of the aircraft is treated as a variable which is iterated to find the optimal solution corresponding to minimum thrust. This flight phase has proven to be the most critical phase with respect to thrust requirements and a second solution

stage iterates the climb angle to find to optimal flight path to meet the thrust requirements. As it is not sensible to operate an engine at full power for long periods, a percentage of the full power is also assumed (which is 97.5% in this analysis). The total altitude attained and distance covered can also be determined for each step to verify the results. The analysis is presented in the flowchart below.

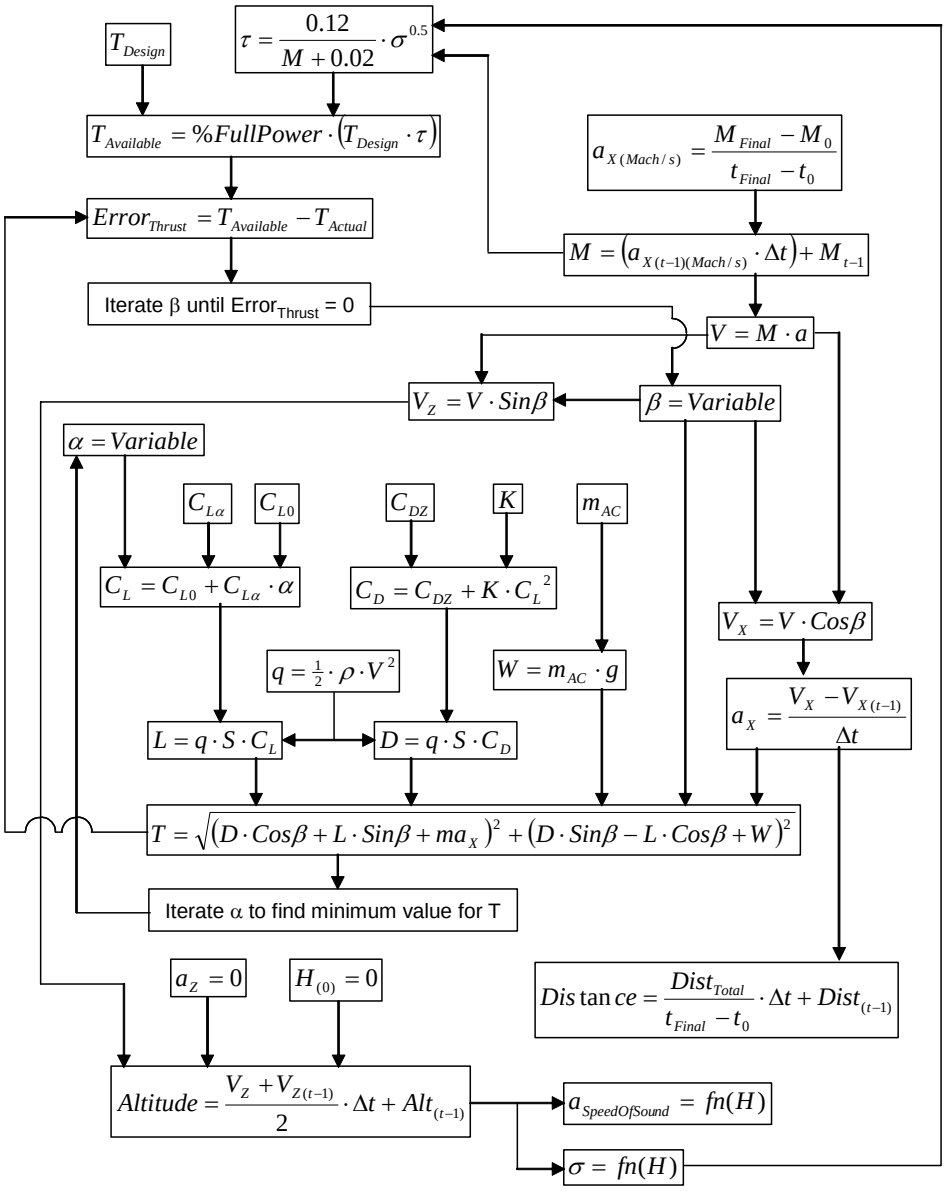

Figure A-6

A1.3.3 MALE second stage

During the second climb phase, the MALE climbs to its final loiter altitude of 7.620km at a constant climb speed of Mach 0.3488. During this analysis, the angle of attack of the aircraft is treated as a variable which is iterated to find the optimal solution corresponding to minimum thrust. In contrast to the last stage, the climb angle attains a fixed value in this analysis. The analysis is presented in the flowchart below.

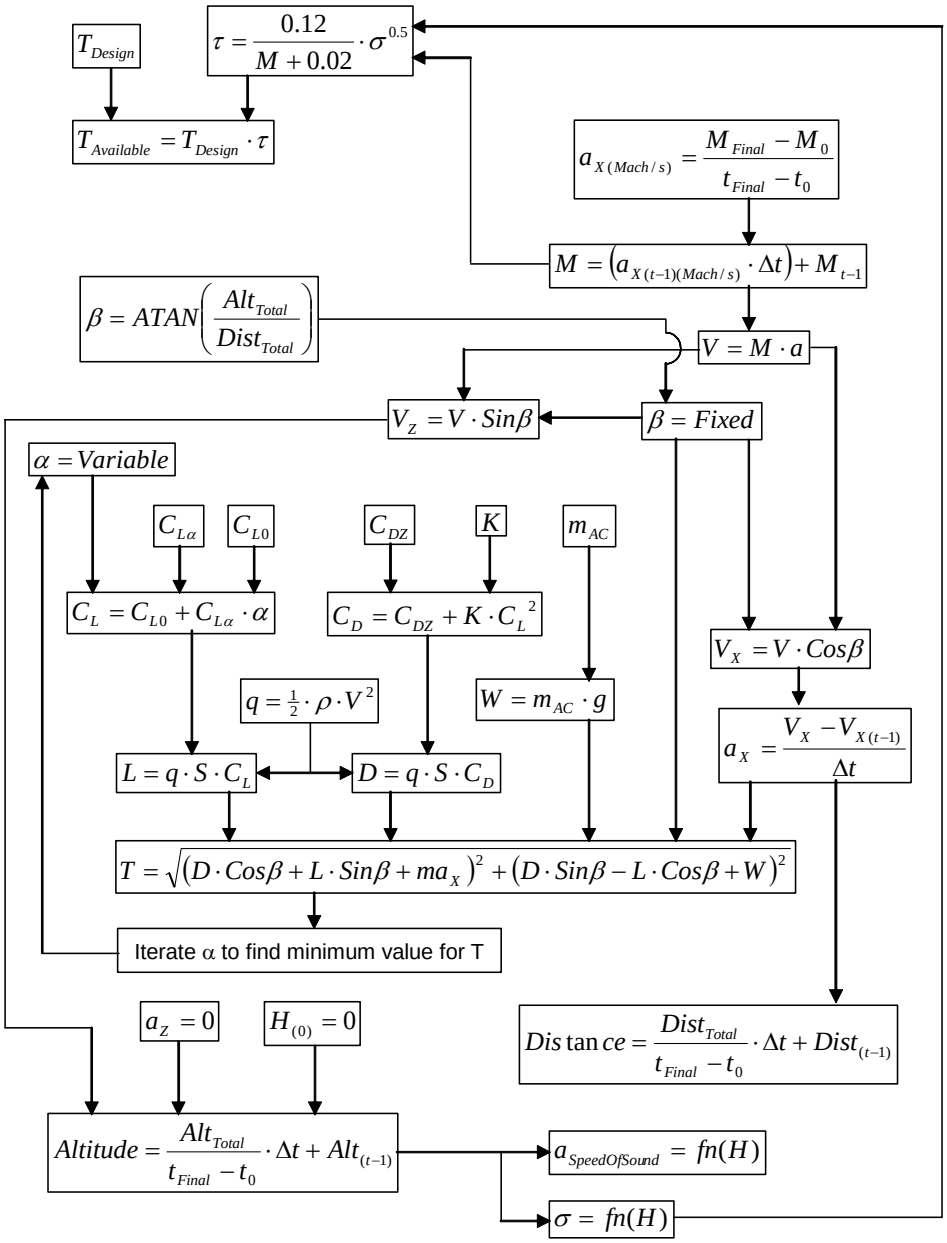

Figure A-7

A1.4 Cruise and loiter performance analysis

The analysis procedure for the cruise and loiter phases of the UCAV and MALE configurations respectively is essentially the same. In the case of the UCAV, we have an outbound and inbound cruise phase, both of which are at an altitude of 12.192km and speed of Mach 0.9. In the case of the MALE, the main loiter phase is at an altitude of 7.62km, and at a speed of Mach 0.2507 for 35 hours. In addition, to this there is a 1 hour loiter phase at sea level and a speed of Mach 0.1046. Both the cruise and loiter phases follow the same analysis procedure whereby the flight phase is fixed and the aircraft angle of attack is a variable which is iterated to find the minimum value of engine thrust. This procedure is presented in the flowchart below, with the only

difference between the analyses of the UCAV and MALE being the flight speed and altitude.

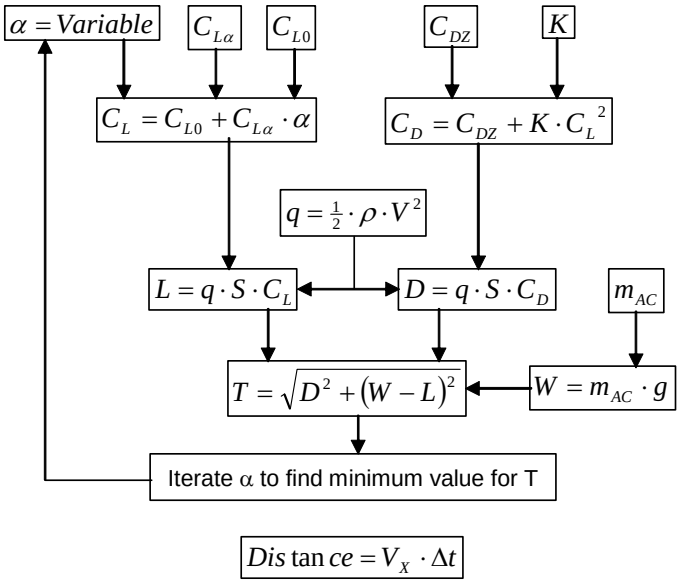

Figure A-8

A1.5 Descent performance analysis

The analysis procedure to determine the descent performance is different for the UCAV and MALE configurations. In the case of the UCAV, the aircraft descends to its approach altitude at a constant vertical descent velocity while decelerating to its approach speed. In the case of the MALE, the descent phase is broken down into 2 stages. The first stage involves a constant speed descent to an intermediate altitude. The second stage then involves a simultaneous descent to sea level and a deceleration. The analysis procedure for each of these will be discussed in the sections which follow.

A1.5.1 UCAV descent

During the descent phase, the UCAV descends from its cruise altitude to a landing approach altitude of 15.24m at a constant vertical velocity of 10m/s. During this time it also decelerates from its cruise speed to an approach speed of Mach 0.1764. During this analysis, the flight path of the aircraft is fixed and its angle of attack is treated as a variable which is iterated to find the optimal solution corresponding to minimum thrust. The total altitude lost and distance covered can also be determined for each step to verify the results. The analysis is presented in the flowchart below.

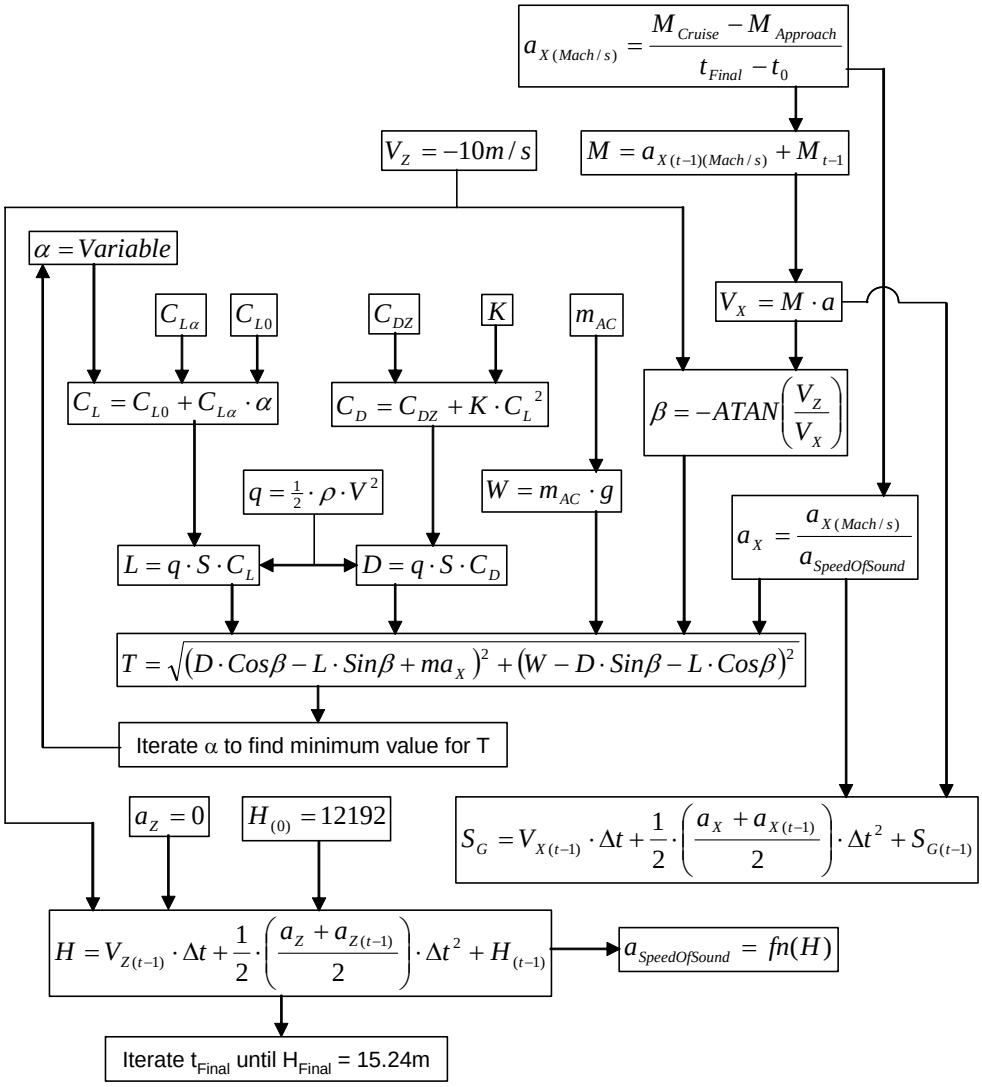

Figure A-9

A1.5.2 MALE first descent stage

During the first descent phase, the MALE descends from its loiter altitude to an intermediate altitude of 4.572km at a constant speed of Mach 0.3488. During this analysis, the flight path of the aircraft is fixed and the angle of attack of the aircraft is treated as a variable which is iterated to find the optimal solution corresponding to minimum thrust. The analysis is presented in the flowchart below.

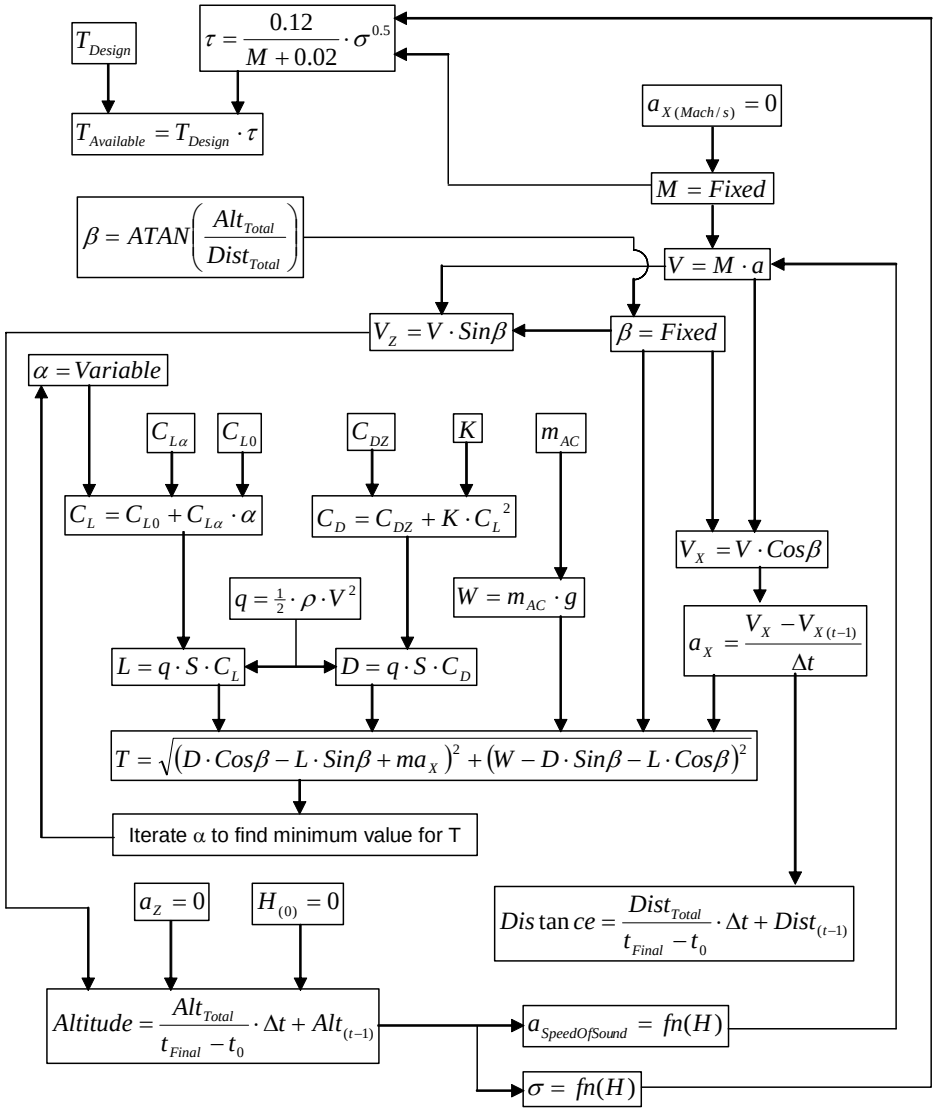

Figure A-10

A1.5.3 MALE second descent stage

During the second descent phase, the MALE descends from its intermediate altitude of the first descent stage to sea level while decelerating to a speed of Mach 0.1073. During this analysis, the angle of attack of the aircraft is treated as a variable which is iterated to find the optimal solution corresponding to minimum thrust. The total altitude lost and distance covered can also be determined for each step to verify the results. The analysis is presented in the flowchart below.

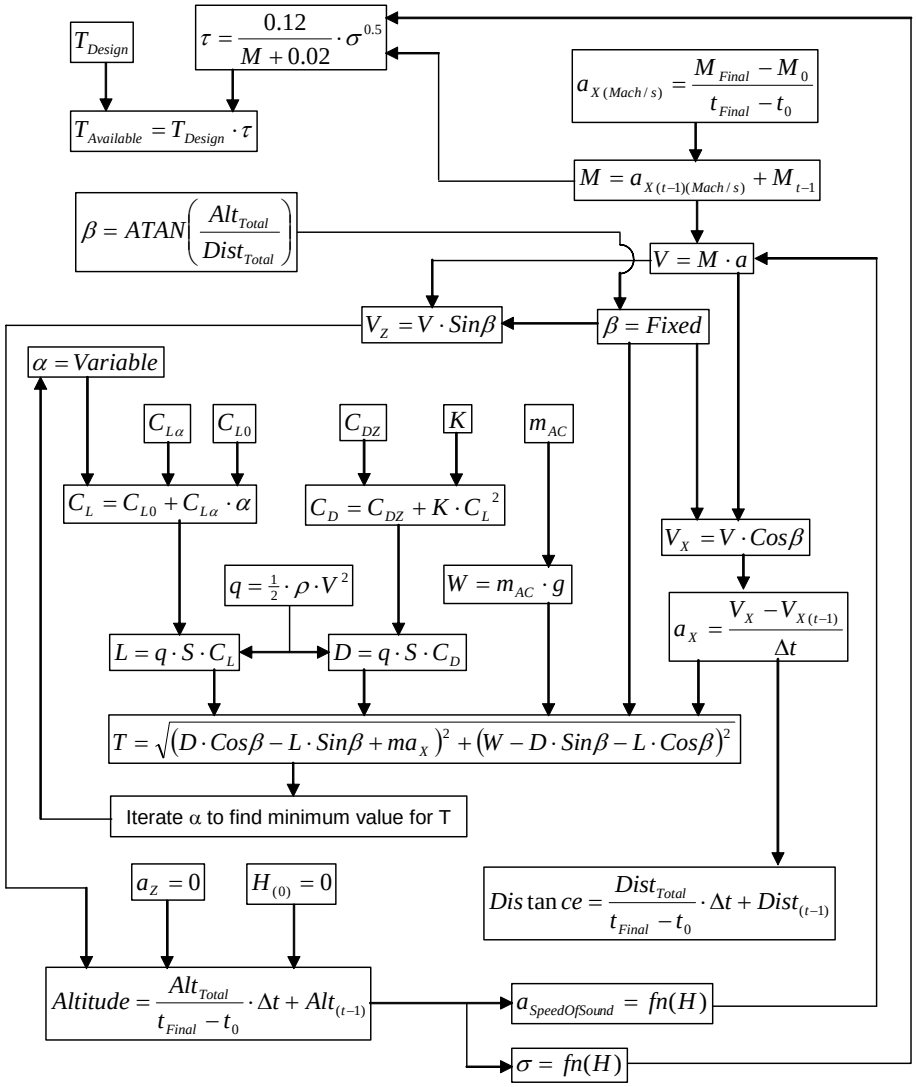

Figure A-11

A1.6 Landing performance analysis

The analysis procedure for landing performance is generic to both the UCAV and MALE, the difference being the field performance, approach speed and regulatory clearance screen height. The landing phase is taken to include: landing approach, flare and ground run, each of which will be presented in the sections which follow.

A1.6.1 Landing approach and flare

The landing approach and flare phase starts at the regulatory screen height and approach speed. The aircraft then descends at a vertical descent velocity specific to that configuration while decelerating to its touchdown speed. As the aircraft speed is reduced, the aircraft angle of attack must be increased accordingly in order to maintain sufficient lift to maintain the desired descent velocity. This gives rise to the characteristic landing flare manoeuvre, whereby the nose of the aircraft is rotated as the

aircraft approaches the ground. This manoeuvre also ensures that the main landing gear wheel makes contact with the ground first to bear the impact of the landing.

During this analysis, the angle of attack of the aircraft is treated as a variable which is iterated to find the optimal solution corresponding to minimum thrust. The total altitude lost and distance covered can also be determined for each step. This phase ends when the aircraft velocity equals the touchdown velocity. The only difference between the analyses of the UCAV and MALE is the vertical decent velocity V_Z and the approach screen height as given in the flowchart below

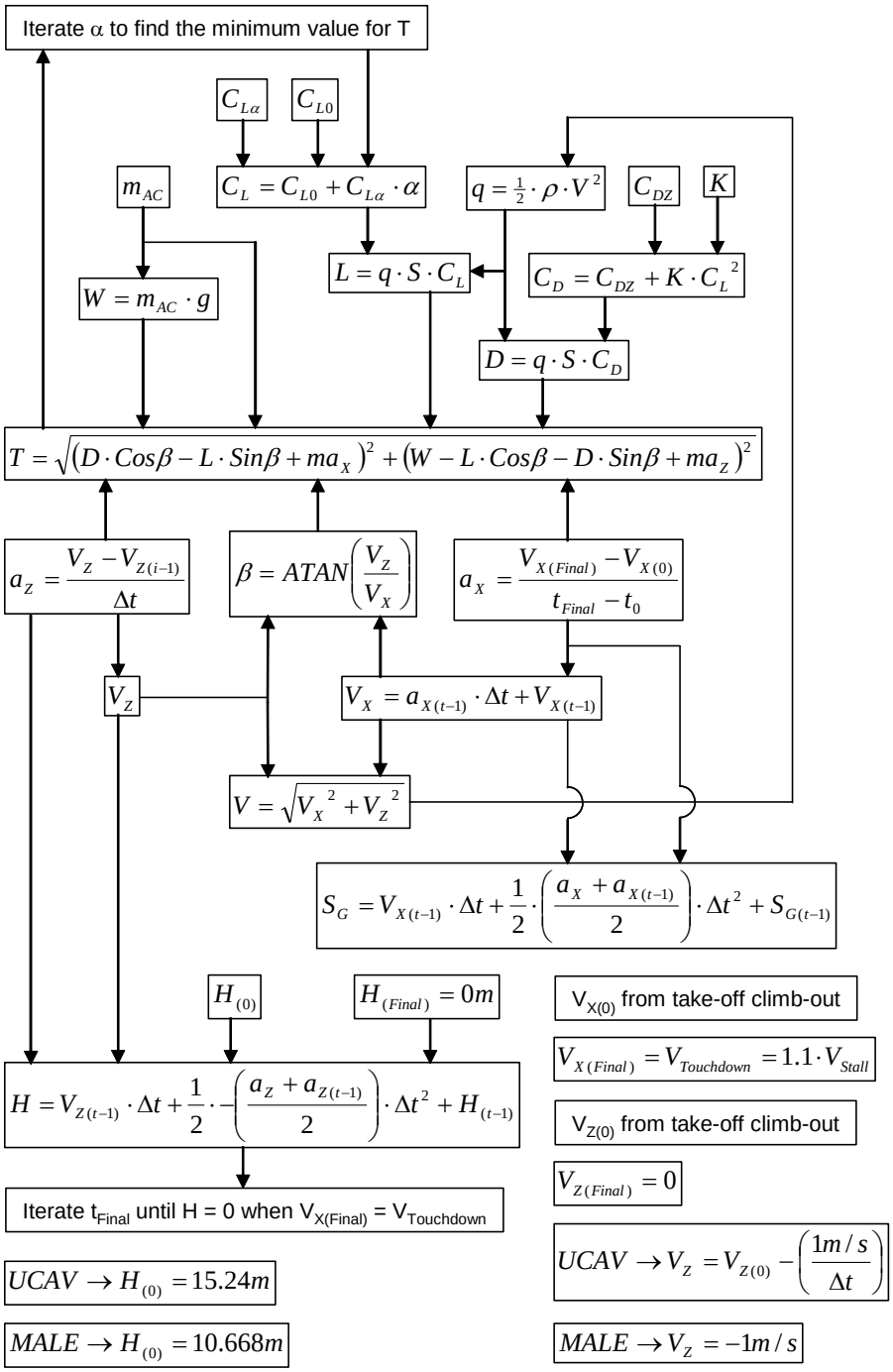

Figure A-12

A1.6.2 Landing ground roll

During the landing ground roll phase, the aircraft decelerates from its touchdown speed along the runway until the aircraft comes to a standstill. In this analysis, the engine thrust is assumed to be exponentially decreased from its landing approach setting at 0.5 second intervals. At the start of this phase, only the main wheels are on the ground and the angle of attack of the aircraft must be gradually reduced until the nose wheel makes full contact with the ground. This analysis is identical for the MALE and UCAV as presented in the flowchart below.

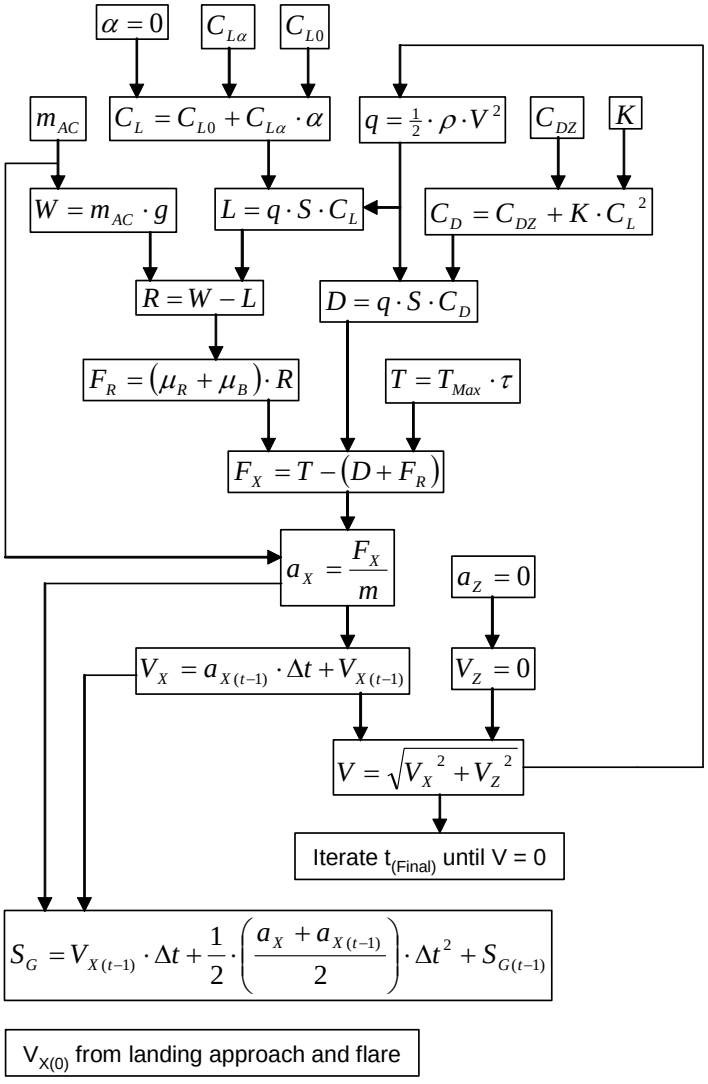

Figure A-13

A1.7 UCAV fuel consumption, weight variation and engine characteristics

As the aircraft flies the course of its flight profile, fuel is gradually consumed which leads to a reduction in the weigh of the aircraft. The approach used to predict the fuel consumption and therefore the weight of the aircraft at any point follows the same procedure for each flight phase. Using generic fuel consumption relations from Howe

[1], this process can be seen to be a function of the aircraft speed, altitude and engine thrust as presented in the flowchart below.

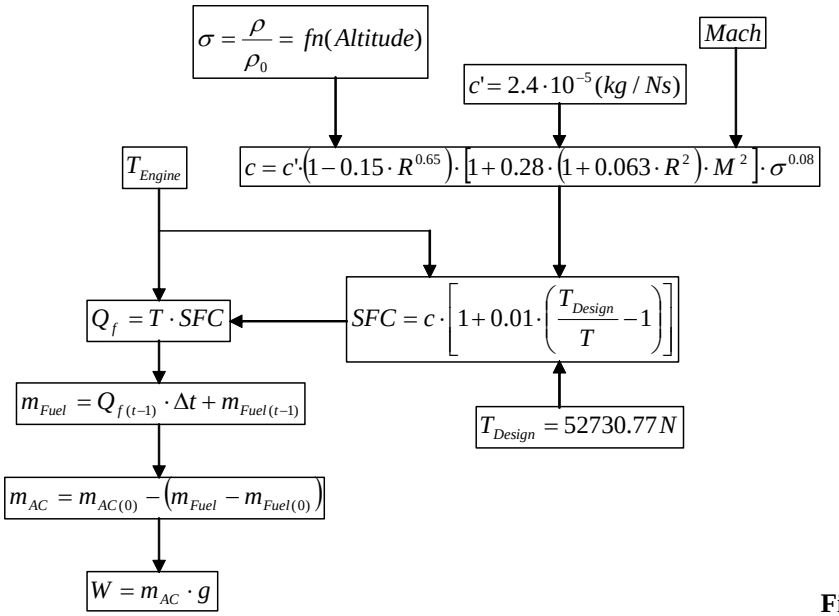

Figure A-14

The maximum achievable value of engine thrust as required for critical flight phases can be determined from a generic relation from Howe as a function of aircraft altitude and speed, as given in the flowchart below. In this case, the design value of thrust is taken to be the maximum value of thrust when the aircraft is at sea level and stationary, as was determined in the conceptual design studies.

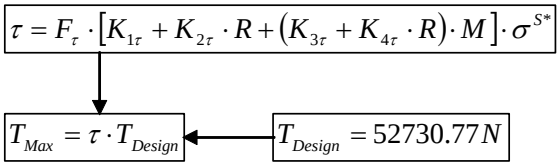

Bypass ratio R	Mach number range	Operating condition	$K_{1\tau}$	$K_{2\tau}$	$K_{3\tau}$	$K_{4\tau}$	s^*
1 or lower	0-0.4	Dry	1.0	0	-0.2	0.07	0.8
		Wet	1.32	0.062	-0.13	-0.27	0.8
	0.4-0.9	Dry	0.856	0.062	0.16	-0.23	0.8
		Wet	1.17	-0.12	0.25	-0.17	0.8
	0.9-2.2	Dry	1.0	-0.145	0.5	-0.05	0.8
		Wet	1.4	0.03	0.8	0.4	0.8
3 to 6	0-0.4	Dry	1.0	0	-0.6	-0.04	0.7
	0.4-09	Dry	0.88	-0.016	-0.3	0	0.7
8	0-0.4	Dry	1	0	-0.595	-0.03	0.7
	0.4-0.9	Dry	0.89	-0.014	-0.3	+0.005	0.7

* Strictly s values apply up to 11 km altitude above which the factor is unity based on the 11 km altitude condition as a datum.

Equation A-1 and Table A-1 [38]

The constants in the expression above can be determined from the accompanying table from Howe for a dry engine with a bypass ratio of 0.8 and Mach number up to 0.9.

A1.8 MALE fuel consumption, weight variation and engine characteristics

As for the UCAV, the approach used to predict the fuel consumption and therefore the weight of the aircraft at any point, follows the same procedure for each flight phase. Using a relation from Mattingly [16] for a turboprop engine, this process can be seen to be a function of the aircraft speed, altitude (via the temperature ratio) and engine thrust as presented in the flowchart below.

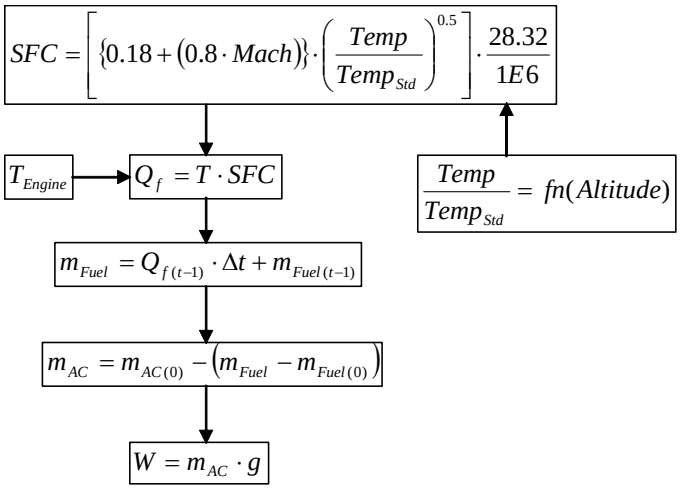

Figure A-15

Once again, the maximum achievable value of engine thrust as required for critical flight phases can be determined from a generic relation from Mattingly as a function of aircraft altitude and speed, as given in the flowchart below. As before, the design value of thrust is taken to be the maximum value of thrust when the aircraft is at sea level and stationary, as was determined in the conceptual design studies.

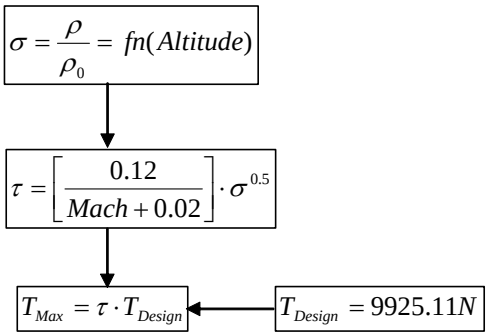

Figure A-16

A1.9 General terms used

The majority of the expressions used in these analyses are self explanatory and will be familiar to any aerospace student. General aerodynamic terms such as C_{DZ}, K, $C_{L\alpha}$ and X_{AC} are presented as convenient polynomial expressions in the baseline aircraft design section of this thesis. Atmospheric terms of particular importance within these analyses are the speed of sound and density of surrounding air. This data, as is readily available from any aerodynamic textbook has been adapted into convenient polynomial expressions as given below, where H is the altitude in km.

$$a_{Air} = -4.02H + 340.5 \qquad \text{Eq A-2}$$

$$\rho_{Air} = 0.0035H^2 - 0.1152H + 1.2239 \qquad \text{Eq A-3}$$

B1 Thrust vectoring source data

Two different data sets were available from NASA for the external vanes vectoring system - that for a military power nozzle and that for a max nozzle (which is aimed at nozzles incorporating an afterburner). Since our engine does not use an afterburner, we will thus only concentrate on the data for the military power engine nozzle. There were also a number of different paddle sizes investigated by NASA but here we are concentrating on the same configuration as that used on the X-31 with a large top vane and two smaller vanes. The test results for the vectored nozzle and baseline nozzle with no vanes installed is given in the sections below. An additional section gives the geometry of the system as tested by NASA.

B1.1 NASA vectored nozzle test results

The results obtained from the NASA tests on the thrust vectoring system are given in the table below at a number of specified values of nozzle pressure ratio and paddle deflection angle. In this work, we are primarily interested in the pitch control of the system and thus only results for deflection of the top vectoring paddle have been included. The two lower vanes are thus assumed to be in their fully retracted position of -10°. These results were taken directly from page 109 to 129 of NASA TM 4359 [61].

Data for the vectored NASA nozzle from tests at different paddle angles

δC (deg)	-10	δB (deg)	-10

δA (deg)	NPR test	NPR	wp/wi	F/Fi	Fr/Fi	δP (deg)	δY (deg)	δR (deg)	Cfg
10	2.0016	2	0.886	0.9973	0.9973	0.27	-0.21	0.342053	0.9973
10	3.0014	3	0.9282	0.9967	0.9967	0.69	-0.2	0.718401	0.9967
10	4.0037	4	0.9358	0.9861	0.9862	0.92	-0.15	0.932148	0.9862
10	5.0024	5	0.9283	0.9684	0.9689	1.75	-0.12	1.754109	0.9689
10	6.0004	6	0.9284	0.9529	0.9541	2.86	-0.16	2.864472	0.9541
15	2.0069	2	0.8864	0.9844	0.9848	1.58	-0.31	1.610124	0.9848
15	3.0044	3	0.9268	0.9819	0.9825	2.14	-0.24	2.153416	0.9825
15	4.0049	4	0.9359	0.9693	0.9704	2.82	-0.24	2.830194	0.9704
15	5.0016	5	0.9285	0.9472	0.9499	4.3	-0.34	4.313421	0.9499
15	6.0038	6	0.9285	0.9286	0.9338	5.99	-0.44	6.006139	0.9338
20	3.0063	3	0.9248	0.9297	0.9362	6.75	-0.45	6.764983	0.9362
20	4.0049	4	0.9349	0.9171	0.9258	7.84	-0.62	7.864477	0.9258
20	4.9997	5	0.9284	0.8999	0.9121	9.34	-0.73	9.368484	0.9121
20	5.997	6	0.9283	0.8856	0.9022	10.97	-0.86	11.00366	0.9022
25	1.996	2	0.8853	0.8867	0.9019	10.51	-0.62	10.52827	0.9019
25	3.006	3	0.9245	0.8759	0.8948	11.74	-0.96	11.77919	0.8948
25	4.002	4	0.9349	0.8655	0.8877	12.8	-1.16	12.85246	0.8877
25	5.0013	5	0.9285	0.8554	0.8808	13.72	-1.23	13.77502	0.8808
25	5.9986	6	0.9282	0.8461	0.8754	14.83	-1.24	14.88175	0.8754
30	2.011	2	0.8875	0.8161	0.8531	16.9	-1.29	16.94916	0.8531
30	2.9988	3	0.9291	0.8011	0.8431	18.09	-1.62	18.16239	0.8431
30	3.9973	4	0.9361	0.7992	0.8435	18.61	-1.44	18.66563	0.8435
30	4.9858	5	0.9303	0.7974	0.8428	18.84	-1.48	18.89804	0.8428
30	5.9901	6	0.9285	0.794	0.8415	19.28	-1.64	19.34963	0.8415
35	2.0002	2	0.8881	0.7475	0.8088	22.27	-3.15	22.49167	0.8088
35	2.999	3	0.9255	0.7352	0.7997	23	-3.17	23.21743	0.7997
35	4.0014	4	0.9355	0.7375	0.8001	22.6	-3.48	22.86636	0.8001
35	4.9983	5	0.9288	0.741	0.8002	21.94	-3.73	22.25481	0.8002
35	6.0032	6	0.9283	0.7419	0.7987	21.43	-4.07	21.81306	0.7987

Table 1-1

B1.2 NASA test results with no vanes installed

The results obtained from NASA TM 4359 [61] pages 97 to 98 for the baseline nozzle with no vanes installed is given in the table below.

Data for the baseline NASA nozzle with no vanes installed
(Averaged values of all the test runs)

NPR	NPR test	wp/wi	F/Fi	Fr/Fi	dP (deg)	dY (deg)	dR (deg)	Cfg
2	2.00128	0.88614	0.99994	0.99996	0.01	-0.178	0.178281	0.99996
3	2.99998	0.92822	0.9992	0.9992	0.276	-0.076	0.286273	0.9992
4	4.00185	0.935183	0.989133	0.989133	0.323333	-0.03667	0.325406	0.989133
5	4.99076	0.93238	0.97814	0.97814	0.324	0.01	0.324154	0.97814
6	5.99996	0.92848	0.96856	0.96858	0.292	0.04	0.294727	0.96858

Table 1-2

B1.3 Geometric data of the vectoring system

Data for the geometry of the system taken from NASA TM 4359 [61] pages 133 to 134 is given below. Additional data can also be obtained from NASA TM 4771 [62], TM 101741 [63], TM 3531 [64] and TM 4341 [65] where required.

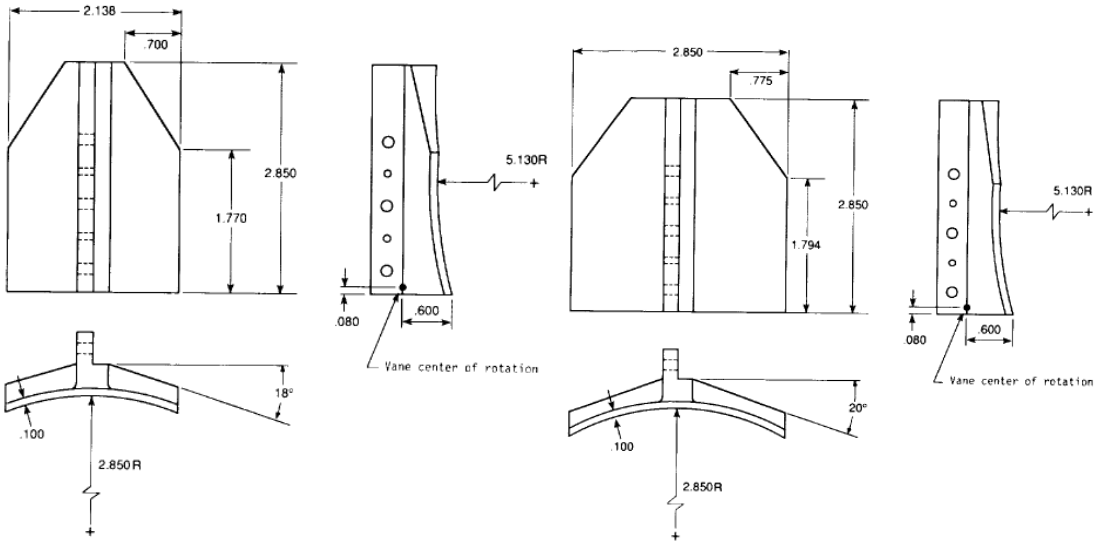

(a) Standard vane. Vane planform area, 5.337 in^2.

(b) Large vane. Vane planform area, 7.304 in^2.

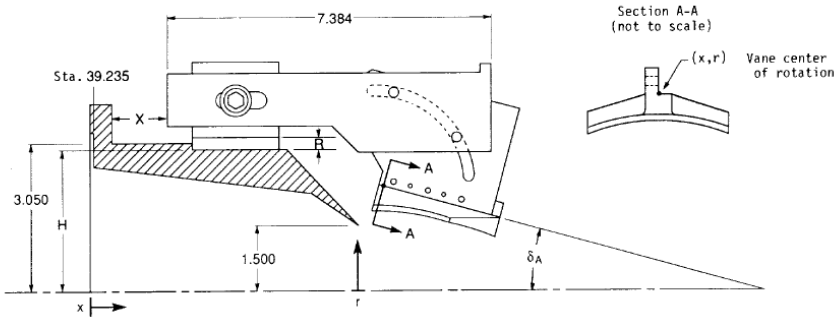

(a) Nozzle and vane geometry.

Figures 1-1, 1-2, 1-3

B2 Rescaling the NASA test data

B2.1 Assumptions and limitations

In this work, we were fortunate enough to have access to test data for the X-31 thrust vectoring system from NASA studies. These tests were however carried out on a scale model of the system and under laboratory conditions. Whilst we can make some attempt to rescale the data to match it to a different nozzle, the data itself makes no allowance for the interaction of external flow conditions on the system. To clarify this point, the installed nozzle performance will be dependent on the flight speed and altitude, giving different results for each case. The performance of the nozzle will also be dependent on its installation within the airframe. In particular, the aircraft after-body will affect the flow field surrounding aircraft and thus the nozzle. We are therefore somewhat restricted as to the accuracy of the results that can be achieved from this study. This work is however considered sufficient for conceptual design and feasibility studies.

B2.2 Background to the approach

In its original format, the NASA test data is only valid for the nozzle on which the original experimental tests were carried out. Since it is not practical to build and test our own nozzle within the time-frame of this project, we have to find a way to adapt the original data to match a different nozzle. Since the terms in the data which govern the flow conditions are non-dimensional, matching of the scale test data to a full scale nozzle should be likened to the matching of models to full scale bodies of other fluid flow studies. This system consists of a simple nozzle which is surrounded by external vectoring vanes, which deflect into the flow stream as required. In its un-vectored state when all the vanes are fully retracted, the nozzle could be viewed in the same way as a standard engine nozzle. Comparison of the operating characteristics of the un-vectored NASA test nozzle with those of our baseline engine did however highlight a mis-match between the two.

In the absence of a better method, the approach adopted here was to rescale the NASA test data in accordance with the differences between the un-vectored nozzles used for the NASA tests and our baseline engine. Some error is expected with this approach but it is expected to serve as a good first approximation. To be able to obtain a better approximation, it would be necessary to carry out more scale tests on a like for like un-vectored nozzle and/or use a CFD model. Either of these approaches would however be time consuming and costly and beyond the scope of these feasibility studies.

B2.3 The data for the un-vectored baseline engine nozzle

In this work, an engine nozzle with PI value of 0.98 was selected as the baseline (un-vectored) configuration. Using the AEDsys software suite, data was generated for this baseline engine-nozzle combination at a number of different engine conditions for cruise and take-off conditions. The full details of this are included with in the engine design section.

B2.4 Rescaling the NASA data to suit the baseline engine nozzle

As mentioned above, a mis-match exists between the operating data of the un-vectored NASA test nozzle and our baseline nozzle. We therefore need to rescale the NASA data to match the characteristics of our nozzle. If we know how much the un-vectored NASA nozzle has to be re-scaled by in order to match the baseline nozzle of our engine, then the vectored data for the NASA nozzle can be rescaled by the same amount. This involves the manipulation of the following parameters from the NASA data:

- Cfg – The nozzle thrust loss factor
- NPR – The nozzle pressure ratio
- dA – The deflection angle of the thrust vectoring vanes
- dR – The deflection of the exhaust jet plume

The NASA data was categorised according to the deflection angle of the vectoring vanes and nozzle pressure ratio (NPR). The NPR parameter is dependent on the nozzle configuration and the engine operating condition and it is therefore difficult to maintain a specific value. Fortunately though, the test conditions for the NASA nozzle were carefully maintained to produce results for a range of fixed NPR and dA values. This simplifies our analysis somewhat as we have fixed points to interpolate between. Since NPR and dA can be regarded as input variables, only Cfg and dR require rescaling.

The rescaling process for the parameter Cfg is presented in the flow chart below. Each data set has been clearly identified by subscripts referring to the NASA or baseline engine data and the vectored or no vanes installed nozzle configurations respectively.

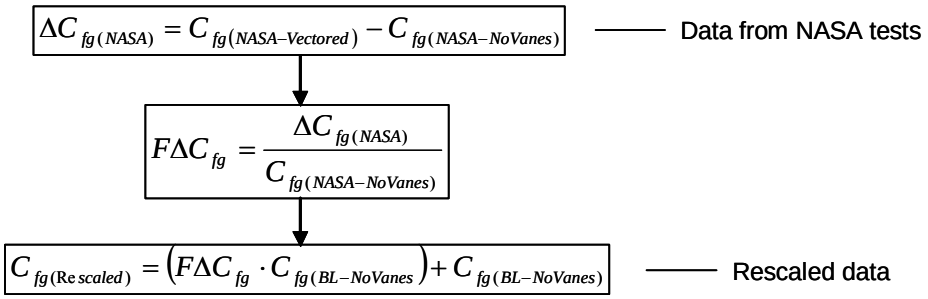

In the first stage of this process, we determine the change in the values that is experienced as a result of deflecting the vanes in to the engines jet stream. In the next stage, we assume that these changes are directly related to the operating characteristics of the nozzle to obtain a relation to rescale the data. Since Cfg is the most widely used standard nozzle parameter amongst propulsion engineers it is reasonable to use this parameter to rescale the changes in the NASA test data. Using these fractional values, we can reverse the process using the Cfg value of the baseline nozzle in place of that of the no-vanes NASA data to obtain the revised and rescaled data.

The parameter dR is rescaled by the same process, as presented in the flow chart below. Here, the $dR_{(no\text{-}vanes)}$ value is omitted when the data is rescaled to the new nozzle. In the case of the NASA nozzle, this figure was used to make allowance for the test rig set-up and nozzle manufacturing tolerances. In the case of our nozzle, these are assumed to be negligible since it is not possible to make a realistic prediction for them.

$$\Delta dR = dR_{(NASA-Vectored)} - dR_{(NASA-NoVanes)}$$ ——— Data from NASA tests

$$F\Delta dR = \frac{\Delta dR_{(NASA)}}{C_{fg(NASA-NoVanes)}}$$

$$dR_{(Rescaled)} = F\Delta dR \cdot C_{fg(BL-NoVanes)}$$ ——— Rescaled data

The procedures above are repeated for each combination of vane vectoring angle and NPR to generate a revised set of data for our nozzle. An example set of results for a NPR of 3 is presented below with similar results for NPR values of 2, 4, 5 and 6.

NPR	3									
Original untouched test data for the NASA nozzle			Incremental changes in original NASA data		Fractional changes for original NASA data		Incremental changes in new nozzle data		Final resized data for new nozzle	
dA (deg)	dR (deg)	Cfg	Δ dR (deg)	Δ Cfg	FΔdR (deg)	FΔCfg	Δ dR (deg)	Δ Cfg	dR (deg)	Cfg
10	0.718401	0.9967	0.4321284	-0.0025	43.247438	-0.2502	0.4203199	-0.00243	0.42032	0.969464
15	2.153416	0.9825	1.8671433	-0.0167	186.86382	-1.67134	1.8161211	-0.01624	1.816121	0.955652
20	6.764983	0.9362	6.4787108	-0.063	648.38979	-6.30504	6.3016712	-0.06128	6.301671	0.910617
25	11.77919	0.8948	11.492912	-0.1044	1150.2114	-10.4484	11.178853	-0.10155	11.17885	0.870348
30	18.16239	0.8431	17.87612	-0.1561	1789.0432	-15.6225	17.387631	-0.15183	17.38763	0.820061
35	23.21743	0.7997	22.931154	-0.1995	2294.9514	-19.966	22.304529	-0.19405	22.30453	0.777847

Table 2-1

B2.5 Matching the nozzle data to the engine operating data

The data rescaling process above, gives us a number of tables of results for nozzle pressure ratios from 2 to 6 in unit steps. Within these are a range of vane deflection angles from 10 to 35 degrees in 5 degree steps. An example of such data is below.

Results for nozzle pressure ratio = 2

dA	NPR	Cfg (Scl'd)	dR (Scl'd)
10	2	0.962961	0.158133
15	2	0.950891	1.382542
20	2	0.910869	5.688082
25	2	0.870846	9.993621
30	2	0.823726	16.19343
35	2	0.780951	21.5451

Results for nozzle pressure ratio = 3

dA	NPR	Cfg (Scl'd)	dR (Scl'd)
10	3	0.969454	0.420316
15	3	0.955642	1.816103
20	3	0.910608	6.301608
25	3	0.87034	11.17874
30	3	0.820053	17.38746
35	3	0.777839	22.3043

Table 2-2

From our engine design work, we have a number of data sets for the baseline engine. Each set corresponds to the engine operating condition such as a different thrust ratio or percentage of bleed. Within each data set, are results corresponding to a number of values of nozzle isentropic stagnation pressure ratio, designated as (π). Is should be emphasised that this is different to the nozzle pressure ratio (NPR). NPR is the ratio of the total to static pressure at the nozzle throat, whereas π is the ratio of the total pressure entering the nozzle to that leaving the component. The NPR of the engine has proven to be invaluable for stitching the engine and nozzle data sets together. Fortunately, this was obtained from the engine design process, as included within our engine data sets.

For the take-off work, we have a number of tables of data for the engine as tested at a range of Pi-Nozzle values from 0.995 to 0.6 in 0.05 steps and engine bleed from 0% to 20% in 2.5% steps. An example take-off analysis data set is given below.

Results for 5% engine bleed

% Thrust	Pi-Nozzle	Cfg (Eng)	NPR (Eng)
100	0.995	0.978	3.217542
100	0.95	0.961	3.217542
100	0.9	0.9405	3.217542
100	0.85	0.918	3.217542
100	0.8	0.8932	3.217542
100	0.75	0.8655	3.217542
100	0.7	0.8343	3.217542
100	0.65	0.7987	3.217542
100	0.6	0.7575	3.217542

Results for 10% engine bleed

% Thrust	Pi-Nozzle	Cfg (Eng)	NPR (Eng)
100	0.995	0.9777	2.898816
100	0.95	0.9588	2.898816
100	0.9	0.9359	2.898816
100	0.85	0.9107	2.898816
100	0.8	0.8827	2.898816
100	0.75	0.8514	2.898816
100	0.7	0.8159	2.898816
100	0.65	0.775	2.898816
100	0.6	0.7276	2.903511

Table 2-3

.

A similar set of data exists for the cruise work. In this case we have a number of tables of data for the engine as tested at a range of Pi-Nozzle values from 0.995 to 0.84 in 0.02 steps and engine throttle settings from 45 to 65% in 5% steps. An example cruise analysis data set is given below.

Results for 50% engine thrust

% Thrust	Pi-Nozzle	Cfg (Eng)	NPR (Eng)
50	0.995	0.9783	3.831136
50	0.98	0.9736	3.837729
50	0.96	0.9673	3.847253
50	0.94	0.9607	3.857143
50	0.92	0.9539	3.867399
50	0.9	0.9464	3.878022
50	0.88	0.9398	3.890842
50	0.86	0.9324	3.902564
50	0.84	0.9247	3.914652

Results for 60% engine bleed

% Thrust	Pi-Nozzle	Cfg (Eng)	NPR (Eng)
60	0.995	0.9785	4.264835
60	0.98	0.9742	4.27033
60	0.96	0.9684	4.279487
60	0.94	0.9624	4.287179
60	0.92	0.9562	4.294872
60	0.9	0.9498	4.303297
60	0.88	0.9432	4.312088
60	0.86	0.9364	4.321245
60	0.84	0.9294	4.331136

Table 2-4

The next stage in this work is to stitch together the data sets for the engine and nozzle, with the aid of linear interpolation techniques. During this process, each engine operating point is interpolated between the corresponding rescaled nozzle data sets to generate a set of data specific to the NPR being analysed. This process is shown diagrammatically below. As a result of the vast amount of data that needed to be analysed, this process was automated with spreadsheet functions to filter and interpolate the data. This automated process will be discussed in more detail in a later section.

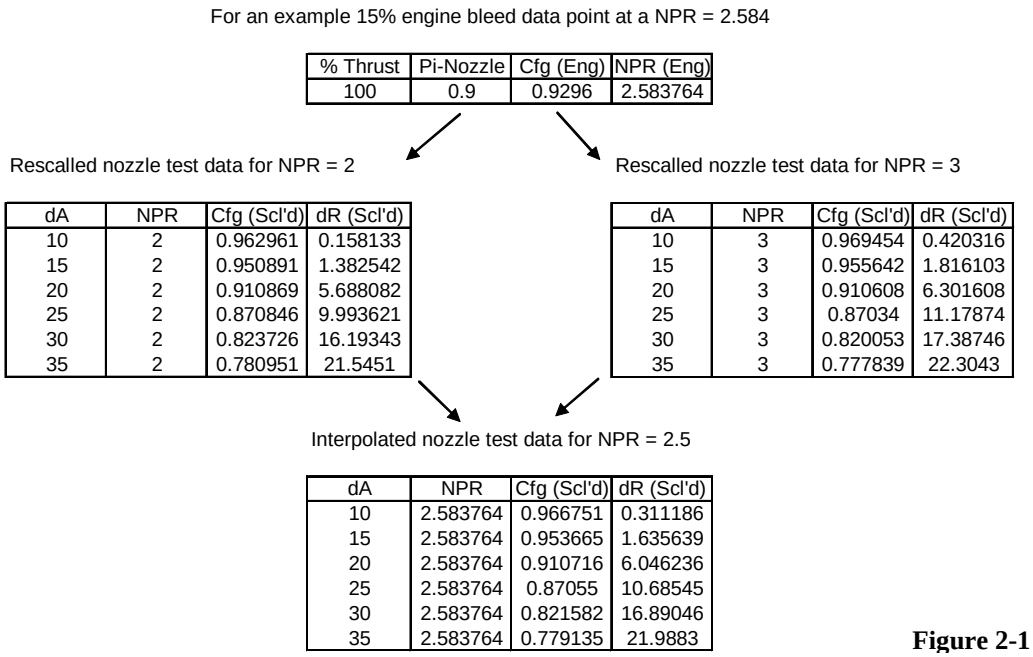

Figure 2-1

A similar process exists for the cruise analysis, in which case the data is given as a function of engine throttle ratio instead of bleed. The equations used for the interpolation of Cfg and dR values are given below. The engine subscript refers to the engine data point being investigated, which would be $NPR_{Engine} = 2.584$ in the example above. The subscripts 1 and 2 refer to upper and lower rescaled nozzle data sets respectively, which would be $NPR_1 = 2$ and $NPR_2 = 3$ in the example above.

$$C_{fg} = \left(\frac{NPR_{Engine} - NPR_1}{NPR_2 - NPR_1} \right) \cdot \left(C_{fg(2)} - C_{fg(1)} \right) + C_{fg(1)} \qquad \text{Eq 2-1}$$

$$dR = \left(\frac{NPR_{Engine} - NPR_1}{NPR_2 - NPR_1} \right) \cdot \left(dR_2 - dR_1 \right) + dR_1 \qquad \text{Eq 2-2}$$

At this stage in the process we now have a table of data points from the rescaled nozzle data, at the NPR point which is being investigated for our engine. The next stage is to further narrow down this data set to the value of Cfg at the engine operating point being investigated. This involves a second stage of interpolation as shown in the figure below.

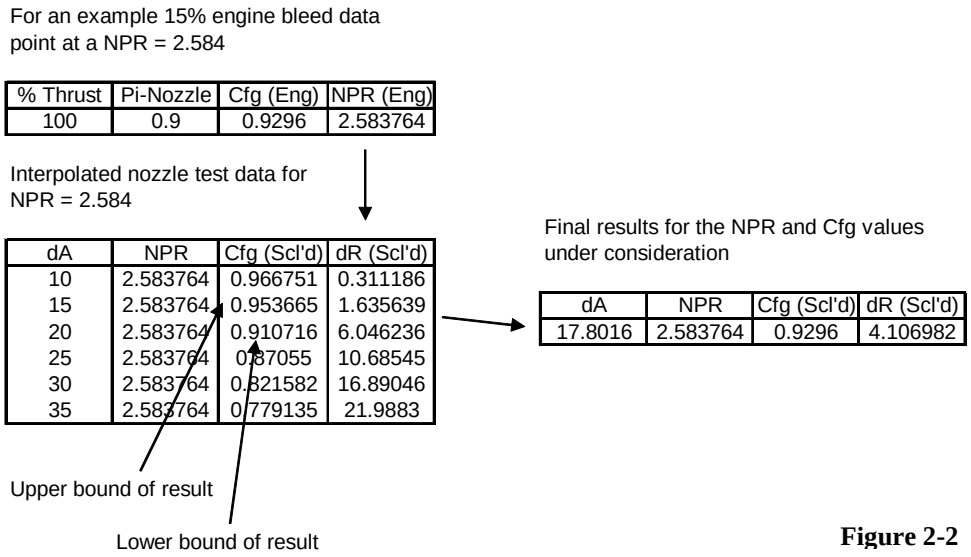

Figure 2-2

As before, a similar process exists for the cruise analysis. The accompanying equations for this interpolation stage are given below for dA and dR respectively, where the subscripts adopt the same terminology as before.

$$dA_{Engine} = \left(\frac{C_{fg(Engine)} - C_{fg(1)}}{C_{fg(2)} - C_{fg(1)}} \right) \cdot \left(dA_2 - dA_1 \right) + dA_1 \qquad \text{Eq 2-3}$$

$$dR_{Engine} = \left(\frac{C_{fg(Engine)} - C_{fg(1)}}{C_{fg(2)} - C_{fg(1)}} \right) \cdot \left(dR_2 - dR_1 \right) + dR_1 \qquad \text{Eq 2-4}$$

Using the process above, we are able to merge the rescaled nozzle data with that for our engine operating at a number of different conditions. The results thus allow us to predict the impact which deflecting the vanes will have on the performance of the engine. Especially in terms of the gross thrust and thrust specific fuel consumption.

B2.6 Dealing with vast quantities of data

As to be expected, it is not practical to manually manipulate the vast quantity of nozzle data for every single engine data point and some form of automation was required. For the range of NPR values encountered in this work, 3 rescaled nozzle NPR datasets were sufficient to cover the entire range of data points. The automation process here utilises a series of tests to filter out the final solution as shown in the example.

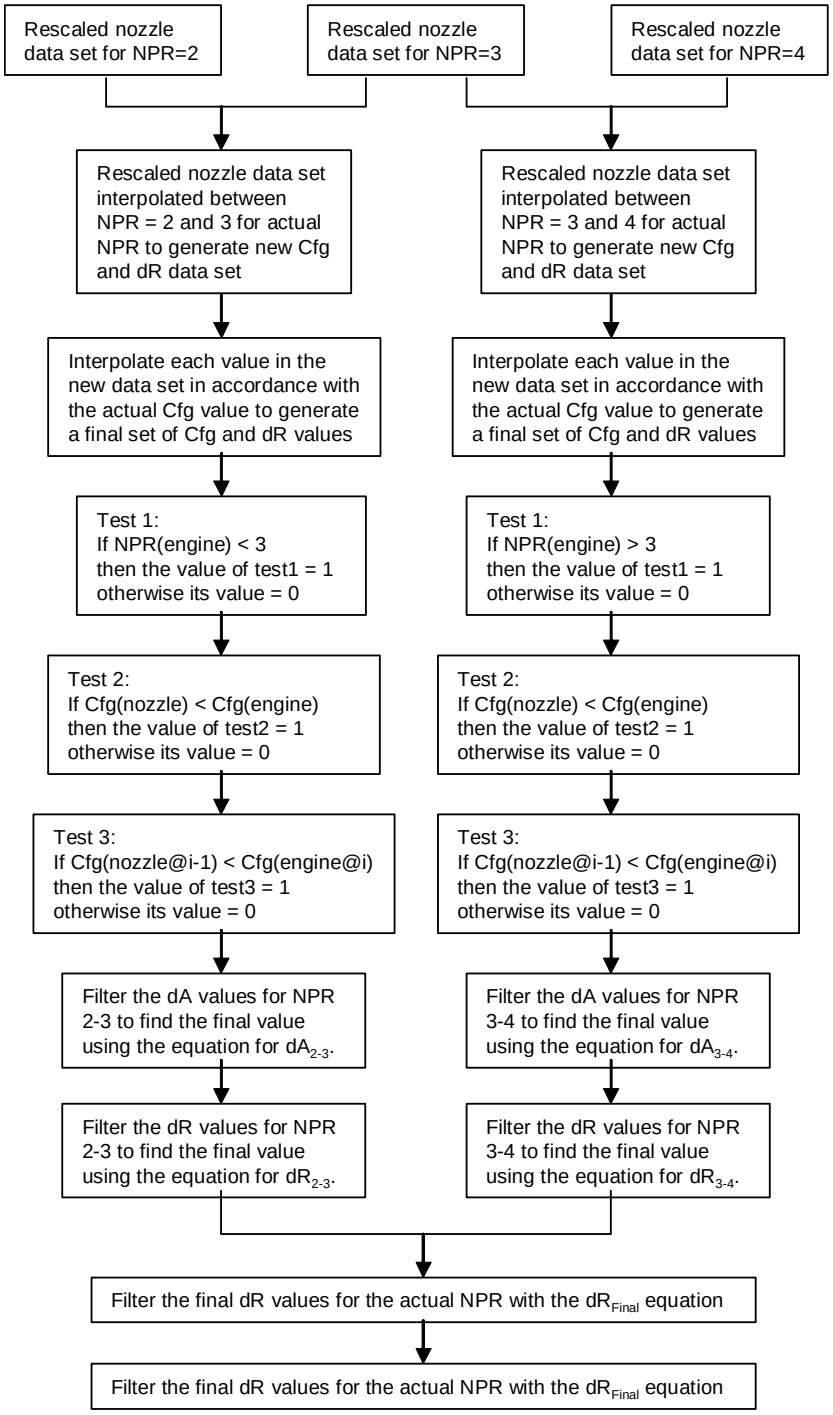

Figure 2-3

The accompanying equations to find dA are:

$$dA_{2-3} = \sum_{i=1}^{n} \left(test1 \cdot test2 \cdot test3 \cdot dA_i \right) \quad \text{AND} \quad dA_{3-4} = \sum_{i=1}^{n} \left(test1 \cdot test2 \cdot test3 \cdot dA_i \right)$$

Eq 2-5, 2-6

Likewise, the equations for dR are:

$$dR_{2-3} = \sum_{i=1}^{n} \left(test1 \cdot test2 \cdot test3 \cdot dR_i \right) \quad \text{AND} \quad dR_{3-4} = \sum_{i=1}^{n} \left(test1 \cdot test2 \cdot test3 \cdot dR_i \right)$$

The final equations for dR and dA are then: Eq 2-7, 2-8

$$dA_{Final} = dA_{2-3} + dA_{3-4}$$ Eq 2-9

$$dR_{Final} = dR_{2-3} + dR_{3-4}$$ Eq 2-10

An example of this process as used in the actual analysis is given below.

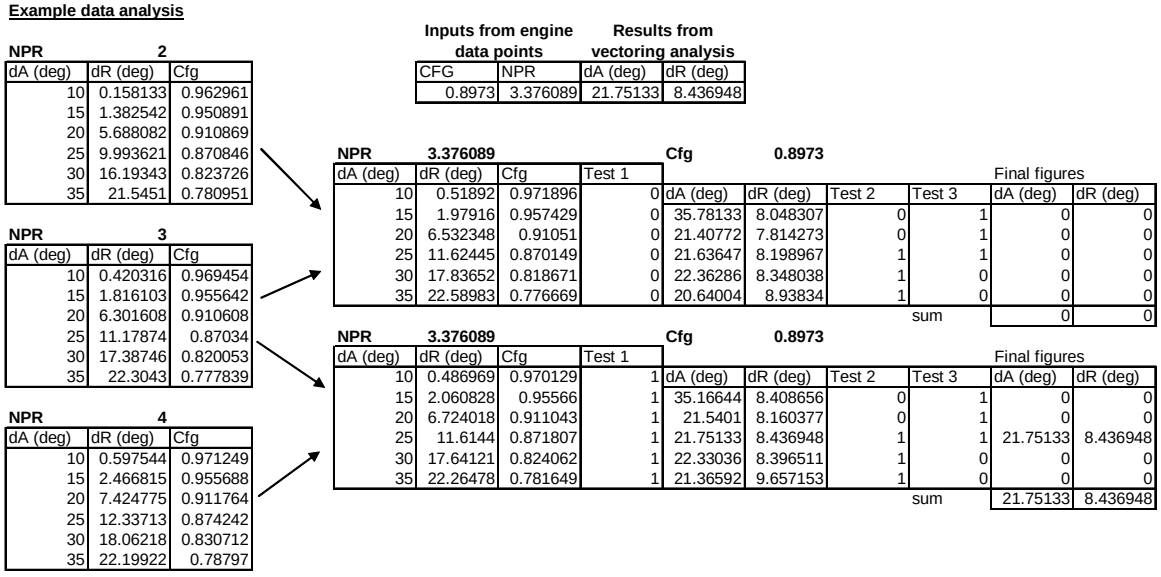

Figure 2-4

The example above is for just one data point and this process must thus be repeated for each of the engine data points to produce a complete table of data. In it entirety, the process completely stitches together the data sets for the engine conditions with the data sets for the rescaled thrust vectoring nozzle.

B2.7 Formatting the results

At this stage in our work, we now have a number of tables of data for the engine and nozzle combination at a number of different vane deflection angles. Each of the tables of data corresponds to a different engine operating condition such as throttle ratio or bleed. An example of such a data table is presented below for a take-off case of 5% bleed. Similar tables exist for the cruise cases within which each data table corresponds to a different throttle ratio. With the data in this format, it is possible to plot the results of each parameter, from each results table. This enables us to fit a polynomial expression to each plot, which puts the data in a format more applicable to analytical analyses. These results are presented in the following sections.

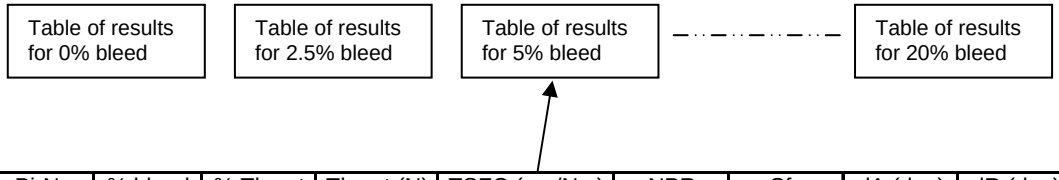

Pi-N	% bleed	% Thrust	Thrust (N)	TSFC (mg/N-s)	NPR	Cfg	dA (deg)	dR (deg)
0.995	5	100	50322.735	22.9473	3.217542	0.978	0	0
0.95	5	100	49353.023	23.397747	3.217542	0.961	13.11596	1.392903
0.9	5	100	48183.141	23.964347	3.217542	0.9405	16.69137	3.50976
0.85	5	100	46902.053	24.621603	3.217542	0.918	19.20294	5.814516
0.8	5	100	45483.07	25.386513	3.217542	0.8932	22.22575	8.720408
0.75	5	100	43903.951	26.298739	3.217542	0.8655	25.58264	12.14197
0.7	5	100	42129.111	27.409275	3.217542	0.8343	28.77826	16.04286
0.65	5	100	40109.618	28.788946	3.217542	0.7987	32.79619	20.18905
0.6	5	100	37774.301	30.56807	3.217542	0.7575	0	0

Figure 2-5

B2.8 Final results for the engine-nozzle in take-off conditions

The analyses of the previous sections, gives us the following results for the engine-nozzle combination operating at its take-off condition. The results presented in this section are given at a number of different engine bleed settings, as a function of plume deflection angle. Those results of particular importance to this work are the maximum available thrust and thrust specific fuel consumption as presented in the charts below. Other useful results but which are not required for this work are, required vanes deflection to achieve a desired plume deflection and required exhaust nozzle exit area. These have thus not been included here due to thesis size limitations.

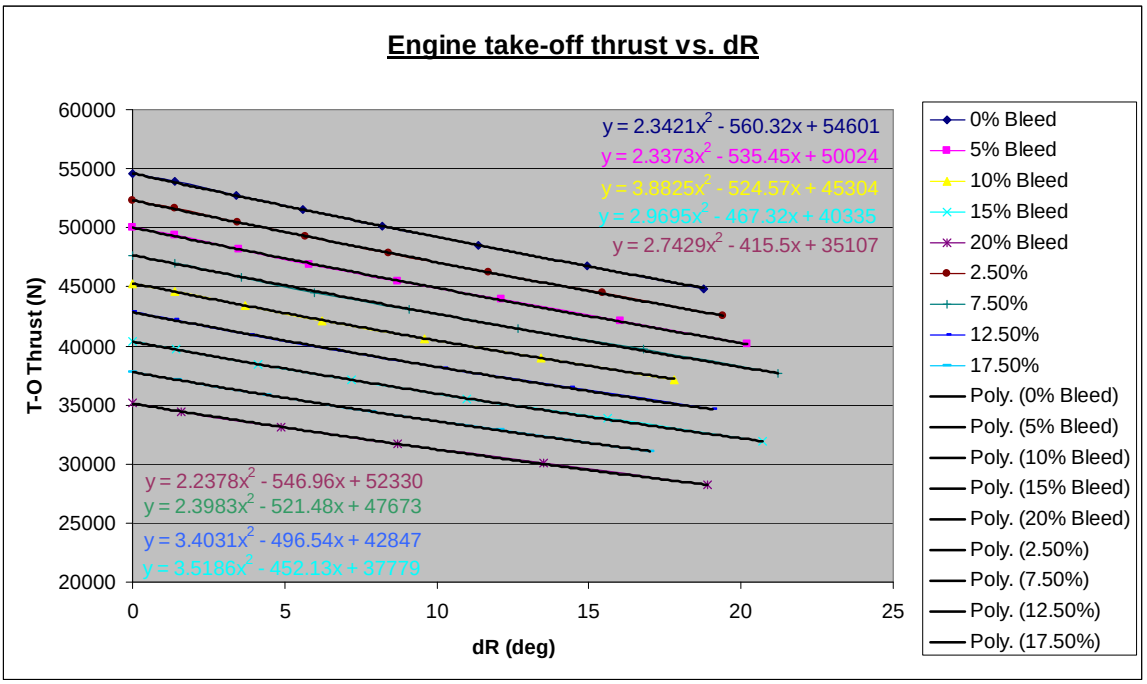

Chart 2-1

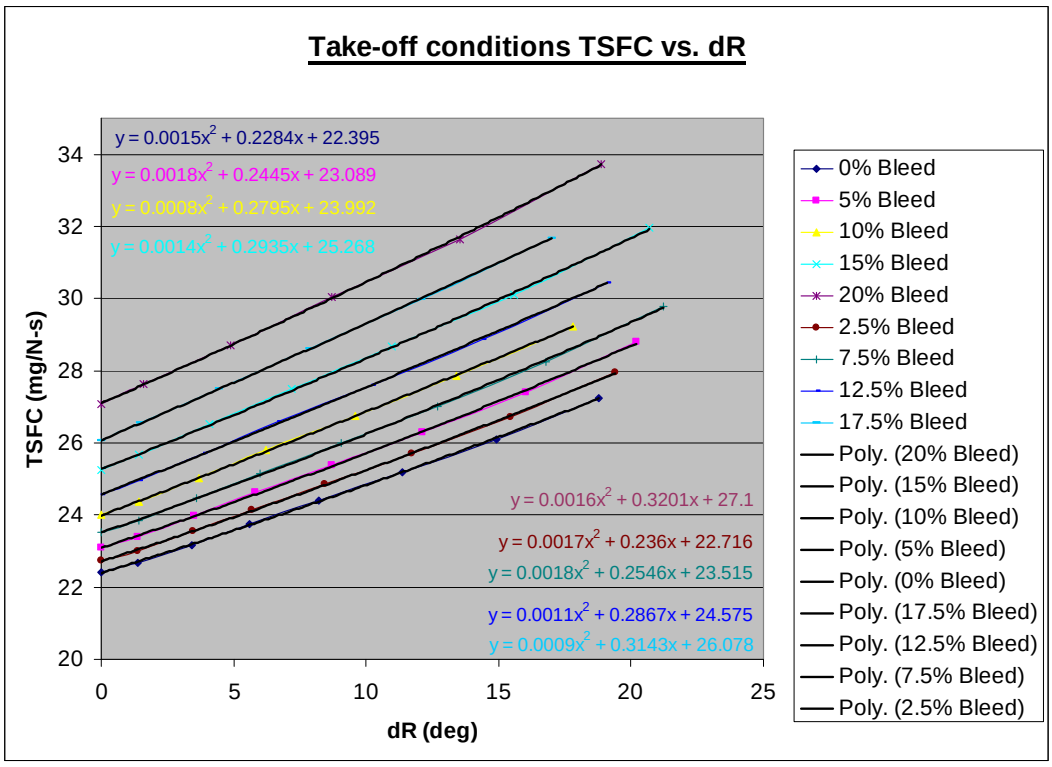

Chart 2-2

B2.9 Final results for the engine-nozzle in cruise conditions

Analysis of the engine-nozzle combination operating at cruise conditions gives us the following results. As for the take-off condition, these are given as a function of plume deflection angle and at a number of different engine thrust settings. Those of particular interest are, engine thrust and thrust specific fuel consumption as presented in the charts below. Other useful results but which are not required for this work are, required vanes deflection to achieve a desired plume deflection and required exhaust nozzle exit area.

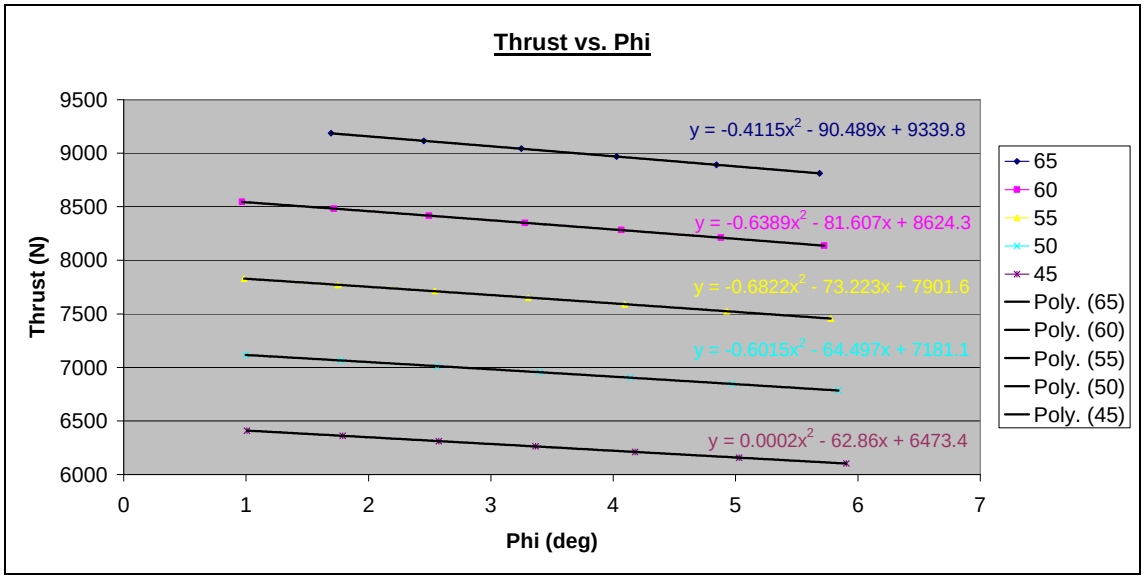

Chart 2-3

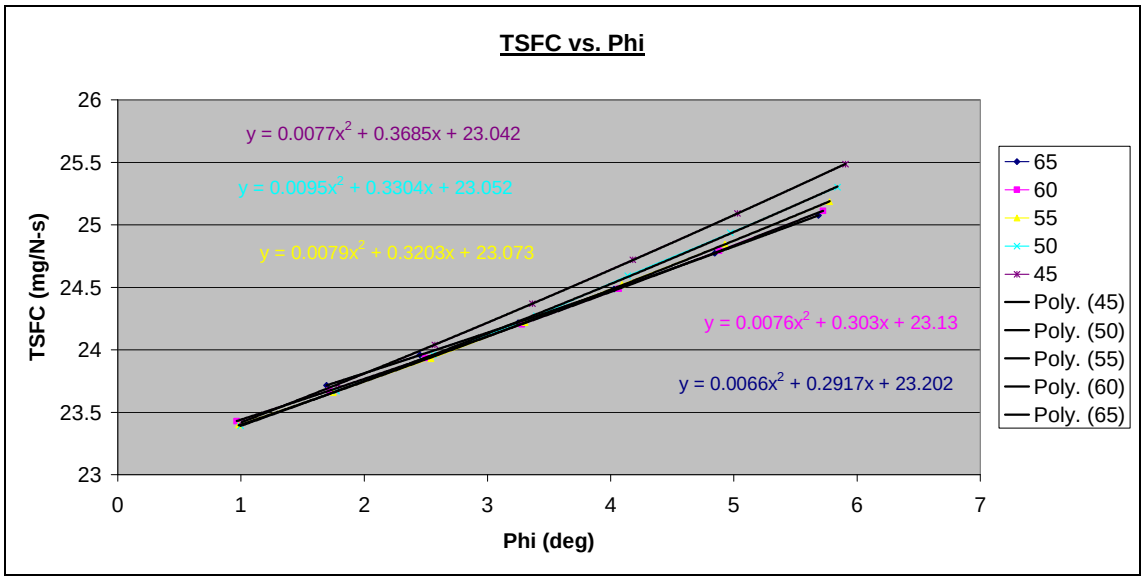

Chart 2-4

B2.10 Variation of Thrust and TSFC with Mach number during the take-off phase

A significant complication in the take-off analysis is due to the fact that the velocity of the aircraft is continually changing as it accelerates down the runway. The problem is that the performance of the engine is also a function of the aircraft velocity and altitude, amongst other parameters. Since the altitude is assumed to be fixed at standard sea level conditions, we only need to consider the velocity effects. The engine performance data used for the take-off analysis was thus derived at an average aircraft take-off speed of Mach 0.2 (assumed to be typical for this type of aircraft).

The velocity effects could be accounted for by repeating the complete engine-nozzle analysis at a number of Mach numbers and interpolating between the data points. This would however require the analysis to be repeated a large number of times, which would prove to be very time consuming. The final result would also be a particularly complicated expression which is a function of plume angle, engine bleed and aircraft velocity. A much simpler approach is to account for the velocity effects with a scale factor. This was generated with ONX and AEDsys [16], which was used to determine the effect of velocites up to Mach 0.4 on the un-vectored baseline configuration (Pi = 0.98) with zero nose jet engine bleed. The Mach 0.2 results were then taken as the baseline values (as presented in the results section above), and all other conditions scaled with reference to this condition. At Mach 0.2, the scale factor thus equals 1. Plotting the results enables us to fit polynomial expressions as a function of Mach number. As given below, these can then be used to the scale the data for thrust and thrust specific fuel consumption.

$$SF_{Thrust} = -3.7672M^4 + 3.459M^3 - 0.7693M^2 - 0.3575M + 1.0804 \qquad \text{Eq 2-11}$$

$$SF_{TSFC} = 3.1881M^4 - 3.04M^3 + 0.9856M^2 + 0.3014M + 0.9196 \qquad \text{Eq 2-12}$$

B3 Deriving a general expression for the engine throttle setting at cruise

The purpose of this work is to transform the thrust vectored engine-nozzle data as obtained in the data rescaling section, into a more manageable format for analytical work. The result is an analytical expression for the engine throttle setting as a function of the resultant engine thrust and engine plume deflection angle. The final expression enables us to determine the thrust specific fuel consumption, given as a function of the throttle ratio. A summary of the procedure used is shown in the flow chart below. The accompanying equations, charts and tables for this process are also given below.

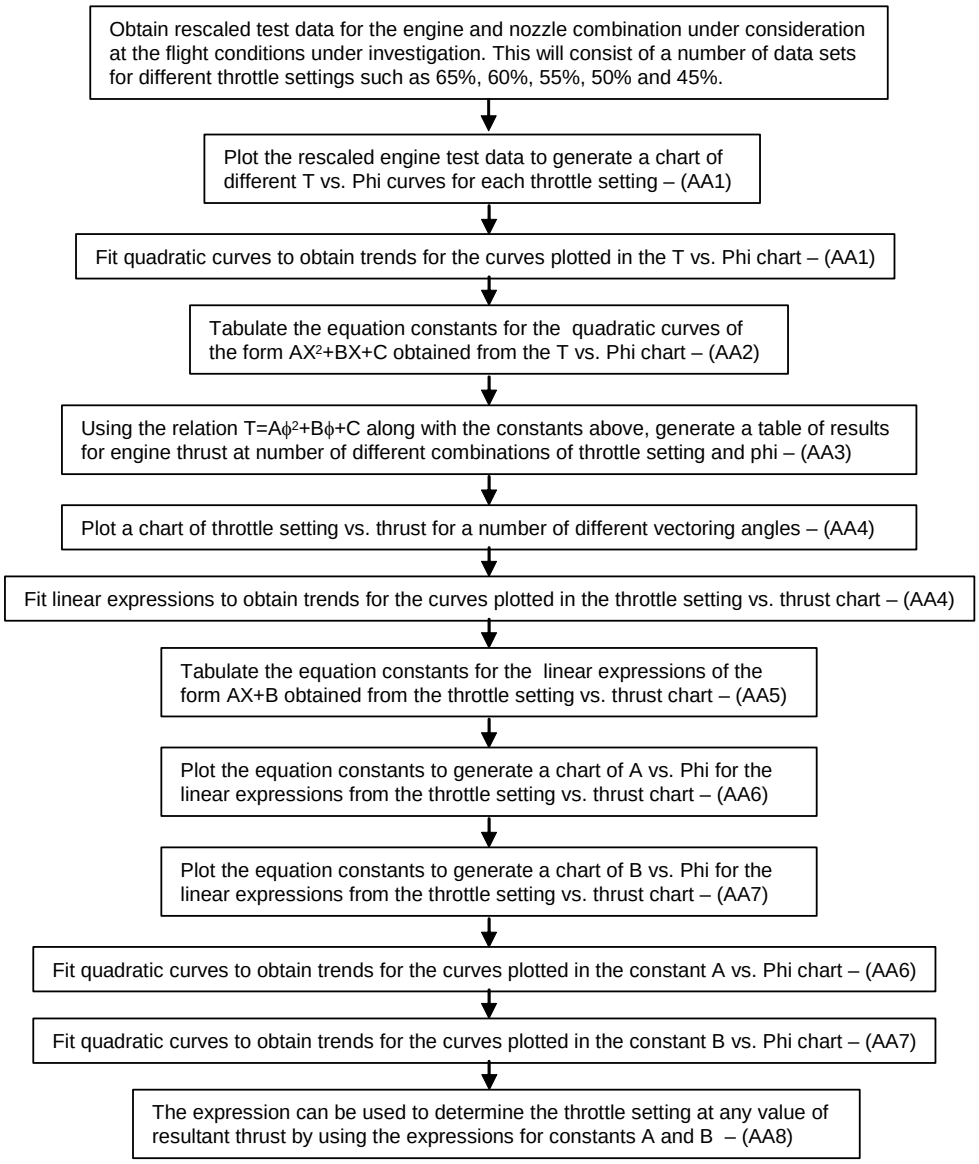

Using the tables of results from the thrust vectored engine-nozzle analysis; we are able to obtain the thrust versus vectoring angle plots given in chart AA1 below. As shown, we are then able to fit a quadratic expression to each curve which corresponds to a different engine throttle setting.

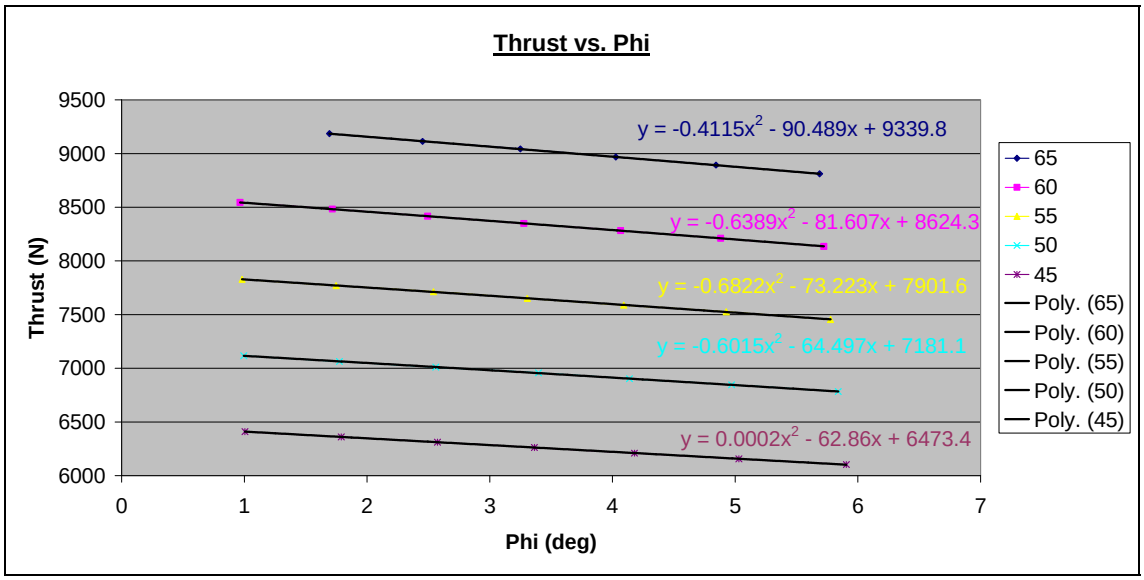

Chart 3-1 (AA3)

The constants from the quadratic expressions can then be tabulated as in AA2 below.

Constants A,B,C for the quadratic expressions of the Thrust vs. Phi plots at different throttle settings

Constants	Throttle settings (%) 65	60	55	50	45
A	-0.4115	-0.6389	-0.6822	-0.6015	0.0002
B	-90.489	-81.607	-73.223	-64.497	-62.86
C	9339.8	8624.3	7901.6	7181.1	6473.4

Table 3-1 (AA2)

Using the expression below we are able to generate the results in table AA3 for engine thrust at a number of different combinations of throttle setting and vectoring angle.

$$T = A \cdot |\phi|^2 + B \cdot |\phi| + C$$

Values of un-vectotred thrust at different combinations of throttle setting and vectoring angle

Phi (deg)	Throttle setting (% - x100) 6500	6000	5500	5000	4500
0	9339.8	8624.3	7901.6	7181.1	6473.4
1	9248.9	8542.054	7827.695	7116.002	6410.54
2	9157.176	8458.53	7752.425	7049.7	6347.681
3	9064.63	8373.729	7675.791	6982.196	6284.822
4	8971.26	8287.65	7597.793	6913.488	6221.963
5	8877.068	8200.293	7518.43	6843.578	6159.105
6	8782.052	8111.658	7437.703	6772.464	6096.247

Table 3-2 (AA3)

The results from table AA3 can then be plotted out to produce chart AA4 below and a linear expression fitted to each curve as shown.

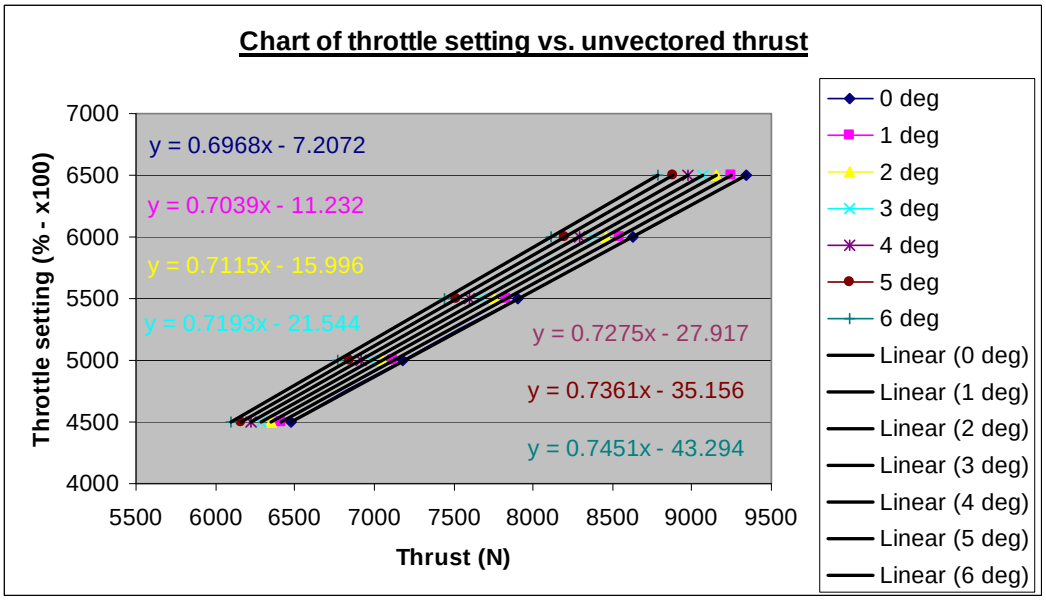

Chart 3-2 (AA4)

The constants from the expressions in the chart AA4 can then be tabulated as in table AA5 below. Where, each linear expression is in the format,

$$\%Throttle = A \cdot (Thrust) + B$$

Constants A,B for the linear expressions of the throttle setting vs. unvectored thrust

Phi (deg)	Constants A	B
0	0.6968	-7.2072
1	0.7039	-11.232
2	0.7115	-15.996
3	0.7193	-21.544
4	0.7275	-27.917
5	0.7361	-35.156
6	0.7451	-43.294

Table 3-3 (AA5)

Each of the columns of constants from the table above can finally be plotted in separate charts and a quadratic expression fitted to each. This gives us equations AA6 and AA7 below for equation constants A and B respectively.

$$B = -0.4118 \cdot |\phi|^2 - 3.5303 \cdot |\phi| - 7.2482 \qquad \text{Eq 3-1 (AA6)}$$

$$A = 0.1821 \cdot |\phi|^2 + 6.9536 \cdot |\phi| + 696.8 \qquad \text{Eq 3-2 (AA7)}$$

The general expression for the engine throttle setting with respect to the resultant engine thrust is then given by the expression AA8 below. Where, the constants A and B are determined by equations AA6 and AA7 respectively as a function of engine plume deflection angle.

$$\%Throttle = \frac{(A \cdot T_{Resultant}) + B}{1000} \qquad \text{Eq 3-3 (AA8)}$$

B4 Deriving a general expression for the thrust specific fuel consumption at cruise

The purpose of this work is to transform the thrust vectored engine-nozzle data as obtained in the data rescaling section, into a more manageable format for analytical work. The result is an analytical expression for the thrust specific fuel consumption as a function of engine throttle setting and engine plume deflection angle. A summary of the procedure used is shown in the flow chart below. The accompanying equations, charts and tables for this process are also given below.

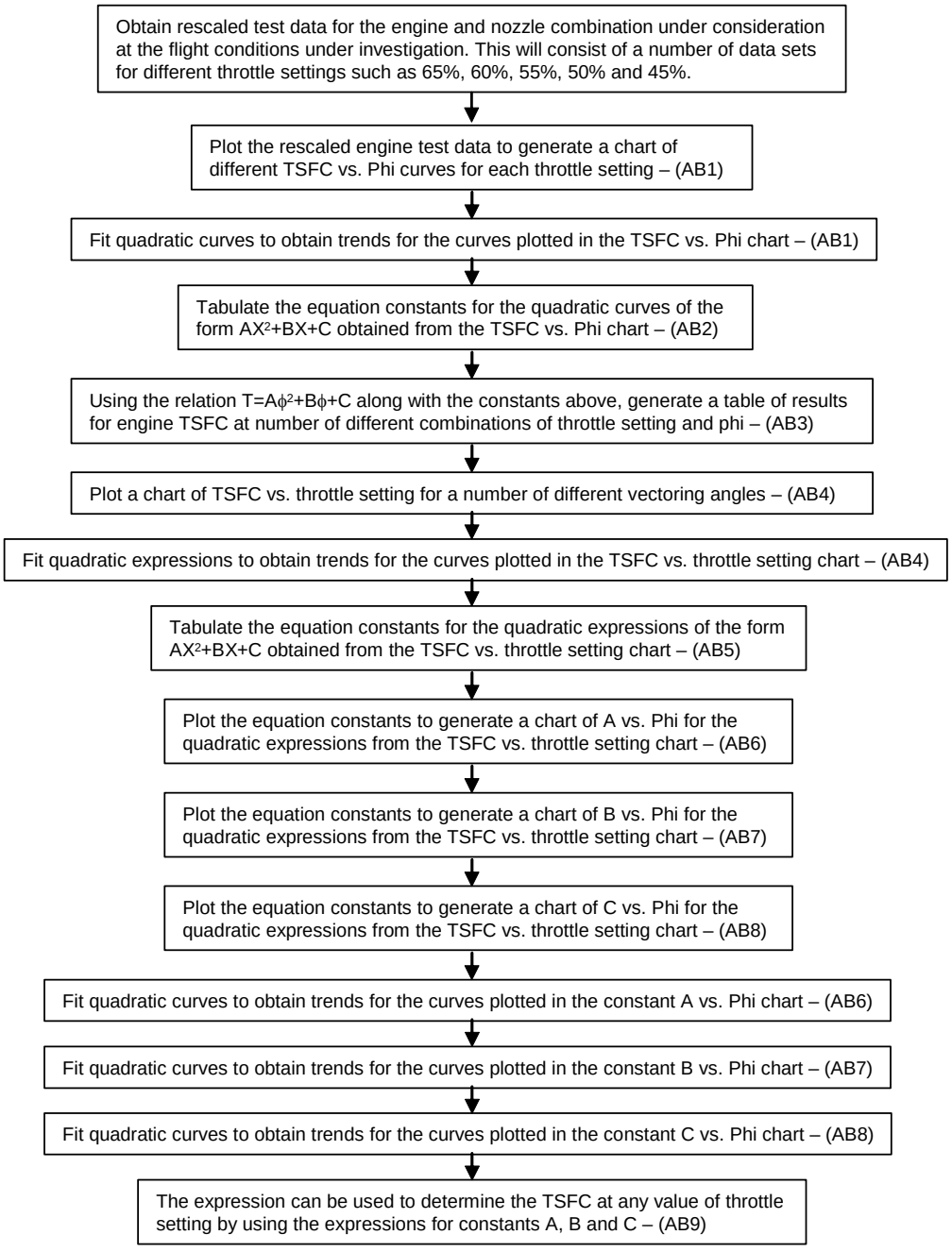

Using the tables of results from the thrust vectored engine-nozzle analysis; we are able to obtain the TSFC versus vectoring angle plots given in chart AB1 below. As shown, we are then able to fit a quadratic expression to each curve which corresponds to a different engine throttle setting.

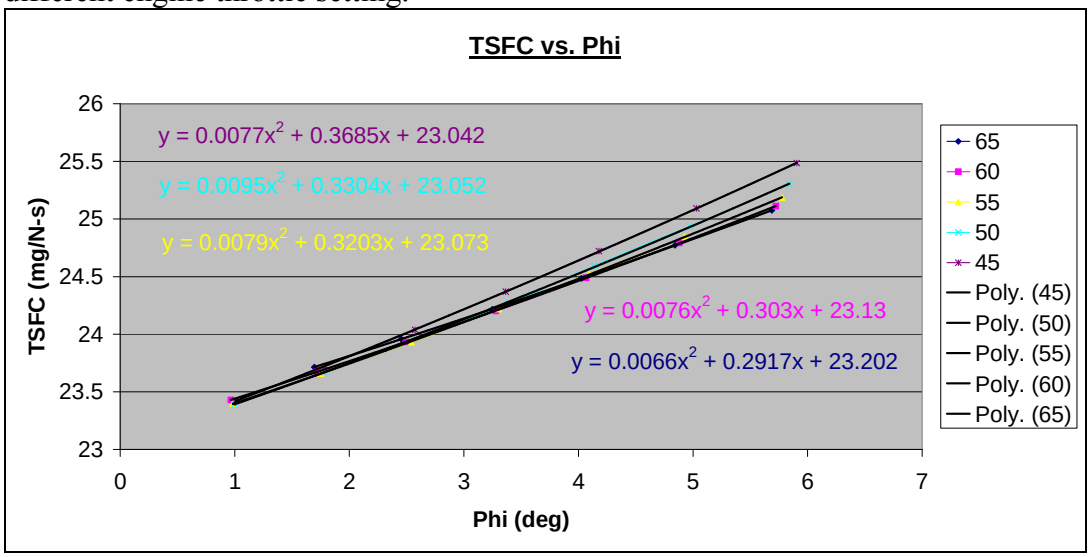

Chart 4-1 (AB1)

The constants from the quadratic expressions can then be tabulated as in AB2 below.

Constants A,B,C for the quadratic expressions of the TSFC vs. Phi plots at different throttle settings

Constants	Throttle settings (%) 65	60	55	50	45
A	0.0066	0.0076	0.0079	0.0095	0.0077
B	0.2917	0.303	0.3203	0.3304	0.3685
C	23.202	23.13	23.073	23.052	23.042

Table 4-1 (AB2)

The expression below we are then able to generate the results in table AB3 for engine TSFC at a number of different combinations of throttle setting and vectoring angle.

$$TSFC = A \cdot |\phi|^2 + B \cdot |\phi| + C$$

Values of TSFC at different combinations of throttle setting and vectoring angle

Phi (deg)	Throttle setting (% - /100) 65	60	55	50	45
0	23.202	23.13	23.073	23.052	23.042
1	23.5003	23.4406	23.4012	23.3919	23.4182
2	23.8118	23.7664	23.7452	23.7508	23.8098
3	24.1365	24.1074	24.105	24.1287	24.2168
4	24.4744	24.4636	24.4806	24.5256	24.6392
5	24.8255	24.835	24.872	24.9415	25.077
6	25.1898	25.2216	25.2792	25.3764	25.5302

Table 4-2 (AB3)

The results from table AB3 can then be plotted out to produce chart AB4 below and a quadratic expression fitted to each curve as shown.

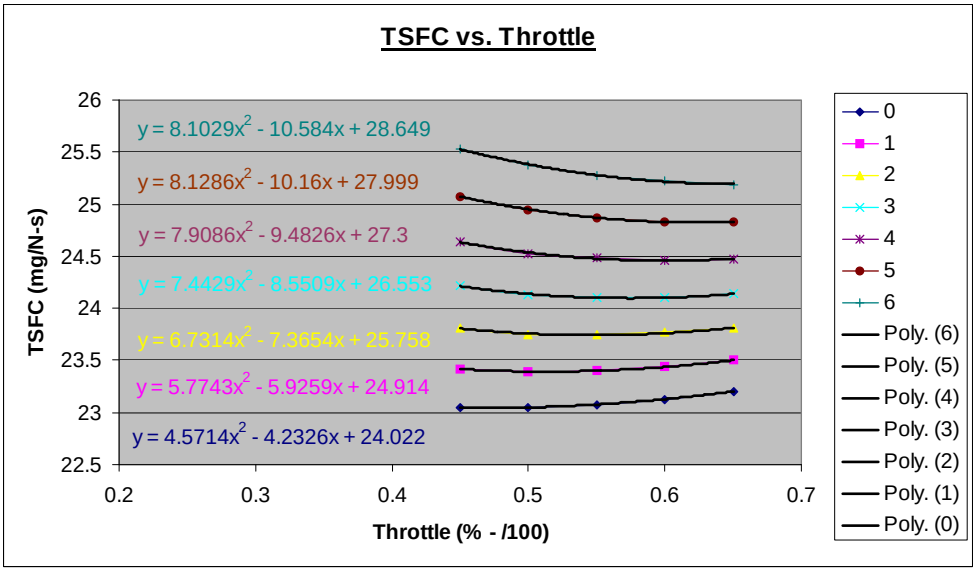

Chart 4-2 (AB4)

The constants from the quadratic expressions in chart AB4 can then be tabulated as in table AB5 below. Where, each quadratic expression is in the format,

$$TSFC = A \cdot (\%Throttle)^2 + B \cdot (\%Throttle) + C$$

Constants A,B,C for the linear expressions of the TSFC vs. throttle setting

Phi (deg)	Constants A	B	C
0	4.5714	-4.2326	24.022
1	5.7743	-5.9259	24.914
2	6.7314	-7.3654	25.758
3	7.4429	-8.5509	26.553
4	7.9086	-9.4826	27.3
5	8.1286	-10.16	27.999
6	8.1029	-10.584	28.649

Table 4-3 (AB5)

Each of the columns of constants from the table above finally be plotted in separate charts and a quadratic expression fitted to each. This gives us equations AB6, AB7 and AB8 below for equation constants A, B and C respectively.

$$A = -0.1229 \cdot |\phi|^2 + 1.3257 \cdot |\phi| + 4.5714 \qquad \text{Eq 4-1 (AB6)}$$

$$B = 0.127 \cdot |\phi|^2 - 1.8203 \cdot |\phi| - 4.2326 \qquad \text{Eq 4-2 (AB7)}$$

$$C = -0.0242 \cdot |\phi|^2 + 0.9163 \cdot |\phi| + 24.022 \qquad \text{Eq 4-3 (AB8)}$$

The general expression for the thrust specific fuel consumption with respect to engine throttle setting is then given by the expression AB9 below. Where, the constants A, B and C are determined from equations AB6, AB7 and AB8 respectively as a function of engine plume deflection angle.

$$TSFC = \left\{ A \cdot \left(\frac{\%T}{100} \right)^2 \right\} + \left\{ B \cdot \left(\frac{\%T}{100} \right) \right\} + C \qquad \text{Eq 4-4 (AB9)}$$

B5 Analysis of the nose jet pitch control system

B5.1 An overview of the system

The layout of the nose jet control system is presented in the figure below.

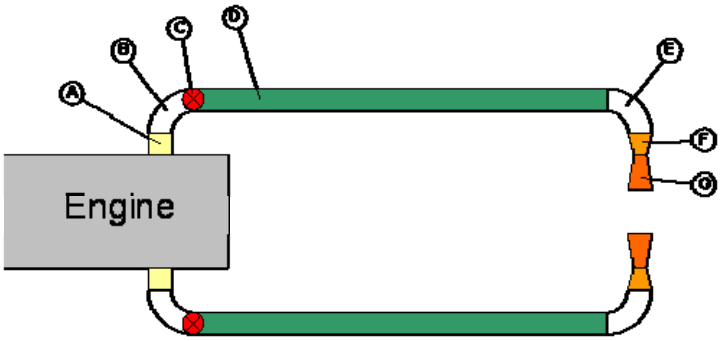

Item	Description
A	Engine bleed port
B	Bleed outlet elbow
C	Bleed valve
D	Front to rear ducting
E	Nozzle elbow
F	Nozzle convergent section
G	Nozzle divergent section

Figure 5-1

This system uses high pressure air which is bled directly from the engine via a bleed port and is connected to a control valve by means of a 90 degree elbow. The air leaving the control valve at the desired flow rate is then ducted to the front of the aircraft before passing through a 90 degree elbow, to interface with the downward pointing nozzle. The convergent-divergent nozzle, which is conveniently located within the nose gear bay, accelerates the flow to generate a reaction force which can be used to lift the nose of the aircraft and thus rotate the aircraft. The control valve is able to regulate the quantity of air which is bled from the engine and thus the reaction force that is generated by the nozzle. This will inevitably be linked into the flight control system. As can be seen in the figure above, the system is symmetrical about the aircraft centreline and thus there will be two nozzles located on either side of the nose landing gear bay.

B5.2 Analysis of the system

In the analysis which follows, the total losses in the system must be determined in order to calculate the flow conditions at the nozzle and thus the reaction force generated. This is achieved by analysing each of the component parts separately. The analysis then involves determining the flow conditions at a number of points along the system and the losses between them. An exploded view of the system is shown below with the reference points used in this analysis marked.

Station	Description
1	Engine bleed port exit
2	Bleed outlet elbow exit
3	Bleed valve exit
4	Front to rear ducting exit
5	Nozzle elbow exit
6	Nozzle throat
7	Nozzle exit

Figure 5-2

5.2.1 Flow conditions at the engine bleed port exit (at station 1)

The results from the ONX\AEDsys analyses at the engine condition under investigation gives us the total temperature, total pressure, ratio of specific heats and bleed mass flow rate at the bleed port exit. As there are two bleed ports (one on each side of the engine), the bleed flow through each port will therefore be half of this value. For the work which follows, we also need to know the Mach number of the flow leaving the bleed port. This is determined with a parameter known as the mass flow function (MFP) which is related to the local Mach number of the flow at any cross section. This is determined with the relation below from ESDU FMI1 [66] as a function of total temperature and pressure.

$$\frac{m\sqrt{RT_H}}{Ap_H} = \sqrt{\gamma}M\left\{1 + \frac{\gamma - 1}{2}M^2\right\}^{\frac{-(\gamma + 1)}{2(\gamma - 1)}}. \qquad \text{Eq 5-1}$$

Fortunately, we have all the terms to be able to calculate the function on the left side of the expression and the only unknown on the right side of the expression is the Mach number. The Mach number can thus be determined by making an initial estimate and iterating this value until the left and right sides of the expression are equal.

We are now able to determine the static temperature and pressure with the expressions below, obtained from ESDU 74028 [67].

$$p/p_t = \left(1 + \frac{\gamma - 1}{2}M^2\right)^{\gamma/(1 - \gamma)} \qquad \text{Eq 5-2}$$

$$T/T_t = \left(1 + \frac{\gamma - 1}{2}M^2\right)^{-1} \qquad \text{Eq 5-3}$$

The density and speed of sound of the gas can be determined with the expressions for the equation of state of a perfect gas from ESDU 74028.

$$\rho = \frac{p}{RT} \qquad \text{Eq 5-4}$$

$$a = \sqrt{\gamma \cdot R \cdot T} \qquad \text{Eq 5-5}$$

The velocity of the flow can then finally be determined from the expression,

$$V = M \cdot a \qquad \text{Eq 5-6}$$

The final fluid property required is the viscosity of the air, which can be determined from the relation below, from ESDU 77021 [68].

$$\mu = \frac{1.458 \cdot 10^{-6} \cdot T^{3/2}}{T + 110.4} \qquad \text{Eq 5-7}$$

We now have all the necessary terms to be able to calculate the Reynolds number of the flow, as given by the expression,

$$\mathrm{Re} = \frac{\rho \cdot V \cdot D}{\mu} \qquad \text{Eq 5-8}$$

The result of this stage is a table of parameters for flow at the bleed port exit, which will be utilised in the analyses which follow.

5.2.2 Bleed elbow loss factor (between stations 1 and 2)

The loss factor for the bleed port exit elbow can be determined by the method given in ESDU 83037 [69]. This method is based on a generic circular arc bend, the geometry of which is defined in figure below.

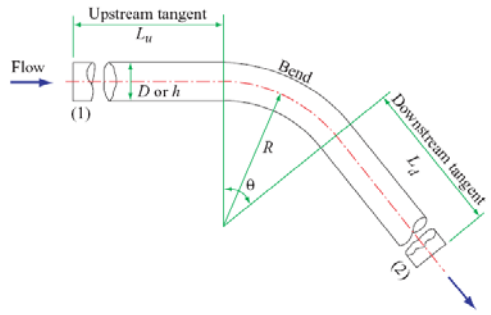

Figure 5-3 [69]

In this study, the important parameters are the pipe diameter, mean bend radius and the turning angle of the bend. The upstream and downstream tangent lengths are assumed to be zero as these are accounted for elsewhere. The elbow diameter is assumed to be the same as the bleed port exit diameter of 50.5mm. The turning angle is 90º and the mean bend radius is assumed to be twice the exit diameter at 101mm.

The procedure followed is that given for turbulent flow (Re≥4000) through short circular arc bends, where the gross static elbow loss factor is determined from,

$$K_{s,\,G} = K_b + K_c + K_d .$$ Eq 5-9

Where, K_b is the loss component due to friction in the bend, which is determined from,

$$K_b = 0.07\theta(R/D)f$$ Eq 5-10

This relation makes use of the fanning friction factor (f) for fully developed flow in a straight pipe. This can be approximated with the relation below from ESDU 66027 [70], which is valid for the 10^4<Re<$2.5\text{x}10^8$ range.

$$f_c = [4\log_{10}(Re/\{4.53\log_{10}(Re) - 3.82\})]^{-2} .$$ Eq 5-11

K_c is the loss component due to bend curvature, which can be determined from,

$$K_c = \frac{\theta}{90}\left(\frac{R}{D}\right)^{0.5}\left[0.03 + 1.3\left(\frac{\varepsilon}{D}\right)^{0.5}\right].$$ Eq 5-12

In this relation, ε is the effective roughness height of the surface. A value of 0.0015mm was chosen as being a typical value for this application. Finally, K_d is the loss component due to flow recovery in the downstream tangent. This can be determined by the relation below, which is valid for R/D≥1.

$$K_d = 0.2(R/D)^{-1.2}\phi_1\phi_2\phi_5$$ Eq 5-13

Where, ϕ_1 is the Reynolds number correction factor as given by the relation,

$$\phi_1 = (1 + 10^4/Re)$$ Eq 5-14

ϕ_2 is the downstream tangent correction factor as given by the relation below. As the length of our downstream tangent is assumed to be zero, the relation reduces to 1.

$$\phi_2 = \left(1 - \exp(-0.1 L_d/D) + \frac{3\exp(-L_d/D)}{(R/D)^2}\right) \exp\left\{-\left[\frac{1}{(L_d/D)+1}\right]^{2(R/D)}\right\}.$$

Eq 5-15

Finally ϕ_5, is the bend angle correction factor, which is given by the expression below as a function of the bend angle. For a 90º bend, this has a value of 1.

$$\phi_5 = 1.04 - [(110 - \theta)^2/10^4].$$

Eq 5-16

5.2.3 Control valve loss factor (between stations 2 and 3)

The loss factor for the control valve can be determined by the method given in ESDU 69022 [71]. This empirical chart based method is based the loss for a typical butterfly valve, whereby the corrected pressure loss coefficient is given by the relation below.

$$C_K = C_K' \times \alpha_1 \times \alpha_2.$$

Eq 5-17

Where, CK' is the basic loss coefficient for a fully open valve with a Re>4000. This can be determined from figure 4 of ESDU 69022, where t/D is taken to equal 0.1.

α_1 is a correction factor for a partially open valve and can be determined from figure 12 of ESDU 69022. In this analysis, the valve is assumed to be fully open in order to generate maximum reaction thrust from the nose jet. In this case, α_1 is taken to be 1. The final term α_2, is a correction factor for flows with a Re<4000 as given by figure 16 of ESDU 69022. Since we are operating in conditions well above Re=4000, this equals 1.

5.2.4 Front to rear ducting loss factor (between stations 3 and 4)

The loss factor for the front to rear ducting can be determined by the method given in ESDU 66027 [70]. The general equation for the friction losses for fully developed flow within a straight pipe is given below.

$$K_f = 4 \cdot f \cdot \frac{L}{D}$$

Eq 5-18

Where, L and D and the length and diameter of the pipe respectively and f is the fanning friction factor which can be approximated with expression below.

$$f_c = [4 \log_{10}(Re / \{4.53 \log_{10}(Re) - 3.82\})]^{-2}.$$

Eq 5-19

5.2.5 Nozzle elbow bend loss factor (between stations 4 and 5)

The analysis for the nozzle bend loss factor follows exactly the same procedure as that used for the bleed elbow. The only difference being the nozzle elbow has a smaller bend radius and is taken to be equal to the pipe diameter with a value of 50.5mm. The pipe diameter has remained constant up to this point in the system.

5.2.6 Nozzle contraction loss factor (between stations 5 and 6)

To determine the nozzle contraction loss factor, reference was made to a similar study which itself referred to an obsolete ESDU data sheet. In the absence of a better approach, the same methodology was adopted here and since the nozzles were of similar geometry, the required coefficients were also considered valid.

Following this approach, the contraction loss coefficient is given by,

$$K_{Con} = \lambda \cdot K_t \cdot \frac{A_2}{A_t} \qquad \text{Eq 5-20}$$

Where, the constants λ and K_t were both taken as 0.1. A_2 is the nozzle elbow exit area, which is the same as the bleed port exit area and A_t is the nozzle throat area, which is determined in a later section.

5.2.7 Total system pressure loss (between stations 1 and 7)

We now have estimates for the loss coefficient of each of the components that make up the system. The total loss coefficient for the system between the bleed port exit and the nozzle throat will then be the sum of these, as in the equation below.

$$K_{Total} = K_{Bleed-Elbow} + K_{Valve} + K_{Ducting} + K_{Nozzle-Elbow} + K_{Nozzle-Con} \qquad \text{Eq 5-21}$$

Using the relations from ESDU FMI1 [66], the total pressure drop between the bleed port outlet and the nozzle throat can then be found from the following relation.

$$\Delta P_{1-7} = \tfrac{1}{2} \cdot \rho \cdot V^2 \cdot K_{Total} \qquad \text{Eq 5-22}$$

Finally, the total pressure at the nozzle throat can be determined from the relation below, where P_{t3} is the total pressure at the bleed port exit.

$$P_{t-Throat} = P_{t3} - \Delta P_{1-7} \qquad \text{Eq 5-23}$$

5.2.8 Nozzle throat sizing (station 6)

To determine the size of the nozzle throat, we make use of a non-dimensional expression for the mass flow rate from ESDU 67035 [72], as given below.

$$\frac{m}{A_1 p_H}(RT_{H1})^{1/2} = \left\{ \frac{2\gamma}{(\gamma-1)} \frac{1}{(p_H/p_0)^{\frac{\gamma+1}{\gamma}}} \left[\left(\frac{p_H}{p_0}\right)^{\frac{\gamma-1}{\gamma}} - 1 \right] \right\}^{1/2}. \qquad \text{Eq 5-24}$$

The terms used in this relation are defined in the figure below. In our analysis, p_H and T_H are the total temperature and pressure of the flow leaving the nozzle elbow.

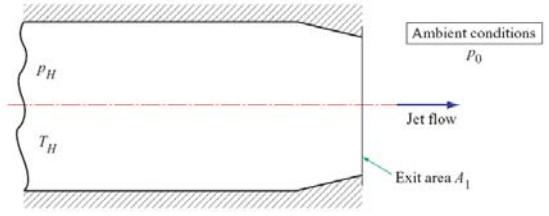

Sketch 2.1 Convergent nozzle configuration

Figure 5-4 [72]

Fortunately, for high pressure ratios where $p_H / p_0 \geq (p_H / p_0)^*$ this equation reduces to the relation below. $(p_H / p_0)^*$ is the critical pressure ratio, which is the condition at which sonic velocity first occurs at the exit of the convergent nozzle. In other words, we are assuming that that at the nozzle throat, the Mach number is always 1.

$$\frac{m}{A_1 p_H}(RT_{H1})^{1/2} = \left[\gamma\left(\frac{2}{\gamma+1}\right)^{\frac{\gamma+1}{\gamma-1}}\right]^{1/2}.$$ Eq 5-25

At this stage, we already have all the necessary terms to be able to calculate the function on the right side of the above expression. In accordance with the continuity of mass, the mass flow rate through the system remains constant and therefore we can use the value calculated at the bleed port exit here. The total temperature is also assumed to remain constant through the system and the value at the bleed port exit is used here, the same being true for the ratio of specific heats. The total pressure at the nozzle throat, taking into account the pressure losses in the system, was determined in the previous section.

The only unknown on the left side of the expression is the nozzle throat area. The nozzle throat area could therefore be found directly from this expression. However, the throat area is required in an earlier section which also an impact on these results and therefore an iterative solution process is required. Firstly, we make an initial estimate of the area, which is used to determine the nozzle contraction loss factor and so forth and then iterate this value until the estimated and calculated values are equal. The nozzle throat diameter can then be determined from the following simple expression.

$$D_t = \sqrt{\frac{4 \cdot A_t}{\pi}}$$ Eq 5-26

5.2.9 Flow conditions at the nozzle throat (station 6)

Fortunately, we have already determined a number of the conditions at the nozzle throat in the work so far. In this section, we determine the remaining terms as required for the following sections. The static pressure and temperature can be determined from the respective relations below, from ESDU 74028 [67]. The reader is reminded that flow at the nozzle throat is sonic and therefore the Mach number at the throat is 1.

$$T/T_t = \left(1 + \frac{\gamma-1}{2}M^2\right)^{-1}$$ Eq 5-27

$$p/p_t = \left(1 + \frac{\gamma-1}{2}M^2\right)^{\gamma/(1-\gamma)}$$ Eq 5-28

The density of the gas and speed of sound of the gas can be calculated with the expressions below from the equation of state for a perfect gas from ESDU 74028.

$$\rho = \frac{p}{RT}$$ Eq 5-29

$$a = \sqrt{\gamma \cdot R \cdot T}$$ Eq 5-30

The velocity of the flow can finally be determined from the expression,

$$V = M \cdot a$$ Eq 5-31

5.2.10 Analysis of the nozzle divergent section (stations 6 to 7)

The layout of a typical convergent-divergent nozzle is presented in the figure below. An important parameter with respect to the nozzle divergent section is the semi-angle θ_{Div}

which is important with respect to maintaining attached flow in the nozzle. In this system, θ_{Div} was taken to be 12.5º, in accordance with similar nozzles.

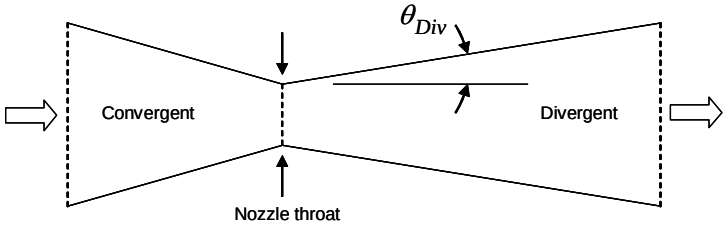

Figure 5-5

With knowledge of the static temperature at the nozzle throat, as determined in the previous section we are able to calculate a revised figure for the ratio of specific heats. For this, we are able to make use of the following curve fitted expression.

$$\gamma_{Throat} = \left(-0.0001 \cdot T_{St-Throat}\right) + 1.434 \qquad \text{Eq 5-32}$$

At this point in our analysis, it is worth double checking our earlier assumption that we are operating in excess of the critical pressure ratio. Where, the critical pressure ratio can be determined from the following expression from ESDU 67035 [72].

$$\left(\frac{p_H}{p_0}\right)^* = \left(\frac{\gamma + 1}{2}\right)^{\frac{\gamma}{\gamma - 1}}. \qquad \text{Eq 5-33}$$

The actual pressure ratio can be determined from the expression below, where P_0 is the ambient pressure (taken as 101.32 kPa).

$$\left(\frac{p_H}{p_0}\right)_{Nozzle} = \frac{P_{t-Throat}}{P_0} \qquad \text{Eq 5-34}$$

In the design of a convergent-divergent nozzle which is operating with a throat Mach number of 1, the divergent section exit area should be correctly matched to the area of the throat for its operating pressure ratio. The nozzle exit area (A_1) to satisfy this requirement can be predicted with the relation below where A* is the nozzle throat area.

$$\frac{A_1}{A^*} = \left\{ \frac{\frac{\gamma - 1}{2}[2/(\gamma + 1)]^{\frac{\gamma + 1}{\gamma - 1}} (p_H/p_0)^{\frac{\gamma + 1}{\gamma}}}{(p_H/p_0)^{\frac{\gamma - 1}{\gamma}} - 1} \right\}^{1/2}, \qquad \text{Eq 5-35}$$

The diameter of the nozzle exit can then be found from the following relation.

$$D_{Exit} = \sqrt{\frac{4 \cdot A_t}{\pi}} \qquad \text{Eq 5-36}$$

The final Mach number of the flow at the exit plane of the nozzle (M_2) can then be found from the expression below, from ESDU 74028 [67]. Where, P_2 is the atmospheric pressure at the nozzle exit and P_1 is the total pressure at the nozzle throat.

$$M_2 = \left\{ \frac{2}{\gamma - 1} \left[\left(\frac{p_2}{p_1} \right)^{(1 - \gamma)/\gamma} - 1 \right] \right\}^{1/2} \qquad \text{Eq 5-37}$$

If we assume that the flow is fully expanded at the nozzle exit then the static temperature at the nozzle exit can then be determined from the relation below. In this

case, the total temperature is taken to be that at the bleed port exit and the Mach number is that at the nozzle exit.

$$T/T_t = \left(1 + \frac{\gamma - 1}{2} M^2\right)^{-1}$$ Eq 5-38

Finally, we are able to calculate the density and speed of sound of the gas with the expression for the equation of state for a perfect gas from ESDU 74028. Since the flow is assumed to be fully expanded then the pressure at the nozzle exit will be the same as the atmospheric pressure.

$$\rho = \frac{p}{RT}$$ Eq 5-39

$$a = \sqrt{\gamma \cdot R \cdot T}$$ Eq 5-40

The velocity of the flow can finally be determined from expression,

$$V = M \cdot a$$ Eq 5-41

B5.3 Calculation of the gross thrust from the pitch control jet

The gross thrust from each nozzle can finally be determined from the expression below.

$$\frac{F}{A_1 p_0} = \frac{m V_1}{A_1 p_0} = \frac{2\gamma}{\gamma - 1}\left[\left(\frac{p_H}{p_0}\right)^{\frac{\gamma - 1}{\gamma}} - 1\right].$$ Eq 5-42

Using the results from the previous sections, we are able to calculate the function on the right hand side of the expression above. In this expression, P_0 is the ambient pressure and A_1 is the nozzle exit area (also referred to as A_3 in the analyses above). The thrust from the nozzle can then be determined from the left hand side of the expression above as,

$$F_{Nozzle} = \left[\frac{F}{A_1 \cdot p_0}\right] \cdot \left(A_3 \cdot P_0\right)$$ Eq 5-43

Since we have two pitch control nozzles at the front of the aircraft (one at either side of the nose landing gear), the total force at the nose of the aircraft will be twice the value obtained above as below.

$$F_{Total} = 2 \cdot F_{Nozzle}$$ Eq 5-44

B5.4 Final results

Following the procedure above, we are able to obtain a complete set of results for the engine operating at its take-off condition, as a function of engine bleed as given in the following chart.

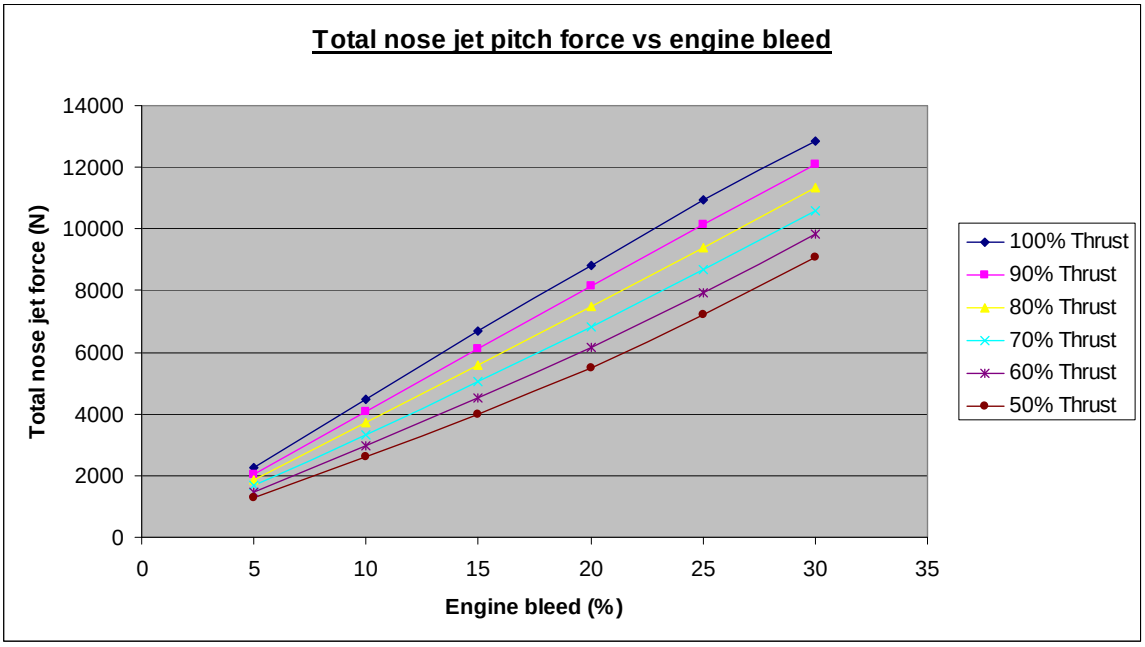

Chart 5-1

For our work, we are however only interested in the results at the maximum thrust take-off condition as given in the table below.

Thrust	Bleed	Nose jet force (N)
100	2.5	1119.966792
100	5	2238.941792
100	7.5	3353.566723
100	10	4465.797366
100	12.5	5572.17656
100	15	6671.088995
100	17.5	7760.114669
100	20	8836.780881
100	25	10926.5119
100	30	12836.68604

Table 5-1

These results are however not without their limitations since they were evaluated for the baseline engine configuration with a nozzle Pi value of 0.98. This corresponds to an engine nozzle deflection angle of 0 degrees. Ideally this analysis should be repeated for each of the engine nozzle deflections being considered but time has proven to be a limiting factor in this project. The engine studies in this thesis have however shown that the effect of the nozzle Pi value on engine bleed is negligible and thus the error in these assumptions in negligible.

B5.5 Mach number scale factors

As already discussed in the sections for the analyses of the engine Thrust and TSFC, the performance of the engine is a function of the aircraft velocity and altitude, amongst other parameters. In the analysis above, the aircraft altitude has been fixed at sea level conditions and its speed fixed at Mach 0.2, which was taken to be the average take-off speed for this type of aircraft. In order to prevent the laborious and time consuming task

of having to repeat the above analysis at a number of different Mach numbers, a scale factor has been applied to the results to account for the ever changing speed of the aircraft during the take-off phase.

In order to generate these scale factors, the analysis above was repeated at a number of different Mach numbers. The un-vectored baseline configuration (Pi = 0.98) with zero nozzle deflection angle was used for this analysis to give the results below.

Nose jet force (N)

	Bleed							
Mach	2.5	5	7.5	10	12.5	15	17.5	20
0	1109.322	2217.201	3322.676	4423.732	5519.019	6607.29	7684.903	8749.135
0.1	1112.146	2222.846	3331.139	4435.45	5533.666	6624.86	7705.384	8773.363
0.2	1119.967	2238.942	3353.567	4465.797	5572.174	6671.089	7760.113	8836.782
0.3	1133.154	2265.301	3394.106	4520.713	5638.025	6750.832	7853.945	8944.005
0.4	1152.219	2302.972	3450.916	4595.045	5735.446	6868.448	7992.667	9103.337

Table 5-2

If the Mach 0.2 results are taken as the baseline values (as presented in the results section above), then a scale factor with reference to this condition can be determined. The results of this analysis are presented below for a number of different values of engine bleed.

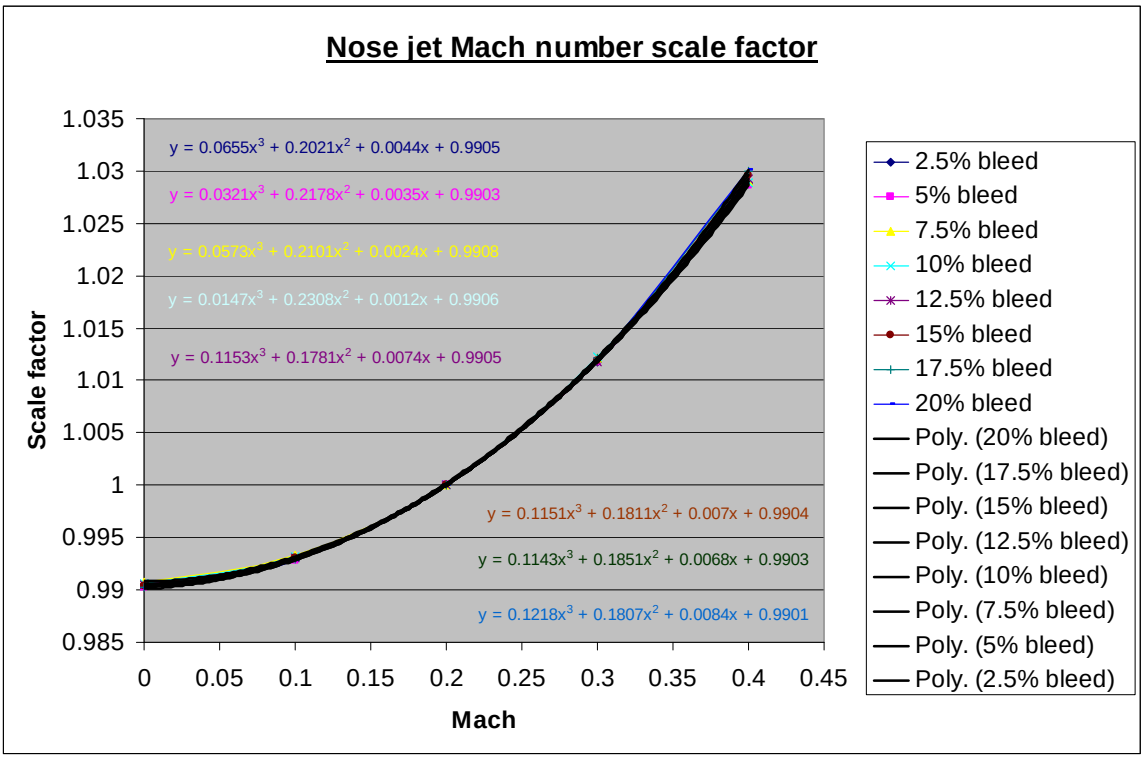

Chart 5-2

C1 Initial propulsion system considerations

C1.1 A brief review of engine exhaust nozzles

The role of the exhaust nozzle is to accelerate the engine exhaust gases generated by the gas generator proportion of the engine to a high velocity and thus generate a propulsive thrust. The engine nozzle can in some cases be required to satisfy other requirements such as stealth requirements or even augment lift by deflecting the thrust. This section givens an overview of some the common nozzle types, which can be arranged into one of the main groups,

- Convergent nozzles - This is the oldest type of engine nozzle which simply consists of a fixed convergent duct. Its exit area is typically selected for optimal cruise. It is still widely used on subsonic aircraft and in cases when the nozzle pressure ratio is less than about 4. Their simplicity and light-weight has helped them retain their popularity.
- Convergent-divergent nozzles - These were developed to overcome the limitations of convergent nozzles, which become chocked when the exit gases reach Mach 1. The addition of a divergent section nozzle downstream of the nozzle throat allows the gases to further accelerate in this section to values in excess of Mach 1. Variable geometry variants allow the nozzle throat to be varied to match the engine operating conditions and thus increase their operational flexibility. When afterburners are used, the operating characteristics of the afterburner can be isolated from the engine by means of the nozzle throat. Even more refined variants allow the nozzle exit area to be varied as well. These nozzles have typically seen application on high performance engines in supersonic aircraft or in cases where the nozzle pressure ratio is greater than about 4.
- Ejector nozzle - An additional airflow from the outside of the nozzle is ejected into the exhaust flow to alter the flow characteristics of the exhaust flow at the nozzle exit. These are not only restricted to use on convergent nozzles but have also been developed as a convergent-divergent configuration. A refinement of this is the two-stage ejector nozzle in which some of the external flow passes through the nozzle. Such a concept allows the nozzle areas to be varied independently.
- Variable geometry nozzle - Such configurations enable the engine to operate more effectively over a wider operating range. The first generation of variable convergent nozzles (as were developed for the early transonic fighters) consisted of flaps which deflected into the flow. Other variants include the translating plug and the later more efficient converging iris designs.
- Thrust vectored nozzle - A detailed description of a number of common thrust vectoring nozzles is presented in the main text. In addition to those discussed, other older configurations include, vectoring flaps, rotating sections, side elbow, bucket and ventral designs.

C1.2 A brief note on engine intakes

Intake design is not the focus of this study but will be briefly mentioned since it can have a considerable impact on engine and nozzle performance. The role of the engine intake is to not only deliver sufficient air to the engine at all flight regimes but also slow the air to prevent breakdown of the flow within the compressor. Other design requirements for an inlet are to minimise pressure losses, flow distortion and swirl. An engine intake consists of two parts, an inlet front face and a diffuser. The free-stream flow is initially slowed outside the inlet and then further slowed within the diffuser. The most common types of subsonic intake are plenum, straight through, podded nacelle, pitot, flush NACA and S-duct. Supersonic inlets include pitot, external compression and mixed compression (internal and external). The location of the engine inlets is an important consideration to prevent problems with inlet distortion. The shape of the aircraft fore-body will being a particular problem. For buried installations, intake locations include, chin, over-fuselage, over-wing, fuselage side and many more. The intake design must also incorporate a means of boundary layer removal to prevent large pressure recovery losses. This can consist of either a boundary layer diverter or a means of bleeding the boundary layer from the inlet entrance.

The engine inlet is sized to be able to deliver sufficient air to the engine at the most critical design condition. As the inlet is responsible for the biggest contribution to propulsion system drag, the designer must ensure that it is not oversized. At other conditions, the excess air will spill around the outside of the intake which results in a drag component called ‘additive drag’. This is due to the loss in momentum of the air approaching the inlet, which is slowed and compressed by the inlet but not used by the engine. This can be offset by cowl-lip suction, which is a result of the turning of the flow around the edge of the engine cowl. Alternatively, the excess air can be ducted and dumped, which results in by-pass drag, but this will still considerably less than the additive drag. A final form of drag within the inlet system arises from the removal of the turbulent boundary layer. Calculation of these drag terms involves complex analytical and empirical tools which are a function of the flow field around the aircraft.

C1.3 Engine nozzle sizing for conceptual design studies

The design of an engine nozzle is a complex process involving numerous trade-offs to deliver the best balance of performance over the flight profile. During aircraft conceptual design studies, an initial estimate of nozzle area will enable the designer to predict components such as wave drag and boat-tail drag. If an existing engine is to be used, this can be easily determined from engine data, otherwise we have to rely on more general statistical relations. A very crude approximation of nozzle area can be made with respect to the capture area of the engine. For the two types of nozzle commonly encountered, the exit area can be determined as,

- Convergent nozzle = 0.5 to 0.7 times the capture area
- Convergent-divergent nozzle = 0.5 to 0.7 times the capture area in the closed position and 1.2 to 1.6 times the capture area in the fully open position.

Where, the engine capture area is determined in the conceptual intake sizing section. The drag component of particular concern in initial studies is boat-tail drag, which results from flow separation on the aft part of the nozzle or fuselage fairing. For a

protruding nozzle, initial guidelines are that the angle of the aft fuselage in this location should not be greater than 15º or 20º.

C1.4 Engine intake sizing for conceptual design studies

As for the exhaust nozzle, the design of an engine intake is a complex and time consuming process which has to take into account factors such as, flow distortion, pressure recovery losses and other pressure losses. Such a process is not viable for conceptual design work. The methods presented in this section relate the mass flow rate of air passing through the engine to the thrust produced. At high subsonic speeds, ram effects can increase the mass flow rate of air into the engine, but these are often offset by a drop in performance in the exhaust nozzle. Up to the transonic regime, the velocity effects can be assumed to cancel out, resulting in relatively linear thrust characteristics. The exception to this is where a supersonic nozzle is used, where ram effects are not offset by the nozzle. Pressure losses in the inlet will however eventually prevail, leading to a loss in engine performance.

Inlet pressure recovery is a complex function of flow behaviour and flight Mach number. In conceptual design work, the internal pressure recovery may be approximated as, straight duct = 0.96, S duct = 0.94 and podded nacelle = 0.98. The intake capture area for a subsonic jet engine can be estimated from the expression below from Roskam [51], where the density and velocity are relative to the flight condition being studied.

$$A_C = \frac{\dot{m}_{Inlet}}{\rho \cdot V} \qquad \text{Eq 1-1}$$

Where, the total inlet mass flow rate is the sum of that required by the engine and that required for cooling, as given by the expression below from Roskam [7].

$$\dot{m}_{Inlet} = \dot{m}_{Engine} + \dot{m}_{Cooling} \qquad \text{Eq 1-2}$$

The air flow requirements of the engine can be determined from the expression below from Roskam [7] as a function of the engine thrust.

$$\dot{m}_{Engine} = k_{Gas} \cdot T \qquad \text{Eq 1-3}$$

The factor k_{Gas} in this expression is a function of the engine by-pass ratio as below:

- 0.0003 for $0 \leq BPR \leq 1$
- 0.0007 for $1 \leq BPR \leq 2$
- 0.0009 for $2 \leq BPR \leq 4$
- 0.0011 for $4 \leq BPR \leq 6$

Likewise, the cooling air requirements can be estimated by the expression below from Roskam [7],

$$\dot{m}_{Cooling} = 0.06 \cdot \dot{m}_{Engine} \qquad \text{Eq 1-4}$$

The final inlet size is then the largest area determined from a number of flight phases tested. For most subsonic aircraft this is usually to meet low speed requirements.

C2 An overview of engine design methodology

C2.1 Engine design specifications and parameter predictions

Any engine design process begins with performance targets. In industry, these will be specified by the aircraft design department or customer. In this study, these were specified in our aircraft conceptual design studies. We also need to make predictions as to the characteristics of the different engine components, relative to the level of technology incorporated in the engine. Data from existing designs enables us to establish technology based trends, which can be used for this purpose.

C2.1.1 Engine performance targets

The engine performance targets of particular importance for the design of a new engine are thrust and specific fuel consumption. The targets for this study are given below.

2.1.1.1 Thrust design targets

The installed thrust requirements for our engine were determined from the constraint analysis used to size the aircraft. These results are however for the engine thrust referred back to standard sea level conditions (SSL). For engine design work; we prefer to have the actual thrust requirements of our engine at their corresponding altitude and speed. These can be easily determined with the thrust scaling and weight scaling factors used in the constraint analysis. As the engine will be designed in isolation from the airframe, we need to factor these results for installation losses to determine the uninstalled values. A figure of 5% has been assumed here as being typical for the losses for a buried engine installation. The table below gives these results in both British and SI units.

		Installed thrust values		Uninstalled thrust values	
Design case	T (N) SSL	T (N) True	T (lbf) True	T (N) True	T (lbf) True
Max. Level Speed Constraint (Low)	36309.5484	31910.94551	7173.864558	33590.46896	7551.436377
Max. Level Speed Constraint (High)	27901.8796	6127.323276	1377.476806	6449.813974	1449.975585
Sustained Turn Rate Constraint	51890.94	45852.4075	10308.02929	48265.6921	10850.55715
Specific Excess Power Constraint	52730.7736	44115.38305	9917.530737	46437.24532	10439.50604
Take-Off Distance Constraint	26604.9163	25838.69475	5808.768544	27198.62605	6114.493204
Cruise Constraint (start of cruise outboard)	36361.71	7941.999429	1785.432155	8359.999399	1879.402269
Acceleration Constraint	47189.527	37334.59428	8393.149071	39299.57292	8834.893759
Cruise Constraint (end of cruise inboard)	32967.6161	7200.673133	1618.775406	7579.655929	1703.974112
Cruise Constraint (end of outboard/start of inboard)	34471.0838	7529.055364	1692.598654	7925.321436	1781.682794

(assume 5% installation loss)

Table 2-1

These results show the sustained turn rate and specific excess power thrust requirements to be the most critical design constraints. In the design work, it is however also worthwhile checking the take-off and cruise constraints.

2.1.1.2 Specific fuel consumption design targets

During our conceptual design work, we had assumed an installed specific fuel consumption value of 0.88 at cruise for our engine. This is therefore the target value for our engine design, to ensure we are able to meet our original requirements. As for the thrust requirements, this figure needs to be expressed as an uninstalled value for engine

design work. Assuming an installation loss of 5%, the uninstalled specific fuel consumption target of our engine is thus 0.84.

C2.1.2 Engine component technology level prediction

Utilising trends for past, current and future engine proposals, we are able to predict the characteristics of the engine components according to the level of technology we are striving for. Although an engine utilising all components with the highest levels of technology will offer the best performance, the development timescale and cost of such an engine will be high. The technology requirements should therefore be kept to a sensible level. A typical list of engine component parameters at different technology levels is given in the figure below from Mattingly [16]. In this study, we are interested in a mix of level 3 and level 4 technologies corresponding to current and future engine designs. This will give us a realistic engine design with a number of high technology features which can be developed within a realistic budget and timeframe.

Table 4.4 Component polytropic efficiencies and total pressure losses

Component	Figure of merit	Type	Level of technology 1	2	3	4
Diffuser	$\pi_{d\,max}$	A[a]	0.90	0.95	0.98	0.995
		B[b]	0.88	0.93	0.96	0.97
		C[c]	0.85	0.90	0.94	0.96
Compressor	e_c	——	0.80	0.84	0.88	0.90
Fan	e_f	——	0.78	0.82	0.86	0.89
Burner	π_b	——	0.90	0.92	0.94	0.96
	η_b		0.88	0.94	0.99	0.995
Turbine	e_t	Uncooled	0.80	0.85	0.89	0.91
		Cooled		0.83	0.87	0.89
Afterburner	π_{AB}	——	0.90	0.92	0.94	0.95
	η_{AB}		0.85	0.91	0.96	0.97
		D[d]	0.95	0.97	0.98	0.995
Nozzle	π_n	E[e]	0.93	0.96	0.97	0.985
		F[f]	0.90	0.93	0.95	0.98
Maximum T_{t4}		(K)	1110	1390	1780	2000
		(°R)	2000	2500	3200	3600
Maximum T_{t7}		(K)	1390	1670	2000	2220
		(°R)	2500	3000	3600	4000

[a]A = subsonic aircraft with engines in nacelles.
[b]B = subsonic aircraft with engine(s) in airframe.
[c]C = supersonic aircraft with engine(s) in airframe.
[d]D = fixed-area convergent nozzle.
[e]E = variable-area convergent nozzle.
[f]F = variable-area convergent-divergent nozzle.
[g]Stealth may reduce $\pi_{d\,max}$, π_{AB}, and π_n.
Note: The levels of technology can be thought of as representing the technical capability for 20-year increments in time beginning in 1945. Thus level 3 technology presents typical component design values for the time period 1985–2005.

Table 2-2 [16]

C2.1.3 Engine parameters – design choices

In this section, we give an overview of a number of the design parameters utilised in the engine design work. This includes parameters for component behaviour, component efficiencies and engine operating temperatures. The initial prediction of these parameters is one of the most important stages in the design process as the engine configuration is designed according to these values. These design choices also become the design targets which the later component level designers must endeavour to meet. Failure to meet these targets later on in the development process may render the final engine configuration unable to meet our original design requirements. These parameters must therefore be selected with care.

2.1.3.1 Component total pressure ratios (Pi value)

The parameter is defined as the ratio of the total (isentropic stagnation) pressures across a component as given by the relation,

$$\pi_{Component} = \frac{P_{Total}(LeavingComponent)}{P_{Total}(EnteringComponent)} \quad \text{Eq 2-1}$$

The Pi value of the exhaust nozzle is of particular importance in this study, which is the ratio of the total pressures at the nozzle exit P_{t9} and entry P_{t7}.

2.1.3.2 Solution boundaries

Typical ranges of the engine parameters for a number of different engine configurations are given in the chart below from Mattingly [16]. As this chart is based on data collated from existing engine designs, it gives a useful reality check for any engine design. It also serves as an indication of the boundaries between which our solution is expected to lie, unless we are dealing with an advanced configuration.

Table 4.1 Typical $F/\dot{m}_0$ and S values

Engine type	Compressor pressure ratio (π_c)	Fan pressure ratio (π_f)	Bypass ratio (α)	T_{t7}, °R	T_{t4}, °R	$F/\dot{m}_0$, lbf/lbm/s	S, 1/h
Turbojet no A/B	10–20	——	——	——	2000	54–58	1.0–1.1
					3000	93–96	1.3–1.4
Turbojet with A/B	10–20	——	——	3600	2000	94–101	2.0–2.2
					3000	115–119	1.7–1.8
Turbofan low α no A/B	20–30	2–4	0.2–1	——	2000	23–47	0.85–1.0
					3000	53–84	0.96–1.5
Turbofan low α with A/B	8–30	2–4	0.2–1	3600	2000	75–98	2.1–2.7
	10–30				3000	102–116	1.7–2.0
Turbofan high α no A/B	30–40	1.4–1.6	5–7.5	——	2000	5.5–12	0.76–0.97
		1.4–4	5–10		3000	13–27	0.67–1.03

Table 2-3 [16]

Thus, in this particular design study, the parameters for our turbofan engine with no afterburner are thus expected to lie between the following boundaries,

- Compressor pressure ratio – 20 to 30
- Turbine inlet temperature – 2000 to 3000ºR
- Specific thrust – 23 to 84 (depending on Tt4)
- Specific fuel consumption – 0.85 to 1.5 (depending on Tt4)

These figures are however, applicable to current technology engine configurations. For next generation developments, we need to make comparisons with similar designs.

2.1.3.3 Comparison with similar designs - UCAV design example

Fortunately, for this study the results for a similar UCAV engine design are available from Mattingly [16]. This was designed to cruise at M0.8 and 40,00ft with a specific fuel consumption goal of 0.76 1/h, which is not too far from our requirements. A mixed flow turbofan with a high bypass ratio engine was chosen to deliver high propulsion efficiency. A throttle ratio of 1 was assumed and the maximum turbine inlet temperature taken to be 3200ºR (which when corrected for control system constraints at cruise, equals 2714ºR). Other engine parameters are given in the table below.

Description	Input Value	
Polytropic Efficiency		
Fan (e_f)	0.890	
Low-pressure Compressor (e_{cL})	0.890	
High-pressure Compressor (e_{cH})	0.900	
High-pressure Turbine (e_{tH})	0.890	
Low-pressure Turbine (e_{tL})	0.910	
Total Pressure Ratio		
Inlet ($\pi_{d\,max}$)	0.90	low value due to stealth
Burner (π_b)	0.960	
Nozzle (π_n)	0.90	low value due to stealth
Mixer ($\pi_{M\,max}$)	0.97	
Component Efficiency		
Burner (η_b)	0.995	
Mechanical		
Low-pressure Spool (η_{mL})	0.995	
High-pressure Spool (η_{mH})	0.995	
Power Takeoff – LP Spool (η_{mPL})	0.995	
Power Takeoff – HP Spool (η_{mPH})	0.995	
Fuel (JP-8) Heating Value (h_{PR})	18,400 Btu/lbm	
Turbine Cooling Air		
$T_{t4\max} > 2400^\circ R$	$\varepsilon_1 = \varepsilon_2 = (T_{t4\max} - 2400)/16{,}000$	
$T_{t4\max} \le 2400^\circ R$	$\varepsilon_1 = \varepsilon_2 = 0$	

Assuming $T_{t4\max}$ = 3200°R in the above equation, then the turbine cooling air requirement is $\varepsilon_1 = \varepsilon_2 = 0.05 = 5\%$. The modified specific heat (MSH) gas model is selected for cycle computations with the following gas properties:

$\gamma_c = 1.4, c_{pc} = 0.240$ Btu/(lbm-°R), $\gamma_t = 1.3, c_{pt} = 0.295$ Btu/(lbm-°R)

Table 2-4 [16]

This gave a final engine configuration of, α =1.236, π_C =36, π_f =3.5, $\dot{m}_0$ =107.1 lbm/s. The similarity between the design requirements of this and our study mean that these figures also serve as useful guidelines for our design. Our engine is still expected to differ somewhat primarily due to different specific fuel consumption constraints.

2.1.3.4 Maximum turbine entry temperature (TET)

The maximum turbine entry temperature (T_{t4}) of an engine is limited by the maximum metallurgical temperature and the method of cooling adopted for the turbine. As seen from the Brayton cycle, increasing the TET temperature does however offer the benefit of improved efficiency. Ingenious cooling methods are therefore employed to enable an engine to operate at temperatures beyond which the turbine would normally be able to withstand. Technological advancements in engine materials are also enabling engineers to push these boundaries even further.

2.1.3.5 Operating turbine entry temperature

As will be discussed in the section for theta break, T_{t4} will be limited by the engine control system to values below the maximum TET to prevent damage to the engine. The free-stream total temperature can be shown to have a strong influence on the behaviour of the engine throughout its flight. This is usually expressed as a ratio of the standard sea level static temperature to arrive at the dimensionless form θ_0. To summarise from below, the actual value of T_{t4} will be limited to values less than T_{t4max} for flight conditions where θ_0 is less than the throttle ratio (TR). Beyond this limit, T_{t4} will attain its maximum value and the engine will be limited by other components instead. The

value of T_{t4} for flight conditions below θ_0 can be determined from the relation below as a function of either the engine throttle ratio or theta break.

$$T_{t4} = \frac{\theta_0}{TR} \cdot T_{t4Mas} = \frac{\theta_0}{\theta_{Break}} \cdot T_{t4Max} \quad \text{Eq 2-2}$$

Where θ_0, is given by the expression,

$$\theta_0 = \frac{T_{t0}}{T_{Std}} = \frac{T_0 \cdot \left(1 + \frac{\gamma_C - 1}{2} M_0{}^2\right)}{T_{Std}} \quad \text{Eq 2-3}$$

In our study, the throttle ratio was fixed at 1. Using the expression above, the turbine inlet temperature was determined for a number of different flight cases as:

- Sustained turn rate = 3507.556ºR – At M0.7 and 250ft
- Specific excess power = 3188.897ºR – At M0.4 and 5,000ft
- Take-off = 3200.064ºR – At M0.01 and 0ft
- Cruise = 2795.753ºR – At M0.9 and 40,000ft

2.1.3.6 Turbine cooling air requirements

Turbine cooling air is required to maintain the temperature of the turbine at an acceptable level. It may not be required however for low temperature engine designs. An estimate of the cooling air requirements can be determined from the following design trends:

- For cases where Tt4 ≤ 2400ºR, the cooling air requirements are typically zero so that, $\varepsilon_1 = \varepsilon_2 = 0$
- For cases where Tt4>2400ºR, the cooling air requirements can be predicted from the expression, $\varepsilon_1 = \varepsilon_2 = \frac{T_{t4Max} - 2400}{16000}$ Eq 2-4

In this study, where $T_{t4Max} = 3200°R$, the cooling requirements are $\varepsilon_1 = \varepsilon_2 = 5\%$

2.1.3.7 Component efficiencies

Within the engine parametric analysis, the efficiency of a number of the engine components must be defined. These are characterised as:

- Polytrophic efficiencies - Used to describe the process efficiency of devices such as compressors and turbines. These account for the deviation of the behaviour of an actual fluid device from the polytrophic idealisation.
- Mechanical efficiencies - Used to account for mechanical inefficiencies such as friction between moving components, windage and seal drag.
- Burner (combustion) efficiency – This is defined as the degree to which complete combustion is achieved. It is calculated as the ratio of the actual thermal rise to the maximum theoretically available thermal energy.
- Nozzle expansion characteristics - The nozzle expansion characteristics are usually quoted as the ratio P_0/P_9 and is used to indicate whether we are dealing with under-expansion, ideal-expansion, over-expansion etc.

These efficiencies vary according to the design and operation of the engine and the components and technological advancements incorporated in its design. Their values

vary between different engine designs and are best predicted by inspection of similar current designs.

2.1.3.8 Theta break and the throttle ratio

Theta break and throttle ratio are properties of the engine control system which impose limits on the operating characteristics of the engine. To prevent the risk of damage to the engine by it exceeding its operating boundaries, the control system is designed to limit the maximum allowable values of π_C and T_{t4} with respect to its operating conditions. The figure below from Mattingly [16], is an example of the control system characteristics applicable to an engine compressor.

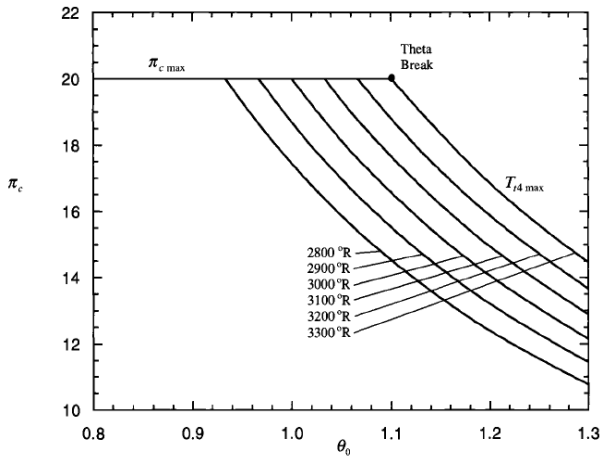

Fig. D.2 Compressor pressure ratio as a function θ_0 of and T_{t4} for a compressor with a reference point of $\pi_c = \pi_{c\,max} = 20$, $T_{t4} = T_{t4\,max} = 3300$ °R (1833 K), and $\theta_0 = 1.1$ [i.e., $C_1 = 0.0004512$ 1/°R (0.0008122 1/K) in Eq. (D.3)].

In this figure, we can see that for low values of θ_0, T_{t4} must be limited to prevent the compressor exceeding π_{C-Max} and thus stalling. At higher values of θ_0, π_C must be limited to prevent $T_{t4-\max}$ from being exceeded. Theta break is the point where the control logic switches between limiting π_C and T_{t4}. At values of θ_0 less than θ_{Break}, Tt4 is less than $T_{t4-\max}$ which results in a loss in specific thrust. Likewise, at values of θ_0 greater than θ_{Break}, π_C is less than π_{C-Max} and the specific fuel consumption is higher that its optimal. θ_{Break} is thus selected by the designer to achieve the best balance of performance throughout the flight profile. For cases where an aircraft is flown with a value of $\theta_0 = 1$ (as in traditional designs), the engine is designed with $\theta_{Break} = 1$.

The throttle ratio is the ratio of the maximum total temperature of gases leaving the main burner at a particular flight condition to the total temperature of the gases leaving the burner at sea level static conditions. This can also be shown to be equal to θ_{Break} and therefore, the two terms can be used interchangeably, which gives, $TR = \theta_{Break}$. A number of advanced engines with throttle ratios greater than one are being developed for future supersonic aircraft. Most current engines are however designed to have a throttle ratio of one, which will also be used for this study.

C2.1.4 Off the shelf engines vs. new developments

With so many existing engines to choose from, why go to the trouble of designing a new engine? Off the shelf engines do offer benefits of immediate availability and reduced cost, but there is unlikely to be one that fits our design requirements exactly. Even after it has been tailored to suit our needs, some compromises would also be required. Existing engine manufacturers are also unlikely to supply such detailed engine

data as required by this project. Therefore a new engine design was considered to be the best approach for this project to generate the required detailed engine data.

C2.2 An overview of the engine design and sizing process

The engine design and sizing process is a very detailed subject and only an overview will be given here. During these studies, a baseline engine was designed and sized with a level of detail sufficient for later analyses. Component level design was not required for this work. In this section, we will therefore only give a brief overview of the subject which is sufficient enough for the reader to understand the engine design process.

C2.2.1 Engine design methodology

The engine model developed for these studies, has a level of detail which is sufficient enough for our needs. This proved adequate to predict parameters such as available thrust and specific fuel consumption, as well as the flow conditions at a number of points within the engine. With our estimates for general engine parameters, we are able to carry out the conceptual design and initial sizing of an engine and analytical model with a level of detail sufficient for our needs. As will be discussed in the following sections, the conceptual engine design process consists of two stages as follows:

- On-design – This stage is used to determine the optimal combination of the unknown engine parameters to meet the needs of our design condition. At the end of this stage, all of our engine design parameters are fixed.
- Off-design – This stage is used to test the engine in conditions other than our design condition and will ultimately determine the size of our engine.

C2.2.2 The on-design design stage

This is the first stage in the design process, which begins with our design requirements and predictions for the characteristics of a number of the engine components. During this stage, we use parametric analysis techniques to explore the undetermined engine parameters and ultimately determine the optimal engine configuration to meet our needs. Such parametric studies can include the investigation of the parameters:

- Turbine inlet temperature- For this study, this has already been fixed in accordance with current metallurgical limits.
- Compressor pressure ratio – This is a design variable for our analysis.
- Fan pressure ratio – This is a design variable for our analysis. Fortunately this is automatically adjusted within the software to meet our engine requirements.
- Bypass ratio – For our study, this was fixed at the conceptual design stage.

The only unknown in this study is therefore the engine compressor ratio, which will be the focus of our parametric analysis. This process involves the generation of plots of uninstalled thrust specific fuel consumption versus uninstalled specific thrust for a range of compressor pressure ratio values, as in the example below. These can then be used to establish a trend between the engine performance and the compressor pressure ratio, which will help us identify the optimal solution. Our primary goal here is to optimise the engine at its design point, such as cruise. It is important however that it retains acceptable performance characteristics over the other flight conditions. This involves

repeating the parametric analysis at a range of thrust critical flight points such as such as take-off, cruise and specific excess power.

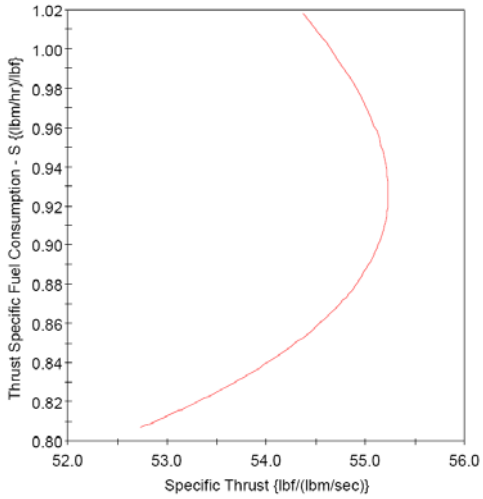

Chart 2-1

The parametric trend for the critical design point enables us to determine the maximum compressor ratio to meet our requirements such as fuel consumption at that point. Once we have fixed the compressor ratio and the design point, we need to verify this result within the trends generated for the other critical flight points. This ensures that the engine retains acceptable performance characteristics over our entire flight profile. The final result may prove to be a trade-off between the difference performance requirements. The ideal engine is one whose key parameters are within their best ranges for all the critical engine operating points. When making our final selection, it is in our best interest to keep the specific thrust as high as possible for the most demanding flight conditions as this is related to the final size of our engine. Keeping the specific thrust as high as possible will ensure that the size, weight and cost of the final engine are kept to a minimum. At the end of this stage, all of our engine design parameters will have been fixed with the aid of the parametric trends but the actual size of the engine is still variable. The result is thus a rubber engine which has been optimised for our design requirements.

C2.2.3 The off-design sizing stage

At the end of the on-design analysis, we have an engine configuration whose parameters have been fixed with respect to a design point. The final size of the engine however remains undetermined, which is represented by the mass flow rate of air passing through it ($\dot{m}_0$).The engine performance parameters we have been using in our on-design analysis were independent of the size of the engine and with $\dot{m}_0$ we are able to determine the actual engine parameters. An iterative process is used to determine the final engine size which begins with an assumed value of $\dot{m}_0$. The engine is then tested at various critical flight points to determine the critical value of $\dot{m}_0$, which is used to size our engine. The flight phases of particular interest include:

- Flight phases which have a high fuel consumption
- Conditions with demanding thrust requirements
- Other extreme operating conditions

The assumed value of $\dot{m}_0$ can then re-scaled accordingly to determine the final engine size which is able to deliver sufficient thrust to meet all of our performance requirements. With its size fixed, the performance of the final engine configuration can be determined within its entire operating envelope. We are also then able to test the engine at different engine throttle settings, which is particularly useful for this study.

The off-design analysis is named as such, since we not only measure the performance characteristics of our engine at our reference design point (used for the on-design analysis) but also at a number of other flight conditions throughout its operating envelope. It is typical to study more that one potential engine configuration up to the off-design stage and then use these results to establish further trends between design choices and therefore further optimise the final engine configuration. The result is an engine with the best balance of performance over the complete flight profile. In this study, our off-design has been based on assumed typical values for the engine installation allowances. We can however, also use an off-design analysis to study more detailed intake and nozzle installation models. This has however not been possible in this study due to the project time constraints.

C2.3 Station numbering

The engine station numbering used in this study is consistent with the ARP755A aerospace recommended practice, as given below.

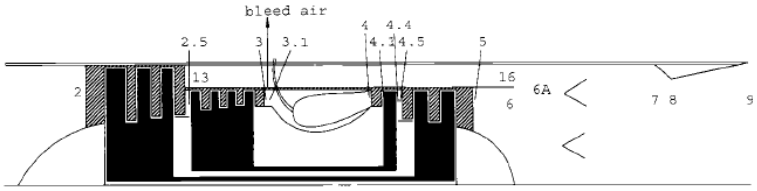

Fig. 4.1a Reference stations—mixed-flow turbofan engine.

Station	Location
0	Far upstream or freestream
1	Inlet or diffuser entry
2	Inlet or diffuser exit, fan entry
13	Fan exit
2.5	Low-pressure compressor exit
	High-pressure compressor entry
3	High-pressure compressor exit
3.1	Burner entry
4	Burner exit
	Nozzle vanes entry
	Modeled coolant mixer 1 entry
	High-pressure turbine entry for π_{tH} definition
4.1	Nozzle vanes exit
	Coolant mixer 1 exit
	High-pressure turbine entry for τ_{tH} definition
4.4	High-pressure turbine exit
	Modeled coolant mixer entry
4.5	Coolant mixer 2 exit
	Low-pressure turbine entry
5	Low-pressure turbine exit
6	Core stream mixer entry
16	Fan bypass stream mixer entry
6A	Mixer exit
	Afterburner entry
7	Afterburner exit
	Exhaust nozzle entry
8	Exhaust nozzle throat
9	Exhaust nozzle exit

C3 Practical software based engine design

C3.1 Engine design with the AEDsys software suite

The conceptual design of an engine can be a very labour intensive activity due to the vast number of relations which are required and the simultaneous solution of each of these. Fortunately, we are able to make use of a reliable software suite called AEDsys, which has already been developed for such purpose by Mattingly [16]. As will be discussed in the sections below, this software is sufficient to be able to handle the on-design and off-design stages as well as perform more detailed analysis of the various components. Only an overview of the programs as applied to this project will be given here and the reader is advised to consult the program user guides for more information.

C3.1.1 On-Design parametric analysis with the ONX module

The ONX module [73] allows the user to define a number of component level engine characteristics and then test the remaining engine parameters over a range of values to perform a parametric analysis. For this study, we opted for the following user selections from the main window:

- Type of cycle – Turbofan with mixed exhaust. The mixed exhaust configuration is particularly good for cooling the hot exhaust gases and therefore reducing the IR signature and increasing the stealth of the aircraft.
- Ideal gas model – The Modified Specific Heat (MSH) Model as this has been shown to give the best results.
- Unit system – The English unit system was used as a program used later on was only able to cope with these units and this enabled the results to be used directly.
- Iteration variable – Our parametric analysis is based on Compressor Pressure Ratio, which is the only unknown design variable. In this work a range of CPR values between 10 and 40, in 0.25 steps were tested.

The component level engine characteristics are finally defined within the engine data input box, which includes choices for:

- Aircraft operating environment – Mach number, Altitude, Temperature, etc
- Fuel characteristics – Heating value
- Burner exit temperature – T_{t4}
- Air off-take requirements – Includes bleed and cooling air requirements
- Power off-take requirements
- Component isentropic stagnation pressure ratios (Pi) – Diffuser, Burner, Nozzle
- Component polytrophic efficiencies – Fan, Compressors and Turbines
- Component efficiencies – Burner, Spools, etc

The values selected for each of these components for this study are shown in the figure below. It should be noted that a Pi-Nozzle value of 0.98 was used for the baseline engine and not the figure of 0.9 shown in the figure. The compressor ratio input box is also normally left black for these parametric analyses. The value of -1 used for the fan pressure ratio enables the software to automatically find the best solution for this

variable. The majority of these variables remain fixed during our tests. Under different test conditions, Mach number, Altitude and T_{t4} must however be adjusted accordingly.

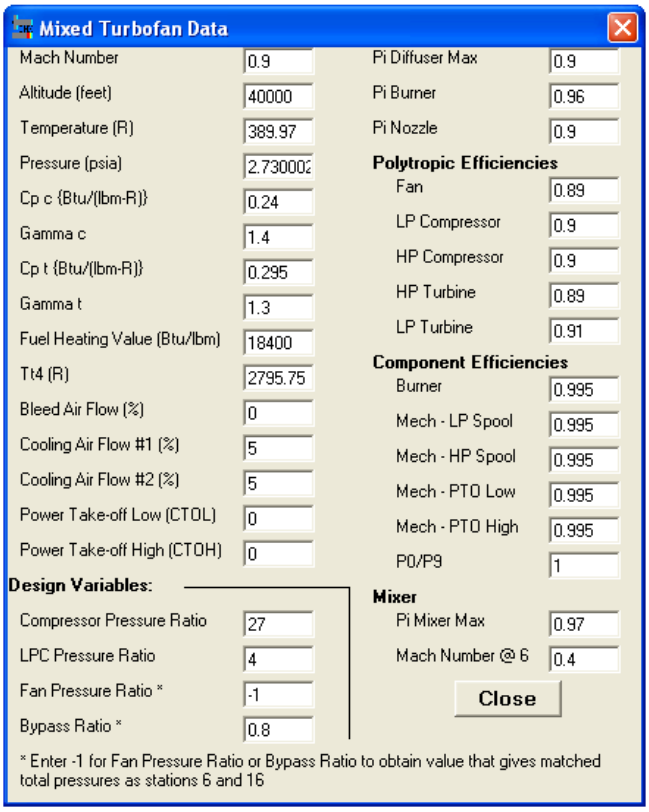

Figure 3-1 – ONX data input window

C3.1.2 Off-Design engine analysis with the engine cycle deck

The on-design work enabled us to determine the best rubber engine configuration from parametric studies, which where primarily focused on one particular engine operating point. The AEDsys engine cycle deck [74] enables us to determine the most critical mass flow rate requirements and thus the size of the engine by examining its performance at the design point and a range of other off-design conditions. The engine cycle deck is not available within the main window of AEDsys on start-up by default. It must be activated by selecting Cycle Deck from the engine pull-down menu, this then puts two additional buttons on the main window, which are used for the off-design analysis work. The first of these is the Engine Data button, which is used to define the reference engine configuration within the program. The second is the Engine Test button, which is used to test the reference engine at any off-design condition.

3.1.2.1 Defining the engine with ONX reference files

Fortunately, the engine data can be transferred directly from the ONX module by the creation of a reference file, which defines the engine configuration at its design condition. To generate a reference file within ONX, we need to select the Single Point Calculation option from the main window. The compressor pressure ratio will now be fixed at its final value of 27 within the view data form. Since the single point calculation is based on an actual engine size, the user must define the mass flow rate of the engine

at its design point. The final engine mass flow rate is however determined by an iterative process and thus we begin by making an initial estimate, which is refined later. The reference file can then be entered into the cycle deck via the Engine Data form. This form has additional options for engine installation allowances, but since these have already been factored into our work, the default constant loss model is retained. The other features within this input window will retain their default values for our work.

3.1.2.2 Engine testing within the cycle deck

We are finally able to test the engine under a variety of off-design test conditions via the Engine Test form. The off-design engine test inputs within this window allow us to modify a variety of operating parameters but for this study we will concentrate on the Mach number, Altitude and Throttle ratio. After testing, the results can be retrieved in either a summary of the main results or a more detailed format (which gives the operating conditions at each engine station).

3.1.2.3 Selecting the final engine size

The process to determine the final size of the engine involves an iterative process between ONX and AEDsys, as follows:

1. Within ONX, create a single point reference file using an initial estimate for the engine mass flow rate. In this analysis, a value of 100 lbm/sec was assumed.
2. Within AEDsys, test this reference engine at each of the critical design points to determine the thrust available at each condition.
3. At each critical design point determine the ratio of required thrust to available thrust from the scale factor relation below.

$$SF = \frac{T_{\text{Required}}}{T_{Available}} \qquad \text{Eq 3-1}$$

4. Rescale the engine mass flow rate in accordance with the most critical condition from above, as given by the relation below.

$$\dot{m}_{New} = SF \cdot \dot{m}_{Guess} \qquad \text{Eq 3-2}$$

5. Repeat the process above to verify the new results.

In this study, the sustained turn rate was identified as the most critical condition, which gave a mass flow rate of 59.48 lbm/sec for the final engine size.

C3.2 Design of the baseline engine

This section gives an overview of the rationale for the selection of the final baseline engine configuration, which is used for further analysis work in this project.

C3.2.1 Design point parametric analysis

In this study, the parametric analysis focused on determining the optimal compressor pressure ratio for the engine. This parameter can have a considerable impact on the thrust and specific fuel consumption characteristics of the final engine configuration and must be selected with care. Since the cruise phase is the largest consumer of fuel, it makes sense to select this as the design point or on-design condition for the parametric

analysis. ONX was used to test a range of compressor ratios and thus generate the parametric trend below of output parameters of most concern to us.

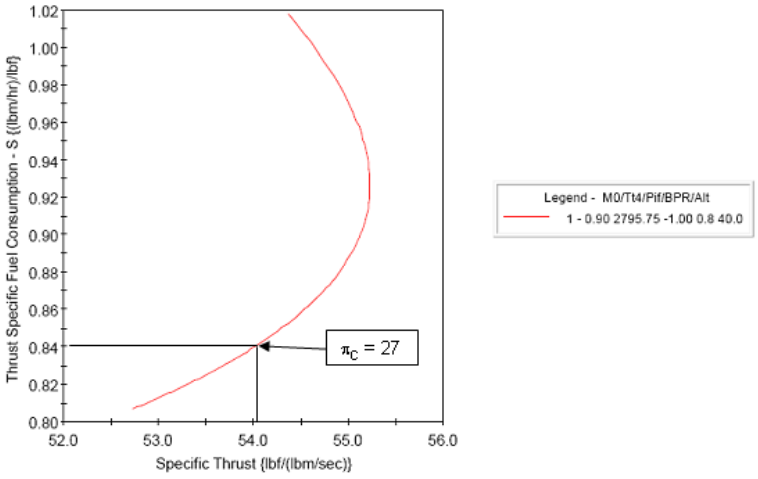

Chart 3-1

With reference to the figure above, there are two possible solutions for the specific thrust, at higher and lower values of specific fuel consumption. The final compressor pressure ratio should be selected at a point sufficiently below the knee of the curve. This ensures that any deviation in the engine operating point does not stray above the knee of the curve and therefore into the unnecessarily higher SFC operating regime. At the same time, we should aim to achieve the highest specific thrust possible, which would have smaller airflow requirements and thus result in a smaller and lighter engine. As can be seen from the figure, this would however be at the expense of thrust specific fuel consumption. We must however also be careful not to select a point too low down on the curve for which the specific thrust is falling rapidly. Selection of the final engine configuration is therefore a trade-off of many factors.

In this study, our configuration was selected to meet our uninstalled cruise specific fuel consumption design target of 0.84. This point is marked on the parametric analysis curve above, which when traced back within our ONX raw data, corresponds to a compressor ratio of 27. Since this point was also situated at an excellent location on the parametric curve, our final engine configuration was fixed at this value.

C3.2.2 Verifying the final configuration

In the last section, the engine compressor ratio was selected to deliver the best performance at cruise. It is essential however to verify this design choice at other critical flight conditions, to ensure the engine retains good performance at these conditions. The flight conditions examined in this way were:

- Specific excess power requirements – At Mach 0.4 and 5,000ft.
- Sustained turn rate requirements – At Mach 0.7 and 250ft.
- Take-off requirements – At Mach 0.01 and 0ft.

ONX is used to generate a parametric curve for each one as presented below, to which the point corresponding to a compressor pressure ratio of 27 has been added.

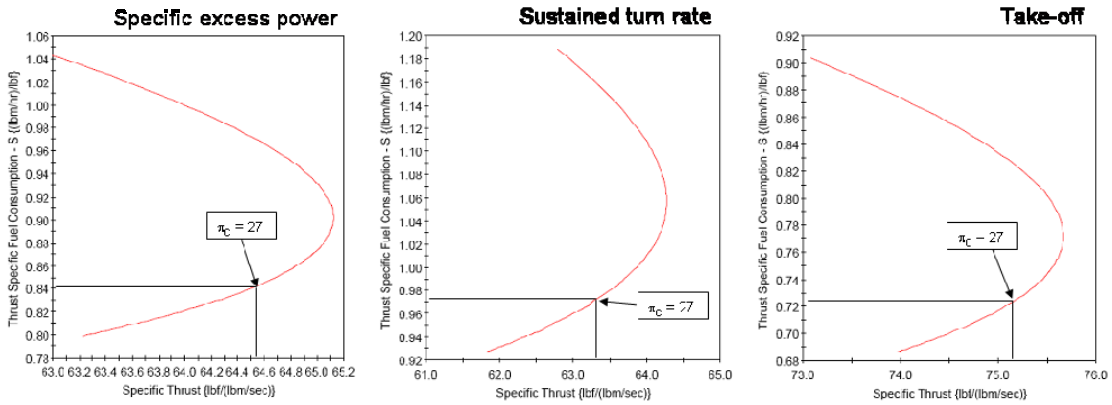

Chart 3-2, 3-3, 3-4

Within each of the analyses above, the engine is shown to operate at a favourable point along the curve with a compressor pressure ratio of 27 and so it will be fixed at this value for the baseline engine.

C3.2.3 Refined engine intake and nozzle sizing

Within the results generated by the AEDsys software are the intake and exhaust areas required for the engine at each flight condition. These were determined as:

- Flow area at 0 (engine intake) = 5.703ft^2 – To meet the SEP requirements
- Flow area at 9 (engine nozzle) = 2.777ft^2 – To meet the cruise requirements

C3.3 The analysis of thrust vectoring nozzles

The work carried out so far has focused on a fixed geometry nozzle with fixed operating characteristics. In this study, the nozzle isentropic stagnation pressure ratio (Pi) was fixed at 0.98 for our baseline design. In the case of variable geometry nozzles however, the value of Pi will be related to its internal flow characteristics, which in turn will be dependent on the nozzle geometry amongst other factors. Pi will therefore vary as the geometry of the nozzle is varied. This concept is illustrated below for a thrust vectoring nozzle operating at a number of different nozzle deflection angles. It should be noted that the values quoted in this figure are arbitrary values to illustrate the concept.

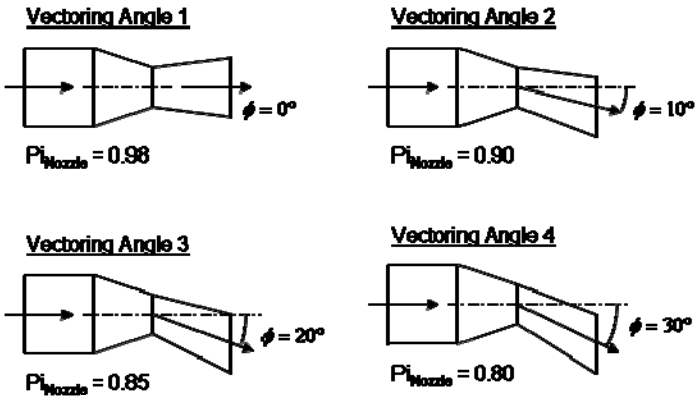

Figure 3-2 – Relationship between nozzle vectoring angle and its Pi value

It should be re-emphasised that the operating characteristics of an engine will be affected by nozzle, by means of the back pressure it generates. This means that, if each of the nozzle configurations above were coupled to an identical engine, its operating characteristics would be different for each case. For a thrust vectoring nozzle, the engine characteristics will therefore vary according to the engine plume deflection angle. In our work so far, we have concentrated on the baseline engine with an un-vectored nozzle ($\phi = 0°$). Our next step is to examine the behaviour of our baseline engine when the characteristics of the engine nozzle are varied. Later on in our work, we can use this data to pair our engine to an existing nozzle and predict its performance.

C3.4 Datasets for take-off and cruise conditions

At this stage in our work we need to gather data which will help us to predict the behaviour of our baseline engine when the nozzle characteristics are varied. Fortunately, we are able to use the AEDsys software suite for this task but even so, a significant amount of work is still required. This process involves the analysis of many different engine configurations at a number of different operating conditions. The difference between each is the nozzle, which is accounted for via the value of Pi_{Nozzle}, which itself is a function of the plume deflection angle. In this work, we are primarily interested in the analysis of the engine at take-off and cruise. Using the process described in the following sections, we are able to test our engine with a number of different nozzles, to generate a set of data for each. The results of most importance to us are:

- Engine thrust (lbf)
- Thrust specific fuel consumption ((lbm/hr)/lbf)
- $\dot{m}_0$ (lbm/s) - Mass flow rate of air through the engine intake
- Tt4 (Rankine) – Total temperature at the burner exit
- $\dot{m}_8$ (lbm/s) – Mass flow rate of exhaust gases through the nozzle throat
- Pt8 (Psia) – Total pressure of the exhaust gases at the nozzle throat
- Tt8 (Rankine) – Total temperature of the exhaust gases at the nozzle throat
- γ_{6A} - Ratio of specific heats of the gases at the nozzle entry (mixer exit)
- A9 (ft^2) – Required area at the exhaust nozzle exit
- A9/A8 – Ratio of areas at the nozzle throat and nozzle exit (this result is given in the main window of the AEDsys engine test form and not the test results)

An overview of the process and the results are given in the sections which follow.

C3.4.1 Take-off analysis datasets

During take-off, the engine thrust is assumed to be held at its maximum value. In this analysis, we also need to consider the effect of engine bleed on engine performance, (which will be used for a pitch control device located at the nose of the aircraft). The amount of bleed required is not known at this stage and our analysis is thus repeated at a number different engine bleed settings to establish a trend. When using AEDsys, engine bleed is fixed for the on-design testing and therefore we have to create a new reference file within ONX for each test point before we can use the cycle deck. The process used to build such a dataset for the take-off phase is as follows:

1. Modify the value of Pi_{Nozzle} and engine bleed within the original ONX data file for the configuration being tested. All the other parameters remaining the same.
2. Generate a single point engine reference file within ONX, using the original reference engine mass flow rate value of 59.48 lbm/sec. The modified form of our baseline engine becomes a new on-design test configuration.
3. Input the ONX reference file into AEDsys and test the engine at the off-design conditions being investigated. Here we are working with fixed values of, Altitude = 0m, Mach number = 0.2 and Throttle setting = 100%.
4. Record the required results and then return to step 1 to repeat the process for the next combination of Pi_{Nozzle} and engine bleed being tested.

This gives us the table of results as presented in the first table below.

The second table gives the results for the properties of the air which is bled from the engine to supply air to the nose pitch control device. Calculation of the rate of air bleed, as is fed to the nose pitch control device, is as follows. The total quantity of air which is bled from the high pressure compressor is determined as the sum of the quantity of air required for the pitch control device and that required for cooling. The cooling air requirements were defined in our original engine requirements as:

- $\dot{m}_{Cooling-1} = 5\%$
- $\dot{m}_{Cooling-2} = 5\%$

The total percentage air bleed, is then given by,

$$\%Bleed_{Total} = \%Bleed_{NoseJet} + \%Bleed_{Cooling-1} + \%Bleed_{Cooling-2} \quad \text{Eq 3-3}$$

The actual bleed mass flow rate (lbm/s) can then be determined from the total mass flow rate of air leaving the high pressure compressor, as given by the expression,

$$\dot{m}_{Bleed(Total)} = \dot{m}_3 \cdot \left[\frac{\%Bleed_{Total}}{100} \right] \quad \text{Eq 3-4}$$

The mass flow rate of air being fed to the pitch control device can finally be determined from the expression,

$$m_{Bleed(NoseJet)} = m_{Bleed(Total)} \cdot \left[\frac{\%Bleed_{NoseJet}}{\%Bleed_{Total}} \right] \quad \text{Eq 3-5}$$

Test variables			Engine properties results				Nozzle properties results					
Pi-Nozzle	% Bleed	% Thrust	Thrust	TSFC	m-dot 0	Tt4	m-dot 8	Pt8	Tt8	Gamma 6A	A9	A9/A8
0.995	0	100	12334	0.7866	178.97	3200	181.66	51.932	1568.94	1.3373	2.168	1.1814
0.995	2.5	100	11828	0.7975	179	3200	179.15	49.615	1543.56	1.3379	2.178	1.1597
0.995	5	100	11313	0.81	179.02	3200	176.62	47.285	1517.38	1.3385	2.193	1.1382
0.995	7.5	100	10789	0.8244	179.06	3200	174.11	44.947	1490.36	1.3391	2.211	1.117
0.995	10	100	10253	0.8412	179.09	3200	171.59	42.601	1462.45	1.3398	2.235	1.0963
0.995	12.5	100	9707	0.8608	179.11	3200	169.05	40.279	1433.7	1.3405	2.264	1.0766
0.995	15	100	9149	0.8839	179.13	3200	166.52	37.971	1404.02	1.3412	2.301	1.058
0.995	17.5	100	8574	0.9119	179.15	3200	163.99	35.666	1373.32	1.3419	2.347	1.0409
0.995	20	100	7979	0.9461	179.18	3200	161.47	33.369	1341.54	1.3427	2.405	1.0259
0.95	0	100	12119	0.8006	178.97	3200	181.66	51.932	1568.94	1.3373	2.229	1.2145
0.95	2.5	100	11611	0.8123	179	3200	179.15	49.615	1543.56	1.3379	2.241	1.1931
0.95	5	100	11095	0.8259	179.02	3200	176.62	47.285	1517.38	1.3385	2.258	1.1719
0.95	7.5	100	10569	0.8415	179.06	3200	174.11	44.947	1490.36	1.3391	2.279	1.1512
0.95	10	100	10031	0.8599	179.09	3200	171.59	42.601	1462.45	1.3398	2.306	1.1311
0.95	12.5	100	9482	0.8812	179.11	3200	169.05	40.279	1433.7	1.3405	2.339	1.1122
0.95	15	100	8920	0.9067	179.13	3200	166.52	37.971	1404.02	1.3412	2.38	1.0947
0.95	17.5	100	8340	0.9374	179.15	3200	163.99	35.666	1373.32	1.3419	2.432	1.079
0.95	20	100	7739	0.9755	179.18	3200	161.47	33.369	1341.54	1.3427	2.499	1.0658
0.9	0	100	11859	0.8181	178.97	3200	181.66	51.932	1568.94	1.3373	2.304	1.2556
0.9	2.5	100	11351	0.831	179	3200	179.15	49.615	1543.56	1.3379	2.319	1.2346
0.9	5	100	10832	0.8459	179.02	3200	176.62	47.285	1517.38	1.3385	2.339	1.2139
0.9	7.5	100	10303	0.8632	179.06	3200	174.11	44.947	1490.36	1.3391	2.363	1.1939
0.9	10	100	9762	0.8835	179.09	3200	171.59	42.601	1462.45	1.3398	2.395	1.1748
0.9	12.5	100	9209	0.9074	179.11	3200	169.05	40.279	1433.7	1.3405	2.433	1.157
0.9	15	100	8642	0.9358	179.13	3200	166.52	37.971	1404.02	1.3412	2.481	1.141
0.9	17.5	100	8055	0.9706	179.15	3200	163.99	35.666	1373.32	1.3419	2.541	1.1274
0.9	20	100	7446	1.0138	179.18	3200	161.47	33.369	1341.54	1.3427	2.619	1.117
0.85	0	100	11576	0.8381	178.97	3200	181.66	51.932	1568.94	1.3373	2.389	1.302
0.85	2.5	100	11065	0.8525	179	3200	179.15	49.615	1543.56	1.3379	2.407	1.2816
0.85	5	100	10544	0.8691	179.02	3200	176.62	47.285	1517.38	1.3385	2.431	1.2617
0.85	7.5	100	10012	0.8884	179.06	3200	174.11	44.947	1490.36	1.3391	2.46	1.2427
0.85	10	100	9466	0.9112	179.09	3200	171.59	42.601	1462.45	1.3398	2.497	1.2248
0.85	12.5	100	8908	0.938	179.11	3200	169.05	40.279	1433.7	1.3405	2.542	1.2087
0.85	15	100	8335	0.9703	179.13	3200	166.52	37.971	1404.02	1.3412	2.598	1.1949
0.85	17.5	100	7740	1.01	179.15	3200	163.99	35.666	1373.32	1.3419	2.669	1.184
0.85	20	100	7121	1.0601	179.18	3200	161.47	33.369	1341.54	1.3427	2.761	1.1775
0.8	0	100	11263	0.8614	178.97	3200	181.66	51.932	1568.94	1.3373	2.487	1.3551
0.8	2.5	100	10749	0.8775	179	3200	179.15	49.615	1543.56	1.3379	2.509	1.3356
0.8	5	100	10225	0.8961	179.02	3200	176.62	47.285	1517.38	1.3385	2.537	1.3168
0.8	7.5	100	9689	0.918	179.06	3200	174.11	44.947	1490.36	1.3391	2.572	1.2992
0.8	10	100	9138	0.9438	179.09	3200	171.59	42.601	1462.45	1.3398	2.616	1.2831
0.8	12.5	100	8574	0.9746	179.11	3200	169.05	40.279	1433.7	1.3405	2.67	1.2693
0.8	15	100	7993	1.0118	179.13	3200	166.52	37.971	1404.02	1.3412	2.736	1.2584
0.8	17.5	100	7388	1.0582	179.15	3200	163.99	35.666	1373.32	1.3419	2.821	1.2515
0.8	20	100	6756	1.1174	179.13	3200	161.41	33.375	1341.77	1.3427	2.93	1.25
0.75	0	100	10916	0.8888	178.97	3200	181.66	51.932	1568.94	1.3373	2.6	1.4167
0.75	2.5	100	10399	0.9071	179	3200	179.15	49.615	1543.56	1.3379	2.627	1.3984
0.75	5	100	9870	0.9283	179.02	3200	176.62	47.285	1517.38	1.3385	2.661	1.3812
0.75	7.5	100	9329	0.9534	179.06	3200	174.11	44.947	1490.36	1.3391	2.703	1.3656
0.75	10	100	8771	0.9833	179.09	3200	171.59	42.601	1462.45	1.3398	2.756	1.352
0.75	12.5	100	8199	1.0191	179.11	3200	169.05	40.279	1433.7	1.3405	2.821	1.3415
0.75	15	100	7608	1.063	179.13	3200	166.52	37.971	1404.02	1.3412	2.902	1.3348
0.75	17.5	100	6991	1.1184	179.12	3200	163.96	35.671	1373.5	1.3419	3.006	1.3333
0.75	20	100	6342	1.1909	178.56	3200	160.84	33.453	1344.76	1.3424	3.126	1.3333
0.7	0	100	10526	0.9216	178.97	3200	181.66	51.932	1568.94	1.3373	2.733	1.4892
0.7	2.5	100	10005	0.9427	179	3200	179.15	49.615	1543.56	1.3379	2.767	1.4728
0.7	5	100	9471	0.9675	179.02	3200	176.62	47.285	1517.38	1.3385	2.809	1.4579
0.7	7.5	100	8923	0.9968	179.06	3200	174.11	44.947	1490.36	1.3391	2.861	1.4452
0.7	10	100	8357	1.0321	179.09	3200	171.59	42.601	1462.45	1.3398	2.926	1.4353
0.7	12.5	100	7774	1.0748	179.11	3200	169.05	40.279	1433.7	1.3405	3.007	1.4295
0.7	15	100	7170	1.128	179.08	3200	166.47	37.981	1404.33	1.3412	3.106	1.4286
0.7	17.5	100	6537	1.1966	178.52	3200	163.35	35.765	1376.76	1.3417	3.22	1.4286
0.7	20	100	5874	1.2873	177.16	3200	159.41	33.647	1352.14	1.3419	3.349	1.4286
0.65	0	100	10086	0.9619	178.97	3200	181.66	51.932	1568.94	1.3373	2.893	1.5764
0.65	2.5	100	9558	0.9868	179	3200	179.15	49.615	1543.56	1.3379	2.935	1.5627
0.65	5	100	9017	1.0162	179.02	3200	176.62	47.285	1517.38	1.3385	2.988	1.5512
0.65	7.5	100	8460	1.0514	179.06	3200	174.11	44.947	1490.36	1.3391	3.054	1.5429
0.65	10	100	7882	1.0943	179.09	3200	171.59	42.601	1462.45	1.3398	3.137	1.5387
0.65	12.5	100	7286	1.1471	178.98	3200	168.92	40.305	1434.47	1.3404	3.236	1.5385
0.65	15	100	6667	1.2139	178.33	3200	165.71	38.11	1408.47	1.3409	3.345	1.5385
0.65	17.5	100	6022	1.3008	176.98	3200	161.78	36.006	1385.15	1.3411	3.468	1.5385
0.65	20	100	5347	1.4173	174.7	3200	156.9	33.994	1365.42	1.341	3.606	1.5385
0.6	0	100	9579	1.0128	178.97	3200	181.66	51.932	1568.94	1.3373	3.09	1.6838
0.6	2.5	100	9044	1.0429	179	3200	179.15	49.615	1543.56	1.3379	3.145	1.6744
0.6	5	100	8492	1.079	179.02	3200	176.62	47.285	1517.38	1.3385	3.214	1.6683
0.6	7.5	100	7922	1.227	179.05	3200	174.09	44.95	1490.43	1.3391	3.299	1.6667
0.6	10	100	7331	1.1769	178.77	3200	171.26	42.67	1464.37	1.3397	3.398	1.6667
0.6	12.5	100	6723	1.2444	177.96	3200	167.88	40.5	1440.27	1.3401	3.505	1.6667
0.6	15	100	6094	1.3304	176.51	3200	163.85	38.43	1418.75	1.3402	3.624	1.6667
0.6	17.5	100	5441	1.4437	174.24	3200	158.98	36.448	1400.58	1.34	3.757	1.6667
0.6	20	100	4761	1.5979	170.91	3200	153.01	34.557	1387.05	1.3394	3.907	1.6667

Table 3-1 – Engine and nozzle data from engine tests at take-off conditions

Test variables			Engine	Properties at station 3				Bleed flow calculations		
Pi-Nozzle	% bleed	% Thrust	m-dot 0	m-dot 3	Gamma 3	Pt3	Tt3	% $bleed_{Total}$	m-dot $bleed_{Total}$	m-dot $bleed_{NoseJet}$
0.995	0	100	178.97	98.99	1.4	359.585	1478.86	10	9.899	0
0.995	2.5	100	179	99	1.4	359.599	1478.87	12.5	12.375	2.475
0.995	5	100	179.02	99.02	1.4	359.613	1478.89	15	14.853	4.951
0.995	7.5	100	179.06	98.98	1.4	359.637	1478.91	17.5	17.3215	7.4235
0.995	10	100	179.09	99	1.4	359.655	1478.93	20	19.8	9.9
0.995	12.5	100	179.11	99.01	1.4	359.684	1478.97	22.5	22.27725	12.37625
0.995	15	100	179.13	99.02	1.4	359.72	1479.01	25	24.755	14.853
0.995	17.5	100	179.15	99.03	1.4	359.758	1479.06	27.5	27.23325	17.33025
0.995	20	100	179.18	99.05	1.4	359.8	1479.11	30	29.715	19.81
0.95	0	100	178.97	98.99	1.4	359.585	1478.86	10	9.899	0
0.95	2.5	100	179	99	1.4	359.599	1478.87	12.5	12.375	2.475
0.95	5	100	179.02	99.02	1.4	359.613	1478.89	15	14.853	4.951
0.95	7.5	100	179.06	98.98	1.4	359.637	1478.91	17.5	17.3215	7.4235
0.95	10	100	179.09	99	1.4	359.655	1478.93	20	19.8	9.9
0.95	12.5	100	179.11	99.01	1.4	359.684	1478.97	22.5	22.27725	12.37625
0.95	15	100	179.13	99.02	1.4	359.72	1479.01	25	24.755	14.853
0.95	17.5	100	179.15	99.03	1.4	359.758	1479.06	27.5	27.23325	17.33025
0.95	20	100	179.18	99.05	1.4	359.8	1479.11	30	29.715	19.81
0.9	0	100	178.97	98.99	1.4	359.585	1478.86	10	9.899	0
0.9	2.5	100	179	99	1.4	359.599	1478.87	12.5	12.375	2.475
0.9	5	100	179.02	99.02	1.4	359.613	1478.89	15	14.853	4.951
0.9	7.5	100	179.06	98.98	1.4	359.637	1478.91	17.5	17.3215	7.4235
0.9	10	100	179.09	99	1.4	359.655	1478.93	20	19.8	9.9
0.9	12.5	100	179.11	99.01	1.4	359.684	1478.97	22.5	22.27725	12.37625
0.9	15	100	179.13	99.02	1.4	359.72	1479.01	25	24.755	14.853
0.9	17.5	100	179.15	99.03	1.4	359.758	1479.06	27.5	27.23325	17.33025
0.9	20	100	179.18	99.05	1.4	359.8	1479.11	30	29.715	19.81
0.85	0	100	178.97	98.99	1.4	359.585	1478.86	10	9.899	0
0.85	2.5	100	179	99	1.4	359.599	1478.87	12.5	12.375	2.475
0.85	5	100	179.02	99.02	1.4	359.613	1478.89	15	14.853	4.951
0.85	7.5	100	179.06	98.98	1.4	359.637	1478.91	17.5	17.3215	7.4235
0.85	10	100	179.09	99	1.4	359.655	1478.93	20	19.8	9.9
0.85	12.5	100	179.11	99.01	1.4	359.684	1478.97	22.5	22.27725	12.37625
0.85	15	100	179.13	99.02	1.4	359.72	1479.01	25	24.755	14.853
0.85	17.5	100	179.15	99.03	1.4	359.758	1479.06	27.5	27.23325	17.33025
0.85	20	100	179.18	99.05	1.4	359.8	1479.11	30	29.715	19.81
0.8	0	100	178.97	98.99	1.4	359.585	1478.86	10	9.899	0
0.8	2.5	100	179	99	1.4	359.599	1478.87	12.5	12.375	2.475
0.8	5	100	179.02	99.02	1.4	359.613	1478.89	15	14.853	4.951
0.8	7.5	100	179.06	98.98	1.4	359.637	1478.91	17.5	17.3215	7.4235
0.8	10	100	179.09	99	1.4	359.655	1478.93	20	19.8	9.9
0.8	12.5	100	179.11	99.01	1.4	359.684	1478.97	22.5	22.27725	12.37625
0.8	15	100	179.13	99.02	1.4	359.72	1479.01	25	24.755	14.853
0.8	17.5	100	179.15	99.03	1.4	359.758	1479.06	27.5	27.23325	17.33025
0.8	20	100	179.13	99.05	1.4	359.817	1479.14	30	29.715	19.81
0.75	0	100	178.97	98.99	1.4	359.585	1478.86	10	9.899	0
0.75	2.5	100	179	99	1.4	359.599	1478.87	12.5	12.375	2.475
0.75	5	100	179.02	99.02	1.4	359.613	1478.89	15	14.853	4.951
0.75	7.5	100	179.06	98.98	1.4	359.637	1478.91	17.5	17.3215	7.4235
0.75	10	100	179.09	99	1.4	359.655	1478.93	20	19.8	9.9
0.75	12.5	100	179.11	99.01	1.4	359.684	1478.97	22.5	22.27725	12.37625
0.75	15	100	179.13	99.02	1.4	359.72	1479.01	25	24.755	14.853
0.75	17.5	100	179.12	99.02	1.4	359.773	1479.08	27.5	27.2305	17.3285
0.75	20	100	178.56	99.09	1.4	360.04	1479.42	30	29.727	19.818
0.7	0	100	178.97	98.99	1.4	359.585	1478.86	10	9.899	0
0.7	2.5	100	179	99	1.4	359.599	1478.87	12.5	12.375	2.475
0.7	5	100	179.02	99.02	1.4	359.613	1478.89	15	14.853	4.951
0.7	7.5	100	179.06	98.98	1.4	359.637	1478.91	17.5	17.3215	7.4235
0.7	10	100	179.09	99	1.4	359.655	1478.93	20	19.8	9.9
0.7	12.5	100	179.11	99.01	1.4	359.684	1478.97	22.5	22.27725	12.37625
0.7	15	100	179.08	99.05	1.4	359.746	1479.05	25	24.7625	14.8575
0.7	17.5	100	178.52	99.12	1.4	360.031	1479.41	27.5	27.258	17.346
0.7	20	100	177.16	99.02	1.4	360.606	1480.15	30	29.706	19.804
0.65	0	100	178.97	98.99	1.4	359.585	1478.86	10	9.899	0
0.65	2.5	100	179	99	1.4	359.599	1478.87	12.5	12.375	2.475
0.65	5	100	179.02	99.02	1.4	359.613	1478.89	15	14.853	4.951
0.65	7.5	100	179.06	98.98	1.4	359.637	1478.91	17.5	17.3215	7.4235
0.65	10	100	179.09	99	1.4	359.655	1478.93	20	19.8	9.9
0.65	12.5	100	178.98	99.05	1.4	359.75	1479.05	22.5	22.28625	12.38125
0.65	15	100	178.33	99.13	1.4	360.09	1479.49	25	24.7825	14.8695
0.65	17.5	100	176.98	99.32	1.4	360.716	1480.29	27.5	27.313	17.381
0.65	20	100	174.7	99.54	1.4	361.672	1481.52	30	29.862	19.908
0.6	0	100	178.97	98.99	1.4	359.585	1478.86	10	9.899	0
0.6	2.5	100	179	99	1.4	359.599	1478.87	12.5	12.375	2.475
0.6	5	100	179.02	99.02	1.4	359.613	1478.89	15	14.853	4.951
0.6	7.5	100	179.05	99.03	1.4	359.644	1478.92	17.5	17.33025	7.42725
0.6	10	100	178.77	99.04	1.4	359.827	1479.15	20	19.808	9.904
0.6	12.5	100	177.96	99.2	1.4	360.253	1479.7	22.5	22.32	12.4
0.6	15	100	176.51	99.39	1.4	360.975	1480.62	25	24.8475	14.9085
0.6	17.5	100	174.24	99.68	1.4	362.037	1481.99	27.5	27.412	17.444
0.6	20	100	170.91	100.06	1.4	363.522	1483.88	30	30.018	20.012

Table 3-2 – Engine bleed data from engine tests at take-off conditions

C3.4.2 Cruise analysis datasets

During the cruise phase, the engine thrust is an extra variable in our analysis which is constantly changing throughout the flight phase. We therefore need to test our engine at a number of different throttle ratios for a range of nozzles. Fortunately, the throttle ratio is defined within AEDsys cycle deck, used for off-design testing. The process used to build such a dataset for the cruise phase is as follows:

1. Modify the value of Pi_{Nozzle} being tested within the original ONX data file. All the other parameters remaining the same.
2. Generate a single point engine reference file within ONX, using the original reference engine mass flow rate value of 59.48 lbm/sec. The modified form of our baseline engine becomes a new on-design test configuration.
3. Input the ONX reference file into AEDsys and test the engine at the off-design conditions being investigated. Here we are working with fixed values of, Altitude = 40kft, Mach number = 0.9 and fixed engine bleed for cooling only.
4. Record the required results and then return to step 1 to repeat the process for the next value of Pi_{Nozzle} being tested.

This gives us the table of results as presented below.

Test variables			Engine properties results				Nozzle properties results					
Pi-Nozzle	% Bleed	% Thrust	Thrust	TSFC	m-dot 0	Tt4	m-dot 8	Pt8	Tt8	Gamma 6A	A9	A9/A8
0.995	0	65	2105	0.8154	48.1	2446.13	48.58	12.228	1197.71	1.3398	2.385	1.311
0.995	0	60	1943	0.8129	46.36	2386.39	46.8	11.643	1168.53	1.3403	2.33	1.2811
0.995	0	55	1782	0.8108	44.6	2323.71	45	11.056	1138.11	1.3408	2.274	1.2512
0.995	0	50	1620	0.8096	42.8	2256.92	43.16	10.459	1105.9	1.3414	2.217	1.2208
0.995	0	45	1458	0.8095	40.96	2186.27	41.29	9.859	1072.11	1.3421	2.16	1.1904
0.98	0	65	2095	0.821	48.14	2447.4	48.62	12.241	1198.33	1.3398	2.406	1.3222
0.98	0	60	1933	0.8188	46.4	2387.92	46.84	11.658	1169.27	1.3403	2.35	1.2925
0.98	0	55	1773	0.8171	44.65	2325.53	45.05	11.073	1138.99	1.3408	2.294	1.2626
0.98	0	50	1611	0.8163	42.85	2259.05	43.22	10.477	1106.92	1.3414	2.238	1.2324
0.98	0	45	1451	0.8167	41.03	2188.76	41.36	9.879	1073.29	1.3421	2.181	1.2021
0.96	0	65	2080	0.8289	48.19	2449.16	48.67	12.259	1199.19	1.3398	2.434	1.3378
0.96	0	60	1921	0.827	46.47	2390.4	46.91	11.683	1170.53	1.3402	2.379	1.3084
0.96	0	55	1760	0.8259	44.72	2328.03	45.12	11.096	1140.2	1.3408	2.323	1.2785
0.96	0	50	1600	0.8257	42.93	2261.99	43.3	10.503	1108.33	1.3414	2.267	1.2484
0.96	0	45	1441	0.8268	41.11	2192.19	41.44	9.908	1074.93	1.342	2.211	1.2183
0.94	0	65	2065	0.8371	48.24	2450.99	48.72	12.277	1200.09	1.3397	2.464	1.354
0.94	0	60	1907	0.8357	46.54	2392.59	46.98	11.704	1171.6	1.3402	2.409	1.3247
0.94	0	55	1747	0.8351	44.79	2330.63	45.2	11.12	1141.46	1.3408	2.353	1.295
0.94	0	50	1588	0.8355	43.01	2265.05	43.38	10.53	1109.8	1.3413	2.297	1.2651
0.94	0	45	1430	0.8374	41.21	2195.76	41.54	9.937	1076.63	1.342	2.241	1.2353
0.92	0	65	2049	0.8457	48.3	2452.9	48.78	12.296	1201.02	1.3397	2.495	1.3708
0.92	0	60	1892	0.8448	46.6	2394.87	47.04	11.725	1172.71	1.3402	2.44	1.3417
0.92	0	55	1734	0.8447	44.87	2333.32	45.28	11.144	1142.77	1.3407	2.385	1.3122
0.92	0	50	1576	0.8458	43.1	2268.23	43.47	10.558	1111.33	1.3413	2.329	1.2825
0.92	0	45	1419	0.8485	41.3	2199.48	41.63	9.968	1078.39	1.342	2.274	1.253
0.9	0	65	2033	0.8548	48.36	2454.89	48.84	12.316	1201.99	1.3397	2.527	1.3885
0.9	0	60	1877	0.8543	46.67	2397.25	47.12	11.748	1173.86	1.3402	2.472	1.3596
0.9	0	55	1720	0.8549	44.94	2336.14	45.35	11.17	1144.13	1.3407	2.417	1.3302
0.9	0	50	1564	0.8567	43.19	2271.55	43.56	10.587	1112.92	1.3413	2.362	1.3008
0.9	0	45	1408	0.8602	41.4	2203.35	41.74	10.001	1080.24	1.3419	2.307	1.2715
0.88	0	65	2016	0.8643	48.42	2456.96	48.9	12.337	1203.01	1.3397	2.56	1.4069
0.88	0	60	1862	0.8644	46.74	2399.73	47.19	11.772	1175.07	1.3402	2.506	1.3782
0.88	0	55	1706	0.8656	45.03	2339.09	45.44	11.198	1145.56	1.3407	2.452	1.349
0.88	0	50	1552	0.8681	43.29	2275.42	43.66	10.622	1114.85	1.3413	2.397	1.3201
0.88	0	45	1396	0.8726	41.5	2207.38	41.84	10.034	1082.16	1.3419	2.343	1.2909
0.86	0	65	1999	0.8744	48.48	2459.08	48.97	12.358	1204.07	1.3397	2.596	1.4262
0.86	0	60	1846	0.8751	46.82	2402.32	47.27	11.797	1176.33	1.3401	2.542	1.3977
0.86	0	55	1692	0.877	45.11	2342.16	45.52	11.226	1147.05	1.3407	2.488	1.3688
0.86	0	50	1539	0.8802	43.38	2279.03	43.76	10.654	1116.58	1.3412	2.434	1.3401
0.86	0	45	1384	0.8857	41.61	2211.59	41.95	10.07	1084.17	1.3418	2.38	1.3113
0.84	0	65	1981	0.8851	48.55	2461.35	49.04	12.381	1205.17	1.3397	2.633	1.4465
0.84	0	60	1829	0.8864	46.9	2405.03	47.35	11.824	1177.65	1.3401	2.579	1.4182
0.84	0	55	1676	0.889	45.2	2345.37	45.61	11.256	1148.6	1.3406	2.526	1.3896
0.84	0	50	1525	0.8931	43.49	2282.79	43.87	10.687	1118.39	1.3412	2.472	1.3612
0.84	0	45	1372	0.8996	41.73	2215.99	42.07	10.107	1086.27	1.3418	2.419	1.3328

Table 3-3 – Analysis dataset at cruise conditions

C3.5 Refined engine nozzle analysis with the Nozzle module

A component level analysis of the nozzle can be carried out with the Nozzle module [75] within AEDsys. In particular, this enables us to determine the nozzle gross thrust coefficient (Cfg) using the engine-nozzle results obtained above. This parameter is the ratio of the actual gross thrust to the ideal gross thrust and as particularly important for further analysis work. A one dimensional nozzle analysis is sufficient for our studies as is selected within the main window. The majority of the input parameters have already been determined from our engine analysis work, the only unknowns being:

- Gas constant – This has a fixed value for air.
- Static pressure – This is the ambient pressure at the flight condition.
- Discharge coefficient – This is a function of the nozzle geometry and was given a value of 0.98 in all of our test cases, which is typical for this type of nozzle.

After entering all the required parameters, the results can be obtained from the Design Calc button and are displayed in the main window.

C3.5.1 Cruise analysis nozzle results

The results from the Nozzle program for the cruise phase are presented below along with the nozzle pressure ratio (NPR) which can be determined from the expression below.

$$NPR = \frac{P_{t8}}{P_0} \qquad \text{Eq 3-6}$$

Pi-Nozzle	% Bleed	% Thrust	Cfg	NPR
0.995	0	65	0.9785	4.479121
0.995	0	60	0.9785	4.264835
0.995	0	55	0.9784	4.049817
0.995	0	50	0.9783	3.831136
0.995	0	45	0.9782	3.611355
0.98	0	65	0.9744	4.483883
0.98	0	60	0.9742	4.27033
0.98	0	55	0.9739	4.056044
0.98	0	50	0.9736	3.837729
0.98	0	45	0.9733	3.618681
0.96	0	65	0.9688	4.490476
0.96	0	60	0.9684	4.279487
0.96	0	55	0.9679	4.064469
0.96	0	50	0.9673	3.847253
0.96	0	45	0.9666	3.629304
0.94	0	65	0.963	4.49707
0.94	0	60	0.9624	4.287179
0.94	0	55	0.9616	4.07326
0.94	0	50	0.9607	3.857143
0.94	0	45	0.9597	3.639927
0.92	0	65	0.9571	4.504029
0.92	0	60	0.9562	4.294872
0.92	0	55	0.9551	4.082051
0.92	0	50	0.9539	3.867399
0.92	0	45	0.9525	3.651282

Pi-Nozzle	% Bleed	% Thrust	Cfg	NPR
0.9	0	65	0.9509	4.511355
0.9	0	60	0.9498	4.303297
0.9	0	55	0.9485	4.091575
0.9	0	50	0.9464	3.878022
0.9	0	45	0.9452	3.66337
0.88	0	65	0.9446	4.519048
0.88	0	60	0.9432	4.312088
0.88	0	55	0.9417	4.101832
0.88	0	50	0.9398	3.890842
0.88	0	45	0.9377	3.675458
0.86	0	65	0.938	4.52674
0.86	0	60	0.9364	4.321245
0.86	0	55	0.9345	4.112088
0.86	0	50	0.9324	3.902564
0.86	0	45	0.9299	3.688645
0.84	0	65	0.9312	4.535165
0.84	0	60	0.9294	4.331136
0.84	0	55	0.9272	4.123077
0.84	0	50	0.9247	3.914652
0.84	0	45	0.9219	3.702198

Table 3-4 – Nozzle analysis results at cruise conditions

C3.5.2 Take-off analysis nozzle results

The results from the Nozzle program for the take-off phase are presented below along with the nozzle pressure ratio (NPR).

Pi-Nozzle	% Bleed	% Thrust	Cfg	NPR
0.995	0	100	0.9782	3.533751
0.995	5	100	0.978	3.217542
0.995	10	100	0.9777	2.898816
0.995	15	100	0.9774	2.583764
0.995	20	100	0.9768	2.270618
0.95	0	100	0.9627	3.533751
0.95	5	100	0.961	3.217542
0.95	10	100	0.9588	2.898816
0.95	15	100	0.9558	2.583764
0.95	20	100	0.9513	2.270618
0.9	0	100	0.944	3.533751
0.9	5	100	0.9405	3.217542
0.9	10	100	0.9359	2.898816
0.9	15	100	0.9296	2.583764
0.9	20	100	0.9201	2.270618
0.85	0	100	0.9235	3.533751
0.85	5	100	0.918	3.217542
0.85	10	100	0.9107	2.898816
0.85	15	100	0.9006	2.583764
0.85	20	100	0.8852	2.270618
0.8	0	100	0.9009	3.533751
0.8	5	100	0.8932	3.217542
0.8	10	100	0.8827	2.898816
0.8	15	100	0.8682	2.583764
0.8	20	100	0.8459	2.271026

Pi-Nozzle	% Bleed	% Thrust	Cfg	NPR
0.75	0	100	0.8759	3.533751
0.75	5	100	0.8655	3.217542
0.75	10	100	0.8514	2.898816
0.75	15	100	0.8317	2.583764
0.75	20	100	0.8034	2.276334
0.7	0	100	0.8478	3.533751
0.7	5	100	0.8343	3.217542
0.7	10	100	0.8159	2.898816
0.7	15	100	0.7898	2.584445
0.7	20	100	0.753	2.289535
0.65	0	100	0.8159	3.533751
0.65	5	100	0.7987	3.217542
0.65	10	100	0.775	2.898816
0.65	15	100	0.7424	2.593223
0.65	20	100	0.6992	2.313146
0.6	0	100	0.7793	3.533751
0.6	5	100	0.7575	3.217542
0.6	10	100	0.7276	2.903511
0.6	15	100	0.6894	2.614997
0.6	20	100	0.6408	2.351456

Table 3-5 – Nozzle analysis results at take-off conditions

C4 Detailed nozzle design an overview

C4.1 Nozzle design requirements

The function of a typical exhaust nozzle is to:

1. Accelerate the exhaust gases to a high velocity – Primary function of the nozzle.
2. Collect the gas flow into a single jet plume – The exhaust gases are typically collated from more than one engine stage into a single exhaust plume. In the case of a mixed flow exhaust, this may be the mixing of the fan and core flows. A two-exhaust turbofan will retain separate core and fan exhaust flows.
3. Straighten the exhaust flow – The rotating parts of the engine, impart a rotary component to the flow passing through it. As the preference is for a uniform exhaust flow, some method of straightening the flow is required.
4. Fully expand the exhaust gases as much as possible - To extract the maximum amount of energy from them.
5. Reduce the impact on engine operation of afterburners - For a correctly sized nozzle throat area; the characteristics downstream of the throat of a convergent-divergent nozzle are completely independent of those upstream. This useful engine operating regime can be extended with the use of a variable throat nozzle.
6. Provide capability for cooling the nozzle walls where required.
7. Provide capability for the use of thrust reversing systems.
8. Provide a means to suppress engine noise from the jet
9. For stealth applications, the nozzle should be able to provide means of reducing the infra-red signature and radar reflection. Such techniques do typically impart an engine performance penalty.
10. Provide capability for the use of thrust vectoring systems.
11. Minimise boat-tail drag – This is related to the external geometry of the nozzle.
12. Maintain a high level of engine reliability

The design engineer has the difficult task of meeting all of these requirements at minimum cost, weight, development time and complexity and with minimum total pressure loss.

C4.2 An overview of nozzle operation

The primary function of a propulsive gas turbine nozzle is to generate a high velocity exhaust jet and thus thrust to propel the aircraft. It is thus a means of converting the excess enthalpy from the gas generator into an exhaust stream of high kinetic energy. The efficiency of a nozzle is by definition, the ratio of the actual performance of the nozzle to the performance of an ideal isentropic expansion process. Since the velocity of the gases entering the nozzle can be neglected in comparison to those leaving the nozzle, this reduces to the ratio of actual to ideal exhaust velocities squared as given below. The expression for the polytrophic efficiency of the nozzle is also given.

$$\eta_{Nozzle} = \frac{V_{Actial}^{\ 2}}{V_{Ideal}^{\ 2}} \qquad e_n = \frac{\gamma}{\gamma - 1} \cdot \frac{\ln\left\{1 - \eta_n \left[1 - \left(P_e / P_{ti}\right)^{(\gamma-1)/\gamma}\right]\right\}}{\ln\left(P_e / P_{ti}\right)} \qquad \text{Eq 4-1, 4-2}$$

An important parameter with respect to nozzle operation is the nozzle pressure ratio. This is related to the expansion of the gases through the nozzle and is governed by the pressure ratio across the nozzle. The ideal case to achieve maximum thrust is when the exit pressure equals the ambient pressure and therefore careful control of the pressure ratio is required to maintain favourable performance. In this optimum operating condition, the gases leaving the exhaust are fully expanded and we are therefore able to extract the maximum possible amount of energy out of the exhaust gases.

C4.3 Engine back-pressure control

A secondary function of the nozzle is engine back pressure. This is used to retain some of the energy of the burner gases to power the turbine and thus the compressor. Engine back-pressure is an important parameter in any engine design and analysis work. It is maintained by the area of the throat of the nozzle and is related to the thrust and fuel consumption characteristics of the engine. In this context, the inter-relation between an engine and its nozzle is clearly apparent and neither the engine nor nozzle can therefore be considered in isolation. The nozzle throat area is therefore an important design variable which affects the performance of both the engine and the nozzle. The throat area is typically fixed for on-design conditions, with respect to the mass flow rate of the engine at its design condition. This is thus ultimately one of the main contributors to the off-design performance of the engine.

Nozzle with a variable throat area offer benefits of a wider operating range and thus improved off-design performance. The capability to increase the mass flow rate through the engine as desired can also reduce the risk of compressor surge. Such a nozzle is essential for engines fitted with an afterburner, to cater for the large temperature changes involved. The ability to reduce the engine back pressure can also make engine starting significantly easier. Such nozzles do however come at a price in terms of increased cost, complexity and weight. The analysis of such engine-nozzle combinations is considerably more complicated since each discrete value of throat area represents a different engine with different on-design and off-design operating characteristics.

C4.4 Exhaust nozzle area ratio

The flow conditions at the nozzle exit are particularly important with respect to the performance of the engine. The ideal condition for any nozzle is when the flow is fully expanded at the nozzle exit. In such case, the nozzle exit pressure equals the ambient and the resultant thrust is at its maximum. A loss in engine performance will be experienced for conditions of under-expansion or over-expansion. The performance of a nozzle can however be improved by varying the nozzle exit area with respect to the throat area. The ultimate configuration is thus one whose throat area can be varied to control engine back pressure and the exit area varied in accordance with the throat area. Such configurations are particularly useful for afterburning engines but have proven to be considerably complex.

C4.5 Thrust reversers

Thrust reversers have traditionally been used during the landing ground run to slow the aircraft but they can also be used to improve the manoeuvrability of fighter aircraft. The clam-shell and the cascade-blocker and the two types most common. The use of a reverser does however have an impact of engine operation and it is sometimes necessary to increase the nozzle throat area to prevent fan and compressor stall. Since this is not the objective our study they will not be discussed in detail here.

C4.6 Nozzle design parameters

The sections which follow give an introduction to a number of common nozzle design parameters. Terms relating to the nozzle geometry are defined in the figure below.

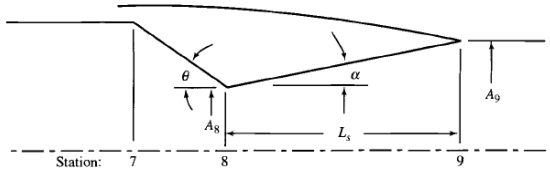

A_8 = Primary nozzle throat area
A_9 = Secondary nozzle exit area
α = Secondary nozzle half angle
θ = Primary nozzle half angle
L_s = Secondary nozzle length

Fig. 10.70 Nozzle geometric parameters.

Figure 4-1 – Nozzle geometric parameters [16]

C4.6.1 Total pressure loss

The biggest contribution to the total pressure loss is viscous effects, which can be determined from the following relation for one-dimensional flow. Where, P_W is the wetter perimeter and C_f is the friction coefficient.

$$\frac{dP_t}{P_t} = -\frac{\gamma}{2} \cdot M^2 \cdot C_f \cdot \frac{P_W}{A} \cdot dx \qquad \text{Eq 4-3}$$

The pressure loss of two-dimensional nozzle can be determined relative to a circular nozzle via following relation. Where, AR is the aspect ratio (Width/Height)

$$\frac{1-(\pi_n)_{\text{Rectangular}}}{1-(\pi_n)_{Circular}} = \frac{AR+1}{\sqrt{\pi \cdot AR}} \qquad \text{Eq 4-4}$$

C4.6.2 Gross thrust and discharge coefficients

The dimensionless gross thrust and discharge coefficients are the two main parameters used to assess nozzle performance. The gross thrust coefficient is a measure of the nozzle efficiency, expressed as the ratio of actual to ideal gross thrust.

$$C_{fg} = \frac{F_{g-Actual}}{F_{g-Ideal}} \qquad \text{Eq 4-5}$$

The parameter is particularly important as it used to account for losses from:

- Exhaust velocity angularity

- Reduction in velocity due to boundary layer friction
- Mass flow leakage thorough the nozzle walls
- Flow non-uniformities

This parameter can differ between companies according to the method adopted.

The discharge coefficient is particularly important to determine the required nozzle throat area to pass a specified mass flow rate. This parameter is the ratio of the actual mass flow to the ideal mass flow for the nozzle, which is also equal to the ratio of the effective 1-D to the ideal throat area as given by the expression,

$$C_D = \frac{\dot{m}_8}{\dot{m}_{8i}} = \frac{\rho_8 \cdot V_8 \cdot A_8}{\rho_8 \cdot V_8 \cdot A_{8e}} = \frac{A_8}{A_{8e}} \quad \text{Eq 4-6}$$

The maximum value of C_D is achieved when the nozzle is choked and is a function of the half angle of the nozzle convergent section. In the case of a convergent nozzle, any NPR below this value sees a reduction in C_D. A convergent-divergent nozzle sees a reduction in C_D for an increase in NPR beyond that for C_{Dmax}.

C4.6.3 Velocity coefficient

The velocity coefficient is the ratio of the actual to the ideal velocity of the exhaust gases as given by the expression below.

$$C_V = \frac{V_{9-Actual}}{V_{9-Ideal}} \quad \text{Eq 4-7}$$

This parameter is a function of the geometry of the nozzle and is related to the adiabatic efficiency of the nozzle since it also represents friction losses in the boundary layer of the nozzle. We are thus able to obtain the alternative expression for adiabatic efficiency.

$$\eta_{Nozzle} = C_V{}^2 \quad \text{Eq 4-8}$$

C4.6.4 Angularity coefficient (C_A)

The angularity coefficient is used to account for the thrust loss due to the non-axial component of the exhaust gases leaving the nozzle. Analytical and chart based methods can be used to determine C_A as a function of nozzle half angle and nozzle area ratio.

C4.7 One dimensional flow approximation

For the preliminary analysis of a nozzle, a one-dimensional adiabatic flow analysis is a reasonable approximation. In such case, the nozzle flow coefficients reduce to the simpler formats, $C_A = 1$ and $C_D = P_{t8}/P_{t7}$. Eq 4-9

Using relations for ideal gross thrust as a function of isentropic exit velocity and treating the exhaust as a calorically perfect gas, we are able to obtain the expression.

$$C_{fg} = C_D \cdot C_V \cdot \left\{ \frac{1 - \left(\frac{P_{9i}}{P_{t8}}\right)^{(\gamma-1)/\gamma}}{1 - \left(\frac{P_0}{P_{t8}}\right)^{(\gamma-1)/\gamma}} \right\}^{1/2} \cdot \left\{ 1 + \frac{\gamma - 1}{2 \cdot \gamma} \cdot \frac{1 - P_0/P_9}{\left(P_{t9}/P_9\right)^{(\gamma-1)/\gamma} - 1} \right\} \quad \text{Eq 4-10}$$

For ideal expansion (P9 = P0), this reduces to $C_{fg} = C_D \cdot C_V$ Eq 4-11

Fortunately, all of the expressions above have already been incorporated into the AEDsys Nozzle program.

C4.8 General relation for nozzle performance

The complete general relation for the gross thrust coefficient incorporating all of the nozzle coefficients above is given below.

$$C_{fg} = \frac{C_V \cdot C_A \cdot \dot{m}_7 \cdot V_{9i} / g_C + (P_{9i} - P_0) \cdot A_9}{\dot{m}_7 V_S / g_C} - \Delta C_{fg} \qquad \text{Eq 4-12}$$

Where, $\dot{m}_7$ is the actual mass flow rate entering the nozzle, V_{9i} and P_{9i} are the ideal velocity and pressure at the nozzle exit and ΔC_{fg} is the sum of the losses due to leakage and changes in the cooling air flow. Thrust losses due to under or over expansion are not included in these expressions and are instead accounted for in the 'off-design' engine analysis. These analytical expressions are however only approximate and the results must be verified by experiment and/or CFD modelling. In this study, the 1-dimensional analysis incorporated into the Nozzle program is sufficient for our needs.

C4.9 Installation considerations

The final size of an engine is based on uninstalled thrust requirements, which require knowledge of the engine installation losses. For initial design work, it is sufficient to assume a typical loss factor but more detailed estimates are required for later studies. The main contributors to these losses are the engine intake and exhaust and therefore careful design of these is required. This design work is not limited to the internal profile of the inlet and exhaust as their external profile can also provide a significant contribution to the total drag of the aircraft. Such an analysis is however a field of study in its own right since the presence of the engine, inlet, nozzle and even the exhaust stream can have an impact on the flow field and pressure distribution around the aircraft.

A further complication is a phenomenon known as throttle dependant drag, in which the engine throttle setting has a considerable impact on the external drag characteristics of the inlet and nozzle. Due to its complexity, such an analysis is not feasible within the time constraints of this project. Therefore, only an overview of the nozzle and intake installation considerations will be given here to provide guidance on making sensible design choices. Since our work is primarily focused on the integration of exhaust nozzles, this will be the main focus of this discussion.

C4.9.1 Revised inlet and exhaust installation loss factors

During initial design work, we can assume an installation loss of 5% and thus the installed thrust of engine can be predicted by the expression, $T = F \cdot 0.95$. Where T and F refer to the installed and uninstalled engine thrust respectively. A more refined estimate for the installed engine thrust (as used for later design work) is given by the expression,

$$T = \dot{m}_0 \cdot \left(\frac{F}{\dot{m}_0} \right) \cdot \left(1 - \phi_{Inlet} - \phi_{Nozzle} \right) \quad \text{Eq 4-13}$$

Where, $\dot{m}_0$ is the engine mass flow rate and $\left(F/\dot{m}_0 \right)$ the specific thrust of the engine, as obtained from the parametric engine design work. ϕ_{Inlet} and ϕ_{Nozzle} are inlet and nozzle installation loss factors, expressed as a function of the uninstalled thrust. These are themselves complex functions of flight condition and throttle setting. The internal behaviour of the inlet and nozzle has already been accounted for in our engine design work, by means of the engine component parameters. These loss factors are thus used to account for losses primarily due to external flow behaviour.

The engine design process incorporating this new model is modified as such:

1. Make an estimate of the size of the critical mass flow rate of the engine.
2. Determine the inlet and nozzle installation loss factors at this mass flow rate for a number of critical design conditions.
3. Determine the thrust of the engine at these conditions
4. Re-scale the mass flow rate until the engine thrust requirements are met.
5. Return to step 2 and determine the installation loss at this new mass flow rate.
6. Repeat steps 2-5 until the solution converges.

The installation loss factors will be discussed in more depth in the sections that follow.

C4.9.2 Inlet installation loss factor

The inlet installation loss factor can be determined by the following expression as a function of the uninstalled thrust and the drag.

$$\phi_{Inlet} = \frac{D_{Inlet}}{F} \quad \text{Eq 4-14}$$

The effects of external friction are not included in this expression and should be covered by the aerodynamics design team instead. The propulsive aspect of inlet drag (often referred to as the additive inlet drag) can be determined from the expression below,

$$D_{Inlet(Additive)} = \int_0^1 \left(P - P_0 \right) \cdot dA \quad \text{Eq 4-15}$$

Where, station 1 is taken at the inlet lip and 0 is the free-stream. A number of analytical expressions can be determined according to the inlet configuration adopted, either subsonic or supersonic. The reader is advised to consult the literature for more details.

C4.9.3 Nozzle installation loss factor

The nozzle installation loss factor can be determined by the following expression as a function of the uninstalled thrust and the drag.

$$\phi_{Nozzle} = \frac{D_{Nozzle}}{F} \quad \text{Eq 4-16}$$

As for the inlet, the effects of external friction are not included in this expression and are covered by the aerodynamics team instead. The propulsive aspect of nozzle drag is associated with separation of the boundary layer on the nozzle afterbody, which results in a pressure drag on the nozzle. The geometry of the nozzle as well as a representation of the region of flow separation is presented in the figure below.

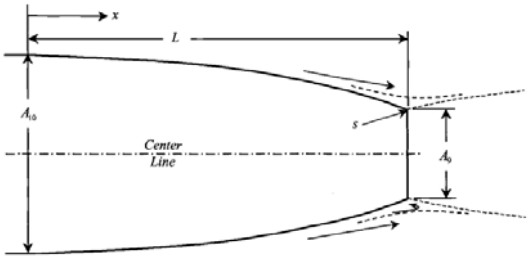

Fig. 6.7 Axisymmetric exhaust nozzle model.

Figure 4-2 – Nozzle boat-tail drag geometric parameters [16]

The propulsive aspect of nozzle drag can be determined from the expression below,

$$D_{Nozzle} = \int_m^9 (P - P_0) \cdot dA \qquad \text{Eq 4-17}$$

Fortunately, simplified empirical expressions exist for determining the nozzle loss factors. One such expression for the subsonic regime (up to Mach 0.8) is given below.

$$\phi_{Nozzle} = \frac{M_0 \cdot \frac{C_D}{2} \cdot (A_{10} - A_9) / A_0}{F \cdot g_C / (\dot{m}_0 \cdot a_0)} \qquad \text{Eq 4-18}$$

For the transonic and supersonic regimes, ($0.8 \leq \text{Mach} \geq 1.2$), we have the expression.

$$\phi_{Nozzle} = \frac{M_0 \cdot \left(\frac{C_D}{2}\right) \cdot \left(\frac{A_{10}}{A_0}\right)}{F \cdot g_C / (\dot{m}_0 \cdot a_0)} \qquad \text{Eq 4-19}$$

For the speed regime $0 < \text{Mach} < 0.8$, the drag coefficient (C_D) can be found from figure 4-3 below from Mattingly. For the speed $0.8 \leq \text{Mach} \leq 1.2$, ($C_D$) can be determined from the figure 4-4 below from Mattingly, as a function of M_0 and L/D_{10}.

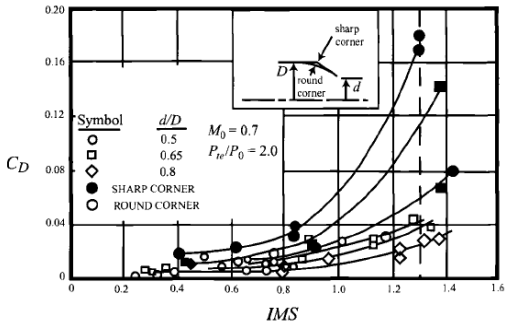

Fig. 6.8 Convergent nozzle boattail pressure drag coefficients.[4.7]

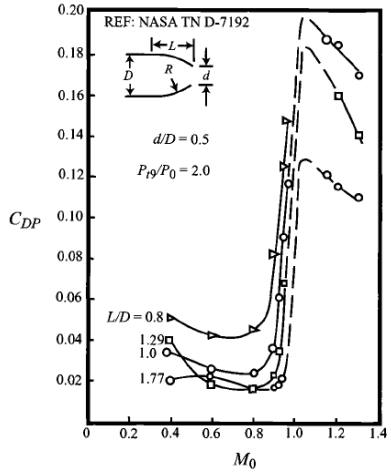

Fig. 6.10 Experimental pressure drag coefficients of some circular—arc boattails.[7]

Figure 4-3 and 4-4 – Boat-tail drag coefficients [16]

The parameter IMS in figure 6.8 is the 'Integral Mean Slope' which is a function of the nozzle geometry. This complex function requires detailed knowledge of the nozzle geometry but for initial design work, the simplified approximation below is used.

$$IMS \approx 1.8 \cdot \left(\frac{D_{10} - D_9}{L}\right) \cdot \left(1 - \frac{D_9}{D_{10}}\right) \qquad \text{Eq 4-20}$$

Fortunately, all of the expressions above have already been incorporated into the AEDsys software.

C4.9.4 Predicting the drag due to a thrust vectoring nozzle

The boat-tail drag determined in the last section is only applicable to fixed geometry nozzles. In the case, of a variable geometry nozzle (in particular a thrust vectoring nozzle), its ever changing geometry can make drag prediction extremely difficult. In addition to the typical factors such as flow-field, nozzle geometry and position, throttle setting and flight condition, the drag is also a function of the nozzle deflection angle. The surrounding flow-field behaviour will also be different to that for a conventional nozzle as a result of nozzle leakages and the presence of additional cooling flows etc. Prediction of the drag of a thrust vectoring nozzle is therefore a complex subject which is specific to a nozzle and whose results can only be really verified by experimentation and/or CFD.

C4.10 Stealth design requirements

It is advantageous for a stealth aircraft to reduce the IR signature from the exhaust of the hot engine as much as possible. Cooling of the exhaust flows does offer some benefit but additional approaches such as hiding the exit of the turbine from direct view and edge alignment have proved to be most effective. One such example is shown in the figure below. It should be noted however that the use of such nozzles does have a negative impact on engine performance, a factor which needs to be incorporated in to the design of such an aircraft and its engine.

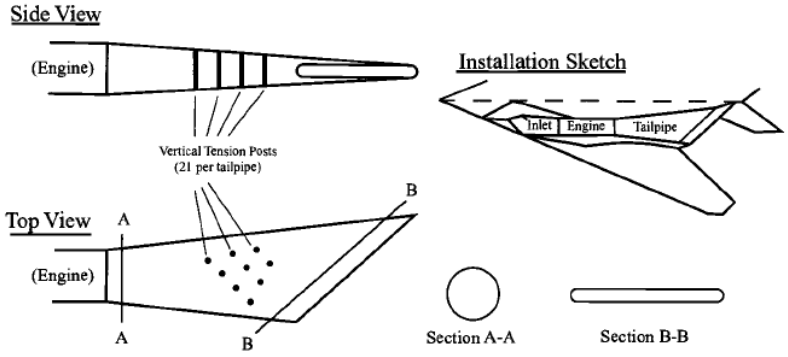

Fig. 10.69 Exhaust nozzle of F-117A [Originally published in *Have Blue and the F-117A: Evolution of the "Stealth Fighter,"* D. Aronstein and A. Piccirillo, AIAA, 1997 (Ref. 12). Copyright 1997 by AIAA. Reprinted with permission.]

Figure 4-5 – Example stealth nozzle design features [Source unknown]

D1 General terms for the performance analyses

This section is a reference for some of the general analysis terms used within the following thrust vectored aircraft performance analyses. Some of these expressions are common to more than one analysis while others are specific to just one.

D1.1 Basic terms

The general aerodynamic terms such as C_{DZ}, K, $C_{L\alpha}$ and X_{AC} as used in the baseline performance analysis work remain valid for this work. These are presented as convenient polynomial expressions in the baseline aircraft design section of this thesis. Other useful basic terms included in the analyses are:

- The basic lift coefficient, for an aircraft operating away the ground is given by,
  $C_{L(Basic)} = C_{L\alpha} \cdot (\alpha + i_W - \alpha_{0L})$ Eq 1-1
- The dynamic pressure (q) of the flow is a common term within the analyses and is given by, $q = \frac{1}{2} \cdot \rho \cdot V^2$ Eq 1-2

D1.2 Analysis of the ground effect for the take-off analysis

Any aircraft operating in a close vicinity to the ground (as in the take-off phase) will experience a phenomena known as the ground effect. The presence of the ground can be considered as a mirror line which reflects the system of vortices and therefore modifies the aerodynamic characteristics of the aircraft. Analytical approaches model the effect of the ground as a reflected set of vortices below the ground with their own sets of sources, sinks and doublets. For this work however, we are merely concerned with the effect that this has on the aerodynamic characteristics of the aircraft. The most common way to account for this effect is to treat the ground effect as a virtual increase in the wing aspect ratio as will be used here. The aerodynamic parameters will then be modified in the same way as for an actual increase in the wing aspect ratio with $C_{L\alpha}$ and K_V being the most affected. When operating away from the ground these retain their standard notation $C_{L\alpha}$, C_{DZ} and K_{Basic}. It is worth noting that the aerodynamic centre of the aircraft remains unaffected. Rather than recalculating $C_{L\alpha}$ and K_V of the virtual wing, analytical approximations can be used to determine the increase of these parameters for the actual wing.

Since $C_{L\alpha}$ has a direct impact on the lift coefficient, it is viable to account for a variation in the lift coefficient instead, as below.

$C_{L(incGE)} = C_{L(Basic)} + \Delta C_{L(GE)}$ Eq 1-3

This increase in lift coefficient can be obtained from below, taken from Datcom [20].

$$\Delta C_{L(GE)} = 57.3 \cdot \left(\frac{C_{L(Basic)} \cdot C_{L\alpha}}{\pi \cdot AR} \right) \cdot \left(1 - \frac{A}{A_G} \right)$$ Eq 1-4

The parameters used in this expression and the accompanying chart are:

1. $C_{L(Basic)}$ - The basic lift coefficient of a wing operating away from the ground.
2. $C_{L\alpha}$ - The basic lift curve slope of a wing operating away from the ground.
3. AR – The actual wing aspect ratio (not the virtually increased value).
4. A/A_G – Ratio of the actual to the virtual aspect ratio as given by the chart below.
5. H – This is the height of the 25% MAC point of the wing above the ground.
6. b – This is the actual wing span of the wing (not the virtually increased value).

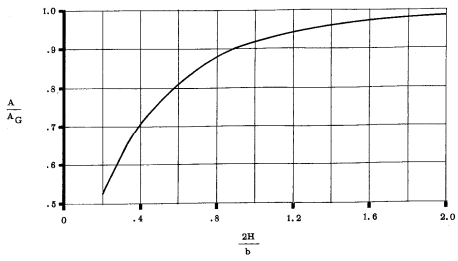

FIGURE 4.4.1-5a EFFECTIVE ASPECT RATIO IN THE PRESENCE OF THE GROUND

Figure 1-1 [20]

In a similar way, the variation in the lift induced drag is determined as the sum of the basic value and a change due to the ground effect as below.

$$K_{(incGE)} = K_{Basic} + \Delta C_{Di(GE)} \quad \text{Eq 1-5}$$

This increase in lift induced drag can be obtained from below, taken from Nicolai.

$$\Delta C_{Di(GE)} = -\sigma' \cdot K_{Basic} \cdot C_L{}^2 \quad \text{Eq 1-6}$$

The parameter σ' is determined by the relation below, where h is the height of the wing above the ground and b is the actual wing span.

$$\sigma' = \frac{1-(1.32 \cdot h/b)}{1.05+(7.4 \cdot h/b)} \quad \text{Eq 1-7}$$

D1.3 The effect of deploying the Kruger flaps

The Kruger flaps are deployed during the take-off and landing phases to extend the useable angle of attack of the aircraft. Although the leading edge Kruger flaps are not camber changing devices, they can still add an extra component of zero lift pitching moment to the aircraft when deployed. The method from Roskam [11] is used to determine this extra component, which consists of a variable expression (Part A) and a fixed expression (Part B) as given below.

$$C_{m0(Krugers)} = \Delta C_{m(Krugers)-A} + \Delta C_{m(Krugers)-B} \quad \text{Eq 1-8}$$

Part B of the expression is dependent on the centre of the gravity of the aircraft and was determined by the expressions from Roskam as:

- In the landing configuration $\Delta C_{m(Krugers)-B} = -0.004292488$
- In the take-off configuration $\Delta C_{m(Krugers)-B} = -0.004319778$

Part A of the expression is more variable and is dependent on the aircraft wing-fuselage pitching moment and lift coefficient as given by the relation below.

$$\Delta C_{m(Krugers)-A} = \left[\left(C_m \cdot \left\{\left(\frac{\bar{c}'_K}{c}\right)^2 - 1\right\}\right) + \left(0.75 \cdot C_L \cdot \frac{\bar{c}'_K}{c} \cdot \left\{\frac{\bar{c}'_K - c}{c}\right\}\right)\right] \cdot \eta_K \quad \text{Eq 1-9}$$

The parameters used in this expression are:

1. C_m – Wing-fuselage pitching moment
2. $\bar{c}_K'$ - Mean aerodynamic chord of the flapped wing section (determined for this configuration as 5.315m)
3. c – The chord of the un-flapped wing at the location of the mean aerodynamic chord for the flapped wing section (determined for this configuration as 5.206m)
4. C_L – Lift coefficient of the wing
5. $\Delta\eta$ - The span of the Kruger flap as a fraction of the wing semi-span (determined for this configuration as 0.25)

Determination of the wing-fuselage pitching moment followed the method given by Roskam which can be complex as it is dependent on many other parameters. To clarify the process to determine the Kruger pitching moment, it is presented in the easy to follow flowchart format below. If relevant, the ground effect must be included in the analysis, but should be omitted if not required.

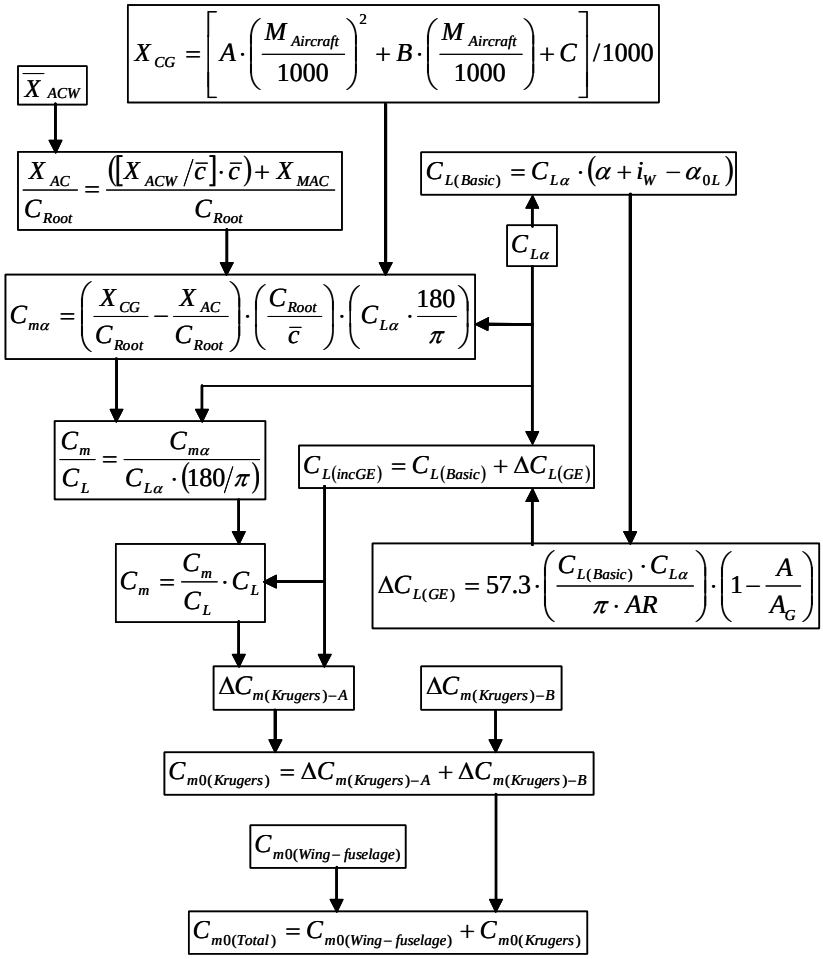

D1.4 Variation in the aircraft centre of gravity with fuel burn

As fuel is consumed, both the weight and centre of gravity of the aircraft will change as a result of this weight loss and a shift in the weight distribution. Fortunately, an expression for the location of the aircraft centre of gravity as a function of the aircraft mass was analytically derived from the conceptual design work, as given below.

$$X_{CG} = \left[-1.3116 \cdot \left(\frac{M_{Aircraft}}{1000} \right)^2 + 29.427 \cdot \left(\frac{M_{Aircraft}}{1000} \right) + 4316.6 \right] / 1000 \qquad \text{Eq 1-10}$$

This value is measured from the nose of the aircraft (the aircraft reference point). It is common to also quote this value relative to the mean aerodynamic chord of the wing. In such cases this can be found from the expression below, where X_{MAC} is the location of the start of the mean aerodynamic chord as measured from the aircraft nose.

$$\overline{X}_{CG} = \frac{X_{CG} - X_{MAC}}{\overline{C}} \qquad \text{Eq 1-11}$$

D1.5 Aircraft drag increase in the landing configuration

When in its landing configuration, the aircraft will experience an increase in drag due to the deployment of high lift devices and the extension of the landing gear. The impact of leading edge devices is typically negligible in comparison with trailing edges devices and so only the trailing edge devices are included here. In such cases, the contribution to the lift induced drag is negligible compared to that due to the zero lift drag. The expression below from Howe [1] proved to be sufficient to predict the increase in the zero lift drag of the aircraft in the landing configuration.

$$\Delta C_{DZ(Landing)} = \left(\frac{0.15 \cdot F_F}{AR^{0.33}} \right) + C_{DL(Landing)} \qquad \text{Eq 1-12}$$

The first part of this expression accounts for the deployed high lift devices and the second the extended landing gear. The parameters used in this expression are:

1. AR – Wing aspect ratio
2. FF – Flap drag factor which is taken as 1.0 for a single slotted trailing edge flap.
3. $C_{DL(Landing)}$ - The drag coefficient of an extended landing gear. This is assumed to have a value of 0.03, typical for this type of aircraft.

D1.6 Control characteristics of the elevons

As part of the analysis work, the effectiveness of the thrust vectoring system for aircraft pitch control was compared to that of conventional elevons control surfaces. In order to be able to carry out such an analysis, we need to predict the impact which the deflection of the elevons will have on the lift, drag and pitching moment of the aircraft.

D1.6.1 Contribution to lift due to elevon deflection

If we treat the elevon as a plain flap, the variation in lift due to elevon deflection can be determined from the expression below from Raymer [3].

$$\Delta C_{L(Flap)} = \frac{dC_L}{d\delta_{Flap}} \cdot \delta_{Flap} \qquad \text{Eq 1-13}$$

The terms required in the determination of this expression are:

1. $dC_L / d\delta_{Flap}$ - Lift increment for plain flaps as determined by the expression below from Raymer [3]. This is a function of the elevon geometry with this arrangement having a $S_{flapped}/S$ ratio of 0.1869 and $Cos\Lambda_{HL} = 1$.

$$\frac{dC_L}{d\delta_f} = 0.9 \cdot K_f \cdot \left(\frac{dC_l}{d\delta_f} \right) \cdot \frac{S_{flapped}}{S} \cdot Cos\Lambda_{HL} \qquad \text{Eq 1-14}$$

2. $dC_l / d\delta_f$ - The 2-dimensional lift increment for plain flaps which is determined from the chart below. For this arrangement, we have a t/c value of 0.0894 at the mid-elevon point and a cf/c ratio of 0.15 which gives us $dC_l / d\delta_f = 3.1$

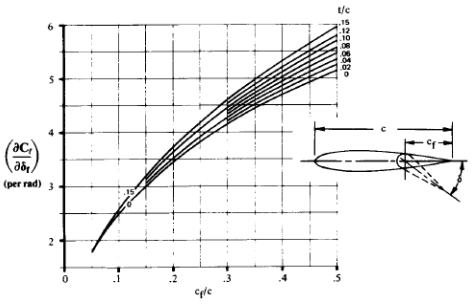

Fig. 16.6 Theoretical lift increment for plain flaps. (Ref. 37)

Figure 1-2 [3]

3. K_f – Flap correction factor for large flap deflection angles. As we are operating at angles of 10 degrees and less, K_f=1.
4. δ_{Flap} - Flap deflection angle measured in radians.

This gives us a value of $dC_L / d\delta_{Flap} = 0.521451$ for our configuration. As required, the expression for the total wing lift coefficient then becomes,

$$C_L = \left[C_{L\alpha} \cdot (\alpha - \alpha_{0L}) \right] + \Delta C_{L(Flap)} \qquad \text{Eq 1-15}$$

D1.6.2 Contribution to pitching moment due to elevon deflection

The pitching moment coefficient due to elevator deflection can be determined by the expression below from Raymer [3].

$$C_{M(elevons)} = -K_{Flap} \cdot \frac{dC_L}{d\delta_{Flap}} \cdot \delta_{Flap} \cdot \left(\overline{X}_{CP(Flap)} - \overline{X}_{CG} \right) \qquad \text{Eq 1-16}$$

The terms required in the determination of this expression are:

1. $dC_L / d\delta_{Flap}$ - Lift increment for plain flaps as determined above.
2. δ_{Flap} - Flap deflection angle measured in radians.
3. $\overline{X}_{CP(Flap)}$ - Location of the centre of pressure of the flap relative to the aircraft reference point as a fraction of the MAC of the wing. The location of the centre of pressure of the flap with respect to the mean aerodynamic chord of the flapped area can be determined from the chart below. Knowing the location of the flapped MAC with respect to the aircraft reference point we are able to convert this to the aircraft reference point. For our configuration this was determined as $\overline{X}_{CP} = 0.7311$.

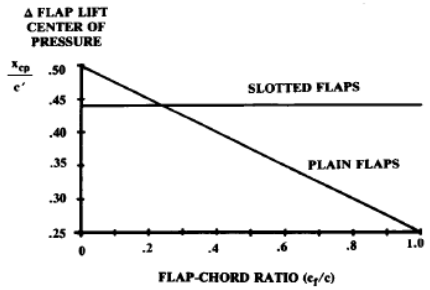

Fig. 16.9 Center of pressure for lift increment due to flaps. (after Ref. 37)

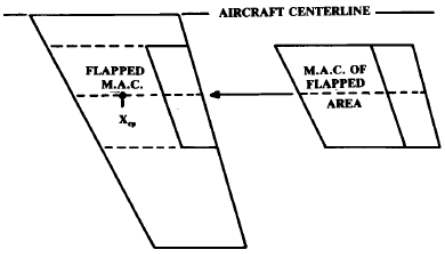

Fig. 16.8 Flapped area and flapped M.A.C. (C′).

Figure 1-3 and 1-4 [3]

4. $\overline{X}_{CG}$ - Location of the aircraft centre of gravity as measured from the aircraft reference point, as a fraction of the MAC of the wing.

D1.6.3 Contribution to drag due to elevon deflection

The total drag coefficient of the aircraft including the components due to elevon deflection can be determined from the modified drag coefficient expression below.

$$C_D = \left(C_{DZ} + \Delta C_{D0(Flap)}\right) + \left[\left(K + \Delta C_{Di(Flap)}\right) \cdot C_L{}^2\right] \qquad \text{Eq 1-17}$$

The contributions due to zero lift drag and lift induced drag are given in sections below.

D1.6.3.1 Contribution to zero lift drag

The variation in the zero lift drag due to elevon deflection is determined by the expression below taken from Stinton [4].

$$\Delta C_{D0(Flap)} = \varepsilon_C \cdot \varepsilon_S \cdot \varepsilon_B \qquad \text{Eq 1-18}$$

The terms required in the determination of this expression are:

1. ε_C - This is a factor to account for the elevon chord in relation to the wing chord as determined from the figure below. This was determined as $\varepsilon_C = 0.75$.
2. ε_S - This is a factor to account for the area of the flap in relation to the total area of the wing as determined from the figure below. This was determined as $\varepsilon_S = 0.475$ for $b_f / b = 0.33$.
3. ε_S - This is a factor to account for flap deflection as determined from the figure below. To save time and effort, an expression was derived from the results for ε_S for this configuration as a function of the absolute value of flap deflection measured in degrees.

$$\varepsilon_B = \left(0.0065 \cdot \left|\delta_f\right|^2 + 2.2696 \cdot \left|\delta_f\right|\right) / 1E3 \qquad \text{Eq 1-19}$$

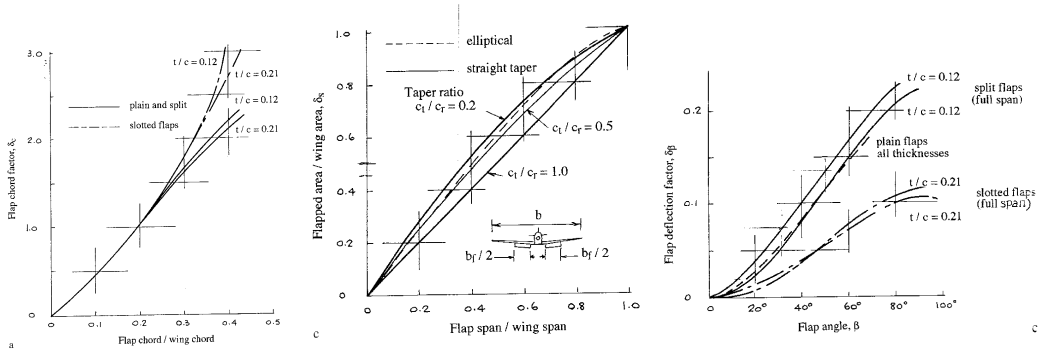

Figure 1-5, 1-6 and 1-7 [4]

D1.6.3.2 Contribution to lift induced drag

The variation in lift induced drag due to elevon deflection is determined by the expression below, taken from Roskam [11].

$$\Delta C_{Di(Flap)} = K_{\Delta CDi}{}^2 \cdot \Delta C_{L(Flap)}{}^2 \cdot Cos\Lambda_{1/4} \qquad \text{Eq 1-20}$$

The terms required in the determination of this expression are:

1. $\Delta C_{L(Flap)}$ - The variation in lift due to elevon deflection as above.
2. $\Lambda_{1/4}$ - The quarter chord sweep angle of the wing.
3. $K_{\Delta CDi}$ - This is an empirical correction factor which is obtained from the charts below as a function of the aspect ratio of the wing and the flap geometry. This was determined as $K_{\Delta CDi} = 0.45$ for this configuration.

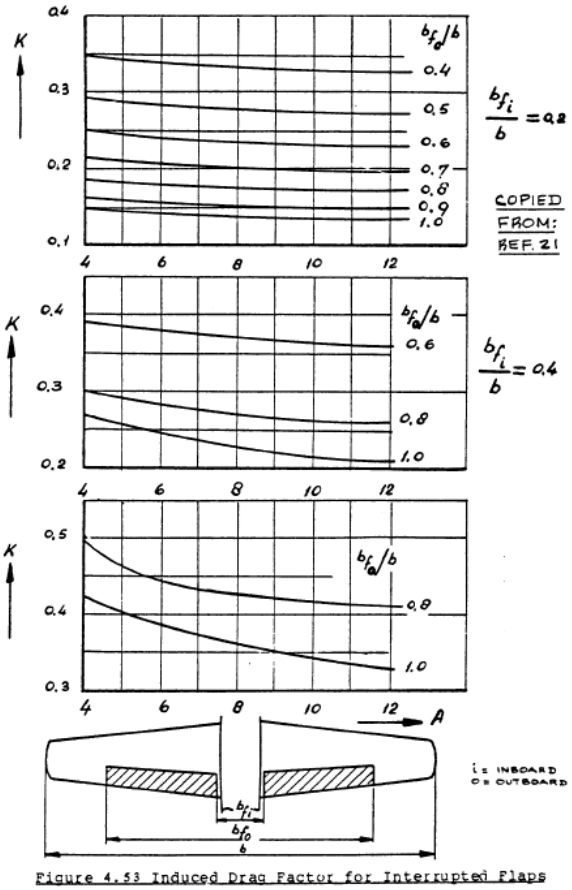

Figure 1-8 [11]

D2 Cruise analysis

The purpose of this analysis is to asses the benefits of using a low cost thrust vectoring system to replace the conventional elevons on an aircraft during the cruise phase. It is hoped that by replacing the elevons, the additional drag penalty associated with their use will also be eliminated. The result is an increase in the aerodynamic efficiency of the aircraft. Since the cruise phase has the largest fuel demands, this will be the key indicator of the viability of such a proposal. This section describes two studies, one for the thrust vectored proposal and the other for a conventional aircraft configuration utilising elevons. A comparison between these results will enable the feasibility of using such a system for trimming an aircraft to be assessed.

D2.1 Analysis parameters

Presented in this section are the parameters required for these analyses. During these analyses, the aircraft is in a clean cruise configuration. As fuel is consumed, the centre of gravity of the aircraft will be displaced as discussed in the general terms section. In the case of the conventional configuration, deflection of the elevons will result in a variation in lift, drag and pitching moment due to their deflection. This is discussed in greater depth in the general terms section.

D2.1.1 The engine throttle setting of the thrust vectored engine

In contrast to a standard fixed configuration engine, the analysis of a thrust vectoring engine-nozzle combination is complicated by the fact that the engine configuration is a function of thrust vectoring nozzle deflection and therefore variable. To cater for this, an expression was derived as part of the engine analysis work which gives the specific fuel consumption as a function of the engine throttle ratio. To be able to use this, we make use of an expression also derived in the engine analysis work for the engine throttle ratio as a function of engine thrust, as given below.

$$\%T = \frac{(A \cdot T) + B}{1E3} \qquad \text{Eq 2-1}$$

The coefficients used in this expression are themselves functions of the absolute value of thrust vectoring angle as given by the following relations.

$$A = \frac{0.1821 \cdot |\phi|^2 + 6.9536 \cdot |\phi| + 696.8}{1E3} \qquad \text{Eq 2-2}$$

$$B = -0.4118 \cdot |\phi|^2 - 3.5303 \cdot |\phi| - 7.2483 \qquad \text{Eq 2-3}$$

D2.1.2 Specific fuel consumption of the thrust vectored configuration

The expression for the specific fuel consumption of the engine as determined from our engine analysis work is given below. As already stated, this is a function of the engine throttle setting determined above.

$$SFC = \frac{\left[A \cdot (\%T)^2 + B \cdot (\%T) + C\right]}{1E6} \qquad \text{Eq 2-4}$$

The coefficients used in this expression are themselves functions of the absolute value of thrust vectoring angle as given by the following quadratic relations.

$$A = -0.1229 \cdot |\phi|^2 + 1.3257 \cdot |\phi| + 4.5714 \qquad \text{Eq 2-5}$$

$$B = 0.127 \cdot |\phi|^2 - 1.8203 \cdot |\phi| - 4.2326 \qquad \text{Eq 2-6}$$

$$C = -0.0242 \cdot |\phi|^2 + 0.9163 \cdot |\phi| + 24.022 \qquad \text{Eq 2-7}$$

D2.1.3 Specific fuel consumption of the conventional configuration

In the case of the conventional fixed configuration engine, an expression for the specific fuel consumption was also derived in our engine work. The resulting expression is a direct function of engine thrust as given below.

$$SFC = \left[A \cdot \left(\frac{T}{1000}\right)^4 + B \cdot \left(\frac{T}{1000}\right)^3 + C \cdot \left(\frac{T}{1000}\right)^2 + D \cdot \left(\frac{T}{1000}\right) + E \right] \cdot 1E - 6 \qquad \text{Eq 2-8}$$

The corresponding coefficients are given in the following table.

Coefficents	A	B	C	D	E
Value	-0.0007	0.0175	-0.1262	0.1578	23.895

D2.2 Thrust vectored cruise analysis

The function of this analysis is to investigate the cruise performance of a thrust vectored variant of the UCAV. During this flight phase, the aircraft is assumed to be flying at a constant speed and attitude and the thrust vectoring system is utilised solely for trim. As the specific fuel consumption is dependent on the engine configuration, this will change throughout the flight phase as the centre of gravity of the aircraft and thus the trim requirements varies.

D2.2.1 Derivations

The arrangement of the aircraft in its cruise configuration is given in the figure below along with the system of forces acting on it. This figure also includes the definitions of the characteristic lengths required to determine the moment coefficients.

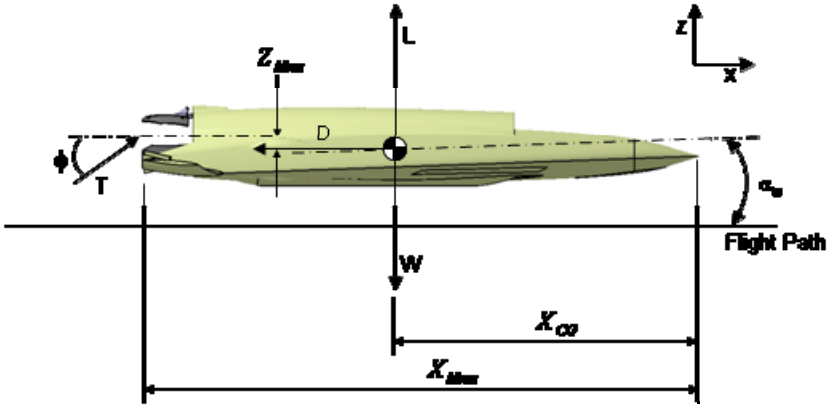

Figure 2-1

As the aircraft will approach the oncoming airflow at an angle of attack, the thrust required to maintain flight will be the resultant of the forces acting on the aircraft in the X and Z directions. Applying Newton's second law of motion to the aircraft we are able to derive a suitable expression as follows. Summing forces along the x-axis, we obtain,

$$ma_x = T\cos\alpha - D\,.$$ Eq 2-9

As the aircraft is moving with constant velocity, $a_x = 0$, so that the above reduces to,

$$T\cos\alpha = D$$ Eq 2-10

In a similar way, summing the forces along the y-axis, we obtain,

$$ma_z = T\sin\alpha + L - W\,.$$ Eq 2-11

As the aircraft is maintaining a constant altitude, $a_z = 0$, so that the above reduces to,

$$T\sin\alpha = W - L$$ Eq 2-12

Solving the above equations simultaneously, we are able to obtain the expression below for the thrust. This is the fundamental equation for the first part of this analysis.

$$T = \sqrt{D^2 + (W-L)^2}$$ Eq 2-13

Summing the moments acting on the aircraft about its centre of gravity, we obtain,

$$C_{M(Total)} = C_{M0(wf)} + C_{M(LW)} + C_{M(HT)} + C_{M(VT)}$$ Eq 2-14

Each of the components in the expression above can be derived from inspection of the figure above. The dimensions are given as a fraction of the wing mean aerodynamic chord, denoted as 'bar' values. The resulting expressions are given below:

1. $C_{M0(wf)}$ - The zero lift pitching moment of the wing-fuselage
2. $C_{M(LW)} = C_L \cdot \left(\overline{X}_{CG} - \overline{X}_{ACW}\right)$ - Due to the lift of the wing Eq 2-15
3. $C_{M(VT)} = \dfrac{-T_Z}{q \cdot S} \cdot \left(\overline{X}_{Nozz} - \overline{X}_{CG}\right)$ - Due to the vertical component of deflected thrust. Eq 2-16
4. $C_{M(HT)} = \dfrac{-T_X}{q \cdot S} \cdot \overline{Z}_{Nozz}$ - Due to the horizontal component of deflected thrust. Eq 2-17

The horizontal and vertical components of deflected thrust can be determined from the simple relations below as a function of vectoring angle ϕ.

$$T_Z = T_{Engine(Vectored)} \cdot Sin(\phi)$$ Eq 2-18

$$T_X = T_{Engine(Vectored)} \cdot Cos(\phi)$$ Eq 2-19

The thrust of the exhaust plume will encounter thrust losses due to deflection of the nozzle which have already been incorporated into the engine performance relations. These relations will now be put into practice in the analyses that follow.

D2.2.2 Analysis approach

The nature of this analysis meant that it had to be broken down into two stages as follows,

1. This stage is used to determine the optimal angle of attack of the aircraft which gives us the minimum thrust requirements at that instance in time.
2. This stage is used to determine the thrust vectoring plume angle required to trim the aircraft and that instance in time.

An iterative solution process is required to solve each analysis. An added complication to this is however the fact that the two analyses are inter-related by means of the engine thrust term. It is therefore necessary to keep alternatively iterating each solution until both solutions converge. This process is summarised below.

Solution procedure for the cruise analysis

Stage 1 – Iterate α to determine the minimum value for T
Stage 2 – Iterate ϕ until $C_m = 0$

Repeat Stage 1 and Stage 2 until both of the solutions converge

Since many of the parameters are continually changing during the cruise phase, it is necessary to break the flight phase down into a number of steps. The accuracy of the analysis increases as the number of time steps used increases. As the number of time steps increase, the corresponding decrease in the interval of each time step therefore reduces the step wise nature of the parameters used. The analysis process described above is then repeated at each of the time steps being analysed. The two analysis stages are discussed in the sections below.

D2.2.3 Analysis stage 1 – Solution for required engine thrust

The analysis process to determine the optimal aircraft angle of attack and thus the thrust is presented in the easy to follow equation flow chart below. This process is repeated for each time step with macros being used to automate the Microsoft Excel Solver function used for the iteration process.

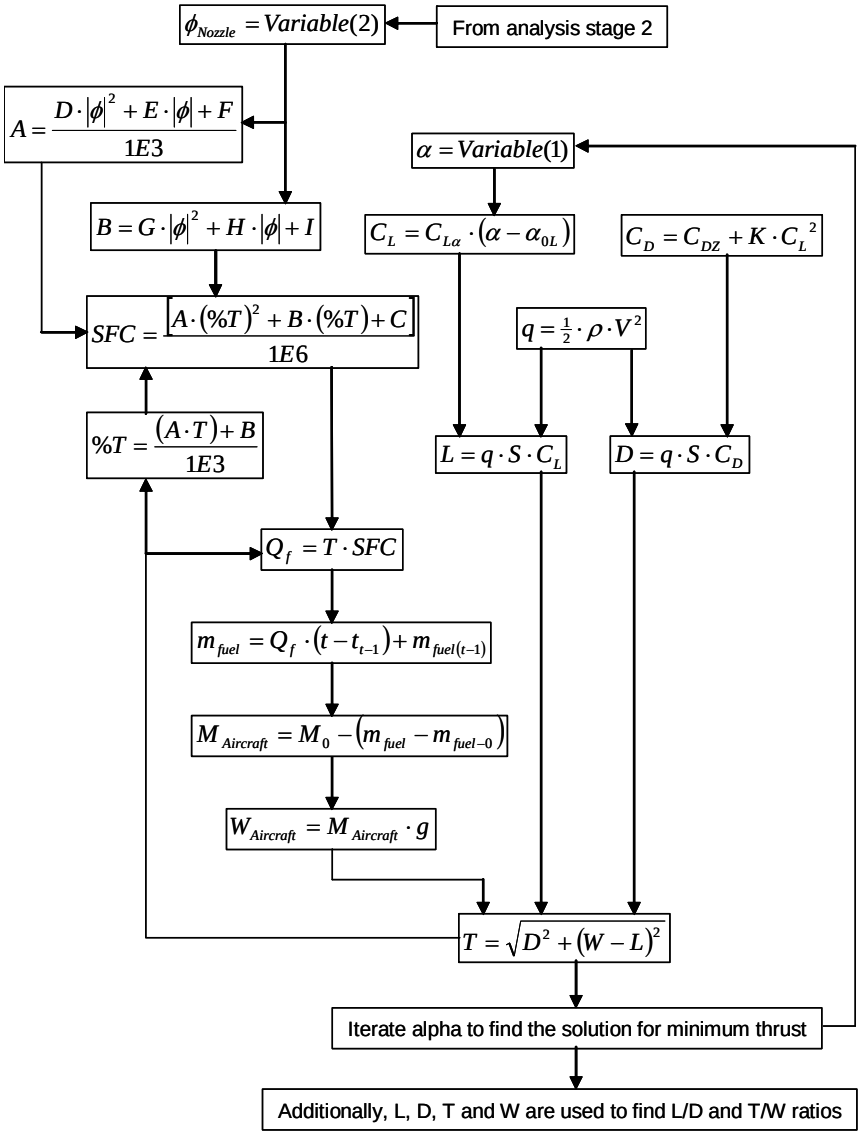

D2.2.4 Analysis stage 2 – Solution for nozzle vectoring angle

The analysis process to determine the nozzle vectoring angle required to trim the aircraft is presented in the easy to follow equation flow chart below. This process is repeated for each time step with macros being used to automate the Microsoft Excel Solver function used for the iteration process.

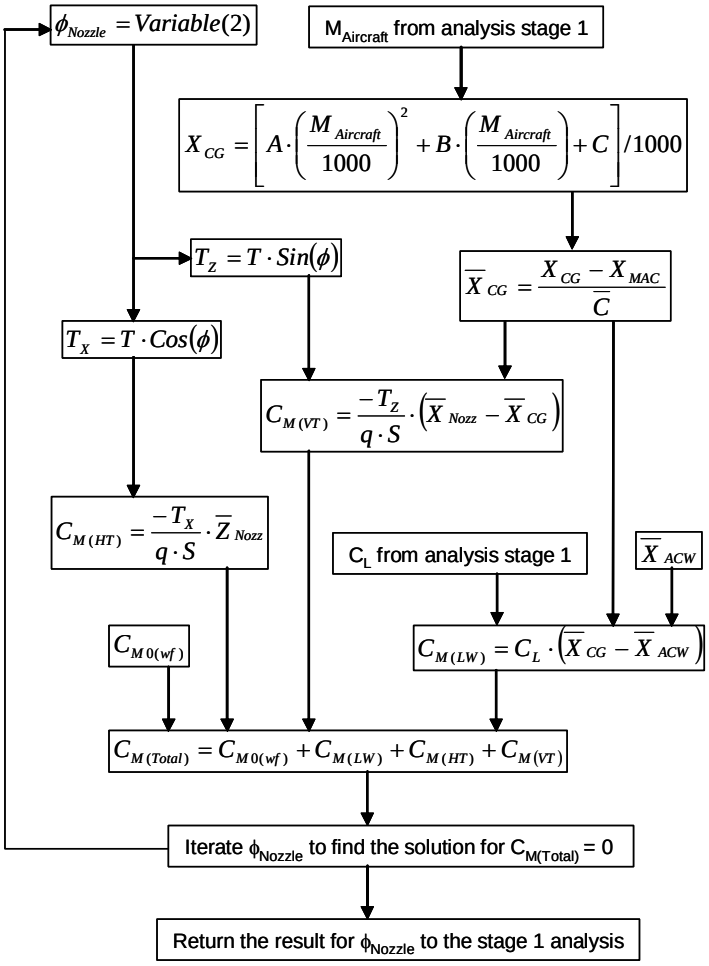

D2.3 Conventional elevons configuration cruise analysis

The function of this analysis is to investigate the cruise performance of the conventional UCAV utilising elevons. As before, the aircraft is assumed to be flying at a constant speed and attitude, with the elevons being utilised solely for trim. In this case, as the engine configuration is fixed, the specific fuel consumption will remain constant throughout the flight phase. The elevon deflection required will however vary as the centre of gravity of the aircraft and thus the trim requirements varies.

D2.3.1 Derivations

The arrangement of the conventional aircraft in its cruise configuration is given in the figure below along with the system of forces acting on it. Also shown are the characteristic lengths required to determine the moment coefficients.

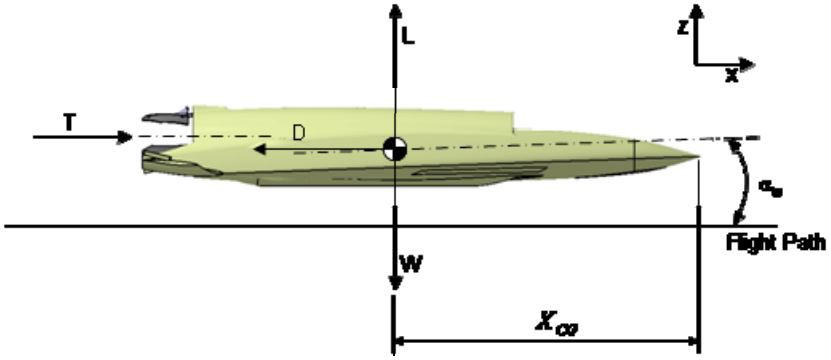

Figure 2-2

The derivations of the forces and moments follow the same procedure as for the thrust vectored variant of the aircraft. Following the same procedure to determine the required thrust from the engine, we obtain the same fundamental equation as before. As before, this is the foundation of the first part of this analysis.

$$T = \sqrt{D^2 + (W - L)^2} \qquad \text{Eq 2-20}$$

In the case of the moments acting on the aircraft about its centre of gravity, the relation for the conventional elevons configuration becomes,

$$C_{M(Total)} = C_{M0(wf)} + C_{M(LW)} + C_{M(elevons)} \qquad \text{Eq 2-21}$$

As before, each of the components in the expression above can be derived by inspection of the figure above with each of the dimensions being quoted as 'bar' values. This results in the expressions given below:

5. $C_{M0(wf)}$ - The zero lift pitching moment of the wing-fuselage
6. $C_{M(LW)} = C_L \cdot \left(\overline{X}_{CG} - \overline{X}_{ACW}\right)$ - Due to the lift of the wing Eq 2-22
7. $C_{M(elevons)}$ - The pitching moment due to deflection of the elevons as determined by the relations presented in the general terms section.

These relations will now be put into practice in the analyses that follow.

D2.3.2 Analysis approach

The analysis for the conventional elevons configuration follows a very similar approach to that presented for the thrust vectored aircraft. As before, the nature of the analysis meant that it had to be broken down into two parts as follows,

1. This stage is used to determine the optimal angle of attack of the aircraft which gives us the minimum thrust requirements at that instance in time.
2. This stage is used to determine the elevon deflection angle required to trim the aircraft and that instance in time.

An iterative solution process is required to solve each analysis. An added complication to this is however the fact that the two analyses are inter-related by means of the engine thrust term. As before, it is therefore necessary to keep alternatively iterating each solution until both solutions converge. This process is summarised below.

Solution procedure for the cruise analysis

Stage 1 – Iterate α to determine the minimum value for T
Stage 2 – Iterate δ_f until $C_m = 0$

Repeat Stage 1 and Stage 2 until both of the solutions converge

As before, since many of the parameters are constantly changing during the cruise phase, it is necessary to break the flight phase down into a number of steps in order to increase the accuracy of the analysis. The analysis process described above is then repeated at each of the time steps being analysed. The two analysis stages are discussed in the sections below.

D2.3.3 Analysis stage 1 – Solution for required engine thrust

The analysis process to determine the optimal aircraft angle of attack and thus the thrust is presented in the easy to follow equation flow chart below. Compared to the analysis for the thrust vectored aircraft, here we have to take account of the additional aerodynamic effects which arise as a result of deflecting the elevons, which includes increases in lift and drag. The process given below is repeated for each time step with macros being used to automate the Microsoft Excel Solver function used for the iteration process.

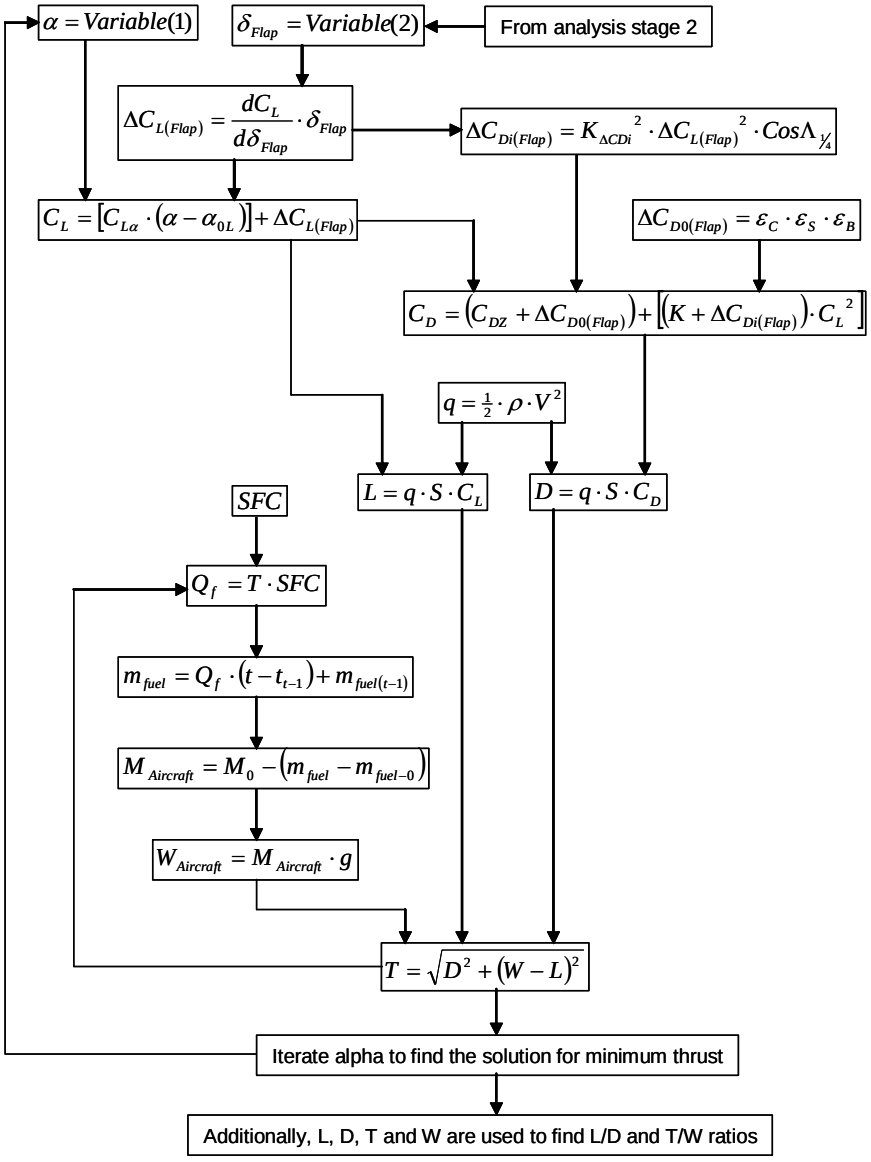

D2.3.4 Analysis stage 2 – Solution for elevon deflection

The analysis process to determine the elevon deflection required to trim the aircraft is presented in the easy to follow equation flow chart below. This follows a similar approach to that used for the thrust vectored aircraft, the main difference between that the thrust vectoring moment terms are replaced with the moment term due to elevon deflection. This process given below is repeated for each time step with macros being used to automate the Microsoft Excel Solver function used for the iteration process.

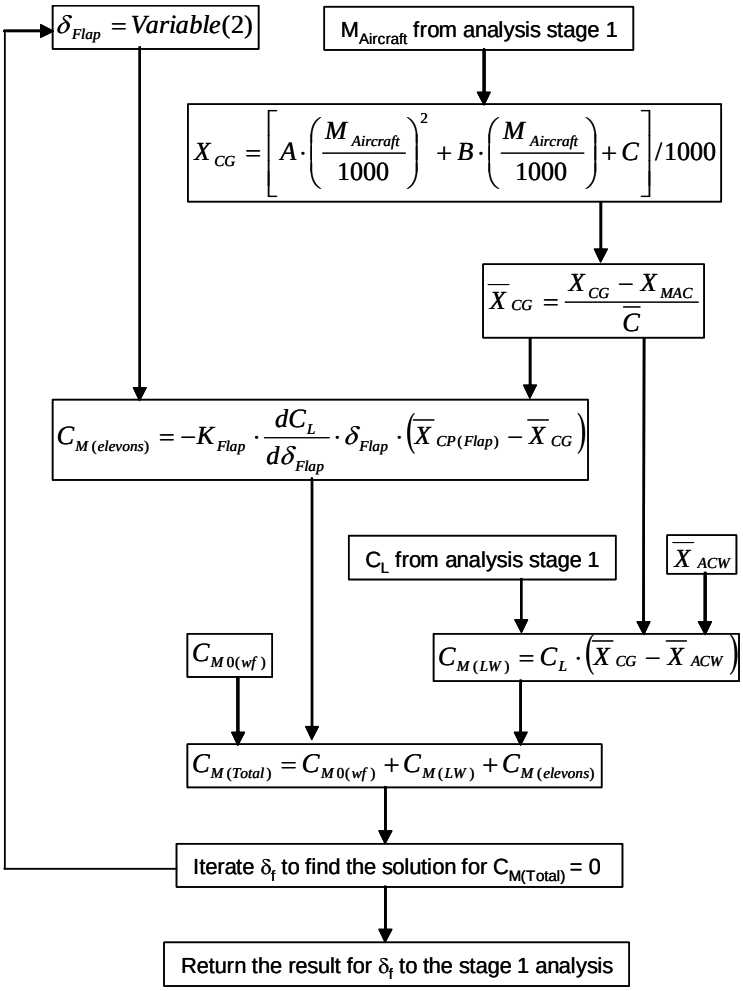
$\delta_{Flap} = Variable(2)$
$M_{Aircraft}$ from analysis stage 1
$X_{CG} = \left[A \cdot \left(\frac{M_{Aircraft}}{1000} \right)^2 + B \cdot \left(\frac{M_{Aircraft}}{1000} \right) + C \right] / 1000$
$\overline{X}_{CG} = \frac{X_{CG} - X_{MAC}}{\overline{C}}$
$C_{M(elevons)} = -K_{Flap} \cdot \frac{dC_L}{d\delta_{Flap}} \cdot \delta_{Flap} \cdot \left(\overline{X}_{CP(Flap)} - \overline{X}_{CG} \right)$
C_L from analysis stage 1
$\overline{X}_{ACW}$
$C_{M0(wf)}$
$C_{M(LW)} = C_L \cdot \left(\overline{X}_{CG} - \overline{X}_{ACW} \right)$
$C_{M(Total)} = C_{M0(wf)} + C_{M(LW)} + C_{M(elevons)}$
Iterate δ_f to find the solution for $C_{M(Total)} = 0$
Return the result for δ_f to the stage 1 analysis

D3 Take-off analysis

The complete take-off phase typically consists of four phases, ground roll, rotation, transition to climb and take-off climb-out. The results of the baseline performance studies showed the contribution of the, rotation, transition and take-off climb out phases to the complete take-off to be small in comparison to the ground run phase. Time constraints have dictated the depth of study which can be achieved and in this analysis it is reasonable to merely concentrate on the ground roll. The work consists of three analyses, the first of which determines the point where there is sufficient speed and thus lift to commence the rotation. The other two analyses determine the point at which there is sufficient control authority available to safely control the aircraft, one of which is for the thrust vectoring system and the other for conventional elevons. These results are finally merged to find the optimal point when the aircraft has sufficient lift and control.

D3.1 Analysis parameters

Presented in this section are the parameters required for this analysis. During this analysis, the aircraft is in its take-off configuration with the Kruger flaps deployed. Its close proximity to the ground means that ground effect is also important. Both of these are discussed in the general terms section.

D3.1.1 Engine parameters

The engine characteristics such as available thrust and thrust specific fuel consumption were determined in the engine analysis work at a number of engine operating points. This covered a range of engine bleed settings and thrust vectoring nozzle deflection angles. A complication comes from the fact that the speed of the aircraft is constantly changing during the take-off run, which will also affect the engine operating parameters. To overcome this, all the parameters were evaluated at an average take-off speed of M0.2, to which a scale factor was applied to account for the Mach number variations. This is given by the respective relations below for thrust and specific fuel consumption.

$$T_{TO} = T_{M\,0.2} \cdot T_{M-Scale} \qquad \text{Eq 3-1}$$

$$SFC_{TO} = SFC_{M\,0.2} \cdot SFC_{M-Scale} \qquad \text{Eq 3-2}$$

The accompanying Mach number scale factors are given by the expressions below. It should be re-emphasised that these are independent of thrust vectoring angle and bleed.

$$T_{M-Scale} = \left(-3.7672M^4\right) + \left(3.459M^3\right) - \left(0.7693M^2\right) - \left(0.3575M\right) + 1.0804 \qquad \text{Eq 3-3}$$

$$SFC_{M-Scale} = \left(3.1881M^4\right) - \left(3.04M^3\right) + \left(0.9856M^2\right) + \left(0.3014M\right) + 0.9196 \qquad \text{Eq 3-4}$$

The available engine thrust at M0.2 is determined from the following relation where the vectoring angle of the engine plume ϕ is in degrees and the thrust is in Newtons.

$$T_{TO-M\,0.2} = \left(A \cdot \phi^2\right) + \left(B \cdot \phi\right) + C \qquad \text{Eq 3-5}$$

The constants in this expression are different for each engine bleed setting as given in the table below. Each set of constants being valid for a range of vectoring angles within that engine bleed setting.

Thrust at M0.2	Bleed setting (%)								
	0	2.5	5	7.5	10	12.5	15	17.5	20
Constant A	2.3421	2.2378	2.3373	2.3983	3.8825	3.4031	2.9695	3.5186	2.7429
Constant B	-560.32	-546.96	-535.45	-521.48	-524.57	-496.54	-467.32	-452.13	-415.5
Constant C	54601	52330	50024	47673	45304	42847	40335	37779	35107

Table 3-1

In a similar way, the thrust specific fuel consumption at M0.2 is determined by the relation below where once again, ϕ is in degrees and SFC is in kg/Ns (x1E-6).

$$SFC_{TO-M\,0.2} = \left(A \cdot \phi^2\right) + \left(B \cdot \phi\right) + C \qquad \text{Eq 3-6}$$

As before, the constants in this expression are different for each engine bleed setting as given in the table below.

TSFC at M0.2	Bleed setting (%)								
	0	2.5	5	7.5	10	12.5	15	17.5	20
Constant A	0.0015	0.0017	0.0018	0.0018	0.0008	0.0011	0.0014	0.0009	0.0016
Constant B	0.2284	0.236	0.2445	0.2546	0.2795	0.2867	0.2935	0.3143	0.3201
Constant C	22.395	22.716	23.089	23.515	23.992	24.575	25.268	26.078	27.1

Table 3-2

Collectively, these relations enable us to predict the thrust and specific fuel consumption of the engine over a range of bleed settings, plume deflection angles and speeds. These have provided a valuable tool for this performance analysis work but they are however only applicable to this particular engine. The reader is advised to refer to the engine design section for further details of their derivation.

D3.1.2 Vectored thrust components

The layout of the thrust vectoring system is shown in the figure below along with expressions for the horizontal and vertical components of thrust. The thrust of the engine plume is the vectored thrust which includes the thrust loss is associated with the vectoring action. In this figure, ϕ is defined as the angle that the engine's exhaust plume and thus the engine thrust is deflected from the engine centre-line.

$$T_X = T_{Engine(Vectored)} \cdot Cos(\phi)$$
$$T_Z = T_{Engine(Vectored)} \cdot Sin(\phi)$$

Eq 3-7 and 3-8

Figure 3-1

D3.1.3 Nose-jet control terms

The function of the nose jet is to generate a pitch force sufficient to rotate the nose of the aircraft at take-off and therefore replace the conventional elevator control surfaces. In such cases, the deflection of the elevons will therefore be zero ($\delta_{Flap} = 0$). In the nose jet analysis section, it was shown that the thrust generated by the nose jet is primarily a function of engine bleed. We could be misled into thinking that the nose jet force would also be a function of the engine vectoring angle, since this has a knock on effect on the engine. However, since the mass flow rate of air through the engine remains the same, the bleed remains unaffected. The nose jet analysis gave us a useful table of results for the nose jet force at M0.2 and at a number of engine bleed settings as presented below.

	Bleed setting (%)								
	0	2.5	5	7.5	10	12.5	15	17.5	20
L-NJ at M0.2 (N)	0	1119.967	2238.942	3353.567	4465.797	5572.177	6671.089	7760.115	8836.781

Table 3-3

As with the engine analyses, these figures are for an average take-off speed of M0.2 and it is necessary to apply a scale factor to account for Mach number effects. The resulting thrust from the nose jet can be determined from the relation below.

$$L_{NJ} = L_{NJ(@M\,0.2)} \cdot Scale_{NJ-Mach} \quad \text{Eq 3-9}$$

The scale factor for the aircraft speed is given by the relation below whose constants are given in the accompanying table for a range of engine bleed settings.

$$Scale_{NJ-Mach} = \left(A \cdot M^3\right) + \left(B \cdot M^2\right) + \left(C \cdot M\right) + D \quad \text{Eq 3-10}$$

$Scale_{NJ-Mach}$	Bleed setting (%)								
	0	2.5	5	7.5	10	12.5	15	17.5	20
Constant A	0	0.0655	0.0321	0.0573	0.0147	0.1153	0.1151	0.1143	0.1218
Constant B	0	0.2021	0.2178	0.2101	0.2308	0.1781	0.1811	0.1851	0.1807
Constant C	0	0.0044	0.0035	0.0024	0.0012	0.0074	0.007	0.0068	0.0084
Constant D	0	0.9905	0.9903	0.9908	0.9906	0.9905	0.9904	0.9903	0.9901

Table 3-4

D3.1.4 Presentation of the results

At the point of initiation of rotation of the aircraft, we are able to determine a number of other parameters. In particular, the distance covered during the ground run can be determined from the relation below. It is important to evaluate this expression over a number of small time steps to account for the ever changing velocity and acceleration.

$$S_G = V_X\left(t - t_{i-1}\right) + \left(\frac{1}{2} \cdot \frac{a_{X(t)} + a_{X(t-1)}}{2}\right)\left(t - t_{i-1}\right)^2 + S_{G(t-1)} \quad \text{Eq 3-11}$$

We are also able to determine the contribution to the total lift from the different lifting mechanisms as given by the relation below. This includes that from the wings, the vertical component of vectored thrust and the lift from the nose jet.

$$L_{Total} = L + T_Z + L_{NJ} \quad \text{Eq 3-12}$$

D3.1.5 Effect of thrust vectoring on the landing gear

When the engine plume is deflected downwards, an additional nose down pitching moment is generated about the main landing gear wheels. This will increase the nose gear load fraction and will thus change the ground handling characteristics of the aircraft. As a result, the nose steering could become too heavy to be able to be used safely. The opposite being true if the engine thrust is instead deflected upwards, which could give rise to steering which is too light with the risk of drift.

Knowing the total pitching moment of the aircraft, as given by analyses which follow, we are able to determine the landing gear reaction forces from the relations below. The terms $X_{Main-gear}$ and $X_{Nose-gear}$ are the locations of the main gear and nose gear respectively, as measured from the reference point of the aircraft.

$$R_{Nose-gear} = \frac{-C_{m(Total)}\left(q \cdot S \cdot \bar{c}\right)}{X_{Main-gear} - X_{Nose-gear}} \quad \text{Eq 3-13}$$

$$R_{Main-gear} = R_{Total} - R_{Nose-gear} \quad \text{Eq 3-14}$$

The nose gear and main gear load fractions can finally be determined from the normal landing gear analysis methods.

D3.2 Numerical analysis to determine the final solution

As will be seen in the sections which follow, the solution to these analyses is found at the point of intersection of two curves. For example, in the case of the control limit analysis, this will be intersection of curves for the control power required and control power available. Although it is possible to estimate these intersection points graphically, numerical interpolation techniques were employed instead to improve the accuracy and automate the process. The system devised was integrated within the analysis spreadsheets to filter out the closest solution points either side of the location of the final solution and then linearly interpolate between these to obtain the final solution.

The first step in this process is to filter out the upper and lower solution boundaries between which the final solution lies from the mass of data within the spreadsheet. Assuming that our two parameters are X and Y (control power required and control power available), the two spreadsheet functions below can be used to fill two auxiliary columns of either ones or zeros depending on where each corresponding data point lies in relation to the final solution.

Top solution filter: $Filter_{Top} = IF(X_{(@t-1)} > Y_{(@t-1)},1,0)$ Eq 3-15

Bottom solution filter: $Filter_{Bottom} = IF(X_{(@t)} < Y_{(@t)},1,0)$ Eq 3-16

The multiplication of these two rows as given in the function below will pinpoint the upper and lower solution boundaries.

Solution filter: $Filter_{Selector} = Filter_{Top} \cdot Filter_{Bottom}$ Eq 3-17

By multiplying the solution filter by the original results, the top and bottom boundaries of each analysis solution can be determined as given below.

Top solution boundary: $Boundary_1 = Variable \cdot Filter_{(@t+1)}$ Eq 3-18

Bottom solution boundary: $Boundary_2 = Variable \cdot Filter_{(@t)}$ Eq 3-19

The final solution can finally be determined by linearly interpolating between the boundaries with the expression below.

$$Variable_{(@Solution-t)} = \left[\frac{t_{Solution} - t_1}{t_2 - t_1}\right]\left(Variable_{(@t2)} - Variable_{(@t1)}\right) + Variable_{(@t1)}$$

Eq 3-20

For small time steps, the result curves are sufficiently linear for the error in using a linear interpolation method to be negligible.

With the solution part of the spreadsheet set up as above, all that remains is to determine time domain solution where the 2 curves intersect ($t_{Solution}$). An iterative solution process was used for this purpose as given by the steps below.

1. Assume a value for the input t-solution, which lies between boundaries 1 and 2.
2. Using the assumed value for t-solution, linearly interpolate variables X and Y between the boundaries 1 and 2.
3. Determine the error between the solutions for X and X. $Error = X - Y$
4. Iterate the assumed value for t-solution with Solver until the error equals zero.

Using the final value for t-solution and the location of the top and bottom solution boundaries, the remaining analysis parameters can be linearly interpolated by the same expression above. As well as the variables X and Y, we are interested in solutions for

time, mass of fuel consumed, ground run, Mach number and the fractions of lift from the nose jet, vertical component of vectored thrust and wing.

D3.3 Take-off analysis – Lift limit

The function of this analysis is to determine the point during the ground run when there is sufficient lift for the aircraft to be able to begin the rotation phase. The total lift acting on the aircraft during this phase is the sum of that due to the wings, control nose jet and vertical component of the deflected engine thrust. To be able to safely initiate the rotation, the aircraft must be moving at a speed of 110% of the stall speed of the wing. The stall speed of the wing will be relative to the load acting on the wing and thus allowance needs to be made for the contribution from the other lifting devices. To improve the accuracy of the results, the flight phase is broken down into a number of smaller steps which can be analysed sequentially. In cases where an iterative solution process is required, this is automated with the Solver function of Microsoft Excel.

D3.3.1 Derivations

The arrangement of the aircraft in its take-off configuration is given in the figure below along with the system of forces acting on it.

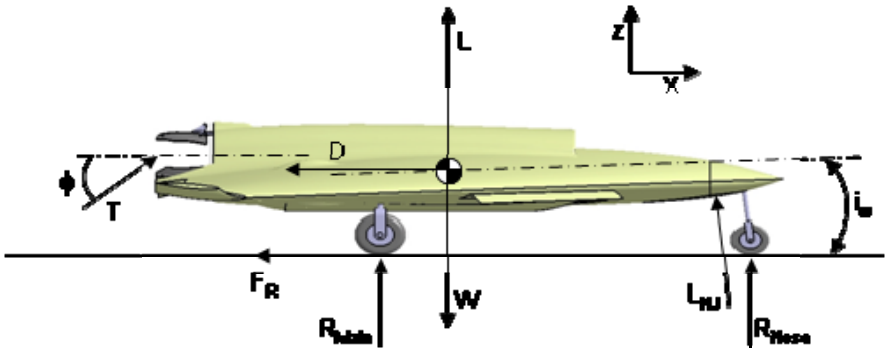

Figure 3-2

Summing the forces acting in the horizontal direction, we obtain the relation below for the resultant force. Here, we are assuming that the angle of the nose jet thrust from the vertical is negligible and therefore does not contribute any horizontal force.

$$F_X = T_{TO-X} - (D + F_R) \qquad \text{Eq 3-21}$$

The rolling resistance of the wheels is given by the expression $F_R = \mu_R \cdot R$, where μ_R is assumed to have a value of 0.02. The term R is the total reaction force acting on the landing gear wheels, which includes components due to weight, lift and the vertical components of thrust, as given by the relation below.

$$R = W - L - F_Z \qquad \text{Eq 3-22}$$

The vertical components of thrust consist of that from the vectored engine thrust and the thrust from the nose jet as given by the expression below.

$$F_Z = T_{TO-Z} + L_{NJ} \qquad \text{Eq 3-23}$$

These relations will now be put into practice in the analyses that follow.

D3.3.2 Analysis approach

This analysis is broken down into two stages, the first being to determine the actual aircraft speed and the second to determine the required aircraft speed. Each process is presented in easy to follow flowchart format in the sections which follow. The result of the analysis being the point of intersection between these two curves.

D3.3.2.1 Actual aircraft speed

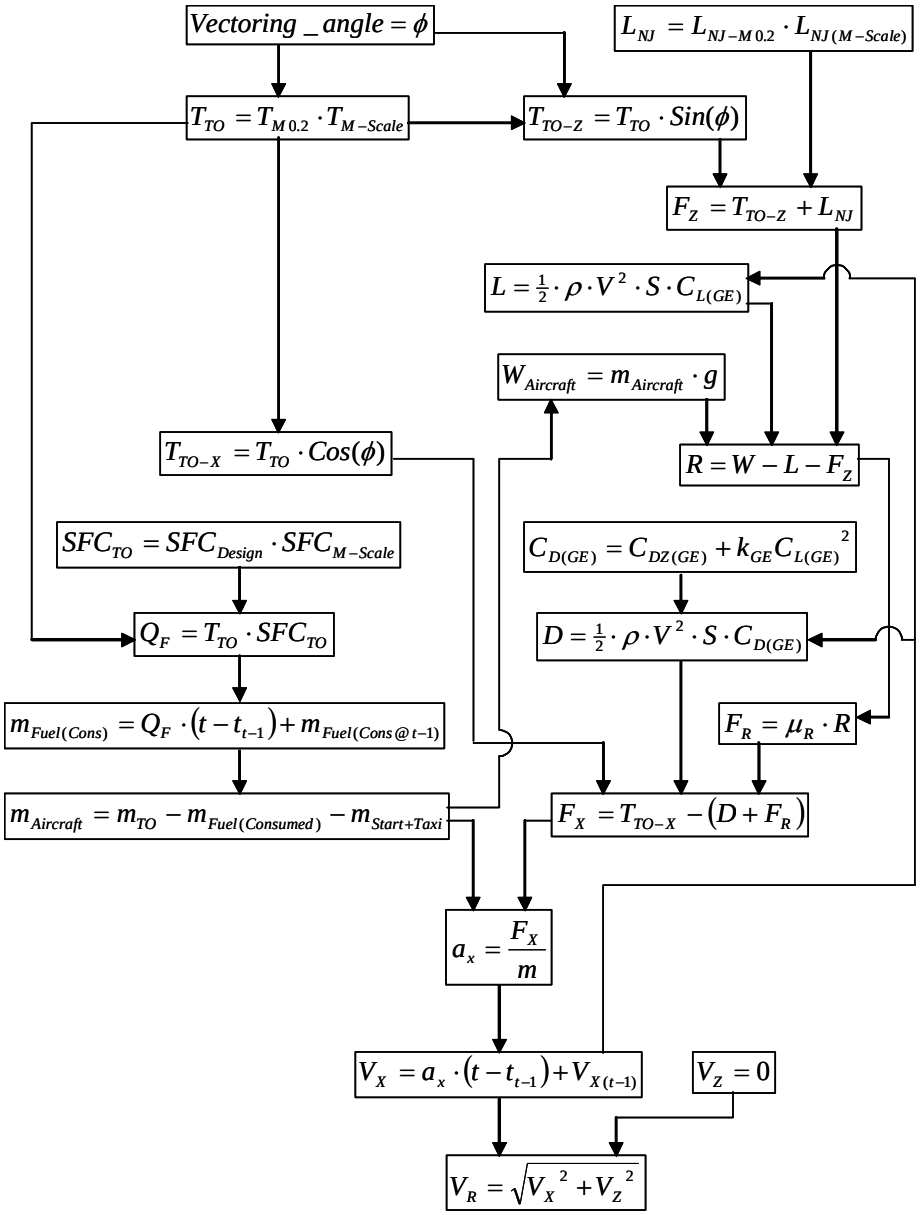

D3.3.2.2 Required aircraft speed

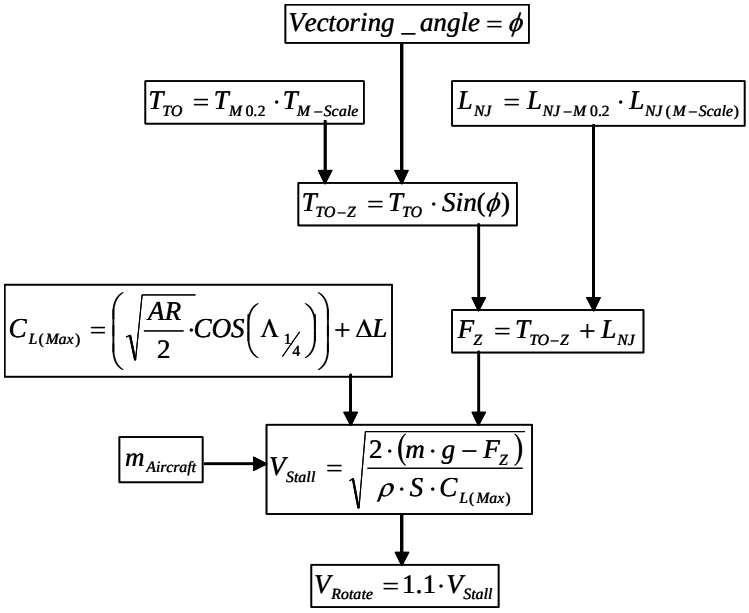

D3.3.3 Finding the final solution

The solution to this analysis corresponds to the intersection between the curves for the required aircraft speed and the actual aircraft speed as shown in the example below. The actual value of this point is determined by numerical analysis techniques.

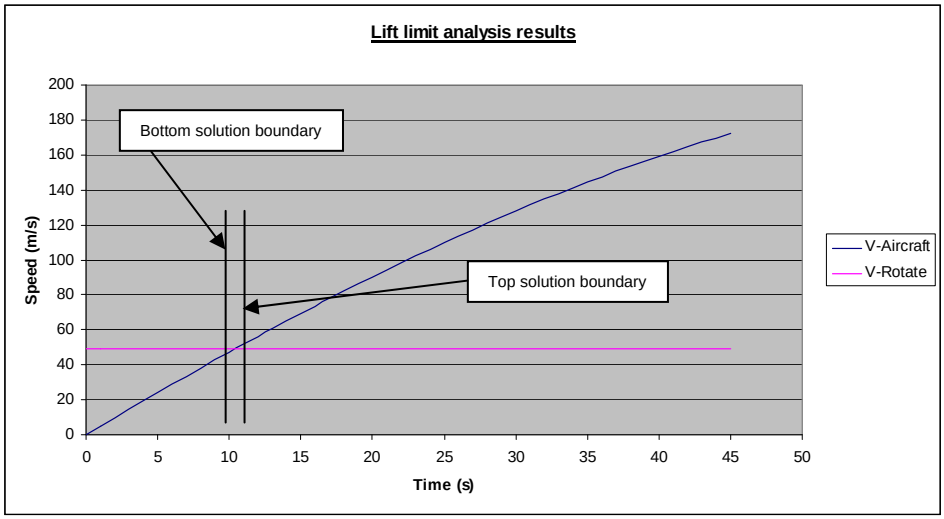

Chart 3-1

D3.4 Take-off analysis – Thrust vectoring control limit

The function of this analysis is to determine the point during the ground run when there is sufficient control authority available from the nose jet control system to be able to safely rotate the nose of the aircraft. To be able to rotate the nose of the aircraft, there needs to be a control moment acting about the main wheel which is sufficient to counteract the sum of the other moments acting on the aircraft. This includes the

angular inertia to initiate a rotational acceleration as specified by the airworthiness regulation. Since the moment due to thrust vectoring is dependent on the deflection of the exhaust plume, the analysis is repeated for a range of thrust vectoring angles. As before, to improve the accuracy of the results, the flight phase is analysed as a number of sequential steps. Iterative solutions are automated with the Excel Solver function.

D3.4.1 Derivations

The arrangement of the aircraft in its take-off configuration is given in the figure below. This shows the system of forces acting on the aircraft as well as their locations as measured from the aircraft reference point. Each of these lengths being expressed as a fraction of the mean aerodynamic chord of the wing, denoted as a 'bar' value. The sum of the forces acting in the horizontal direction is given by the expression used earlier.

$$F_X = T_{TO-X} - (D + F_R) \qquad \text{Eq 3-24}$$

The force required to rotate the nose of the aircraft is determined from the sum of the moments acting on the aircraft about the main landing gear wheels. Each of these being determined from inspection of the figure which gives the forces and characteristic lengths used to arrive at the moment expressions below.

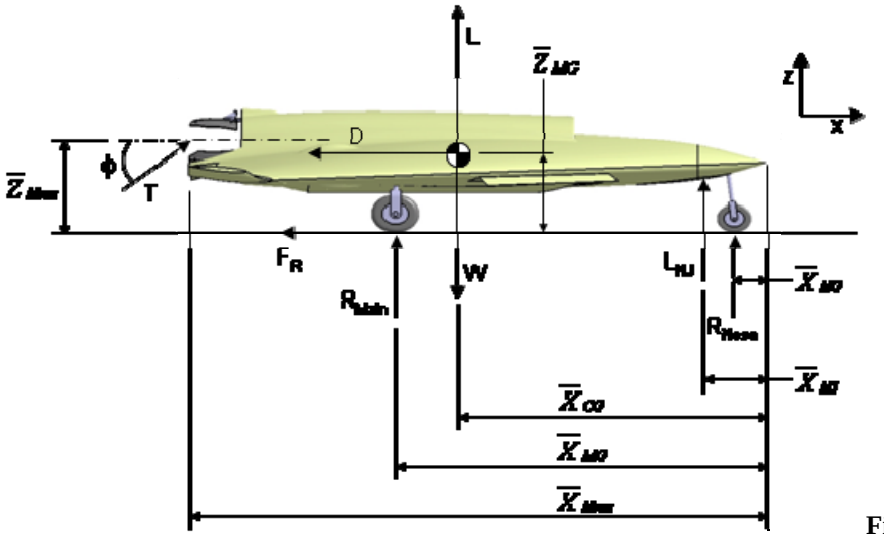

Figure 3-3

The total zero lift pitching moment is the sum of that due to the wing-fuselage and that due to the deflection of the leading edge Kruger flaps as given by,

$$C_{M\,0(Total)} = C_{M\,0(Wing-fuselage)} + C_{M\,0(Krugers)} \qquad \text{Eq 3-25}$$

The moment due to the lift from the wing-fuselage combination is given by,

$$C_{M(LW)} = C_{L(GE)} \cdot \left(\overline{X}_{MG} - \overline{X}_{ACW}\right) \qquad \text{Eq 3-26}$$

The moment due to the vertical component of vectored engine thrust is given by,

$$C_{M(TZ)} = \frac{-T_Z}{q \cdot S}\left(\overline{X}_{NOZZ} - \overline{X}_{MG}\right) \qquad \text{Eq 3-27}$$

The moment due to the horizontal component of vectored engine thrust is given by,

$$C_{M(TX)} = \frac{-T_X}{q \cdot S}\left(\overline{Z}_{MG} + \overline{Z}_{NOZZ}\right)$$ Eq 3-28

The moment due to the drag of the wing-fuselage combination is given by,

$$C_{M(D)} = C_D \cdot \overline{Z}_{MG}$$ Eq 3-29

The moment due to the inertia of the accelerating aircraft, which is assumed to act at the centre of gravity of the aircraft, is given by,

$$C_{M(ax)} = \left(\frac{m_{Aircraft} \cdot a_X}{q \cdot S}\right) \cdot \overline{Z}_{MG}$$ Eq 3-30

The moment due to the vertical thrust from the nose jet is given by,

$$C_{M(NJ)} = \frac{L_{NJ}}{q \cdot S} \cdot \left(\overline{X}_{MG} - \overline{X}_{NJ}\right)$$ Eq 3-31

The moment due to the weight of the aircraft acting at its centre of gravity is given by,

$$C_{M(mg)} = \frac{-m \cdot g}{q \cdot S} \cdot \left(\overline{X}_{MG} - \overline{X}_{CG}\right)$$ Eq 3-32

The final moment contribution acting on the aircraft is the rotational inertia of the aircraft at the point of rotation of the nose. This required the second moment of area of the aircraft about the main landing gear wheels $I_{YY(MainGear)}$ which was approximated from statistical methods from Roskam [10] as $I_{YY(MainGear)} = 40692m^4$. $\ddot{\theta}$ is the rotational acceleration of the aircraft at the initial point of rotation as specified by airworthiness requirements. In this example, this was taken as $\ddot{\theta} = 8\,\mathrm{deg}/s^2$ which is consistent with this size of aircraft. The rotational inertia moment can then be determined from,

$$C_{M(RI)} = \frac{-I_{YY(MainGear)} \cdot \ddot{\theta} \cdot (\pi/180)}{q \cdot S \cdot \overline{c}}$$ Eq 3-33

The total moment acting on the aircraft is the sum of all the components above. From this we are able to determine the nose jet force required to rotate the nose of the aircraft as given by the expression below.

$$L_{NJ(\mathrm{Re}qd)} = -C_{m(Total)} \cdot \left(\frac{q \cdot S}{\overline{X}_{MG} - \overline{X}_{NJ}}\right)$$ Eq 3-34

These relations will now be put into practice in the analyses that follow

D3.4.2 Analysis approach

This analysis is broken down into two stages, the first being to determine the available nose jet force and the second to determine the required nose jet force. Each process is presented in the sections which follow. The result of the analysis being the point of intersection between these two curves.

D3.4.2.1 Available nose jet force

The available nose jet force is given by the expression below from the nose jet control terms given in the analysis parameters section of this appendix.

$$L_{NJ\,(Available)} = L_{NJ-M\,0.2} \cdot L_{NJ\,(M-Scale)}$$ Eq 3-35

D3.4.2.2 Required nose jet force

The process to find the required nose jet force is presented in easy to follow flowchart format below utilising the expressions derived above.

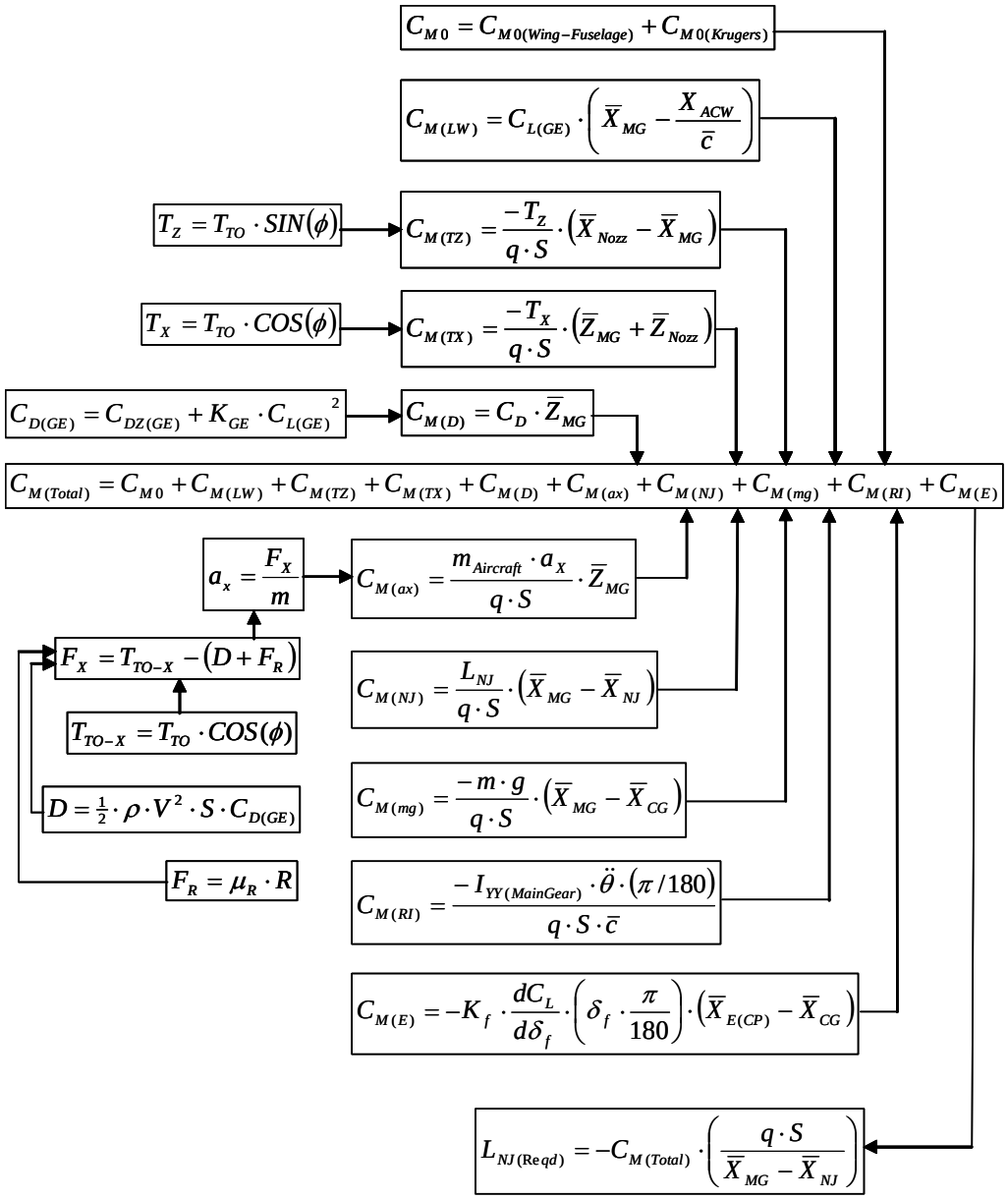

D3.4.3 Finding the final solution

The solution to this analysis corresponds to the intersection between the curves for the nose jet lift required and the nose jet lift available as shown in the example below. The actual value of this point is determined by numerical analysis techniques.

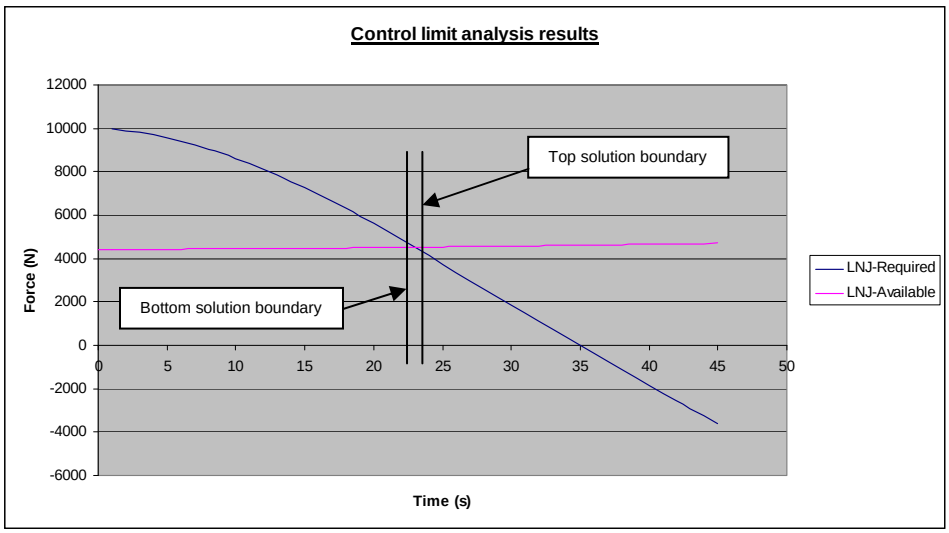

Chart 3-2

D3.5 Take-off analysis – Conventional elevons control limit

The function of this analysis is to determine the point during the ground run when there is sufficient control authority available from conventional elevons to be able to safely rotate the nose of the aircraft. This analysis allows us to determine the effect of using the elevons for pitch control as opposed to using the thrust vectoring/nose jet system. For a true comparison, the elevon control requirements were analysed at a number of different engine plume deflection angles. As before, to improve the accuracy of the results, the flight phase is analysed as a number of sequential steps. Iterative solutions are automated with the Microsoft Excel Solver function

D3.5.1 Derivations

For this analysis, we make use of the expression for pitching moment due to elevon deflection as given below and discussed in the general terms section.

$$C_{M(E)} = -K_f \cdot \frac{dC_L}{d\delta_f} \cdot \left(\delta_f \cdot \frac{\pi}{180} \right) \cdot \left(\overline{X}_{CP(E)} - \overline{X}_{CG} \right) \qquad \text{Eq 3-36}$$

Upon rearranging this expression, we are able to determine the elevator deflection required to rotate the nose of the aircraft as a function of the resultant moment acting on the aircraft as given below.

$$\delta_{E(Rotate)} = \frac{C_{m(Total)}}{-K_f \cdot \frac{dC_L}{d\delta_f} \cdot \left(\overline{X}_{CP(E)} - \overline{X}_{CG} \right)} \cdot \frac{180}{\pi} \qquad \text{Eq 3-37}$$

D3.5.2 Analysis approach

This analysis is broken down into two stages, the first being to determine the maximum elevon available elevon deflection and the second to determine the required elevon deflection. Each process is presented in the sections which follow. The result of the analysis being the point of intersection between these two curves.

D3.5.2.1 Maximum available elevon deflection

In this analysis, the maximum elevon deflection during take-off has been assumed to be 10 degrees. Although it is possible for a conventional control surface to effectively exceed this figure, this figure makes allowance for reserve control authority for roll control as may be required.

D3.5.2.2 Required elevon deflection

The analysis to determine the required elevon deflection follows the same process as used for the nose jet control force with the elevon deflection becoming the objective variable instead as given below. All the other parameters remain the same.

$$C_{M(Total)} = C_{M0} + C_{M(LW)} + C_{M(TZ)} + C_{M(TX)} + C_{M(D)} + C_{M(ax)} + C_{M(NJ)} + C_{M(mg)} + C_{M(RI)} + C_{M(E)}$$

$$\delta_{E(Rotate)} = \frac{C_{m(Total)}}{-K_f \cdot \frac{dC_L}{d\delta_f} \cdot \left(\overline{X}_{CP(E)} - \overline{X}_{CG}\right)} \cdot \frac{180}{\pi}$$

where $\frac{dC_L}{d\delta_{Flap}}$ and K_{Flap} feed into the denominator.

D3.5.3 Finding the final solution

The solution to this analysis corresponds to the intersection between the curves for the elevon deflection required and the maximum elevon deflection as shown in the example below. The actual value of this point is determined by numerical analysis techniques.

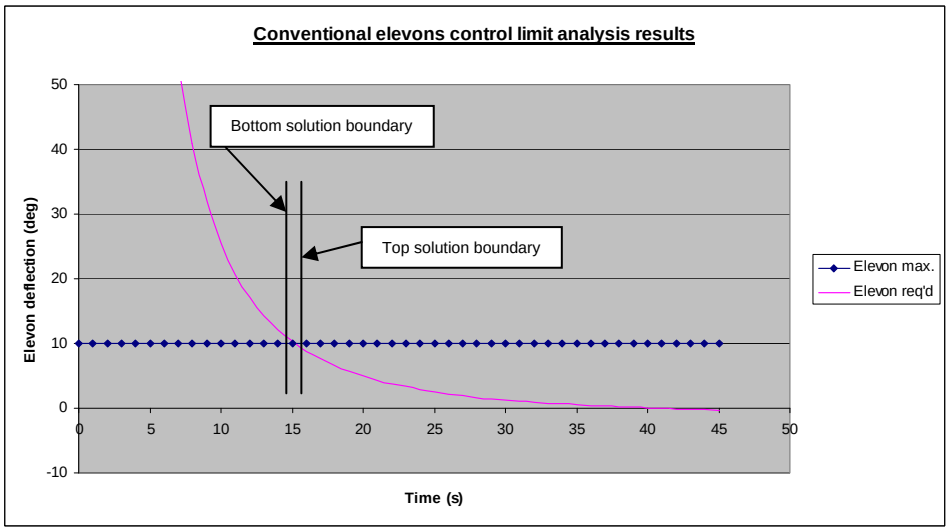

Chart 3-3

D3.6 Finding the final overall solution

At this stage in the work, we have a matrix of results for a range of nozzle vectoring angles and engine bleed settings. This includes a set of results for the point during the take-off when sufficient lift is available and another for when there is sufficient control authority available. As discussed, the control authority for the thrust vectored aircraft is dependent on the force from the nose control jet which itself is dependant on the bleed from the engine. As the performance of the engine is also dependent on the amount of bleed extraction, it is necessary to keep the bleed to a minimum to prevent inferior engine performance. The optimum solution for each thrust vectoring nozzle angle will therefore be the engine bleed setting which results in a control limit which coincides with the lift limit.

Using the results for the minimum ground run required for the lift limit and control limit analyses; it is possible to find the point of intersection between these two curves. This point represents the minimum ground run distance required to safely generate sufficient lift from the wings as well as achieve sufficient control power to be able to safely rotate the nose of the aircraft. As for the other analyses, actual value of this intersection point is determined by numerical analysis techniques. In this analysis however, engine bleed becomes the solution variable as opposed to time (as used in earlier analyses). This process is illustrated in the example figure below.

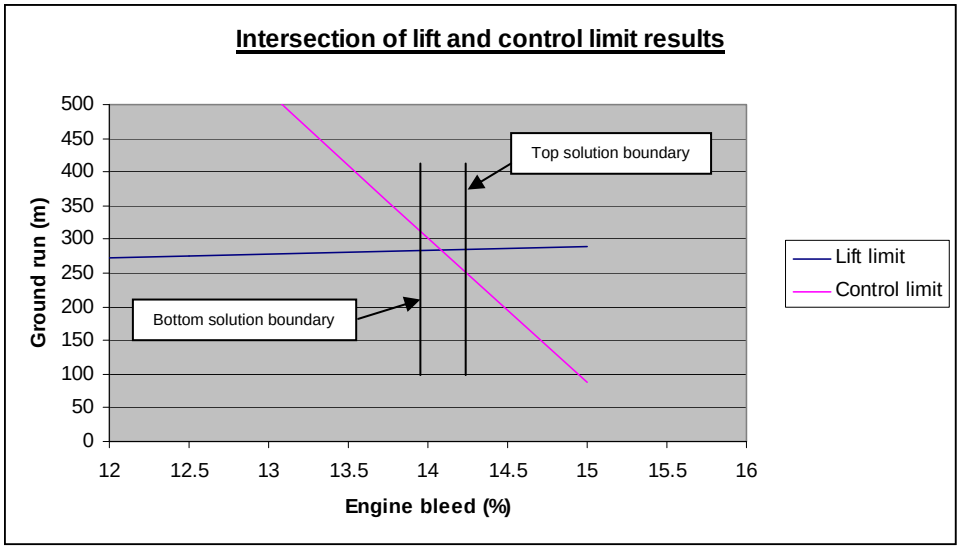

Chart 3-4

D4 Landing analysis

The complete landing phase typically consists of three phases, approach, flare and ground run. In this work, the flare has been integrated into the landing approach analysis resulting in two analyses to describe the landing performance of the aircraft. The first of these analyzes the flight path from the screen height to the point where the vertical velocity is zero and the aircraft is firmly on the ground. The second then analyzes the ground run to bring the aircraft to rest. The landing approach analysis is an iterative solution process involving a complex balance of the forces and moments acting on the aircraft, within which a range of vectoring angles and initial descent velocities are explored. The ground run analysis is a less complex balance of the deceleration forces acting on the aircraft. An additional analysis has investigated the potential of landing on an aircraft carrier, by means of a lower landing approach speed.

D4.1 Analysis parameters

Presented in this section are the parameters required for these analyses. During these analyses, the aircraft is in its landing configuration with the Kruger flaps deployed and landing gear extended. These are discussed in the general terms section.

D4.1.1 Engine specific fuel consumption

During the landing phases, the engine is throttled back and it is sufficient to use a typical figure of $c' = 2.10 \times 10^{-5}$ (kg/Ns) for the specific fuel consumption. This figure is however relative to the engine operating at its design condition, when it is delivering a thrust of 52730.77N. When the engine is operated at partial load, the SFC will vary from its design value as can be predicted by the expression below. Here T is the thrust of the engine at the off-design condition.

$$SFC = c' \cdot \left(1 + \left[0.01 \cdot \left\{ \frac{T_{Design}}{T} - 1 \right\} \right] \right) \qquad \text{Eq 4-1}$$

D4.2 Landing approach analysis

The function of this analysis is to determine the performance of the aircraft during the landing approach phase. The exact process is a complex balance of the forces and moments acting on the aircraft to arrive at a solution for the performance of the aircraft at any instant.

D4.2.1 Derivations

The arrangement of the aircraft in its descent configuration is given in the figure below along with the system of forces acting on it.

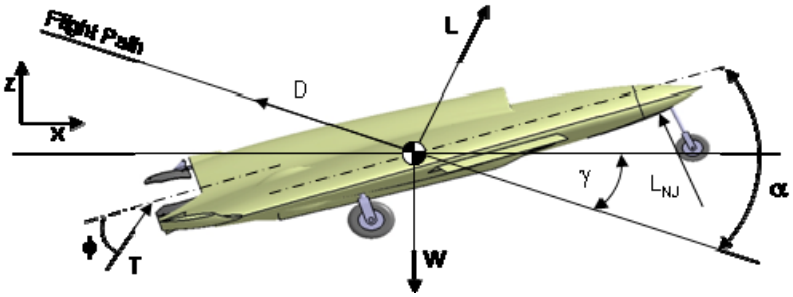

Figure 4-1

Summing the forces acting in the vertical direction, we obtain the relation below for the resultant force.

$$\sum F_Z = -L_{Thrust} + W - L_{Lift} - L_{Drag} + Z_{Inertia} + L_{NoseJet} \quad \text{Eq 4-2}$$

Inspection of the above figure, allows us to derive relations for each component as given below. As the aircraft is descending, the flight path angle in this analysis is negative. This results in the need for an extra minus sign in the relations.

1. $L_{Thrust} = T \cdot Sin(\alpha + \phi - (-\gamma))$ Eq 4-3
2. $W = m \cdot g$ Eq 4-4
3. $L_{Lift} = L \cdot Cos(\gamma)$ Eq 4-5
4. $L_{Drag} = D \cdot Sin(\gamma)$ Eq 4-6
5. $Z_{Inertia} = m \cdot a_Z$ Eq 4-7
6. $L_{NoseJet} = L_{NJ} \cdot Cos(\alpha - (-\gamma))$ Eq 4-8

In a similar way, summing the forces acting in the horizontal direction allows us to obtain the relation below for the resultant force.

$$\sum F_X = T_{Engine-X} + T_{Lift} + T_{Drag} + X_{Inertia} + T_{NoseJet} \quad \text{Eq 4-9}$$

This is made up of the following components as derived from the figure above.

1. $T_{Engine-X} = T_{Engine} \cdot Cos(\alpha + \phi - (-\gamma))$ Eq 4-10
2. $T_{Lift} = L \cdot Sin(\gamma)$ Eq 4-11
3. $T_{Drag} = -D \cdot Cos(\gamma)$ Eq 4-12
4. $X_{Inertia} = -m \cdot a_X$ Eq 4-13
5. $T_{NoseJet} = -L_{NJ} \cdot Sin(\alpha - (-\gamma))$ Eq 4-14

These relations will now be put into practice in the analyses that follow

D4.2.2 Analysis approach

The complexity of this analysis has necessitated the need to break it down into a number of smaller sections in order to be able to present the procedure here. This is shown in the diagram below, which is intended to help the reader trace their steps. This diagram not only presents the function of each block but also highlights their inputs/outputs so that the inter-relation between the blocks can be better understood. Due to the complexity of the analysis, it is not possible to illustrate all the links between the blocks, as this could potentially obscure the function of the diagram. Instead, arrows between each block are used to remind the reader that a complex network of links exists.

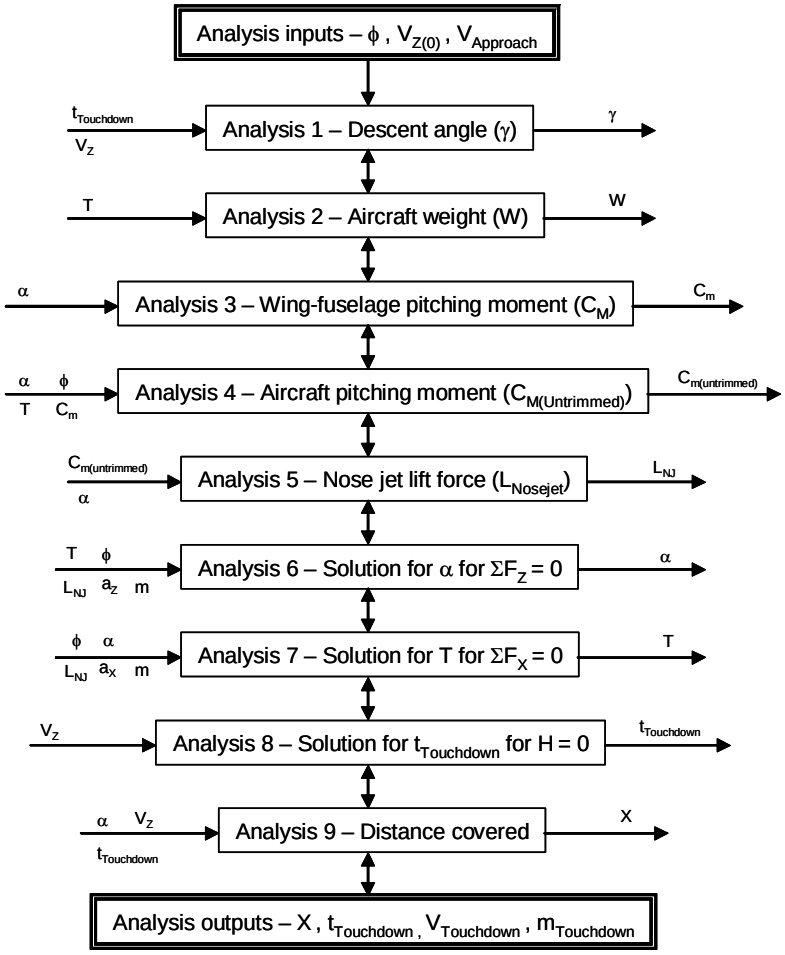

To be able to solve this analysis, an iterative solution process is required for the aircraft angle of attack and the engine thrust. The solution for the aircraft angle of attack is found as that value which gives a resultant vertical force of zero. In a similar way, the solution for the engine thrust is found as that value which gives a resultant horizontal force of zero. As an added complication, the angle of attack and engine thrust can be seen to be related to each other and it is therefore necessary to keep alternatively iterating each solution until both solutions converge. This process is summarised below.

Solution procedure for the landing approach analysis

Stage 1 – Iterate a until $\Sigma F_Z = 0$
Stage 2 – Iterate T until $\Sigma F_X = 0$

Repeat Stage 1 and Stage 2 until ΣF_Z and $\Sigma F_X = 0$

This analysis is repeated for an array of combinations of the input parameters being investigated. This includes variations of the parameters:

1. ϕ - Thrust vectoring nozzle deflection angle
2. $V_{Z(0)}$ - Initial vertical descent velocity of the aircraft at the screen height
3. $V_{Approach}$ - Approach speed of the aircraft at the screen height

The approach speed ($V_{Approach}$) is different for land based and carrier based aircraft. In this particular analysis, the aircraft is assumed to be land based but a carrier variant is considered in a later section. In this analysis, the approach speed is $V_{Approach} = 1.2 \cdot V_{Stall}$.

The array of values of ϕ and $V_{Z(0)}$ investigated in this analysis are presented in the table below which gave a total of 28 analysis cases for each combination of input variables.

Inputs		Vectoring angle (ϕ)						
		0	**5**	**10**	**15**	**20**	**25**	**30**
$V_{Z(0)}$	**2.5**	C1	C2	C3	C4	C5	C6	C7
	5	C8	C9	C10	C11	C12	C13	C14
	7.5	C15	C16	C17	C18	C19	C20	C21
	10	C22	C23	C24	C25	C26	C27	C28

Table 4-1

The analysis outputs of particular importance include:

- X – Ground distance covered to the point of touchdown.
- $t_{Touchdown}$ – The time taken until the vertical descent velocity equals zero.
- $V_{Touchdown}$ – The aircraft velocity at the point when the vertical velocity is zero.
- $m_{Touchdown}$ – The aircraft mass at the point when the vertical velocity equals zero.

In the sections which follow, each of the individual analysis blocks making up the complete analysis will be presented to the reader in an easy to follow flow chart format. To improve the accuracy of the results, the flight phase is broken down into a number of smaller steps which can be analysed sequentially. In cases where an iterative solution process is required, this is automated with the Solver function of Microsoft Excel.

D4.2.3 Analysis stage 1 – Descent angle

The function of this stage of the analysis is to determine the descent angle of the aircraft at each time step, as required by the other analysis stages. In this flight phase, the descent angle not fixed and can be seen to vary throughout the flight stage in relation to the changes in the aircraft X and Z velocity components. The solution to this stage is therefore a function of the horizontal and vertical velocity components as is presented in the equation flowchart below.

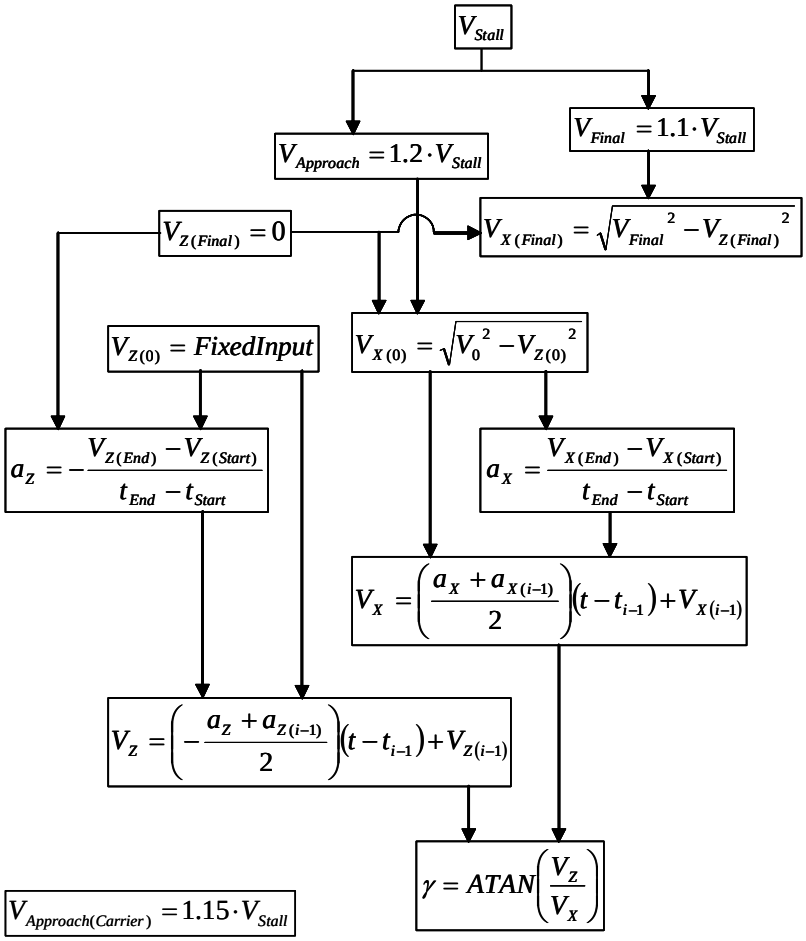

D4.2.4 Analysis stage 2 – Aircraft weight

The function of this stage of the analysis is to determine the mass and weight of the aircraft at each time step, as required by the other analysis stages. The solution is directly related to the engine thrust and specific fuel consumption, as presented in the flow chart below. As clarification, $m_{AC(0)}$ is the mass of the aircraft at the start of the approach phase and $m_{Fuel(0)}$ is the total mass of fuel used up to that point.

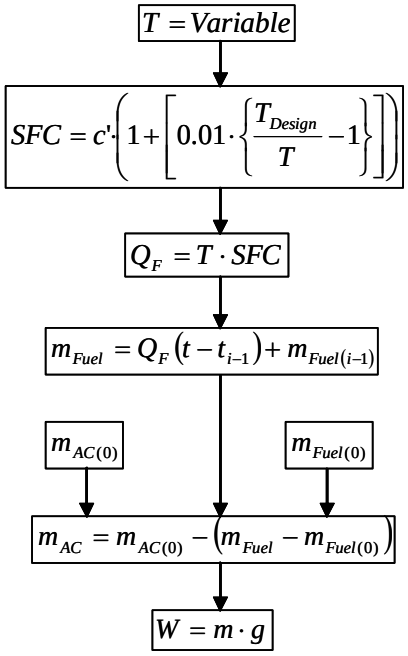

D4.2.5 Analysis stage 3 – Wing-fuselage pitching moment

The function of this stage of the analysis is to determine the wing-fuselage pitching moment coefficient at each step, as presented in the flow chart below. The solution is a function of the variable aircraft angle of attack, as required by analysis stage 4 to determine the untrimmed pitching moment of the aircraft.

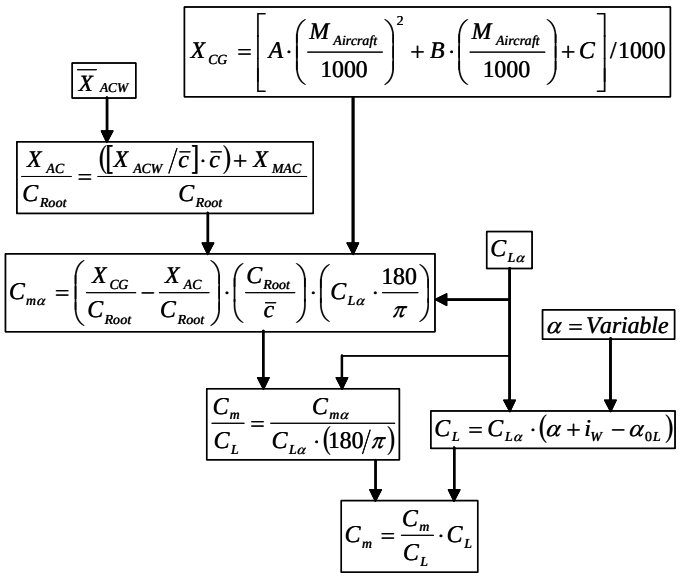

D4.2.6 Analysis stage 4 – Aircraft pitching moment

The function of this stage of the analysis is to determine the total aircraft pitching moment coefficient at each time step, as presented in the flow chart below. The solution, which is a function of α, ϕ and T as well as the wing-fuselage pitching

moment C_m is required for analysis stage 5 to determine the nose jet lift required to be able to trim the aircraft.

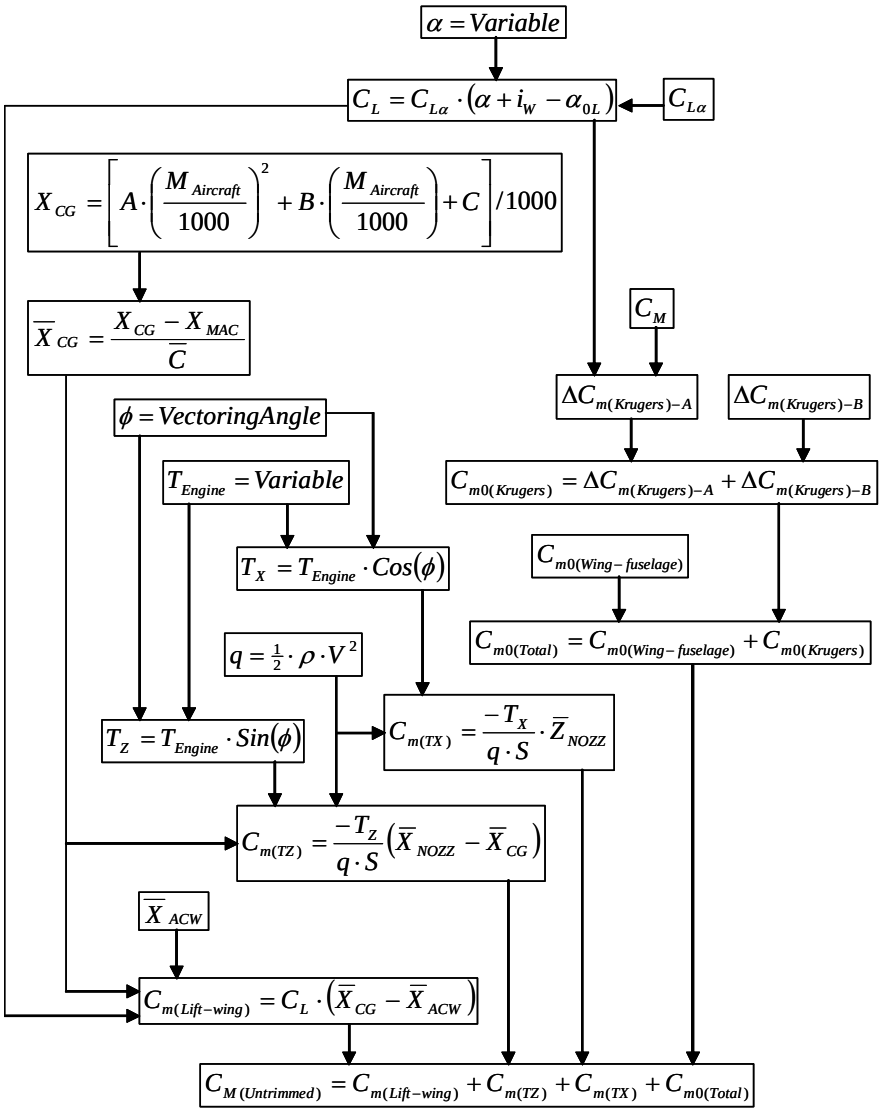

D4.2.7 Analysis stage 5 – Nose lift jet force

The function of this stage of the analysis is to determine the nose jet lift force required to trim the aircraft at each time step, as presented in the flow chart below. The output from this stage is integrated with the solution stages 6 and 7 for angle of attack and thrust respectively.

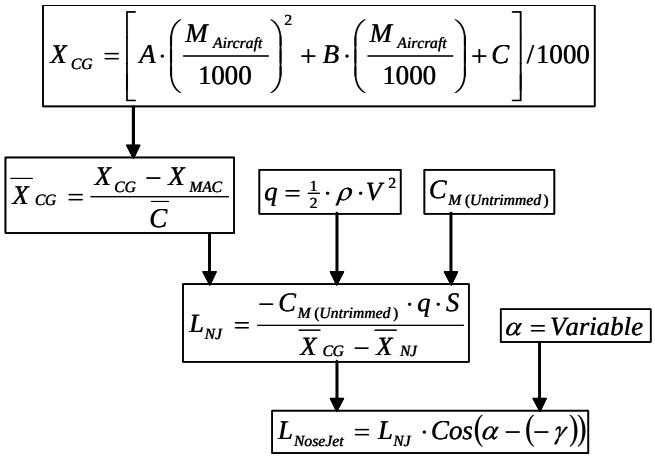

D4.2.8 Analysis stage 6 – Solution for angle of attack

The function of this stage is to determine the solution for the optimal angle of the aircraft at each time step, as presented in the flow chart below. The solution is a function of the input parameters T, ϕ, L_{NJ}, a_z and m, which are used to determine the sum of the vertical force components acting on the aircraft at any moment in time. By iterating the input variable α, we are able to determine the value required to achieve a resultant vertical force of zero. This analysis block is therefore the basis of the first stage of the solution process.

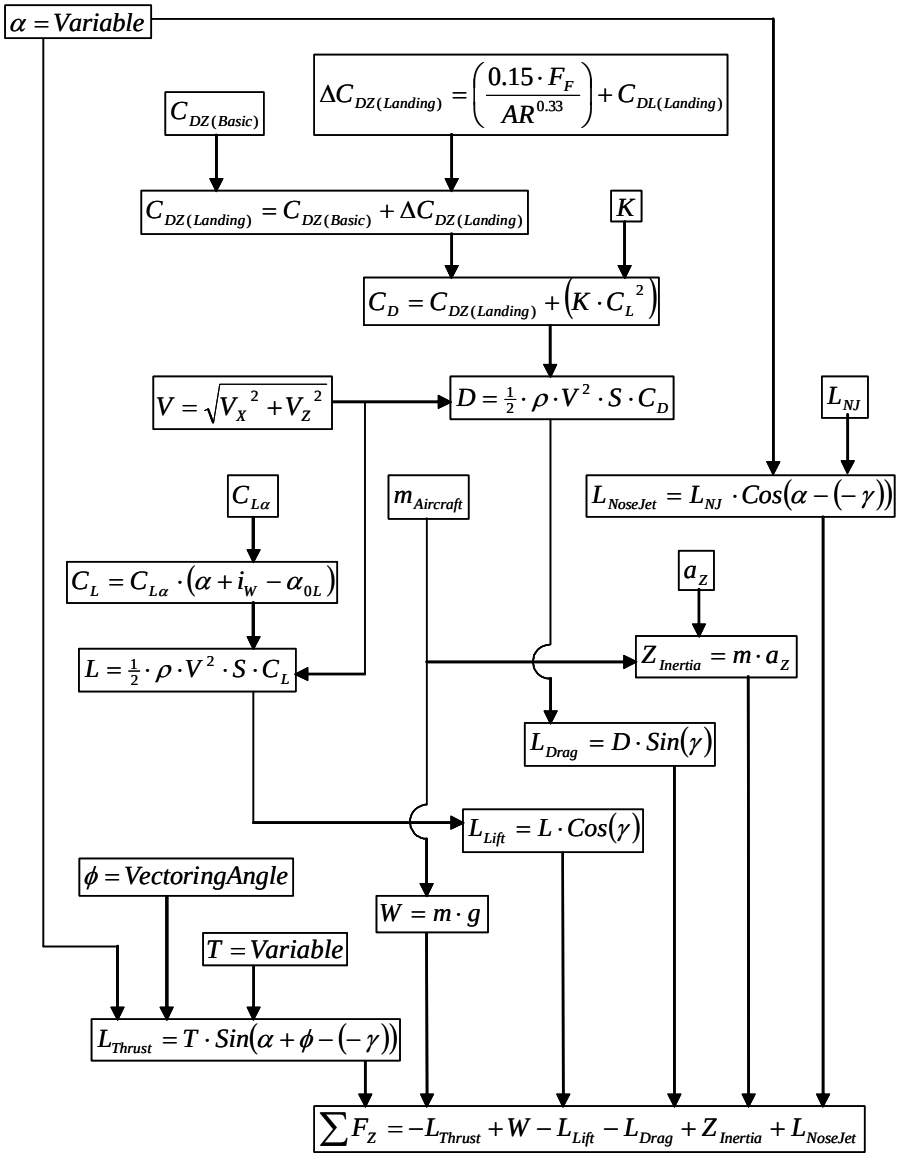

D4.2.9 Analysis stage 7 – Solution for thrust

The function of this stage is to determine the solution for the optimal engine thrust of the aircraft at each time step, as presented in the flow chart below. The solution is a function of the input parameters α, ϕ, L_{NJ}, a_x and m, which are used to determine the sum of the horizontal force components acting on the aircraft at any moment in time. By iterating the input variable T, we are able to determine the value of T required to achieve a resultant horizontal force of zero. This analysis block is therefore the basis of the second stage of the solution process.

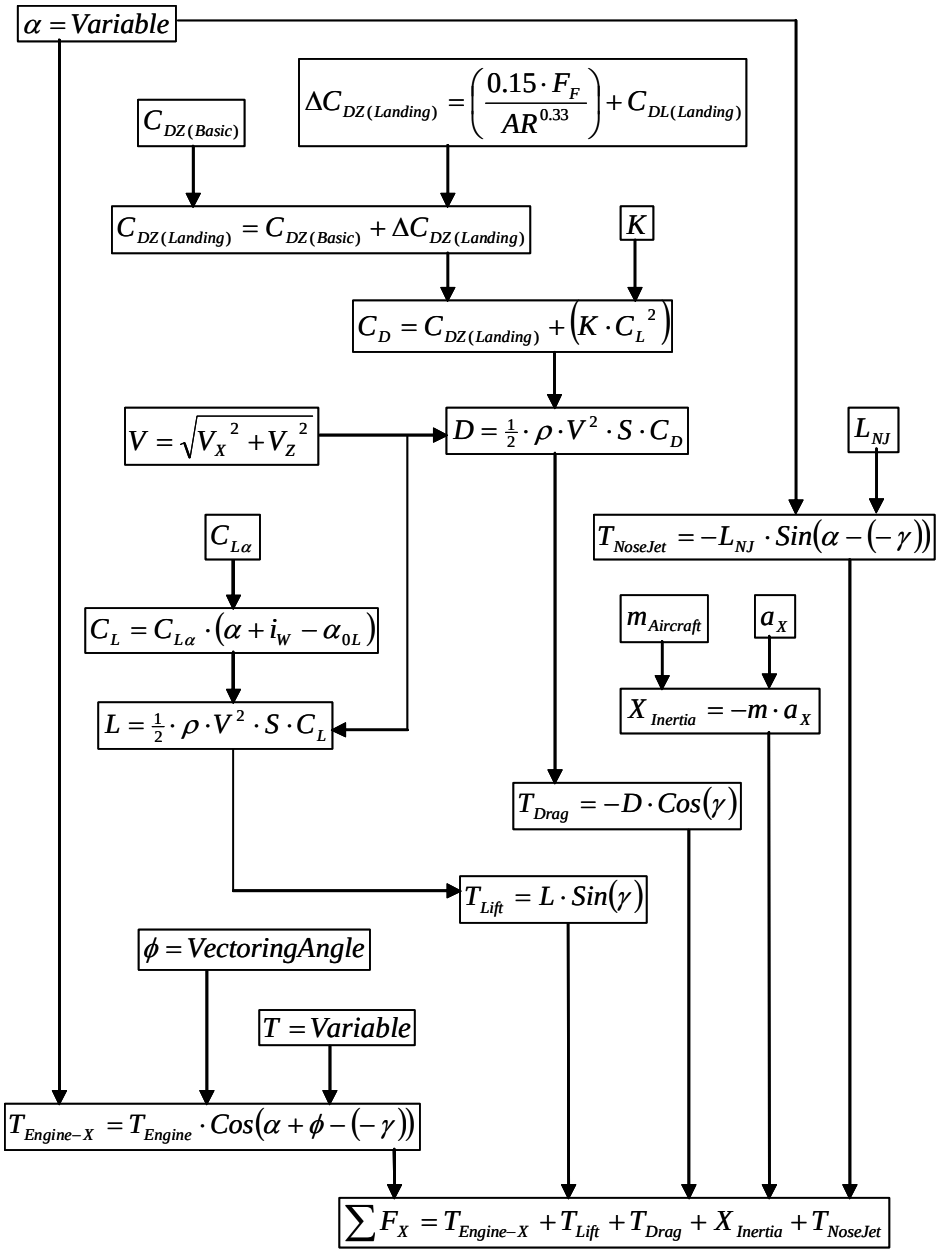

D4.2.10 Analysis stage 8 – Time to touchdown

The function of this stage is to determine the total time taken to complete the approach phase of the complete landing phase, as is presented in the flow chart below. This is based on the time taken to descent from the screen height, utilising expressions to determine the altitude at each time step. The time to touchdown is not only the time taken to descend from the screen height but also the time to reach the point where the vertical velocity equals zero. A particularly important factor within this analysis is the initial vertical descent velocity, which is one of the input variables under investigation.

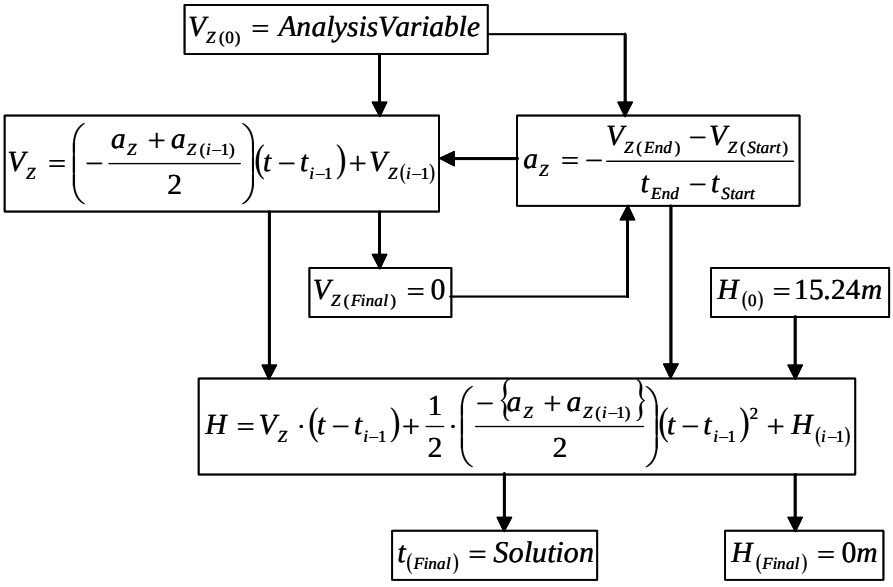

D4.2.11 Analysis stage 9 – Distance covered

The function of this stage is to determine the total horizontal distance covered during the approach phase as presented in the flow chart below. This process enables the distance to be determined at each time step which collectively gives the total distance covered. The total distance in this flight phase is the horizontal distance flown between the point of the screen height and the point where the vertical velocity equals zero. The input variables in this analysis are α, V_Z and $t_{Touchdown}$ (from the previous analysis stages) and the output X is one of the final analysis solutions.

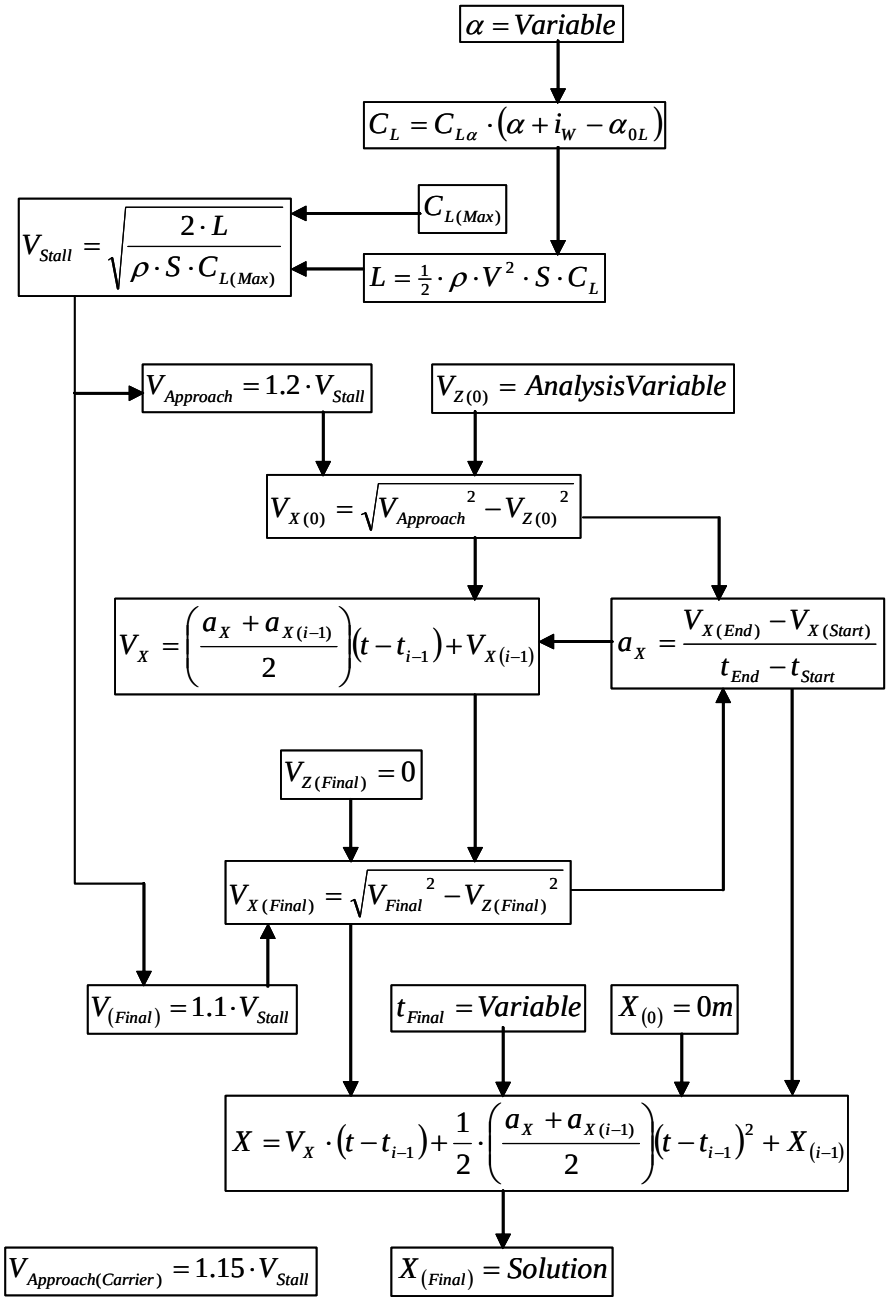

D4.3 Landing ground run analysis

The function of this analysis is to determine the performance of the aircraft during the landing ground run phase. The starting point for this analysis is the results from the landing approach phase. This process is however a less complex balance of the deceleration forces acting on the aircraft.

D4.3.1 Derivations

The arrangement of the aircraft in its landing ground run configuration is given in the figure below along with the system of forces acting on it.

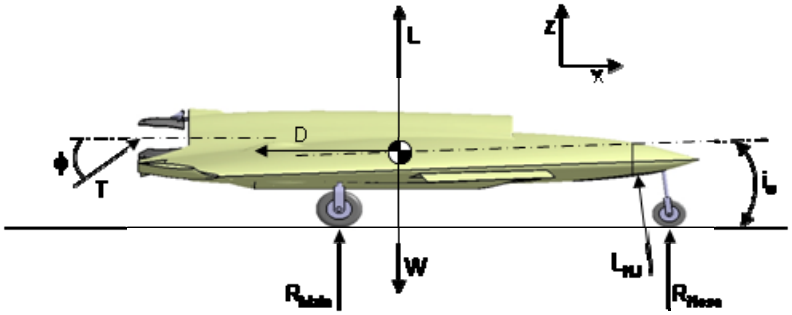

Figure 4-2

In this analysis, the aircraft is assumed to have all its wheels in contact with the ground and the vertical acceleration $a_Z = 0$. We have also assumed that the engine is at idle and therefore any thrust is negligible. Since no pitch control is required, the lift force from the nose jet is assumed to be zero. At this stage we could be misled into thinking that the lift from the wings is zero since the angle of attack of the aircraft is assumed to be zero. This is not the case however since the wing is still being presented to the airflow at an angle due to the setting angle of the landing gear as well as the angle of zero lift for the wing. This can be observed in the relation for C_L, $C_L = C_{L\alpha} \cdot (\alpha + i_W - \alpha_{0L})$. In reality however, the effect of the landing gear setting angle is likely to be less than that assumed here. The forward inertia of the aircraft as a result of the aircraft braking will generate a moment about the rear wheels which will compress the nose landing gear strut and therefore reduce the setting angle.

Inspection of the forces acting on the aircraft in the vertical direction gives the expression, $R = W - L$. Here R is the ground reaction from the wheels which is directly related to the aircraft braking force F_R. In a similar way, the forces acting in the aircraft in the horizontal direction, gives the expression, $F_X = T - (D + F_R)$ Eq 4-15

This is made up of the following components:

1. $T_{Engine@Idle} = 0$
2. $D = \frac{1}{2} \cdot \rho \cdot V^2 \cdot S \cdot C_{D(Landing)}$ Eq 4-16
3. $F_R = (\mu_R + \mu_B) \cdot R$ Eq 4-17

F_R is the total horizontal decelerating friction force, which is the sum of that due to the rolling friction of the tyres ($\mu_R = 0.03$) and that due to the application of the brakes ($\mu_B = 0.3$). These relations will now be put into practice in the analyses that follow.

D4.3.2 Analysis approach

The analysis for the landing ground run is considerably less complex than that for the landing approach phase as given by the flowchart below. As with the landing approach analyses, to improve the accuracy of the results, the flight phase is broken down into a number of smaller steps which can be analysed sequentially. Where required, the Solver function Microsoft Excel is used for iterative solutions. By this method, the summation of the ground run distance as determined at each time step gives the total ground distance covered until the aircraft comes to a rest.

Although the aircraft is on the ground, the setting angle of the landing gear means that the wing is still generating a small amount of lift, which will affect the vertical reaction force on the wheels and thus the decelerating force. The input parameters for this phase are the output parameters from the previous landing approach flight phase. The ones of particular concern here are $V_{Touchdown}$ and $m_{Touchdown}$. The parameter $m_{Touchdown}$ is assumed to remain constant during this phase since no (or negligible) fuel is being consumed when the engine is at idle.

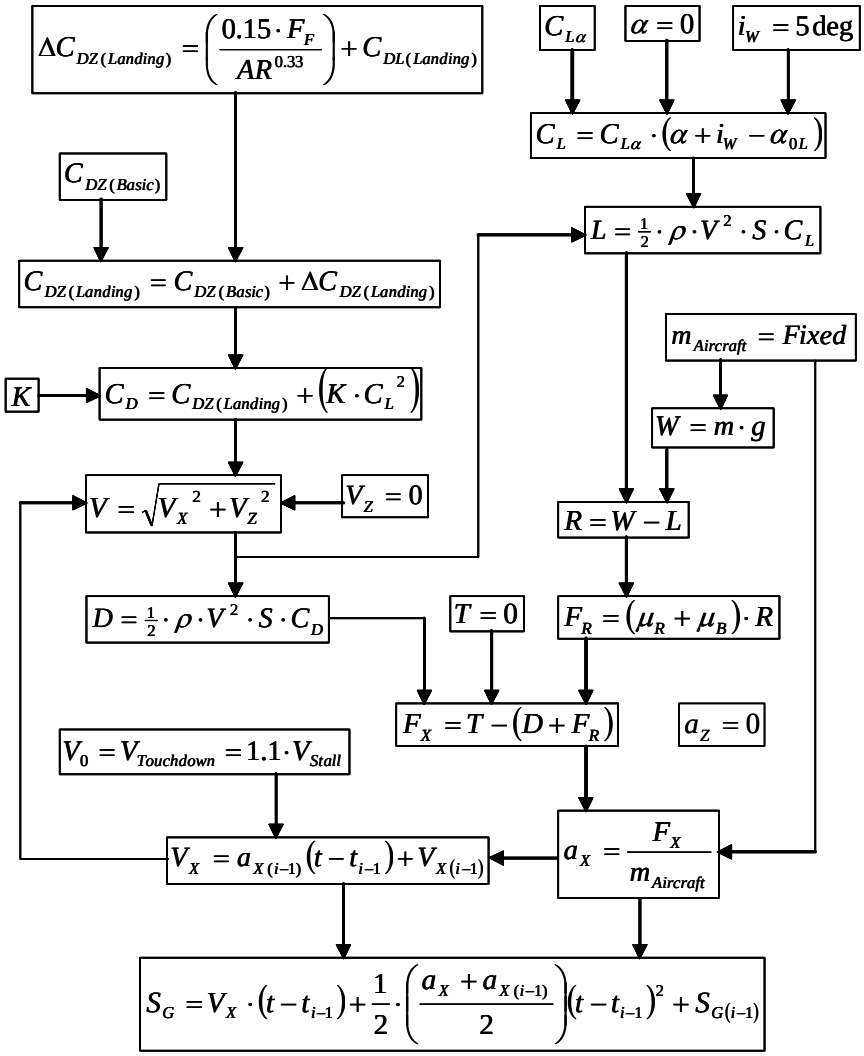

D4.4 Aircraft carrier landing analysis

In the case of the analysis for landing on an aircraft carrier, the only difference is the landing approach speed which now becomes $V_{Approach} = 1.15 \cdot V_{Stall}$. This is considered to be the only variation between the land based and carrier base analyses. In reality however, a carrier aircraft is unlikely to be subject to the requirement to clear a landing approach screen height. In addition, there is likely to be an additional braking force due to an arresting hook. In this analysis however we have assumed that an arresting hook is not used. We are therefore making an assessment of the viability of landing a land based aircraft on an aircraft carrier without any modifications to the aircraft.

D5 Wing size reduction investigation

The take-off analysis studies carried out on the thrust vectored variant of the baseline aircraft raised the question whether the incorporation of such a system would enable a smaller wing to be used. The rationale for this is that, compared to the baseline aircraft, the thrust vectored aircraft has additional components of lift from the thrust vectoring system. These include the vertical components of thrust from the deflected thrust vectoring nozzle and the thrust from the nose jet.

Our initial thoughts are that these additional components of lift should mean that the lift requirements of our wing during the take-off phase are reduced. The same argument is also true for the aircraft during the landing phase. If we refer back to the constraint analysis which was carried out for our baseline design, we can see that the final size of a wing is typically governed by either the take-off or landing boundaries. Our initial thoughts are therefore that the addition of a thrust vectoring system would result in our wing being oversized to meet our original requirements.

The aim of this study was therefore to test these predictions and examine the impact of reducing the size of the wing and how this compares with the performance of our baseline design. The approach adopted in this study was to test a number of variants of the thrust vectored aircraft, each with a different wing size. The results of which will enable us to establish a trend between wing size and take-off performance for the thrust vectored aircraft.

D5.1 Wing resizing

As mentioned above, the approach adopted in this study was to analyse the performance of a number of variants of the baseline design. Each of which has a different wing size and therefore different characteristics. If we take another look at the aircraft conceptual design process, we will see that a reduction in the wing area is accompanied by variations in:

- Aircraft mass (empty and take-off)
- Mission fuel requirements (as result of revised L/D characteristics)
- Drag (lift induced drag and zero lift)
- Wing geometry
- T/W and W/S boundaries

Since the wing area has such a considerable impact on many other parts of the aircraft and its characteristics, it was necessary to repeat the conceptual design process for each aircraft variant. This process is discussed below.

Although variations in wing area will have a considerable impact on the vast majority of the aircraft parameters, some of these are expected to retain their original figures as derived for the baseline design. This includes:

- Fuselage mass – Fixed at 1318.99kg
- Systems mass – Fixed at 1038.06kg
- Powerplant mass – Fixed at 1505.06kg
- Take-off thrust – Fixed at 52730.77N

- Wing t/c ratio – Fixed at 12%
- Wing aspect ratio – Fixed at 2.54

The process followed was to fix the aircraft wing area at a number of values, which were a fraction of the original wing area as given by the following expression. The values tested in this study were, 50-100% in 10% steps. Where, $S_{Baseline} = 53.4194 m^2$.

$$S_{Variant(i)} = S_{Baseline} \cdot \frac{\%S_{Variant(i)}}{100} \qquad \text{Eq 5-1}$$

This design exercise gave us the following results for the different variants.

Aircraft configurations

$\%S_{Variant(i)}$	$S_{Variant}$ (m^2)	Mo (kg)	M_{Empty} (kg)	M_{Fuel} (kg)	M_{Wing} (kg)	Cdz_{Cruise}	Kv_{Cruise}	L/D_{Cruise}
100	53.4194034	8650.487	4523.54385	2312.574	661.43728	0.010393	0.177667	9.572682
90	48.077463	8616.954	4490.71431	2311.871	628.60774	0.010503	0.177667	9.522385
80	42.7355227	8582.28	4456.10471	2311.806	593.99814	0.010628	0.177667	9.466471
70	37.3935824	8546.323	4419.35347	2312.6	557.2469	0.010771	0.177667	9.403478
60	32.051642	8508.921	4379.96049	2314.591	517.85392	0.010938	0.177667	9.331279
50	26.7097017	8469.896	4337.19993	2318.327	475.09336	0.011139	0.177667	9.246601

Table 5-1

Wing geometry for aicraft confiurations

$\%S_{Variant(i)}$	$S_{Variant}$ (m^2)	C_{Root} (m)	b (m)	MAC (m)
100	53.4194034	8.338155	11.6484	5.609304
90	48.077463	7.910268	11.05065	5.321453
80	42.7355227	7.457873	10.41865	5.017114
70	37.3935824	6.976201	9.745753	4.693081
60	32.051642	6.458707	9.022814	4.344948
50	26.7097017	5.895966	8.236665	3.966377

Table 5-2

D5.2 Take-off analyses

Since the take-off phase is the critical flight phase with respect to lift requirements, this study is limited to this phase. The take-off performance analysis, as performed on each of the variants being studied, follows exactly the same process as that used in the thrust vectoring take-off performance analysis. The obvious difference being the substitution of different aircraft parameters as determined above. To reiterate, the analyses covered by this study includes:

1. Lift limit analysis
2. Thrust vectoring control limit
3. Conventional elevons control limit

Whereas, the original take-off analysis study also considered the effect of varying the landing gear setting angle, it is assumed to be fixed at 5 degrees in this study.

E1 Fuel cell system design requirements

In our baseline aircraft constraint analysis, we determined the thrust required from our propeller to meet our performance constraints. As part of our design work, we were also able to predict the propeller efficiency, which enables us to determine the propeller input shaft power required. The purpose of this section is to determine the fuel cell system power requirements, taking into account losses within the power train. This includes all the losses between the fuel cell output and the propeller. In this analysis we are particularly interested in those losses from, the propeller, gearbox and controller. Losses from other power train components are assumed to be negligible in comparison.

E1.1 An overview of the fuel cell system power train

A schematic of the fuel cell system power train is presented below to help the reader familiarise themselves with the power train.

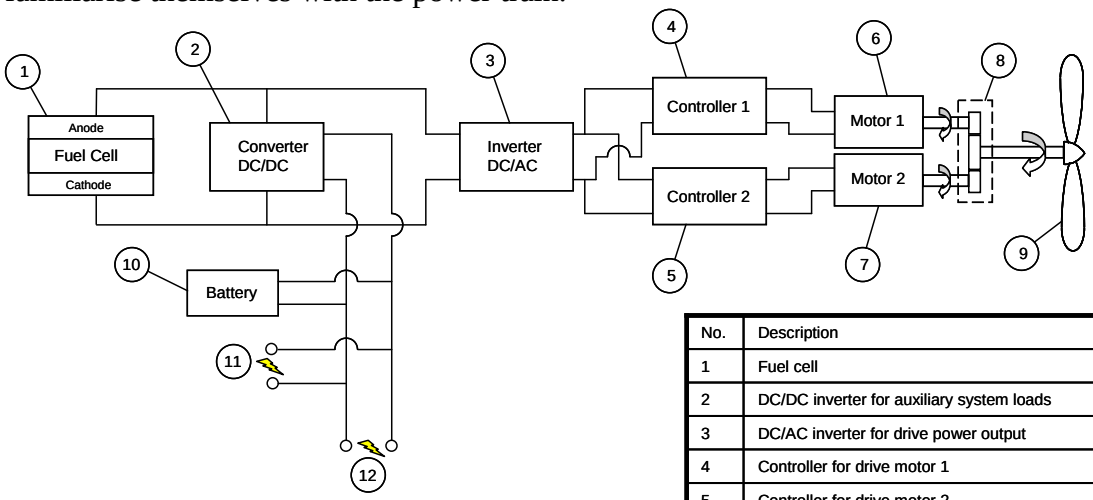

No.	Description
1	Fuel cell
2	DC/DC inverter for auxiliary system loads
3	DC/AC inverter for drive power output
4	Controller for drive motor 1
5	Controller for drive motor 2
6	Drive motor 1
7	Drive motor 2
8	2 into 1 reduction drive gearbox
9	Aircraft propeller
10	Battery for system start-up and back-up
11	Power off-takes for fuel cell system balance of plant
12	Power off-takes for other aircraft external loads

Figure 1-1

The power delivered by the fuel cell is DC and must therefore first pass through an inverter to change it to the AC power required by the electrical traction components. This AC power is then fed to the AC traction motor via a motor controller, which is used to regulate the speed and torque of the motor. As can be seen from the figure, there is also the need to draw DC power from the fuel cell output, which is used for power off-takes such as auxiliary equipment and other aircraft loads. A DC/DC converter is included in the system in order to condition and regulate this DC power off-take. Also included in this circuit is a battery which will be used to aid system start-up and supply power to the essential systems in the event of a failure. The most suitable battery for this

application would be either a Nickel Metal Hydride (NiMH) or Lithium Lon (Li-lon) battery.

Research into existing traction motors has shown there to be no motor currently available which is capable of meeting our power demands. Therefore two motors are required which are arranged in parallel, each of which is accompanied with its own controller. The two parallel traction motors are coupled by means of a 2 into 1 reduction gearbox, which will also bring the speed of the motors inline with that of the propeller. The mechanical shaft power out of the gearbox is finally fed to the propeller.

E1.2 Commercially available traction motors

Research into suitable existing high-power light-weight traction motors has generated the table of currently available candidate traction motors given below.

High power light weight traction motors

Manufacturer	Model	Type	Rated voltage (V)	Peak voltage (V)	Peak power (kW)	Peak power duration (s)	Continuous power (kW)	Max torque (Nm)	Rated torque (Nm)	Rated RPM	Efficency - peak power	Efficency - continuous	Nominal speed	Length (mm)	Width (mm)	Height (mm)	Diameter (mm)	Weight (kg)	Cooling method	Notes
Siemens	1PV5135WS28	3-phase induction	650	900	200	<15	67	430	160	3500				425	245	245		90	Water/glycol	
Siemens	1PV5135WS24	3-phase induction	520	900	150		61	370	160	3500				425	245	245		90	Water/glycol	
Brusa	HSM1-6.17.12		400	400	108		64	220	130			95	4700	245			270	51	Water/glycol	
AC propulsion	AC-150		336-360		150		50				91	91		350			245	50	Forced air	
UQM	HPM-150	Brushless		420	150	30-90	100	650	400	1650	92.5	95		241			405	91	Liquid	
Toshiba	Traction motor						275			3010				717			458	392	Forced air	
Raser	P-200				200		100	415	207			93		457			279	112	Liquid	
Yuneec	Power drive 60	Brushless	166.5	190			60			2400				209			280	30		Aviation
Evo Electric	AFM-240	PM axial flux			335	60	150	800	440			96.5		222			400	80	Water/glycol	
AC propulsion	AC-200	Copper rotor			200									381			305	50	Forced air	tzero package
Lynx Motion	E-813	Axial flux	574				130	900	450	2750	98	98		162.4			813	295		
Tesla motors	Sport	AC induction			215			400			80	90						52	Air cooled	Tesla roadster
LE	M40L2				140		90			3250				191			410	90		
LE	M40B2				120		78			3000				191			510	95		
Azure	AC90	AC-induction			97		50			1350		92		520			394	189	Air cooled	
UQM	HPM 125				125		45					94		252			280	41	Liquid	
UQM	SMP218-143-3				145		85					94		279			280	50	Liquid	

Table 1-1

For the needs of this project, the AC-200 motor as manufactured by AC Propulsion was selected as the candidate most able to match our requirements. This motor has the added benefit of being air cooled and therefore offers a weight saving compared to similar designs. The long and narrow geometry of this motor also offers the benefits of being able to fit within the narrow part of a rear fuselage. As already mentioned, two of these motors in parallel were necessary to meet the power requirements of this aircraft.

E1.3 Commercially available traction motor controllers

Research into suitable existing high-power motor controllers has generated the table of currently available candidate motor controllers given below.

Controllers suitable for high power traction motors

Manufacturer	Evisol	Raser	UQM	AC propulsion	Centric-AutoMotive	Saminco	AC propulsion	Azure
Model		PCU-200	DD45-500L	AC-150 Gen-2	EVI-200	M600	AC-200	DMOC645
Peak power (kW)	200	215		150		220	200	97
Continuous power (kW)		110						
Efficency		94-95					95-98	
Nominal voltage (V)	750-DC		240-420		750			
Max voltage (V)	900-DC		340-420		900			
Output form	3-phase				3-phase			
Length (mm)		224x330x358	380	186x313x760		585x470x215	186x313x760	585
Width (mm)			365					260
Height (mm)			119					310
Weight (kg)	24	36	15.9	30	24	58	30	27.5
Cooling method	Water/glycol	Liquid	Liquid	Forced air	Water/glycol	Liquid	Forced air	Air cooled
Notes		Dual control				300kW cont capable	tzero package	

Table 1-2

For the needs of this project, the AC-200 motor controller as manufactured by AC Propulsion was selected as candidate most able to match our requirements. This controller also has the benefit of being designed specifically for the AC-200 traction motor selected above and has the same benefits of air cooling. Two of these controllers are required to meet our power demands with one being allocated to each motor.

E1.4 Fuel cell power requirements

The analysis described in this section is used to determine the fuel cell system output power required to be able to meet the performance constraints of the aircraft, whilst making allowance for losses in the aircraft power train. The analytical procedure is summarised in the following flow chart. The accompanying equations are also given below.

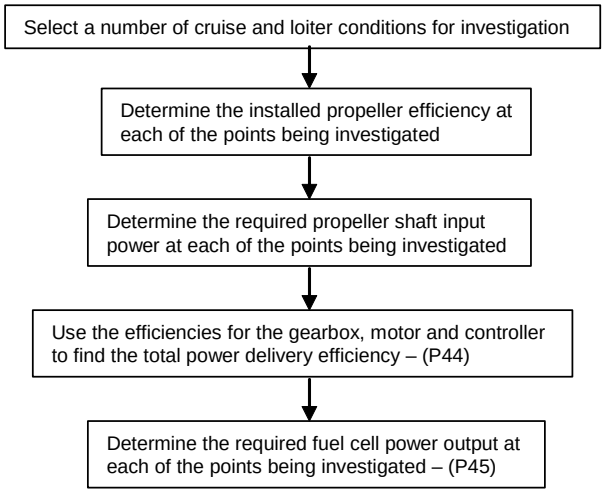

The total efficiency of the fuel cell power train, between the fuel cell output and the propeller, is determined from equation P44 below. This is made up of the following component efficiencies:

- $\eta_{Gearbox}$ - Efficiency of the 2 into 1 reduction gearbox (which is taken to be 0.98)
- η_{Motor} - Efficiency of the traction motors (which is taken to be 0.93)
- $\eta_{Controller}$ - Efficiency of the motor controllers (which is taken to be 0.97)
- $\eta_{\mathrm{Pr}opeller}$ - Efficiency of the propeller (which is determined by the methods presented in the baseline aircraft design section)

$$\eta_{Total-Delivery} = \eta_{Gearbox} \cdot \eta_{Motor} \cdot \eta_{Controller} \cdot \eta_{Propeller} \qquad \text{Eq 1 (P44)}$$

The required fuel power output can finally be determined from equation P45, which is analysed at a number of flight conditions to determine the most critical constraint.

$$P_{Output-FuelCell} = \frac{P_{Propeller-Input}}{\eta_{Total-Delivery}} \qquad \text{Eq 2 (P45)}$$

E1.5 Results for fuel cell system power output required

The final results for the required fuel cell system power output (taking into account the power train losses) for this project are presented in the figure below for the range of flight conditions experienced by the aircraft.

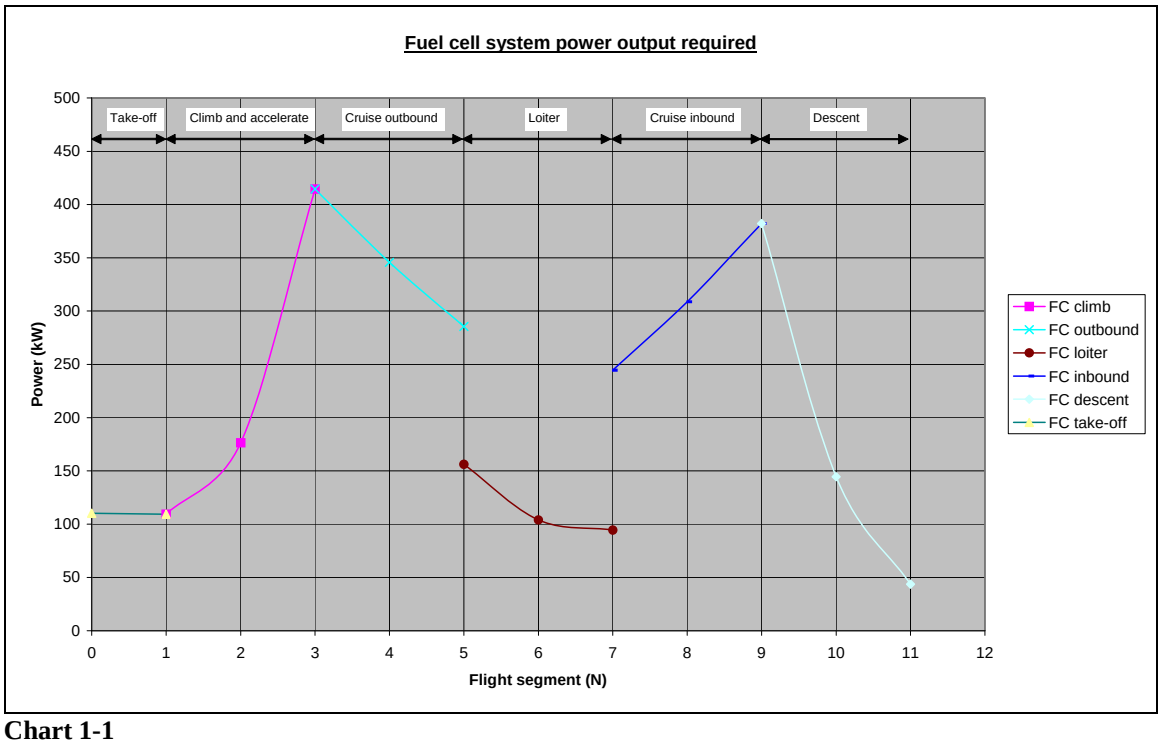

Chart 1-1

From the chart above, the most critical points in terms of fuel cell power requirements can be easily identified, which are:

- End of climb/start of cruise outboard = 414.51kW. This will be the design condition to ensure that a fuel cell system is capable of delivering sufficient power at out most demanding flight condition.
- Start of loiter = 156.16kW. This will be the design condition for a fuel cell system which is capable of delivering sufficient power for the loiter phase only.

E2 An overview of the fuel cell systems

The objective of this section is to introduce the reader to the various systems designed by the author for a methanol fuelled fuel cell powered aircraft. The systems which are of particular importance to this study and are thus presented here are:

- The main fuel cell system – This system is responsible for generating the DC power used to supply the aircraft electric powertrain.
- The aircraft electric powertrain – This system is responsible for converting the electrical power from the fuel cell into thrust via the propeller.
- Fuel cell powered aircraft control systems – These systems are responsible for controlling the various components of the fuel cell system to meet the flight commands.

Each of these systems will be discussed in more detail in the sections that follow.

E2.1 An overview of the main fuel cell system

The schematic for the main fuel cell system is shown overleaf. The reader is advised to familiarise themselves with this system in order to be able to understand the fuel cell system analysis work which follows in the rest of this thesis.

The complete system can be broken down into a number of subsystems which are each identified by a different colour in the schematic. These are:

1. Air supply – This includes an air compressor which is used to pressurise the air entering the fuel cell and a humidifier to control the air quality.
2. Fuel supply – This includes the methanol delivery circuit and the fuel processor, as well as means of cooling and recovering water from the reformate.
3. Exhaust stream power recovery – This includes a burner and turbine to generate mechanical power using the excess hydrogen leaving fuel cell. This mechanical power is used to power the air compressor via a direct mechanical connection. The hydrogen flow rate entering the fuel cell is carefully controlled so that there is only just sufficient excess hydrogen and thus turbine power output to meet the demands of the compressor.
4. Water recovery and humidification – This includes separators which are used to recover water from the anode and cathode streams. This recovered water is then re-circulated to the fuel processor and humidifier.
5. Cooling system – This includes a pumped coolant circuit which is used to remove waste heat from the various components. Where possible, this heat is reused within the system and aircraft for de-icing and other heating needs. The excess waste heat is dispensed into the atmosphere by means of a air/water heat exchanger.

Further details of these systems will be presented later on in the thesis, in the sections which make up the fuel cell system analysis.

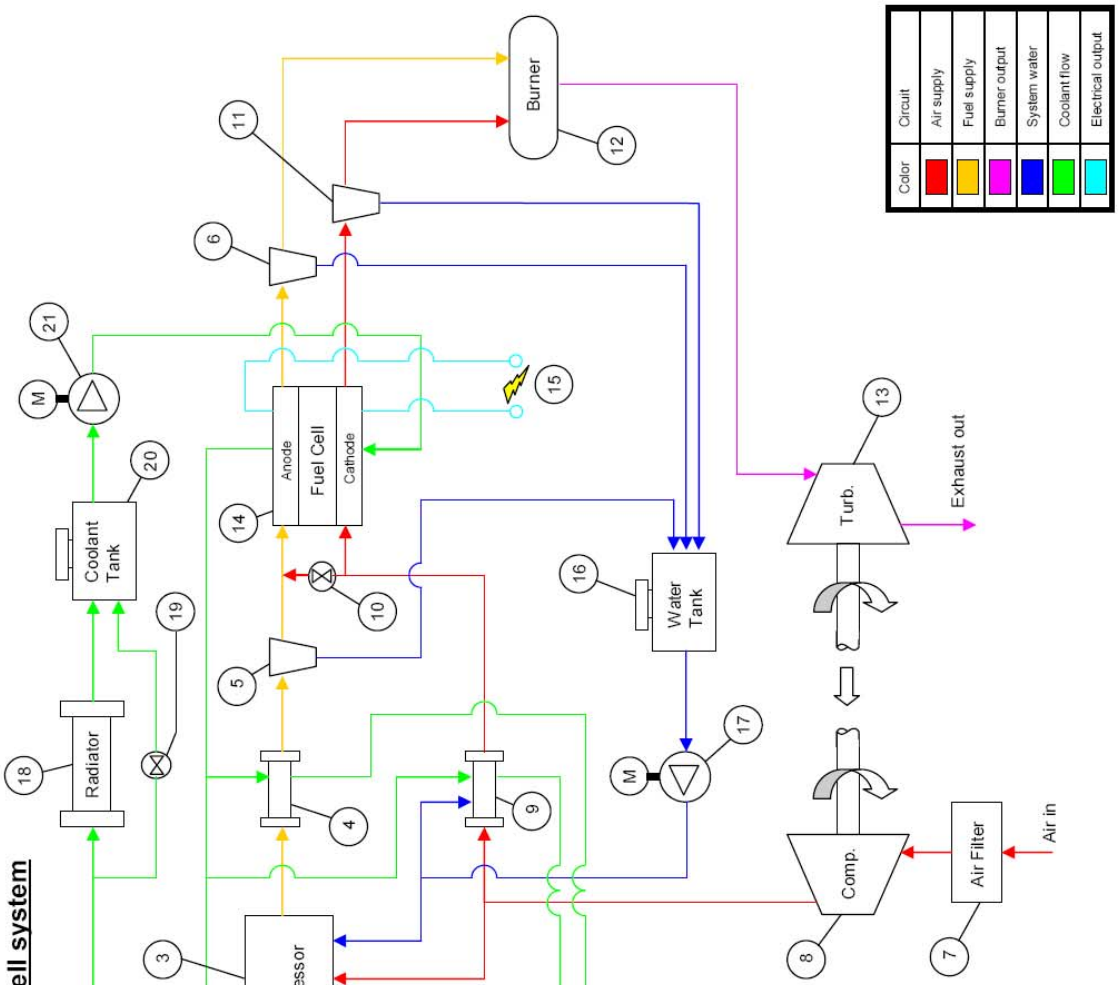

No	Description
1	Methanol fuel tank
2	Fuel pump
3	Fuel processor
4	Anode reactants cooler
5	Anode in water separator
6	Anode out water separator
7	Air filter
8	Air compressor
9	Cathode air cooler & humidifier
10	Air bleed valve
11	Cathode water separator
12	Burner
13	Turbine
14	Fuel cell
15	Power output terminals
16	System water tank
17	System water pump
18	Radiator
19	Coolant by-pass valve
20	Coolant tank
21	Coolant pump

E2.2 An overview of the fuel cell powered aircraft powertrain

The aircraft electric powertrain converts the electrical power output from the fuel cell into mechanical power at the propeller input shaft and ultimately thrust. This system has already been extensively discussed in the fuel cell system requirements section of this thesis and the reader is advised to refer to this for further details.

E2.3 An overview of an example fuel cell control system

The schematic of an example control system for a fuel cell powered aircraft is shown overleaf. This system is not necessarily right or wrong but serves the purpose of giving the reader an idea of the scale of the task required to integrate a fuel cell system into an aircraft. This is made up of the following parts:

1. Flight control unit – This compares flight commands from the pilot with data for the aircraft flight conditions to devise the action required to ensure that the pilots commands are met. In the case of an autonomous aircraft, this is also responsible for the generation of an aircraft flight path.
2. Power delivery unit – This is used to compare the power needs of the motors with the power output from the fuel cell. It is then able to make a decision as to whether the fuel cell output needs to be increased, decreased or maintained at its current value.
3. Fuel cell control unit – This is used to control the power output from the fuel cell to meet the needs of the output demanded from the power delivery unit. This control unit authorises the fuel processor control unit and air delivery unit to supply air and fuel in the proportions required to maintain the power output of the fuel cell.
4. Fuel processor control unit – This is used to regulate the output from the fuel processor and its associated ancillary equipment to generate the hydrogen flow rate demanded by the fuel cell control unit.
5. Air delivery unit – This is used to regulate the quantity of air delivered to the fuel processor and fuel cell, as demanded by the fuel cell control unit.
6. Power switching and conditioning unit – This is used to condition the DC power output from the fuel cell and convert it the AC format required by the motors. This unit also allows the power supply to be switched between a battery supply for starting and in the event of an emergency. Under normal operating conditions, any excess power from the fuel cell is used to charge the battery.
7. Motor controllers – These are used to control the speed and torque of the AC traction motors.

As already stated, this is just one example of a possible fuel cell control system and many other different variants are possible. Hopefully however, it will have given the reader an appreciation of the complexity of such a control system.

Schematic of an example fuel cell powered aircraft control system

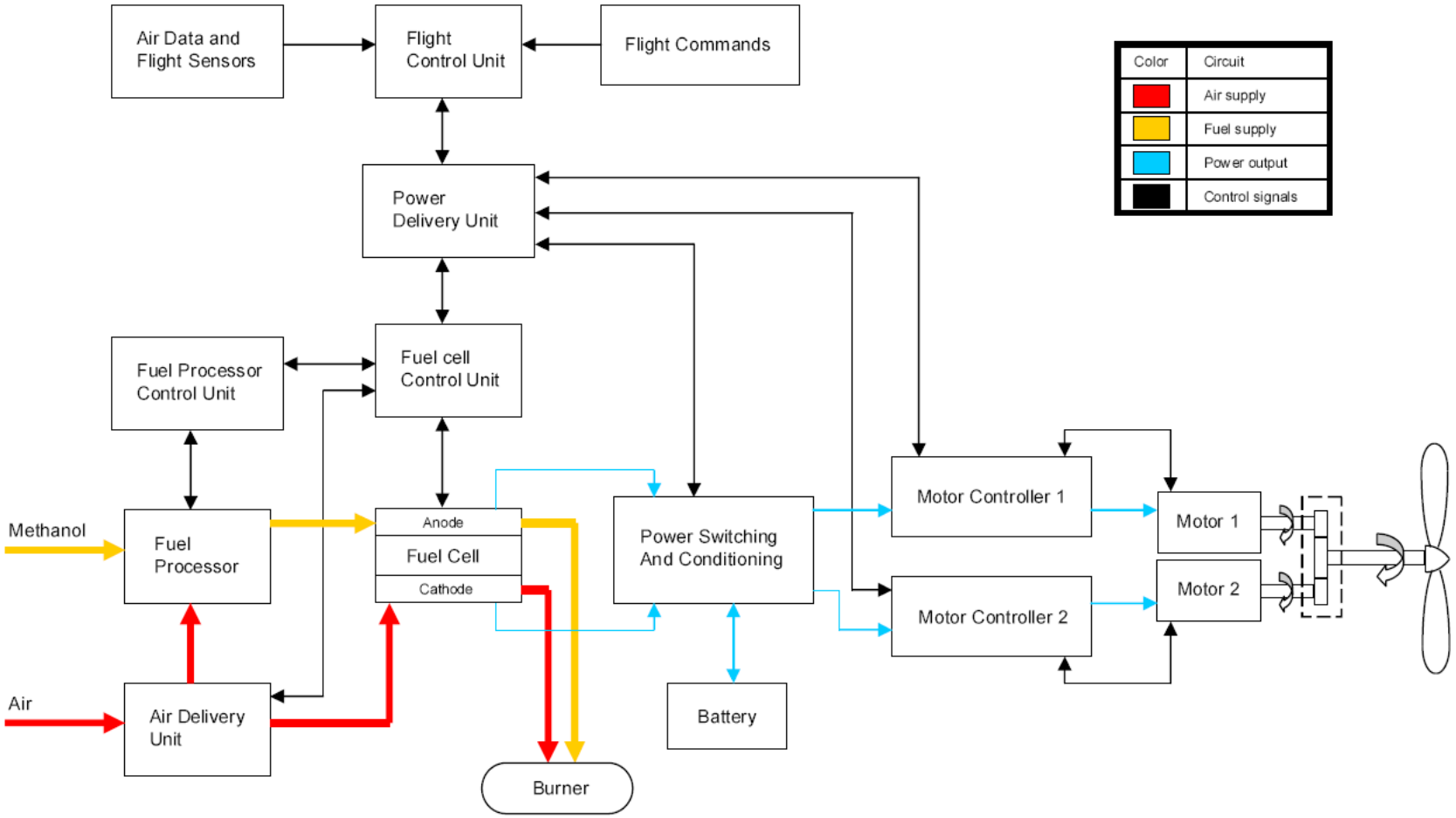

E3 An overview of the fuel processors

In the schematic of the complete fuel cell system, the fuel processor was represented as a simple block but it is actually a system in its own right. The purpose of this section is to give the reader a brief overview of the fuel processor used in this project; they are however advised to refer to the analysis for further details. The two fuel processors discussed briefly in the sections below are the autothermal and the steam reformer.

E3.1 An overview of the autothermal based fuel processor

The layout of the autothermal based fuel processor is presented in the figure below, which also shows the composition of the reformate at each stage within the fuel processor.

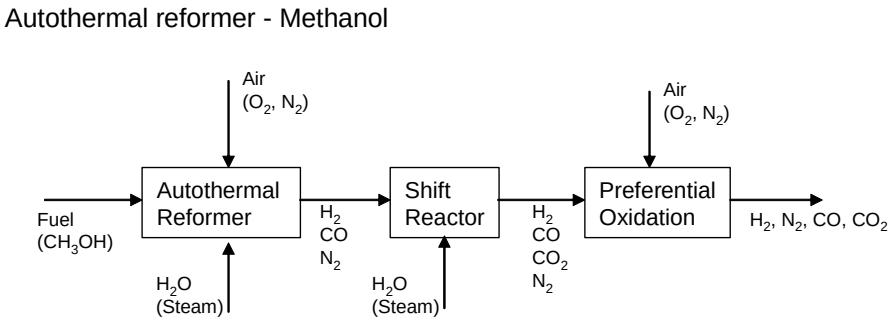

Figure 3-1

The fuel processor block within our complete fuel cell system schematic, then becomes as in the figure below, in which we are merely concerned with the inputs and outputs of the fuel processor.

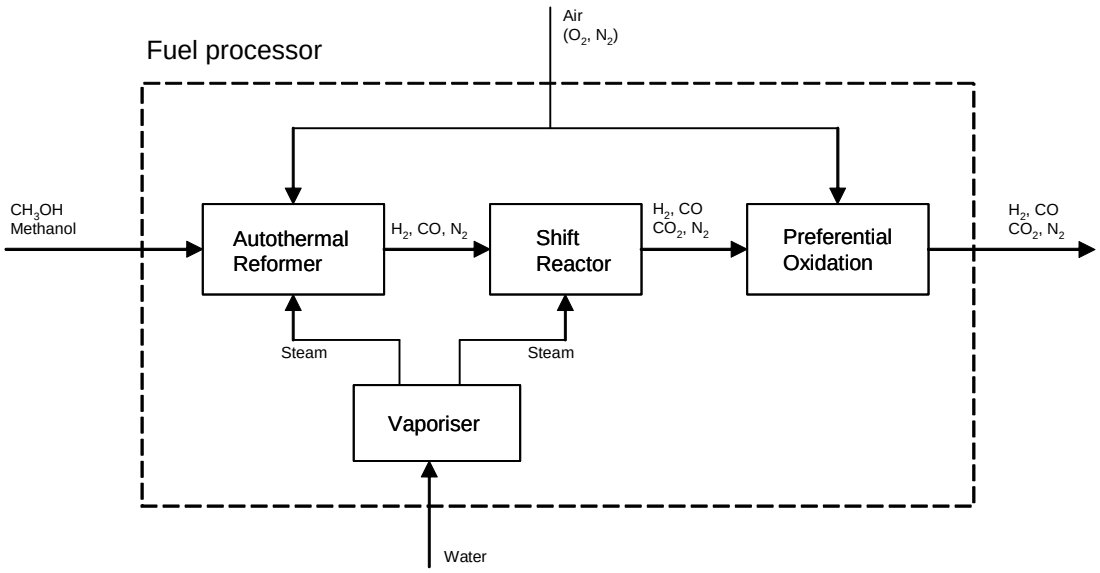

Figure 3-2

E3.2 An overview of the steam reformer based fuel processor

The layout of the steam reformer based fuel processor is presented in the figure below, which also shows the composition of the reformate at each stage within the fuel processor.

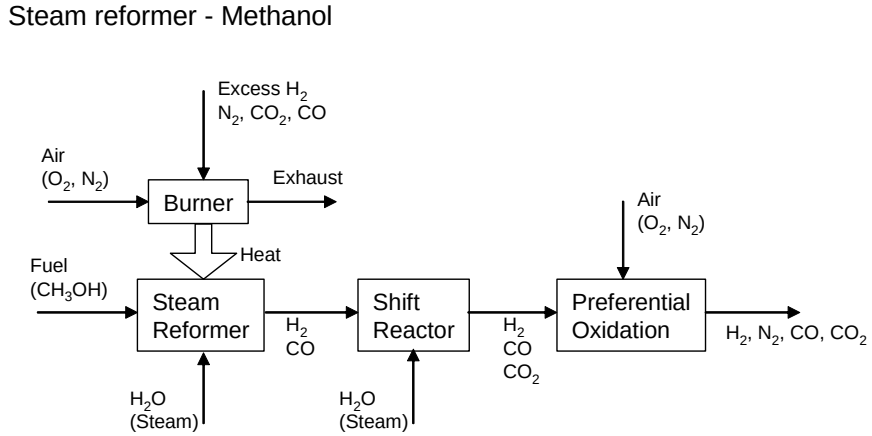

Figure 3-3

The fuel processor block within our complete fuel cell system schematic, then becomes as in the figure below, in which we are merely concerned with the inputs and outputs of the fuel processor.

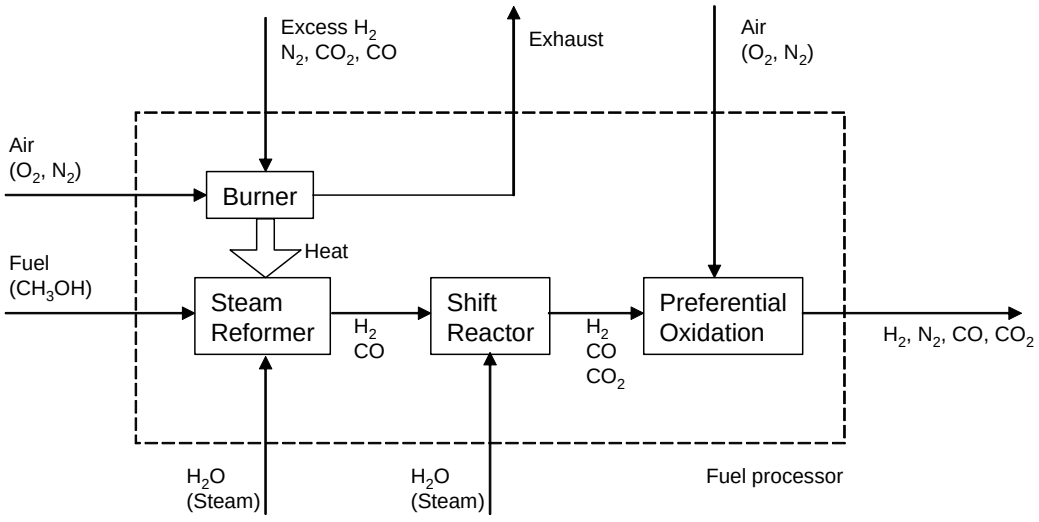

Figure 3-4

E4 Sizing the fuel cell stacks

E4.1 Fuel cell system design requirements

In the fuel cell system requirements section, the end of climb was identified as the most critical point in terms of fuel cell power requirements. This gave us a power demand of 414.51 kW, which our fuel cell system must be sized to meet.

E4.2 Sizing the fuel cell stacks

Since each fuel cell stack is built up of a number of cells which are connected in series, the desired output voltage is achieved by using a relative number of cells in the stack. Each cell is able to deliver the same voltage and thus the total number of cells required in all the stacks to meet our requirements can be determined from the expression below.

$$N_{Cells(Total)} = \frac{P_{Max}}{I_{MaxP} \cdot V_{Cell(MaxP)}} \qquad \text{Eq 4-1}$$

The terms included in this expression are:

- P_{Max} - The maximum power output demands (414.51 kW in this system).
- I_{MaxP} - Typical total system current at maximum power. In this system, a value of 300A was assumed which is consistent with similar existing fuel cell systems (as used by the Ballard Mk 902).
- $V_{Cell(MaxP)}$ - Typical cell voltage at maximum power. In this system, a value of 0.65V was assumed which is consistent with similar existing fuel cells.

When rounded up to the nearest whole number, a total number of cells of 2126 are required in order to be able to meet our power requirements. It is however not practical to construct a single fuel cell stack from so many cells and so this number of cells must be divided over a number of separate stacks instead. This gives us added benefits of:

- Better fuel cell performance – Since there will be a better distribution of reactants within a smaller stack and thus they are more likely to be able to reach each of the separate cells.
- Maintainability – Smaller stacks are more easily removed from the aircraft and rebuilt.
- Operational aspects – A number of the stacks can be shut-down when they are not required. This not only increases the lifespan of the fuel cell stacks but also gives better fuel cell performance, since we are able to avoid low power operation where the internal fuel cell losses (activation losses) are greatest.
- Safety – A system built from a number of separate stacks, enables an individual stack to be safely shut-down in the event of a catastrophic failure. It should be pointed out that a fuel cell system will normally continue to operate with one or more failed cells, although at a much lower power output. Only a serious failure would necessitate the need to shut-down the complete stack.
- Installation – Smaller stacks can be more readily installed within any space requirements, since they are able to be stacked on top of each other if required.

A review of comparable existing fuel cell stacks indicated that a figure of about 600 cells per stack is typical for larger fuel cell stacks. Thus, the number of stacks required to meet our requirements can then be determined from the expression below.

$$N_{Stacks} = \frac{N_{Cells(Total)}}{600} \qquad \text{Eq 4-2}$$

When rounded up to the nearest whole number, this gives us a number of fuel cell stacks of 4. The actual number of cells in each stack is then given by the equation.

$$N_{Cells(Stack)} = \frac{N_{Cells(Total)}}{N_{Stacks}} \qquad \text{Eq 4-3}$$

When rounded up, this gives us a figure of 532 cells per stack and the total number of cells in all the stacks becomes 2128. The maximum power output required from each stack can finally be determined by the equation.

$$P_{Stack} = \frac{P_{Max}}{N_{Stacks}} \qquad \text{Eq 4-4}$$

This gives us a power output requirement of 103.63 kW per stack.

E4.3 The cell active area and total bi-polar plate area

The fuel cell active area is simply the working area of the fuel cell plate, on which the electro-chemical reactions take place to generate the output power. This is an important design parameter within any fuel cell system, which not only defines the maximum power output of each cell but also its size. The layout of a typical fuel cell bi-polar plate is shown in the figure below, with an indication of the fuel cell active area highlighted.

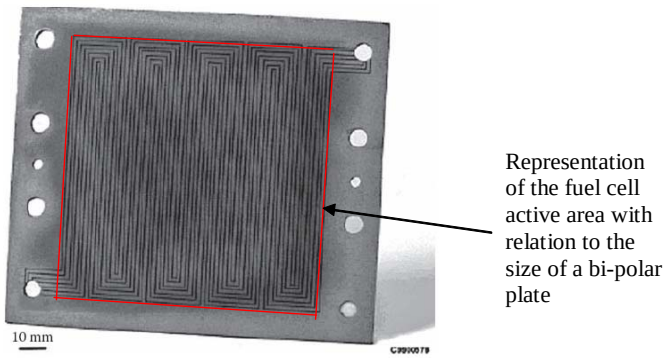

FIGURE 5.3

Figure 4-1 – Fuel cell active area representation [76]

It should be noted that the bi-polar plate does not actually have an active area but since its flow field pattern comes into contact with the active area then this gives a reasonable representation. This concept can be seen in the figure below which shows how the flow field plate makes contact with the anode/membrane/cathode assembly and is therefore a reasonable representation of the fuel cell active area.

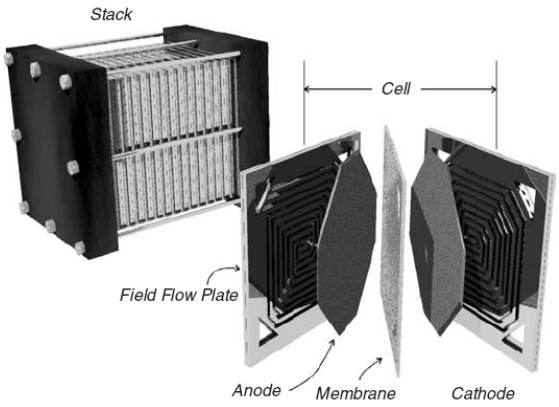

FIGURE 4.2 Fuel cell stack made up of flow field plates (or bipolar plates) and MEAs (shown in the insert).

Figure 4-2 – Fuel cell stack construction [77]

The fuel cell active area is a design variable, the selection of which is influenced by requirements such as power output, voltage, efficiency and physical factors (such as size and mass). A large active area is however not always desirable since this implies a greater current (which leads to bigger connecting cables) and larger fuel cell plates. Another limiting factor with large plates is that it can prove difficult to generate uniform flow conditions within each cell, which can affect fuel cell performance. At the other extreme, a small active area would imply the use of a large number of cells to achieve the same power output. The sheer number of cells required for a large system would make assembly of such a unit difficult. Such a unit would also have problems with reactant distribution and large internal pressure drops within long distribution channels. Typical trends for fuel cell active area with respect to the total number of cells in the stack and the stack power output are presented in the figure below.

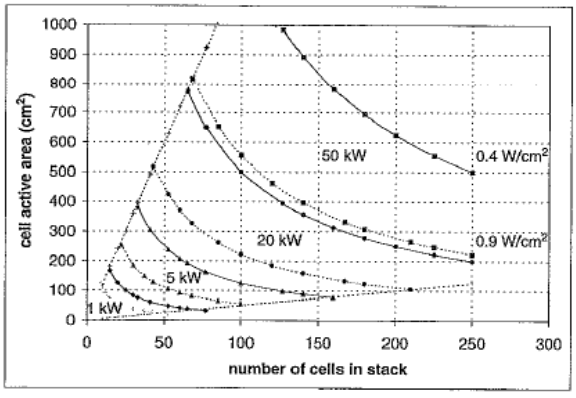

FIGURE 6-1. Fuel cell stack sizing—number of cells and cell active area for different power outputs (solid lines are for 0.4 W/cm² and dashed lines are for 0.9 W/cm²).

Figure 4-3 – Fuel cell active area [57]

In our example, the stack power output and number of cells in the stack is beyond the extremities of the chart above and therefore we must make an estimate from comparable sized existing stacks. A review of similar sized existing stacks manufactured by Ballard

and GM, indicated a active area of 400cm^2. The curves in the above figure also tend towards this value for a large numbers of cells.

An estimate of total area of the bi-polar plate can be made by including an allowance for sufficient overhang around the perimeter of the active area. This overhang is required for sealing the edge of the flow field, aligning and clamping the stack and for distribution of the reactants. In the case of the cells within the Ballard MK4 stacks, the active area was 31% of the electrode area. This figure was increased by a considerable amount to 56% in the Ballard MK5 stacks. As a guideline, the ratio of total plate area to cell active area as used in existing designs is in the range 1.4 to 1.8, though newer designs are likely to be significantly less than this.

E4.4 The overall stack geometry

The procedure used to determine the size and mass of the stack is based on predictions from similar existing designs. In particular, we make use of the parameters, power density and specific power, which are measures of the power per unit volume and power per unit mass respectively. The figures for a number of exiting designs are given in the table below, which also includes some target figures for future fuel cell designs.

Manufacturer	Model	Power density (kW/l)	Specific power (kW/kg)
GM	Gen 7	1.1	0.47
GM	Stack 2000	1.6	0.94
GM	Stack 2001	1.75	1.22
Ballard	Mk 902	1.13	0.8854
Nucellsys	HY80	0.9	N/A
Ballard	Targets for 2010	2.5	N/A
U.S. DOE	Targets for 2010	2	N/A

Table 4-1

The data from this table shows the Stack 2001 as manufactured by GM to be most representative of the current level of fuel cell system technology. The Ballard and U.S. DOE targets show slightly better figures for the power density but in the absence of more accurate data, these may prove to be too optimistic. As development targets are not always achieved by manufacturers, it seems more sensible to rely on actual figures.

In our configuration, we have assumed a fuel cell total area/active area ratio of 1.435 which corresponds to the figures reported for Stack 2001 developed by GM. For a fuel cell active area of 400cm^2 (0.04m^2), this gives us a total cell area of 0.0574m^2. If we also adopt the power density figures reported for Stack 2001 of 1.75 kW/l, then the total volume of each of the four stacks can be determined as below.

$$V_{Stack} = \frac{P_{Stack}}{PowerDensity} = \frac{103.63}{1.75} = 0.05922m^3 \qquad \text{Eq 4-5}$$

Using our estimate of total cell area from above, the stack length is as below.

$$L_{Stack} = \frac{V_{Stack}}{A_{Cell(Total)}} = \frac{0.05922}{0.0574} = 1.03166m \qquad \text{Eq 4-6}$$

If we assume that each cell is square, then the height and width of each cell can be determined from the total cell area as below.

$$W_{Cell(Total)} = H_{Cell(Total)} = \sqrt{A_{Cell(Total)}} = 239.6mm \quad \text{Eq 4-7}$$

Design recommendations in the literature suggest that the maximum number of cells in a stack is typically between 200 and 250. Therefore, in this design we have opted for two rows of cells in our stack in order to make the required number of 532 cells per stack. This gives us the final stack configuration below.

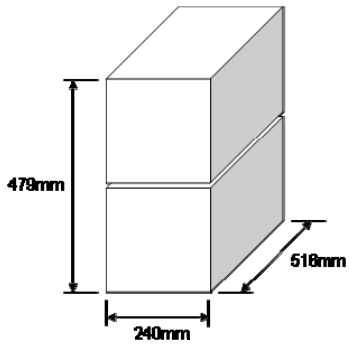

Figure 4-4

In a similar way, the mass of the stack can be predicted from the specific power figures of similar existing units. Using the figures from GM for their Stack 2001, the specific power was estimated to be 1.2439 kW/kg. The stack mass was thus determined as.

$$M_{Stack} = \frac{P_{Stack}}{SpecificPower} = \frac{103.63}{1.2439} = 83.31kg \quad \text{Eq 4-8}$$

E4.5 The cell flow field geometry

Any fuel cell must have some sort of flow field pattern cut into the bi-polar plate in order to distribute the reactants to the fuel cell anode and cathode. Some of the patterns commonly encountered include, parallel channel, serpentine flow field (patented by Ballard), mirrored flow field (patented by GM), interdigitated flow field and mesh. This list is by no way exhaustive and there are numerous different patterns available, each of which has its own advantages and disadvantages. Important considerations for flow field designs are:

- Adequate membrane electrode assembly support – Sufficient support must be available to securely hold the MEA.
- Ability to distribute the reactants effectively and uniformly – There must be an adequate distribution of reactants to all parts of the fuel cell. This distribution should also be as uniform as possible to prevent an undesired mix of concentration hot spots and concentration depleted areas which would result in undesirable voltage variations across the fuel cell.
- Blockage – The layout of the flow field should be able to prevent blockage of the channel due to factors such as a build-up of the by-product of water.
- Manufacture – More complex flow field patterns can be significantly more complicated and timely to manufacture and are therefore more costly.

In these studies, we have opted for a multiple parallel serpentine design as used by Ballard, which is illustrated in the figure below.

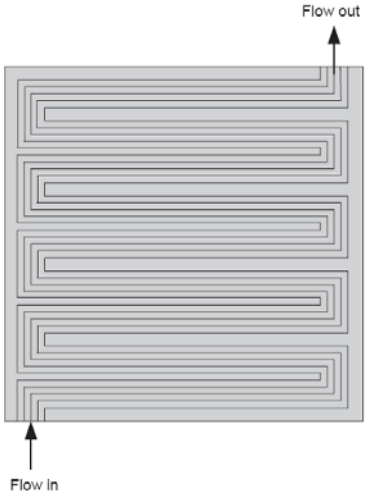

FIGURE 10-3. Multiple serpentine flow channel design.

Figure 4-5 – Flow field channel design [78]

To further aid visualisation of the concept, a cross section of serpentine anode and cathode flow channels in contact with the fuel cell is given in the figure below.

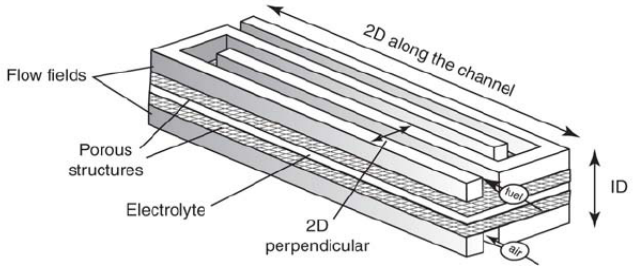

FIGURE 15.1 Schematic of a slice through a fuel cell. Dimensions indicated are: 1D, orthogonal to the electrolyte; 2D along the channel, combining the 1D and the direction along the channel; 2D perpendicular, combining the 1D and the direction perpendicular to the main flow.

Figure 4-6 – Flow field cross section [79]

As well as the design of the flow field, the dimensions of the flow field channels have an important influence on the performance of the fuel cell. Large channels are able to distribute the reactants effectively but offer little support for the fuel cell. At the other end of the scale, small channels are more susceptible to blockages. For square channel profiles, channels with dimensions of 1mm by 1mm (width by depth) with 1mm spacing between channels are typically used in current designs. Studies have however reported that channels with dimensions of 1.5mm by 1.5mm with 0.5mm spacing between the channels are the optimal configuration. These dimensions have thus been taken as the next generation of technology within the fuel cell industry and have been used for the purposes of our high technology studies. These larger reactant channels will be especially useful in our configuration since they will help to reduce the pressure drop across the channels. This is especially important for high altitude and low pressure operation as with our design and will reduce our compressor power requirements.

As well as being able to distribute the oxygen and hydrogen reactants, the bi-polar plate must also have sufficient provision for cooling. In small fuel cell systems, cooling can be achieved by supplying an excess of air to the fuel cell. In larger systems however an additional means of cooling must be used, which is typically achieved by passing coolant through the bi-polar plate as well. An example of such a configuration is shown in the figure below.

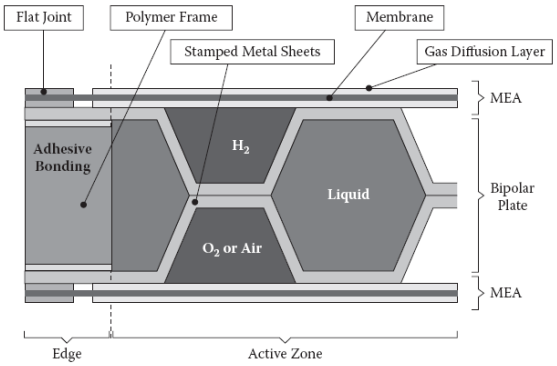

FIGURE 5.8
Architecture of stamped metal plate concept with MEAs. (Reprinted with permission from Granier, J. 2004–2005. *CLEFS CEA* 50/51: 76–78.)

Figure 4-7 – Cross section through fuel cell assembly [76]

E4.6 The fuel cell control unit

In the absence of better data the fuel cell control unit of the NuCellSys HY-80 was scaled up with respect to the ratio of fuel cell power outputs (from 68kW to 103.63kW). The unit was therefore scaled up from 80x181x168mm to 92x208x193mm.

E5 Sizing the fuel processor

The fuel processor must be sized to be able to deliver sufficient hydrogen to the fuel cell to enable it to operate effectively at its maximum power condition. Since our system utilises four separate fuel cell units, it makes sense to use four separate fuel processors as well. As such, each fuel cell unit has its own corresponding fuel processor. As for the fuel cell units, such a configuration enables the fuel processors that are not required to be shut down in order to improve the efficiency of the system.

In practice, a fuel processor would be sized according to the maximum hydrogen output it must be able to deliver. Such hydrogen flow rate data is readily available for our analysis but is not so readily available for existing fuel processors. Fortunately, it is now convention for the size and mass of a fuel processor to be defined with respect to the maximum power output of the fuel cell which it supplies hydrogen to. We are therefore able to determine the size and mass of the fuel processor using statistical estimates from existing designs. The parameters of particular importance are the power density and specific power, which are measures of the power per unit volume and power per unit mass respectively. The figures for a number of exiting designs are given in the table below, which also includes targets for future fuel processor designs.

Manufacturer	Model	Power density (kW/l)	Specific power (kW/kg)
U.S. DOE	Targets for 2010	0.8	0.8
Ballard	ME-75-6	1.172	N/A
Daimler	Necar 3	1.1	0.44
GM	Fuel Processor	0.5	0.44

Table 5-1

Since the Ballard ME-75-6 is a current unit, it is reasonable to use these figures for our system. In the absence of a specific power figure from the literature, this has been assumed to be the same as the figure for the power density, which correlates with the figures given for the U.S. DOE 2010 targets. Using the power density figures reported for the Ballard ME-75-6 the total volume of each of the four fuel processors can be determined as below.

$$V_{Stack} = \frac{P_{Stack}}{PowerDensity} = \frac{103.63}{1.172} = 0.08843m^3 \qquad \text{Eq 5-1}$$

In a similar way, the mass of each fuel processor can be determined from the Ballard ME-75-6 specific power estimate as given below.

$$M_{Stack} = \frac{P_{Stack}}{SpecificPower} = \frac{103.63}{1.172} = 88.43kg \qquad \text{Eq 5-2}$$

If the dimensions of the ME-75-6 fuel processor are rescaled in the correct proportions, to achieve the volume figures predicted above, the final dimensions of each of the four fuel processors will be as given in the figure.

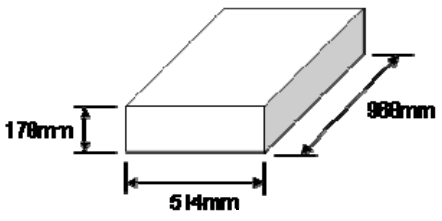

Figure 5-1

F1 Evaluation of the NFCC altitude predictions

F1.1 Derivation of a general relation

The purpose of this work was to convert the experimental test results from the AIAA paper [50], as given below, into a format more suitable for analytical work. We are able to use this chart to generate a table of Flow vs. Pressure, which enables the data to be re-plotted as stack voltage vs. airflow at a number of pressures, as below.

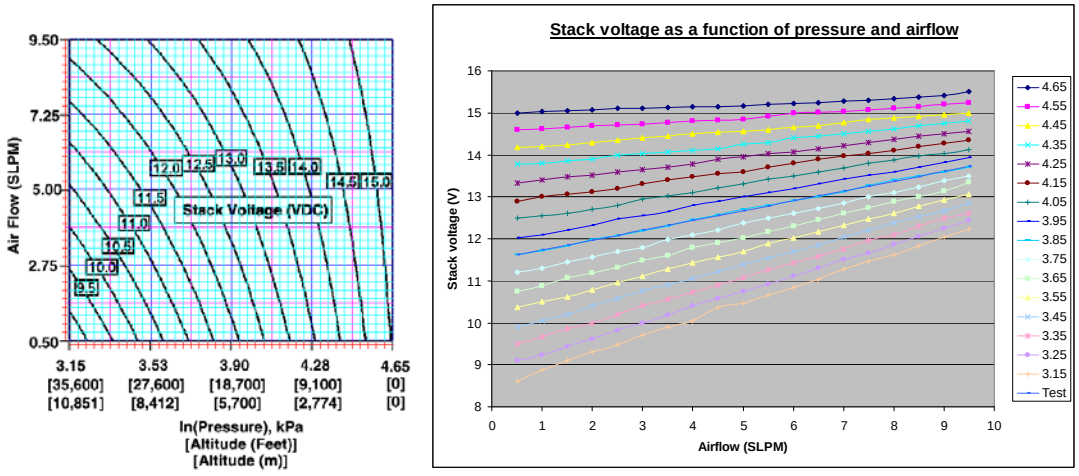

Figure 1 [50] and Chart 2 – Voltage vs. airflow

To each of the curves in the chart above, a trend line can be fitted and a polynomial expression obtained. Examination of the coefficients of each of these polynomial expressions then enables us to determine a global expression for the stack. The voltage of a single cell within the 23 cell experimental stack as a function of atmospheric pressure and flow rate can then determined from,

$$V_{Cell} = \frac{1}{23}\left[\{-0.232(\ln P)+1.1273\}(AF)+\{4.3395(\ln P)\}-5.2091\right] \quad \text{Eq 1}$$

Where ln P is given by the relation below and H is the altitude in meters.

$$(\ln P) = \ln\left(1.01325E2\cdot\left[\frac{288.15}{288.15-(H\cdot 6.5E-3)}\right]^{-5.25588}\right) \quad \text{Eq 2}$$

Using this expression, the variation in voltage due to either a change in pressure from P1 to P2 or a change in airflow from AF1 to AF2 can be determined as the ratio of V_2 and V_1. After simplifying, the voltage variation from sea level conditions becomes,

$$\frac{V_2}{V_{SL}} = \frac{\{-0.232(\ln P_2)+1.1273\}(AF_2)+\{4.3395(\ln P_2)\}-5.2091}{0.05585(AF)+14.8322} \quad \text{Eq 3}$$

The term AF in the above relations is the equivalent airflow given in standard litres per minute at 20ºC and 1atm. This can be converted in to actual LPM with the expression,

$$LPM = \left(\frac{P_{1Atm}}{P_{Actual}}\right)\cdot\left(\frac{T_{Actual}}{T_{20°C}}\right)\cdot SLPM \quad \text{Eq 4}$$

F1.2 Evaluation of the results

There were plans to convert the expressions above to use stoichiometric ratio instead of the airflow rate and thus be in a format more general to any fuel cell. However, such a task would require knowledge of the operational characteristics of the fuel cell at any given point. In particular, to be able to determine the stoichiometric ratio, we need to be able to determine the theoretical airflow. This is however dependent on parameters such as pressure, concentration, temperature and current density. In the original experiments, the tests were carried out with a fixed external resistance load and thus if the voltage across the resistor in known, the current through it can be easily determined. The concentration can be assumed to be constant since atmospheric air was used and the operating pressure is also known (being an experiment variable). The only temperature given in the results is that of the air entering the fuel cell, which is not indicative of fuel cell operating temperature. The operating temperature is thus an unknown.

Using a number of ball-park assumptions and a first pass analysis, it was believed that the temperature was variable throughout the experiments, as shown below. This is to be expected since operation at high stoichiometric ratios is known to have a cooling effect.

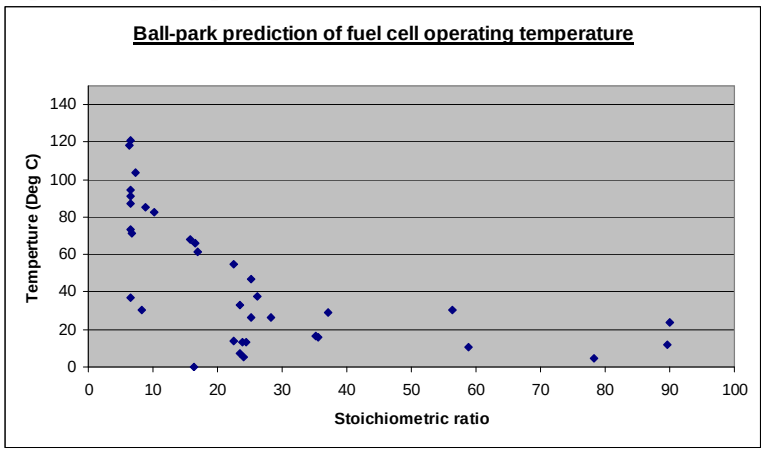

Figure 2 – Ballpark predictions for the effect of temperature

If we were to test a fuel cell at standard conditions over a range of temperatures, the dependency of the output voltage on the operating temperature would be apparent. The results from the AIAA study are thus deemed questionable. This study also makes reference to another research paper which discusses the effect that variations in stoichiometric ratio can have on fuel cell output voltage. The AIAA study however was for an estimated range of stoichiometric ratios from 3 to 60 and the research paper referred to is only valid for stoichiometric ratios up to 3.

Although the results in the AIAA paper showed initial promise, the author of this thesis had no further choice but to abandon the use of the data. Much later on in this project, the author of the AIAA paper finally responded to questions put to him about his work and produced additional data which was not included in the AIAA paper. This data did confirm that considerable variations in the operating temperature of the fuel cell were experienced during testing. There is therefore a strong possibility that the voltage variations experienced are predominantly due to variation in operating temperature and not pressure and airflow. It was however unfortunately too late in this project to be able to revisit this work and alternative theoretical approaches had already been adopted.

G1 Derivation of equations for the fuel cell

In order to be able to derive the equations required for the analysis of the fuel cell it is necessary to understand the electrochemical reactions taking place. The process typically involves simultaneous reactions at the anode and cathode as given below for a hydrogen fuel cell.

The anode reaction: $H_2 \rightarrow 2H^+ + 2e^-$ Eq 1-1

The cathode reaction: $\frac{1}{2}O_2 + 2H^+ + 2e^- \rightarrow H_2O$ Eq 1-2

The combined reaction is then: $H_2 + \frac{1}{2}O_2 \rightarrow H_2O$ Eq 1-3

Air requirements

From inspection of the cathode reaction it is evident that 4 electrons must travel around the electrical circuit for each mole of oxygen used in order to complete the reaction. The quantity of charge transferred is then as below, where F is the Faraday Constant (which is the charge on one mole of electrons) and $\dot{N}$ is the flow rate of moles per second.

$$Q = 4 \cdot F \cdot \dot{N}_{O2}$$ Eq 1-4

For a stack of n cells, the oxygen usage then becomes,

$$\dot{N}_{O2} = \frac{In}{4F}$$ Eq 1-5

Using the relation below for the power of a fuel cell stack, a more convenient form of the equation above can be obtained on a molar mass basis as given below.

Power of a fuel cell stack: $P_{St} = V_{Cell} \cdot I \cdot n$ Eq 1-6

The mass flow rate of oxygen: $\dot{m}_{O2} = \frac{P_{St}}{4 \cdot V_{Cell} \cdot F} \cdot M_{O2}$ Eq 1-7

Air is however typically used instead of O_2 for practical reasons and allowance must be made in the equations by including an oxygen fraction. As well as this, it is also practical to supply air in excess of that predicted by theory, which is defined by an oxygen stoichiometric ratio. The final form of the equation then becomes.

$$\dot{m}_{Air} = \frac{P_{St}}{4 \cdot V_{Cell} \cdot F} \cdot \frac{S_{O2}}{r_{O2}} \cdot M_{O2}$$ Eq 1-8

Hydrogen requirements

From inspection of the cathode reaction, it is apparent that in order to complete the reaction 2 electrons must travel around the circuit for each mole of hydrogen. By following the same procedure as before, the mass flow rate of hydrogen is obtained. In this case, direct hydrogen is used which for practical reasons must also supplied in excess, as is defined by a hydrogen stoichiometric ratio.

$$\dot{m}_{H2} = \frac{P_{St}}{2 \cdot V_{Cell} \cdot F} \cdot S_{H2} \cdot M_{H2}$$ Eq 1-9

Water production in the fuel cell

The equation for the production of water in the fuel cell is derived by the same process as for the air and hydrogen requirements. In this case however, examination of the

cathode reaction shows that 2 electrons must travel around the circuit for each mole of water produced. The required equation is then as below.

$$\dot{m}_{H_2O-FC(Gen)} = \frac{P}{2 \cdot V_{Cell} \cdot F} \cdot M_{H_2O} \quad \text{Eq 1-10}$$

Quantity of nitrogen entering the fuel cell from the air

The derivation for the quantity of nitrogen entering the fuel cell is the same as that for the air but with the addition of the fraction of nitrogen present in the air as below.

$$\dot{m}_{N2-air(in)} = \frac{P}{4 \cdot V_{Cell} \cdot F} \cdot S_{O2} \cdot \frac{(1 - r_{O2})}{r_{O2}} \cdot M_{N2} \quad \text{Eq 1-11}$$

Quantity of water vapour entering the fuel cell from the air

The definition of humidity ratio gives us: $\omega = \frac{m_w}{m_a}$ Eq 1-12

Where the subscripts w and a represent water and air respectively. Noting that the mass of an element is the product of its partial pressure and molecular mass, this gives us.

$$\omega = \frac{P_w \cdot M_w}{P_a \cdot M_a} \quad \text{Eq 1-13}$$

Here, we also make use of the definition of relative humidity, which is a function of the partial pressure of water (P_w) and the saturated vapour pressure of the water (P_{Sat}).

The relative humidity is defined as: $\phi = \frac{P_w}{P_{Sat}}$ Eq 1-14

It should be noted that the partial pressure of air can also be obtained from the total pressure of air and the partial pressure of water as below.

$$P_a = P - P_w \quad \text{Eq 1-15}$$

Substitution of these into the humidity ratio then gives us.

$$\omega = \frac{m_w}{m_a} = \frac{M_w \cdot \phi \cdot P_{Sat}}{M_a \cdot (P - \phi \cdot P_{Sat})} \quad \text{Eq 1-16}$$

After rearranging, the above becomes.

$$\dot{m}_w = \frac{M_w \cdot \phi \cdot P_{Sat}}{M_a \cdot (P - \phi \cdot P_{Sat})} \cdot \dot{m}_a \quad \text{Eq 1-17}$$

Substitution for the mass flow of air entering the fuel cell we then finally obtain.

$$\dot{m}_{H_2O-FC(Air-in)} = \dot{m}_{Air-FC(in)} \cdot \frac{M_{H_2O}}{M_{Air}} \cdot \frac{\phi_{Amb} \cdot P_{VS}(@T_{FC(in)})}{P_{FC(in)} - \phi_{Amb} \cdot P_{VS}(@T_{FC(in)})} \quad \text{Eq 1-18}$$

The total volumetric flow rate of humid air entering the fuel cell can then be obtained by dividing the derivations for air and water vapour entering the fuel cell by the density of humid air. The result is as given below.

$$Q_{Stack} = \frac{P}{4 \cdot V_{Cell} \cdot F} \cdot \left(\frac{S_{O2}}{r_{O2}} \right) \cdot \frac{R \cdot T_{FC(in)}}{P_{FC(in)} - \phi_{FC(in)} \cdot P_{VS}(@T_{FC(in)})} \cdot 10^6 \quad \text{Eq 1-19}$$

Saturated vapour pressure at the exit of a operational fuel cell

One of the problems associated with fuel cell operation at low pressures is an increase in water content of the air at these conditions. This can result in a decrease in

performance of the fuel cell and therefore must be carefully controlled. Since the vast majority of existing fuel cells work at standard sea level conditions, it makes sense to replicate these conditions as much as possible at altitude. This would mean operating the fuel cell with the same humidity ratio under these different conditions.

To solve this problem, it is first necessary to determine what a typical humidity ratio is for standard sea level operation. Using the general equation above for humidity ratio, this maximum allowable humidity ratio can be derived by substitution of the relevant parameters for standard sea level operation, as given below.

$$\omega_{Max} = \frac{M_w \cdot \phi \cdot P_{Sat}}{M_a \cdot \left(P - \phi \cdot P_{Sat}\right)} \qquad \text{Eq 1-20}$$

The next stage then involves the use of the alternative form of the equation for the humidity ratio as given below.

$$\frac{m_w}{m_a} = \frac{M_w \cdot \phi \cdot P_{Sat}}{M_a \cdot \left(P - \phi \cdot P_{Sat}\right)} \qquad \text{Eq 1-21}$$

Rearranging this equation to solve for P_{Sat} gives the following.

$$P_{Sat-FC(exit)} = \frac{P_{@\,i-1}}{\phi_{Air(in)} \cdot \left(\left\{ \frac{M_{H_2O}}{\omega_{Air-Max(in)} \cdot M_{Air}} \right\} + 1 \right)} \qquad \text{Eq 1-22}$$

The P_{Sat} result can then be used to determine the associated T_{Sat}, and therefore the desired operating temperature of the fuel cell.

G2 Derivation of the equations for the analysis of the autothermal reformer

Analysis of the autothermal reformer

The overall equation for an autothermal process (including shift reaction) is,

$$C_mH_nO_p + \chi O_2 + (2m - p - 2\chi)H_2O \rightarrow mCO_2 + \left(2m + \frac{n}{2} - p - 2\chi\right)H_2 \qquad \text{Eq 2-1}$$

Where χ represents the quantity of oxygen (in moles of oxygen per mole of fuel) which is required to attain either an endothermic, exothermic or thermoneutral reaction (autothermal). Since χ varies with fuel composition, the standard practice is to use an equivalence ratio, as defined below.

$$\varepsilon = \frac{m + \frac{n}{4} - \frac{p}{2}}{\chi} \qquad \text{Eq 2-2}$$

The equivalence ratio is directly related to the efficiency of the reforming process with a gain in hydrogen output being experienced with an increase in the equivalence ratio. The theoretical efficiency limit is 100% but there is a practical limit to prevent carbon formation in the fuel processor. As a result, the equivalence ratio used is always less than the theoretical value required to achieve an autothermal process.

Incorporating the equivalence ratio, the equation for an autothermal process becomes.

$$C_mH_nO_p + \frac{m + \frac{n}{4} - \frac{p}{2}}{\varepsilon}O_2 + \frac{(\varepsilon - 1)(2m - p) - \frac{n}{2}}{\varepsilon}H_2O \rightarrow mCO_2 + \left(2m + \frac{n}{2} - p\right)\left(1 - \frac{1}{\varepsilon}\right)H_2 \qquad \text{Eq 2-3}$$

In addition to operation at lower values of equivalence ratio, the problem of carbon formation can be alleviated somewhat by adding excess steam to the reaction. A steam to carbon ratio σ (molar fraction of steam to carbon in the fuel) in the range of 2-3 is typically used for this purpose.

In an actual reforming process, allowance also needs to be made for other limiting factors such as the composition of air, fuel slip and incomplete reactions. An actual reforming reaction including all these factors can thus be defined as.

$$C_mH_nO_p + \frac{m + \frac{n}{4} - \frac{p}{2}}{\varepsilon}O_2 + \frac{1 - r_{O2}}{r_{O2}}\frac{m + \frac{n}{4} - \frac{p}{2}}{\varepsilon}N_2 + \sigma H_2O \qquad \text{Eq 2-4}$$

$$\rightarrow aC_mH_nO_p + bCH_4 + cCO_2 + dCO + eN_2 + fH_2 + gH_2O$$

The output from an actual reactor can thus be seen to consist of following elements (as defined by their coefficients). Also listed is the role of each of the elements within a PEM fuel cell.

a – Fuel slip
b – Incomplete reactions (dilutant)
c – Carbon dioxide (dilutant)
d – Carbon monoxide (poisonous to a PEM fuel cell)

e – Nitrogen (from the air) (dilutant)
f – Hydrogen (fuel)
g – Water (dilutant)

In the case of methanol (CH_3OH) as used in this study, the actual reforming reaction will be as given below, where the composition for methanol is, m=1, n=4 and p=1. The fuel slip in this case is typically minimal in comparison to the other elements and is often disregarded.

$$CH_3OH + \frac{1.5}{\varepsilon}O_2 + \frac{1-r_{O2}}{r_{O2}}\frac{1.5}{\varepsilon}N_2 + \sigma H_2O \rightarrow bCH_4 + cCO_2 + dCO + eN_2 + fH_2 + gH_2O$$

Eq 2-5

The equation above can be solved by means of an atom balance of the constituent parts, in order to determine the different reformate quantities leaving the reformer.

Carbon balance: $1 = b + c + d$

Oxygen balance: $\frac{3}{\varepsilon} + \sigma = 2c + d + g$

Hydrogen balance: $4 + 2\sigma = 4b + 3f + 2g$

Nitrogen balance: $e = \frac{1.5}{\varepsilon}\left(\frac{1-r_{O2}}{r_{O2}}\right)$

The atom balances above gives four of the six equations needed to solve the six unknown coefficients in the equation above. The remaining two equations required can be found from the required hydrogen and carbon monoxide content in the dry reformate gas, as given below.

CO content: $r_{CO} = \frac{d}{b + c + d + e + f}$ Eq 2-6

By substitution of the relations for the carbon and nitrogen into the expression above, this reduces to the form below. An operating requirement of PEM fuel cells is that the carbon monoxide in any reformate must be kept below 1% to prevent the fuel cells from being poisoned. Substitution of this figure thus enables the equation to be solved.

$$r_{CO} = \frac{d}{1 + \frac{1.5}{\varepsilon}\left(\frac{1-r_{O2}}{r_{O2}}\right) + f} = 0.01$$ Eq 2-7

In a similar way, the hydrogen content in the dry reformate gas gives.

$$r_{H2} = \frac{f}{1 + \frac{1.5}{\varepsilon}\left(\frac{1-r_{O2}}{r_{O2}}\right) + f}$$ Eq 2-8

From the definition of fuel processor efficiency, the hydrogen output can be determined as below.

$$f = \eta_{Actual}\frac{\Delta H_{Fuel}}{\Delta H_{H2}}$$ Eq 2-9

In cases where the hydrogen fraction is known, then the equation for hydrogen content can be solved for the hydrogen output as below.

$$f = \frac{r_{H2} \cdot \left(1 + \frac{1.5}{\varepsilon}\left[\frac{1 - r_{O2}}{r_{O2}}\right]\right)}{1 - r_{H2}} \quad \text{Eq 2-10}$$

Solving for the other unknown constants gives,

$$a = 0 \quad \text{Eq 2-11}$$

$$e = \frac{1.5}{\varepsilon}\left(\frac{1 - r_{O2}}{r_{O2}}\right) \quad \text{Eq 2-12}$$

$$d = r_{CO}\left(1 + \frac{1.5}{\varepsilon}\left[\frac{1 - r_{O2}}{r_{O2}}\right] + f\right) \quad \text{Eq 2-13}$$

$$b = \frac{8 - 2f - 2d - \frac{6}{\varepsilon}}{8} \quad \text{Eq 2-14}$$

$$c = \frac{\frac{6}{\varepsilon} + 2f - 6d}{8} \quad \text{Eq 2-15}$$

$$g = \frac{\frac{3}{\varepsilon} + 2\sigma - f + d}{2} \quad \text{Eq 2-16}$$

The quantity of hydrogen required by the fuel cell (on a molar basis) is given by the expression below from the fuel cell derivations.

$$\dot{N}_{H2} = S_{H2} \cdot \frac{P}{2 \cdot V_{Cell} \cdot F} \quad \text{Eq 2-17}$$

Multiplication of this result by the molar mass of hydrogen gives the result on a mass flow basis instead. This result can then be used to find the mass flow rate of methanol entering the reformer by using f from above, the reciprocal of which gives the moles of methanol required to achieve the required hydrogen output.

$$\dot{m}_{Fuel} = S_{H2} \cdot \frac{P}{2 \cdot V_{Cell} \cdot F} \cdot \frac{M_{Fuel}}{f} \quad \text{Eq 2-18}$$

The quantity of air required for the fuel processor can be seen to be proportional to the mass flow rate of methanol entering the system. The relationship between these can be obtained from the general form of the actual reforming relation given above. This also includes an O_2 fraction to allow for the use of air as opposed to oxygen.

$$\dot{m}_{Air-FP(in)} = S_{H2} \cdot \frac{P}{2 \cdot V_{Cell} \cdot F} \cdot \frac{1}{f} \cdot \frac{m + n/4 - p/2}{\varepsilon} \cdot \frac{M_{Air}}{r_{O2}} \quad \text{Eq 2-19}$$

Water consumed by the fuel processor is once again relative to the rate of methanol entering the system. In this case however, for simplicity the relationship is obtained from the ideal relation for an autothermal process. The error in doing so can be considered minimal.

$$\dot{m}_{H_2O-FP(Cons)} = S_{H2} \cdot \frac{P}{2 \cdot V_{Cell} \cdot F} \cdot \frac{1}{f} \cdot \frac{(\varepsilon - 1)(2m - p) - n/2}{\varepsilon} \cdot M_{H_2O}$$ Eq 2-20

Analysis of the preferential oxidation unit

The purpose of the preferential oxidation unit is to reduce the CO content of the reformate and therefore the air for the unit will be proportional to the CO content. This process is defined by the reaction $CO + \frac{1}{2} O_2 \rightarrow CO_2$. Eq 2-21

The first part of the derivation below presents the CO flow rate as a function of the hydrogen flow rate and then the remaining part takes into account the air requirements as a function of the CO rate. Here, the divisor of 2 relates to the PROX reaction of moles of air per mole of CO. The PROX stoichiometric ratio (S_{PROX}) ensures that there is sufficient O_2 for the reaction and as before the O_2 fraction allows for the use of air instead of O_2.

$$\dot{m}_{Air-PROX(in)} = S_{H2} \cdot \frac{P}{2 \cdot V_{Cell} \cdot F} \cdot \frac{r_{CO}}{f} \cdot \left(1 + \frac{m + n/4 - p/2}{\varepsilon} \cdot \frac{1 - r_{O2}}{r_{O2}} + f \right) \cdot \frac{S_{PROX}}{2} \cdot \frac{M_{Air}}{r_{O2}}$$ Eq 2-22

Water generated by the preferential oxidation unit is derived in a similar way as for the air requirement of the PROX unit but with a different final relation in accordance with the PROX reaction.

$$\dot{m}_{H_2O-PROX(Gen)} = S_{H2} \cdot \frac{P}{2 \cdot V_{Cell} \cdot F} \cdot \frac{r_{CO}}{f} \cdot \left(1 + \frac{m + n/4 - p/2}{\varepsilon} \cdot \frac{1 - r_{O2}}{r_{O2}} + f \right) \cdot (S_{PROX} - 1) \cdot M_{H_2O}$$ Eq 2-23

Other elements included in the composition of the reformate

The other elements which leave the fuel processor along with the hydrogen include nitrogen, water vapour, carbon monoxide and carbon dioxide. Since the water vapour and CO are typically small in comparison to the other elements, these are however often neglected. Using the derivation above for the hydrogen output from the fuel processor, the total reformate output can be obtained. Division of the hydrogen output by the hydrogen fraction leaving the fuel processor gives the result below (on a molar basis).

$$\dot{N}_{\text{Re } formate} = \frac{P}{2 \cdot V_{Cell} \cdot F} \cdot \frac{S_{H2}}{r_{H2}}$$ Eq 2-24

The mass flow rate of nitrogen leaving the fuel reformer is easily obtained from the product of the total reformate output, the nitrogen fraction for the reformate and the molar mass of nitrogen. This gives the result as follows.

$$\dot{m}_{N2-fuel(in)} = \frac{P}{2 \cdot V_{Cell} \cdot F} \cdot \frac{S_{H2}}{r_{H2}} \cdot r_{N2} \cdot M_{N2}$$ Eq 2-25

In a similar way, mass flow rate of carbon dioxide can be derived as.

$$\dot{m}_{CO2-fuel(in)} = \frac{P}{2 \cdot V_{Cell} \cdot F} \cdot \frac{S_{H2}}{r_{H2}} \cdot r_{CO2} \cdot M_{CO2}$$ Eq 2-26

G3 Derivation of the equations for the analysis of the steam reformer

Analysis of the steam reformer fuel processor

The overall equation for a steam reforming process is,

$$C_m H_n O_p + mH_2O + Heat_{SR} \rightarrow (m-p)CO + pCO_2 + \left(m + \frac{n}{2}\right)H_2 \quad \text{Eq 3-1}$$

The steam reforming process must be preceded by a gas shift reaction, given below.

$$CO + H_2O(g) \rightarrow CO_2 + H_2 + Heat_{GSR} \quad \text{Eq 3-2}$$

The combined reaction for the complete fuel processor including the steam reforming process and the gas shift reaction is then.

$$C_m H_n O_p + (2m-p)H_2O + X_{Heat} \rightarrow mCO_2 + \left(2m + \frac{n}{2} - p\right)H_2 \quad \text{Eq 3-3}$$

In the case of systems which use an additional quantity of fuel (k) to generate the steam for the process, the additional combustion process is given by.

$$kC_m H_n O_p + k\left(m + \frac{n}{4} - p\right)O_2 \rightarrow kmCO_2 + k\left(\frac{n}{2}\right)H_2O + X_{Heat} \quad \text{Eq 3-4}$$

In this case, the efficiency of the steam reforming process is,

$$\eta = \frac{\left(2m + \frac{n}{2} - p\right)}{(1+k)} \cdot \frac{\Delta H_{H2}}{\Delta H_{Fuel}} \quad \text{Eq 3-5}$$

Where the steam for the process is obtained from some source other than the combustion of additional fuel, the efficiency becomes.

$$\eta = \left(2m + \frac{n}{2} - p\right) \cdot \frac{\Delta H_{H2}}{\Delta H_{Fuel}} \quad \text{Eq 3-6}$$

Keeping the same convention as for the autothermal reformer, the output from a steam reformer can be obtained from inspection of the reaction above, as given below.

$$f = 2m + \frac{n}{2} - p \quad \text{Eq 3-7}$$

As before, the fuel input required to achieve a desired hydrogen output is given by the equation below.

$$\dot{m}_{Fuel} = S_{H2} \cdot \frac{P}{2 \cdot V_{Cell} \cdot F} \cdot \frac{M_{Fuel}}{f} \quad \text{Eq 3-8}$$

As can be seen from the reaction above, the reforming reaction does not involve any combustion process and thus no oxygen input is required, as defined below.

$$\dot{m}_{Air-FP(in)} = 0 \quad \text{Eq 3-9}$$

The water quantity required for the fuel processor can be derived as for the autothermal reformer. In this case, the water quantity required is obtained from the relation above on a molar basis and the required substitution made to derive the equation below.

$$\dot{m}_{H_2O-FP(Cons)} = S_{H2} \cdot \frac{P}{2 \cdot V_{Cell} \cdot F} \cdot \frac{1}{f} \cdot (2m - p) \cdot M_{H_2O} \quad \text{Eq 3-10}$$

Analysis of the PROX unit

Air for the preferential oxidation unit is derived in a similar way as for the autothermal reforming process. The difficulty here is that CO does not appear as an output component in the steam reforming reaction that we have been using so far. For the autothermal process we utilised the actual reaction but this is not possible here due to the complexity of the steam reforming process. An actual steam reforming analysis can however be seen to include reverse reactions which are responsible for the generation of the traces of CO.

In this study, it is reasonable to assume that the CO output is comparable with that of an autothermal reformer, as given below.

$$r_{CO} = \frac{d}{1 + \frac{1.5}{\varepsilon}\left(\frac{1 - r_{O2}}{r_{O2}}\right) + f} = 0.01 \quad \text{Eq 3-11}$$

In the case of an autothermal reformer, the middle function in the denominator can be traced back to the oxygen leaving the reformer. For a steam reformer, this term will become zero and thus the relation can be reduced as below.

$$r_{CO} = \frac{d}{1 + f} \quad \text{Eq 3-12}$$

After rearranging the above relation, the CO content per unit fuel input can be determined as below.

$$d = r_{CO}(1 + f) \quad \text{Eq 3-13}$$

This finally gives us an estimate for the air requirement for the PROX unit as given below. The error in such an assumption is considered to be minimal with a better estimate only really be obtainable by experimentation.

$$\dot{m}_{Air-PROX(in)} = S_{H2} \cdot \frac{P}{2 \cdot V_{Cell} \cdot F} \cdot \frac{r_{CO}}{f} \cdot (1 + f) \cdot \frac{S_{PROX}}{2} \cdot \frac{M_{Air}}{r_{O2}} \quad \text{Eq 3-14}$$

In a similar way, the relation for water generation from the autothermal reformer can be modified to arrive at the relation below.

$$\dot{m}_{H_2O-PROX(Gen)} = S_{H2} \cdot \frac{P}{2 \cdot V_{Cell} \cdot F} \cdot \frac{r_{CO}}{f} \cdot (1 + f) \cdot (S_{PROX} - 1) \cdot M_{H_2O} \quad \text{Eq 3-15}$$

G4 Derivation of equations for the burner analysis

In this analysis it is assumed that only the excess hydrogen from the fuel cell is utilised in the burner, other flammable components such as fuel slip and incomplete reformate are considered to be of negligible quantity. Other reformate components are therefore treated as dilatants in the combustion process with their only effect being to reduce the temperature of the combustion process.

G4.1 Products entering the burner

Stoichiometric ratio

The reaction for the combustion of hydrogen is as given below.

$$2H_2 + O_2 \rightarrow 2H_2O + Heat \qquad \text{Eq 4-1}$$

Inspection of this reaction shows us that the minimum quantity of O_2 required for complete combustion is ½ of the H_2 available. Referring back to the derivations for the fuel cell, the mass flow rate of O_2 required is thus as given below.

$$\dot{m}_{O2-Req'd} = \frac{1}{2} \cdot (S_{H2} - 1) \cdot \frac{P}{2 \cdot V_{Cell} \cdot F} \cdot M_{Air} \qquad \text{Eq 4-2}$$

In a similar way, the quantity of O_2 that is available at the burner can be shown to be.

$$\dot{m}_{O2-Ava} = (S_{O2} - 1) \cdot \frac{P}{4 \cdot V_{Cell} \cdot F} \cdot M_{Air} \qquad \text{Eq 4-3}$$

The stoichiometric ratio of the O_2 at the burner is finally given by the expression below.

$$S_{Burner} = \frac{\dot{m}_{Air-Ava}}{\dot{m}_{Air-Req'd}} = \frac{S_{O2} - 1}{S_{H2} - 1} \qquad \text{Eq 4-4}$$

Quantity of water generated by combustion

The quantity of water which is generated in the burner as a result of the combustion process can be derived from inspection of the reaction above. This shows us that one mole of water is generated for each mole of hydrogen burnt. Incorporating the hydrogen mass flow rate entering the burner into this definition gives us the following result.

$$\dot{m}_{H_2O-BURN(Gen)} = (S_{H2} - 1) \frac{P}{2 \cdot V_{Cell} \cdot F} \cdot M_{H_2O} \qquad \text{Eq 4-5}$$

Quantity of hydrogen entering the burner

Since there are no losses between the fuel cell and burner, the mass flow rate of hydrogen entering the burner will be the same as that of the unused hydrogen leaving the fuel cell. For reference, the hydrogen entering the fuel cell is given below.

$$\dot{m}_{H2} = \frac{P}{2 \cdot V_{Cell} \cdot F} \cdot S_{H2} \cdot M_{H2} \qquad \text{Eq 4-6}$$

The quantity of unused hydrogen leaving the fuel cell will be the difference between that entering the fuel cell (as defined by the hydrogen stoichiometric ratio) and that

consumed by the fuel cell (as defined by a hydrogen stoichiometric ratio of 1). This leads us to the derivation below.

$$\dot{m}_{H2-fuel(in)} = \frac{P}{2 \cdot V_{Cell} \cdot F} \cdot (S_{H2} - 1) \cdot M_{H2} \qquad \text{Eq 4-7}$$

Quantity of oxygen entering the burner

In a similar way as for the derivation of hydrogen entering the burner, the quantity of oxygen entering the burner can be derived as below.

$$\dot{m}_{O2-air(in)} = \frac{P}{4 \cdot V_{Cell} \cdot F} \cdot (S_{O2} - 1) \cdot M_{O2} \qquad \text{Eq 4-8}$$

Quantity of nitrogen entering the burner

Since nitrogen does not play an active part in any of the reactions with the fuel cell, it merely acts as a dilutant and passes straight through the fuel cell and thus into the burner untouched. The quantity of nitrogen entering the burner will thus be the sum of that entering the fuel cell from the air and that from the fuel processor as below.

$$\dot{m}_{N2-Burn(in)} = \dot{m}_{N2-Air(FC-in)} + \dot{m}_{N2-Fuel(FC-in)} \qquad \text{Eq 4-9}$$

The mass flow rate of nitrogen entering the fuel cell is given in the relevant sections for fuel cell derivations.

Quantity of water vapour entering the burner along with the oxygen depleted air

This derivation is based on the fact that the air enters the fuel cell with a standard atmospheric composition and leaves the fuel cell in an oxygen depleted state as a result of the oxygen being consumed within the fuel cell. This leads to the following result for the oxygen depleted air leaving the fuel cell.

$$\dot{N}_{Air-burn(in)} = \frac{P}{4 \cdot V_{Cell} \cdot F} \cdot \left(\frac{S_{O2}}{r_{O2}} - 1 \right) \qquad \text{Eq 4-10}$$

From the fuel cell derivations, the following result can be used to find the mass flow rate of water vapour at any point in a system as a function of the mass flow rate of air and the operating conditions at that point.

$$\dot{m}_w = \frac{M_w \cdot \phi \cdot P_{Sat}}{M_a \cdot (P - \phi \cdot P_{Sat})} \cdot \dot{m}_a \qquad \text{Eq 4-11}$$

Combining the two results above, gives us the derivation below. This can also be seen to include a fraction factor to account for the quantity of water recovered by the water separator. The remainder of this fraction as given by the expression below gives us the quantity of water remaining in the air stream.

$$\dot{m}_{H_2O-air(in)} = \frac{P}{4 \cdot V_{Cell} \cdot F} \cdot \left(\frac{S_{O2}}{r_{O2}} - 1 \right) \cdot \frac{\phi_{FC(out)} \cdot P_{VS}(@T_{Burn(in)})}{P_{Burn(in)} - \phi_{FC(out)} \cdot P_{VS}(@T_{Burn(in)})} \cdot M_{H_2O} \cdot (1 - X_{Air-Fract}) \qquad \text{Eq 4-12}$$

Quantity of water vapour entering the burner along with the hydrogen input

From above, the quantity of hydrogen leaving the fuel cell is given as.

$$\dot{m}_{H2-fuel(in)} = \frac{P}{2 \cdot V_{Cell} \cdot F} \cdot (S_{H2} - 1) \cdot M_{H2} \qquad \text{Eq 4-13}$$

Following the same process as in the previous section and thus combining this result with the derivation for the mass flow rate of water as a function of the mass flow rate of air, the following result is obtained. As before, a fraction is included to account for the quantity of water recovered by the water separator located in the fuel cell hydrogen output stream.

$$\dot{m}_{H_2O-H2(in)} = \frac{P}{2 \cdot V_{Cell} \cdot F} \cdot (S_{H2} - 1) \cdot \frac{\phi_{FC(out)} \cdot P_{VS}(@T_{Burn(in)})}{P_{Burn(in)} - \phi_{FC(out)} \cdot P_{VS}(@T_{Burn(in)})} \cdot M_{H_2O} \cdot (1 - X_{H2-Fract})$$

Eq 4-14

G4.2 Products leaving the burner

Quantity of unused oxygen leaving the burner

The quantity of unused oxygen leaving burner will be the remainder of that entering the burner and that consumed by the combustion process in the burner. From above, the quantity of oxygen entering the burner is as follows.

$$\dot{m}_{O2-air(in)} = \frac{P}{4 \cdot V_{Cell} \cdot F} \cdot (S_{O2} - 1) \cdot M_{O2}$$

Eq 4-15

Also from above, the quantity of oxygen consumed in the burner is.

$$\dot{m}_{O2-\mathrm{Req'd}} = (S_{H2} - 1) \cdot \frac{P}{4 \cdot V_{Cell} \cdot F} \cdot M_{Air}$$

Eq 4-16

The quantity of oxygen is then given by.

$$\dot{m}_{O2-Burn(out)} = \dot{m}_{O2-Burn(in)} - \dot{m}_{O2-Burn(Consumed)}$$

Eq 4-17

Substitution of the above equations, allows us to arrive at the following result.

$$\dot{m}_{O2-Burn(out)} = \frac{P}{4 \cdot V_{Cell} \cdot F} \cdot (S_{O2} - S_{H2}) \cdot M_{O2}$$

Eq 4-18

Quantity of nitrogen leaving the burner

Since nitrogen only serves as a dilutant within the burner, the quantity of nitrogen leaving the burner will be the same as that entering the burner. This in turn will be the same as the sum of that entering the fuel cell, as given below.

$$\dot{m}_{N2-Burn(in)} = \dot{m}_{N2-Air(FC-in)} + \dot{m}_{N2-Fuel(FC-in)}$$

Eq 4-19

From the fuel cell derivations, the nitrogen entering the fuel cell with the air can be determined from.

$$\dot{m}_{N2-air(in)} = \frac{P}{4 \cdot V_{Cell} \cdot F} \cdot S_{O2} \cdot \frac{(1 - r_{O2})}{r_{O2}} \cdot M_{N2}$$

Eq 4-20

Likewise, the nitrogen entering the fuel cell from the fuel processor is given by.

$$\dot{m}_{N2-fuel(in)} = \frac{P}{2 \cdot V_{Cell} \cdot F} \cdot \frac{S_{H2}}{r_{H2}} \cdot r_{N2} \cdot M_{N2}$$

Eq 4-21

Substitution of these terms into the equation above leads to the following expression.

$$\dot{m}_{N2-Burn(out)} = \frac{P}{2 \cdot V_{Cell} \cdot F} \left(\left\{ S_{H2} \cdot \frac{r_{N2}}{r_{H2}} \right\} + \left\{ \frac{S_{O2}}{2} \cdot \left[\frac{1 - r_{O2}}{r_{O2}} \right] \right\} \right) \cdot M_{N2}$$

Eq 4-22

Quantity of carbon dioxide leaving the burner

As for the nitrogen passing through the system, the carbon dioxide is a mere dilutant, therefore the quantity of CO_2 leaving the burner is the same as that entering the fuel cell. The main source of CO_2 entering the system is from the fuel processor as derived in the fuel processing section and reiterated below.

$$\dot{m}_{CO2-Burn(out)} = \frac{P}{2 \cdot V_{Cell} \cdot F} \cdot \frac{S_{H2}}{r_{H2}} \cdot r_{CO2} \cdot M_{CO2} \qquad \text{Eq 4-23}$$

Quantity of water leaving the burner

As for the N2 and CO2 passing through the system, any water vapour in the system will also act as a mere dilutant. The total quantity of water leaving the burner will therefore be the sum of:

- The water that enters the burner with the air and is not removed by the air water separator. As derived above.
- The water that enters the burner with the hydrogen and is not removed by the hydrogen water separator. As derived above.
- The water generated by combustion in the burner. As derived above.

This leads to the result below.

$$\dot{m}_{H_2O-Burn(out)} = \left(\frac{P}{2 \cdot V_{Cell} \cdot F} \cdot \{S_{H2} - 1\} \cdot M_{H_2O} \right) + \dot{m}_{H_2O-Air(in)} + \dot{m}_{H_2O-H2(in)} \qquad \text{Eq 4-24}$$

Quantity of water vapour leaving the burner with the exhaust gases

As for the water vapour entering the burner, the following relation can be used to determine the quantity of water present in vapour form in the exhaust gas flow.

$$\dot{m}_w = \frac{M_w \cdot \phi \cdot P_{Sat}}{M_a \cdot (P - \phi \cdot P_{Sat})} \cdot \dot{m}_a \qquad \text{Eq 4-25}$$

In this case, the mass flow rate of air becomes the mass flow rate of exhaust gases leaving the burner and the molar mass of air becomes the composite molar mass of the exhaust gases. This leads us to the result below.

$$\dot{m}_{H_2O-Exh(Out)} = \dot{m}_{Exh(Out)} \cdot \frac{M_{H_2O}}{M_{Exh}} \cdot \frac{\phi_{Exh} \cdot P_{VS}(@T_{Exh(Out)})}{P_{Exh(Out)} - \phi_{Exh} \cdot P_{VS}(@T_{Exh(Out)})} \qquad \text{Eq 4-26}$$

G5 Derivation of a general relation to determine the fuel cell output voltage

This section will give an overview of the derivation of a simple expression which is capable of predicting the voltage output from a fuel cell as a function of its power output and operating temperature. The first stage in this work is to predict the fuel cell output voltage at a number of different values of operating temperature and over a range of current densities. Knowledge of the current and voltage then allows us to determine the output power at each point and ultimately the point of maximum power. We are then able to plot relations for fuel cell output voltage versus output power fraction at a number of different operating temperatures. By fitting polynomial expressions to these relations we are then able to derive a global relation by examination of the coefficients. A summary of the analytical procedure is shown in the flow chart below. The accompanying equations and background to the analysis procedure is also given below.

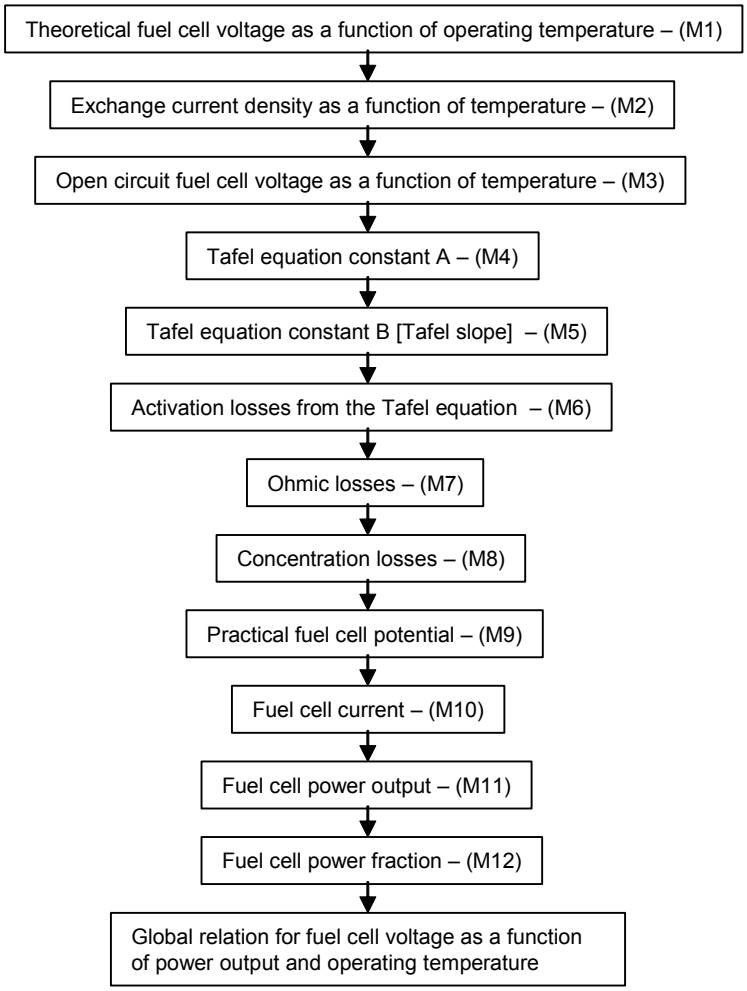

The first stage in this analysis is to determine the theoretical fuel cell voltage from the reactions involved. As a reminder, the general reaction for a hydrogen fuel cell is,

$$H_2 + \tfrac{1}{2}O_2 \rightarrow H_2O \qquad \text{Eq 5-1}$$

If we consider the chemistry of the reaction in greater detail, we will see that there is an energy change associated with the reaction. For our purposes, it is most convenient to express this change as the change in the Gibbs free energy of formation. This is the difference between the Gibbs energy of the reactants and products as below.

$$\Delta G = G_{f-\mathrm{Pr}oducts} - G_{f-\mathrm{Re}actants} \quad \text{Eq 5-2}$$

These values are typically determined on a molar basis as denoted by a bar value. The value of the change in Gibbs free energy of formation can be seen to be dependant on the temperature of the reaction and final state of the products and is thus variable.

Calculation of the molar specific change in Gibbs free energy of formation can be a lengthy process. Fortunately, for the basic hydrogen fuel cell reaction above the data is already available in a tabulated format for a number of different conditions as given below. The sign convention used is consistent with energy being released.

Table 2.1 $\Delta\bar{g}_f$ for the reaction $H_2 + \frac{1}{2}O_2 \rightarrow H_2O$ at various temperatures

Form of water product	Temperature (°C)	$\Delta\bar{g}_f$ (kJ mol^{-1})
Liquid	25	−237.2
Liquid	80	−228.2
Gas	80	−226.1
Gas	100	−225.2
Gas	200	−220.4
Gas	400	−210.3
Gas	600	−199.6
Gas	800	−188.6
Gas	1000	−177.4

Table 5-1 – Change in Gibbs free energy of formation [56]

If we look back at the working principles of the fuel cell, we can see that in order to complete the reaction, two electrons must pass round the external circuit per mole of hydrogen. Each electron will carry a charge as predicted by the Faradays constant F. The electrical work done to move this charge around the circuit is then determined as the product of the charge and voltage. If we assume that the reaction is reversible and therefore there are no losses in the fuel cell, this electrical work done will equal the change in Gibbs free energy of the reaction as below

$$\Delta\bar{g}_f = charge \times voltage = -2F \cdot E \quad \text{Eq 5-3}$$

By rearranging the equation above, we have a method of predicting the reversible open circuit voltage of the fuel cell, as below.

$$E = \frac{-\Delta\bar{g}_f}{2F} \quad \text{Eq 5-4}$$

If we then use the above relation to determine the EMF at a number of different operating temperatures, we are then able to plot the results and obtain a relation for EMF versus operating temperature as given below.

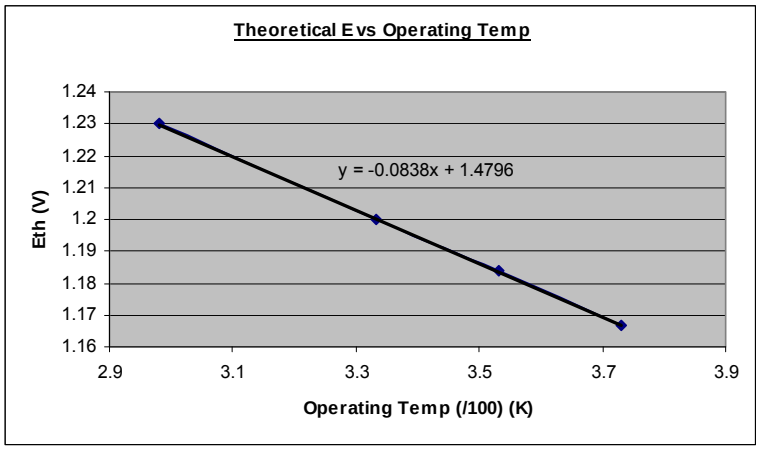

Eq 5-5 (M1)

The next stage in the work is to predict the actual open circuit voltage of the fuel cell by taking into account the operating losses. The first part of this analysis is to determine the exchange current density i_0 from equation M2 as a function of operating temperature. The exchange current density is a particularly important parameter which can be deemed as a measure of the readiness of the electrode to proceed with the electrochemical reaction. A higher exchange current density implies a more active electrode surface and thus higher currents can be generated for any over potential.

Equation M2: $$i_0 = i_{0-\mathrm{Re}f} \cdot a_c \cdot L_c \cdot \left(\frac{P_r}{P_{r-\mathrm{Re}f}} \right)^{\gamma} \exp\left[-\frac{E_c}{RT}\left(1 - \frac{T}{T_{\mathrm{Re}f}} \right) \right]$$ Eq 5-6 (M2)

The terms included in the above equation are:

- $i_{0-\mathrm{Re}f}$ - This is the exchange current density at a reference condition (typically 25°C and 1atm). This is normally quoted per unit catalyst surface area (with the units $Acm^{-2}Pt$). Determination of this parameter will be discussed further below.
- a_c - This is the catalyst specific area. Modern catalysts have a value which lies between 600 and $1000cm^2mg^{-1}$. In the absence of better data, an average value of $800cm^2mg^{-1}$ has been assumed for this analysis.
- L_c - This is the catalyst loading. Modern electrodes have a value which lies between 0.3 and $0.5mgPtcm^{-2}$. In the absence of better data, an average value of $0.4mgPtcm^{-2}$ has been assumed for this analysis.
- Pr – This is the reactant partial pressure, measured in kPa. This is assumed to be 1atm in this analysis.
- Pr^{ref} – This is the reference pressure, measured in kPa. This is assumed to be 1atm in this analysis.
- γ – This is the pressure coefficient which can be anywhere between 0.5 and 1.0 but in this analysis a value of 1 is used.
- E_c – This is the activation energy and is assumed to have a value of $66kJmol^{-1}$ for oxygen reduction on a Pt catalyst.
- R – This is the standard gas constant which has a value of $8.314Jmol^{-1}K^{-1}$.
- T and T_{ref} – This is the temperature and reference temperature (at 25°C) in K. The temperature being the independent variable in this analysis.

The reference exchange current density can be determined from a standard value of exchange current density with the following relation. A standard value of 0.001 has been assumed for i_0 in this analysis which is consistent with data obtained for a modern Ballard fuel cell.

$$i_{0-\mathrm{Re}f} = \frac{i_0}{a_c \cdot L_c} \qquad \text{Eq 5-7}$$

The denominator $a_c L_c$ of the relation above is the product of the catalyst specific area and the catalyst loading, which is also known as the electrode roughness. Using the figures above, a value of 3.125E-6 was determined for i_0.

The practical open circuit voltage can then be determined from the theoretical open circuit voltage with Equation M3. The unknown parameters in this equation are:

- i_{loss} - This is the loss in current density due to internal currents and fuel crossover through the polymer membrane electrolyte. Examination of analysis data for existing fuel cells has deemed a value of 3mAcm^{-2} as being a typical.
- α – This is the charge transfer coefficient which typically assumes a value of 1.

$$E_{OC} = E_{th} - \left[\frac{R \cdot T}{\alpha_a \cdot F} \cdot \ln\left(\frac{i_{loss}}{i_0} \right) \right] \qquad \text{Eq 5-8 (M3)}$$

Until now we have only considered the open circuit voltage for the fuel cell. The next stage of the analysis is to determine the losses which are encountered as a result of useful current being drawn. We will then finally be able to determine the actual fuel cell output voltage in the presence of an external load. The fuel cell working losses are characterised as, activation, ohmic and concentration as will be examined below.

Activation losses are associated with the anode and cathode electrode kinetics and the initiation of the electrochemical reaction. These are related to the exchange current density with lower losses being experienced at higher values of exchange current density. Activation losses can be determined from the Butler-Volmer equation but are most effectively predicted by equation M6 which is known as the Tafel equation. The equation coefficients A and B are given by equations M4 and M5 respectively. Where i_0 is the exchange current density and i is the current density (mA/cm^2), which is obtained by dividing the current by the fuel cell active area. The fuel cell active area is a design variable for fuel cells with a value of 400cm^2 being assumed for this analysis.

$$A_{Act} = -2.3 \cdot \frac{R \cdot T}{\alpha_a \cdot F} \cdot \log(i_0) \qquad \text{Eq 5-9 (M4)}$$

$$B_{Act} = 2.3 \cdot \frac{R \cdot T}{\alpha_a \cdot F} \qquad \text{Eq 5-10 (M5)}$$

$$\Delta V_{Act} = A_{Act} + B_{Act} \cdot \log(i) \qquad \text{Eq 5-11 (M6)}$$

The ohmic losses are not only a result of the resistance of the flow of electrons in the conductive components but also the resistance of the flow of ions in the electrolyte. These losses can be predicted with equation M7, which has values of R between 0.1 and 0.2Ωcm^2. In this analysis, an average value of 0.15Ωcm^2 has been assumed.

$$\Delta V_{Ohm} = i \cdot R \qquad \text{Eq 5-12 (M7)}$$

The final source of losses is the concentration losses, which result from concentration gradients at the fuel cell electrodes due to the rapid consumption of reactants at various points on the electrodes. These are best predicted by the empirical relation M8, with typical values of C = 3E-5V and D = 0.125Acm^{-2} being assumed for this analysis.

$$\Delta V_{Conc} = C \cdot \exp\left(\frac{i}{D}\right) \qquad \text{Eq 5-13 (M8)}$$

The final voltage output from a fuel cell, which is being subjected to an external load, is given by equation M9.

$$V_{Cell} = E_{OC} - \Delta V_{Act} - \Delta V_{Ohm} - \Delta V_{Conc} \qquad \text{Eq 5-14 (M9)}$$

The process presented above is repeated for a range of values of current density to produce a plot of V_{Cell} against current density (i). If equation M10 is used to determine the current from the current density, the fuel cell power output can be determined from equation M11. The $A_{Cell-Act}$ term in equation M10 is the fuel cell active area, which as mentioned above has been assumed to be 400cm^2 in this analysis.

$$I_{Cell} = \frac{i \cdot A_{Cell-Act}}{1000} \qquad \text{Eq 5-15 (M10)}$$

$$P_{Cell} = V_{Cell} \cdot I_{Cell} \qquad \text{Eq 5-16 (M11)}$$

The results of equation M11 can then be used to generate a plot of power against current, from which the maximum value of power output can then be determined. Using equation M12, we are then finally able to generate another plot of percentage maximum power output against current.

$$\%P = \frac{P_{Cell}}{P_{Cell(Max)}} \qquad \text{Eq 5-17 (M12)}$$

This whole process is then repeated for a range of fuel cell operating temperatures and for values of current density up to that for the maximum power. The results are finally plotted against percentage power output to generate something similar to the plot shown in figure 5-1 below. This shows the characteristic fuel cell polarization curves for a number of different operating temperatures from 30 to 100°C.

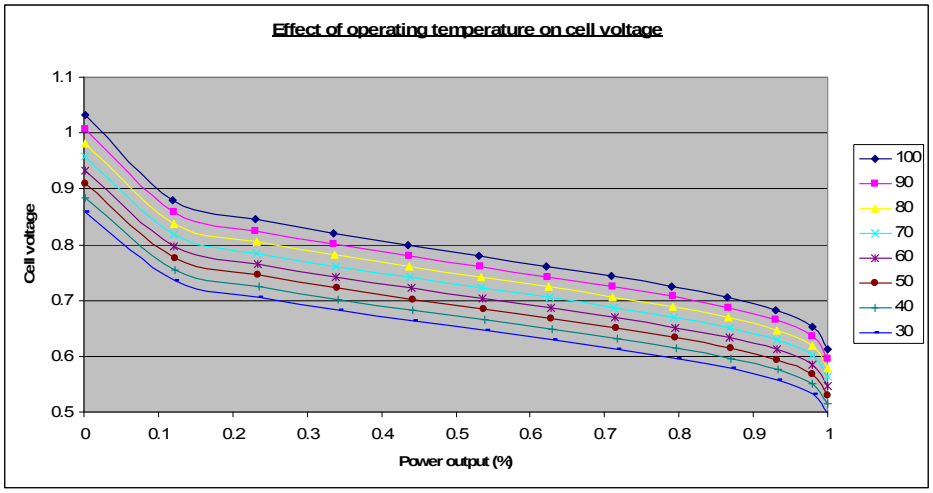

Figure 5-1

The final stage in this analysis is to transform the results given in the above chart into a more easily manageable format for use within the main spreadsheet. Step one of this process is to fit a polynomial expression to each of the curves in the above plot. We are then able to examine the trend between coefficients of each expression to arrive at the global expression given by equation M13. The accompanying coefficients can be determined from equations M14 through to M18.

$$V_{Cell-Basic} = \left(C_{X4} \cdot F_{Pwr}{}^{4}\right) + \left(C_{X3} \cdot F_{Pwr}{}^{3}\right) + \left(C_{X2} \cdot F_{Pwr}{}^{2}\right) + \left(C_{X} \cdot F_{Pwr}\right) + C_{C}$$

Eq 5-18 (M13)

$$C_{X4} = -1.5486 \cdot \frac{T_{FC}}{1000} - 0.8708$$

Eq 5-19 (M14)

$$C_{X3} = 2.6579 \cdot \frac{T_{FC}}{1000} - 1.7465$$

Eq 5-20 (M15)

$$C_{X2} = -1.2895 \cdot \frac{T_{FC}}{1000} - 1.2305$$

Eq 5-21 (M16)

$$C_{X} = 0.4107 \cdot \left(\frac{T_{FC}}{1000}\right)^{2} - 0.2492 \cdot \frac{T_{FC}}{1000} + 0.1772$$

Eq 5-22 (M17)

$$C_{C} = 2.0758 \cdot \frac{T_{FC}}{1000} + 0.6517$$

Eq 5-23 (M18)

H1 Analysis of the fuel cell system

Due to its size, it has been necessary to break this analysis down into a number of smaller sections so that the procedure can be presented here in an easy to understand format. This process is shown in the diagram below to help the reader trace their steps. It has not however been possible to illustrate all the links between the blocks in this diagram due to the complexity of the analysis and the risk of obscuring the meaning of the diagram.

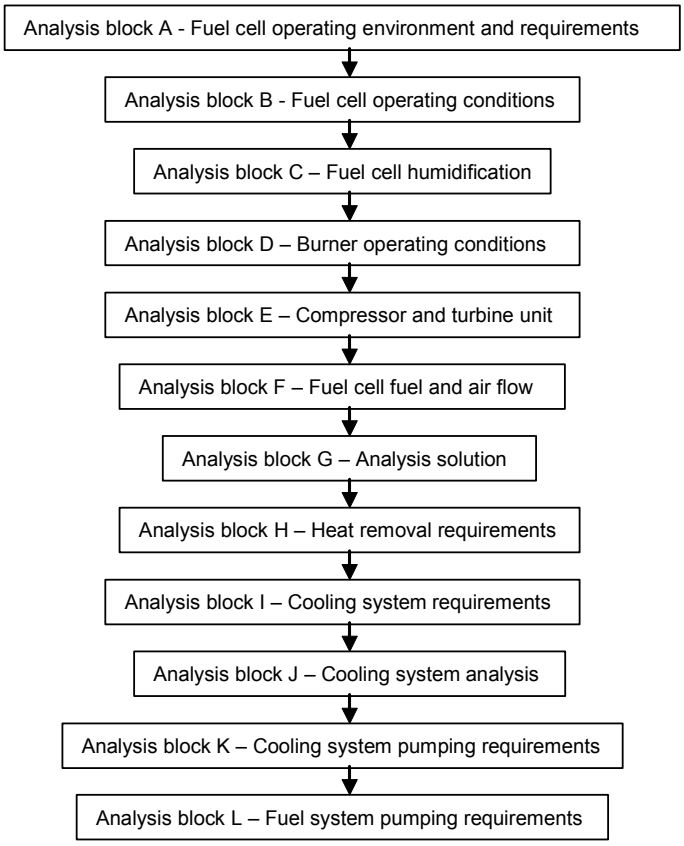

Each of the blocks in the chart above represents a complex analysis for a particular part of the fuel cell system or an operating condition. This includes analysis of the system operating environment, operating conditions (including the analysis of flows entering and leaving the system) and auxiliary systems used to regulate the operating conditions of the system (such as the cooling and humidification systems). Each of these blocks will be discussed in depth in the sections which follow.

H1.1 Analysis block A – Fuel cell operating environment

H1.1.1 Atmospheric variables

Within this section the relations will be presented which are used to determine the properties of the atmosphere at the altitudes under consideration. These relations, as given below, were obtained from ESDU 77021 [68] and the reader is advised to refer to this data sheet for further information.

$$T = T_i + \left(L_i \cdot H\right) \qquad \text{Eq A-1}$$

$$P = P_i \cdot \left(\frac{T_i}{T}\right)^{\frac{g0m0}{RL_i}} \qquad \text{Eq A-2}$$

$$\rho = \frac{P \cdot m_0}{R \cdot T} \qquad \text{Eq A-3}$$

$$\mu = \frac{1.458 \cdot 10^{-6} \cdot T^{3/2}}{T + 110.4} \qquad \text{Eq A-4}$$

H1.2 Other useful fuel cell system analysis fluid parameters

H1.2.1 Cooling system parameters

The kinematic viscosity (nu) and thermal diffusivity (α) of the ambient air are given by the polynomial expressions below which were obtained by fitting curve-fit expressions to existing data. Where, H is the altitude in km and T is the temperature in Kelvins.

$$\upsilon = \left(0.0023H^4 - 0.0412H^3 + 0.3195H^2 + 0.6524H + 14.725\right)/1E6 \qquad \text{Eq A-5}$$

$$\alpha = \left(9.1018E - 11\right)\cdot T^2 + \left(8.8197E - 8\right)\cdot T - \left(1.0654E - 5\right) \qquad \text{Eq A-6}$$

Also required for the cooling system analysis are the Cp and k values of air which can be determined from the relations below. Where, T_{Air} is the temperature of the air in the immediate vicinity of the fuel cell in Kelvins and the accompanying constants are given in the table below.

$$Cp(air) = \left[A \cdot \left(\frac{T_{Air}}{1000}\right)^4 + B \cdot \left(\frac{T_{Air}}{1000}\right)^3 + C \cdot \left(\frac{T_{Air}}{1000}\right)^2 + D \cdot \left(\frac{T_{Air}}{1000}\right) + E\right] \cdot 1000 \qquad \text{Eq A-7}$$

Constants	A	B	C	D	E
Cp (W/mdegC)	13.333	-15.259	6.7556	-1.3456	1.1066

$$k_{Air} = \frac{2.648151E - 3 \cdot \left(T_{Ait}\right)^{3/2}}{T_{Air} + \left(245 \cdot 10^{-12/T_{Air}}\right)} \qquad \text{Eq A-8}$$

The fuel cell coolant is assumed to be a mix of 30% glycol and 70% water, the properties of which can be determined from the expression below developed by the

author. Where, $T_{Coolant}$ is the temperature of the glycol/water mix in Kelvins and the equation constants for each parameter are given in the accompanying table.

$$X = \left[A \cdot \left(\frac{T_{Coolant}}{1000} \right)^4 + B \cdot \left(\frac{T_{Coolant}}{1000} \right)^3 + C \cdot \left(\frac{T_{Coolant}}{1000} \right)^2 + D \cdot \left(\frac{T_{Coolant}}{1000} \right) + E \right] \cdot 1000 \qquad \text{Eq A-9}$$

Constants	A	B	C	D	E
k (W/mdegC)	0	0	-7.5625	5.8258	-0.567
Rho (kg/m3)	0	0	-2565.7	1150.5	918.14
Cp (W/mdegC)	2720.1	-3620.6	1809	-400.48	36.705
mu (kgm-1s-1)	0	-21.369	22.722	-8.0691	0.9582

H1.2.2 Specific heats

The specific heat of each of the substances utilised within the fuel cell system can be determined from the expression below. Where T is the temperature of the gas in Kelvins and M is the molecular mass of the substance. The accompanying equation constants and molecular masses are given in the table below.

$$C_P = \left[A + (B \cdot T) + \left(C \cdot T^2\right) + \left(D \cdot T^3\right) \right] / M \qquad \text{Eq A-10}$$

Specific heat constants - Cp (kJ/kg.K)

Substance	a	b	c	d
H2	29.11	-1.916E-03	4.003E-06	-8.704E-10
O2	25.48	1.520E-02	-7.155E-06	1.312E-09
H2O(g)	32.24	1.923E-03	1.055E-05	-3.595E-09
N2	28.9	-1.571E-03	8.081E-06	-2.873E-09
CO2	22.26	5.981E-02	-3.501E-05	7.469E-09
CO	28.16	1.675E-03	5.372E-06	-2.222E-09
Air	28.11	1.967E-03	4.802E-06	-1.966E-09

Molecular mases

Substance	M (kg/kmol)
H2	2.0158
O2	31.9988
H2O(g)	18.0152
N2	28.0134
CO2	44.0099
CO	28.0105
Air	28.848

A separate relation was derived for the specific heat of water in its liquid state, as given by the expression below, where T is in °C and CP is in kJ/kg.K. The accompanying equation constants are given in the table below.

$$C_{P(H_20(l))} = A \cdot \left(\frac{T}{100} \right)^6 + B \cdot \left(\frac{T}{100} \right)^5 + C \cdot \left(\frac{T}{100} \right)^4 + D \cdot \left(\frac{T}{100} \right)^3 + E \cdot \left(\frac{T}{100} \right)^2 + F \cdot \left(\frac{T}{100} \right) + G$$

Constants	A	B	C	D	E	F	G
H2O(l)	0.4782	-1.7887	2.8164	-2.3940	1.2311	-0.3441	4.2171

Eq A-11

H1.2.3 Other useful parameters

The ratio of specific heats of air can be determined from the expression below.

$$\gamma_{Air} = \frac{C_{P(Air)}}{C_{P(Air)} - 0.287} \qquad \text{Eq A-12}$$

The remaining parameters required for the analysis are,

- Lower heating value of hydrogen = 240 kJ/mol
- Lower heating value of methanol = 643 kJ/mol
- Molecular mass of methanol = 32.0424 kg/kmol
- Higher heating value of hydrogen (HHV@25°C) = 141.9 kJ/g
- Heat of evaporation of H_20 at 0°C = 2.5kJ/g

H1.3 Analysis block B – Fuel cell operating conditions

H1.3.1 Theoretical background

It should be noted that the operational temperature of a fuel cell is actually not an independent parameter and is dependant on the fuel cell operating pressure and humidification requirements. In this analysis, the fuel cell can be considered to be a constant volume device within a control volume as shown in figure 1 below.

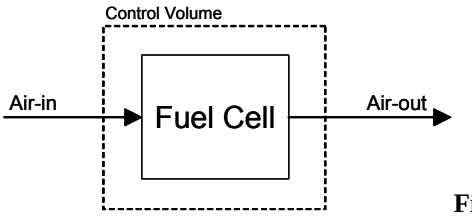

Figure B-1

In order for the fuel cell to operate effectively, its water content must be kept within carefully controlled limits. If there is too much water, the reactant channels will become flooded and if there is insufficient water, the membrane will dry out. In either case, a serious reduction in performance will occur. The optimum operating condition is when the oxygen depleted air leaves the fuel cell with an average relative humidity of 0.9 (within the limits of 80 to 100%). In other words, the exhaust air must be 90% saturated. From a thermodynamics perspective of a constant volume device, this would imply that the operating temperature of the fuel cell must be carefully maintained to keep its operating point within the saturated vapour dome. This concept is clarified in the P-V diagram of figure 2 below.

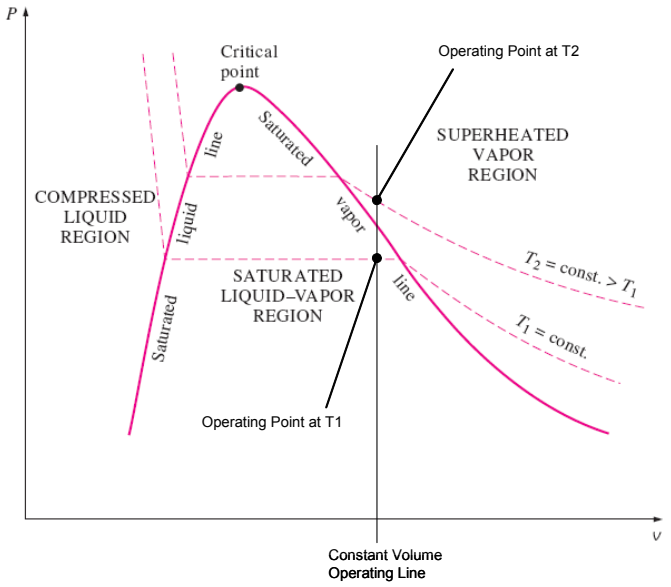

Figure B-2

In the P-V diagram above, we can see that the operating temperature of a fixed volume fuel cell would have to be decreased from temperature T2 to T1 in order to move its operating point from the superheated region to within the desired saturated vapour region (to within the vapour dome). It is also evident that if the relative humidity of the air is known then the temperature required to achieve this condition can be determined.

H1.3.2 Analysis to determine of the operational fuel cell voltage

The purpose of this analysis is to determine the operational voltage output from the fuel cell as a function of the fuel cell operating conditions. In particular, the fuel cell voltage can be shown to be a function of operating temperature, pressure, reactant concentration and power output. A summary of the analytical procedure used to determine the output voltage as a function of these parameters is shown in the flow chart below.

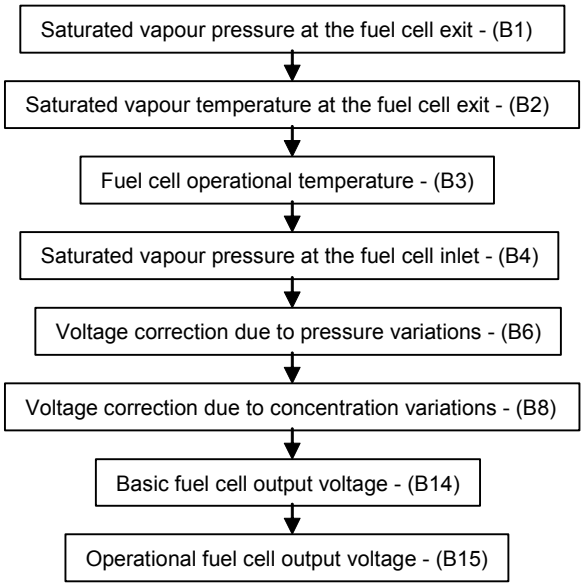

The output voltage can be seen to consist of a basic and an operational fuel cell output voltage. The basic fuel cell voltage is determined as a function of the power output of a fuel cell operating at standard sea level conditions and thus at standard atmospheric pressure and oxygen concentration. The operational fuel cell output voltage is the actual fuel cell output voltage. This is the basic voltage corrected for non-standard operating pressures and concentrations. The accompanying equations are discussed below.

Using the relations from the fuel cell derivations section, it is possible to derive equation B1 below. This enables the saturated vapour pressure of the exit air to be determined as a function of the pressure, humidity ratio and relative humidity at the fuel cell exit. The pressure at the fuel cell exit is determined in the next analysis. The only unknown in this expression is the humidity ratio, which can be seen to vary with pressure and can be considerable at low pressure (as much as 40% for low temperatures). Since it is not sensible to use air with a particularly high humidity ratio, a humidity ratio equivalent to sea level conditions has been assumed. This corresponds to the operating environment of the majority of the currently available tried and tested existing fuel cells. For a relative humidity of 0.9 with a saturated vapour pressure at 60º and at standard sea level pressure (as is common for a number of existing fuel cells), this gives us a maximum relative humidity of $\omega = 0.1339$. This value is thus taken as the maximum value of humidity ratio which we are confident that a fuel cell can comfortably operate with. The humidity ratio was therefore fixed at this value for all our test conditions.

$$P_{Sat-FC(exit)} = \frac{P_{@i-1}}{\phi_{Air(in)} \cdot \left(\left\{ \frac{M_{H_2O}}{\omega_{Air-Max(in)} \cdot M_{Air}} \right\} + 1 \right)} \quad \text{Eq B-1}$$

By plotting the saturated vapour temperature verses the saturated vapour pressure of air; it is possible to obtain the relation given in equation B2. This relation enables us to determine the saturated vapour temperature of the air leaving the fuel cell, with respect to the saturated vapour pressure determined in the relation above. For our work, an accuracy of 1 decimal place is deemed sufficient.

$$T_{Sat-FC(exit)} = W\left(LOG(P_{Sat})\right)^3 + X\left(LOG(P_{Sat})\right)^2 + Y\left(LOG(P_{Sat})\right) + Z \quad \text{Eq B-2}$$

The constants for equation B2 are given in the table below.

Constant	W	X	Y	Z
Value	1.2166	-7.0857	43.351	-92.121

It should be noted that there is a limit to the actual operating temperature which a fuel cell can operate at, which is dictated by the material limits of the components that make up the fuel cell assembly. Since 80ºC is generally regarded as the maximum allowable temperature for a PEM fuel cell, this figure is adopted here. The operating temperature of the fuel cell can then thus be determined from equation B3 below as the lesser of the saturated vapour temperature and the maximum allowable limit.

$$T_{FC-Operational} = IF(T_{Sat} < T_{Max(Mat)}, T_{Sat}, T_{Max(Mat)}) \quad \text{Eq B-3}$$

In a similar way as above, the saturated vapour pressure of the air entering the fuel cell can be determined from the curve fitted expression given in equation B4 below.

$$P_{Sat(Air)} = EXP\left[\left(a \cdot T^{-1}\right) + b + \left(c \cdot T\right) + \left(d \cdot T^2\right) + \left(e \cdot T^3\right) + \left(f \cdot \ln(T)\right)\right] \quad \text{Eq B-4}$$

The constants for equation B4 are given in the table below.

Constant	a	b	c	d	e	f
Value	-5.800E+03	1.391E+00	-4.864E-02	4.176E-05	-1.445E-08	6.546E+00

The effect of variations in fuel cell operating pressure is traditionally predicted by the analytical Nernst equation given below.

$$\Delta E_{\Delta P} = \frac{R \cdot T_{FC}}{4 \cdot F} \cdot \ln\left(\frac{P_2}{P_1}\right)$$

This relation has been shown to give reasonable results for high temperature fuel cells operating at temperatures of about 1000ºC. In the case of low temperature fuel cells however, a significant error between those figures predicted by this relation and those reported in practice, is evident. To overcome this problem, the author of this thesis has derived a fudge factor from analytical and experimentally reported data, to correct the predictions made by the Nernst equation. This is given in equation B5 as a function of temperature, since the error is proportional to the operating temperature of the fuel cell.

$$Fud_{\Delta P} = \left(-0.0108 \cdot T_{FC}\right) + 8.4535 \qquad \text{Eq B-5}$$

The corrected Nernst equation to predict the effect of pressure variations is then given by equation B6 below.

$$\Delta E_{\Delta P} = \frac{R \cdot T_{FC}}{4 \cdot F} \cdot \ln\left(\frac{P_2}{P_1}\right) \cdot Fud_{\Delta P} \qquad \text{Eq B-6}$$

In a similar way as for the relation to predict the effect of pressure changes, an alternative form of the Nernst equation can be used to predict concentration changes as given below.

$$\Delta E_{\Delta \beta} = \frac{R \cdot T_{FC}}{4 \cdot F} \cdot \ln\left(\frac{\beta_2}{\beta_1}\right)$$

As before, there is some disagreement between those values predicted by this analytical expression and those reported in practice and so another fudge factor was derived by the author of this thesis to correct for this effect. This is given by equation B7 below.

$$Fud_{\Delta \beta} = 5.2743 \cdot \left(\beta_2 - \beta_1\right) \qquad \text{Eq B-7}$$

The corrected Nernst equation to predict the effect of concentration variations is then given by equation B8 below.

$$\Delta E_{\Delta \beta} = \frac{R \cdot T_{FC}}{4 \cdot F} \cdot \ln\left(\frac{\beta_2}{\beta_1}\right) \cdot Fud_{\Delta \beta} \qquad \text{Eq B-8}$$

Using the global analytical relation derived by this author in the fuel cell operating temperature relations derivations section, we are able to determine the basic fuel cell voltage. This is given by equation B14 as a function of the fuel cell output power fraction. The corresponding equation constants are given by equations B9 through to B13 as a function of the fuel cell operating temperature.

$$C_{X4} = -1.5486 \cdot \frac{T_{FC}}{1000} - 0.8708 \qquad \text{Eq B-9}$$

$$C_{X3} = 2.6579 \cdot \frac{T_{FC}}{1000} - 1.7465 \qquad \text{Eq B-10}$$

$$C_{X2} = -1.2895 \cdot \frac{T_{FC}}{1000} - 1.2305 \qquad \text{Eq B-11}$$

$$C_X = 0.4107 \cdot \left(\frac{T_{FC}}{1000}\right)^2 - 0.2492 \cdot \frac{T_{FC}}{1000} + 0.1772 \qquad \text{Eq B-12}$$

$$C_C = 2.0758 \cdot \frac{T_{FC}}{1000} + 0.6517 \qquad \text{Eq B-13}$$

$$V_{Cell-Basic} = \left(C_{X4} \cdot {F_{Pwr}}^4\right) + \left(C_{X3} \cdot {F_{Pwr}}^3\right) + \left(C_{X2} \cdot {F_{Pwr}}^2\right) + \left(C_X \cdot F_{Pwr}\right) + C_C \qquad \text{Eq B-14}$$

The operational fuel cell voltage is finally determined as the sum of the basic voltage and the corrections for pressure and concentration, as given by equation B15 below.

$$V_{Cell-Out} = V_{Cell-Basic} + \Delta E_{\Delta P} + \Delta E_{\Delta \beta} \qquad \text{Eq B-15}$$

H1.3.3 Pressure at the fuel cell exit

In order to complete the analysis in the last section, we need to determine the pressure of the oxygen depleted air leaving the fuel cell. We are then able to determine the saturated vapour pressure at the fuel cell exit as required for our fuel cell voltage predictions. A summary of the analytical procedure followed to determine the total pressure drop within the fuel cell stack and ultimately the pressure at the fuel cell exit is presented in the flow chart below.

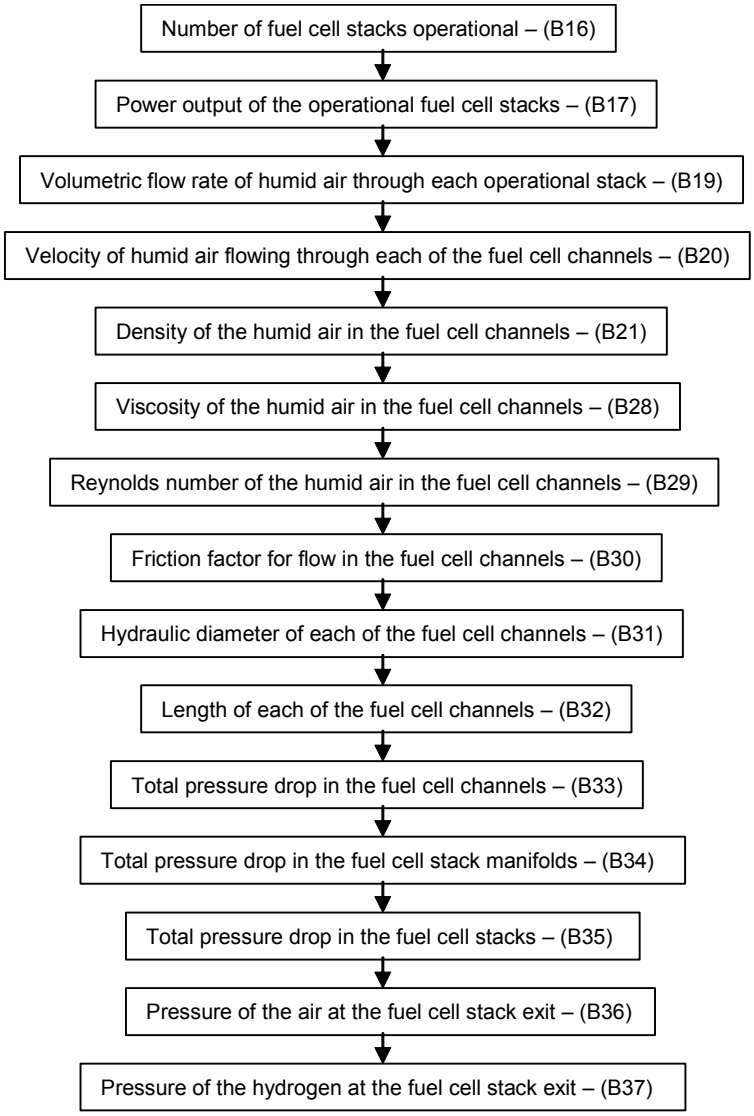

As is mentioned elsewhere in this thesis, it is more efficient to operate fuel cells at higher rather than lower power outputs. This is due to fuel cell activation losses which are predominant at low currents. For this reason, the fuel cell system in this study has been designed to shut-down any fuel cell stack not required. For example, if it is possible to achieve the same power output from 3 stacks instead of 4, then the forth is shut-down and the remaining 3 are run at a higher and more efficient power output. The accompanying equations for this analysis are discussed below.

The number of fuel cell stack which are operational can be determined from equation B16 below as a function of the power output required and the maximum power output each stack is able to deliver (which is 103.63kW in this analysis).

$$N_{Op-Stacks} = ROUNDUP\left(\left(\frac{P_{Out}}{P_{Stack(Max)}}\right),0\right) \quad \text{Eq B-16}$$

The power output and the percentage of maximum power of each operational fuel cell stack can then be determined from equations B17 and B18 respectively.

$$P_{Stack} = \frac{P_{Out}}{N_{Op-Stacks}} \quad \text{Eq B-17}$$

$$\%P_{Stack} = \frac{P_{Stack}}{P_{Stack(Max)}} \cdot 100 \quad \text{Eq B-18}$$

The total volumetric flow rate of the humid air passing through each operational fuel cell stack is given by equation B19 below. This is derived from expressions for the total mass flow rate of air entering the fuel cell and the density of the air with respect to its temperature and pressure.

$$Q_{Stack} = \frac{P}{4 \cdot V_{Cell} \cdot F} \cdot \left(\frac{S_{O2}}{r_{O2}}\right) \cdot \frac{R \cdot T_{FC(in)}}{P_{FC(in)} - \phi_{FC(in)} \cdot P_{VS}(@T_{FC(in)})} \cdot 10^6 \quad \text{Eq B-19}$$

The velocity of the humid air flowing through each channel on the bi-polar plate can be determined from equation B20 as a function of the internal geometry of the fuel cell stack. This requires knowledge of the number of cells in the stack (532 in this analysis), the number of parallel serpentine channels on each bi-polar plate (10 in this analysis) and the cross-sectional area of each reactant channel (0.0225cm^2 in this analysis).

$$V_{Ch-Cell} = \frac{Q_{Stack}}{N_{Cell} \cdot N_{Ch-Cell} \cdot A_{Ch}} \quad \text{Eq B-20}$$

The density of the humid air entering the fuel cell can then be determined from equation B21 as a function of the temperature and pressure of the air.

$$\rho_{Air-Humid} = \frac{\left(P_{FC(in)} - P_{Sat(in)}\right) \cdot M_{Air} + P_{Sat(in)} \cdot M_{H_2O}}{R \cdot T_{FC(in)} \cdot 1000} \quad \text{Eq B-21}$$

Determination of the viscosity of the humid air entering the fuel cell is more complex than for the other parameters and is typically determined as a composition of its component parts (air and water vapour). This first stage is to determine the viscosity of the air and water vapour at the temperature of the humid air. The viscosity of air and water vapour is typically given at a reference temperature of 25, which can then be determined at the required temperature from equations B22 and B23.

$$\mu_{1-Air(T-FC(in))} = \mu_{Air(25)} \cdot \frac{T_{25} + C_{Air}}{T_{FC(in)} + C_{Air}} \cdot \left(\frac{T_{FC(in)}}{T_{25}}\right)^{3/2} \quad \text{Eq B-22}$$

$$\mu_{2-WV(T-FC(in))} = \mu_{WV(25)} \cdot \frac{T_{25} + C_{WV}}{T_{FC(in)} + C_{WV}} \cdot \left(\frac{T_{FC(in)}}{T_{25}}\right)^{3/2} \quad \text{Eq B-23}$$

The parameters and constants used in these relations are,

Parameter	Value	Description
mu-air 25 (kgm-1s-1)	0.0000181	Viscosity of air at 25 deg C
mu-wv 25 (kgm-1s-1)	0.0000163	Viscosity of water vapor at 25 deg C
C-air	120	Sutherlands constant for air
C-water vapor	660	Sutherlands constant for water vapor

The next stage is to determine the volume fractions of air and water vapour present from equations B24 and B25 respectively.

$$r_{1-Air} = \frac{\phi_{FC(in)} \cdot P_{VS(@T-FC(in))}}{P_{FC(in)}} \quad \text{Eq B-24}$$

$$r_{2-WV} = \frac{P_{FC(in)} - \left(\phi_{FC(in)} \cdot P_{VS(@T-FC(in))}\right)}{P_{FC(in)}} \quad \text{Eq B-25}$$

We are then able to determine the functions required for the next stage of the analysis, for the air and water vapour, from equations B26 and B27 respectively.

$$\Psi_{1-Air} = \frac{\sqrt{2}}{4}\left[1 + \left(\frac{\mu_{1-Air}}{\mu_{2-WV}}\right)^{0.5}\left(\frac{r_{2-WV}}{r_{1-Air}}\right)^{0.25}\right]^2 \left(1 + \frac{r_{1-Air}}{r_{2-WV}}\right)^{-0.5} \quad \text{Eq B-26}$$

$$\Psi_{2-WV} = \frac{\sqrt{2}}{4}\left[1 + \left(\frac{\mu_{2-WV}}{\mu_{1-Air}}\right)^{0.5}\left(\frac{r_{1-Air}}{r_{2-WV}}\right)^{0.25}\right]^2 \left(1 + \frac{r_{2-WV}}{r_{1-Air}}\right)^{-0.5} \quad \text{Eq B-27}$$

The viscosity of the humid air mixture can finally be determined from equation B28 as a function of the parameters determined above.

$$\mu_{Air-Humid} = \frac{\mu_{1-Air}}{1+\Psi_{1-Air}\dfrac{M_{2-WV}}{M_{1-Air}}} + \frac{\mu_{2-WV}}{1+\Psi_{2-WV}\dfrac{M_{1-Air}}{M_{2-WV}}} \qquad \text{Eq B-28}$$

The Reynolds number of the flow within the bi-polar plate serpentine channels can then be determined from equation B29. The characteristic dimension in this expression is the hydraulic diameter of each of the channels, as will be determined below.

$$\mathrm{Re}_{Ch} = \frac{\rho_{Air-Humid} \cdot V_{Ch} \cdot D_{H-Ch}}{\mu_{Air-Humid}} \qquad \text{Eq B-29}$$

The friction factor for steady laminar flow in a channel can be determined from the expression below where $\mathrm{Re}-f$ has a constant value of 56 for a square channel.

$$f_{Ch} = \frac{\mathrm{Re}-f}{\mathrm{Re}_{Ch}} \qquad \text{Eq B-30}$$

The hydraulic diameter of the reactant channels can be determined from equation B31 as a function of width and depth of the channel (taken as 0.15 x 0.15 cm in this study).

$$D_{H-Ch} = \frac{2 \cdot W_{Ch} \cdot D_{Ch}}{W_{Ch} + D_{Ch}} \qquad \text{Eq B-31}$$

The length of each of the serpentine channels can be determined from equation B32, where the parameters used in this relation are,

- $A_{Cell(Act)}$ - Cell active area (400cm^2 in this example)
- $N_{Ch(P)}$ - Number of parallel serpentine channels in each bi-polar plate (10 in this example)
- W_{Ch} - Width of a channel (0.15cm in this example)
- S_{Ch} - Separation between the serpentine channels (0.05cm in this example)

$$L_{Ch} = \frac{A_{Cell(Act)}}{N_{Ch(P)} \cdot \left(W_{Ch} + S_{Ch}\right)} \qquad \text{Eq B-32}$$

The pressure drop in each of the serpentine channels can then be determined from equation B33. This expression can be seen to consist of two parts. The first of these is used to determine the pressure drop in the straight sections of the serpentine channel. The second part of this expression gives the additional pressure drop due to the presence of local loss a factors such as bends and obstructions. Many of the parameters in this expression have already been defined with the exception of,

- K_L - Local loss factor (in this analysis, this is given a value of 30 for each of the 90º bends in the serpentine path)
- N_{Bends} - The number of 90º bends in the serpentine path (18 in this example)

- f - Friction factor (assumed to be the same as for the straight channel lengths)

$$\Delta P_{Ch} = f_{Ch} \cdot \frac{L_{Ch}}{D_{H-Ch}} \cdot \rho_{Air-H} \cdot \frac{V_{Ch-Cell}^{2}}{2} + \sum \left(K_L \cdot f\right) \cdot \rho_{Air-H} \cdot \frac{V_{Ch-Cell}^{2}}{2} \quad \text{Eq B-33}$$

Since each of the cells in our stack are in parallel and in addition, each of the serpentine channels are parallel, the total pressure drop across the fuel cell stack is therefore equal to the result for the pressure drop in an single serpentine channel. The pressure drop in the fuel cell stack manifolds can be determined from equation B34 in which it is assumed to be 10% of the total pressure drop in the fuel cell stack channels.

$$\Delta P_{Man} = \frac{\Delta P_{Ch}}{10} \quad \text{Eq B-34}$$

The total pressure drop in the complete fuel cell stack assembly is then given by equation B35. Since the assembly of fuel cell stacks are in parallel, the pressure drop is the same for each stack and all the operational stacks collectively.

$$\Delta P_{Stack} = \Delta P_{Ch} + \Delta P_{Man} \quad \text{Eq B-35}$$

The pressure of the air at the fuel cell stack exit is then given by equation B36 as the difference between the air entering the fuel cell and the pressure drop.

$$P_{FC-Air(Out)} = P_{Stack-Op(Air)} - \Delta P_{Stack} \quad \text{Eq B-36}$$

In a fuel cell, it is important that the pressure is balanced on either side of the bipolar plate, to prevent damage to the membrane. Therefore the pressure at the hydrogen side exit will the same as for the air side exit, as given by equation B37.

$$P_{FC-H2(Out)} = P_{FC-Air(Out)} \quad \text{Eq B-37}$$

H1.4 Analysis block C – Fuel cell humidification

As already discussed, it is important that the fuel cell is kept with sufficient hydration limits, as failure to do so will cause the performance to be severely impaired. In this system, fuel cell humidification is achieved by humidifying the air supply stream entering the fuel cell with water recovered from the fuel cell outlet. The purpose of this analysis is to determine the quantity of water that has to be recovered from the fuel cell output streams, to feed the fuel processor and hydrate the fuel cell. A summary of the analytical procedure is shown in the flow chart below. A simplified representation of the humidification system is included at the end of this section for reference.

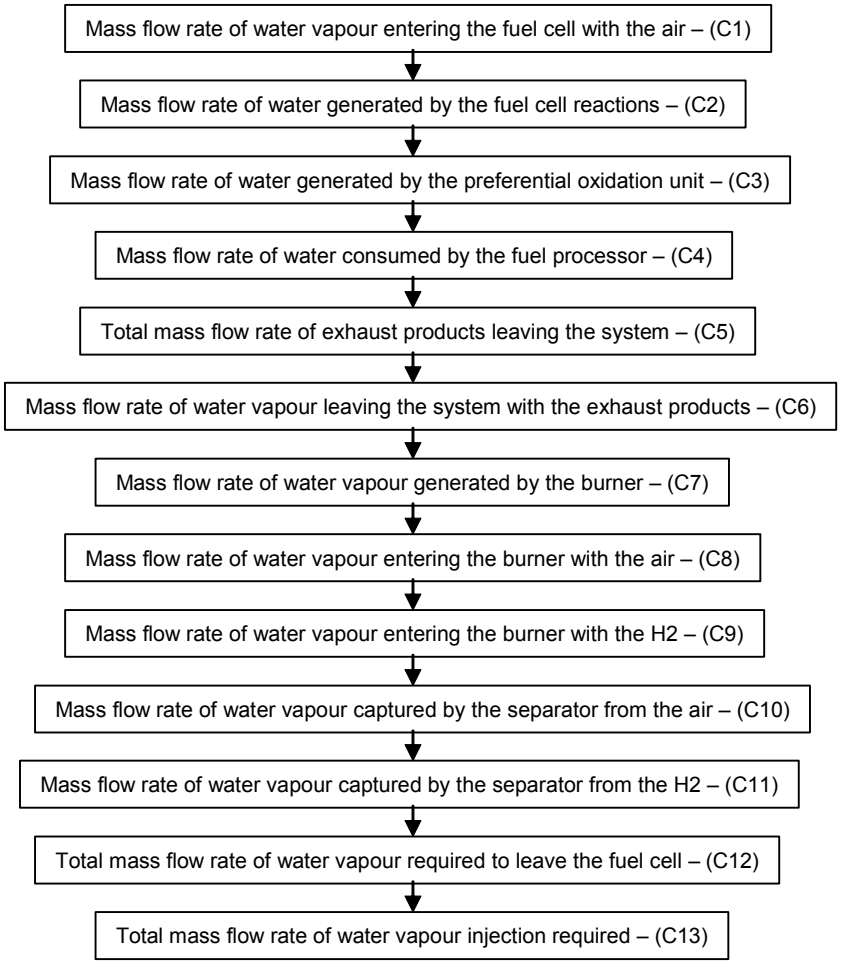

The accompanying equations are given below. A certain amount of water enters the system along with the ambient air via the air supply, as given by equation C1.

$$\dot{m}_{H_2O-FC(Air-in)} = \dot{m}_{Air-FC(in)} \cdot \frac{M_{H_2O}}{M_{Air}} \cdot \frac{\phi_{Amb} \cdot P_{VS}(@T_{FC(in)})}{P_{FC(in)} - \phi_{Amb} \cdot P_{VS}(@T_{FC(in)})} \qquad \text{Eq C-1}$$

Other sources of water in the system are, that generated by the fuel cell reaction and that generated by the PROX unit of the fuel processor, as given by C2 and C3 respectively.

$$\dot{m}_{H_2O-FC(Gen)} = \frac{P}{2 \cdot V_{Cell} \cdot F} \cdot M_{H_2O} \qquad \text{Eq C-2}$$

$$\dot{m}_{H_2O-PROX(Gen)} = S_{H2} \cdot \frac{P}{2 \cdot V_{Cell} \cdot F} \cdot \frac{r_{CO}}{f} \cdot \left(1 + \frac{m + n/4 - p/2}{\varepsilon} \cdot \frac{1 - r_{O2}}{r_{O2}} + f \right) \cdot (S_{PROX} - 1) \cdot M_{H_2O} \qquad \text{Eq C-3}$$

Now we know how much water is available, the next stage is to determine the water demands of the fuel processor as given by C4.

$$\dot{m}_{H_2O-FP(Cons)} = S_{H2} \cdot \frac{P}{2 \cdot V_{Cell} \cdot F} \cdot \frac{1}{f} \cdot \frac{(\varepsilon - 1)(2m - p) - n/2}{\varepsilon} \cdot M_{H_2O} \qquad \text{Eq C-4}$$

The mass flow rate of dry exhaust products leaving the burner can be determined from equation C5, which is determined from the balance of the products entering, leaving and generated by the system as given by $\sum \dot{m}_{In} = \sum \dot{m}_{Out} + \sum \dot{m}_{Gen}$. Where,

$$\sum \dot{m}_{In} = \dot{m}_{Fuel} + \dot{m}_{Air} + \dot{m}_{H_2O-FP} + \dot{m}_{H_2O-INJ}$$

$$\sum \dot{m}_{Out} = \dot{m}_{Exh} + \dot{m}_{H_2O-Seperator}$$

$$\sum \dot{m}_{Gen} = \dot{m}_{H_2O-FC} + \dot{m}_{H_2O-Burn} + \dot{m}_{H_2O-PROX}$$

$$\dot{m}_{Exh(Out)} = \dot{m}_{Fuel} + \dot{m}_{Air} - \dot{m}_{H_2O-FC} - \dot{m}_{H_2O-BURN} - \dot{m}_{H_2O-PROX} + \dot{m}_{H_2O-FP} + \dot{m}_{H_2O-INJ} \qquad \text{Eq C-5}$$

If we know the temperature, pressure and the relative humidity of the exhaust gas then the mass flow rate of water leaving the system with the burner exhaust gases can be determined from C6.

$$\dot{m}_{H_2O-Exh(Out)} = \dot{m}_{Exh(Out)} \cdot \frac{M_{H_2O}}{M_{Exh}} \cdot \frac{\phi_{Exh} \cdot P_{VS}(@T_{Exh(Out)})}{P_{Exh(Out)} - \phi_{Exh} \cdot P_{VS}(@T_{Exh(Out)})} \qquad \text{Eq C-6}$$

The majority of the terms used in equation C5 have already been derived in earlier analyses. The exception to this being the quantity of water generated in the burner as a by-product of the combustion process and the quantity of water required to be injected into the air stream for humidification. The quantity of water generated in the burner can be derived from C7.

$$\dot{m}_{H_2O-BURN(Gen)} = (S_{H2} - 1) \frac{P}{2 \cdot V_{Cell} \cdot F} \cdot M_{H_2O} \qquad \text{Eq C-7}$$

From earlier work, we know how much water must leave the fuel cell in order to keep it sufficiently hydrated. We also know how much water is generated in the fuel cell and how much enters the fuel cell along with the reactants. The required quantity of water to be injected into the air stream for hydration can then be determined from equation C8.

$$\dot{m}_{H_2O-INJ} = \dot{m}_{H_2O-FC(Out)} - \dot{m}_{H_2O-Air(in)} - \dot{m}_{H_2O-H2(in)} - \dot{m}_{H_2O-FC(Gen)} \quad \text{Eq C-8}$$

In equation C8, the quantity of water leaving the fuel cell is equal to the sum of that entering the burner with the reactant streams and that recovered by the separators as in equation C9.

$$\dot{m}_{H_2O-FC(Out)} = \dot{m}_{H_2O-BURN(Air-In)} + \dot{m}_{H_2O-SEP(Air-In)} + \dot{m}_{H_2O-BURN(H2-In)} + \dot{m}_{H_2O-SEP(H2-In)} \quad \text{Eq C-9}$$

The terms in equation C9 can be determined from the relations C10 to C13. Where X in the relations is the fraction of water recovered by each of the separators. In particular C11 and C13 give the quantity of water recovered from the fuel and air streams. C10 and C12 then give the remainder of water that enters the burner along with each of the streams.

$$\dot{m}_{H_2O-BURN(Air-In)} = \dot{m}_{H_2O-FC(Air-out)} \cdot (1 - X_{Air-Fract}) \quad \text{Eq C-10}$$

$$\dot{m}_{H_2O-SEP(Air-In)} = \dot{m}_{H_2O-FC(Air-out)} \cdot (X_{Air-Fract}) \quad \text{Eq C-11}$$

$$\dot{m}_{H_2O-BURN(H2-In)} = \dot{m}_{H_2O-FC(H2-out)} \cdot (1 - X_{H2-Fract}) \quad \text{Eq C-12}$$

$$\dot{m}_{H_2O-SEP(H2-In)} = \dot{m}_{H_2O-FC(H2-out)} \cdot (X_{H2-Fract}) \quad \text{Eq C-13}$$

H1.4.1 Simplified representation of the humidification system

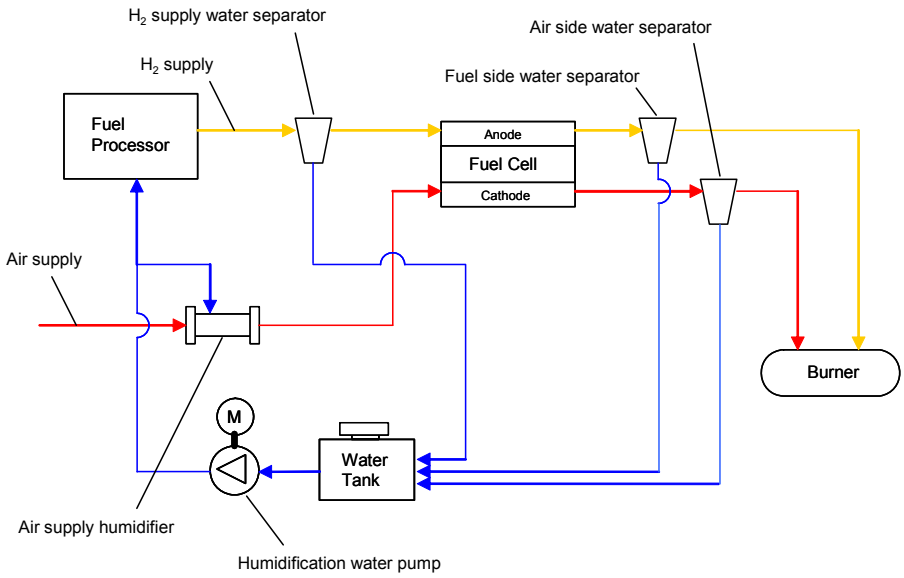

Figure C-1

H1.5 Analysis block D – Burner operating conditions

H1.5.1 Mass flow of the products entering the burner

This part of the analysis is used to determine the mass flow rate of the products entering the burner. A summary of the analytical procedure is shown in the flow chart below.

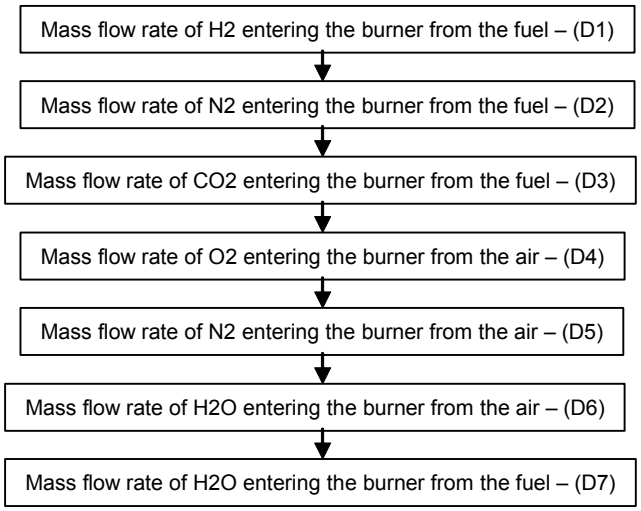

The accompanying equations are given below. The reader is advised to refer to the section on derivation of burner equations for further details of the terms used in these equations. The mass flow rate of hydrogen, nitrogen and carbon dioxide entering the burner from the fuel supply is given by equations D1 to D3 respectively.

$$\dot{m}_{H2-fuel(in)} = \frac{P}{2 \cdot V_{Cell} \cdot F} \cdot (S_{H2} - 1) \cdot M_{H2} \qquad \text{Eq D-1}$$

$$\dot{m}_{N2-fuel(in)} = \frac{P}{2 \cdot V_{Cell} \cdot F} \cdot \frac{S_{H2}}{r_{H2}} \cdot r_{N2} \cdot M_{N2} \qquad \text{Eq D-2}$$

$$\dot{m}_{CO2-fuel(in)} = \frac{P}{2 \cdot V_{Cell} \cdot F} \cdot \frac{S_{H2}}{r_{H2}} \cdot r_{CO2} \cdot M_{CO2} \qquad \text{Eq D-3}$$

The mass flow rate of oxygen and nitrogen entering the burner from the oxygen depleted air supply is given by equations D4 and D5 respectively.

$$\dot{m}_{O2-air(in)} = \frac{P}{4 \cdot V_{Cell} \cdot F} \cdot (S_{O2} - 1) \cdot M_{O2} \qquad \text{Eq D-4}$$

$$\dot{m}_{N2-air(in)} = \frac{P}{4 \cdot V_{Cell} \cdot F} \cdot S_{O2} \cdot \frac{(1 - r_{O2})}{r_{O2}} \cdot M_{N2} \qquad \text{Eq D-5}$$

The mass flow rate of water which accompanies the air and fuel streams entering the burner is given by equations D6 and D7 respectively.

$$\dot{m}_{H_2O-air(in)} = \frac{P}{4 \cdot V_{Cell} \cdot F} \cdot \left(\frac{S_{O2}}{r_{O2}} - 1 \right) \cdot \frac{\phi_{FC(out)} \cdot P_{VS}(@T_{Burn(in)})}{P_{Burn(in)} - \phi_{FC(out)} \cdot P_{VS}(@T_{Burn(in)})} \cdot M_{H_2O} \cdot (1 - X_{Air-Fract})$$

Eq D-6

$$\dot{m}_{H_2O-H2(in)} = \frac{P}{2 \cdot V_{Cell} \cdot F} \cdot (S_{H2} - 1) \cdot \frac{\phi_{FC(out)} \cdot P_{VS}(@T_{Burn(in)})}{P_{Burn(in)} - \phi_{FC(out)} \cdot P_{VS}(@T_{Burn(in)})} \cdot M_{H_2O} \cdot (1 - X_{H2-Fract})$$

Eq D-7

H1.5.2 Mass flow rate of the products leaving the burner

This part of the analysis is used to determine the mass flow rate of the products leaving the burner. A summary of the analytical procedure is shown in the flow chart below.

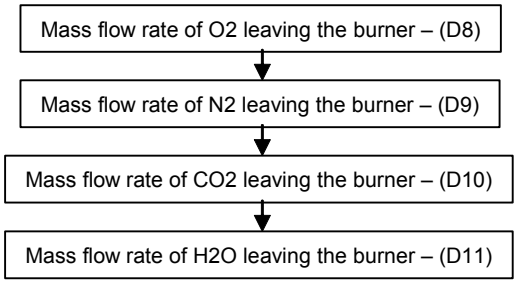

The accompanying equations are given below. The reader is advised to refer to the section on derivation of burner equations for further details of the terms used in these equations. The mass flow rate of oxygen, nitrogen and carbon dioxide leaving the burner is given by equations D8 to D10 respectively. This analysis assumes that the presence of any carbon monoxide to be minimal.

$$\dot{m}_{O2-Burn(out)} = \frac{P}{4 \cdot V_{Cell} \cdot F} \cdot (S_{O2} - S_{H2}) \cdot M_{O2}$$

Eq D-8

$$\dot{m}_{N2-Burn(out)} = \frac{P}{2 \cdot V_{Cell} \cdot F} \left(\left\{ S_{H2} \cdot \frac{r_{N2}}{r_{H2}} \right\} + \left\{ \frac{S_{O2}}{2} \cdot \left[\frac{1 - r_{O2}}{r_{O2}} \right] \right\} \right) \cdot M_{N2}$$

Eq D-9

$$\dot{m}_{CO2-Burn(out)} = \frac{P}{2 \cdot V_{Cell} \cdot F} \cdot \frac{S_{H2}}{r_{H2}} \cdot r_{CO2} \cdot M_{CO2}$$

Eq D-10

The mass flow rate of water leaving the burner, as given by equation D11, is assumed to be the same as that entering the burner as it merely acts as a dilutant.

$$\dot{m}_{H_2O-Burn(out)} = \left(\frac{P}{2 \cdot V_{Cell} \cdot F} \cdot \{S_{H2} - 1\} \cdot M_{H_2O} \right) + \dot{m}_{H_2O-Air(in)} + \dot{m}_{H_2O-H2(in)}$$

Eq D-11

H1.5.3 Mass flow rate of products recovered by the separators

This part of the analysis is used to determine the mass flow rate of the water which has been recovered by the separators, for reuse within the fuel cell system. A summary of the analytical procedure is shown in the flow chart below.

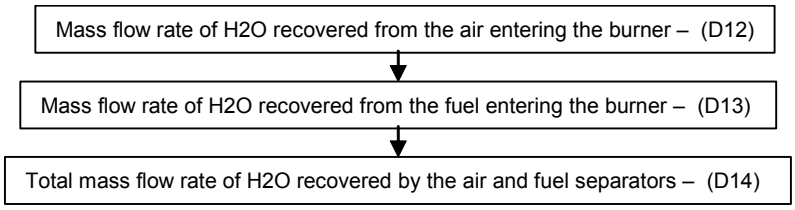

The accompanying equations are given below. If we refer back to the relations to determine the mass flow rate of water entering the burner we will see that this is governed by the fraction (1-X). Where X is the fraction of water captured by each of the separators and is assumed to be the same for each in this analysis. If we therefore replace the (1-X) simply with X then we obtain the quantity of water captured by each of the separators, as given by equations D12 and D13.

$$\dot{m}_{H_2O-air(SEP)} = \frac{P}{4 \cdot V_{Cell} \cdot F} \cdot \left(\frac{S_{O2}}{r_{O2}} - 1 \right) \cdot \frac{\phi_{FC(out)} \cdot P_{VS}(@T_{Burn(in)})}{P_{Burn(in)} - \phi_{FC(out)} \cdot P_{VS}(@T_{Burn(in)})} \cdot M_{H_2O} \cdot X_{Air-Fract}$$

Eq D-12

$$\dot{m}_{H_2O-H2(SEP)} = \frac{P}{2 \cdot V_{Cell} \cdot F} \cdot (S_{H2} - 1) \cdot \frac{\phi_{FC(out)} \cdot P_{VS}(@T_{Burn(in)})}{P_{Burn(in)} - \phi_{FC(out)} \cdot P_{VS}(@T_{Burn(in)})} \cdot M_{H_2O} \cdot X_{H2-Fract}$$

Eq D-13

The total amount of water recovered is then the sum of that from the fuel and air stream separators, as given by equation D14.

$$\dot{m}_{H_2O-SEP(total)} = \dot{m}_{H_2O-Air(SEP)} + \dot{m}_{H_2O-H2(SEP)}$$

Eq D-14

H1.5.4 Enthalpy of the products entering the burner

This part of the analysis is used to determine the enthalpy of the products entering the burner. A summary of the analytical procedure is shown in the flow chart below.

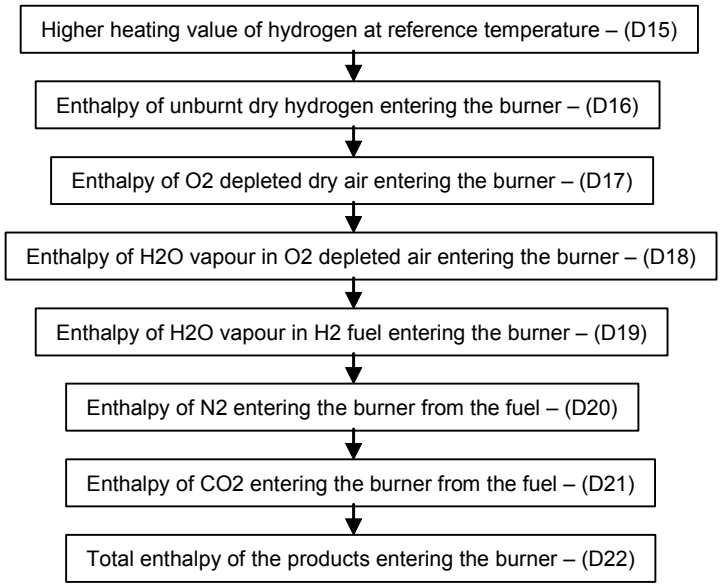

The accompanying equations are given below. The enthalpy of a gas or liquid can be determined by one of four ways according to its properties, as given below.

1) In the case of dry gases – The enthalpy is given by the relation $H = \dot{m} \cdot C_p \cdot t$ where $\dot{m}$ is the mass flow rate, C_p is the specific heat and t is the temperature.
2) In the case of combustible gases – Since any combustible gas has a heating value, this must be included in the enthalpy calculation which is given by $H = \dot{m} \cdot \left(C_p \cdot t + h_{HHV(0)}\right)$
3) In the case of liquid water – The enthalpy is determined from $H = \dot{m} \cdot C_p \cdot t$ with the corresponding values used for water in its liquid state.
4) In the case of water vapour – The enthalpy of the water will now include an extra term h_{fg} to allow for the heat of evaporation. When taken at 0°C this has a value of 2500jg^{-1}. The relation then becomes $H = \dot{m} \cdot \left(C_p \cdot t + h_{fg(0)}\right)$

It should be noted that the higher heating value parameter is temperature dependent. The values quoted in the literature are typically given at 25°C but for the expressions here we require them to be referenced to 0°C. This can be achieved with equation D15.

$$h_{HHV(0)} = h_{HHV(25)} - \left(C_{P-H2} + \frac{1}{2}\frac{M_{O2}}{M_{H2}} C_{P-O2} - \frac{M_{H_2O}}{M_{H2}} C_{P-H_2O(l)} \right) \cdot 25 \qquad \text{Eq D-15}$$

Since hydrogen is a combustible gas then its enthalpy is given by the relation of D16. This relation also includes and efficiency factor η_{Burn} to allow for combustion inefficiencies in the burner. In the absence of better information, a value of 0.9925 was assumed for this value which is in line with the efficiency of the burner of a gas turbine.

$$H_{H2-Burn(in)} = \dot{m}_{H2-Burn(in)} \cdot \left(C_{P-H2} \cdot t_{H2-Burn(in)} + h_{HHV(0)}\right) \cdot \eta_{Burn} \qquad \text{Eq D-16}$$

The air entering the burner will be oxygen depleted since some of this will have been used up in the fuel cell. The most efficient way to determine the enthalpy of this is to break it down into its major component parts (oxygen and nitrogen), as in D17.

$$H_{N2+O2-Burn(air-in)} = \dot{m}_{O2-Burn(air-in)} \cdot \left(C_{P-O2} \cdot t_{O2-Burn(air-in)}\right) + \dot{m}_{N2-Burn(air-in)} \cdot \left(C_{P-N2} \cdot t_{N2-Burn(air-in)}\right)$$

Eq D-17

The water that enters the burner does so along with the fuel and air streams. Since this water is in vapour form, its enthalpy can be determined from equations D18 and D19.

$$H_{H_2O-Burn(Air-in)} = \dot{m}_{H_2O(g)-Burn(Air-in)} \cdot \left(C_{P-H_2O(g)} \cdot t_{H_2O-Burn(Air-in)} + h_{fg(0)}\right) \quad \text{Eq D-18}$$

$$H_{H_2O-Burn(H2-in)} = \dot{m}_{H_2O(g)-Burn(H2-in)} \cdot \left(C_{P-H_2O(g)} \cdot t_{H_2O-Burn(H2-in)} + h_{fg(0)}\right) \quad \text{Eq D-19}$$

The enthalpy of the remaining dry gases which originate from the reformed fuel (nitrogen and carbon dioxide) can be determined from equations D20 and D21.

$$H_{N2-Burn(fuel-in)} = \dot{m}_{N2-Burn(fuel-in)} \cdot \left(C_{P-N2} \cdot t_{N2-Burn(fuel-in)}\right) \quad \text{Eq D-20}$$

$$H_{CO2-Burn(fuel-in)} = \dot{m}_{CO2-Burn(fuel-in)} \cdot \left(C_{P-CO2} \cdot t_{CO2-Burn(fuel-in)}\right) \quad \text{Eq D-21}$$

The total enthalpy of the products entering the burner is finally the sum of the components above, as given in equation D22.

$$\sum H_{Burn(in)} = H_{H2(fuel)} + H_{N2+O2(Air)} + H_{CO2(fuel)} + H_{H_2O(H2)} + H_{H_2O(Air)} + H_{N2(fuel)}$$

Eq D-22

H1.5.5 Enthalpy of the products leaving the burner

This part of the analysis is used to determine the enthalpy of the products leaving the burner. A summary of the analytical procedure is shown in the flow chart below.

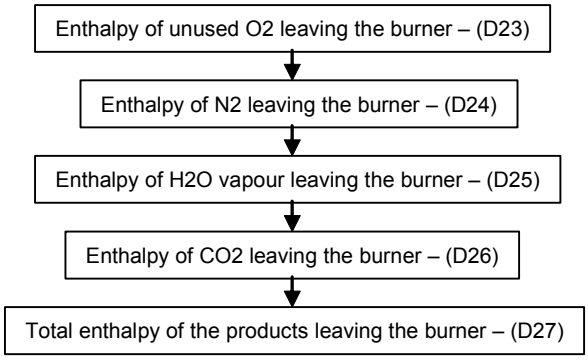

The accompanying equations are given below. The dry gases leaving the burner are unused oxygen, nitrogen and carbon dioxide and their enthalpies are determined from D23, D24 and D26 respectively. Since the water leaving the burner is in vapour form, it can be determined from equation D25.

$$H_{O2-Burn(out)} = \dot{m}_{O2-Burn(out)} \cdot \left(C_{P-O2} \cdot t_{O2-Burn(out)}\right) \quad \text{Eq D-23}$$

$$H_{N2-Burn(out)} = \dot{m}_{N2-Burn(out)} \cdot \left(C_{P-N2} \cdot t_{N2-Burn(out)}\right) \quad \text{Eq D-24}$$

$$H_{H_2O-Burn(out)} = \dot{m}_{H_2O(g)-Burn(out)} \cdot \left(C_{P-H_2O(g)} \cdot t_{H_2O-Burn(out)} + h_{fg(0)}\right) \quad \text{Eq D-25}$$

$$H_{CO2-Burn(out)} = \dot{m}_{CO2-Burn(out)} \cdot \left(C_{P-CO2} \cdot t_{CO2-Burn(out)}\right) \quad \text{Eq D-26}$$

The summation of the enthalpy of the products leaving the burner is finally given by equation D27.

$$\sum H_{Burn(out)} = H_{O2-Burn(out)} + H_{N2-Burn(out)} + H_{CO2-Burn(out)} + H_{H_2O-Burn(out)} \quad \text{Eq D-27}$$

H1.5.6 Enthalpy difference between burner entry and exit

This part of the analysis determines the difference in the enthalpy of the products entering and leaving the burner and forms part of the solution process. In this analysis, the burner temperature is an unknown and the analysis must be solved by iterating an initial estimate until the enthalpy difference across the burner is zero. The enthalpy of the water captured by the air and fuel stream separators is also determined at this point but is required in a different analysis. A summary of the analytical procedure is shown in the flow chart below.

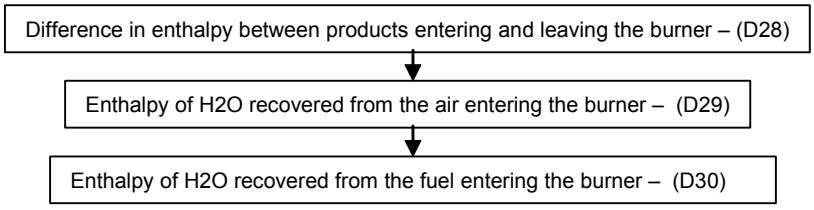

The accompanying equations are given below. The difference in enthalpy between the products entering and leaving the burner can be determined from equation D28.

$$\Delta H = \sum H_{Burn(in)} - \sum H_{Burn(out)} \quad \text{Eq D-28}$$

Equations D29 and D30 give the enthalpy of the water vapour captured by the air and fuel stream water separators respectively. Although the water will be in liquid form when it leaves the separator and not vapour form, it is useful for a later analysis to determine the enthalpy loss as a result of the initial recovery of the water vapour.

$$H_{H_2O-SEP(Air)} = \dot{m}_{H_2O(g)-SEP(Air)} \cdot \left(C_{P-H_2O(g)} \cdot t_{H_2O-SEP(Air)} + h_{fg(0)}\right) \quad \text{Eq D-29}$$

$$H_{H_2O-SEP(H2)} = \dot{m}_{H_2O(g)-SEP(H2)} \cdot \left(C_{P-H_2O(g)} \cdot t_{H_2O-SEP(H2)} + h_{fg(0)}\right) \quad \text{Eq D-30}$$

H1.5.7 Properties of the exhaust gas leaving the burner

The purpose of this final stage of the analysis is to determine the composition and thus the properties of the exhaust gas leaving the burner. Of most importance are the specific heat (constant pressure) and the ratio of specific heats which are used in a different

section for the analysis of turbine output power. A summary of the analytical procedure is shown in the flow chart below.

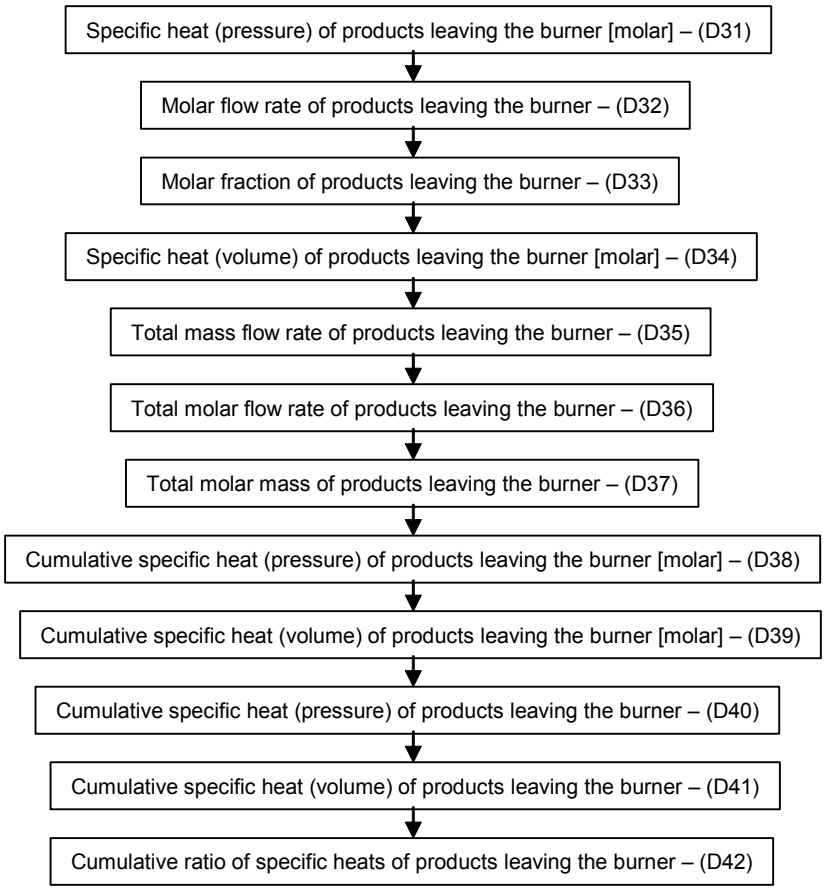

The accompanying equations to determine the properties of each of the products leaving the burner are given below. The specific heat at constant pressure is given by equation D31 on a molar basis.

$$\overline{C_{Pi}} = a + (b \cdot t) + (c \cdot t^2) + (d \cdot t^3) \qquad \text{Eq D-31}$$

The constants for the above equation are given in the following table for each of the components that make up the exhaust gases

	a	b	c	d
O2	25.48	1.52E-02	-7.16E-06	1.31E-09
N2	28.9	-1.57E-03	8.08E-06	-2.87E-09
H2O (vapour)	32.24	1.92E-03	1.06E-05	-3.60E-09
CO2	22.26	5.98E-02	-3.50E-05	7.47E-09

To be able to make use of the above expression, it is necessary to change the mass flow rates into molar flow rates, with equation D32.

$$N_i = \frac{m_i}{M_i} \qquad \text{Eq D-32}$$

The molar fraction of each of the products leaving the burner can be determined from equation D33, where the denominator is the sum of the moles of all the gases.

$$y_i = \frac{N_i}{\sum N_i} \qquad \text{Eq D-33}$$

The specific heat of each of the products at constant volume can be determined from equation D34, where R_u is the universal gas constant. (R_u = 8.3143 kJ/kmol.K)

$$\overline{C_{Vi}} = \overline{C_{Pi}} - R_u \qquad \text{Eq D-34}$$

The total mass flow rate of the gases leaving the burner can then be determined from equation D35 and the total molar flow rate from equation D36.

$$\dot{m}_{Total} = \sum \dot{m}_i \qquad \text{Eq D-35}$$

$$N_{Total} = \sum N_i \qquad \text{Eq D-36}$$

The total molar mass of the exhaust gas mixture leaving the burner can be determined as the sum of the products of the molar mass of each of the individual gases and their molar fraction. This is given by equation D37.

$$M_{Total} = \sum \left(M_i \cdot y_i \right) \qquad \text{Eq D-37}$$

In a similar way, the specific heats at constant pressure and volume for the exhaust gas mixture on a molar basis are given by equations D38 and D39 respectively.

$$\overline{C_{Pm}} = \sum \left(\overline{C_{Pi}} \cdot y_i \right) \qquad \text{Eq D-38}$$

$$\overline{C_{Vm}} = \sum \left(\overline{C_{Vi}} \cdot y_i \right) \qquad \text{Eq D-39}$$

The specific heat at constant pressure and constant volume for the exhaust gas mixture can then be converted to a mass basis with equations D40 and D41.

$$C_{Pm} = \frac{\overline{C_{Pm}}}{M_{Total}} \qquad \text{Eq D-40}$$

$$C_{Vm} = \frac{\overline{C_{Vm}}}{M_{Total}} \qquad \text{Eq D-41}$$

Finally, the ratio of specific heats (also referred to as gamma) is given by equation D42.

$$k = \frac{C_{Pm}}{C_{Vm}} \qquad \text{Eq D-42}$$

H1.6 Analysis block E – Compressor and turbine analysis

The purpose of this analysis is to determine the power demands of the compressor and the power available from the turbine. The solution for our system is found when the power available from the turbine exactly matches the demands of the compressor. For our work, it is also necessary to determine the temperatures of the gasses leaving the compressor and turbine. The outlet temperature of the compressor gives an indication of the demands of a charge cooler, required to bring the temperature inline with that of the fuel cell inlet. The exit temperature of the turbine is used to determine the quantity of water leaving the system, if required. The relevant equations are given below but since these are standard equations for compressors and turbines, they will not be discussed in detail here.

The outlet temperature of the compressor can be determined from equation E1 and its power demands from equation E2. In each case, the efficiency η_{Comp} is taken to be 0.65, which is a typical figure for an air compressor.

$$T_{Comp(Out)} = \frac{T_{Comp(in)}}{\eta_{Comp}} \left[\left(\frac{P_{Out}}{P_{In}} \right)^{\frac{\gamma-1}{\gamma}} - 1 \right] + T_{Comp(in)} \qquad \text{Eq E-1}$$

$$W_{Comp} = C_{P(Air)} \cdot \frac{T_{Comp(in)}}{\eta_{Comp}} \left[\left(\frac{P_{Out}}{P_{In}} \right)^{\frac{\gamma-1}{\gamma}} - 1 \right] \cdot \dot{m}_{Comp} \qquad \text{Eq E-2}$$

In the case of the turbine, its outlet temperature and power output can be determined from equations E3 and E4 respectively. In each case, the efficiency η_{Turb} is taken to be 0.65, which again is a typical figure for a turbine.

$$T_{Turb(Out)} = T_{Turb(in)} \cdot \eta_{Turb} \cdot \left[\left(\frac{P_{Out}}{P_{In}} \right)^{\frac{\gamma-1}{\gamma}} - 1 \right] + T_{Turb(in)} \qquad \text{Eq E-3}$$

$$W_{Turb} = C_{P(Exh)} \cdot \eta_{Turb} \cdot T_{Turb(in)} \left[\left(\frac{P_{Out}}{P_{In}} \right)^{\frac{\gamma-1}{\gamma}} - 1 \right] \cdot \dot{m}_{Turb} \qquad \text{Eq E-4}$$

H1.7 Analysis block F – Fuel cell air and fuel requirements

H1.7.1 Fuel cell system with autothermal fuel processor

The purpose of this analysis is to determine the mass flow rate of air and fuel, which is required by the complete fuel cell system. A summary of the analytical procedure is shown in the flow chart below. The accompanying equations are also given below. The reader is however advised to refer to the sections on fuel cell derivations and fuel processor derivations for further details of the terms included in the expressions.

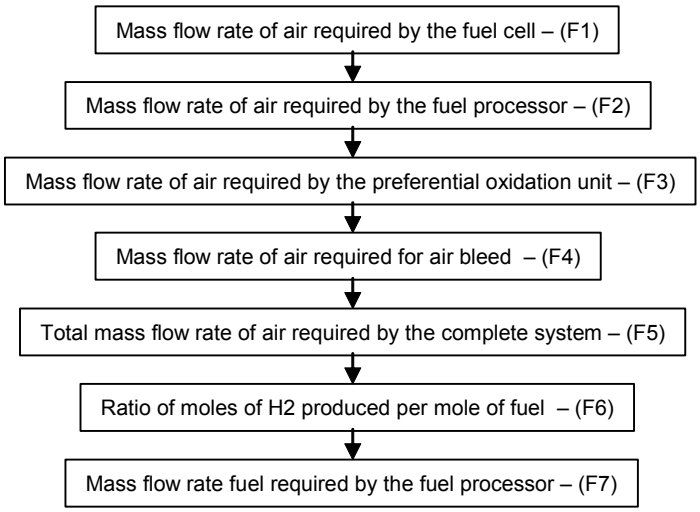

The theoretical mass flow rate of air required by the fuel cell is given by equation F1.

$$\dot{m}_{Air-FC(in)} = \frac{S_{O2}}{r_{O2}} \cdot \frac{P}{4 \cdot V_{Cell} \cdot F} \cdot M_{Air} \qquad \text{Eq F-1}$$

The additional air required for the autothermal fuel processor and PROX clean up unit can be determined from equations F2 and F3 respectively.

$$\dot{m}_{Air-FP(in)} = S_{H2} \cdot \frac{P}{2 \cdot V_{Cell} \cdot F} \cdot \frac{1}{f} \cdot \frac{m + n/4 - p/2}{\varepsilon} \cdot \frac{M_{Air}}{r_{O2}} \qquad \text{Eq F-2}$$

$$\dot{m}_{Air-PROX(in)} = S_{H2} \cdot \frac{P}{2 \cdot V_{Cell} \cdot F} \cdot \frac{r_{CO}}{f} \cdot \left(1 + \frac{m + n/4 - p/2}{\varepsilon} \cdot \frac{1 - r_{O2}}{r_{O2}} + f \right) \cdot \frac{S_{PROX}}{2} \cdot \frac{M_{Air}}{r_{O2}} \qquad \text{Eq F-3}$$

As already discussed, to reduce carbon formation, a small amount of air is typically bled from the air supply and fed into the fuel cell along with the hydrogen supply. This is typically 2% of the hydrogen flow rate as given by equation F4.

$$\dot{m}_{Air-Bleed} = 0.02 \cdot \frac{S_{H2}}{r_{H2}} \cdot \frac{P}{2 \cdot V_{Cell} \cdot F} \cdot M_{Air} \quad \text{Eq F-4}$$

The total mass flow rate of air required by the fuel cell system can then be determined from equation F5 as the sum of the terms above.

$$\dot{m}_{Air-Total(in)} = \dot{m}_{Air-FC(in)} + \dot{m}_{Air-FP(in)} + \dot{m}_{Air-PROX(in)} + \dot{m}_{Air-Bleed} \quad \text{Eq F-5}$$

From our earlier analyses, we know what the theoretical flow rate of hydrogen for the fuel cell is. Equation F6 from the autothermal fuel processor derivations section then allows us to determine the molar mass flow rate of fuel required to achieve a unit hydrogen output.

$$f = \frac{r_{H2} \cdot \left(1 + \frac{1.5}{\varepsilon}\left[\frac{1 - r_{O2}}{r_{O2}}\right]\right)}{1 - r_{H2}} \quad \text{Eq F-6}$$

Using the expression for the flow rate of hydrogen for the fuel cell, the required mass flow rate of fuel can be determined as in equation F7, which incorporates equation F6.

$$\dot{m}_{Fuel} = S_{H2} \cdot \frac{P}{2 \cdot V_{Cell} \cdot F} \cdot \frac{M_{Fuel}}{f} \quad \text{Eq F-7}$$

H1.7.2 Fuel cell system with steam reformer fuel processor

In the case of a fuel cell system with a steam reformer based fuel processor, the same analysis approach is adopted as given above but some of the equation will differ. The reader is advised to refer to the sections on fuel processor derivations for more details. In this case, equation F2 will be replaced by F8, F3 by F9 and F6 by F10.

$$\dot{m}_{Air-FP(in)} = 0 \quad \text{Eq F-8}$$

$$\dot{m}_{Air-PROX(in)} = S_{H2} \cdot \frac{P}{2 \cdot V_{Cell} \cdot F} \cdot \frac{r_{CO}}{f} \cdot (1 + f) \cdot \frac{S_{PROX}}{2} \cdot \frac{M_{Air}}{r_{O2}} \quad \text{Eq F-9}$$

$$f = 2m + \frac{n}{2} - p \quad \text{Eq F-10}$$

It is also worth noting that the water generated and consumed by the fuel processor will also be different to the autothermal system, as is required for another analysis section. Where, the replacement expressions are given by equations F10 and F12 below.

$$\dot{m}_{H_2O-PROX(Gen)} = S_{H2} \cdot \frac{P}{2 \cdot V_{Cell} \cdot F} \cdot \frac{r_{CO}}{f} \cdot (1 + f) \cdot (S_{PROX} - 1) \cdot M_{H_2O} \quad \text{Eq F-11}$$

$$\dot{m}_{H_2O-FP(Cons)} = S_{H2} \cdot \frac{P}{2 \cdot V_{Cell} \cdot F} \cdot \frac{1}{f} \cdot (2m - p) \cdot M_{H_2O} \quad \text{Eq F-12}$$

H1.8 Analysis block G - Analysis solution procedure

In the fuel cell system analysis overview section, the reader was given an introduction to the complexity of this analysis. The true complexity of the complete analysis however soon becomes evident when we consider the links between the blocks that make up the analysis. Within this analysis, there are a number of variables which have to be solved one-by-one in order to find the global solution, as shown in the flowchart below. This process is however very tedious since each of the variables also have an impact on each other and thus an iterative solution within an iterative solution must be adopted as shown in the figure below. The global solution therefore involved a slowly converging spiral of the solution variables. The author developed a macro based Microsoft Excel spreadsheet for the very purpose of solving this analysis, but this still took a reasonable amount of time to find the final solution for each operating point being tested. Thus, many hours were devoted to determining all the results required at the different power requirements and flight conditions being studied.

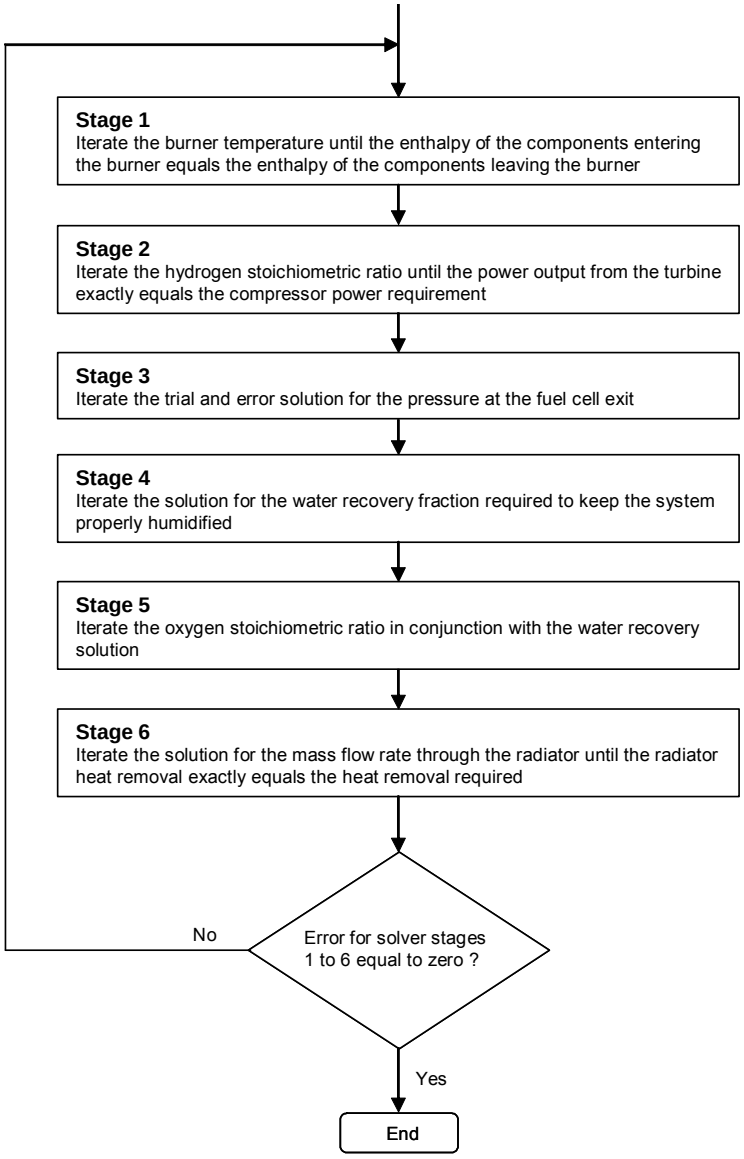

H1.9 Analysis block H – Heat removal requirements

H1.9.1 Mass flow rate of products entering and leaving the fuel cell

This part of the analysis is used to determine the mass flow rate of the products entering and leaving the fuel cell. A summary of the analytical procedure is shown in the flow chart below. The accompanying equations are also given below.

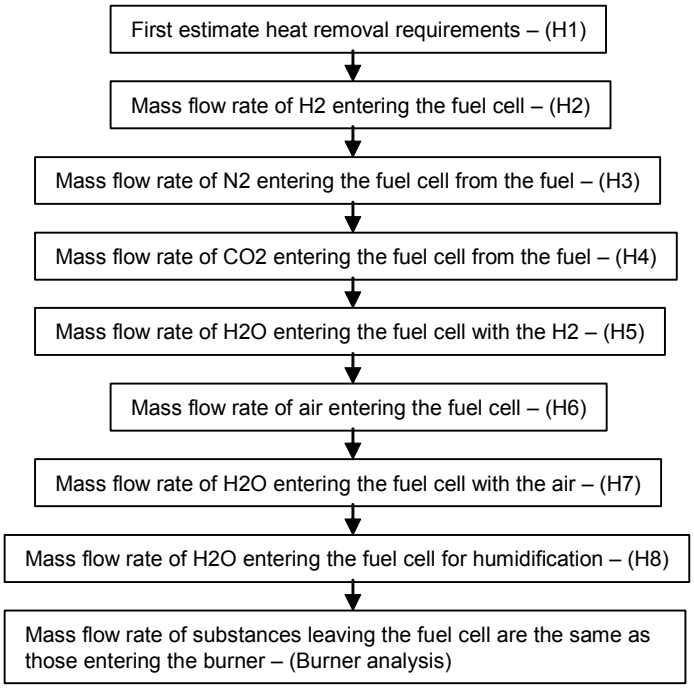

A first pass estimate of the waste heat generated by a fuel cell can be obtained from consideration of the inefficiencies within an operational fuel cell which is drawing power. This is given by equation H1 below.

$$Q_{Heating} = P \cdot \left(\frac{1.25}{V_{Cell}} - 1 \right) \qquad \text{Eq H-1}$$

This is however a very basic first approximation and does not give a very accurate estimate of the waste heat which has to be removed by the cooling system. To obtain a better estimate, we must also take into account the heat which is being taken into and out of the system by the reactants and products which enter and leave the system respectively. To be able to carry out such an analysis, it is first necessary to determine the mass flow rate of the products entering and leaving the system. The reader is advised to refer to the section on fuel cell derivations for further details of the terms used in the following equations. The mass flow of hydrogen entering the fuel cell is given by equation H2.

$$\dot{m}_{H2} = \frac{P}{2 \cdot V_{Cell} \cdot F} \cdot S_{H2} \cdot M_{H2} \qquad \text{Eq H-2}$$

Since nitrogen and carbon dioxide are not involved in the fuel cell reactions, they merely pass straight through and act as dilutants. The mass flow rate of these products leaving the fuel cell and entering the burner will therefore be identical to that entering the fuel cell. The mass flow rate of the products entering the burner can be obtained from the burner analysis section. The quantity of N_2 and CO_2 entering the fuel cell from the fuel can be determined from equations H3 and H4 respectively.

$$\dot{m}_{N2-FC:Fuel(in)} = \dot{m}_{N2-Burn:Fuel(in)} \quad \text{Eq H-3}$$

$$\dot{m}_{CO2-FC:Fuel(in)} = \dot{m}_{CO2-Burn:Fuel(in)} \quad \text{Eq H-4}$$

The hydrogen entering the fuel cell is assumed to be dry and therefore any water attached to this stream will be zero as defined in equation H5.

$$\dot{m}_{H_2O-FC:H2(in)} = 0 \quad \text{Eq H-5}$$

The mass flow rate of air entering the fuel cell can be determined from equation H6 and any water attached to it can be determined from equation H7.

$$\dot{m}_{Air-FC(in)} = \frac{S_{O2}}{r_{O2}} \cdot \frac{P}{4 \cdot V_{Cell} \cdot F} \cdot M_{Air} \quad \text{Eq H-6}$$

$$\dot{m}_{H_2O-FC(Air-in)} = \dot{m}_{Air-FC(in)} \cdot \frac{M_{H_2O}}{M_{Air}} \cdot \frac{\phi_{Amb} \cdot P_{VS}(@T_{FC(in)})}{P_{FC(in)} - \phi_{Amb} \cdot P_{VS}(@T_{FC(in)})} \quad \text{Eq H-7}$$

The water entering the fuel cell will also be supplemented with an additional mass flow rate of water as required for the humidification of the fuel cell. This is given by equation H8, which is used to decipher positive mass flow rates only.

$$\dot{m}_{H_2O-INJ} = IF(\dot{m}_{H_2O-INJ} > 0, \dot{m}_{H_2O-INJ}, 0) \quad \text{Eq H-8}$$

The mass flow rates of other products leaving the fuel cell are identical to those entering the burner and the reader should refer to this section for more details. The reader should however be aware of the presence of the water separators. The mass flow rate of water leaving the fuel cell will thus also include that captured by the separators.

H1.9.2 Quantity of waste heat to be removed by the cooling system

This part of the analysis is used to determine the quantity of waste heat which must be removed by the cooling system, from a first law of thermodynamics analysis of the system. A summary of the analytical procedure is shown in the flow chart below. The accompanying equations are also given below.

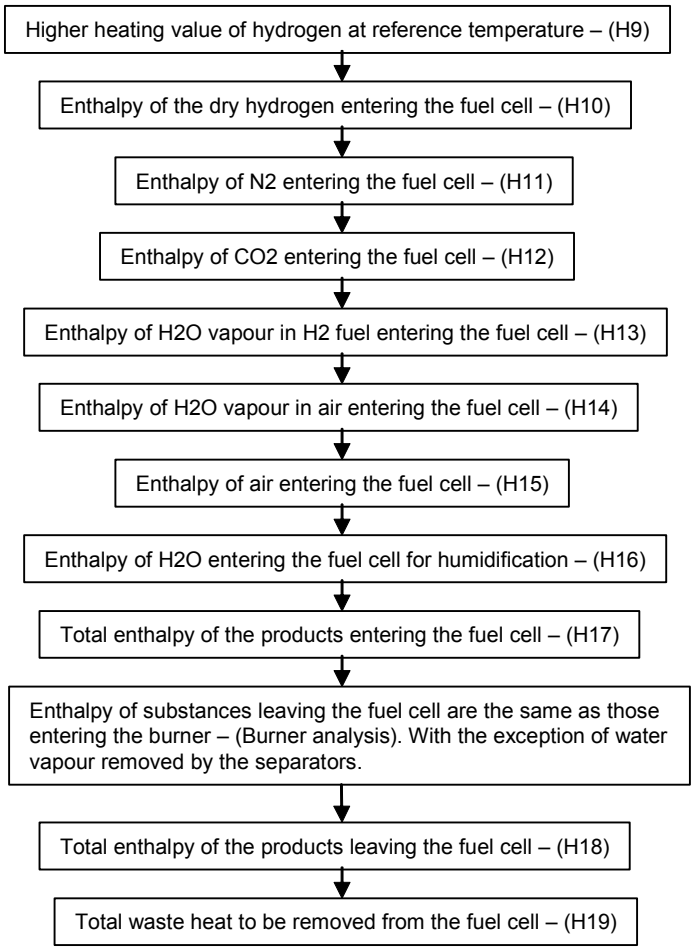

Determination of the enthalpy of the fuel cell gases follows the same procedure as used in the burner analysis section, in accordance with the properties of the gases. As a refresher, there are four possible cases for, dry gases, combustible gases, liquid water and water vapour. To prevent the discussion being repeated here, the reader is advised to refer to the burner analysis section for further details. As before, the higher heating value of hydrogen figures given in the literature at 25ºC must be converted to values at 0ºC. This can be performed with equation H9.

$$h_{HHV(0)} = h_{HHV(25)} - \left(C_{P-H2} + \frac{1}{2}\frac{M_{O2}}{M_{H2}} C_{P-O2} - \frac{M_{H_2O}}{M_{H2}} C_{P-H_2O(l)} \right) \cdot 25 \qquad \text{Eq H-9}$$

The N_2, CO_2 and Air entering the fuel cell are taken as dry gases whose enthalpies can be determined from equations H11, H12 and H14 respectively. The only combustible gas entering the fuel cell is the H_2 which is given by equation H10. The total water vapour entering the fuel cell consists of that from the fuel and air streams and that injected into the air stream for humidification, as given by equations H13, H15 and H16 respectively.

$$H_{H2(in)} = \dot{m}_{H2-FC(in)} \cdot \left(C_{P-H2} \cdot t_{H2-FC(in)} + h_{HHV(0)} \right) \qquad \text{Eq H-10}$$

$$H_{N2(in)} = \dot{m}_{N2-FC(in)} \cdot \left(C_{P-N2} \cdot t_{N2-FC(in)}\right) \quad \text{Eq H-11}$$

$$H_{CO2(in)} = \dot{m}_{CO2-FC(in)} \cdot \left(C_{P-CO2} \cdot t_{CO2-FC(in)}\right) \quad \text{Eq H-12}$$

$$H_{H_2O(Fuel-in)} = \dot{m}_{H_2O(g)-FC(Fuel-in)} \cdot \left(C_{P-H_2O(g)} \cdot t_{H_2O-FC(Fuel-in)} + h_{fg(0)}\right) \quad \text{Eq H-13}$$

$$H_{Air(in)} = \dot{m}_{Air-FC(in)} \cdot \left(C_{P-Air} \cdot t_{Air-FC(in)}\right) \quad \text{Eq H-14}$$

$$H_{H_2O(Air-in)} = \dot{m}_{H_2O(g)-FC(Air-in)} \cdot \left(C_{P-H_2O(g)} \cdot t_{H_2O-FC(Air-in)} + h_{fg(0)}\right) \quad \text{Eq H-15}$$

$$H_{H_2O(Inj)} = \dot{m}_{H_2O(g)-Inj} \cdot \left(C_{P-H_2O(g)} \cdot t_{H_2O-Inj} + h_{fg(0)}\right) \quad \text{Eq H-16}$$

The total enthalpy entering the fuel cell can then be determined as the sum of above, as given by equation H17.

$$H_{FC(in)} = H_{H2(in)} + H_{N2(in)} + H_{CO2(in)} + H_{H_2O(fuel)} + H_{Air(in)} + H_{H_2O(Air)} + H_{H_2O(INJ)} \quad \text{Eq H-17}$$

The total enthalpy of the products leaving the fuel cell can be determined from equation H18, which is the sum of the enthalpy of the products entering the burner and the enthalpy of the water vapour captured by the separators. The enthalpy of the products entering the burner was determined in the burner analysis and the enthalpy of the water vapour captured by the separators was determined in the humidification analysis.

$$H_{FC(out)} = H_{H_2O-SEP(Air-FC:Out)} + H_{H_2O-SEP(H2-FC:Out)} + \sum H_{Burn(in)} \quad \text{Eq H-18}$$

The total heat output can finally be determined from the first law of thermodynamics as applied to the fuel cell. After dropping unwanted terms and rearranging, this gives us equation H19, where Q is the heat output and P is the fuel cell power output.

$$Q_{Heat} = H_{FC(in)} - H_{FC(out)} - P \quad \text{Eq H-19}$$

H1.10 Analysis block I – Cooling system requirements

The purpose of this analysis is to obtain an estimate of the waste heat which must be removed by the radiator/s. This analysis first determines the quantity of heat with is lost from the fuel cell by radiation and conduction, the remaining waste heat in the fuel cell must then be removed the cooling system. A summary of the analytical procedure is shown in the flow chart below. The accompanying equations are also given below.

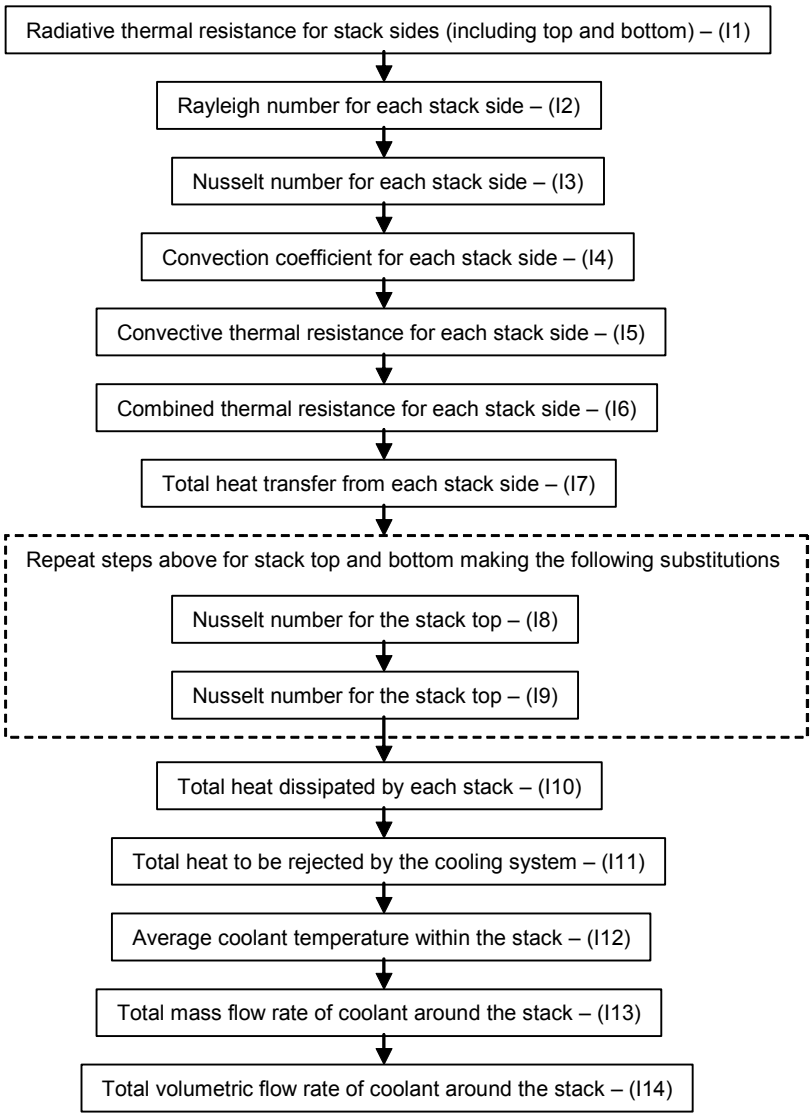

In this work, each of the stack external surfaces is assumed to be of the same size. The radiative thermal resistance for each can then be determined from equation I1.

$$R_{Rdv} = \frac{1}{\sigma \cdot F \cdot A_{St} \cdot \left(T_{St} + T_{Air}\right)\left(T_{St}^{\ 2} + T_{Air}^{\ 2}\right)} \qquad \text{Eq I-1}$$

We will now turn our attention to determining the terms for the convective heat transfer. We start by analysing the sides of the stack, the analysis for the top and bottom uses

slightly different expressions for the Nusselt number as will be discussed below. The Rayleigh number, Nusselt number and finally the convection coefficient can be determined from equations I2 to I4 respectively. It should be noted that the expression given for the Nusselt in equation I3 is for the vertical stack sides only.

$$Ra = \frac{g \cdot \beta \cdot \left(T_{St} - T_{Air}\right) \cdot L_{Ch}^{\ 3}}{nu \cdot \alpha} \qquad \text{Eq I-2}$$

$$Nu_{Sides} = 0.56 \cdot Ra^{0.25} \qquad \text{Eq I-3}$$

$$h = \frac{k}{L_{Ch}} \cdot Nu \qquad \text{Eq I-4}$$

The convective thermal resistance for each stack side can be obtained from equation I5. The combined thermal resistance for convection and radiation can then be determined from equation I6.

$$R_{Con} = \frac{1}{h \cdot A_{St}} \qquad \text{Eq I-5}$$

$$R_{Th} = \frac{1}{\frac{1}{R_{Con}} + \frac{1}{R_{Rdv}}} \qquad \text{Eq I-6}$$

The heat transfer from each of the stack sides by dissipation can finally be determined by equation I7.

$$Q_{Dis} = \frac{T_{St} - T_{Air}}{R_{Th}} \qquad \text{Eq I-7}$$

The procedure to determine the heat transfer by dissipation from the stack top and bottom surfaces is the same as for that used for the stack sides, the only difference being the expression used for the Nusselt number. Where, the Nusselt number for the stack top and bottom is given by equations I8 and I9 respectively.

$$Nu_{Top} = 0.54 \cdot Ra^{0.25} \qquad \text{Eq I-8}$$

$$Nu_{Bottom} = 0.25 \cdot Ra^{0.25} \qquad \text{Eq I-9}$$

The total heat loss from all the surfaces of all the operational fuel cell stacks is then given by equation I10.

$$Q_{Dis-total} = N_{Stacks-Op} \cdot \left[\left(2 \cdot Q_{Dis-side}\right) + Q_{Dis-top} + Q_{Dis-bottom}\right] \qquad \text{Eq I-10}$$

The waste heat to be removed by the cooing system is finally determined from equation I11, where the heat output from the cooling system $Q_{Heat-out}$ was determined in the previous heat removal requirements analysis.

$$Q_{Cooling} = Q_{Heat-out} - Q_{Dis-total}$$ Eq I-11

To be able to determine the mass flow rate of coolant required to meet this cooling requirement, it is necessary to estimate the coolant temperature change as it passes through the fuel cell $\Delta T_{Cooling}$. Which is assumed to be 10ºC in this analysis. The average temperature of the coolant within the fuel cell is then given by equation I12.

$$T_{Coolant-Av} = T_{FC} - \frac{\Delta T_{Cooling}}{2}$$ Eq I-12

Along with the specific heat capacity of the coolant, the coolant temperature drop can be used to determine the total mass flow rate of coolant required through the operational fuel cell stacks. This is given by equation I13 and the corresponding volumetric flow rate is given by equation I14.

$$\dot{m}_{FCC} = \frac{Q_{Cooling}}{C_{P-Coolant} \cdot \Delta T}$$ Eq I-13

$$Q_{FCC} = \frac{\dot{m}_{FCC}}{\rho_{Coolant}}$$ Eq I-14

The characteristic lengths which are required for the analysis are given by equations I15 and I16. The characteristic length of the sides is equal to the width of a cell which itself is equal to the height of a cell. The characteristic length of the top and bottom stack surfaces is determined by the area/perimeter ratio for the surface as given by the bi-polar plate geometry. Finally, the area of each stack surface can be determined from equation I17.

$$L_{Ch-sides} = W_{Cell}$$ Eq I-15

$$L_{Ch-top\&bottom} = \frac{A_{Cell}}{4 \cdot W_{Cell}}$$ Eq I-16

$$A_{St} = W_{Cell} \cdot L_{Stack}$$ Eq I-17

The air properties, kinematic viscosity (nu) and thermal diffusivity (α) as required for this analysis are defined in the parameters section. The exception to this is the thermal expansion coefficient of the ambient air which is simply the inverse of the temperature in Kelvins, as given by equation I18.

$$\beta = \frac{1}{T}$$ Eq I-18

H1.11 Analysis block J – Cooling system analysis

This section is used to analyse the heat transfer properties of the cooling system heat exchanger as well as the pressure drop in its matrix and connecting pipe work. A simplified representation of the cooling system is presented at the end of this section for reference. In this work, the radiator is analysed as a number of repeating blocks whose properties were defined in Kays and London [80] and have been included at the end of this section for reference. In a different section, the radiator is sized according to the number of repeating blocks required to meet our heat transfer requirements. During this study, a two row and a three row radiator configuration were investigated in parallel to determine the optimal configuration for our needs, as will be discussed later section.

H1.11.1 Heat exchanger air side heat transfer coefficient

This part of the analysis is used to determine the heat transfer coefficient for the air side of the heat exchanger matrix. A summary of the analytical procedure is shown in the flow chart below. The accompanying equations are also given below.

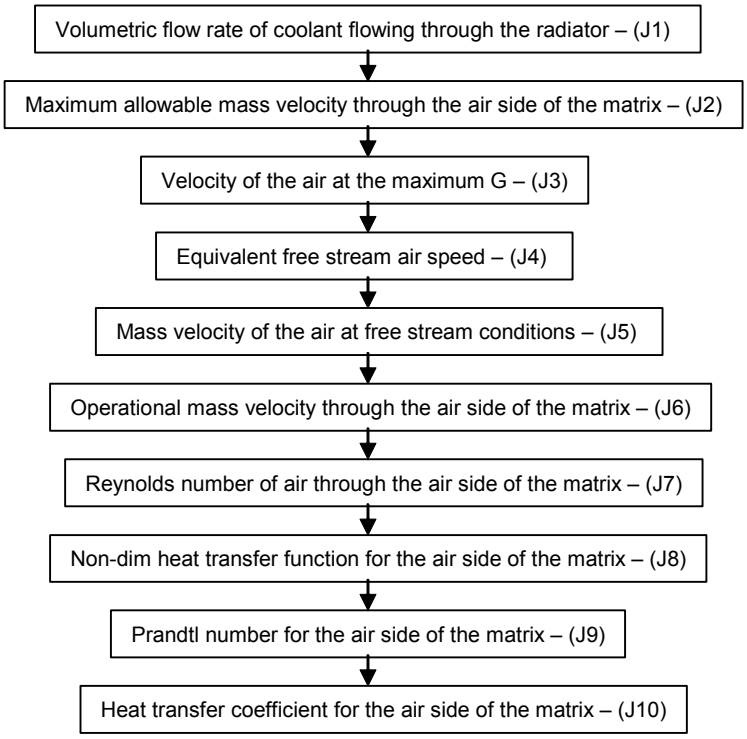

The radiator volumetric flow rate is determined from J1, which is a function of the radiator mass flow rate $\dot{m}_{Rad}$, which itself is determined by Stage 6 of the solver block. Equation J2 is then used to determine the maximum value of mass velocity consistent with the maximum Reynolds number for the heat exchanger. The velocity of the air passing through the matrix at this condition can then be determined by equation J3 below.

$$Q_{Rad} = \frac{\dot{m}_{Rad}}{\rho_{Coolant}} \quad \text{Eq J-1}$$

$$G_{Air(Max)} = \frac{\mathrm{Re}_{Air(Max)} \cdot \mu_{Air}}{D_{h(Air)}} \quad \text{Eq J-2}$$

$$V_{Air(G:Max)} = \frac{G_{Air(Max)} \cdot \sigma_{Air}}{\rho_{Air}} \quad \text{Eq J-3}$$

This analysis uses the equivalent air speed, as derived from J4, which is a function of the true airspeed as determined above.

$$V_{Air-EAS(Flight)} = V_{Air(Flight)} \cdot \left(\frac{\rho}{\rho_{SL}} \right)^{0.5} \quad \text{Eq J-4}$$

The free stream mass velocity as determined by equation J5 is used unless the maximum limit is reached. In which case, the value of maximum mass velocity is used as defined by equation J6 below.

$$G_{Air(Free)} = \frac{\rho_{Air} \cdot V_{Air-EAS(Flight)}}{\sigma_{Air}} \quad \text{Eq J-5}$$

$$G_{Air(Used)} = IF(G_{Air(Free)} > G_{Air(Max)}, G_{Air(Max)}, G_{Air(Free)}) \quad \text{Eq J-6}$$

Equation J7 then determines the Reynolds number corresponding to the actual value of mass velocity used.

$$\mathrm{Re}_{Air(Used)} = \frac{G_{Air(Used)} \cdot D_{h(Air)}}{\mu_{Air}} \quad \text{Eq J-7}$$

By fitting a polynomial curve to the non-dimensional heat exchanger data given at the end of this section, a cubic relation can be obtained as given by equation J8.

$$X_{HT} = \left\{ A_R \cdot \left[LOG(\mathrm{Re}) \right]^3 + B_R \cdot \left[LOG(\mathrm{Re}) \right]^2 + C_R \cdot \left[LOG(\mathrm{Re}) \right] + D_R \right\} / 1000 \quad \text{Eq J-8}$$

In this analysis, curves have been fitted to the data for both the 2-row and 3-row heat exchanger configurations. The above relation is applicable to both of the configurations and the equation constants are given in the table below.

Config/Const	A_R	B_R	C_R	D_R
2-Row	-1.9141	21.579	-84.051	117.26
3-Row	-6.0672	67.857	-256.24	332.68

The Prandtl number, as given by equation J9 below is actually a fluid property and is independent of the heat exchanger configuration.

$$\mathrm{Pr}_{Air} = \frac{C_{P(Air)} \cdot \mu_{Air}}{k_{Air}} \qquad \text{Eq J-9}$$

The air side heat transfer coefficient is finally obtained from equation J10 below.

$$h_{Air} = \frac{X_{HT} \cdot G_{Air(Used)} \cdot C_{P(Air)}}{\mathrm{Pr}_{Air}^{2/3}} \qquad \text{Eq J-10}$$

H1.11.2 Heat exchanger coolant side heat transfer coefficient

This part of the analysis is used to determine the heat transfer coefficient for the coolant side of the heat exchanger matrix. A summary of the analytical procedure is shown in the flow chart below. The accompanying equations are also given below.

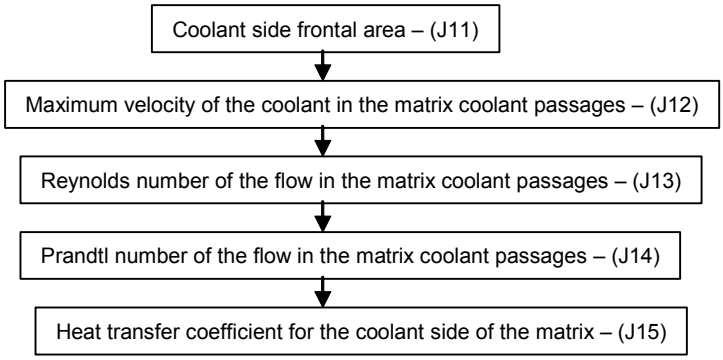

The first stage of the analysis is to determine the total frontal area of the coolant side of the heat exchanger matrix as given by equation J11 below. The velocity of the coolant in each of the coolant passages can then be determined from the mass flow rate of the coolant in each of the coolant passages, as in J12. This includes the necessary terms to determine the total coolant passage area from the coolant side frontal area.

$$A_{fr(Coolant)} = w_{Matrix} \cdot d_{Matrix} \qquad \text{Eq J-11}$$

$$u_{Rad-CP(\max)} = \frac{\dot{m}_{Rad}}{\rho_{Coolant} \cdot \sigma_{Coolant} \cdot A_{fr(Coolant)}} \qquad \text{Eq J-12}$$

The Reynolds number for the flow is given by equation J13. As before, the Prandtl number is a fluid property which is determined for the coolant from equation J14.

$$\mathrm{Re}_{Rad-CP} = \frac{\rho_{Coolant} \cdot u_{Rad-CP(\max)} \cdot D_{h(Rad-CP)}}{\mu_{Coolant}} \qquad \text{Eq J-13}$$

$$\mathrm{Pr}_{Coolant} = \frac{C_{P(Coolant)} \cdot \mu_{Coolant}}{k_{Coolant}} \qquad \text{Eq J-14}$$

If we use the Dittus-Boelter equation to determine the Nusselt number, the coolant side heat transfer coefficient can finally be determined from equation J15 below.

$$h_{Coolant} = 0.023 \cdot \frac{k_{Coolant}}{D_{h(Rad-CP)}} \cdot \mathrm{Re}_{Rad-CP}^{\ 0.8} \cdot \mathrm{Pr}_{Coolant}^{\ 0.4} \qquad \text{Eq J-15}$$

H1.11.3 Determination of the total heat exchanger heat transfer rate

This part of the analysis is used to determine the total heat transfer coefficient rate for the heat exchanger matrix. A summary of the analytical procedure is shown in the flow chart below. The accompanying equations are also given below.

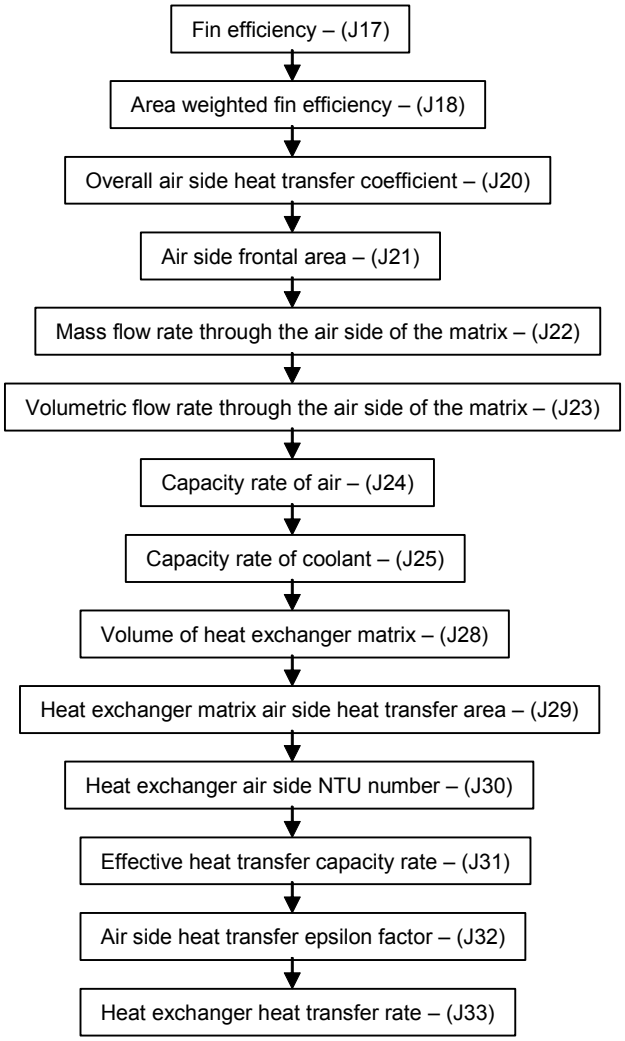

Equation J16 below is used to determine a function required for the fin efficiency relation as given by J17 below.

$$mL = \sqrt{\frac{2 \cdot h_{Air}}{k_{Metal} \cdot t_{Fin}}} \cdot L_{Eff-Plate} \qquad \text{Eq J-16}$$

$$\eta_{Fin} = \frac{\tanh(mL)}{mL} \qquad \text{Eq J-17}$$

The fin efficiency from J17 must then be corrected for the geometry being used with the area-related expression J18 below. This requires the fin area ratio given by J19 below.

$$\eta_{W-Fin} = 1 - \beta_{Fin}\left(1 - \eta_{Fin}\right) \quad \text{Eq J-18}$$

$$\beta_{Fin} = \frac{A_{Fin}}{A_{Total}} \quad \text{Eq J-19}$$

The overall heat transfer coefficient, which includes the effect of the matrix fins, is then given by equation J20 below.

$$\frac{1}{U_{Air}} = \frac{1}{\eta_{W-Fin} \cdot h_{Air}} + \frac{1}{\left(\alpha_{Coolant} / \alpha_{Air}\right) \cdot h_{Coolant}} \quad \text{Eq J-20}$$

The air side total frontal area is determined from equation J21 below, which is used in equation J22 to determine the mass flow rate of air passing through the heat exchanger. The volumetric flow rate can then be determined from equation J23 below.

$$A_{fr(Ait)} = w_{Matrix} \cdot h_{Matrix} \quad \text{Eq J-21}$$

$$\dot{m}_{Air} = G_{Air(Used)} \cdot \sigma_{Air} \cdot A_{fr(Air)} \quad \text{Eq J-22}$$

$$Q_{Air} = \frac{\dot{m}_{Air}}{\rho_{Coolant}} \cdot 1000 \quad \text{Eq J-23}$$

The next stages of the analysis require knowledge of the maximum and minimum values of the heat exchanger capacity rates for the air and coolant fluids, as given by equations J24 to J27.

$$C_{Rate-air} = \dot{m}_{Air} \cdot C_{P(Air)} \quad \text{Eq J-24}$$

$$C_{Rate-coolant} = \dot{m}_{Rad} \cdot C_{P(Coolant)} \quad \text{Eq J-25}$$

$$C_{Min} = Min\left(C_{Rate-air}, C_{Rate-coolant}\right) \quad \text{Eq J-26}$$

$$C_{Max} = Max\left(C_{Rate-air}, C_{Rate-coolant}\right) \quad \text{Eq J-27}$$

The heat exchanger matrix total volume and air side free flow area are then given by equations J28 and J29 respectively and the heat transfer NTU number is given by J30.

$$V_{Matrix} = A_{fr(Air)} \cdot d_{Matrix} \quad \text{Eq J-28}$$

$$A_{HT(Air)} = \sigma_{Air} \cdot V_{Matrix} \quad \text{Eq J-29}$$

$$NTU = \frac{A_{HT(Air)} \cdot U_{Air}}{C_{Min}} \quad \text{Eq J-30}$$

To determine the heat transfer epsilon factor as given by equation J32, we require the effective heat transfer rate which is given by equation J31.

$$C_{Eff} = \frac{C_{Min}}{C_{Max}} \qquad \text{Eq J-31}$$

$$\varepsilon = 1 - \exp\left[\frac{1}{C_{Eff}} \cdot NTU^{0.22} \cdot \left\{\exp\left(-C_{Eff} \cdot NTU^{0.78}\right) - 1\right\}\right] \qquad \text{Eq J-32}$$

With the relations above, the heat exchanger heat transfer rate can finally be determined from Equation J33 below. The temperatures are a function of the operating environment and fuel cell operating conditions and are incorporated in the analysis solution process.

$$Q_{Heat} = \varepsilon \cdot C_{Min} \cdot \left(T_{h(in)} - T_{c(in)}\right) \qquad \text{Eq J-33}$$

H1.11.4 Pressure drop within the matrix coolant passages

This part of the analysis is used to determine the total pressure drop within the coolant passages the heat exchanger matrix. A summary of the analytical procedure is shown in the flow chart below. The accompanying equations are also given below.

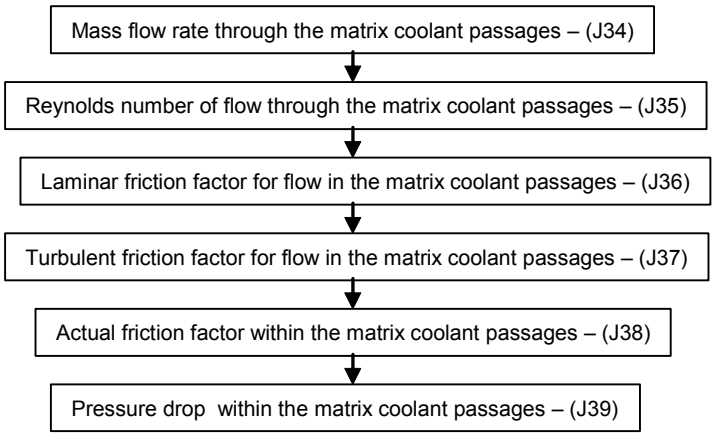

Equations J34 and J35 give the mass velocity and Reynolds number respectively for the flow through the coolant side of the heat exchanger.

$$G_{Coolant} = \frac{\dot{m}_{Rad}}{A_{fr(Coolant)} \cdot \sigma_{Coolant}} \qquad \text{Eq J-34}$$

$$\mathrm{Re}_{Coolant} = \frac{G_{Coolant} \cdot D_{h(Coolant)}}{\mu_{Coolant}} \qquad \text{Eq J-35}$$

The friction factor for the coolant flow passages is determined from equation J38 in accordance with the Reynolds number of the flow regime being encountered. The flow is considered turbulent for flows above 4000 and laminar in other cases. The laminar and turbulent friction factors are given by equations J36 to J38 respectively.

$$f_{Laminar} = \frac{64}{\mathrm{Re}} \qquad \text{Eq J-36}$$

$$f_{Turbulent} = 0.079 \cdot \mathrm{Re}^{-0.25} \qquad \text{Eq J-37}$$

$$f_{Actual} = IF(\mathrm{Re}_{Coolant} > 4000, f_{Turbulent}, f_{La\min ar}) \qquad \text{Eq J-38}$$

The pressure drop across the coolant passages within the fuel cell can finally be determined from equation J39.

$$\Delta P_{Coolant} = f_{Actual} \cdot \frac{G_{Coolant}{}^{2}}{2 \cdot \rho_{Coolant}} \cdot \left(\frac{L}{r_H} \right) \qquad \text{Eq J-39}$$

H1.11.5 Determination of the pressure drop and velocity of the air passing through the air side of the heat exchanger matrix

This part of the analysis is used to determine the pressure drop and velocity of the air passing through the air side of the heat exchanger matrix. A summary of the analytical procedure is shown in the flow chart below. The accompanying equations are also given below.

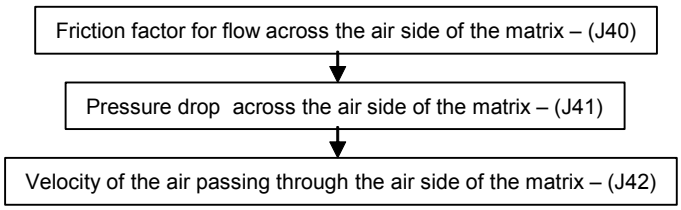

The flow conditions across the air side of the heat exchanger matrix have already been determined. The remaining unknown required to be able to determine the pressure drop across the air side is the friction factor, which is determined from the heat exchanger data. By fitting a polynomial curve to the non-dimensional heat exchanger data given at the end of this section, a cubic relation can be obtained as given by equation J40.

$$f_{Matrix} = \left\{ A_M \cdot [LOG(\mathrm{Re})]^3 + B_M \cdot [LOG(\mathrm{Re})]^2 + C_M \cdot [LOG(\mathrm{Re})] + D_M \right\} / 1000 \qquad \text{Eq J-40}$$

In this analysis, curves have been fitted to the data for both the 2-row and 3-row heat exchanger configurations. The above relation is then applicable to both of the configurations, where the equation constants are given in the table below.

Config/Const	A_M	B_M	C_M	D_M
2-Row	-18.629	206.44	-770.96	991.16
3-Row	-31.797	347.99	-1280.7	1610.6

The pressure drop across the air side of the heat exchanger matrix and the velocity of the air passing through it can finally be found from Equations J41 and J42 respectively.

$$\Delta P_{Air} = f_{Actual} \cdot \frac{G_{Air}{}^{2}}{2 \cdot \rho_{Air}} \cdot \left(\frac{A}{A_{Min}} \right) \qquad \text{Eq J-41}$$

$$V_{Air-Matrix} = \frac{G_{Air} \cdot \sigma_{Air}}{\rho_{Air}}$$ Eq J-42

H1.11.6 Mass flow rate of coolant in the by-pass pipe work

This part of the analysis is used to determine the final geometry of the heat exchanger matrix from the number of repeating blocks required, as determined by the cooling system solution. This also determines the mass flow rate of coolant which by-passes the radiator. A summary of the analytical procedure is shown in the flow chart below. The accompanying equations are also given below.

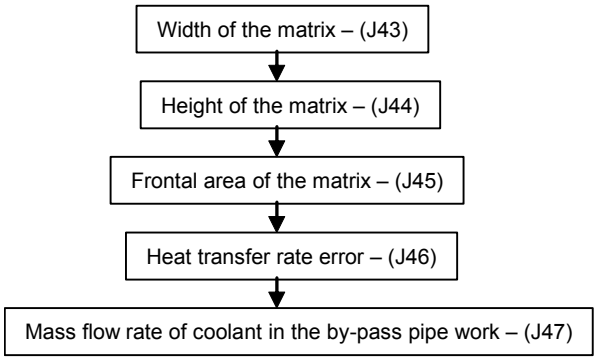

Equations J43 to J45 are used to determine the final geometry of the heat exchanger matrix from the geometry of a single repeating block, the number of repeating blocks and the heat exchanger aspect ratio.

$$w_{Matrix} = w_{Block} \cdot N_{Blocks}$$ Eq J-43

$$h_{Matrix} = \frac{w_{Matrix}}{AR_{Matrix}}$$ Eq J-44

$$A_{Matrix} = w_{Matrix} \cdot h_{Matrix}$$ Eq J-45

Equation J46 is used as part of the solution procedure, in which the mass flow through the radiator is iterated until the error reduces to zero. In other words, the coolant mass flow is set so that the heat removal required by the radiator exactly equals the heat removal actually achieved.

$$Q_{Heat(Error)} = Q_{Heat(Cooling)} - Q_{Heat(Radiator)}$$ Eq J-46

The mass flow rate of coolant which passes through the by-pass circuit is then given by equation J47. This is the difference between that leaving the fuel cell and that passing through the heat exchanger.

$$\dot{m}_{By-Pass} = \dot{m}_{FC-Coolant} - \dot{m}_{Radiator}$$ Eq J-47

H1.11.7 Simplified representation of the cooling system

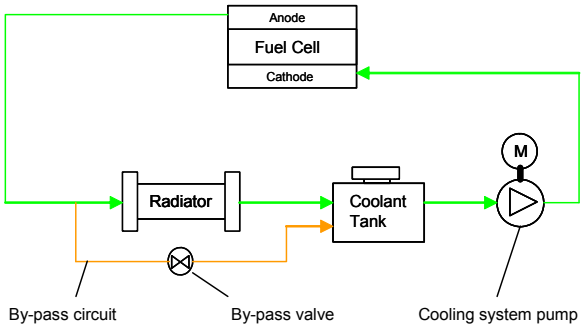

Figure J-1

H1.11.8 Heat exchanger properties

Data for the 2 and 3 row heat exchanger configurations used in this analysis is given in the respective figures below, from Kays and London [80] Figures 10.95 and 10.96.

Fig. 10-95 Finned flat tubes, surface 9.68 – 0.87-R.

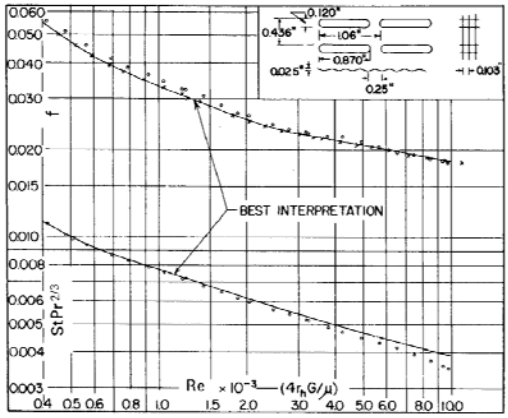

Fin pitch = 9.68 per in = 381 per m
Flow passage hydraulic diameter, $4r_h$ = 0.01180 ft = 3.597 x 10^{-3} m
Fin metal thickness = 0.004 in, copper = 0.102 x 10^{-3} m
Free-flow area/frontal area, σ = 0.697
Total heat transfer area/total volume, α = 229 ft²/ft³ = 751 m²/m³
Fin area/total area = 0.795

Fig. 10-96 Finned flat tubes, surface 9.29 – 0.737-SR.

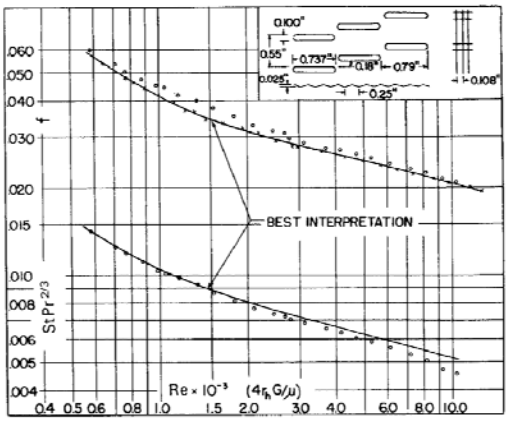

Fin pitch = 9.29 per in = 366 per m
Flow passage hydraulic diameter, $4r_h$ = 0.01352 ft = 4.12 x 10^{-3} m
Fin metal thickness = 0.004 in, copper = 0.102 x 10^{-3} m
Free-flow area/frontal area, σ = 0.788
Total heat transfer area/total volume, α = 228 ft²/ft³ = 748 m²/m³
Fin area/total area = 0.814

Figure J-2

Data for the heat exchangers as used in the analysis work is given in the table below.

Parameter	2-Row Heat Ex.	3-Row Heat Ex.
$D_{h(Air)}$ (m)	3.60E-3	4.12E-3
σ_{Air}	0.697	0.788
$\sigma_{Coolant}$	0.173	0.161
$D_{h(Rad-CP)}$ (m)	5.4838E-3	4.5776E-3
$L_{Eff-Plate}$ (m)	4.01E-3	5.72E-3
k_{Metal} (W/mdegC)	173	173
t_{Fin} (m)	1.02E-4	1.02E-4
$\alpha_{Coolant} / \alpha_{Air}$ (m-1)	0.168	0.188
d_{Matrix} (m)	6.8326E-2	6.1544E-2
$D_{h(Coolant)}$	5.4838E-3	4.5776E-3
r_H (m)	1.3710E-3	1.1444E-3

Table J-1

H1.12 Analysis block K – Cooling system pumping requirements

H1.12.1 Pressure drop across the fuel cell stack coolant channels

This part of the analysis is used to determine the pressure drop across the fuel cell coolant channels. A summary of the analytical procedure is shown in the flow chart below. The accompanying equations are also given below.

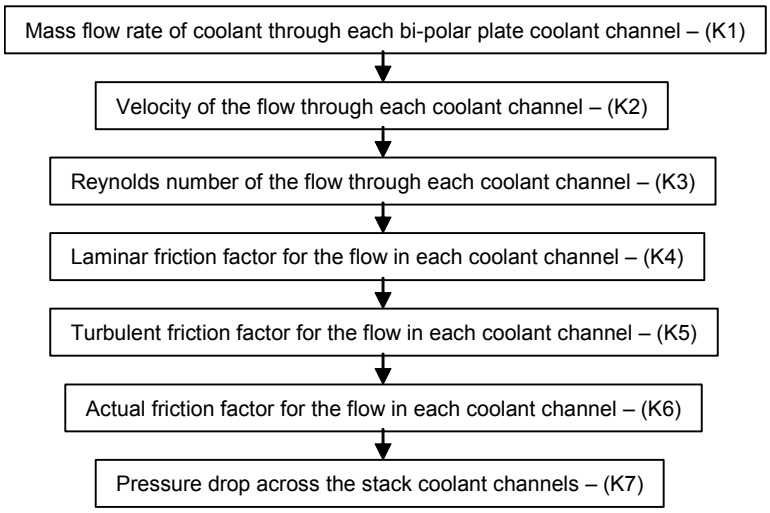

The first stage in this analysis is to determine the geometry of the coolant channels within each bi-polar plate, which are assumed to be of a serpentine layout to match the reactant channels. If the cross sectional area of the coolant channel is taken to be a fraction of the cross sectional area of the reactant channel, then its area can be determined from the equation below. In this particular analysis, the cross sectional area of the coolant channel is assumed to be the same as for the reactant channels.

$$A_{Coolant-Ch} = A_{\mathrm{Re}\,ac\,\tan t-Ch} \cdot \frac{A_{Coolant-Ch}}{A_{\mathrm{Re}\,ac\,\tan t-Ch}}$$

If we assume that the coolant channels are circular, then its diameter can be determined from the equation below, otherwise we can use the equivalent diameter of the channel.

$$D_{Coolant-Ch} = \sqrt{\frac{4 \cdot A_{Coolant-Ch}}{\pi}}$$

The mass flow rate through each of the bi-polar plate coolant channels can be determined from equation K1. In this relation, the total mass flow of coolant circulating the system is first divided by the number of operational stacks to find the coolant passing through each stack. This is then divided by the number of bi-polar plates in each stack (531 in this case) to find the coolant in each plate. This figure is finally divided again by the number of parallel serpentine channels in each bi-polar plate (10 in this case) to arrive at the mass flow rate of coolant passing through each coolant channel.

$$\dot{m}_{FCC} = \frac{\dot{m}_{Stacks-Total}}{N_{Stacks-Op} \cdot N_{Stack-Plates} \cdot N_{Bi-Channels}} \quad \text{Eq K-1}$$

The average velocity of the coolant in the fuel cell channel can be determined from the basic relation given in equation K2.

$$V_{FCC} = \frac{\dot{m}_{FCC}}{\rho_{Coolant} \cdot A_{FCC}} \quad \text{Eq K-2}$$

The Reynolds number of the flow can be determined from K3, in which the critical length D is the diameter of the coolant channel.

$$\mathrm{Re}_{FCC} = \frac{\rho_{Coolant} \cdot V_{FCC} \cdot D_{H-FCC}}{\mu_{Coolant}} \quad \text{Eq K-3}$$

The next stage of the analysis is to determine the friction factor for flow in the channels. In the case of the flow being laminar, equation K4 is used, otherwise in the case of turbulent flow, K5 is used. Equation K6 is used to determine the actual state of the flow, with Reynolds numbers above 4000 being turbulent, otherwise the flow is laminar.

$$f_{Laminar} = \frac{64}{\mathrm{Re}} \quad \text{Eq K-4}$$

$$f_{Turbulent} = 0.079 \cdot \mathrm{Re}^{-0.25} \quad \text{Eq K-5}$$

$$f_{Actual} = IF(\mathrm{Re}_{FCC} > 4000, f_{Turbulent}, f_{Laminar}) \quad \text{Eq K-6}$$

Finally, the pressure drop across each serpentine channel can be determined from equation K7. The first part of this relation determines the pressure drop due to the length of the serpentine channel, quoted as L_{FCC} (4m in this case and can be thought of as the serpentine channel being laid out flat). The second part of the relation determines the pressure drop due to the bends in the serpentine path. In this analysis, K_L is the friction factor for 90 degree bends (which was taken as 30) and N is the number of 90 degree bends (which was calculated as 26).

$$\Delta P = f \cdot \frac{L_{FCC}}{D_{H-FCC}} \cdot \rho_{Coolant} \cdot \frac{V_{FCC}^{\ 2}}{2} + \sum_{1}^{N} K_L \cdot f \cdot \rho_{Coolant} \cdot \frac{V_{FCC}^{\ 2}}{2} \quad \text{Eq K-7}$$

Equation K7 gives us the pressure drop across a single serpentine channel, but since the channels are parallel to each other, this is same for the sum of the channels. Since each of the bi-polar plates are also parallel, then the pressure drop is also for the complete fuel cell stack. Likewise, each of the fuel cell stacks are also in parallel to each other.

H1.12.2 Cooling pump power requirements

This part of the analysis is used to determine the power requirements of a cooling system pump. To aid understanding of this analysis a schematic of the cooling system is given below along with the key pipe dimensions.

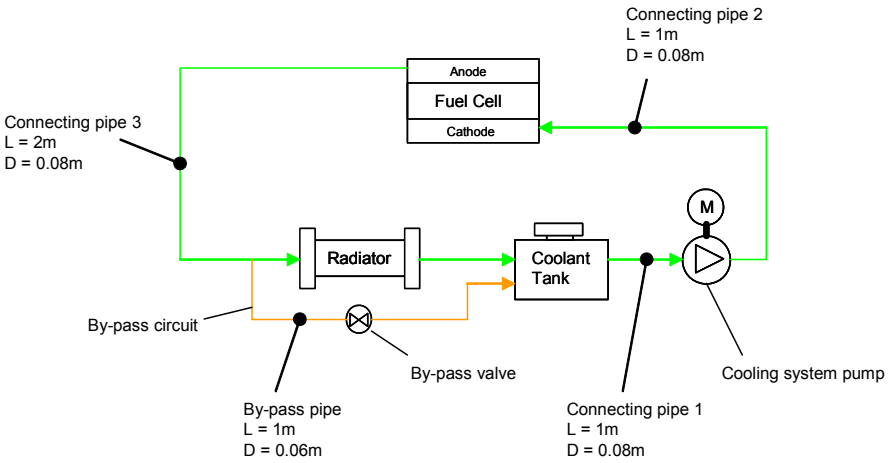

Figure K-1

A summary of the analytical procedure is shown in the flow chart below. The accompanying equations are also given below.

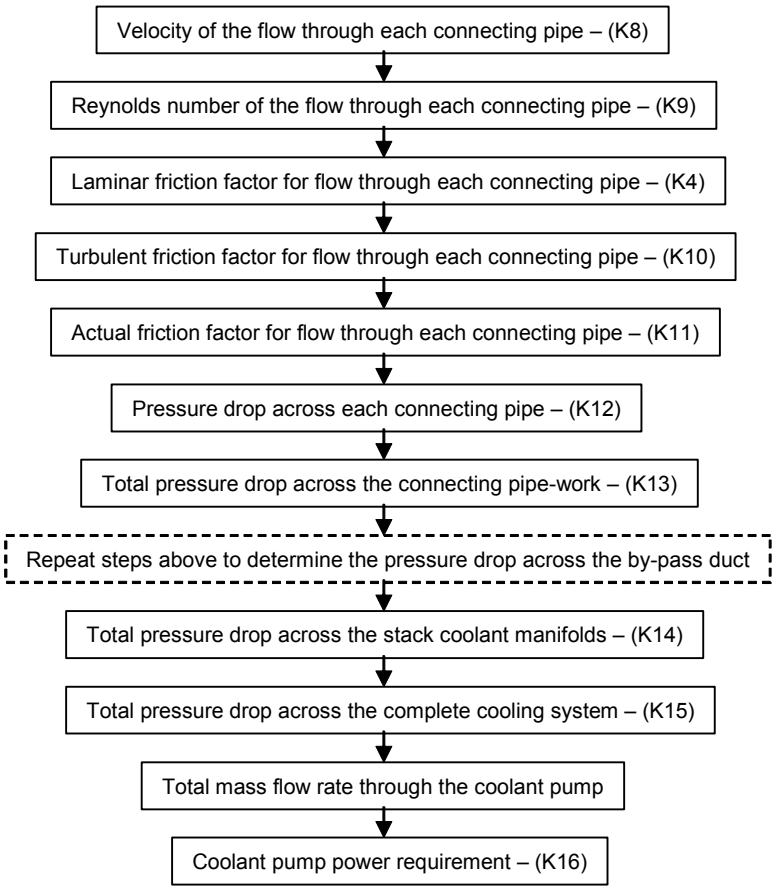

The first part of this analysis determines the pressure drop in the cooling system connecting pipe work, which is added to the pressure drop in the fuel cell coolant circuit. The result is then used along with the total coolant mass flow rate to determine the coolant pump power requirements. Equation K8 gives us the average velocity of the coolant passing through the connecting pipe work in terms of its mass flow rate.

$$V_{CPW} = \frac{\dot{m}_{CPW}}{\rho_{Coolant} \cdot A_{CPW}} \qquad \text{Eq K-8}$$

The Reynolds number of the flow in the pipe is then given by equation K9, where the critical dimension D is the diameter of each connecting pipe.

$$\mathrm{Re}_{CPW} = \frac{\rho_{Coolant} \cdot V_{CPW} \cdot D_{CPW}}{\mu_{Coolant}} \qquad \text{Eq K-9}$$

The laminar friction factor can then be determined from equation K4 and the turbulent friction factor from Equation K10. Equation K10 was obtained from a curve fitted to the turbulent flow curve of a moody chart for a drawn tube of roughness 0.0015mm.

$$f = 2.0656\left[\frac{LOG(\mathrm{Re})}{10}\right]^4 - 5.5851\left[\frac{LOG(\mathrm{Re})}{10}\right]^3 + 5.6666\left[\frac{LOG(\mathrm{Re})}{10}\right]^2 - 2.5596\left[\frac{LOG(\mathrm{Re})}{10}\right] + 0.456 \qquad \text{Eq K-10}$$

The actual friction factor expression used is relative to the Reynolds number of the flow regime as given by equation K11.

$$f_{Actual} = IF(\mathrm{Re}_{CPW} > 4000, f_{Turbulent}, f_{La\min ar}) \qquad \text{Eq K-11}$$

The pressure drop in each of the connecting pipes can then be determined from equation K12, where L is the length of each pipe.

$$\Delta P = f \cdot \frac{L_{CPW}}{D_{CPW}} \cdot \rho_{Coolant} \cdot \frac{V_{CPW}^{\ 2}}{2} \qquad \text{Eq K-12}$$

This process is repeated for each of the connecting pipes with the total pressure drop for all the connecting pipe work being the sum of all these, as given by equation K13.

$$\Delta P_{CPW-Total} = \sum_{1}^{N} \Delta P_{CPW} \qquad \text{Eq K-13}$$

Each fuel cell stack will have a manifold which distributes the coolant to each of the bi-polar plates. The pressure drop in these cooling manifolds is estimated as being 10% of the total stack coolant channels pressure drop as given by equation K14.

$$\Delta P_{TSCM} = \frac{\Delta P_{TSCS}}{10}$$ Eq K-14

The total pressure drop across the complete cooling system is finally the sum of that for the connecting pipe work, stack coolant channels, stack manifolds, external radiator and the by-pass pipe work. This is summarised in equation K15.

$$\Delta P_{TCS} = \Delta P_{CPW-Total} + \Delta P_{TSCS} + \Delta P_{TSCM} + \Delta P_{Rad} + \Delta P_{CSBP}$$ Eq K-15

The power required by the cooling system pump can finally be determined from equation K16. In this analysis, the pump efficiency (η) is taken to be 0.8 which is a typical value for a centrifugal pump.

$$\dot{W}_{Pump} = \frac{\Delta P_{TCS} \cdot \dot{m}_{Pump}}{\rho_{Coolant} \cdot \eta_{Pump}}$$ Eq K-16

H1.13 Analysis block L – Fuel system pumping requirements

This analysis is used to determine the power requirements of a fuel system pump. This follows a similar procedure as for the cooling pump power requirements analysis above. In this case, the power required is given by the expression,

$$\dot{W}_{Pump} = \frac{\Delta P_{FuelSystem} \cdot \dot{m}_{Fuel}}{\rho_{Methanol} \cdot \eta_{Pump}}$$ Eq L-1

Here, the pump is assumed to be a centrifugal pump, in which case η is given a typical value of 0.8. $\dot{m}_{Fuel}$ is the required fuel feed to the fuel processor, which is a solution from another analysis block. The density of methanol can be determined from the expression below which was fitted to data from fuel property charts.

$$\rho_{Methanol} = -14.452 \cdot \left(\frac{T_{Methanol}}{100}\right)^2 - 80.366 \cdot \left(\frac{T_{Methanol}}{100}\right) + 809.21$$ Eq L-2

Where, $T_{Methanol}$ is the temperature of fuel in the fuel tanks, which is assumed to be the same as the ambient temperature for the purpose of this work.

The final term $\Delta P_{FuelSystem}$ is the pressure differential across the fuel pump which can be determined from the expression, $\Delta P_{FuelPump} = \left(P_{FuelSystem} - P_{Ambient}\right) + \Delta P_{Loss(Fuel\ Processor)}$
The operating pressure of the fuel system is taken to be equal to the operating pressure of the air supply, in order to keep the pressures across the fuel cell membrane balanced. The final unknown $\Delta P_{Loss(Fuel\ Processor)}$ is the pressure loss in the fuel processor. This is characteristic of the design of the fuel processor and is not possible to predict analytically. Inspection of a number of existing fuel processors enabled the Author to determine the following very approximate first pass estimate. Where, $\Delta P_{Loss(Fuel\ Processor)}$ is in Pa and $P_{Output(FuelCell)}$ is the fuel cell power output in kW.

$$\Delta P_{Loss(Fuel\ Processor)} = 1000 \cdot P_{Output(FuelCell)}$$ Eq L-4

I1 Sizing the cooling system

This section commences with an overview of the fuel cell powered aircraft cooling system, which is followed by a description of the trade-off studies used to determine the optimal configuration. Finally, an overview is given of the procedures followed to size and integrate the cooling system.

I1.1 Layout of the cooling system

The layout of the final cooling system is presented in the schematic below. It should be noted however that an actual cooling system would also be used to cool a number of additional system components besides the fuel cell. The impact of these on the cooling system is however small in comparison with the contribution from the fuel cell and have therefore been neglected from this analysis in order to keep it simple. The reader is advised to refer to the full fuel cell system schematic for further details.

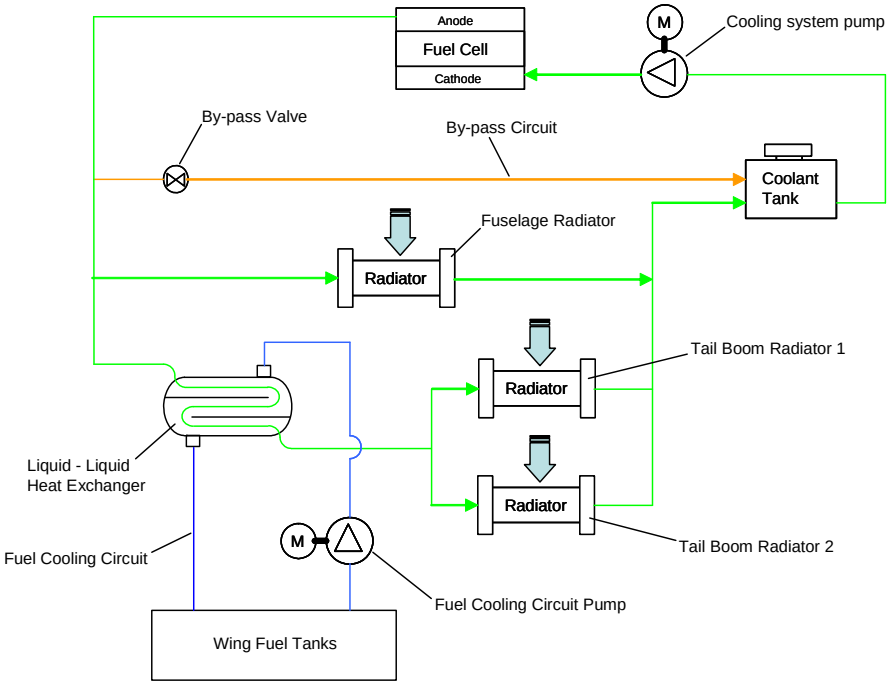

Figure 1-1

To aid understanding, the cooling system can be envisioned as four interconnected flow circuits, as discussed below:

1. By-pass circuit – This is used to divert the flow from the radiators and is therefore used to control the heat load supplied to the radiators. By regulating the flow through the radiators in this way, we are able to accurately control the temperature of the fuel cell.
2. Fuselage radiator circuit – The coolant flow which is not diverted through the by-pass circuit, is split between the fuselage radiator and the tail boom radiators. The larger space available within the rear fuselage in comparison with the booms means that the fuselage radiator is the largest of all the radiators.

3. Tail boom radiator circuit – The remaining coolant that does not pass through either of the circuits above, passes through the radiators in the tail booms instead. Before entering the radiators, the coolant first passes through a liquid-liquid heat exchanger in which some of the heat is transferred to the fuel stored in the wing fuel tanks. This not only provides an additional means of heat dispersal but also provides a means to ensure that the temperature of the fuel is maintained at a level sufficient to prevent the risk of ice formation. After the coolant leaves the liquid-liquid heat exchanger, it is then split equally between the port and starboard heat exchangers located in the tail booms.
4. Fuel cooling circuit – This is used to circulate fuel between the wing fuel tanks and the liquid-liquid heat exchanger, used for the tail boom radiator circuit above.

The coolant flows eventually re-converge and enter the coolant tank, from which it is pumped through the fuel cell and other components not included above.

I1.2 Analysis of the cooling system

If we isolate the fuel cell from the rest of the system and consider it from a first law of thermodynamics perspective, we are able to arrive at the following expression.

$$Q_{CoolingSystem} = \sum H_{FC(In)} - \sum H_{FC(Out)} - P_{FC(Out)} - Q_{Radiation\&Convection} \qquad \text{Eq 1-1}$$

This gives us the quantity of waste heat that the cooling system is required to remove. The terms that make up this expression are,

- $Q_{CoolingSystem}$ - Quantity of waste heat to be removed by the cooling system
- $\sum H_{FC(In)}$ - Total enthalpy of the reactants entering the fuel cell
- $\sum H_{FC(Out)}$ - Total enthalpy of the unused reactants and products leaving the fuel cell
- $P_{FC(Out)}$ - Fuel cell electrical power output
- $Q_{Radiation\&Convection}$ - Quantity of heat rejected from the fuel cell external surfaces by radiation and convection

Since the requirements of the cooling system are dependant on the fuel cell system operating parameters, then analysis of the cooling system must be carried out in conjunction with the analysis of the fuel cell system. In this study, the cooling system was therefore incorporated into the analysis described in Appendix H and the reader is advised to refer to this section for further details.

I1.3 The impact of the fuel cell operating parameters on the cooling system

The fuel cell system analysis described in Appendix H was used to study the impact of the fuel cell operating parameters on the cooling system. The results of this study enabled us to make the best selection of operating parameters for our fuel cell with respect to the complete installation (including the performance of the aircraft).

The first such analysis was to study the impact of the fuel cell pressure ratio on the minimum total radiator frontal area required to meet our cooling requirements. In this analysis, the methods of Appendix H were used to determine the radiator size required to meet our cooling demands at our most critical condition (top of climb). This was repeated for a number of fuel cell pressure ratios to generate the results below. These results are for a single large radiator and are therefore representative of the total radiator frontal area. It is worth pointing out that the final results might be slightly different to these results, but at this stage it is the trend that is most important to us. These results clearly demonstrate the benefit of operating the fuel cell system at higher pressure ratios. In this analysis, the oxygen stoichiometric ratio was fixed at 3 since this is known to have a cooling effect. An example of this is that smaller fuel cells can be cooled solely by supplying air to the fuel cell at higher flow rates.

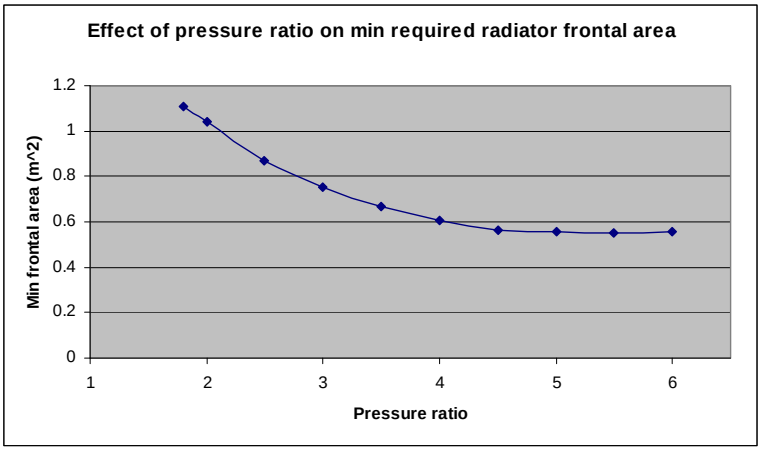

Chart 1-1

A separate analysis was carried out to study the impact of the oxygen stoichiometric ratio on the required minimum radiator frontal area, the results of which are given in the chart below. In this analysis, the fuel cell system was tested at its most critical condition (top of climb) for a number of different values of oxygen stoichiometric ratio. For the purposes of this analysis, the pressure ratio was fixed at a value of 3. Taking into consideration the scale used in the chart below compared to that for the pressure ratio, it is evident that the effect of oxygen stoichiometric ratio is negligible for values over 2.5.

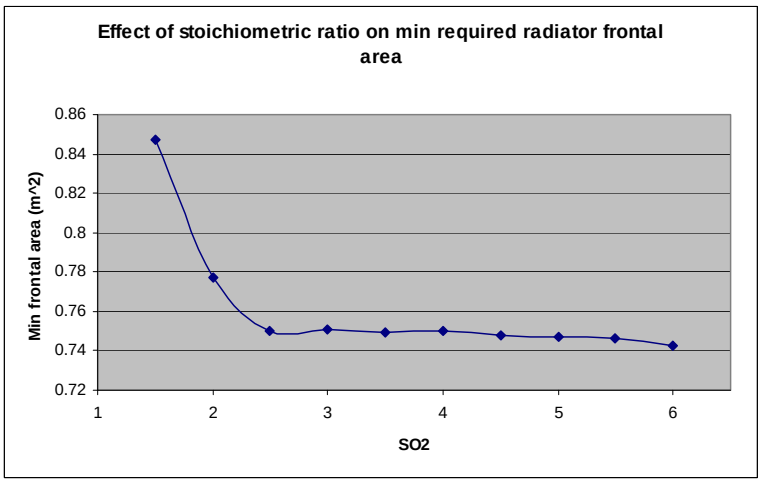

Chart 1-2

I1.4 Heat exchanger selection

There is an endless choice of different heat exchanger configurations available but the type most applicable to our needs is a compact air-liquid heat exchanger (as used for automotive radiators). As to be expected, the best possible configuration can only be achieved by the design and development of a purpose built unit. There is however a vast number of off the shelf compact heat exchangers already available, from which it would be possible to find a reasonable match. The difficulty in such an approach however comes from the lack of technical data available for such units, which is essential to make the correct selection. Fortunately, a number of generic relations already exist for different compact heat exchanger configurations as reported by Kays and London [80].

There are a number of different air-liquid compact heat exchanger configurations available, each with their own set of merits. The most effective of which has been reported to be the two and three row finned flat tube configurations. Fortunately, data for these is readily available from London and Kays. To make the best selection, it is necessary to test each of these configurations at a number of important points throughout the flight profile using the analysis methods of Appendix H. This enables us to determine the minimum heat exchanger frontal area required to meet our cooling needs at that point. The analysis procedure adopted was to vary the size of the heat exchanger until the mass flow rate of coolant through the by-pass circuit is zero. This process was repeated for the two and three row heat exchanger configurations at each points being analysed in the flight phase. This gives us the results in the chart below

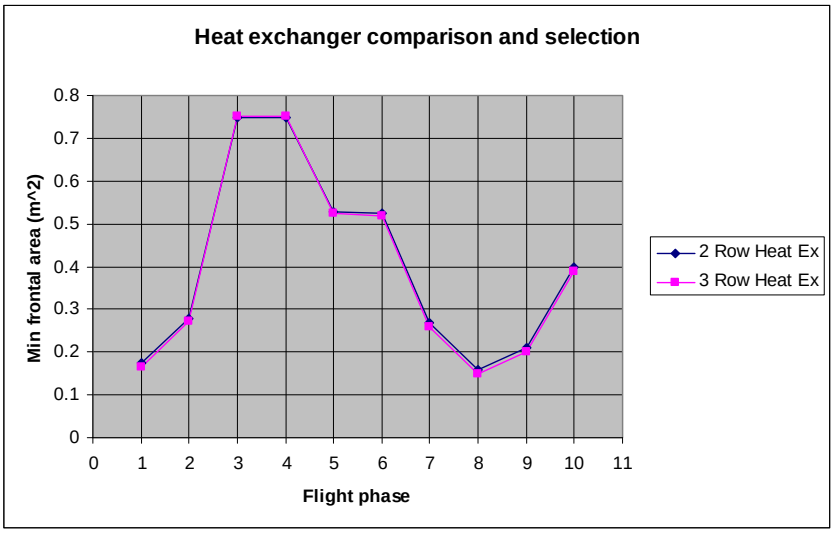

Key to flight phases
1. Climb start
2. Climb mid
3. Climb end
4. Outbound start
5. Outbound mid
6. Outbound end
7. Loiter start
8. Loiter mid
9. Loiter end
10. Inbound start

Chart 1-3

Another parameter of significant importance to our work is the air side pressure drop across the heat exchanger, since this is directly related to the drag generated by the air passing through the matrix. As before, our analysis gave us the results below for the two and three row heat exchangers at a number of different flight phases. The analysis of frontal area above has demonstrated that a two and three row heat exchanger would be of comparable size. However, a considerable reduction in the pressure drop across the air side has been demonstrated for the three row heat exchanger. On this basis, the three row heat exchanger has been selected for our system.

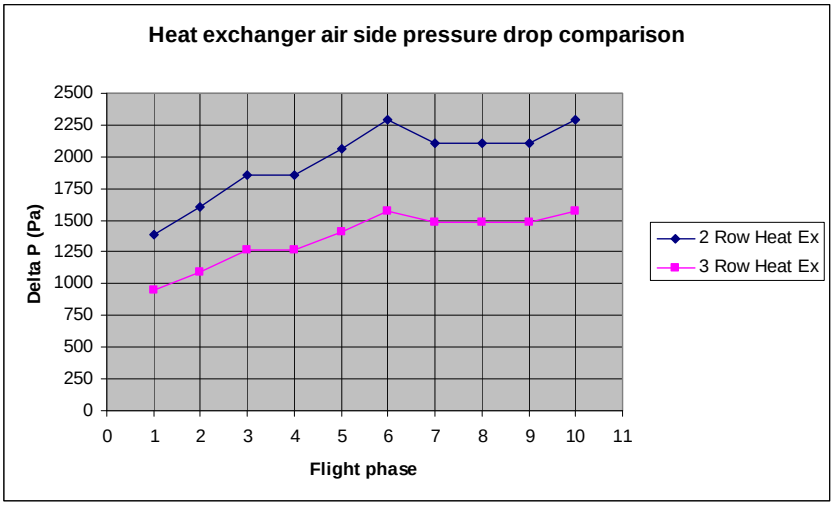

Chart 1-4

I1.5 Sizing the external heat exchangers

In our work so far, the end of climb was identified as the critical design point for our radiator. The methods of Appendix H were used to determine the minimum size of heat exchanger required to meet our needs at this design point. The procedure used involved iterating the size of the heat exchanger until the mass flow rate of coolant through the by-pass circuit is zero. The radiator is thus working at maximum capacity at this critical design point. The problem is however not as straightforward as it first seems as a number of design choices must be made, which include:

- The aspect ratio of each radiator – Long and thin or short and fat?
- The proportion of the heat load carried by each radiator – Should the fuselage radiator be doing the most work, or visa versa, or even carrying equals loads?
- The orientation of each radiator – Whether the matrix tubes are arranged horizontally or vertically when installed.
- The number of repeating blocks – The radiator is built up from a number of repeating elements, the dimensions of which are predefined.

Thus, such a design process involves numerous iterations of the design choices above until a solution is found which meets all our requirements as well as fitting into the space available. The final solutions for the fuselage and tail boom radiators are given in the table below. The dimensions are defined in the figure and refer to the matrix only and therefore do not include the end manifolds or fittings. In the final configuration, 65% of the waste heat is disposed of by the fuselage radiator. The remaining 35% of which is disposed of by the fuel system heat exchanger and tailboom radiators.

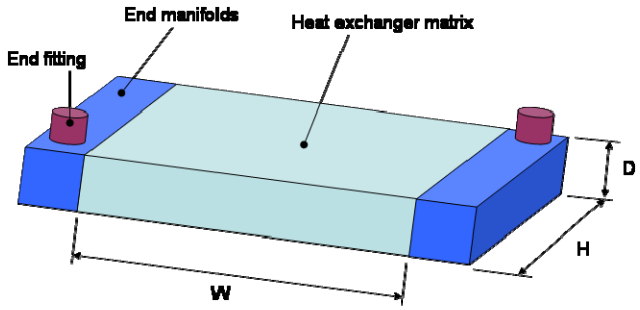

Final radiator matrix configurations

Parameters	Fuselage	Tailboom
No. of rads.	1	2
W (mm)	433.07	195.58
H (mm)	860.2	529.7
D (mm)	61.544	61.544
Aspect ratio	0.5035	0.3692
N-Blocks	31	14

Figure 1-2 and Table 1-1

I1.6 Integrating the tailboom heat exchangers

A number of locations were initially explored for the tailboom radiators. These locations included:

- Fore fuselage – The radiators would be located within the fuselage. Doors can be used to seal off the entry and exit ductwork to reduce aircraft drag when they are not in use. This installation has the benefits of reduced drag and increased cooling efficiency. The downsides are that the ducting would take up a lot of space within the forward fuselage and the coolant would have to be pumped a considerable distance.
- Under wing pods – In this arrangement, the radiators would be housed within pods underneath the wing. This offers the benefits of good cooling efficiency and minimal impact of the existing space within the wings and fuselage. The main drawback is increased aircraft drag.
- Internal wing installation – The radiators would be housed within the wing itself, with just an inlet and exhaust protruding from the wing surface. The radiator is located just fore of the front spar with the inlet just below the leading edge. The exhaust is located just aft of the front spar. The advantage of this arrangement is reduced drag. The disadvantages are that some of the space within the wing is taken up by the inlet and exhaust ducting and therefore there is a slight reduction in the volume of the wing fuel tanks.
- Internal tailboom installation – In this configuration, a radiator would be housed within each of the tailbooms. This arrangement has the advantage of reduced drag and has the least impact on the aircraft structure and other components and assemblies. The disadvantage of this arrangement is that the coolant has to be pumped a long way out to the tailbooms.

Of all the configurations investigated, the tailboom installation showed the most promise for our needs.

I1.7 Integrating the fuselage heat exchanger

As mentioned above, the fuselage radiator is the largest of the heat exchangers and as a result is responsible for the removal of 65% of the total waste heat. This radiator is located within the aft portion of the fuselage, underneath the electric drive train. Air is supplied via flush NACA inlets which are integrated into either side of the aft fuselage. The air is then internally ducted to the radiator, after which it is expelled through a single exhaust located on the rear of the aircraft, just below the propeller drive train.

I2 Sizing of miscellaneous components

I2.1 Radiator mass estimation

This part of the analysis is used to make an initial estimate of the mass of the radiator assembly. A summary of the analytical procedure is shown in the flow chart below.

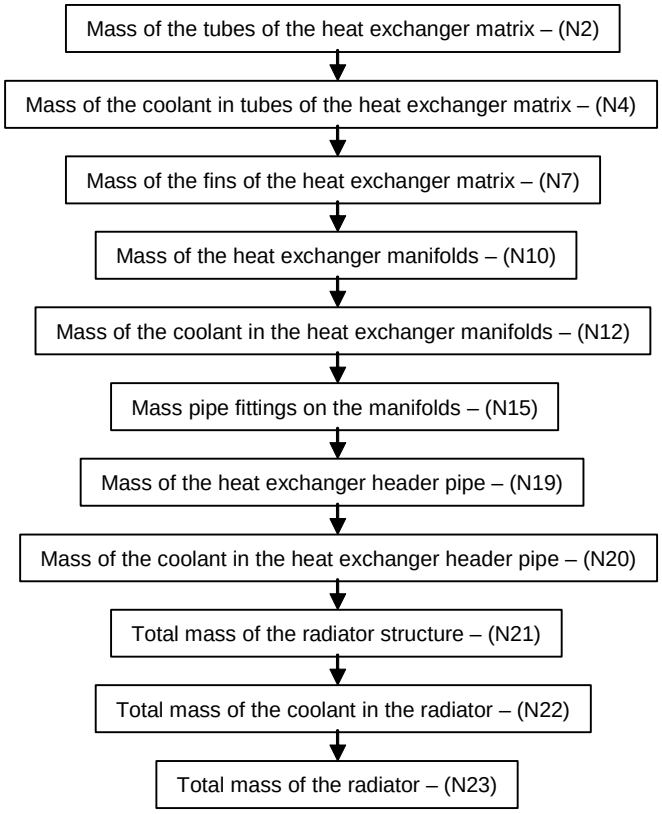

The accompanying equations are discussed below. To aid understanding, a picture of the heat exchanger configuration is shown below.

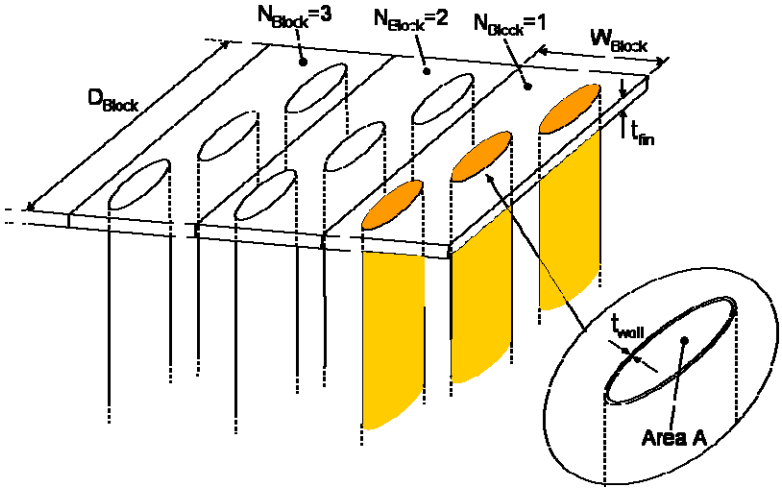

Figure 2-1

An understanding of the heat exchanger configuration, as presented in the figure above, is valuable to aid understanding of the equations presented in this analysis. The heat exchanger is analysed as a number of N repeating identical blocks. Each block has the dimensions WxDxH, with W being the width and D the depth of the block end plates. H is the length of the tubes between end plates. The number of tubes in each block is dependant on the configuration chosen, which is 3 in this analysis (3-row heat exchanger).

The total volume of the material that makes up the tubes of the matrix is given by equation N1, where P is the perimeter of a cross-section through one of the tubes and t is the wall thickness of each tube. The total mass of the tubes is given by equation N2.

$$V_{Tubes-Matrix} = P_{Tube-Each} \cdot N_{Tubes-Block} \cdot N_{Blocks} \cdot h_{Matrix} \cdot t_{Tube-Wall} \quad \text{Eq 2-1 (N1)}$$

$$M_{Tubes-Matrix} = V_{Tubes-Matrix} \cdot \rho_{Matrix-Mat} \quad \text{Eq 2-2 (N2)}$$

An operational heat exchanger will also be completely filled with coolant and allowance must be made for this additional mass. The total volume of the coolant contained in the heat exchanger tubes can be determined from equation N3, where A is the internal cross-sectional area of one of the tubes. The mass of the coolant in the tubes can then be determined from N4.

$$V_{Tubes-Coolant} = A_{CSA-Tube} \cdot N_{Tubes-Block} \cdot N_{Blocks} \cdot h_{Matrix} \quad \text{Eq 2-3 (N3)}$$

$$M_{Tubes-Coolant} = V_{Tubes-Coolant} \cdot \rho_{Coolant} \quad \text{Eq 2-4 (N4)}$$

Matrix fins are used to improve the effectiveness of the heat exchanger, which are equally spaced along the entire length H of the heat exchanger tubes. For the configuration chosen, the fin pitch is defined by the data from Kays and London. The total number of fins can then simply be determined from equation N5.

$$N_{Fins-Block} = \{ROUND[(h_{Matrix} / Pitch_{Fin}),0]\} - 1 \quad \text{Eq 2-5 (N5)}$$

The total volume of the material that makes up the fins in the heat exchanger is given by equation N6, where $A_{Fin\text{-}Block}$ is the platform area of a single fin within each block and t_{Fin} is the material thickness of a fin. The total mass of the matrix fins can then be determined from equation N6.

$$V_{Fins} = A_{Fin-Block(Net)} \cdot N_{Fins-Block} \cdot N_{Block} \cdot t_{Fin-Each} \quad \text{Eq 2-6 (N6)}$$

$$M_{Fins} = V_{Fins} \cdot \rho_{Matrix-Mat} \quad \text{Eq 2-7 (N7)}$$

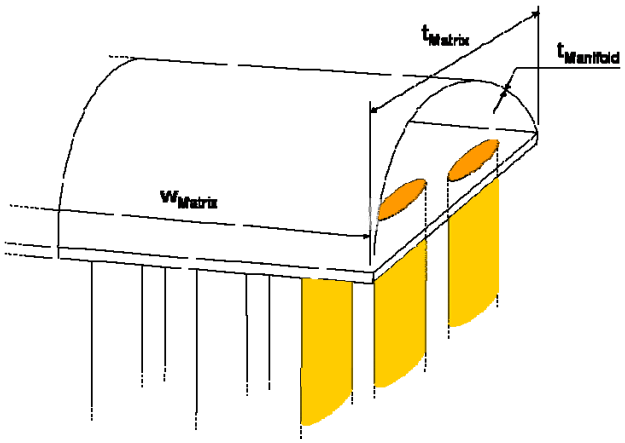

Figure 2-2

The radiator end manifolds are assumed to adopt the semi-circular configuration shown in the figure above. The total volume of material making up the manifolds (one on each end of the matrix) can be determined from equation N8. As defined by equation N9, the wall thickness of the end manifolds is assumed to be twice that of the matrix tubes. The mass of the end manifolds is finally given by equation N10.

$$V_{Manifold} = \pi \cdot t_{Matrix} \cdot w_{Matrix} \cdot t_{Manifold} \qquad \text{Eq 2-8 (N8)}$$

$$t_{Manifold} = 2 \cdot t_{Tube-Wall} \qquad \text{Eq 2-9 (N9)}$$

$$M_{Manifold} = V_{Manifold} \cdot \rho_{Matrix-Mat} \qquad \text{Eq 2-10 (N10)}$$

The volume of the coolant within the end manifolds is given by equation N11 and its mass is given by N12.

$$V_{Manifold-Coolant} = \frac{\pi \cdot t_{Matrix}^{2}}{4} \cdot w_{Matrix} \qquad \text{Eq 2-11 (N11)}$$

$$M_{Manifold-Coolant} = V_{Manifold-Coolant} \cdot \rho_{Coolant} \qquad \text{Eq 2-12 (N12)}$$

The general layout of the complete radiator is shown in the figure below. Besides the heat exchanger matrix and end manifold which have already been discussed, this also includes end fittings for connecting pipes. It is typical for the inlet and outlets of a heat exchanger to be at opposite corners of the matrix, to improve its performance. A header pipe can however be used so that both of the connections are at the same end, as shown.

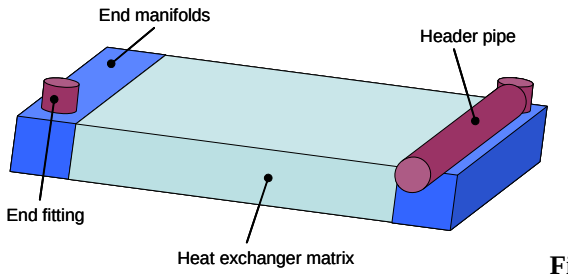

Figure 2-3

In this analysis, we have assumed that the length and diameter of the end fitting are equal, as given by equation N13. The volume of material that makes up the end fitting is

given by equation N14 and its mass is given by N15, where $N_{Fitting}$ is the number of end fittings in the configuration (2 in this case).

$$L_{Fitting} = D_{Fitting} \quad \text{Eq 2-13 (N13)}$$

$$V_{Fitting} = t_{Fitting-Wall} \cdot \pi \cdot L_{Fitting} \cdot D_{Fitting} \quad \text{Eq 2-14 (N14)}$$

$$M_{Fitting} = V_{Fitting} \cdot N_{Fitting} \cdot \rho_{Matrix-Mat} \quad \text{Eq 2-15 (N15)}$$

The length of the header pipe is assumed to be equal to the height of the heat exchanger, as given by equation N16. Its diameter is also assumed to be the same as that of the end fitting, as given by equation N17.

$$L_{Pipe-Header} = h_{Matrix} \quad \text{Eq 2-16 (N16)}$$

$$D_{Pipe-Header} = D_{Fitting} \quad \text{Eq 2-17 (N17)}$$

The volume of material that makes up the header pipe is given by N18, where $t_{Pipe-Header(wall)}$ is the wall thickness of the header pipe and is assumed to be the same as the manifold wall thickness. The mass of the header pipe is then given by equation N19.

$$V_{Pipe-Header} = t_{Pipe-Header(wall)} \cdot \pi \cdot D_{Pipe-Header} \cdot L_{Pipe-Header} \quad \text{Eq 2-18 (N18)}$$

$$M_{Pipe-Header} = V_{Pipe-Header} \cdot \rho_{Matrix-Mat} \quad \text{Eq 2-19 (N19)}$$

The mass of the coolant contained in the header pipe is given by equation N20.

$$M_{Pipe-Header(Coolant)} = \pi \cdot \frac{D_{Pipe-Header}^{2}}{2} \cdot L_{Pipe-Header} \cdot \rho_{Coolant} \quad \text{Eq 2-20 (N20)}$$

The total mass of the empty radiator can finally be determined from equation N21 as the sum of the components above. Likewise, the total mass of the coolant within the radiator is given by equation N22. The total mass of the radiator is finally determined as the sum of the empty mass and the coolant, as given by equation N24.

$$M_{Radiator} = M_{Tubes-Matrix} + M_{Fins} + M_{Manifold} + M_{Fitting} + M_{Pipe-Header} \quad \text{Eq 2-21 (N21)}$$

$$M_{Coolant-Rad} = M_{Tubes-Coolant} + M_{Manifold-Coolant} + M_{Pipe-Header(Coolant)} \quad \text{Eq 2-22 (N22)}$$

$$M_{Rad-Total} = M_{Radiator} + M_{Coolant-Rad} \quad \text{Eq 2-23 (N23)}$$

I2.2 Feed pipe sizing for a split radiator system

Due to size constraints, it is necessary to use two separate radiator circuits instead of one, which will mean splitting the mass flow into two smaller diameter pipes. The cross-sectional area of each split pipe can be determined from equation N24 and its diameter from N25.

$$A_{Pipe-Split} = 0.5 \cdot \pi \cdot \frac{D_{Original}^{\ 2}}{4}$$ Eq 2-24 (N24)

$$D_{Pipe-Split} = \sqrt{\frac{4 \cdot A_{Pipe-Split}}{\pi}}$$ Eq 2-25 (N25)

I2.3 Heat transfer from aircraft wing fuel tanks

This part of the analysis is used to determine the heat transfer from the wing fuel tanks, which thus reduces the quantity of heat which must be dissipated by the boom radiators. Since the depth of the wing fuel tank is small in comparison to its other dimensions, heat loss from the fuel tank is assumed to be from its upper and lower surfaces only. A summary of the analytical procedure is shown in the flow chart below. The accompanying equations are also given below.

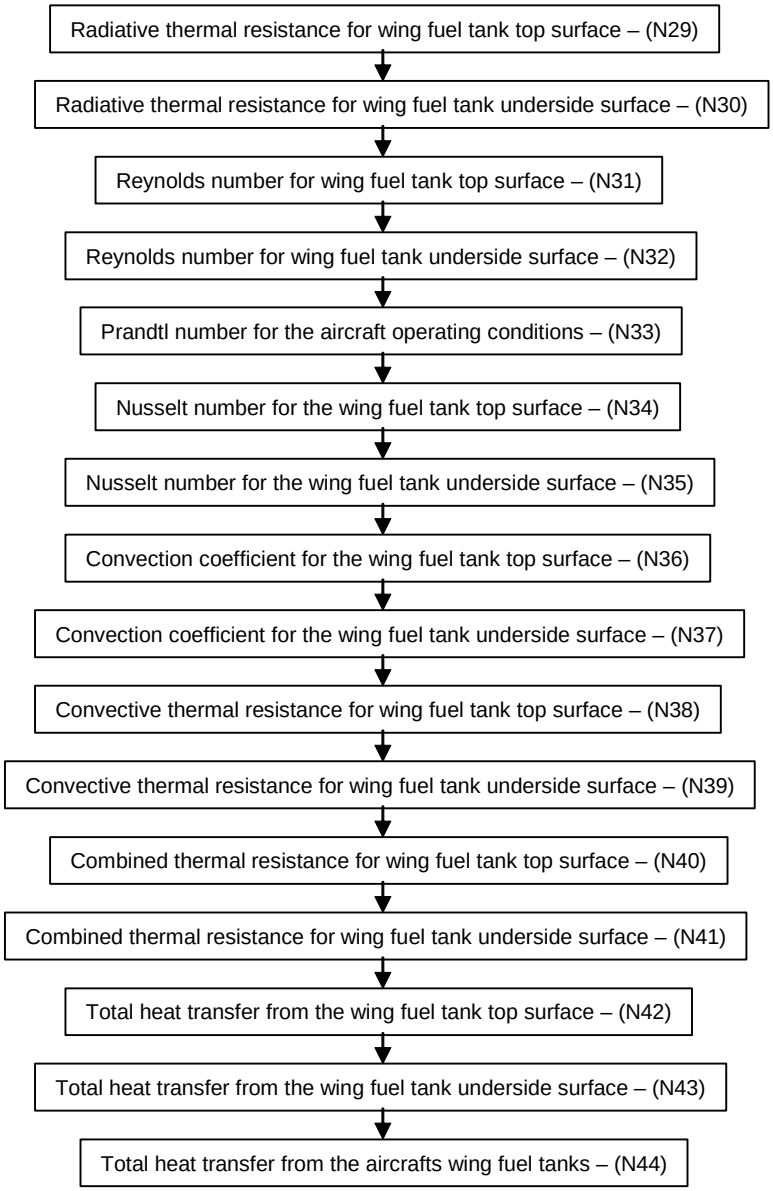

This analysis requires knowledge of a number of properties of the atmospheric air, which are given by equations N26 to N27. It should also be noted that the fuel temperature has been fixed at 15 degrees during the analysis. This analysis follows a similar procedure to that used for heat loss from the external surfaces of a fuel cell as presented in the cooling system requirements section and so the depth of discussion will be somewhat limited here. The main difference here is that heat transfer will involve forced convection as opposed to natural convection used before.

$$k = \frac{2.648151 * 10^{-3} \cdot T^{3/2}}{T + 245.4 * 10^{(-12/T)}} \quad \text{Eq 2-26 (N26)}$$

$$\beta = \frac{1}{T} \quad \text{Eq 2-27 (N27)}$$

$$\alpha = A_{\alpha} \cdot t_{air}{}^{2} + B_{\alpha} \cdot t_{air} - C_{\alpha} \quad \text{Eq 2-28 (N28)}$$

Constant	A_α	B_α	C_α
Value	9.1018E-11	8.8197E-8	-1.0654E-5

The radiative thermal resistance for the top and underside fuel tank surfaces can be determined from equations N29 and N30 respectively.

$$R_{R(top)} = \frac{1}{\sigma \cdot F \cdot A_{Tank-Top} \cdot \left(T_{Fuel} + T_{Air}\right)\left(T_{Fuel}{}^{2} + T_{Air}{}^{2}\right)} \quad \text{Eq 2-29 (N29)}$$

$$R_{R(bottom)} = \frac{1}{\sigma \cdot F \cdot A_{Tank-Bottom} \cdot \left(T_{Fuel} + T_{Air}\right)\left(T_{Fuel}{}^{2} + T_{Air}{}^{2}\right)} \quad \text{Eq 2-30 (N30)}$$

Equations N31 and N32, able us to determine the Reynolds number for the top and underside fuel tank surfaces, where L is the mean surface width and V is the free stream flight speed.

$$\mathrm{Re}_{Top} = \frac{\rho_{Air} \cdot V_0 \cdot L_{Tank-Top}}{\mu_{Air}} \quad \text{Eq 2-31 (N31)}$$

$$\mathrm{Re}_{Bottom} = \frac{\rho_{Air} \cdot V_0 \cdot L_{Tank-Bottom}}{\mu_{Air}} \quad \text{Eq 2-32 (N32)}$$

Another fluid dependant property known as the Prandtl number, as given by equation N33, is required in order to determine the Nusselt number.

$$\mathrm{Pr} = \frac{C_{P-Air} \cdot \mu_{Air}}{k_{Air}} \quad \text{Eq 2-33 (N33)}$$

The Nusselt number for the top and underside fuel tank surface can then be determined from equations N34 and N35 respectively.

$$Nu_{Top} = 0.332 \cdot \mathrm{Re}_{Top}^{0.5} \cdot \mathrm{Pr}^{0.33} \cdot \left(\frac{t_{fuel}}{t_{air}} \right)^{0.177}$$ Eq 2-34 (N34)

$$Nu_{Bottom} = 0.332 \cdot \mathrm{Re}_{Bottom}^{0.5} \cdot \mathrm{Pr}^{0.33} \cdot \left(\frac{t_{fuel}}{t_{air}} \right)^{0.177}$$ Eq 2-35 (N35)

The convection coefficient for the top and underside surfaces can then be determined from equations N36 and N37 respectively.

$$h_{Top} = \frac{k_{Air}}{L_{Tank-Top}} \cdot Nu_{Top}$$ Eq 2-36 (N36)

$$h_{Bottom} = \frac{k_{Air}}{L_{Tank-Bottom}} \cdot Nu_{Botom}$$ Eq 2-37 (N37)

The convective thermal resistance for each fuel tank surface can then be obtained from equations N38 and N39. Equations N40 and N41 can then be used to find the combined thermal resistance for convection and radiation.

$$R_{Con-Top} = \frac{1}{h_{Top} \cdot A_{Tank-Top}}$$ Eq 2-38 (N38)

$$R_{Con-Bottom} = \frac{1}{h_{Bottom} \cdot A_{Tank-Bottom}}$$ Eq 2-39 (N39)

$$R_{Th-Top} = \frac{1}{\frac{1}{R_{Con-Top}} + \frac{1}{R_{R-Top}}}$$ Eq 2-40 (N40)

$$R_{Th-Bottom} = \frac{1}{\frac{1}{R_{Con-Bottom}} + \frac{1}{R_{R-Bottom}}}$$ Eq 2-41 (N41)

The heat transfer from each of the fuel tank surfaces by dissipation can finally be determined by equations N42 and N43. The total heat transfer for the top and underside fuel tank surfaces on both sides of the aircraft is finally given by equation N44.

$$Q_{Dis-Top} = \frac{T_{Fuel} - T_{Air}}{R_{Th-Top}}$$ Eq 2-42 (N42)

$$Q_{Dis-Bottom} = \frac{T_{Fuel} - T_{Air}}{R_{Th-Bottom}}$$ Eq 2-43 (N43)

$$Q_{Dis-Total} = 2 \cdot \left(Q_{Dis-Top} + Q_{Dis-Bottom} \right)$$ Eq 2-44 (N44)

I2.4 Liquid-liquid heat exchanger sizing

The purpose of this analysis is to obtain a first pass estimate of the size of a liquid-liquid heat exchanger, which is used to transfer heat between the cooling system and fuel in the wing tanks. A summary of the analytical procedure is shown in the flow chart below. The accompanying equations are also given below.

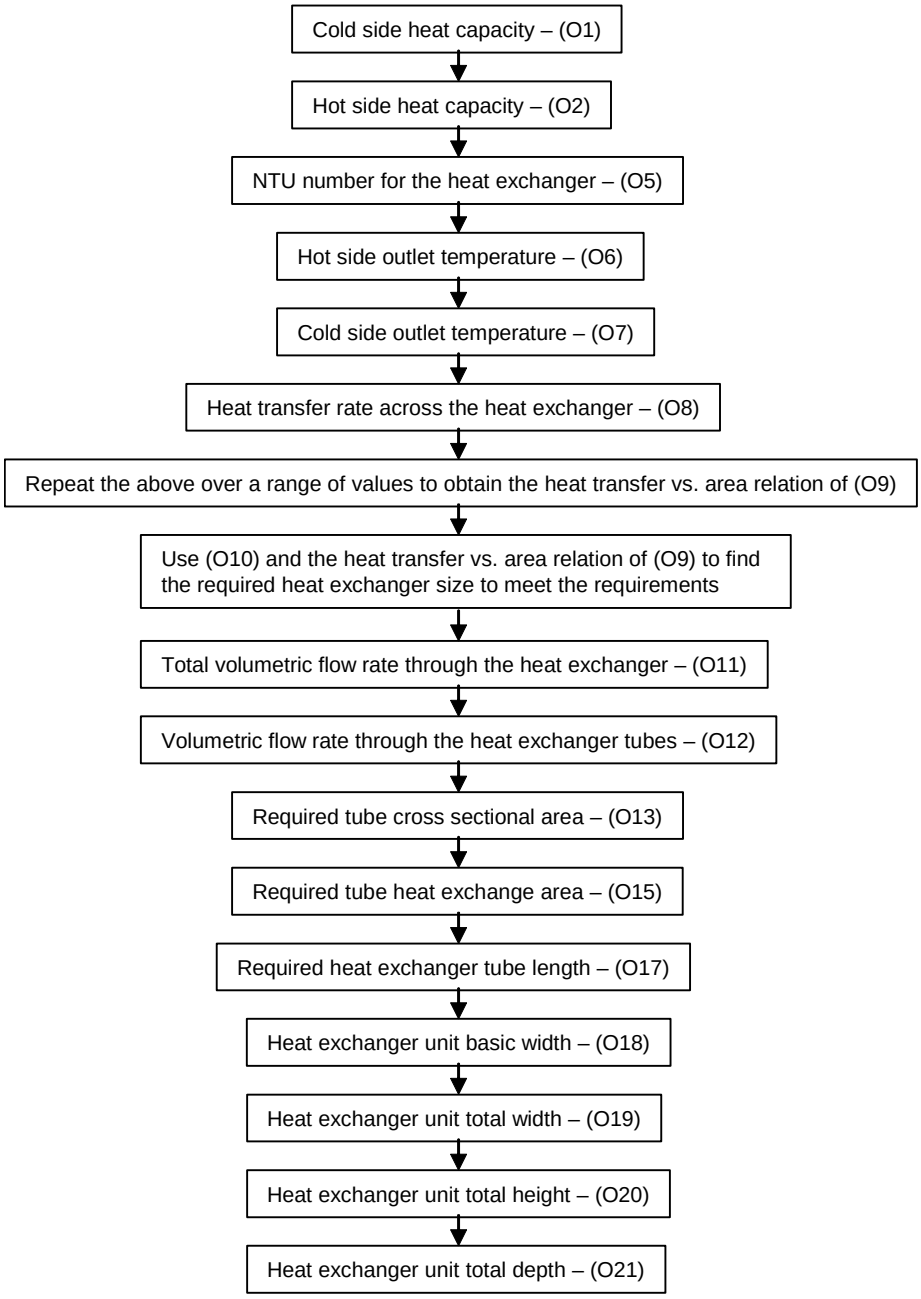

This analysis follows the methodology given in ESDU 92013 [81]. A brief overview of the method will be given here but the reader is advised to refer to the datasheet for further details. Equations O1 to O4 are used to determine the values of maximum and minimum heat capacity for the hot and cold sides of the heat exchanger. The hot side is representative of the coolant at $T_{H(In)}$ = 78.3º which gives C_{pc} = 3727 J/(kg.K). The cold

side is representative of the methanol in the wing tanks at $T_{C(In)}$ = 15° which gives C_{pc} = 3727 J/(kg.K). A trial and error approach was used to determine the best balance of mass flow rates, which gave, m_C =0.9kg/s and m_H =0.13kg/s.

$$C_C = C_{PC} \cdot m_C \qquad \text{Eq 2-45 (O1)}$$

$$C_H = C_{PH} \cdot m_H \qquad \text{Eq 2-46 (O2)}$$

$$C_{Min} = \min(C_C : C_H) \qquad \text{Eq 2-47 (O3)}$$

$$C_{Max} = \max(C_C : C_H) \qquad \text{Eq 2-48 (O4)}$$

Equation O5 gives the NTU number required, where the heat transfer coefficient U_m =600 W/m^{2}K (from ESDU 94042 [82] table 12.1). A_{HT} is the heat transfer area which is an analysis variable, for which a range of values between 0.8 and 2m^2 were explored.

$$NTU = \frac{A_{HT} \cdot U_m}{C_{Min}} \qquad \text{Eq 2-49 (O5)}$$

Using NTU from above and C* (C* =C_{min}/C_{max}) we are able to determine the effectiveness from the corresponding tables in ESDU 92013. The hot side and cold side exit temperatures can then be determined from equations O6 and O7.

$$T_{H(Out)} = T_{H(In)} - \frac{\varepsilon \cdot C_{Min} \cdot \left(T_{H(In)} - T_{C(In)}\right)}{C_H} \qquad \text{Eq 2-50 (O6)}$$

$$T_{C(Out)} = T_{C(In)} + \frac{\varepsilon \cdot C_{Min} \cdot \left(T_{H(In)} - T_{C(In)}\right)}{C_C} \qquad \text{Eq 2-51 (O7)}$$

Finally, the heat exchanger heat transfer rate can be determined from equation O8.

$$Q_{Heat} = C_H \cdot \left(T_{H(In)} - T_{H(Out)}\right) \qquad \text{Eq 2-52 (O8)}$$

After repeating the steps above at a number of different estimates of heat transfer area, the heat transfer versus area relation O9 is obtained, as shown in the chart below.

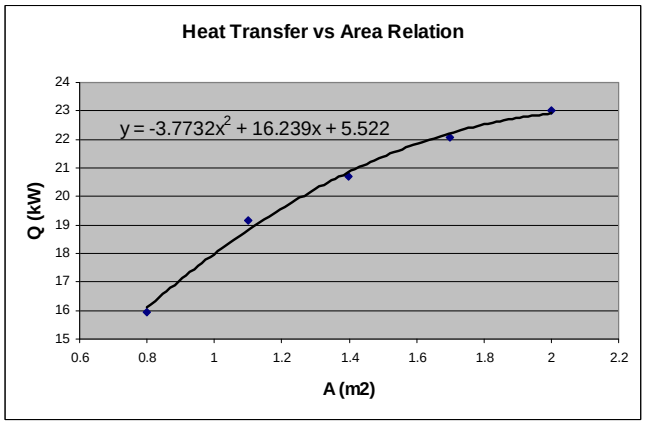

Eq 2-53 (O9)

The relation O9 given above can then be solved to determine the size of heat exchanger required. In which case, the optimal configuration is one whose calculated heat transfer rate will equal the required heat transfer rate, as given in equation O10.

$$Q_{Error} = Q_{Calculated} - Q_{Target} \quad \text{Eq 2-54 (O10)}$$

Relations O11 and O12 enable the volumetric flow rate through the heat exchanger and each of the flow tubes to be determined. The number of tubes used in this analysis is 4.

$$Q_{Flow-Total} = \frac{\dot{m}_H}{\rho_{Coolant}} \quad \text{Eq 2-55 (O11)}$$

$$Q_{Flow-Tube} = \frac{Q_{Flow-Total}}{N_{Tubes}} \quad \text{Eq 2-56 (O12)}$$

The cross sectional area of each of the flow tubes can be determined from equation O13 and the corresponding tube diameter from equation O14.

$$A_{Tube} = \frac{Q_{Flow-Tube}}{V_{Flow-Tube}} \quad \text{Eq 2-57 (O13)}$$

$$D_{Tube} = \sqrt{\frac{4 \cdot A_{Tube}}{\pi}} \quad \text{Eq 2-58 (O14)}$$

The total heat transfer area can now be divided according to the number of tubes used in the configuration as given in equation O15.

$$A_{HT-Tube} = \frac{A_{HT-Total}}{N_{Tubes}} \quad \text{Eq 2-59 (O15)}$$

The circumference of each of the tubes can be determined from equation O16 and then the required length of each of the tubes can be determined from equation O17.

$$C_{Tube} = \frac{D_{Tube}}{1000} \cdot \pi \quad \text{Eq 2-60 (O16)}$$

$$L_{Tube} = \frac{A_{Tube}}{C_{Tube}} \quad \text{Eq 2-61 (O17)}$$

Finally, an estimate of the unit size can be made from the results obtained above and the configuration assumed. In this case, there is assumed to be 4 shells in total with 2 tube passes in each shell, which gives a total of 8 passes for each tube. There is also assumed to be 4 parallel tubes for this arrangement. Using this data and some basic assumptions, an estimate of the unit width can be determined from equation O18.

$$w_{Unit} = \frac{L_{Tube}}{N_{Passes-Total}} \quad \text{Eq 2-62 (O18)}$$

The dimensions of the heat exchanger can then be obtained from equations O19 to O21.

$$w_{HeatEx} = w_{Unit} + \left(4 \cdot D_{Tube}\right) \quad \text{Eq 2-63 (O19)}$$

$$h_{HeatEx} = 4 \cdot \left(\left\{3 \cdot D_{Tube}\right\} + \left\{2 \cdot D_{Tube}\right\}\right) \quad \text{Eq 2-64 (O20)}$$

$$d_{HeatEx} = \left\{5 \cdot D_{Tube}\right\} + \left\{4 \cdot D_{Tube}\right\} \quad \text{Eq 2-65 (O21)}$$

I2.4.1 Liquid-liquid heat exchanger integration

Naturally, the best location for the liquid-liquid heat exchanger is within the fuselage in close proximity to the fuel tanks. This will ensure that the power demands of the pumps required to circulate the hot and cold flows are kept to a minimum and that it is located as close as possible to the aircraft centre of gravity.

I2.5 Fuel cell intake sizing

The minimum fuel cell system intake area required to meet the air supply demands can be determined from the equation below, where $\dot{m}_{Air}$ is determined by the analysis methods given in appendix H.

$$A_{Intake} = \frac{\dot{m}_{Air}}{\rho_{Air} \cdot V_0} \quad \text{Eq 2-66}$$

It should be emphasised however that this is the minimum size to meet the air demands of the fuel cell system only. The actual area of the intake must be larger than this to provide sufficient additional air for cooling. A cooling air requirement of 5% of the core airflow was quoted for a gas turbine engine and in the absence of a better estimate, it seems reasonable to adopt this figure for a fuel cell system. The minimum intake size for a fuel cell system then becomes.

$$A_{Intake(Total)} = 1.05\frac{\dot{m}_{Air}}{\rho_{Air} \cdot V_0} \quad \text{Eq 2-67}$$

J1 Fuel cell powered MALE performance analysis

The purpose of this section is to present an overview of the different fuel cell system configurations which were proposed and the methodology used to evaluate their performance. This covers following fuel cell system variants:

- Autothermal reformer system
- Steam reformer system
- Hybrid autothermal reformer system
- Hybrid steam reformer system
- Fuel cell system with oxygen injection

In the sections which follow, a brief description of each of the fuel cell propulsion system variants will be given. This is followed with an overview of the procedure used to generate an analytical model which can be used to predict the fuel consumption of each system. This analytical model is finally integrated into the existing performance analyses used for the baseline aircraft to enable us to predict the performance of such a system in contrast to the baseline turboprop configuration. The final results for these analyses are presented in the evaluation section on the main text.

J1.1 Autothermal reformer system performance analysis

A simplified schematic of the autothermal reformer based fuel cell system is presented in the figure below. The reader is advised to refer to the section, an overview of the fuel cell powered aircraft systems for further details of the accompanying systems.

Schematic of the autothermal reformer system

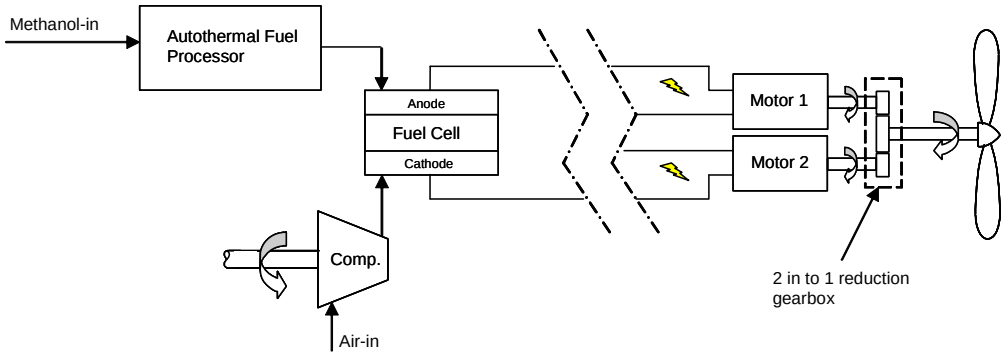

Figure 1

J1.1.1 System analysis

Using the analysis methods discussed in Appendix H (fuel cell system design and analysis), this system was tested over a range of combinations of fuel cell power output and altitude. The results of this analysis work are presented in the chart below as number of trends lines of fuel consumption versus power output. Each curve in this chart represents a different test altitude, which includes a range of values between sea level and the loiter altitude of 7620m.

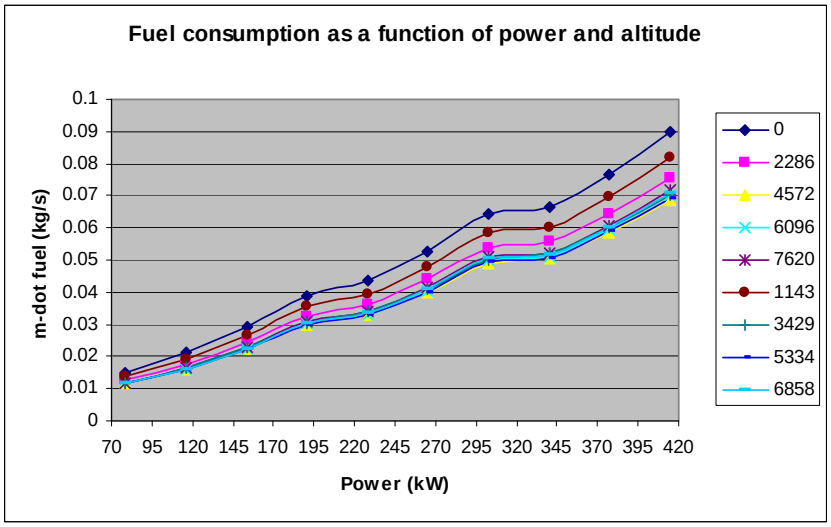

Chart 1

At this point, the reader may question the irregular nature of the curves in the above chart. The shape of the curves is however correct and is a result of the operating characteristics of the fuel cell system. To explain this phenomenon, we shall take a closer look at the characteristics of one of the curves. For this discussion, the curve for the 1143m altitude condition was selected at random, as presented below. The other curves exhibit the same operating characteristics.

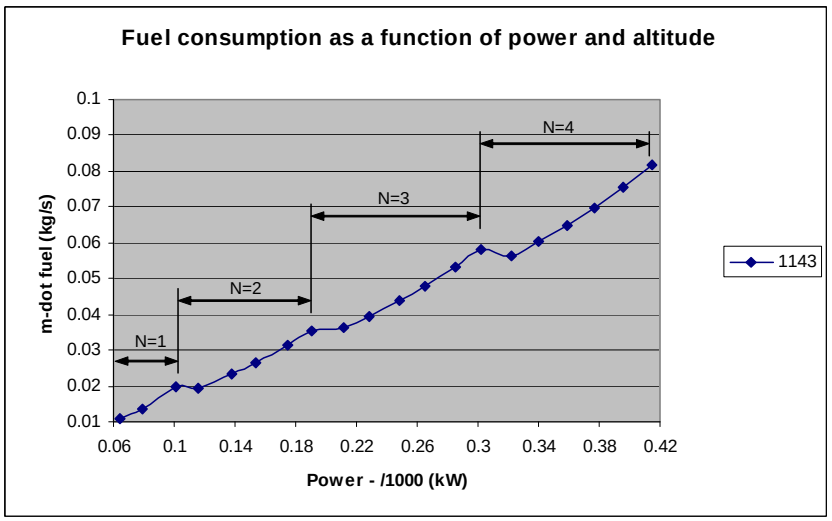

Chart 2

Upon close inspection of the irregular curve in the above chart, we can see that its profile actually consists of a number of steps along its length. It could in fact be considered to be constructed from four smaller segments, each of which corresponds to a different number of fuel cells in operation. For example, the first curve represents 1 of the 4 fuel cells in operation; the second curve corresponds to 2 of the 4 fuel cells in operation and so on. The characteristics are thus a function of the switching of the individual fuel cell stacks. In an actual fuel cell system, the control system will tailor the switching of each fuel cell system to deliver smoother operating characteristics for the complete system. It would therefore be reasonable to draw a best fit curve through the points which begins and end on the first and last points.

J1.1.2 Analysis results

The raw data from our analysis for a number of different altitudes and fuel cell power outputs is given in the table below for reference.

Results for autothermal reformer system

Fuel (kg/s)		Altitude (m)								
		0	1143	2286	3429	4572	5334	6096	6858	7620
Power (kW)	64.47933	0.011967	0.010851	0.009993	0.009314	0.009019	0.009063	0.009112	0.009165	0.009239
	78.7569	0.015121	0.013716	0.012638	0.011784	0.011436	0.011499	0.011567	0.011662	0.011785
	101.3247	0.021567	0.019588	0.018071	0.016874	0.01649	0.016605	0.016761	0.01696	0.017175
	116.0628	0.021234	0.01925	0.017726	0.016519	0.015964	0.016039	0.016121	0.016211	0.016336
	138.17	0.025908	0.023494	0.02164	0.020173	0.019536	0.019635	0.019744	0.019897	0.020061
	153.3687	0.029285	0.026562	0.024472	0.022818	0.022142	0.022261	0.022392	0.022573	0.022768
	175.0153	0.03456	0.03136	0.028904	0.026962	0.026224	0.026378	0.026593	0.026826	0.027077
	190.6746	0.039035	0.035436	0.032676	0.030496	0.02973	0.02992	0.030182	0.030466	0.030828
	211.8607	0.039864	0.036151	0.0333	0.031044	0.030066	0.03022	0.03039	0.030627	0.030882
	227.9805	0.043455	0.039413	0.036311	0.033856	0.032853	0.033028	0.033221	0.033489	0.033777
	248.706	0.048334	0.04385	0.040408	0.037686	0.036644	0.03685	0.037078	0.037391	0.037729
	265.2864	0.052574	0.047708	0.043974	0.041022	0.0399	0.040137	0.040467	0.040824	0.041282
	285.5513	0.058409	0.053023	0.048893	0.04563	0.044483	0.044768	0.045159	0.045582	0.046123
	302.5923	0.064184	0.058292	0.053777	0.050211	0.049066	0.049406	0.049866	0.050455	0.051093
	322.3967	0.062221	0.056443	0.052009	0.048501	0.047073	0.047333	0.047701	0.048015	0.048526
	339.8982	0.066508	0.060342	0.055611	0.051869	0.05044	0.05073	0.051049	0.051486	0.052049
	359.242	0.071598	0.064976	0.059895	0.055878	0.054356	0.054683	0.055138	0.055629	0.056259
	377.2041	0.076791	0.069706	0.064273	0.059978	0.058467	0.058837	0.059346	0.059898	0.060603
	396.0873	0.082933	0.075308	0.069463	0.064846	0.063242	0.063779	0.06436	0.064991	0.065793
	414.51	0.089878	0.081651	0.075348	0.070373	0.068794	0.069415	0.070087	0.070944	0.071872

Table 1

J1.1.3 Derivation of a general relation from the analysis data

The raw data from the last section needs to be converted into a more manageable format if it is to be used within our performance analysis. In this section, we describe the process followed to create a complex analytical expression from the raw data. A summary of the procedure used is shown in the flow chart below. The accompanying equations are also given below.

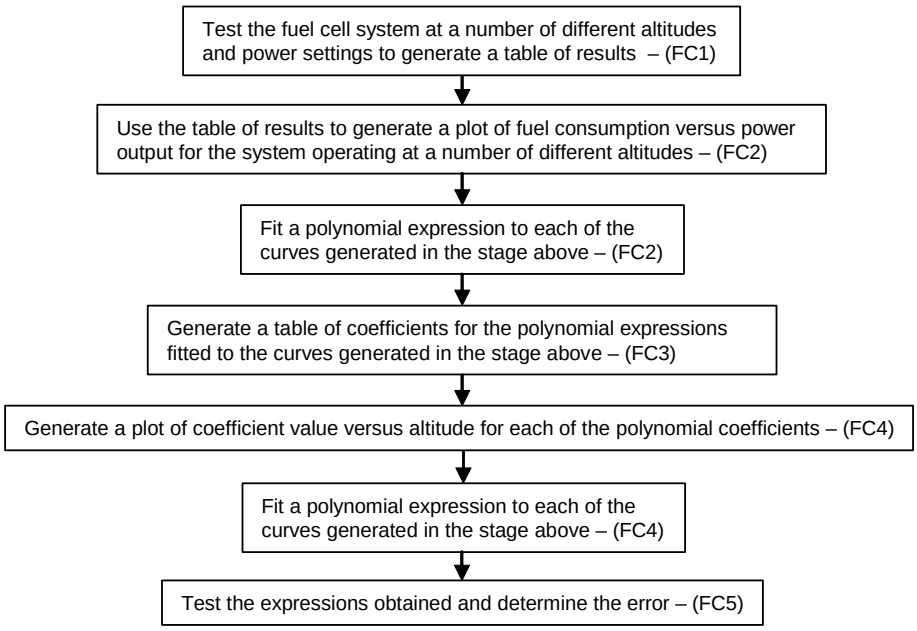

The first stage in this work is to use the raw data from the last section to generate a number of plots of fuel consumption against fuel cell power output, with each plot corresponding to a different altitude. An example of one such plot is presented in the chart below for the 1143m altitude case.

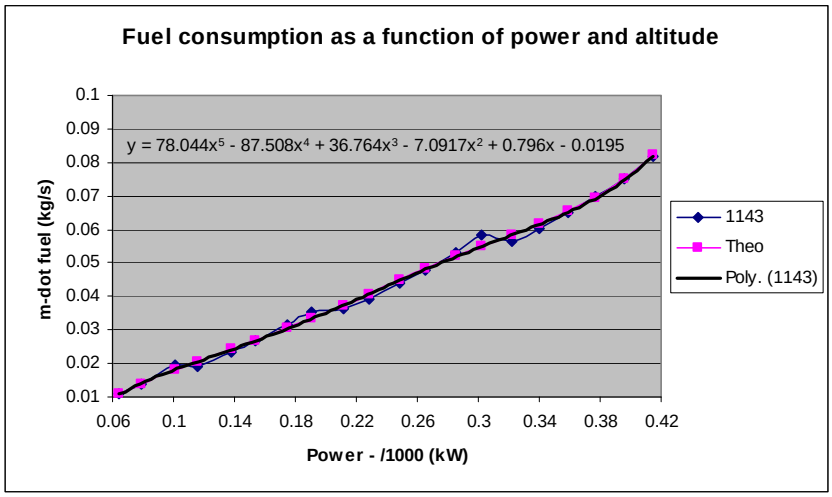

Chart 3 (FC2)

To this plot, we are then able to fit a polynomial best fit curve, which is taken as an average of the data points. The corresponding polynomial expression for each best fit curve takes the form given by the general expression below, which expresses the fuel consumption as a function of the fuel cell power output.

$$\dot{m}_{Fuel} = X_5 \cdot \left(\frac{P}{1E3}\right)^5 + X_4 \cdot \left(\frac{P}{1E3}\right)^4 + X_3 \cdot \left(\frac{P}{1E3}\right)^3 + X_2 \cdot \left(\frac{P}{1E3}\right)^2 + X \cdot \left(\frac{P}{1E3}\right) + C$$

Eq 1 (FC2)

This process is repeated to obtain a plot and corresponding best fit polynomial expression for each of the altitudes tested. This ultimately gives us nine independent expressions, whose constants can be tabulated as in table FC3 below.

Expression constants for autothermal reformer system

		Expresssion constants					
		X5	X4	X3	X2	X	C
Altitude	0	84.883	-95.176	39.985	-7.713	0.8683	-0.0212
	1143	78.044	-87.508	36.764	-7.0917	0.796	-0.0195
	2286	72.895	-81.735	34.339	-6.624	0.7413	-0.0182
	3429	68.93	-77.29	32.472	-6.2639	0.6989	-0.0172
	4572	71.124	-79.762	33.508	-6.4617	0.7116	-0.0177
	5334	73.131	-81.933	34.39	-6.6272	0.7265	-0.0182
	6096	75.196	-84.28	35.392	-6.8232	0.7449	-0.0187
	6858	78.968	-88.5	37.159	-7.1643	0.7761	-0.0197
	7620	82.035	-92.055	38.702	-7.4696	0.8046	-0.0205

Table 2 (FC3)

If we then generate a plot of expression coefficient versus altitude for each column of coefficients from the table above, it is possible to identify a trend with respect to altitude. An example of such a plot for the coefficients X3 is shown in the chart below.

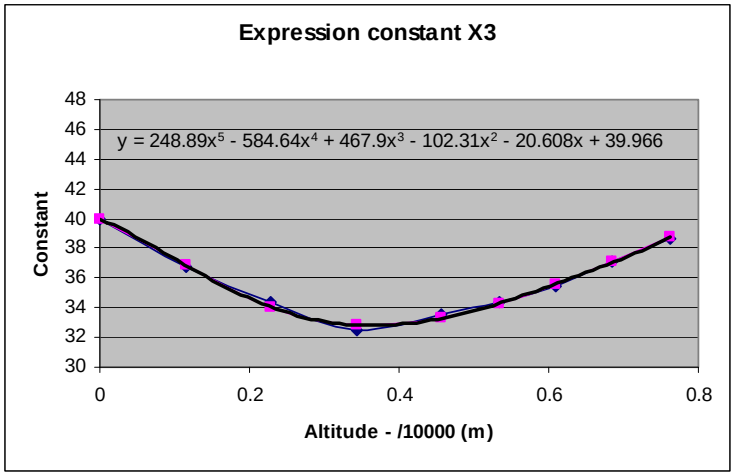

Chart 4 (FC4)

To this plot, we are then able to fit a polynomial best fit curve, which gives us a corresponding best fit polynomial expression. This expression takes the form given by the general expression below which gives the expression coefficient as a function of the operating altitude.

$$X_N = Y_{5(N)} \cdot \left(\frac{h}{1E4}\right) + Y_{4(N)} \cdot \left(\frac{h}{1E4}\right) + Y_{3(N)} \cdot \left(\frac{h}{1E4}\right) + Y_{2(N)} \cdot \left(\frac{h}{1E4}\right) + Y_{(N)} \cdot \left(\frac{h}{1E4}\right) + D_{(N)}$$

Eq 2 (FC4)

This process is repeated to obtain a plot and corresponding best fit polynomial expression for each column of coefficients in table FC3 above. This gives us six independent expressions, whose constants can be tabulated as below.

Expression constants for autothermal reformer system

	Y5	Y4	Y3	Y2	Y	D
X5	500.67	-1204	978.28	-215.15	-43.819	84.842
X4	-579.66	1375.8	-1108.4	243.04	49.053	-95.131
X3	248.89	-584.64	467.9	-102.31	-20.608	39.966
X2	-47.993	112.17	-89.552	19.506	3.9955	-7.7094
X (/10)	40.048	-97.985	80.697	-16.703	-5.1069	8.6793
C (/100)	-11.345	27.677	-22.883	5.0421	1.1134	-2.1191

Table 3 (FC4)

The corresponding expressions for each of the equation coefficients X5, X4, X3, X2, X and C can then determined from the respective relations below. Where, the corresponding expression coefficients Y_5 to D are given in the table above.

$$X_5 = Y_5 \cdot \left(\frac{h}{1E4}\right) + Y_4 \cdot \left(\frac{h}{1E4}\right) + Y_3 \cdot \left(\frac{h}{1E4}\right) + Y_2 \cdot \left(\frac{h}{1E4}\right) + Y \cdot \left(\frac{h}{1E4}\right) + D$$

$$X_4 = Y_5 \cdot \left(\frac{h}{1E4}\right) + Y_4 \cdot \left(\frac{h}{1E4}\right) + Y_3 \cdot \left(\frac{h}{1E4}\right) + Y_2 \cdot \left(\frac{h}{1E4}\right) + Y \cdot \left(\frac{h}{1E4}\right) + D$$

$$X_3 = Y_5 \cdot \left(\frac{h}{1E4}\right) + Y_4 \cdot \left(\frac{h}{1E4}\right) + Y_3 \cdot \left(\frac{h}{1E4}\right) + Y_2 \cdot \left(\frac{h}{1E4}\right) + Y \cdot \left(\frac{h}{1E4}\right) + D$$

$$X_2 = Y_5 \cdot \left(\frac{h}{1E4}\right) + Y_4 \cdot \left(\frac{h}{1E4}\right) + Y_3 \cdot \left(\frac{h}{1E4}\right) + Y_2 \cdot \left(\frac{h}{1E4}\right) + Y \cdot \left(\frac{h}{1E4}\right) + D$$

$$X = \left[Y_5 \cdot \left(\frac{h}{1E4} \right) + Y_4 \cdot \left(\frac{h}{1E4} \right) + Y_3 \cdot \left(\frac{h}{1E4} \right) + Y_2 \cdot \left(\frac{h}{1E4} \right) + Y \cdot \left(\frac{h}{1E4} \right) + D \right] / 10$$

$$C = \left[Y_5 \cdot \left(\frac{h}{1E4} \right) + Y_4 \cdot \left(\frac{h}{1E4} \right) + Y_3 \cdot \left(\frac{h}{1E4} \right) + Y_2 \cdot \left(\frac{h}{1E4} \right) + Y \cdot \left(\frac{h}{1E4} \right) + D \right] / 100$$

Eqs 3 to 8

The final expression for the fuel consumption with respect to fuel cell power output is then given below. Whose constants are a function of operating altitude, as given by the expressions above.

$$\dot{m}_{Fuel} = X_5 \cdot \left(\frac{P}{1E3} \right)^5 + X_4 \cdot \left(\frac{P}{1E3} \right)^4 + X_3 \cdot \left(\frac{P}{1E3} \right)^3 + X_2 \cdot \left(\frac{P}{1E3} \right)^2 + X \cdot \left(\frac{P}{1E3} \right) + C \qquad \text{Eq 9}$$

The final stage in our work is to test the expression at the original raw data points and thus determine the magnitude of any numerical analysis error. The error associated with this expression in respect to the source data, can be found from the expression below,

$$Error = \left(\frac{\dot{m}_{Equation} - \dot{m}_{Analysis}}{\dot{m}_{Analysis}} \right) \cdot 100\% \qquad \text{Eq 10}$$

For this study, this gave us an error range between 0.1 and 7% with an average value of 2.97%. The biggest source of error originates from the smooth curve approximation to the stepped raw data curves. In a practical fuel cell system however, the operating characteristics of the fuel cell system are likely to be tailored to match those of the smooth curve approximation and therefore the error range is not a significant problem.

This expression has been shown to give very good results for medium to high power flight phases but is less satisfactory for low powers which will be covered in the next section. The expression given in this section can thus only be used with confidence within for the following phases:

- Take-off (including ground roll, rotation, climb-out and second segment climb)
- Climb (stage 1 and 2)
- Loiter
- Descent (stage 1 and 2)

J1.1.4 Derivation of a low power relation

As mentioned above, at low powers the general expression given above deviates somewhat from the raw data and thus its accuracy is questionable. In such cases, an alternative expression must be used which is applicable to the following flight phases:

- Sea level loiter
- Landing (including approach and flare and ground roll)

Since the low power flight phases all take place at sea level, it is reasonable to restrict our analysis to a sea level altitude. Not only does this have the benefit of a considerably reduced workload but also results in a much simpler expression than before.

The derivation of such an expression utilises the methods of Appendix H to determine the low power characteristics of the fuel cell at sea level conditions. The fuel cell system is then tested at a number of low power settings to determine the fuel consumption of the fuel cell at these conditions. These results can then be used to generate a plot of fuel consumption versus power as in the chart below.

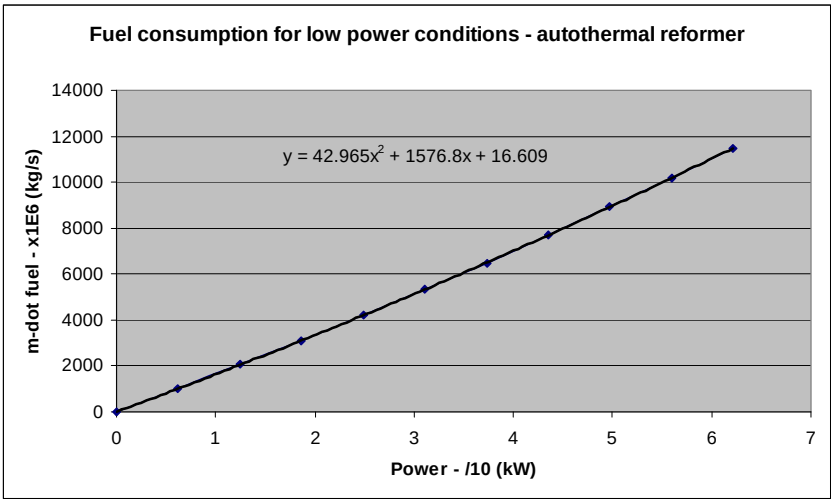

Chart 5

A quadratic curve and corresponding quadratic expression can then be fitted to this chart to generate the manageable final relation below.

$$\dot{m}_{Fuel} = \left[42.965 \cdot \left(\frac{P_{KW}}{10} \right)^2 + 1576.8 \cdot \left(\frac{P_{kW}}{10} \right) + 16.609 \right] / 1E6 \qquad \text{Eq 11}$$

J1.2 Steam reformer system performance analysis

A simplified schematic of the steam reformer based fuel cell system is presented in the figure below. The reader is advised to refer to the section, 'an overview of the fuel cell powered aircraft systems' for further details of the accompanying systems.

Schematic of the steam reformer system

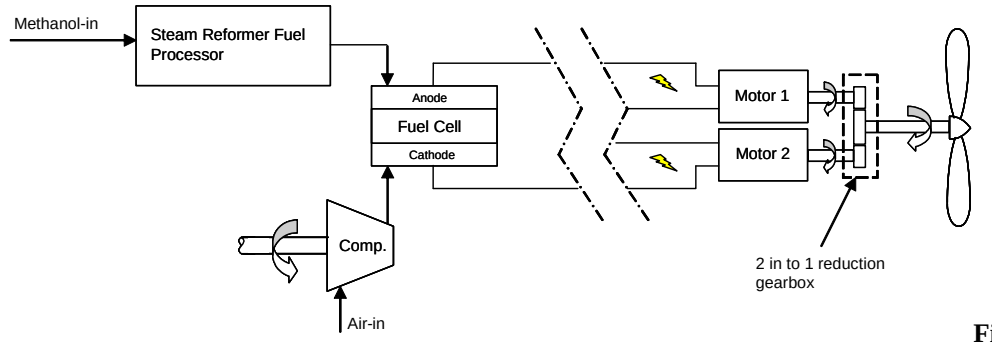

Figure 2

As with the autothermal system, this system is tested at a number of conditions to generate a table of raw data. This raw data can then be used to generate an analytical

model to predict the fuel consumption of the system, which is in a format which can be easily integrated into the performance analysis work. As before, we are then able to predict the performance of such a system in contrast to other propulsion devices.

J1.2.1 Analysis results

The raw data from our analysis for a number of different altitudes and fuel cell power outputs is given in the table below for reference.

Results for steam reformer system

Fuel (kg/s)		Altitude (m)								
		0	1143	2286	3429	4572	5334	6096	6858	7620
Power (kW)	64.47933	0.011967	0.010851	0.009993	0.009314	0.009019	0.009063	0.009112	0.009165	0.009239
	78.7569	0.015121	0.013716	0.012638	0.011784	0.011436	0.011499	0.011567	0.011662	0.011785
	101.3247	0.021567	0.019588	0.018071	0.016874	0.01649	0.016605	0.016761	0.01696	0.017175
	116.0628	0.021234	0.01925	0.017726	0.016519	0.015964	0.016039	0.016121	0.016211	0.016336
	138.17	0.025908	0.023494	0.02164	0.020173	0.019536	0.019635	0.019744	0.019897	0.020061
	153.3687	0.029285	0.026562	0.024472	0.022818	0.022142	0.022261	0.022392	0.022573	0.022768
	175.0153	0.03456	0.03136	0.028904	0.026962	0.026224	0.026378	0.026593	0.026826	0.027077
	190.6746	0.039035	0.035436	0.032676	0.030496	0.02973	0.02992	0.030182	0.030466	0.030828
	211.8607	0.039864	0.036151	0.0333	0.031044	0.030066	0.03022	0.03039	0.030627	0.030882
	227.9805	0.043455	0.039413	0.036311	0.033856	0.032853	0.033028	0.033221	0.033489	0.033777
	248.706	0.048334	0.04385	0.040408	0.037686	0.036644	0.03685	0.037078	0.037391	0.037729
	265.2864	0.052574	0.047708	0.043974	0.041022	0.0399	0.040137	0.040467	0.040824	0.041282
	285.5513	0.058409	0.053023	0.048893	0.04563	0.044483	0.044768	0.045159	0.045582	0.046123
	302.5923	0.064184	0.058292	0.053777	0.050211	0.049066	0.049406	0.049866	0.050455	0.051093
	322.3967	0.062221	0.056443	0.052009	0.048501	0.047073	0.047333	0.047701	0.048015	0.048526
	339.8982	0.066508	0.060342	0.055611	0.051869	0.05044	0.05073	0.051049	0.051486	0.052049
	359.242	0.071598	0.064976	0.059895	0.055878	0.054356	0.054683	0.055138	0.055629	0.056259
	377.2041	0.076791	0.069706	0.064273	0.059978	0.058467	0.058837	0.059346	0.059898	0.060603
	396.0873	0.082933	0.075308	0.069463	0.064846	0.063242	0.063779	0.06436	0.064991	0.065793
	414.51	0.089878	0.081651	0.075348	0.070373	0.068794	0.069415	0.070087	0.070944	0.071872

Table 4

J1.2.2 Derivation of a general relation from the analysis data

As for the autothermal reformer, the raw data from the last section needs to be converted into a more manageable format if it is to be used within our performance analysis. The process used to generate the complex analytical expression from the raw data is the same as that for the autothermal reformer, which enables us to arrive at the expression below.

$$\dot{m}_{Fuel} = X_5 \cdot \left(\frac{P}{1E3}\right)^5 + X_4 \cdot \left(\frac{P}{1E3}\right)^4 + X_3 \cdot \left(\frac{P}{1E3}\right)^3 + X_2 \cdot \left(\frac{P}{1E3}\right)^2 + X \cdot \left(\frac{P}{1E3}\right) + C$$

Eq 12

As before, an expression for each of the equation coefficients X5, X4, X3, X2, X and C can then determined in the form of the general relation below. The accompanying coefficients are given in the table below. As before, the constants X and C must be further divided by 10 and 100 respectively to arrive at the final answer.

$$X_N = Y_{5(N)} \cdot \left(\frac{h}{1E4}\right) + Y_{4(N)} \cdot \left(\frac{h}{1E4}\right) + Y_{3(N)} \cdot \left(\frac{h}{1E4}\right) + Y_{2(N)} \cdot \left(\frac{h}{1E4}\right) + Y_{(N)} \cdot \left(\frac{h}{1E4}\right) + D_{(N)}$$

Eq 13

Expression constants for steam reformer system

	Y5	Y4	Y3	Y2	Y	D
X5	360.66	-867.72	704.05	-155.95	-29.651	60.826
X4	-417.05	990.58	-797.03	175.98	33.211	-68.203
X3	179.5	-421.73	336.99	-74.209	-13.942	28.654
X2	-34.57	80.843	-64.455	14.141	2.7041	-5.5272
X (/10)	28.531	-70.043	57.745	-12.057	-3.4913	6.2293
C (/100)	-10.974	24.351	-18.439	3.8015	0.7872	-1.5194

Table 5

This expression is however, only applicable to the medium to high power flight phases, since its accuracy is questionable at the low power flight regimes. An alternative expression must therefore be used for the low power conditions.

J1.2.3 Derivation of a low power relation

As before, an alternative expression was required for low power sea level flight regimes. The derivation of such an expression utilises the methods of Appendix H to generate a table of results and then generate a plot of fuel consumption versus power as given in the chart below.

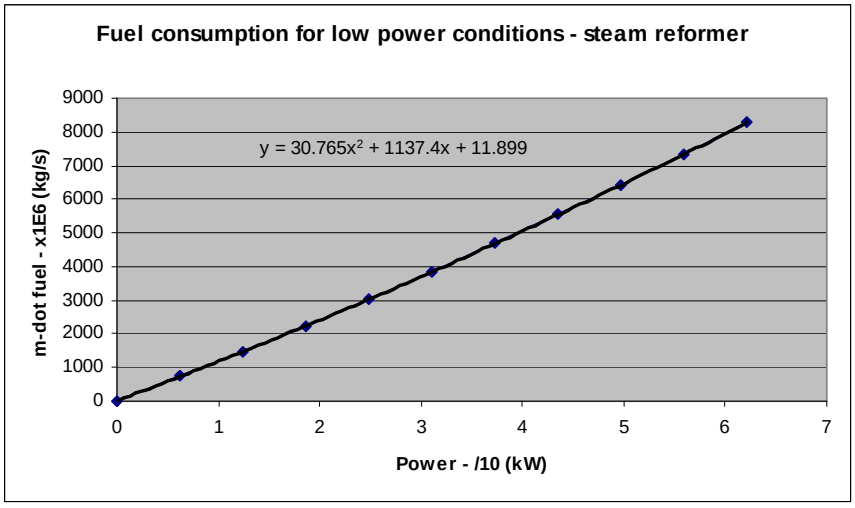

Chart 6

A quadratic curve and corresponding quadratic expression can then be fitted to this chart to generate the final relation below.

$$\dot{m}_{Fuel} = \left[30.765 \cdot \left(\frac{P_{KW}}{10} \right)^2 + 1137.4 \cdot \left(\frac{P_{kW}}{10} \right) + 11.899 \right] / 1E6 \qquad \text{Eq 14}$$

J1.3 Hybrid autothermal reformer system performance analysis

The original analysis of the fuel cell system power requirements highlighted the final climb phase as being the most critical. This flight phase will thus also be the largest consumer of methanol fuel. As discovered in the analyses carried out so far, the fuel consumption of the reformer based fuel cell systems is significantly higher than that of a turboprop engine. This means that the range of our baseline aircraft would be

significantly reduced as a result. To overcome this problem, in this section we investigate the potential of retaining the turboprop engine for the entire flight except the loiter phase. In such a hybrid system, the turboprop engine is disengaged for the loiter phase and the propeller is instead driven by the motor which is fed by the fuel cell system. For all other flight phases, the fuel cell system is disengaged and the propeller power is delivered entirely by the turboprop.

A simplified schematic of the hybrid autothermal reformer system is presented in the figure below. As before, the reader is advised to refer to the section on an overview of the fuel cell powered aircraft systems for further details of the accompanying systems. The only difference between this and the other fuel systems is that one of the motors that feeds the 2 into 1 reduction gearbox, has been replaced with a turboprop engine. Since the loiter phase has a significantly lower power demand than the other flight phases, the size of the fuel cell system can be reduced accordingly. This weight saving is intended to offset the additional weight of the turboprop engine.

Schematic of the hybrid autothermal reformer system

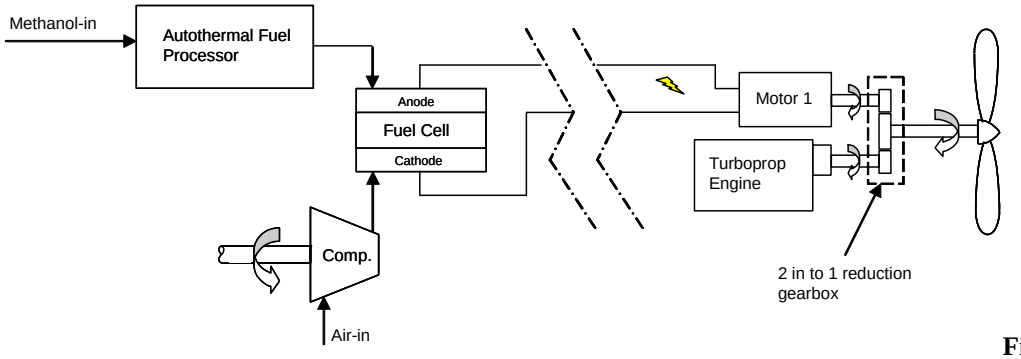

Figure 3

Fortunately, with this system we are able to reuse the analytical model generated for the autothermal system to predict the fuel consumption of the fuel cell part of the system. The relevant expressions are thus integrated into the flight phases of the performance analysis work in which the fuel cell system is operative. The remaining flight phases retain the engine performance expressions for the baseline turboprop configuration.

J1.4 Hybrid steam reformer system performance analysis

The steam reformer based hybrid system offers the same benefits as the autothermal based hybrid system in terms of a reduction in fuel consumption. As before, the turboprop engine is used to supply power to the propeller in all the flight phases except the loiter phase. In the loiter phase, the turboprop engine is disengaged and the propeller is driven by the motor which is fed by fuel cell system instead. The only difference between this and the autothermal reformer based hybrid system is the fuel processor.

A simplified schematic of the hybrid steam reformer system is presented in the figure below. As before, the reader is advised to refer to the section on an overview of the fuel cell powered aircraft systems for further details of the accompanying systems. As with the hybrid autothermal system, the 2 into 1 reduction gearbox is driven by both a motor

and a turboprop engine. As before, the size of the fuel cell system can also be reduced, since in this configuration it only needs to meet the requirements of the loiter phase.

Schematic of the hybrid steam reformer system

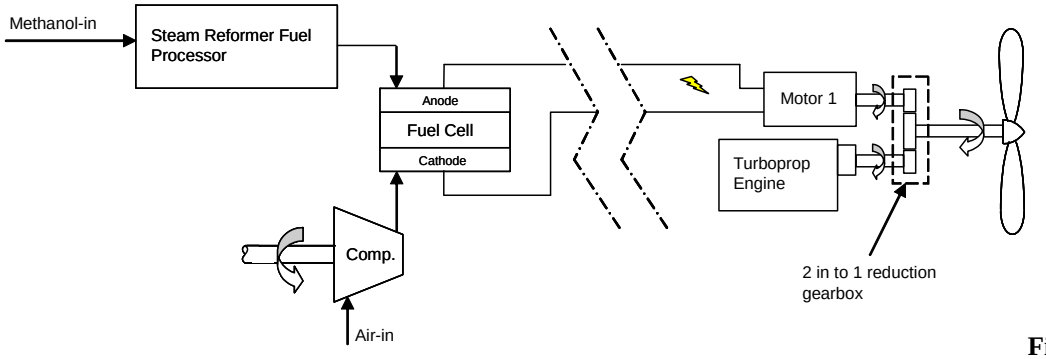

Figure 4

Fortunately, with this system, we are able to reuse the analytical model generated for the fuel consumption of the steam reformer system. The relevant expressions are thus integrated into the flight phases of the performance analysis work in which the fuel cell system is operative. The remaining flight phases retain the engine performance expressions for the baseline turboprop configuration.

J1.5 Investigation into the use of oxygen injection

In the systems above, hydrogen is being fed to the fuel cell in excess of that actually required. This is so that the excess leaving the fuel cell can be burned to generate the hot gases needed to drive a turbine, which is linked to the system air compressor. We therefore have to burn an additional quantity of fuel in order to be able to deliver oxygen in sufficient quantity and at the required pressure for the fuel cell. If we consider the fact that air is only made up of approximately only 21% oxygen, then we are wasting a significant amount of energy (via the additional amount of fuel) to deliver the fractions of air that are not actually required. In particular, the compressor has to work hard to deliver nitrogen (which makes up 79% of the air), which is not actually required. The nitrogen in the air serves no useful purpose within the fuel cell and merely acts as a dilutant which is eventually discarded. We are therefore expending work and fuel to deliver it to the fuel cell in order to throw it away.

If we could find a way to either sieve the oxygen from the air before it enters the compressor or use oxygen from a purer source, then the fuel consumption of our system could be reduced. Sieving the air is however not practical since the air must be delivered to the sieve in a considerable quantity to start with. The only other option is therefore to carry either a compressed or liquefied source of oxygen on-board the aircraft. Such a oxygen supply would be able to at least in part, meet the oxygen needs of the fuel cell. Since space is at a premium inside our aircraft and liquefied oxygen takes up a significantly smaller volume than compressed oxygen, only a liquefied oxygen source will be considered here.

Since a large quantity of oxygen is required for a fuel cell system of this size, it was unlikely that we would be able to carry sufficient oxygen on-board the aircraft to meet our needs. There is still however benefits to be gained by using such an oxygen source to supplement the oxygen already available within the air. In such a system, the air would be mixed with pure oxygen to increase the oxygen content of the air. The feasibility of such a system is considered in the work which follows.

J1.5.1 System description

A simplified schematic of a system which is able to incorporate additional oxygen is presented in the figure below. This system is the same as for a standard fuel cell system, with the exception of the addition of a mixing chamber between the fuel cell and the air compressor. Within this chamber, the air from the compressor is mixed with pure oxygen supplied from an alternative source. The reader is advised to refer to the section 'an overview of the fuel cell powered aircraft systems' for further details of the accompanying systems.

Schematic of a fuel cell system with oxygen injection

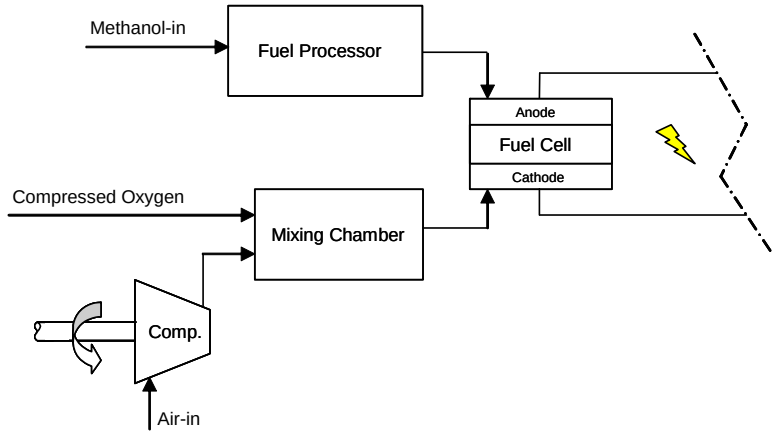

Figure 5

J1.5.2 Analysis of the mixing chamber

As already stated, the mixing chamber is used to mix air from the compressor with pure oxygen from an alternative source. The output stream from the mixing chamber is thus an air stream with an higher oxygen content. In this section, we will determine the revised oxygen fraction of the air mixture for varying quantities of oxygen injection. It is a reasonable approximation that air typically consists of 21% oxygen and 79% nitrogen. This therefore gives us, 21 parts of O_2 per 100 parts of air. If we now add an additional percentage of 'X' O_2 to the air, this will give us additional 'X' parts of O_2 out of 100. The total parts of O_2 in the mixture will then become,

$$O_{2(Total)} = O_{2(Air)} + O_{2(Additional)} = 21 + X \qquad \text{Eq 15}$$

This gives us a mixture made up of a total number of parts,

$$Mix_{(Total)} = Air + O_{2(Additional)} = 100 + X \qquad \text{Eq 16}$$

The total fraction of O_2 in the mixture then becomes,

$$Fraction(O_2) = \frac{O_{2(Total)}}{Mix_{(Total)}} \quad \text{Eq 17}$$

The percentages of air and additional O_2 in the mixture are then given by respective relations below.

$$Percentage(Air) = \frac{Air}{Mix_{(Total)}} \quad \text{Eq 18}$$

$$Percentage(O_{2-Additional}) = \frac{O_{2(Additional)}}{Mix_{(Total)}} \quad \text{Eq 19}$$

Following this procedure, we are able to obtain the table of results given below.

$O_{2(Additional)}$ (%)	Parts $O_{2(from\ air)}$	Parts of air	Parts $O_{2(Additional)}$	Parts of $O_{2(Total)}$	Parts Total	Fraction $O_{2(in\ mixture)}$	% Air	% $O_{2(Additional)}$
0	21	100	0	21	100	0.21	100	0
5	21	100	5	26	105	0.247619048	95.2381	4.761904762
10	21	100	10	31	110	0.281818182	90.90909	9.090909091
15	21	100	15	36	115	0.313043478	86.95652	13.04347826
20	21	100	20	41	120	0.341666667	83.33333	16.66666667
25	21	100	25	46	125	0.368	80	20
30	21	100	30	51	130	0.392307692	76.92308	23.07692308
35	21	100	35	56	135	0.414814815	74.07407	25.92592593
40	21	100	40	61	140	0.435714286	71.42857	28.57142857
45	21	100	45	66	145	0.455172414	68.96552	31.03448276
50	21	100	50	71	150	0.473333333	66.66667	33.33333333
55	21	100	55	76	155	0.490322581	64.51613	35.48387097
60	21	100	60	81	160	0.50625	62.5	37.5
65	21	100	65	86	165	0.521212121	60.60606	39.39393939
70	21	100	70	91	170	0.535294118	58.82353	41.17647059
75	21	100	75	96	175	0.548571429	57.14286	42.85714286
80	21	100	80	101	180	0.561111111	55.55556	44.44444444

Table 6

In a similar way, the molecular mass of the gas mixture at different oxygen concentrations was evaluated and a linear expression fitted to the data as given below. Where, M has the units of kg/kmol and X is oxygen volume fraction.

$$M_{Mixture} = 3.8328 \cdot X + 28.167 \quad \text{Eq 20}$$

J1.5.3 System performance prediction at loiter

Since the aircraft spends the majority of its time at loiter, it makes sense to initially asses the viability of an oxygen injection system at this flight phase. This also fits in well with the proposals for a hybrid fuel cell system, in which the fuel cell is restricted to use at loiter. Since the steam reformer system has already been shown to give the best fuel consumption results, the steam reformer system will form the basis of this study. This analysis thus follows the same analysis procedure as presented for the steam reformer based fuel cell system. The only difference between this analysis and that for the standard steam reformer system is the O_2 fraction of air entering the system. This was determined in the section above, as the oxygen concentration of the air leaving the mixing chamber for a number of different additional O_2 injection settings.

This analysis utilises the methods of appendix H to give us the results for the required mass flow rate of methanol and additional injection oxygen at the mid loiter phase. The quantity of additional oxygen required in each case be then determined from the expression,

$$\dot{m}_{O2(Additional)} = \dot{m}_{Air(Total)} \cdot \left(\frac{\%O_{2(Additional)}}{100} \right) \qquad \text{Eq 21}$$

If we base our initial estimates on the original loiter phase duration of 35 hours, then the total mass of methanol and liquid oxygen for that flight duration can then be determined from the expression below.

$$m_{\mathrm{Re}\,ac\,\tan t(Total)} = \dot{m}_{\mathrm{Re}\,actat} \cdot t_{LoiterPhase} \qquad \text{Eq 22}$$

This analysis gives us the results given in the table below.

Results for mid loiter — Duration of loiter flight phase (s) 126000

$\%O_{2(Additional)}$	Fraction $O_{2(in\ mixture)}$	% Air	$\%O_{2(Additional)}$	m-dot$_{(methanol)}$ (kg/s)	m-dot$_{(LOX)}$ (kg/s)	Mehanol$_{(loiter)}$ (kg)	LOx$_{(loiter)}$ (kg)
0	0.21	100	0	0.01058676	0	1333.93182	0
10	0.281818182	90.90909	9.09090909	0.010066604	0.010226248	1268.392086	1288.507259
20	0.341666667	83.33333	16.6666667	0.009643394	0.018641275	1215.067662	2348.800684
30	0.392307692	76.92308	23.0769231	0.009290876	0.025689793	1170.650402	3236.913976
40	0.435714286	71.42857	28.5714286	0.008992716	0.031677725	1133.08226	3991.393394
50	0.473333333	66.66667	33.3333333	0.008737453	0.036825896	1100.919112	4640.062849
60	0.50625	62.5	37.5	0.008516657	0.041298084	1073.098792	5203.558551
70	0.535294118	58.82353	41.1764706	0.00832396	0.045218359	1048.818956	5697.513206
80	0.561111111	55.55556	44.4444444	0.008154455	0.048682357	1027.461377	6133.976958

Table 7

If we present these results graphically as in the chart below, we can see that a system using oxygen injection is clearly not viable. It is evident that the mass of the liquid oxygen which must be carried on-board the aircraft far exceeds the fuel mass saved with the use of such a system.

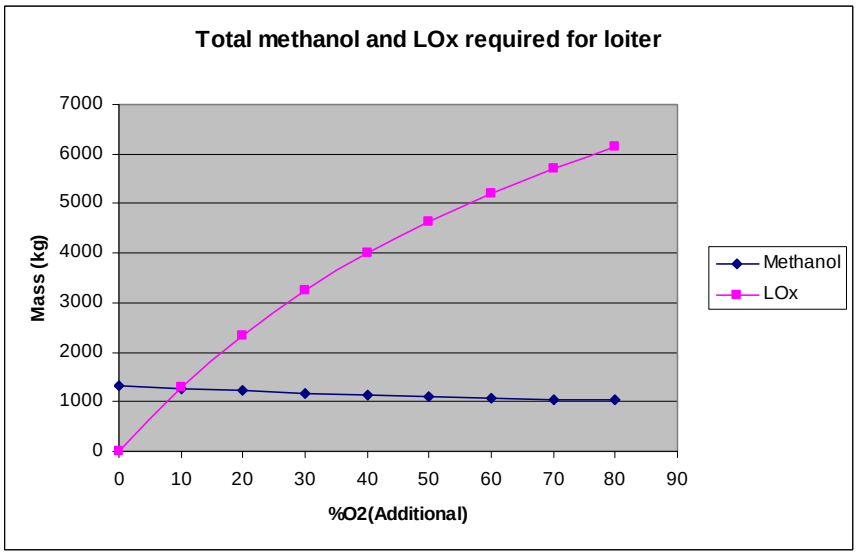

Chart 7